177(2), 2019

COMBUSTION ENGINES

PTNSS Supporting Members
Członkowie wspierający PTNSS

BOSMAL Automotive Research and Development Institute Ltd
Instytut Badań i Rozwoju Motoryzacji BOSMAL Sp. z o.o.

Motor Transport Institute
Instytut Transportu Samochodowego

The Institute for Sustainable Technologies
Instytut Technologii Eksploatacji

Institute of Aviation
Instytut Lotnictwa

Automotive Industry Institute
Przemysłowy Instytut Motoryzacji

The Rail Vehicles Institute TABOR
Instytut Pojazdów Szynowych TABOR

Institute of Mechanised Construction and Rock Mining
Instytut Mechanizacji Budownictwa i Górnictwa Skalnego

Industrial Institute of Agricultural Engineering
Przemysłowy Instytut Maszyn Rolniczych

AVL List GmbH

Solaris Bus & Coach S.A.

Air Force Institute of Technology
Instytut Techniczny Wojsk Lotniczych

COMBUSTION ENGINES
A Scientific Magazine
2019, 177(2)
Year LVIII
PL ISSN 2300-9896

Editor:
Polskie Towarzystwo Naukowe Silników Spalinowych
43-300 Bielsko-Biała, Sarni Stok 93 Street, Poland
tel.: +48 33 8130402, fax: +48 33 8125038
E-mail: sekretariat@ptnss.pl
WebSite: http://www.ptnss.pl
Papers available on-line: http://combustion-engines.eu

Editorial:
Institute of Combustion Engines and Transport
Poznan University of Technology
60-965 Poznan, Piotrowo 3 Street
tel.: +48 61 2244505, +48 61 2244502
E-mail: papers@ptnss.pl

Prof. Jerzy Merkisz, DSc., DEng. (Editor-in-chief)
Miłosław Kozak, DSc., DEng. (Editorial Secretary for Science)
– papers@ptnss.pl
Prof. Ireneusz Pielecha, DSc., DEng.,
Wojciech Cieślik, DEng. (Technical Editors)
Joseph Woodburn, MSci (Proofreading Editor)
Wojciech Serdecki, DSc., DEng. (Statistical Editor)
and Associate Editors

Contents

Editor
Polish Scientific Society
of Combustion Engines
43-300 Bielsko-Biała, Sarni Stok 93 Street, Poland
tel.: +48 33 8130402, fax: +48 33 8125038
E-mail: sekretariat@ptnss.pl
WebSite: http://www.ptnss.pl

Subscriptions
Send subscription requests to the Publisher's address.
Cost of a single issue PLZ30 + VAT.

Preparation for print
ARS NOVA Publishing House
60-782 Poznań, ul. Grunwaldzka 17/10A

Circulation: 650 copies

Printing and binding

Zakład Poligraficzny Moś i Łuczak, sp. j.,
Poznań, ul. Piwna 1

The journal is registered in the Polish technical journals content database – **BAZTECH** www.baztech.icm.edu.pl

The journal is listed in the international database **IC Journal Master List – Index Copernicus** www.indexcopernicus.com

Declaration of the original version
The original version of the Combustion Engines journal is the printed version.

Papers published in the *Combustion Engines* quarterly receive 13 points as stated by the Notification of the Minister of Science and Higher Education dated 26 January 2017.

Cover
I – Cadillac 4.2L Twin-Turbo V8 (*fot. www.autoevolution.com*);
background (Architectural design architecture blue *© Photo by Pixabay from Pexels*)
IV – Precombustion chamber
with combustion feedback control (*fot. prometheus-at.com*)

Article citation info:
TKACZYK, M., SKRĘTOWICZ, M., KRAKOWIAN, K. Analysis of influence of using catalyst and polar additives on engine performance and exhaust emission. *Combustion Engines*. 2019, **177**(2), 3-6. DOI: 10.19206/CE-2019-201

Marcin TKACZYK
Maria SKRĘTOWICZ
Konrad KRAKOWIAN

CE-2019-201

Analysis of influence of using catalyst and polar additives on engine performance and exhaust emission

In the paper researches of influence of using catalyst and polar additives on engine performance and emission of exhaust were carried out. The tests were made on diesel engine DuraTorq-TDDi/TDCi 16v with a capacity of 1998cm3 produced by Ford company. Two additives were investigated: FMAX – catalytic additive to fuel and HDOS – polar additive to lubricating oil in different proportions. The results indicated that using tested additives has a positive effect on exhaust composition (lower concentrations of nitrogen oxides, soot and carbon monoxide) and also decreased fuel consumption.

Key words: *catalytic additives, polar additives, diesel engine, exhaust*

1. Introduction

Diesel fuel is the basic energy carrier which is used for driving self-ignition engines. As the fuel, it has to meet requirements specified in legal acts and norms. The most important features of the fuel is possibility of pumping, filtering, low corrosivity, chemical stability and ability of self-ignition characterized by cetane number [1, 2]. On the quality of fuels for diesel engines also level of lubrication also has significant influence. Lubricating properties could be increased by addition high hydrocarbons and sulphur compounds. However, that additives could destroy construction materials used for fuel and lubrication systems. Sulphur has detrimental effect on heat and thermooxidative stability and tends to corrode the metal. In addition, products of burning the sulphur, sulphur dioxide and sulphur trioxide, form acids in water environment, what is the reason of corrosion of exhaust system and atmospheric air pollution. Due to necessity of reduction of sulfur content in petroleum products to value below 50 mg/kg, their lubrication properties have deteriorated significantly [2, 3]. Therefore it is necessary to use a non-toxic and environmental friendly lubricating additives to the fuel. Actually, that standards could be met by used additives containing derivatives of fatty acid methyl esters (FAME) made of vegetable oils. On the European and world markets esters are used as additives to diesel fuel or in its pure form, as biodiesel. Biodiesel has a lot of benefits compared to conventional diesel fuel. The main of them are that biodiesel is biodegradable, doesn’t include harmful substances and aromatic hydrocarbons. Additionally, biodiesel has higher cetane number, what improves external engines parameters and at the same time, at higher temperature of ignition ensures safety of storage. Esters has more than 20% of oxide bonded in fatty acids, what caused that combustion process is more effectively and emission of soot and particular matter to the atmosphere decreases [4–7].

2. Fuel additive characteristic

One of the factors affecting the engine performance and exhaust toxicity is efficiency of energy source, i.e. the fuel. In the case of vehicles already in use, the general efficiency of the drive source is the most important parameter of the assessment allowing calculations of the economic suitability of the vehicle. In turn, economics is the most important criterion when assessing vehicles used for commercial purposes.

On the automotive market there are available many products (additives to fuel) which improve the economy of the drive and exhaust emissions. One of them, the additive Fuel Maximizer (FMAX) developed by ProOne Extreme Lubricants company was tested. The producer of the additive provides information that the product decreases fuel consumption and exhaust emission, improves lubricating properties of diesel fuel, increases the engine efficiency and cleans fuel system and injectors [8]. Fuel Maximizer is a catalyser, which reduces a activation energy and improve the reaction of combustion of fuel. Additionally, according to the manufacturer, the combustion process is more effective with FMAX through fragmentation the large particles of fuel and acceleration of initiation of combustion reaction.

The Fuel Maximizer was tested in 2018 by Polish Automotive Industry Institute and got the certificate of that Institution [9]. The Laboratory confirmed that the diesel fuel with FMAX meets all fuel requirements according to standards PN/ISO and using that product is safe for the engine.

The second object of the tests was additive to lubricating oil Heavy Duty Oil Stabilizer (HDOS). That product among others extends the life of the oil, protects against extreme pressures, prevents oil burning and leaks, improves performance and reduces fuel consumption, etc. the producer recommends supplying to lubricating oil about 10–20% volume of HDOS.

3. Material and methods

The main aim of the tests was to evaluate the effect of changes caused by addition products of ProOne Extreme Lubricants on engine parameters. The researches were conducted on the turbocharged diesel engine DuraTorq-TDDi/TDCi 16v with a capacity of 1998 cm^3 produced by Ford company. The engine was supplied by Common Rail fuel supplied system and got exhaust gas recirculation. With these solutions, the engine has met the EURO 3 standard [10]. The power unit has been used for 14 years and had mileage about 306 000 km. In Fig. 1 full load characteristic of maximum load and power values for engine is presented. Considering the direct dependence of power and torque, authors of this publication, wishing to avoid duplication of information, will only discuss the course of torque curves. Before starting the tests, to stabilize the engine's operating conditions, the lubricating oil was changed for a new one, approved by the manufacturer Mobil 1 0W40 with the CF quality class. This type of oil has been used for the last 6 years in tested engine.

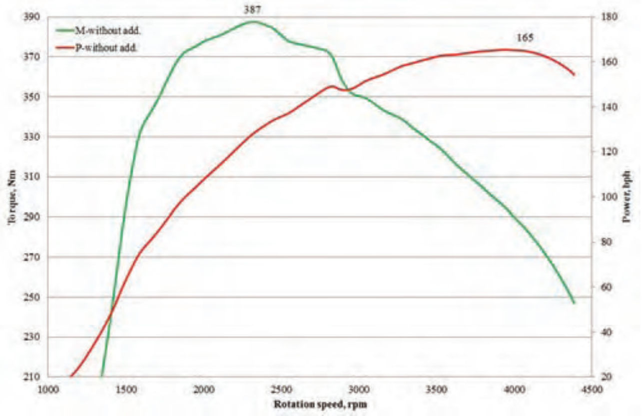

Fig. 1. Full load characteristic of tested engine supplied by diesel fuel without additives

Research was focused on the effect of used additives to fuel (FMAX) and to lubricating oil (HDOS) on parameters of engine's work such as correct operation of some systems (fuel supplied system, air intake system, engine control system, etc.) and exhaust concentrations. In the test full load characteristics were made for engine supplied by fuel without and with additive and without or with additive to lubricating oil. Characteristics were made on the chassis dynamometer MAHA LSP 3000. That tests allowed for evaluation maximum engine performance. Additionally, in chosen points of engine's work (with constant load of engine) measurements of exhaust concentration were conducted. The following components of fumes were analysed:

- nitrogen oxides (NO_x), carbon monoxide (CO), carbon dioxide (CO_2), oxygen (O_2) measured with used Horiba PG 350 analyser (NO_x by chemiluminescence detection method CLD; CO and CO_2 by non-dispersive infrared method NDIR; O_2 by galvanic cell method), accuracy of the measurement was ±0,5% in range $NO_x \geq 100$ ppm and ±1% for other substances in full range;
- soot with used AVL 415 smoke meter, which is able to measure soot concentration in units FSN (filter smoke number) or in mg/m^3 with measurement range to 0,02 mg/m^3.

Additionally, during the tests conditions were controlled using weather station HD32.1 produced by Delta OHM company. Accuracy of temperature measurement of the device is ±0.1°C.

The engine work conditions for exhaust composition measurement were selected to cover the engine operation areas with closed and open EGR valve. In table 1 characteristic of chosen points of engine work conditions are presented.

Table 1. Characteristic of points of engine operation conditions

No.	Rotation speed, rpm	Power, bhp	Comments
1	2100	10	– low engine load value (low air flow and dose of fuel), – opened EGR valve (large proportion of exhaust in fresh inlet air)
2	2100	50	– medium engine load, – semi-open EGR valve (low proportion of exhaust)
3	3000	65	– rotation speed close to nominal, – medium engine load, – closed EGR valve
4	760	idle	– important point to evaluation of engine work in city traffic

Three variants of supplying the engine were tested: diesel fuel without any additives, with FMAX as additive to fuel in proportion 1:4000 (manufacturer's recommendations) and 1:1000 (four times greater than manufacturer's recommendations) and with HDOS as additive to lubricating oil, and the last, with FMAX as additive to fuel in proportion 1:4000 and with HDOS.

4. Results and discussion

In Figure 2 results of full load characteristic for three variants of tests (pure diesel fuel with FMAX in proportion 1:4000 and fuel with FMAX and lubricating oil with HDOS) are presented.

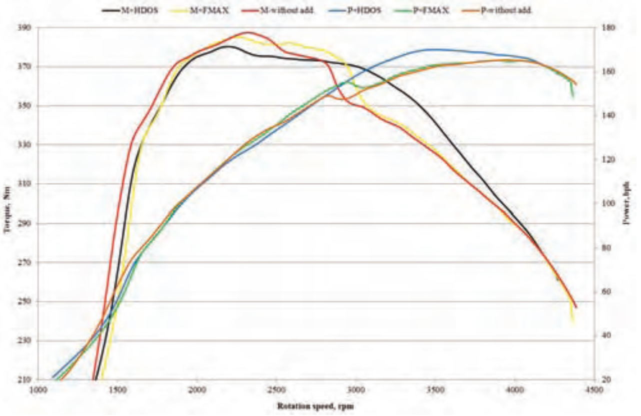

Fig. 2. Results of full load characteristic conducted on the chassis dynamometer

As it can be noticed, the highest torque value is obtained for pure diesel fuel, but in case with FMAX as additive to fuel in proportion 1:4000, the range of high torque values is the widest, between 1700 and 3000 rpm. The best course of power curve was registered in test with FMAX as additive to fuel and HDOS as additive to lubricant oil. Power for variants with pure diesel fuel and for FMAX was similar.

In the test also concentrations of ingredients of exhaust for all variants were measured. In Figs 3–5 measured concentrations of toxic components of exhaust such as NO_x, soot and CO are shown and in figures 6 and 7 respectively concentrations of CO_2 and O_2.

From the figures appears that the lowest concentrations of all of analysed toxic components in each measuring point were obtained for variant with diesel fuel and FMAX in proportion 1:1000. In point 1 (at 2100 rpm and 10 Nm) concentrations of NO_x for all variants are similar. It may be due to similar content of oxygen (Fig. 7) and temperature of combustion process in low load. Generally, it was noticed that concentration of NO_x was the highest in the first variant – with pure diesel fuel and using any additive allows reduce NO_x emission. Emission of soot is the highest for pure diesel almost in all of measuring points. Only in point 2 (at 2100 rpm and 50 Nm) is the lowest for that variant. In terms of emission CO, the worst results were obtained for mixture of fuel and FMAX in proportion 1:4000 in points 1, 3 and 4 and for pure diesel oil in point 2. On the other side, the lowest CO concentrations measured for variant with FMAX added to diesel fuel in proportion 1:1000.

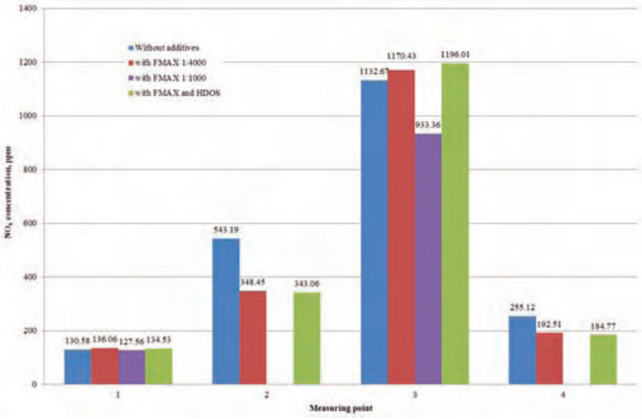

Fig. 3. Concentrations of NO_x measured in tests

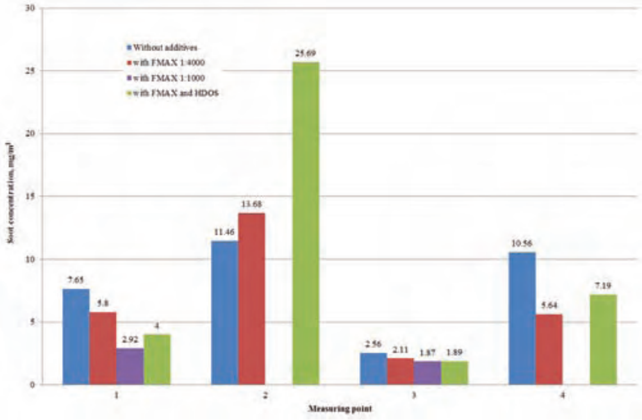

Fig. 4. Concentrations of soot measured in tests

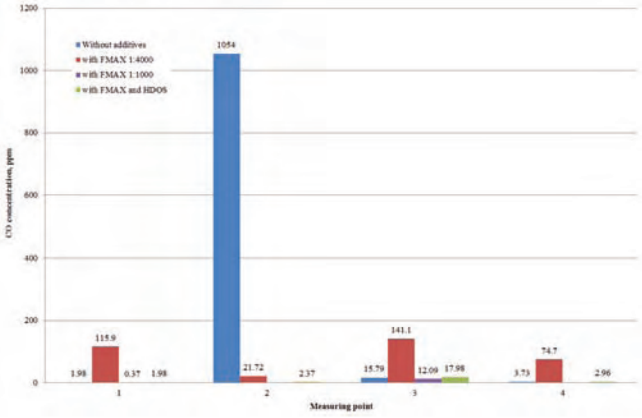

Fig. 5. Concentrations of CO measured in tests

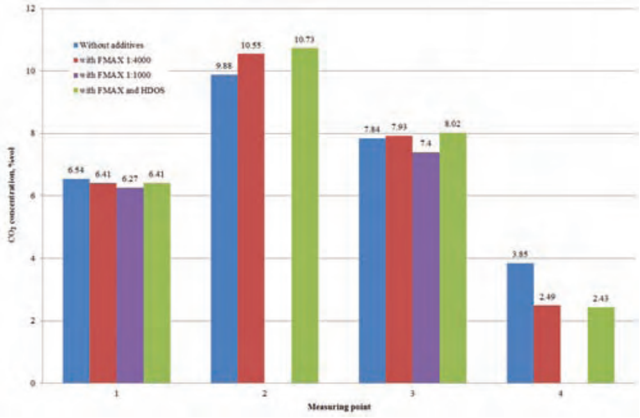

Fig. 6. Concentrations of CO_2 measured in tests

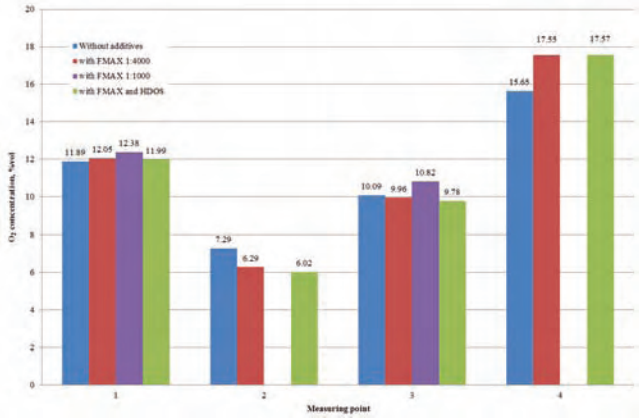

Fig. 7. Concentrations of O_2 measured in tests

In all points of engine's work (except point 2) concentration of CO_2 were lower for at least one variant with additive that for variant with pure diesel fuel. In addition, content of O_2 was highest in variants with additives. It could testify to reducing of fuel consumption in case of using FMAX and HDOS as additives to fuel and lubricant oil. The best result was received for variant with FMAX with fuel in proportion 1:1000.

5. Summary and conclusion

In the paper additives to diesel fuel (FMAX) and to lubricant oil (HDOS) produced by company ProOne Extreme Lubricants were tested, in terms of engine performance and content of exhaust gases. In researches turbocharged diesel engine DuraTorq-TDDi/TDCi 16v with a capacity of 1998 cm^3 produced by Ford company was used. Tests was carried out in 4 variants:

1) combustion of pure diesel fuel
2) combustion of diesel fuel with added FMAX in proportion 1:4000
3) combustion of diesel fuel with added FMAX in proportion 1:1000 and with HDOS as additive to lubricant oil
4) combustion of diesel fuel with added FMAX in proportion 1:4000 and with HDOS as additive to lubricant oil

Measurements of concentration of toxic compounds of exhaust such as NO_x, soot and CO were made. Also the full load characteristic for 3 of variants were prepared. Additionally CO_2 and O_2 content in fumes was analysed.

Based on the results it was noticed that generally additions to diesel and lubricant oil had positive influence on combustion process in relation to emission of exhaust and fuel consumption, but not so good in terms of achieved the maximum torque – the maximum value was obtained for pure diesel fuel. However, the torque above 370 Nm engine achieved in wider range for tests with additives. Also the maximum value of power is the higher for diesel oil with additives, especially FMAX with HDOS. Producer recommends using FMAX in proportion with fuel 1:4000. As in was presented in previous chapter with results, benefits of using mixture in that composition was well in a lot of points of engine operations, but even better results was obtained in proportion FMAX with fuel 1:1000. Concentration of NO_x for that variant was reduced by an average of 10%, concentration of soot of 45% and CO more than 50%.

Acknowledgements

The authors of the article would like to special thank the company Lubrication Plus Business Consulting AB Bogdanowicz Artur for sharing research materials documented in this publication.

Bibliography

[1] KARDASZ, K., KĘDZIERSKA, E., KONOPKA, M. et al. Fatty acid methyl esters as diesel oil lubricating additive, *Exploitation Problems*. 2003, **1**, 191-201.

[2] MITCHELL, K. Lubricity of winter diesel fuels. *SAE Technical Paper* 952370, 1995. DOI:10.4271/952370.

[3] Essential methods of the quality assessment of industrial lubricants and their exploitation meaning, Total. Part IV, *ELF Company Information*. 2002, 8-26.

[4] SULEK, M.W., KULCZYCKI, A., MALYSA, A. Quality assessment of fuels based on biocomponents. *Polish Journal of Commodity Science*. 2006, **2**(7), 30-40.

[5] SULEK, M.W., KULCZYCKI, A., MALYSA, A. Lubricating properties of fatty acid methyl esters and fuel oil compositions. *Tribology*. 2006, **2**.

[6] GELLER, D.P., GOODRUM, J.W. Effects of specific fatty acid methyl esters on diesel fuel lubricity. *Fuel*. 2004, **83**, 2351-2356.

[7] WAIN, K.S., PEREZ, J.M., CHAPMAN, E. et al. Alternative and low sulfur fuel options: boundary lubrication performance and potential problems. *Tribology International*. 2005, **38**, 313-319. DOI:10.1016/j.triboint.2004.08.014.

[8] ProOne Extreme Lubricants information materials;

[9] Research report of Polish Automotive Industry Institute "Tests of physical and chemical parameters for the supplied sample according the order" no. PLN.022.18B/Z1, 19.03.2018.

[10] www.motodiesel.pl/silniki/3015-silnik-20-duratorq-tdci.html. Access: 26.10.2018.

Marcin Tkaczyk, DEng. – Faculty of Mechanical Engineering at Wroclaw University of Science and Technology.
e-mail: *Marcin.Tkaczyk@pwr.edu.pl*

Konrad Krakowian, DEng. – Faculty of Mechanical Engineering at Wroclaw University of Science and Technology.
e-mail: *Konrad.Krakowian@pwr.edu.pl*

Maria Skrętowicz, DEng. – Faculty of Mechanical Engineering at Wroclaw University of Science and Technology.
e-mail: *Maria.Skretowicz@pwr.edu.pl*

Article citation info:
CHŁOPEK, Z., LASOCKI, J., STRZAŁKOWSKA, K., ZAKRZEWSKA, D. Impact of pollutant emission from motor vehicles on air quality in a city agglomeration. *Combustion Engines*. 2019, **177**(2), 7-11. DOI: 10.19206/CE-2019-202

Zdzisław CHŁOPEK
Jakub LASOCKI
Katarzyna STRZAŁKOWSKA
Dagna ZAKRZEWSKA

CE-2019-202

Impact of pollutant emission from motor vehicles on air quality in a city agglomeration

In the large urban areas, in middle latitudes, as in case of Poland, the cause of poor air quality is immission: in winter particulate matter PM10 and PM2.5, in summer – ozone and nitrogen oxides (or nitrogen dioxide). In the whole country, road transport is significantly responsible for the emission of nitrogen oxides (30%), carbon monoxide (20%) and less for emission of particulate matter (a few percent). In the case of other pollutants, the emission of non-metallic organic compounds is less than 10% (including polycyclic organic compounds – just over 0.5%), and sulfur oxides – only 0.03%!

To analyze impact of automotive industry on air quality, pollutant emission data from two stations in Krakow were selected. These stations are known for poor air quality – the stations are: Dietla Street – with a high level of traffic and Kurdwanów – place located far from traffic routes. It was found that other objects than automotive vehicles are the dominant source of dust. These are industrial sources and – above all – energy sources, especially individual heating installations. Particularly large dust pollution occurs in winter and it is not always in areas with intense traffic. There was a strong dependence between immission of pollutants and road traffic, however, this dependence is not dominant in assessing the risk of air quality in urban agglomerations.

Key words: *emission of pollutants, immission of pollutants, motor vehicles*

1. Introduction

There is social acceptance, especially in liberal consumer societies, for determining the dominant influence of automotive on air pollution, especially in urban agglomerations. Such views are common even in scientific environments, and in the opinion-forming circles they even adopt hysterical instead of factual character. Undoubtedly, the impact of automotive pollution is important for the air quality, especially on a local scale and at a time when traffic is very intense [1–8]. It is known that usually other sources are dominant, and not only related to anthropogenic sources of pollutant emission, but also to natural phenomena [7, 9]. These natural phenomena include commonly known risks associated with winds from great deserts. Anthropogenic sources of pollutant emission, especially dangerous for air quality, are primarily energy, and especially distributed energy associated with local heating of buildings. This condition is confirmed by numerous research results of air quality [3–5].

The air quality is controlled in many measuring stations – which is in line with international agreements. In Poland, to assess the air quality, the Polish Air Quality Index has been introduced by the Chief Inspectorate of Environmental Protection.

Table 1 presents limit values of immission[1] of pollutants for the Polish Air Quality Index for individual substances.

Immission of pollutants is determined at air quality monitoring stations by automatic measurement method and averaged over 1 h.

Polish Air Quality Index (pl. Polski Indeks Jakości Powietrza, PIJP) is a detailed index determined for pollution, which is dominating during the averaging of measurements in the area of the province.

$$\mathrm{PIJP} = \mathrm{Max}\left[\mathrm{PIJP_s}\right]$$

where: Max – operator of the maximum value.

Tab. 1. Limit values of pollution immission for the Polish Air Quality Index for specific substances – PIPSs

		PM10	PM2.5	O_3	NO_2	SO_2	C_6H_6	CO
		[μg/m^3]						[mg/m^3]
Very good	1	20	12	70	40	50	5	2
Good	2	60	36	120	100	100	10	6
Moderate	3	100	60	150	150	200	15	10
Sufficient	4	140	84	180	200	350	20	14
Bad	5	200	120	240	400	500	50	20
Very bad	6	>200	>120	>240	>400	>500	>50	>20
No index		–	–	–	–	–	–	–

Practice indicates that the dominant pollutants due to air quality are: in the winter, the immission of particle size fractions PM10 and PM2.5 and in the summer the nitrogen dioxide and ozone emission.

For the summer, poor air quality can be bound to automotive pollution, although this is not the only pollution source. In the winter, however, the heating sector has the dominating influence on air quality.

In general, the impact of road transport on the air quality is not as dominant as it is believed, even among some scientists. Table 2 presents the contribution of national annual emission of pollutants from the road transport sector in the total national annual emission of pollutants from all civilization sources in Poland in 2017 [10].

---

[1] Immission is the concentration of pollutants dispersed in the atmosphere, measured at 1.5 m above the ground.

Tab. 2. Share of the annual emission of pollutants from the road transport sector in the total national annual emission of pollutants from all civilization sources in Poland in 2017

Pollutant	Share [%]
CO	20.7
NMVOC	8.9
PAH	0.6
NOx	29.9
TSP	4.5
PM10	5.3
PM2.5	7.8
SOx	0.03

As it is shown, a large share of automotive emission are nitrogen oxides (about 30%), which contribute to the threat of photochemical smog in the summer and carbon monoxide (about 20%). The share of dust emission is a few percent – in the case of particulate matter PM10, the dominant pollution in winter, the share is about 5%. The participation of polycyclic aromatic hydrocarbons (0.6%), and especially of sulfur oxides (0.03%!) is completely trace.

Since Krakow is commonly used as an example of the environmental threat posed by the automotive industry, it was decided to analyze the results of measurements carried out at two stations of air quality monitoring: at Dietla Street which is located in the area of heavy traffic of motor vehicles and in Kurdwanów – in the area deprived of the dominating share of automotive industry in air pollution.

2. Results of empirical measurements

The pollutant emission data was provided by the air quality monitoring stations. This data is publicly available (for instance on relevant websites) in accordance with applicable law.

Figure 1 shows the immission of particulate matter PM10 values obtained from Kraków–Dietla station and Kraków–Kurdwanów station in 2016.

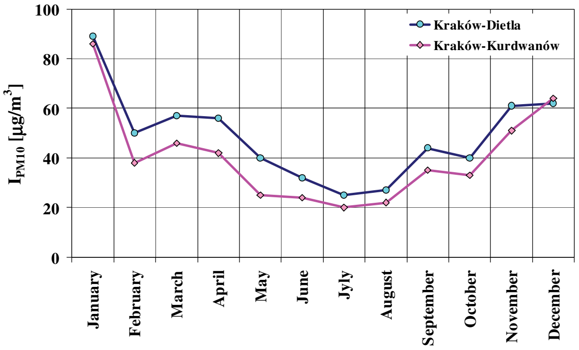

Fig. 1. The immission of particulate matter PM10 values obtained from Kraków–Dietla station and Kraków–Kurdwanów station in 2016

It is clearly visible that, in the so-called ‘heating period’, the immission of particulate matter PM10 is significantly higher comparing to summer months. The particulate matter immission PM10 values obtained from Kraków–Dietla station are stably higher, although the difference is not significant and does not indicate dominant influence of automotive industry.

Figure 2 shows the immission of particulate matter PM10 on 6 January 2016.

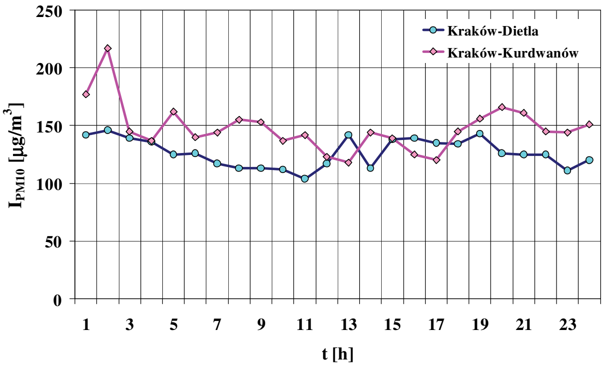

Fig. 2. The immission of particulate matter PM10 on 6 January 2016

In most part of the day the immission of particulate matter PM10 is significantly higher on Kraków–Kurdwanów station – impact of automotive industry on the immission of particulate matter is not striking even at rush hours.

Figure 3 shows the immission of particulate matter PM10 on 8 June 2016.

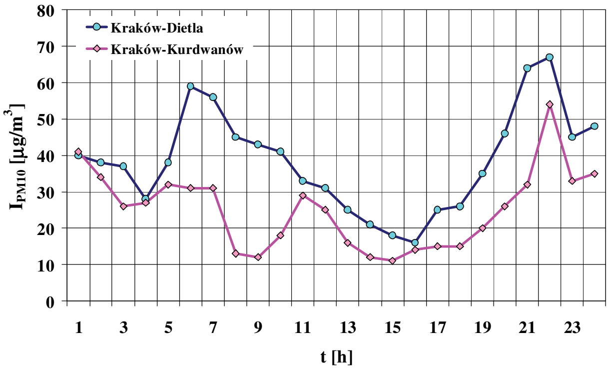

Fig. 3. The immission of particulate matter PM10 on 8 June 2016

The mean value of the immission of particulate matter PM10 in this particular case is considerably higher at the Kraków–Dietla station. This indicates that the automotive industry has a major impact on air pollution. However, these values of the immission are four times lower than in winter season.

The impact of the dust emission from municipal sources is particularly visible in Figs 4 and 5.

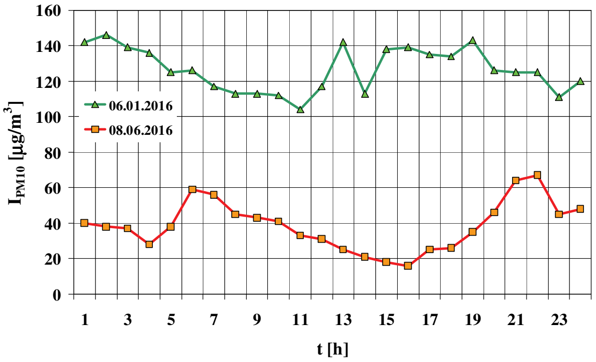

Fig. 4. The immission of particulate matter PM10 values obtained from Kraków–Dietla station on 6 January 2016 and 8 June 2016

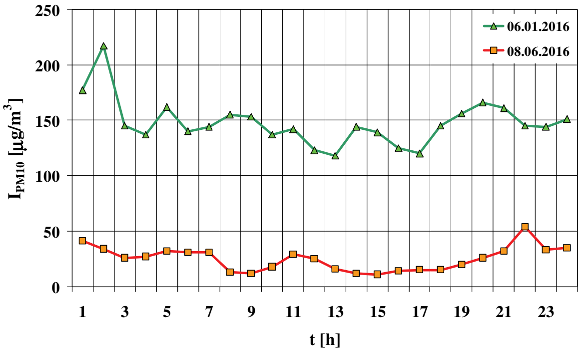

Fig. 5. The immission of particulate matter PM10 values obtained from Kraków–Kurdwanów station on 6 January 2016 and 8 June 2016

The similar comparison was made for the immission of nitrogen dioxide, a dominant pollutant in summer months.

Figure 6 shows the immission of the nitrogen dioxide in 2016 obtained from Kraków-Dietla station and Kraków–Kurdwanów station.

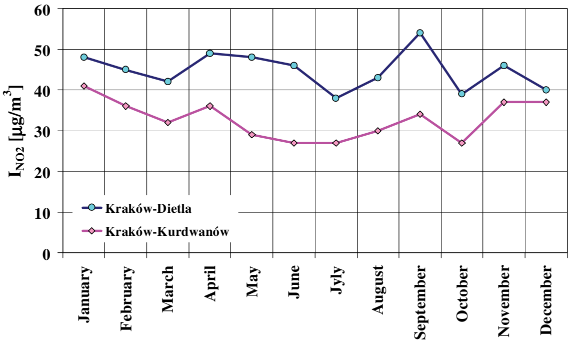

Fig. 6. The immission of nitrogen dioxide values obtained from Kraków–Dietla station and Kraków–Kurdwanów station in 2016

Figure 6 shows the impact of automotive indutsry on nitrogen dioxide immission at Kraków–Dietla station.

Figures 7 and 8 shows immission of nitrogen dioxide on 6 January 2016 and 8 June 2016.

Figures 7 and 8 show the impact of automotive industry on nitrogen dioxide immission – higher values were observed at Dietla station at rush hours.

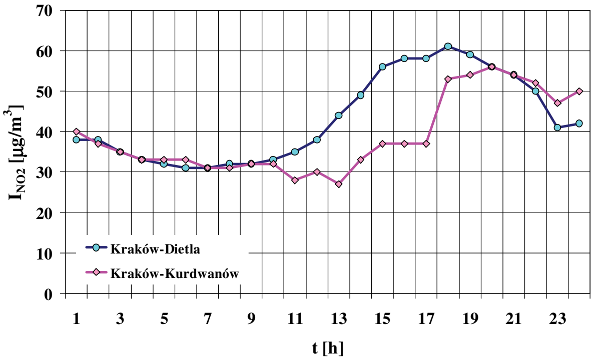

Fig. 7. The immission of nitrogen dioxide on 6 January 2016

Figures 9 and 10 show a comparison of nitrogen dioxide immission. The data was collected by both stations in winter and summer time respectively.

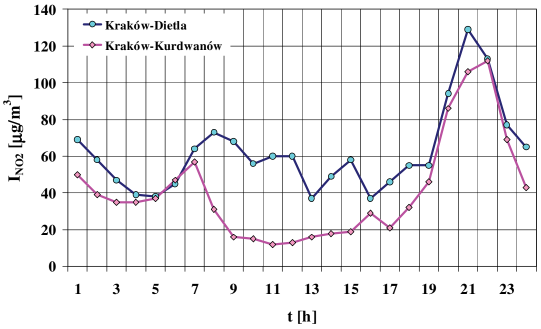

Fig. 8. The immission of nitrogen dioxide on 8 June 2016

As it is shown in Figures 9 and 10, automotive industry is a major source of nitrogen dioxide emission, especially in summer.

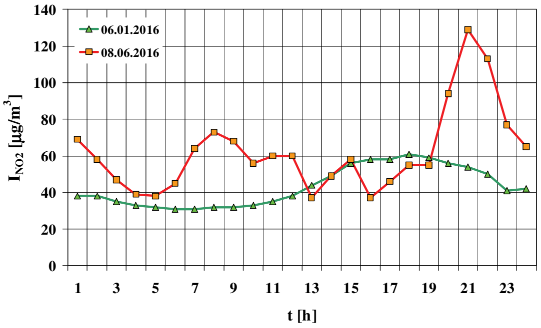

Fig. 9. The immission of nitrogen dioxide values obtained from Kraków–Dietla station on 6 January 2016 and 8 June 2016

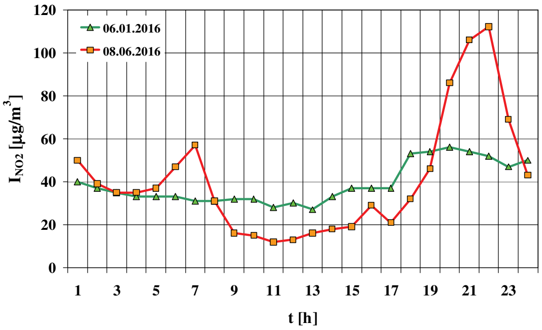

Fig. 10. The immission of nitrogen dioxide values obtained from Kraków–Kurdwanów station on 6 January 2016 and 8 June 2016

It is similar to nitrogen oxides immission – Figs 11–15.

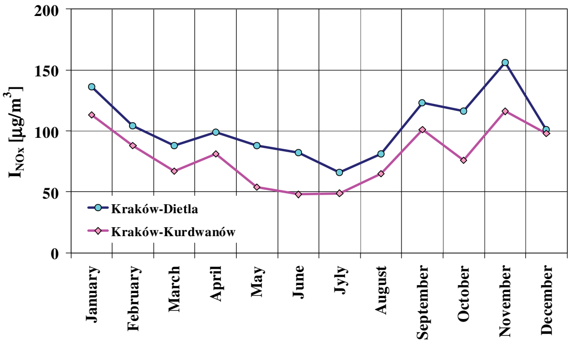

Fig. 11. The immission of nitrogen oxides values obtained from Kraków–Dietla station and Kraków–Kurdwanów station in 2016

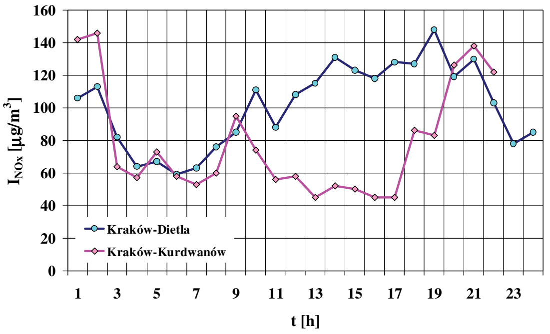

Fig. 12. The immission of nitrogen oxides on 6 January 2016

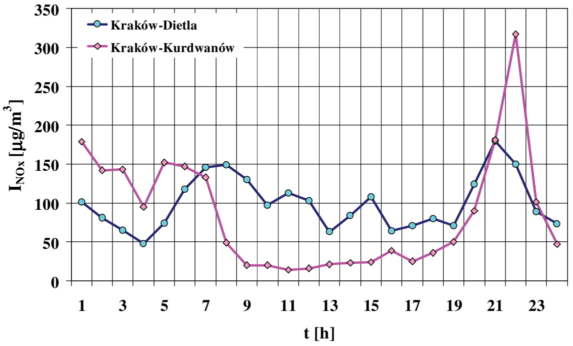

Fig. 13. The immission of nitrogen oxides on 8 June 2016

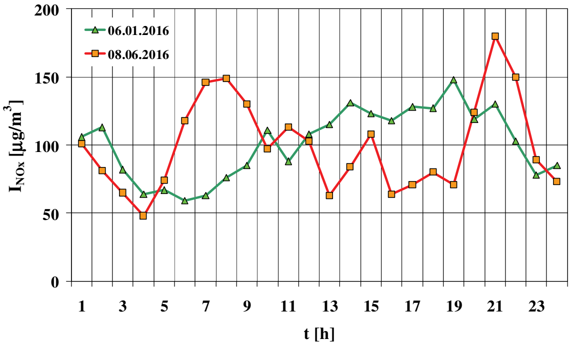

Fig. 14. The immission of nitrogen oxides values obtained from Kraków–Dietla station on 6 January 2016 and 8 June 2016

The results from the research confirm moderate impact of motor vehicles on air quality in a city agglomeration. Other revelations from a number of quality scientific journals confirm such assessment [1–8]. Of course, automotive industry threats are not to be underestimated but only rational actions supported by objective evaluation of the situation should be taken. Propagandistic and unprofessional actions such as mass checking of exhaust components concentration in spark-ignition engines at idling speed in winter time when there are large exceedances of dust immission not only do not bring any benefits but are also quite harmful as social resources are unnecessarily wasted.

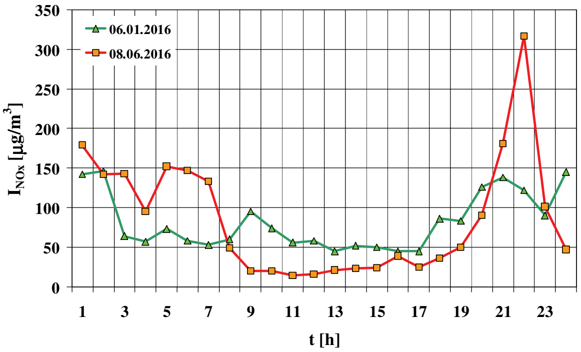

Fig. 15. The immission of nitrogen oxides values obtained from Kraków–Kurdwanów on 6 January 2016 and 8 June 2016

3. Recapitulation

By summarizing the above data, it possible to draw the following conclusions:

1. The cause of poor air quality is immission: in winter particulate matter PM10 and PM2.5, in summer – ozone and nitrogen oxides.
2. Road transport is significantly responsible for the emission of nitrogen oxides (30%), carbon monoxide (20%) and less for emission of particulate matter (a few percent).
3. The dominant sources of dust are other objects different than automotive vehicles. These are industrial sources and – above all – energy sources, especially individual heating installations. Particularly large dust pollution occurs in winter and it is not always in areas with intense traffic.
4. The research from a number of other air quality monitoring stations confirms the conclusions drawn in this paper.

Nomenclature

I	immission
CO	carbon monoxide
NMVOC	non-methane volatile organic compounds
NO_2	nitrogen dioxide
NO_x	nitrogen oxides
PM10	particular matter PM10
PM2.5	particular matter PM2.5
SO_x	sulphur oxides
TSP	total suspended particles
PAH	polycyclic aromatic hydrocarbons

Bibliography

[1] CANAGARATNA, M. Chase studies of particulate emissions from in-use New York City vehicles. *Aerosol Science and Technology*. 2004, **38**(6), 555-573.

[2] CHŁOPEK, Z., ŻEGOTA, M. The emission of particulate matter PM10 from vehicles. *Eksploatacja i Niezawodność – Maintenance and Reliability*. 2004, **21**(1), 3-13.

[3] CHŁOPEK, Z. Testing of hazards to the environment caused by particulate matter during use of vehicles. *Eksploatacja i Niezawodnosc – Maintenance and Reliability*. 2012, **14**(2), 160-170.

[4] CHŁOPEK, Z., SUCHOCKA, K. Risk posed by particulate master to the human and environment near transport router. *The Archives of Automotive Engineering – Archiwum Motoryzacji*. 2014, **63**(1), 3-22.

[5] CHŁOPEK, Z. Examination of a particulate matter PM10 immission model in the environment around road transport routes. *The Archives of Automotive Engineering – Archiwum Motoryzacji*. 2012, **55**(1), 23-38.

[6] XIE, X. et al. A review of urban air pollution monitoring and exposure assessment methods. *SPRS International Journal of Geo-Information,* 2017, 6(389). DOI:10.3390/ijgi6120389.

[7] OBANYA, H.E. et al. Air pollution monitoring around residential and transportation sector locations in Lagos Mainland. *Journal of Health and Pollution*. 2018, **8**(19), 180903.

[8] KRZYZANOWSKI, M. et al. Air pollution in the megacities. *Current Environmental Health Reports*. 2014, **1**(3), 185-191.

[9] HOUTHUJIS, D. et al. PM10 and PM2.5 concentrations in central and eastern Europe: Results from the CESAR study. *Atmospheric Environment*. 2001, **35**, 2757-2771.

[10] Poland's Informative Inventory Report 2018. Submission under the UN ECE Convention on Long-range Transboundary Air Pollution and the Directive (EU) 2016/2284 Warszawa, National Centre for Emission Management (KOBiZE) at the Institute of Environmental Protection – National Research Institute. February 2018.

Prof. Zdzisław Chłopek, DSc., DEng. – Automotive and Construction Machinery Engineering, Warsaw University of Technology.

e-mail: *zdzislaw.chlopek@pw.edu.pl*

Jakub Lasocki, DEng. – Faculty of Automotive and Construction Machinery Engineering, Warsaw University of Technology.

e-mail: *jakub.lasocki@pw.edu.pl*

Katarzyna Strzałkowska, MEng. – Grupa TOPEX.

e-mail: *k.strzalkowska@grupatopex.com*

Dagna Zakrzewska, MEng. – Analitycal Laboratory, Automotive Industry Institute.

e-mail: *d.zakrzewska@pimot.eu*

Article citation info:
CZARNIGOWSKI, J., SKIBA, K., DUBIEŃSKI, K. Investigations of the temperature distribution in the exhaust system of an aircraft piston engine. *Combustion Engines*. 2019, **177**(2), 12-18. DOI: 10.19206/CE-2019-203

Jacek CZARNIGOWSKI
Krzysztof SKIBA
Kamil DUBIEŃSKI

CE-2019-203

Investigations of the temperature distribution in the exhaust system of an aircraft piston engine

Ultralight aviation is based on piston engines requiring both performance and reliability. An important aspect is also the requirements for the installation of such an engine on an airframe, especially its heat emission. This is firstly because of the need to ensure proper engine cooling and secondly because composite elements of the airframe skin are not exposed to excessive overheating. For this purpose, bench tests of the temperature distribution of the exhaust system of ROTAX 912 engine were carried out. Measurements were taken at 6 points of the exhaust system, where the temperature of the exhaust gases and exhaust pipes were measured. The tests covered a wide range of engine operation. The paper presents the temperature distribution at selected points in relation to the engine speed and load.

Key words: *aircraft engine, exhaust system, temperature distribution*

1. Introduction

Ultralight aviation is one of the fastest growing fields of aviation industry. According to reports describing this market [6, 8], there are currently 50,000 ultralight aircraft in use in Europe and about 5.5% of them are added every year. This trend has been maintained for a period of 10 years [6]. According to the data [6], most of these aircraft (over 95%) are powered by piston engines. Most of the European market is occupied by one manufacturer: ROTAX. Its engines are reliable and have a very good power-to-weight ratio. The disadvantage of these motors, however, is the low power of the electric generator.

Current aviation regulations [7] require aircraft manufacturers to install equipment that needs electrical power supply. These include: radio, transponder, contour lighting, stroboscopic lighting and avionics. In addition, very often the components related to easier use are installed: satellite navigation, lighting and heating of the cabin, charging external devices (e.g. mobile phones), etc. This results in a lack of energy. According to the authors [1, 2, 4] in some operating conditions the amount of electric energy consumed by on-board devices exceeds the amount of energy produced by the generator. This is contrary to the applicable aviation regulations [7].

It is therefore necessary to equip aircraft with additional sources of electrical energy. These may be additional batteries [2] or alternators driven by the motor shaft [6]. Another approach is the use of independent generator systems. The generators used are independent generators based on additional internal combustion engines [5] or thermogenerators [3]. The last proposal seems to be very promising due to the use of waste energy from the exhaust gas from the primary source of propulsion.

However, in developing a thermogenerator it is necessary to know the amount of available energy and the temperature of the medium interacting with the thermogenerator element. This temperature must not exceed the limits resulting from the materials used for this part.

This work is the initial stage of the development of a thermogenerator compatible with the ROTAX 912 engine. Its aim is to determine the temperature range of the exhaust system and the exhaust gases themselves in the whole range of engine operation.

2. Research description

2.1. Research objects

The object of the research is a ROTAX 912 ULS piston engine. The engine is a 4 cylinder 4 stroke reciprocating piston engine (boxer) – Fig. 1. The engine is cooled by air (cylinders) and coolant (cylinder heads). It is equipped with a dry oil sump system with an additional oil tank. The engine is integrated with the main reducer which reduces the rotational speed to the requirements of the propeller. The tested engine was equipped with authored fuel system – a sequential multi-point fuel injection system into the intake manifold. Engine parameters are described in Table 1.

Fig. 1. ROTAX 912 ULS Engine

Table 1 Engine Parameters [2]

Engine configuration	Flat engine (boxer)
Cylinder number	4
Displacement	1352 cm^3
Maximal power	73.5 kW (100 HP) at 5800 RPM – limited to 5 minutes
Continuous power	69 kW (93 HP) at 5500 RPM
Maximal torque	128 Nm at 5100 RPM
Weight	56.6 kg
Gearbox ratio	2.43
Bore	84 mm
Stroke	61 mm
Compression ratio	10.8:1
Fuel	RON95

2.2. Test stand

The tests were carried out on a test stand located in the Centre for Innovation and Advanced Technologies of the Lublin University of Technology – Fig. 2. The dynamometer stand is made up of:

- Electro-mechanical brake: EMX – 200/6000 manufactured by Elektromex Centrum, with braking power up to 200 kW at the rotational speed up to 6000 rpm;
- Control system of the dynamometer: ATMX 2000 manufactured by ODIUT Automex SP. z o.o.;
- Gravimetric fuel meter with fuel conditioning: ATMX 2400 manufactured by ODIUT Automex SP. z o.o. has a fuel temperature and pressure control system.
- The system of oil heat exchangers, engine cooling water and brake cooling.

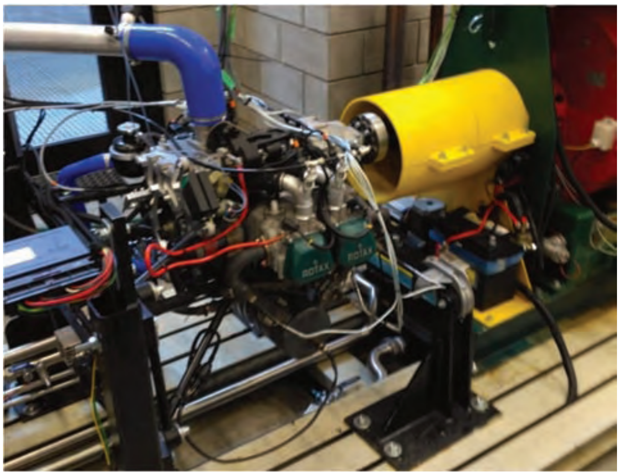

Fig. 2. Test stand

Exhaust system temperature measurements were carried out on a standard ROTAX engine exhaust system. Temperature sensors were placed in the exhaust system at specific distances from cylinders – 30, 180, 400, 600 and 1000 mm, both inside the system (gas temperature measurement) and outside (wall temperature measurement). The location of measurement points is shown in Fig. 3.

Fig. 3. Exhaust system of ROTAX 912 ULS engine

Thermocouples type K (NiCr–NiAl) manufactured by Czaki Thermo – Product were used during the research. Sensors TP-204K-1b-150-1 were used to measure the temperature of exhaust gases and sensors TP-203K-1b-150-1 to measure the temperature of exhaust system elements, the insulation of the cable was a glass fibre with a screen. The location of the sensors is shown in Fig. 4.

Fig. 4. Temperature sensor mounting

Measurements of signals from sensors were made with the use of NI 9213 measuring devices produced by National Instruments embedded in a four-socket, Ethernet and USB transmission. The DAQ module processes signals from the measuring card and sends them via digital transmission to the computer. To analyze the results, the program was developed in an National Instruments – LabVIEW – Fig. 5.

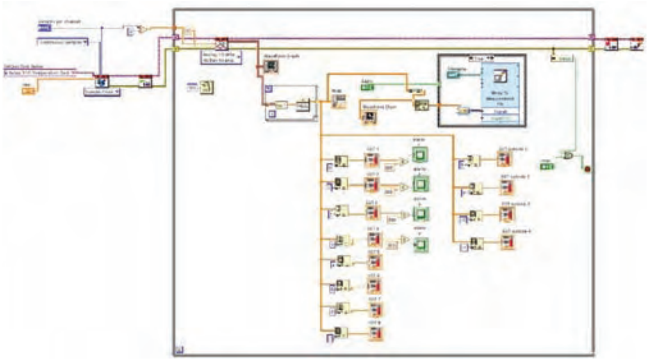

Fig. 5. Analyze program layout

2.3. Scope of research

The aim of the tests was to analyze the distribution of exhaust gas temperature and the external temperature of the exhaust system in a wide range of engine operation on a test stand. The analysis covered both the distribution of temperatures at particular operating points and their difference in charges from the distance from the cylinder.

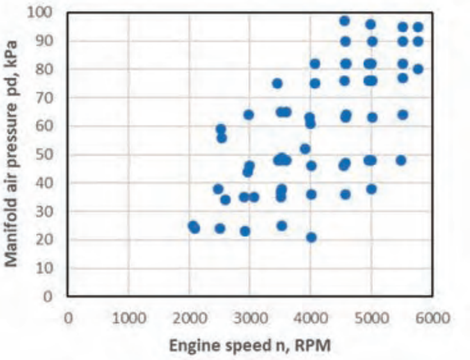

Fig. 6. Engine operational point use in the research

The scope of work included measurements of temperatures in points described in chapter 2.2 in steady state of engine operation at test points determined by the rotational speed and manifold air pressure. The tests were carried out in 61 points (Fig. 6) covering the range of rotational speed 2060 – 5770 RPM, and the manifold air pressure 21 – 97 kPa. The tests were carried out in steady state of engine operation.

10 temperature signals were recorded in the exhaust system at specific distances from the cylinders – 30, 180, 400, 600 and 1000 mm, both inside the system (gas temperature measurement) and outside (wall temperature measurement).

3. Results

The following figures show the results of temperature distribution tests at selected points of the exhaust system. The results are presented as a function of engine speed and manifold air pressure. The measured values and approximation of the second degree polynomial surface were presented.

Figure 7 shows the distribution of exhaust gas temperatures at the first measuring point 30 mm from the cylinder head number 1. The lowest recorded temperature is 536°C and occurs at idling of this engine: rotational speed 2060 RPM and manifold air pressure 25 kPa. An increase in rotational speed and manifold pressure leads to an increase in exhaust gas temperatures. At full engine power (5770 RPM and pressure 98 kPa) the temperature reaches 762°C.

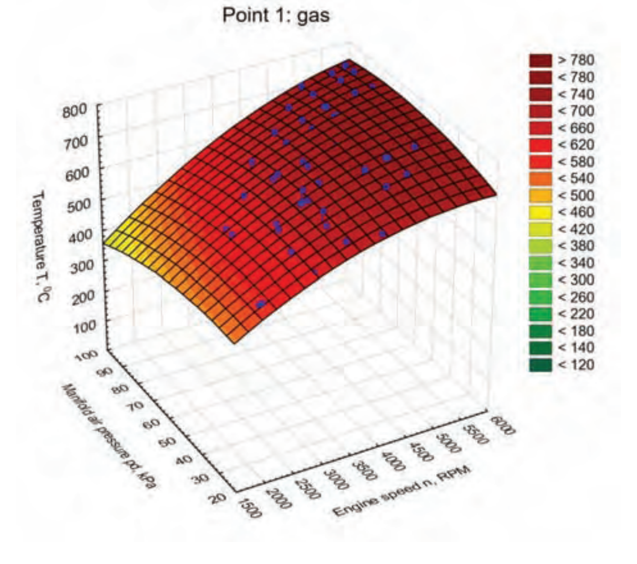

Fig. 7. Exhaust gas temperature at point 1 as a function of rotational speed and manifold air pressure

The temperature of the exhaust system walls at this point also increases with an increase in engine speed and manifold air pressure – Fig. 8. For idling, this temperature is 423°C and for maximum power 661°C.

Similar relationships are also visible for the second measuring point 180 mm from the cylinder head 1 – Figs 9 and 10. The lowest temperatures recorded are at idle and are 384°C for gas and 291°C for the exhaust wall, respectively. They are approximately 130°C lower than at the previous measuring point. The highest recorded temperature is 764°C for gas and 603°C for the wall, respectively. It is noticeable that the maximum gas temperature is practically identical to the temperature at point 1 and the wall temperature is only 58°C cooler.

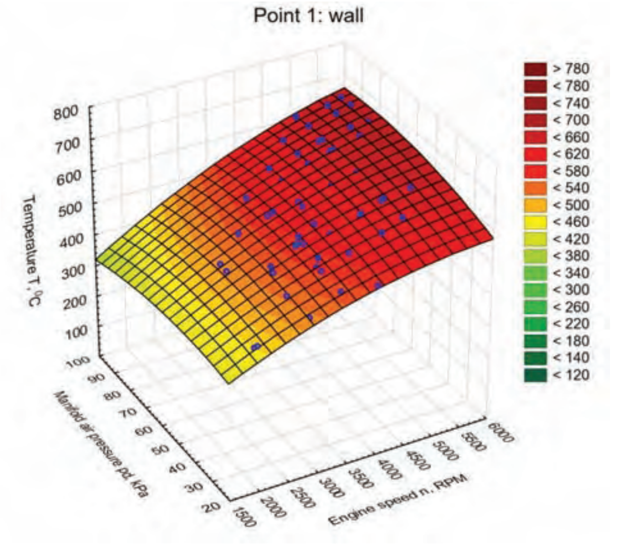

Fig. 8. Exhaust wall temperature at point 1 as a function of rotational speed and manifold air pressure

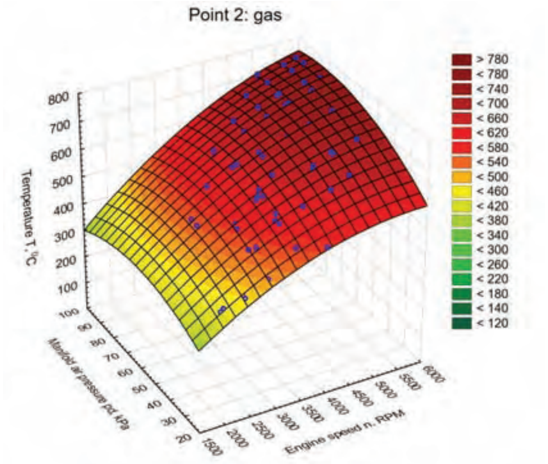

Fig. 9. Exhaust gas temperature at point 2 as a function of rotational speed and manifold air pressure

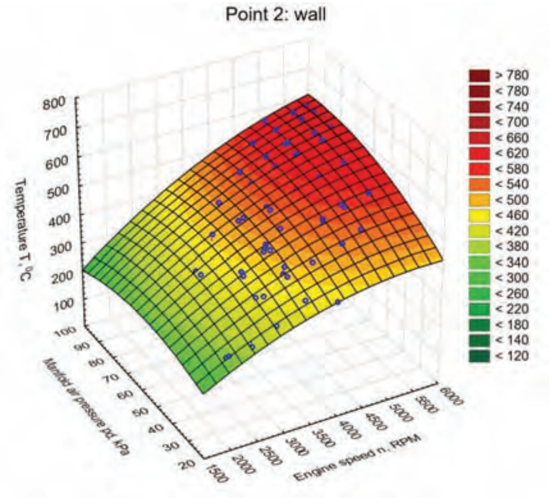

Fig. 10. Exhaust wall temperature at point 2 as a function of rotational speed and manifold air pressure

The third measuring point is located in the silencer, which is a central exhaust manifold and is about 400 mm away from the cylinders. Here too, the rotational speed and manifold air pressure directly affect the temperature increase – Figs 11 and 12. The lowest recorded temperature also occurs at idle and is 306°C for gas and 207°C for the exhaust manifold wall, respectively. This represents a decrease of about 80°C compared to the previous point. The maximum temperature (occurring at maximum engine load) was 750°C for gas and 589°C for exhaust manifold walls, respectively. It is only 14°C lower than the values obtained in the previous point.

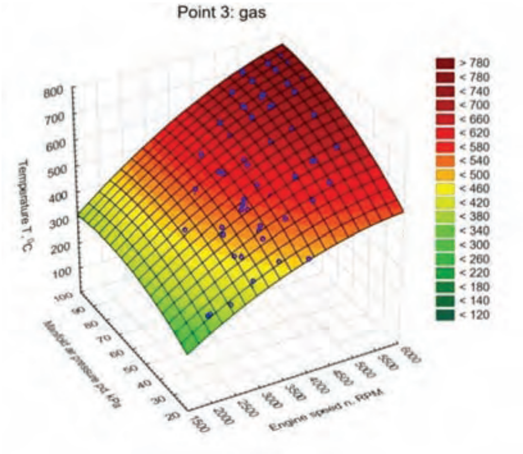

Fig. 11. Exhaust gas temperature at point 3 as a function of rotational speed and manifold air pressure

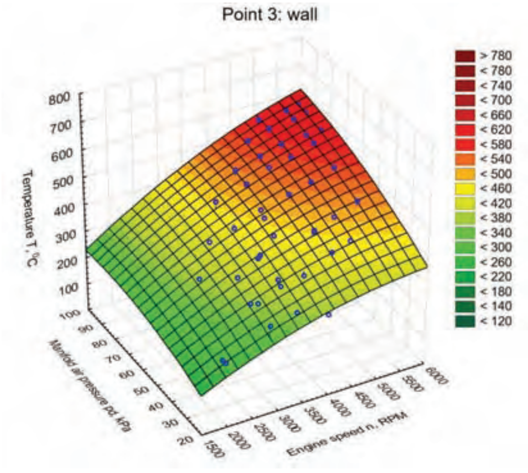

Fig. 12. Exhaust wall temperature at point 3 as a function of rotational speed and manifold air pressure

Another measuring point is located at the silencer exit 600 mm from cylinder head no. 1. At this point, as in the previous ones, an increase in rotational speed and manifold pressure leads to an increase in temperature – Figs 13 and 14. The lowest temperature also occurs at idle and is 316°C and 231°C for the manifold walls, respectively. The highest recorded temperatures are 752°C for gas and 648°C for the manifold wall, respectively. These temperatures are about 10°C higher than in the previous point for gas and up to 60°C for the wall. This is due to two facts: Firstly, the gases are compressed here again by the geometry of the manifold, which increases their temperature and the heat dissipation area is much smaller than at point 3.

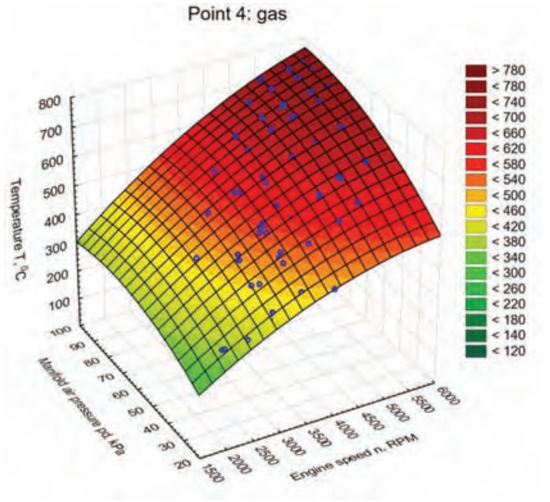

Fig. 13. Exhaust gas temperature at point 4 as a function of rotational speed and manifold air pressure

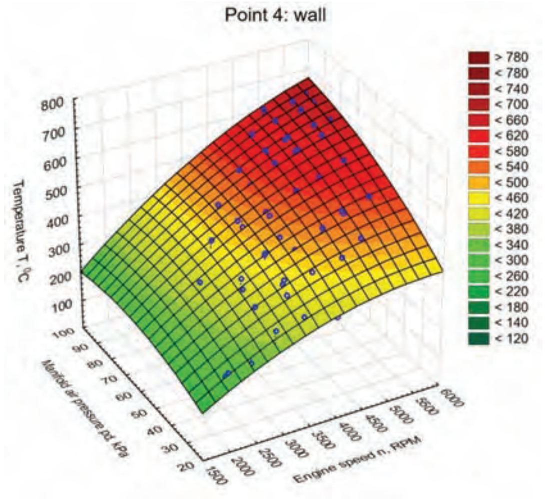

Fig. 14. Exhaust wall temperature at point 4 as a function of rotational speed and manifold air pressure

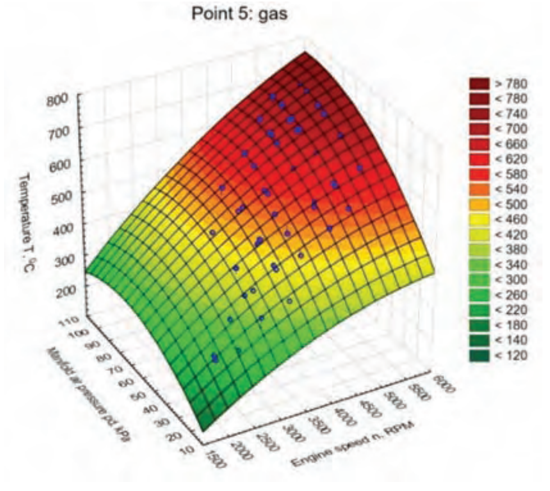

Fig. 15. Exhaust gas temperature at point 5 as a function of rotational speed and manifold air pressure

The last measuring point is 1000 mm from the cylinder head 1 practically at the end of the engine outlet manifold. Again, an increase in speed and manifold air pressure causes an increase in temperature – Figs 15 and 16. The lowest recorded temperature occurs when the engine is idle and is 278°C for gas and 170°C for the manifold wall, respectively. The highest occurs for the highest engine load I is 731°C for gas and 637°C for the manifold wall, respectively. Therefore, the temperature of both gases and the wall temperature drops again compared to the previous point.

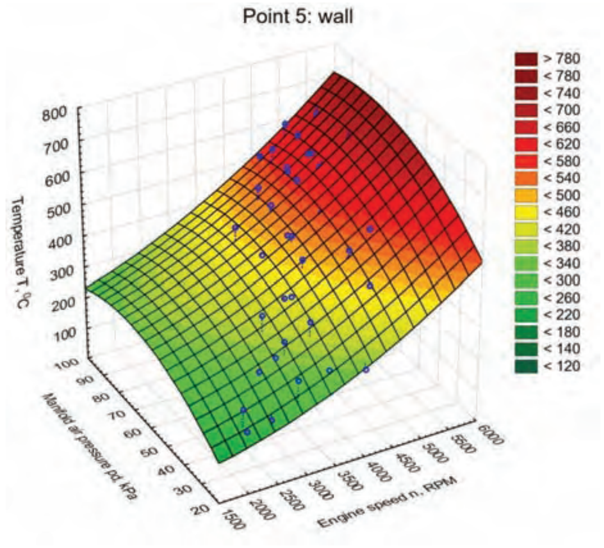

Fig. 16. Exhaust wall temperature at point 5 as a function of rotational speed and manifold air pressure

Temperature differences between the gas and the exhaust manifold wall were also analyzed. For the first measuring point, Fig. 17, it is visible that the increase in speed leads to an increase of the difference and the increase in manifold air pressure decrease of this difference. The smallest difference of 71°C was recorded for the rotational speed of 4555 rpm and manifold air pressure of 21 kPa. The largest one, i.e. 14°C, was recorded at 4015 rpm and 21 kPa.

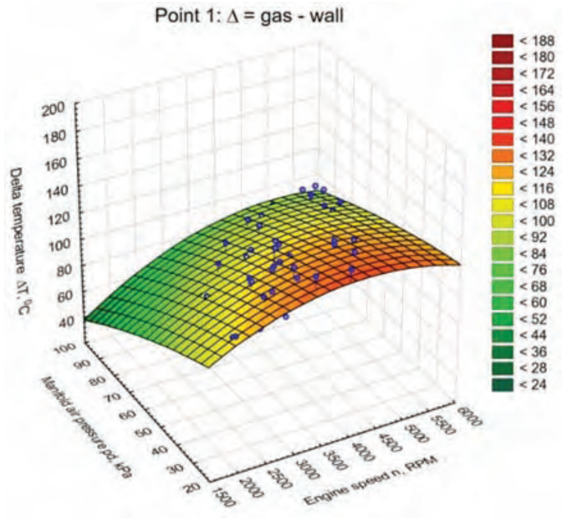

Fig. 17. Temperature difference between exhaust gas and exhaust manifold wall at point 1 as a function of engine speed and manifold air pressure

A different relationship was observed for point 2 – Fig. 19. At this point, the increase in engine speed and manifold air pressure results in an increase in the difference in temperature analyzed. The lowest value equal to 93°C was recorded for idling and the highest value of 161°C for maximum power.

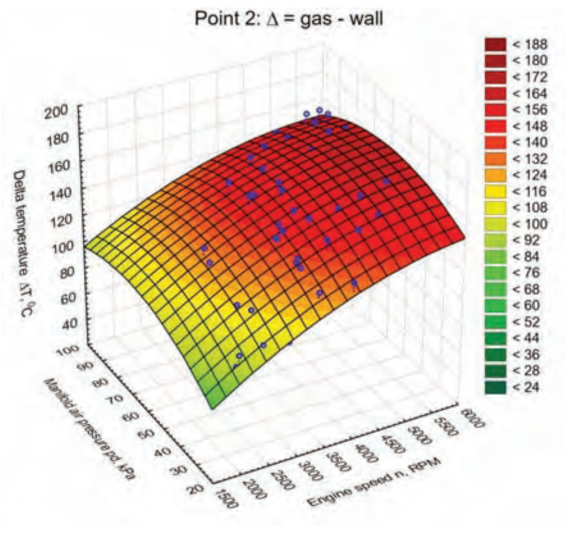

Fig. 19. Temperature difference between exhaust gas and exhaust manifold wall at point 2 as a function of engine speed and manifold air pressure

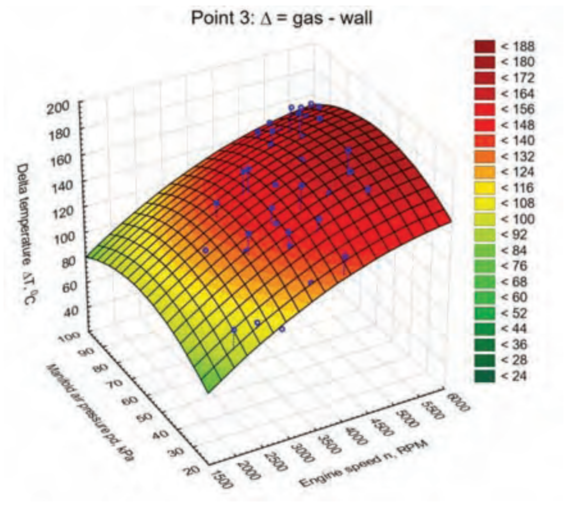

Fig. 20. Temperature difference between exhaust gas and exhaust manifold wall at point 3 as a function of engine speed and manifold air pressure

A similar relationship can be seen at point 3 – Fig. 20. The lowest value of 92°C was recorded for idling and the highest value of 186°C for maximum power.

Also at point 4, the dependence of the temperature difference on the engine speed and manifold air pressure is similar to the previous points – Fig. 20. The lowest value of 56°C was recorded for idling and the highest value of 118°C for maximum power. However, there is a significant flattening of the analysed difference at higher rotational speeds and intake manifold pressures. In the speed range above 4000 rpm and pressure above 60 kPa, the temperature difference is almost unchanged.

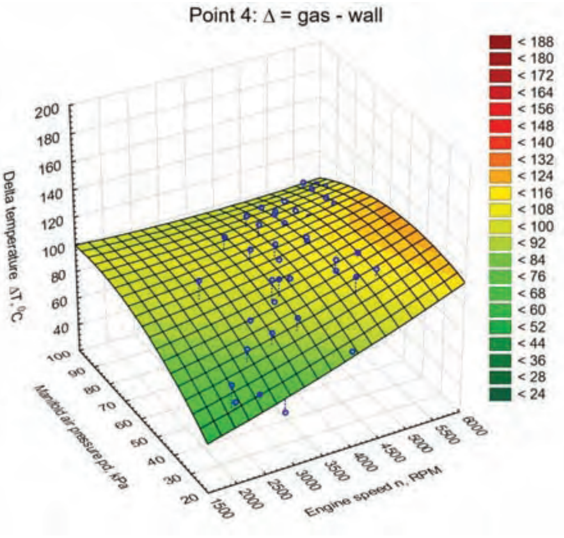

Fig. 21. Temperature difference between exhaust gas and exhaust manifold wall at point 4 as a function of engine speed and manifold air pressure

The smallest changes, i.e. the greatest stability of the temperature difference between the gas and the walls of the exhaust manifold, are shown in point 5 – Fig. 22. The approximated value of the differences oscillates around 80–100°C and the visible deviation of measurement points from the approximated surface results from a random sequence of measurements.

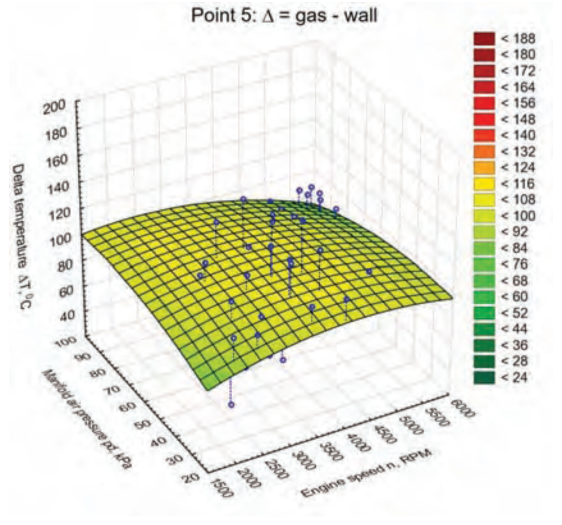

Fig. 22. Temperature difference between exhaust gas and exhaust manifold wall at point 5 as a function of engine speed and manifold air pressure

4. Conclusions

Conducted tests of temperature distribution along the exhaust manifold allowed the following conclusions to be made: The temperature distribution along the outlet manifold is the result of the study:

1. The temperature of the exhaust gases and the temperature of the exhaust manifold walls is proportional to the engine speed and the load degree expressed by the manifold air pressure. The operating conditions have a significant influence on the temperature level. At a point 30 mm from cylinder head no. 1, the minimum exhaust temperature was 536°C and the maximum temperature was 762°C.
2. The temperature of the exhaust gas and the temperature of the exhaust manifold walls decreases with the distance from the cylinder head. An exception to this rule is the exhaust outlet from the silencer to the exhaust pipe, where the temperature rises relative to the silencer temperature as a result of re-compression.
3. The maximum exhaust gas temperature does not decrease significantly with length. It is 762°C at point 1 and 731°C at point 5 (1000 mm from cylinder head no. 1). A similar gradient is visible at the temperature of the exhaust manifold wall: 661°C at point 1 and 637°C at point 5, respectively.
4. The lowest average temperatures of exhaust gas and manifold walls are at point 3 – silencer. This is due to the temperature drop due to the expansion of the exhaust gases.
5. At all measuring points, the temperature difference between the exhaust gas and the walls remains within a similar range. The average value is about 120°C and results from the thermal conductivity of the exhaust manifold material and the degree of heat transfer to the surroundings.

To summarize, it can be stated that the engine exhaust manifold can be used as a heat source for the thermogenerator. Due to the level of maximum temperatures exceeding the limit values for thermocouples, it is not possible to install them directly on the manifold walls. It is therefore necessary to use heat-conducting elements that allow the temperature to be lowered to acceptable levels.

Acknowledgements

This work was financed from the core funds for statutory R&D activities by the Polish Ministry of Science and Higher Education. The authors gratefully acknowledge the support.

Bibliography

[1] CZARNIGOWSKI, J., SKIBA, K. Electric energy balance of the ROTAX 912 with fuel injection. *Journal of KONES Powertrain and Transport*. 2017, **24**(1). DOI: 10.5604/01.3001.0010.2834.

[2] KANG, G.-W., HU, Y., LI, Y.-D., JIANG, W.-H. Parameters matching of ultralight electric aircraft propulsion system. *Hangkong Dongli Xuebao/Journal of Aerospace Power*. 2013, **28**(12), 2641-2646. www.scopus.com/inward/record.uri?eid=2-s2.0-84891890860&partnerID=40&md5=b9e3dab95eb862a2441425fefd7848bc

[3] STOCKHOLM, J.G. Applications in thermoelectricity. *Materials Today: Proceedings*. 2018, **5**(4), 1, 10257-10276, DOI:10.1016/j.matpr.2017.12.273.

[4] TOMAŽIČ, J., TOMAŽIČ, T., ŽEMVA, A. Battery-cell balancing in electric-powered ultralight aircraft [Napetostno izenačevanje akumulatorjev v ultralahkih letalih na električni pogon]. *Elektrotehniski Vestnik/Electrotechnical Review*. 2010, **77**(4), 188-193, www.scopus.com/inward/record.uri?eid=2-s2.0-79551613076&partnerID=40&md5=6d7e93c2b8b848245c2bde2a25aa311e

[5] ZHU, Q., FORSYTH, A., TODD, R. Investigation of hybrid electric aircraft operation on battery degradation. *2018 IEEE International Conference on Electrical Systems for Aircraft, Railway, Ship Propulsion and Road Vehicles and International Transportation Electrification Conference.* ESARS-ITEC 2018, art. 8607617, 2019. www.scopus.com/inward/record.uri?eid=2-s2.0-85062082639&doi=10.1109%2fESARSITEC.2018.8607617&partnerID=40&md5=67fc1d4b18d7bb37a139a17c9d0d0d7e

[6] *2015 General Aviation Statistical Databook & 2016 Industry Outlook* General Aviation Manufacturers Association.

[7] European Aviation Safety Agency. *Certification Specifications for Very Light Aeroplanes CS-VLA.* ED Decision 2009/003/R.

[8] *Light Aircraft Global Market Growth, CAGR, Trend Status and Forecast 2018- 2025.* ReportHive 2018.

[9] Regulatory Options for the European Light Aircraft (ELA1) Phase 3 FINAL REPORT". november 2010 EASA.

Jacek Czarnigowski, DSc., DEng. – Faculty of Mechanical Engineering, Lublin University of Technology.

e-mail: *j.czarnigowski@pollub.pl*

Kamil Bubeński, Eng. – Faculty of Mechanical Engineering, Lublin University of Technology.

e-mail: *kamil.dubenski@pollub.edu.pl*

Krzysztof Skiba, MEng. – Faculty of Mechanical Engineering, Lublin University of Technology.

e-mail: *k.skiba@pollub.pl*

Article citation info:
SZYMLET, N., LIJEWSKI, P., RYMANIAK, Ł. et al. Comparative analysis of exhaust emissions from passenger and motorcycles. *Combustion Engines*. 2019, **177**(2), 19-22. DOI: 10.19206/CE-2019-204

Natalia SZYMLET
Piotr LIJEWSKI
Łukasz RYMANIAK
Barbara SOKOLNICKA
Maciej SIEDLECKI

CE-2019-204

Comparative analysis of exhaust emissions from passenger cars and motorcycles

The subject of this article is a comparative analysis of exhaust emissions for: HC (hydrocarbons), CO (carbon monoxide), CO_2 (carbon dioxide), NO_x (nitrogen oxides) from a passenger vehicle and a motorcycle in laboratory conditions on a dynamometer station. The first vehicle category was represented by a compression-ignition engine with a displacement volume of 1.3 dm^3 and a power of 66 kW. The exhaust aftertreatment system included a catalytic converter and a particulate filter. The second category was a motorcycle, equipped with an engine with a displacement of 0.7 dm^3 and a maximum power of 55 kW. The two-wheeled vehicle was equipped with a three-way catalytic converter. Speeds were modeled on the European type approval test – NEDC (New European Driving Cycle). In order to conduct a comparative analysis of exhaust emissions and fuel consumption from vehicles of different categories, the obtained results were presented in the form of emissions converted into passenger-kilometers (g/pkm). The research used modern equipment belonging to the PEMS (Portable Emissions Measurement Systems) group of devices. The analyzes carried out enable the decision making on which vehicles have a greater environmental impact due to their exhaust emissions, taking into account the distance and the number of passengers carried.

Key words: *combustion engines, passenger car, motorcycle, emission*

1. Introduction

Globalization, leading towards the integration and interdependence of countries worldwide, not only in the cultural but also in the economic aspect, results in a smoother exchange of goods and their mass consumption. This also applies to the automotive industry. The effect of this phenomenon is excessive degradation of the natural environment by the road transport sector, which is particularly evident in urban agglomeration centers. For example, in Poznań in 2017, the number of newly registered passenger cars reached 425 383, so there were 790 of them per 1000 inhabitants [6]. If the total number of vehicles is taken into account, they exceeded the number of inhabitants by over 24 thousand (Fig. 1). This trend is expected to continue and now this indicator is even larger.

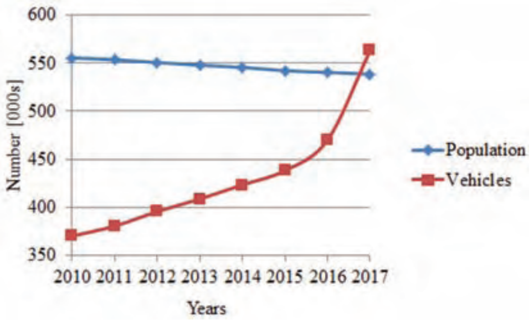

Fig. 1. The number of vehicles registered in Poznań in 2017 and the number of inhabitants [6]

Motor vehicles usually have 3 or 4 seats for passengers. The literature analysis carried out by the authors regarding the rate at which the seats in passenger cars are used allowed to estimate it at 1.2 [3]. The scientific work describing the average number of passengers per car in the Białystok agglomeration on various days of the week was on average 1.54 [2]. This results in exacerbating the phenomenon of congestion, resulting in the losses of not only to time and economic losses but also environmental losses. Many studies have shown that the highest exhaust emission values of toxic compounds can be observed for the idle engine operation, where the vehicle uses a significant amount of fuel to overcome its own internal motion resistance, without producing any useful work [5].

An easy solution to problems related to urban mobility in the aspect of the congestion phenomenon is the use of urban single-track vehicles, whose share is significant in densely populated Asian countries. However, in highly developed countries (e.g. European countries), motorcycle units with larger displacement engines enjoy greater popularity, which does not improve the emission rates in the city, also taking into account their limited transport capacity. In addition, the approval rules for two-wheeled vehicles are more liberal compared to other motor vehicles. In Poznań, there is a continuous increase in the number of vehicles of both categories, as shown in Fig. 2 [6].

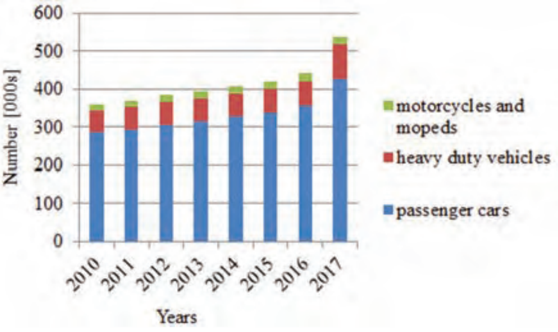

Fig. 2. Vehicles registered in Poznań by type and year [6]

In the light of these problems, this publication is related to considerations regarding the emissivity of various types of vehicles (motorcycles and mopeds and passenger cars) in terms of their transport capacity. For this purpose, the authors have compared the emissions of toxic compounds and the fuel consumption of a motorcycle and passenger car per one passenger kilometer.

2. Research metodology

2.1. Research objects

In order to compare the emissivity of different category vehicles, a motorcycle and a passenger car were used for the research. The test object representing the PC group (*Passenger Car*) was a light vehicle, equipped with a compression-ignition engine, with a displacement of 1.3 dm^3 and with 66 kW of power. The exhaust aftertreatment system consisted of a catalytic converter and a particulate filter, the vehicle was manufactured in 2011 and it complied with the Euro 5 emission norms. The second category was represented by a motorcycle equipped with an engine with a displacement of 0.7 dm^3 and a maximum power of 55 kW. The vehicle was manufactured in 2017, so it was manufactured to meet the Euro 4 standard. Before the start of the test, its mileage was recorded at 740 km, and the exhaust aftertreatment system consisted of a three-way catalytic converter (TWC).

2.2. Chassis dynamometer

The simulation of the NEDC type approval test drive (*New European Driving Cycle*) for a passenger car was performed on the laboratory engine stand, equipped with a dynamic brake – DynoRoad (Fig. 3).

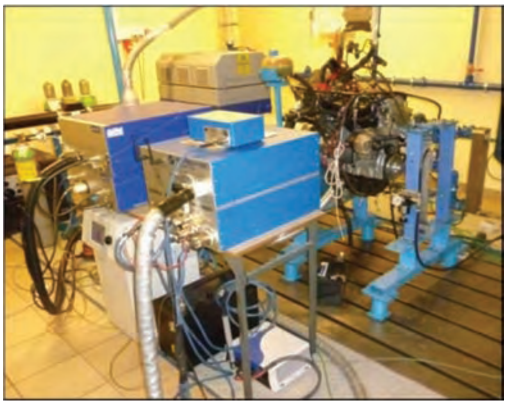

Fig. 3. Dynamometer test bench with the measuring apparatus

This test bench allows to define and input the design features of the tested vehicle such as: mass, type of drive, wheel size, air resistance coefficients or characteristics of the gearbox. The diagram of the procedure is shown in Figure 4. During operation, the combustion engine generates mechanical work converted into electricity by the brake, which after voltage and frequency transformation is transferred to the external network, and excess heat removed by the air cooling system.

Motorcycle tests were carried out using a chassis brake station with a single brake roll, designed for testing two-wheeled vehicles. The DYNOmite motorcycle test bench was manufactured by LAND&Sea [7]. The device can record the vehicle's operational parameters (instantaneous power, torque, speed, acceleration) as well as the distance traveled.

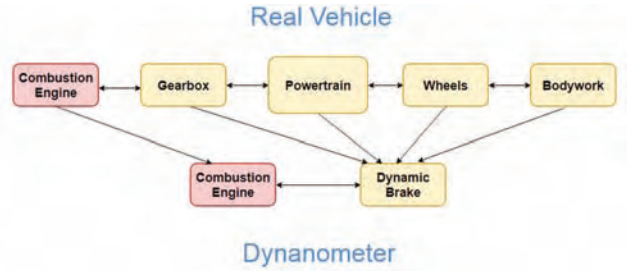

Fig. 4. Diagram of the vehicle simulation process on a test bench

2.3. Measurement equipment

The exhaust emissions and fuel consumption measurement were carried out using mobile devices from the PEMS (*Portable Emissions Measurement System*) group.

SEMTECH DS apparatus (Fig. 5) was used to conduct the exhaust emissions measurement of: HC, CO, CO_2, NO_x from a passenger vehicle. To measure individual exhaust gas compounds, the exhaust sample taken from the mass flow sensor had to pass through a series of analyzers. However, first the sample is subjected to filtration in order to separate out the solid particles. The first analyzer where the sample is sent for testing was the FID (*Flame Ionization Detector*) analyzer, enabling the determination of hydrocarbon emission. After cooling the exhaust gas to about 4°C, the sample was then transported to the NDUV (*Non-dispersive Ultraviolet*) analyzer, which determined the content of nitrogen oxides. The content of carbon monoxide and dioxide was determined using the NDIR (*Non-dispersive Infrared*) analyzer. In the last stage, the sample was sent to the electrochemical analyzer, where oxygen content was measured [9].

Fig. 5. The SEMTECH DS. exhaust emission analyzer.

Measurements of the above-mentioned harmful exhaust compounds emissions in the case of the four-wheel passenger vehicle were made using the AxionR/S+ device.

The device consists of two sets of analyzers working in parallel. Electrochemical analyzers are used to determine the emission of hydrocarbons, carbon monoxide and dioxide, and oxygen and nitrogen oxide measurements are made using the NDIR analyzer. What's more, the AxionR/S+ device allows the registration and measurement of motor and vehicle data, i.e. acceleration, vehicle speed or intake air temperature [8]. The key advantage of this device, in the aspect of testing of two-wheelers, is its lightweight and compact nature (low weight and small dimensions). Figure 6 shows the test object on the brake station with the measuring apparatus.

Both measuring instruments were calibrated and zeroed before the tests in order to make the results independent from background noise or ambient impurities.

Fig. 6. Picture of the tested motorcycle along with the measuring apparatus on the designated dynamometer

2.4. NEDC test

The tests were carried out in accordance with the European NEDC type approval test, dedicated to light motor vehicles. The test consists of two parts: the UDC urban cycle (constituting four ECE 15 tests) and the extra-EUDC cycle. The first test lasted 800 seconds, the second one – 400 seconds, each of them was characterized by different maximum value of the vehicle speed (Fig. 7). The total test time is therefore 1200 seconds, and the distance traveled during the test is approximately 11 km.

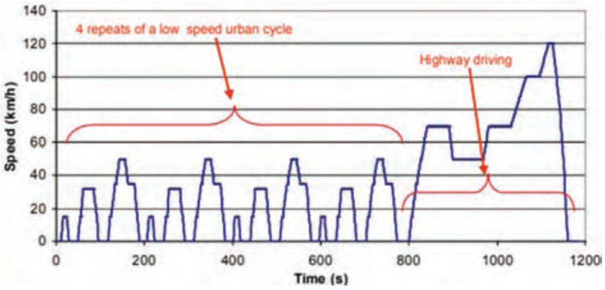

Fig. 7. The NEDC test drive cycle speed profile [1]

3. Results and analysis

Data obtained during the NEDC test (the mass of individual exhaust gas compounds, distance and number of passengers) allowed to determine the emission per passenger kilometer for each of the measured exhaust compound. The emission values obtained for various categories of vehicles (motorcycle and passenger car) were used for comparison (Fig. 8). For a light vehicle, the drive was simulated with three passengers, while the NEDC test in the case of the two-wheel vehicle was performed only considering the driver himself. What's more, based on the data concerning the exhaust emission values of carbon containing compounds, the fuel consumption for each of the tested vehicles was calculated using the Carbon Balance method. The comparison showed a significantly higher CO_2 and FC emissions (by 157% and 151% respectively) obtained during the motorcycle drive tests. This is mainly due to the less efficient operation of spark-ignition engines (increased unit fuel consumption), in particular when idling and in the case of low engine loads that often occur in the NEDC test. Undoubtedly, differences in fuel consumption and CO_2 emissions would be much less significant if the passenger vehicle was only transporting the driver, and if the total fuel consumption and emissions were taken into account. For the motorcycle the emission values of CO and NO_x were recorded to be 47 and 92% lower respectively relative to the passenger car. This outcome was the result of the high exhaust gas aftertreatment system efficiency of the motorcycle, which existed in the form of a three-way catalytic converter (allowing oxidation of carbon monoxide and hydrocarbons with simultaneous reduction of nitrogen oxides). Moreover, the low emission values also resulted from the fact that the vehicle had a lower mileage, in contrast to the passenger car.

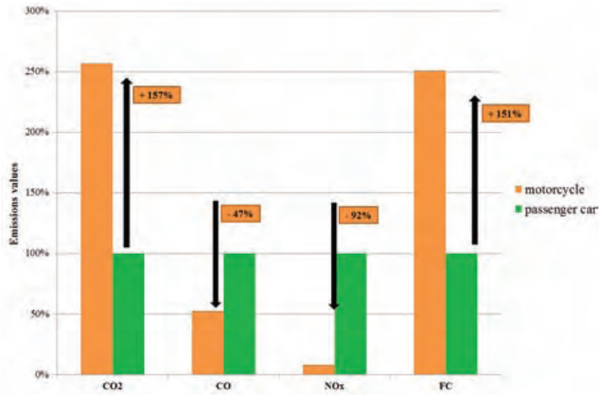

Fig. 8. Exhaust emissions comparison of gaseous compounds and fuel consumption in a passenger-kilometer conversion from the two tested types of vehicles

4. Conclusions

The tests and their analysis, which are the subject of this article, were carried out in laboratory conditions at dynamometer stations. The results allowed to formulate conclusions on the impact of particular types of vehicles on emissivity in urban agglomerations. The emission per one passenger kilometer was calculated, and thus the aspect of transport possibilities of particular types of vehicles and their impact on urban emissivity is discussed in this paper. The comparison showed significantly higher CO_2 and FC emissions (respectively by 157% and 151%) obtained during the motorcycle tests relative to the passenger car. However, lower values of CO and NO_x were recorded for the motorcycle, respectively by 47 and 92%, than for the car. This result can be explained by the high efficiency of the exhaust aftertreatment system in the form of a three-way catalytic converter. This is a positive phenomenon in the aspect of long-term engine operation and exhaust aftertreatment systems, because over time their consumption will adversely affect the ecological indicators. It is estimated that, over time, the differences between the emission values from the analyzed vehicles would gradually decrease.

Poznań is one of the largest cities in Poland, and is thus facing an increasing problem of congestion, lack of parking spaces, air pollution and noise. The solution to these issues is the introduction of the concept of sustainable transport, described in more detail in the White Book of Transport, which assumes that mass transport should prevail in the city urban core, with individual transport prevalent in suburban areas. The main purpose of this document is: "Decrease in the number of cars with conventional drive in urban transport by 2030". In addition, policies aimed at reducing the problem of congestion, and thus emissivity in urban agglomeration centers, resulted in the emergence of the concept of carpooling. Carpooling (literally translating "filling the car") means a paid system of traveling together by a private or company vehicle by several people (usually up to five), based around using all the available space in the car during the trip. In the United States of America, such a system is very popular. This publication has shown that the use of full transport capacity has a positive effect on emissions in the urban environment.

Bibliography

[1] BARLOW, T.J., LATHAM, S., McCRAE, I.S. et al. A reference book of driving cycles for use in the measurement of road vehicle emissions. 2009.

[2] DOBRZYŃSKA, E. Measurement and analysis of the use of cars in city traffic – the case of Bialystok urban area. *Economics and Management*. 2012, **4**, 73-87.

[3] ELLIS, E., CASTLE, A., FARRER K. et al. Great Manchester Transportation Unit. *GMTE Report*. 2006.

[4] EUROPEAN COMMISSION. Roadmap to a single European transport area – towards a competitive and resource-efficient transport system. *White paper of transport*. 2011

[5] PIELECHA, J. *Badania emisji zanieczyszczeń silników spalinowych*. Wyd. Politechniki Poznańskiej. Poznań 2017.

[6] Satistical Office in Poznań, Poznań statistical bulletin, 1st quarter 2018

[7] www.dynomitedynamometer.com

[8] www.globalmrv.com

[9] www.sensors-inc.com

Natalia Szymlet, MEng. – Faculty of Transport Engineering, Poznan University of Technology.
e-mail: *Natalia.R.Szymlet@doctorate.put.poznan.pl*

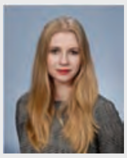

Barbara Sokolnicka, MEng. – Faculty of Transport Engineering, Poznan University of Technology
e-mail: *Barbara.D.Sokolnicka@doctorate.put.poznan.pl*

Piotr Lijewski, DSc., DEng. – Faculty of Transport Engineering, Poznan University of Technology.
e-mail: *Piotr.Lijewski@put.poznan.pl*

Maciej Siedlecki, MEng. – Faculty of Transport Engineering, Poznan University of Technology.
e-mail: *Maciej.S.Siedlecki@doctorate.put.poznan.pl*

Łukasz Rymaniak, DEng. – Faculty of Transport Engineering, Poznan University of Technology.
e-mail: *Lukasz.Rymaniak@put.poznan.pl*

Article citation info:
SZRAMA, S. F-16 turbofan engine monitoring system. *Combustion Engines*. 2019, **177**(2), 23-35. DOI: 10.19206/CE-2019-205

Sławomir SZRAMA

CE-2019-205

F-16 turbofan engine monitoring system

The multirole F-16 is the most advanced aircraft in the Polish Air Forces. It has been equipped with the very modern, sophisticated and advanced turbofan engine F100-PW-229. Due to the fact, that there is only one engine, its reliability, durability, efficiency and performance are the crucial factors for the safety reasons. In the article author researched maintenance system of the F100 turbofan engines, to describe Engine Monitoring System features. Engine Monitoring System (EMS) is the key element in the engine prognostic and health monitoring. The EMS provides engine fault indicators to the pilots and technicians and with the engine performance trending affects the F-16 flight safety risk and enhanced engine maintenance management concept. The main goal of this article was to provide information on the F-16 Engine Monitoring System and its impact on the aircraft airworthiness and F-16 fleet readiness resulting from the engine reliability. It is also an introduction to the F-16 Engine Health Management concept.

Key words: *F100 turbofan engine, F-16, Engine Monitoring System (EMS), EDU, DEEC, Engine Health Management (EHM)*

1. Introduction

The F-16 engine indicating and monitoring system allows the operator, either a pilot or technician to follow and monitor engine operation and performance.

F-16 Engine Monitoring System (EMS) (Fig. 1) provides an electronic flow of engine life usage data to the engine tracking systems. The EMS also collects information during engine operation to support maintenance personnel during engine troubleshooting. These features allow for increased aircraft availability, reduced maintenance man-hours per Engine Flight Hour (EFH), and more accurate tracking [8].

The Engine Monitoring System (EMS) forms an integral part of the overall engine maintenance management plan. The EMS acquires relevant engine data during flight. It analyzes the data and provides a concise output at the Aircraft Maintenance Unit (AMU) being flightline level to define required maintenance actions and to allow transfer of data to ground support equipment for appropriate levels of analysis and usage [1].

The main purpose of the EMS is to:

a) Determine which control system is installed and select the appropriate set of diagnostic algorithms for accurate Line Replaceable Unit (LRU) isolation.
b) Detect in-flight failures, set faults and isolate failures to the appropriate LRUs where possible.
c) Record pre- and post-event data when specific operational limits are exceeded.
d) Establish EMS fault and engine NO-GO indications that lead to determination of appropriate maintenance actions required at the flightline.

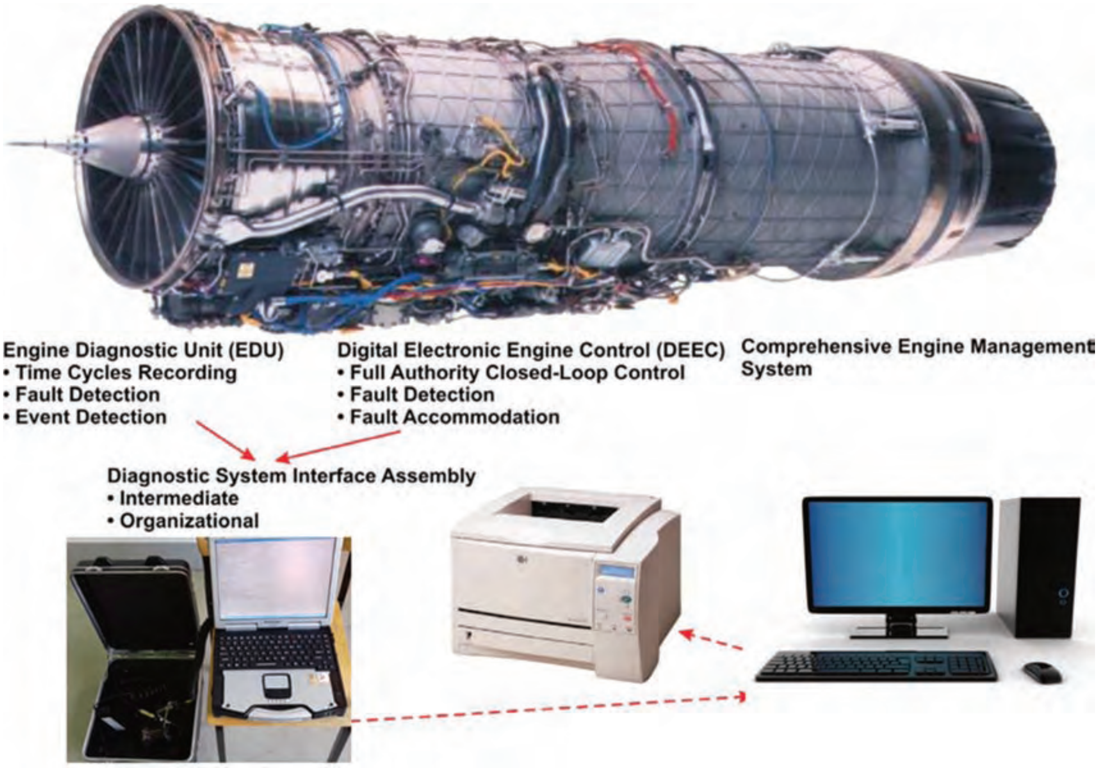

Fig. 1. Engine Monitoring System

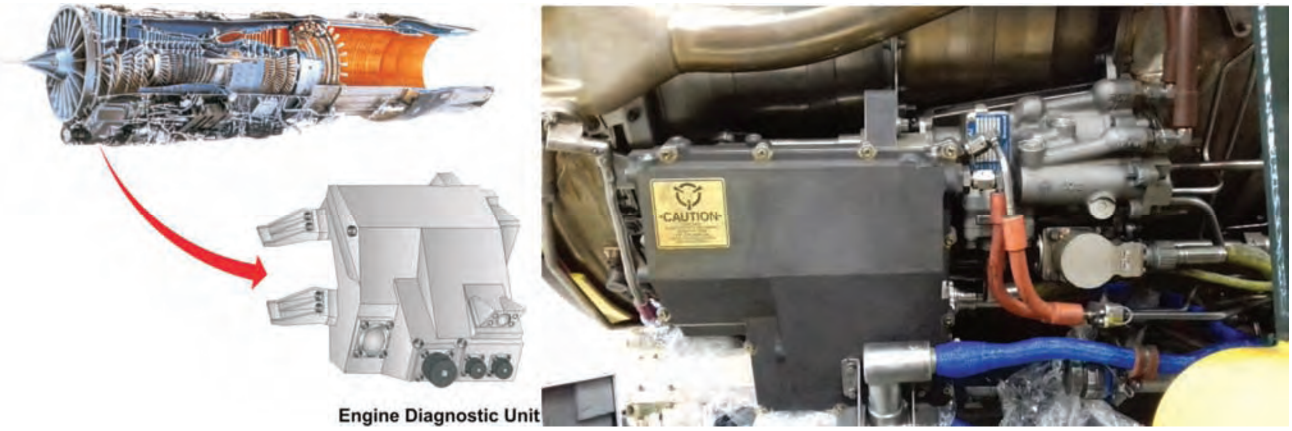

Fig. 2 Engine Diagnostic Unit (EDU)

e) Acquire parts life tracking and trending data for processing by ground support equipment and parts tracking systems.

The EMS is composed of these basic units:

a) A Digital Electronic Engine Control (DEEC) – engine mounted (Fig. 3).
b) An Engine Diagnostic Unit (EDU) – engine mounted (Fig. 2).
c) Comprehensive Engine Diagnostic Set (CEDS) (Fig. 10), Common Engine Transfer System (CETS), or Data Transfer Set (DTS) – ground equipment.
d) Comprehensive Engine Trending And Diagnostic System (CETADS) and Intelligent Trending and Diagnostic System (ITADS) or equivalent Ground Station Computer (GSC) – ground equipment.

The heart of the F100 EMS is the Engine Diagnostic Unit (EDU) (Fig. 2). This computer acquires control system and engine data from the DEEC, engine sensors, and aircraft inputs. In addition to the DEEC, the EDU (with the aircraft integrated diagnostic system), provides fault detection using acquired data. These data are also used to record maintenance information on faults and engine operation. This computer contains logic software that analyzes engine sensor data to determine engine operational integrity. The EDU records an engine anomaly as a fault message and identifies the event during flight. The EDU records fault codes, selected engine operating parameters, and time/cycle data. This fault and event data is transmitted to the Modular Mission Computer (MMC) and can be accessed in the F-16 cockpit on the Multifunctional Display (MFD) in the form of a Maintenance Fault List (MFL). Faults that require pilot action or reduce mission capabilities are displayed on the Pilot Fault List (PFL) [11].

The EDU provides the engine-to-airframe communications interface. The EDU acts as the main interconnect box for engine/aircraft signals. An event or control system fault that requires maintenance action or indicates potential engine damage will cause the EDU to trip a no-go maintenance alert flag on the Avionics Status Panel (ASP). After each flight the maintenance crew checks the ASP. If the engine no-go flag is tripped (Fig. 4), the maintenance crew uses the CEDS to retrieve the maintenance information within the EDU. If the engine no-go flag is not tripped, the engine is released for flight or the CEDS can be used to retrieve time/cycle data (at the end of the flying day). Faults requiring maintenance action before the next flight will set an EMS indicator.

Aircraft specific Fault Isolation (FI) manuals provide troubleshooting trees for fault message) and direct appropriate maintenance actions.

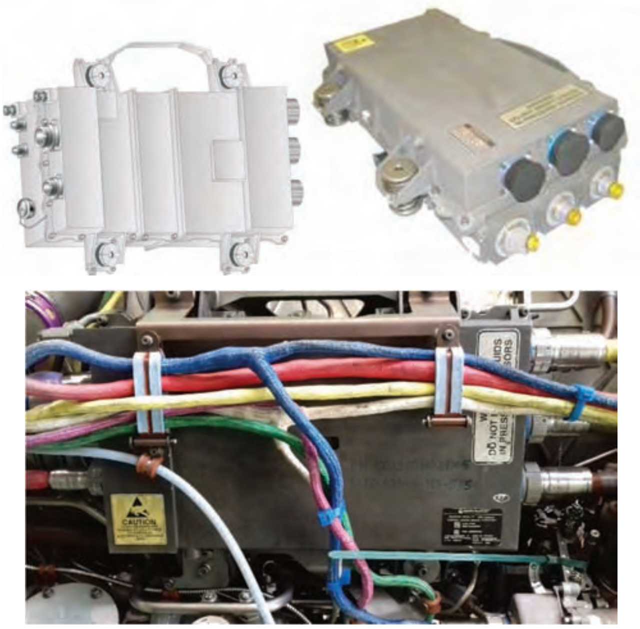

Fig. 3 Digital Electronic Engine Control (DEEC)

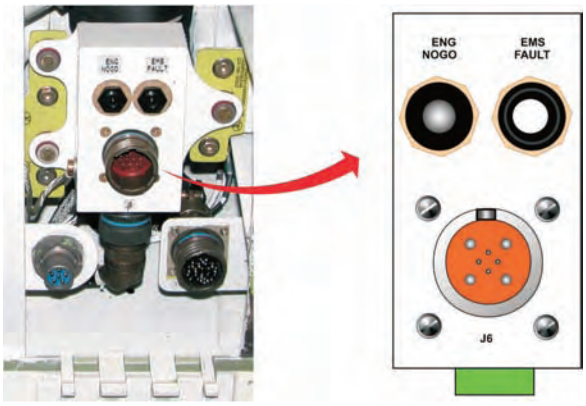

Fig. 4. F-16 System Fault Flags

2. EMS data flow

The EMS becomes operative at engine start and records performance data at takeoff. There are two types of Takeoff performance data: MIL-POWER (PLA between 83 and 90 degrees) and MAX-POWER (PLA at or above 90 degrees).

Sensor inputs from the engine are processed by the DEEC. The DEEC conditions and digitizes these signals for transmission to the engine mounted EDU. The EDU receives these signals, as well as signal inputs from the aircraft and performs diagnostic logic and data storage. Data downloading from the EDU is accomplished by connecting the CEDS, CETS or DTS to the engine. There are six types of DEEC and EDU fault or code categories: Event (EVT) codes-1000 series, DEEC faults-2000 series, EDU faults-3000 series, System faults-4000 series, Advisory faults-5000 series and Performance advisories-6000 series. ITADS faults are the 8000 series. This data is then downloaded into the ground station software, which is currently CETADS and ITADS.

EMS data flow is presented at Fig. 5.

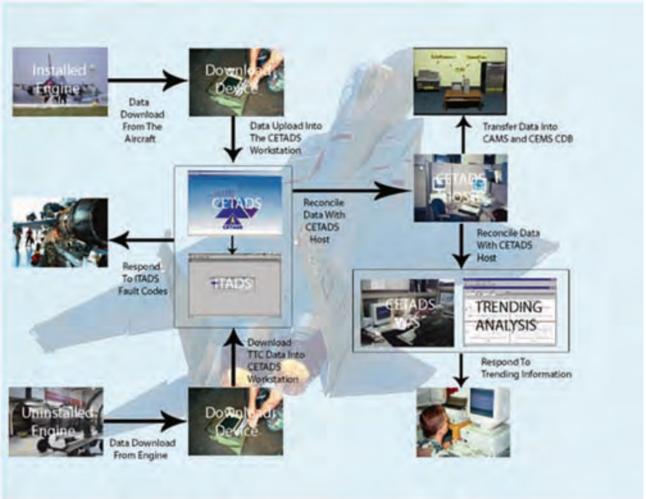

Fig. 5. EMS Data Flow

The Engine Diagnostic Unit (EDU) (Fig. 2) is an engine mounted, fuel cooled, self-contained diagnostic computer used in Monitoring System that operates with conjunction with the DEEC gr. V to acquire and record diagnostic data when the engine is operating. EDU stores data that could be collected later on with Engine Monitoring Support Equipment (EMSE) for further evaluation and analysis. The EDU receives and stores engine and aircraft sensor data, and control system data from the DEEC. These signals and data are monitored by the EDU to detect control system faults and engine malfunctions. When the EDU detects a system fault or anomaly, it records a 3-digit fault code, along with the time of event. This information is stored in the EDU and is retrievable at the flightline level for troubleshooting. The EDU receives and stores data in six basic engine usage data groups: (Fig. 6) [1].

1. Time/Cycle Data. The EDU monitors the engine for overlimit conditions. In addition, it accumulates low cycles fatigue counts and engine flight hours.
2. Event Data. The EDU monitors the engine for overlimit conditions and anomalies. The data is stored in three parts: a three digit code number which identifies the event, the elapsed time when the event occurred and critical parameters to establishing minimum maintenance requirements.
3. Fault Data. The EDU records engine control system, DEEC and EDU faults. The fault data is used to determine maintenance requirements. Faults are stored in two parts: three digit code number which uniquely identifies the source of the fault.
4. Transient Data is recorded in the EDU when an auto transfer to SEC has occurred, a random or recurrent event has taken place or when requested by the operator by positioning the AB RESET switch to ENG DATA position.
5. Performance Data. During any of the two engine operating conditions, the EDU automatically records nine parameters. The operating conditions are: on the ground at intermediate power or takeoff at intermediate or maximum power.
6. Documentary Data. It is used to for parts life tracking and configuration management.

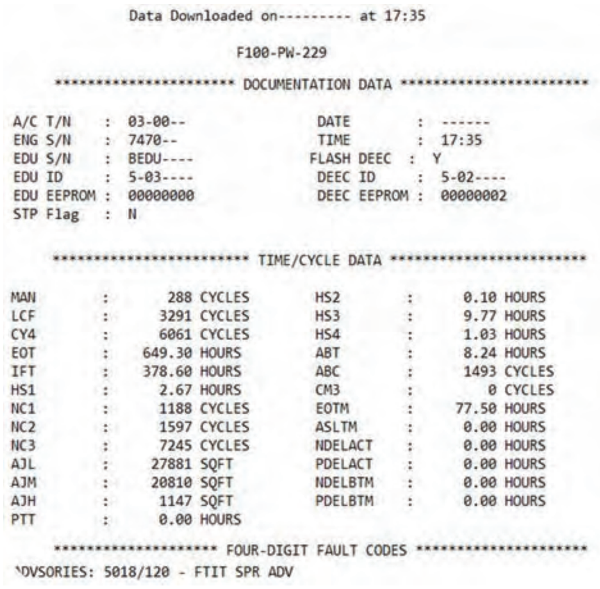

```
              Data Downloaded on--------- at 17:35

                          F100-PW-229

     ********************** DOCUMENTATION DATA **********************

A/C T/N    :  03-00--                DATE        :  ------
ENG S/N    :  7470--                 TIME        :  17:35
EDU S/N    :  BEDU----              FLASH DEEC  :  Y
EDU ID     :  5-03----               DEEC ID     :  5-02----
EDU EEPROM :  00000000               DEEC EEPROM :  00000002
STP Flag   :  N

     *********************** TIME/CYCLE DATA ***********************

MAN          :      288 CYCLES      HS2         :      0.10 HOURS
LCF          :     3291 CYCLES      HS3         :      9.77 HOURS
CY4          :     6061 CYCLES      HS4         :      1.03 HOURS
EOT          :   649.30 HOURS       ABT         :      8.24 HOURS
IFT          :   378.60 HOURS       ABC         :      1493 CYCLES
HS1          :     2.67 HOURS       CM3         :         0 CYCLES
NC1          :     1188 CYCLES      EOTM        :     77.50 HOURS
NC2          :     1597 CYCLES      ASLTM       :      0.00 HOURS
NC3          :     7245 CYCLES      NDELACT     :      0.00 HOURS
AJL          :    27881 SQFT        PDELACT     :      0.00 HOURS
AJM          :    20810 SQFT        NDELBTM     :      0.00 HOURS
AJH          :     1147 SQFT        PDELBTM     :      0.00 HOURS
PTT          :     0.00 HOURS

     ****************** FOUR-DIGIT FAULT CODES ******************
`DVSORIES: 5018/120 - FTIT SPR ADV
```

Fig. 6. EDU Engine Data

The F-16C/D Block 52 is powered by the Pratt & Whitney F100-PW-229 low-bypass, high compression ratio, fully ducted, twin–spool turbofan engine which incorporates a FADEC Digital Electronic Engine Control (DEEC).

The Digital Electronic Engine Control (DEEC) is a fuel cooled, engine mounted, full authority, electronic control, digital computer (Fig. 3). It is mounted to the front fan duct, on the left side, at approximately the 8 o'clock position. The DEEC provides precise management of thrust and airflow in response to Power Lever Angle (PLA) changes while in the Primary (PRI) mode of operation. It monitors engine temperature, speed, and pressure limits, while maintaining stall margin during steady state and transient conditions. The DEEC continually examines and accommodates control system faults. These faults are recorded as a three-digit code and stored in the DEEC, and then transferred to the EDU. If the DEEC cannot control the engine due to an engine fault, or a problem with the system itself, engine control is transferred to the Secondary (SEC) mode portion of the Main Fuel Control (MFC), thus placing the engine in SEC mode of operation.

The DEEC responds to approximately 50 input parameters and provides approximately 20 outputs to the hydromechanical components (Fig. 7). The DEEC provides the engine system with maximum level of save operation along with fault detection and accommodation. Polish Air Force are using two series of DEEC: group V and Group VI. The Group VI DEEC will incorporate all functionality of the EDU [3].

Input signals for DEEC gr V:

a) Fan inlet static pressure (Ps2)
b) Burner pressure (Pb)
c) Fan turbine discharge pressure (Pt6m)
d) Fan inlet temperature (Tt2)
e) Fan turbine inlet temperature (FTIT)
f) Front compressor speed (N1)
g) Rear compressor speed (N2)
h) Geometry position signals from Resolvers
i) Augmentor light-off detector (LOD)
j) Ps2 resistance temperature detector (RTD)
k) Metering/sequencing Valve position
l) Several airframe signals
m) Automatic warning system

DEEC VI Series: DEEC group VI has additional features:

a) Temperature sensor TT3
b) Instead of EDU there is Prognostic Health Monitor (PHM) built in DEEC (more memory available, higher resolution of data scan)
c) Predictive Prognostics
d) Useful Life Remaining Predictions
e) Component Life Tracking
f) Performance Degradation Trending
g) Selective Fault Reporting – Only tells pilot what NEEDS to be known immediately – Informs Maintenance of the rest of the engine information
h) Supports Maintenance Decision Making & Resource Management
i) Fault Accommodation
j) Information Management

The DEEC monitors engine operation for possible anomalies. If an anomaly is detected, the DEEC will record the anomaly and inform the Engine Diagnostic Unit (EDU). The DEEC also takes corrective action depending on the severity of the anomaly.

There are 5 Engine Control Loops (Fig. 8):

a) Compressor Inlet Variable Vanes (CIVV)
b) Rear Compressor Variable Vanes (RCVV)
c) Main Fuel Control (MFC)
d) Augmentor Fuel Control (AFC)
e) Exhaust Nozzle Area (AJ)

Compressor Inlet Variable Vanes - its purpose is to improve fan efficiency and stall margin by controlling the air entering the fan.

a) Primary Mode Control
– Scheduled as a function of fan speed and TT2
b) Secondary Mode Control
– Move to fully cambered position

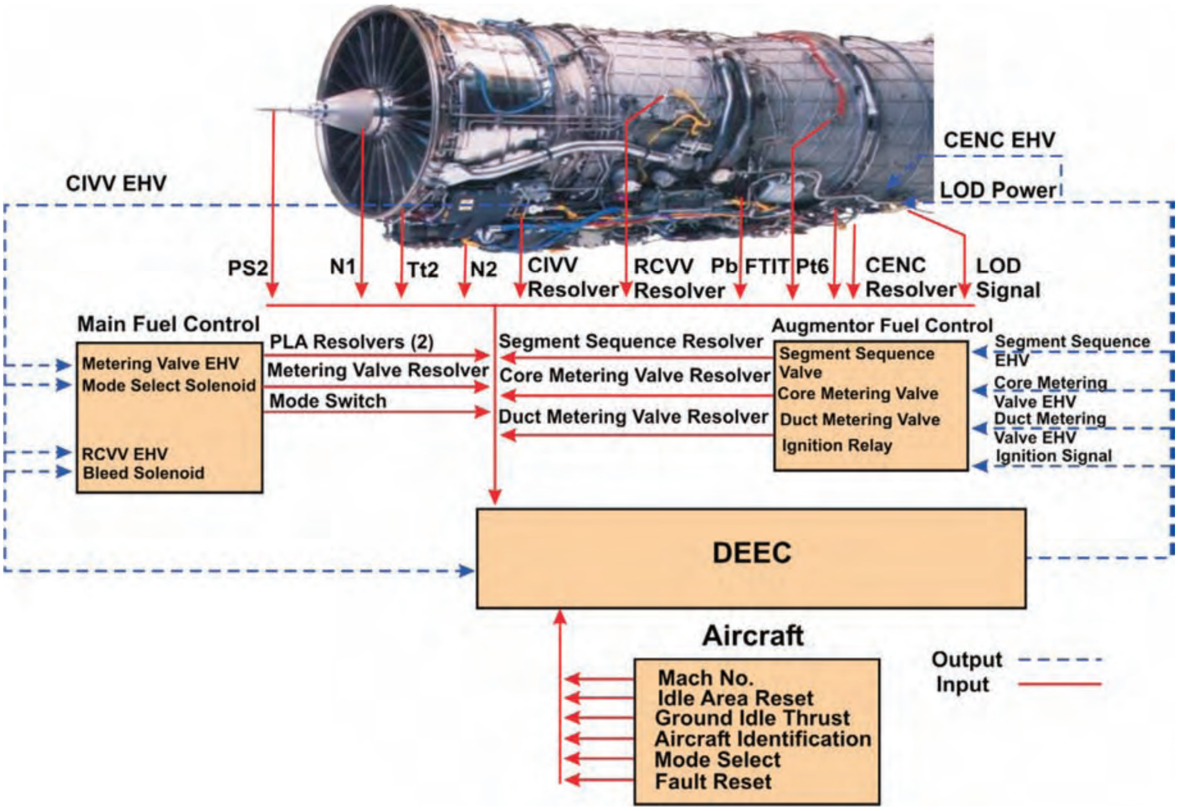

Fig. 7. F-16 Engine sensors and control - DEEC Inputs and Outputs [3]

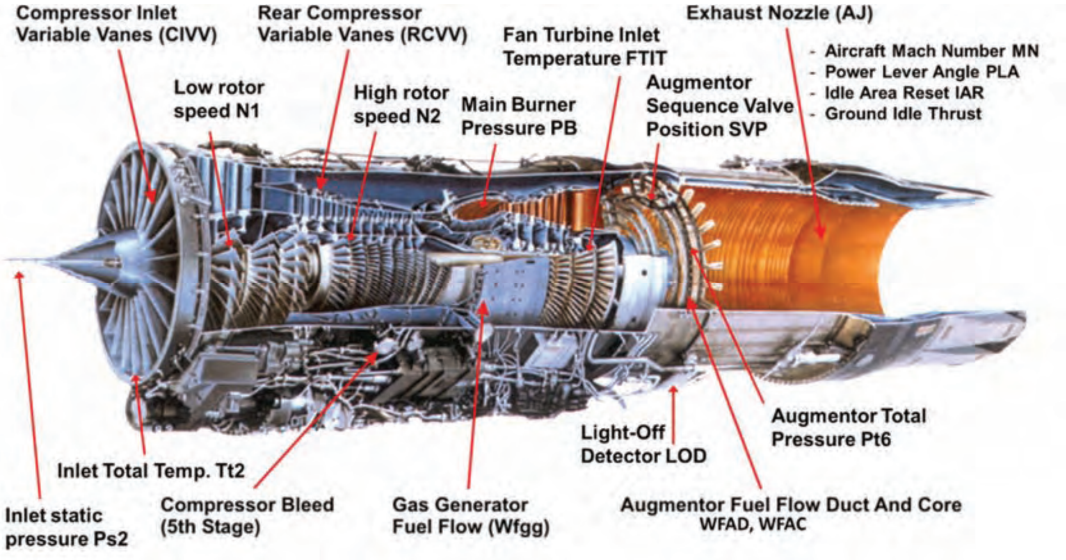

Fig. 8. Digital Electronic Engine Control Inputs and Outputs [7]

Rear Compressor Variable Vanes – its purpose is to maintain satisfactory compressor performance and stall margin over a range of operating conditions by varying the angle of the core inlet guide vanes and the following 3 stages of core stator vanes

a) Primary Mode Control

– Scheduled as a function of core speed, fan speed and TT2

b) Secondary Mode Control

– Scheduled as a function of core speed and TT2

Main Fuel Control – its purpose is to meter fuel to the core engine to increase thrust levels as a function of pilot demand.

a) Primary Mode Control

– Scheduled to maintain fan speed and EPR request, but can be overridden to ensure adequate speed, pressure temperature limits are maintained. In order to support normal engine operation in this mode MFC controls the following actions:

- increases and decreases fuel flow as scheduled by the DEEC;
- provides actuation pressure to CIVV control and cylinder;
- actuates RCVV system as scheduled by the DEEC;
- sends primary/secondary mode signal to DEEC and airframe;
- provides washed/filtered fuel regulated servo pressure to engine servos;
- actuates compressor bleed system as scheduled by the DEEC.

b) Secondary Mode Control

– Scheduled to maintain safe temperature, speed and stall margins in the absence of active speed and temperature limits. In this mode MFC reacts on:

- hydro-mechanical control of fuel flow using PLA, TT2 and PS2 as inputs.
- schedules RCVV system with TT2 and N2 as inputs.
- provides washed/filtered fuel regulated servo pressure to engine servos.
- actuates compressor bleed system during start.

During routine/daily maintenance data stored in the EDU and DEEC can be manually downloaded after every flight and viewed. Then fault data if used for troubleshooting and also to check the EDU and DEEC for any malfunctions. Data is also sent to the engine tracking section where the documentation data is checked for proper numbers.

There are five basic types of faults identified. Each fault is identified with a four digit-code.

1. DEEC V fault series:

a) 1000 series Event Fault : engine anomalies such as hung start and FTIT overtemperatures.

b) 2000 series: DEEC Fault

c) 3000 series: EDU Fault

d) 4000 series: System Faults (any control system anomalies)

e) 5000 series: Advisories

2. DEEC VI Series:

a) 1000 series: Engine anomailes

b) 2000 series: DEEC Fault

c) 4000 series: System Faults

d) 5000 series: Advisories

3. Engine Tracking System

Engine data is permanently stored by the Engine Tracking System (ETS). Complete engine history can be recalled in various reports from this system. The ETS consists of either: Comprehensive Engine Management System Increment IV (CEMS IV) used by the United States Air Force (USAF) to track engines, or Advanced Compact Engine Tracking System (ACETS) used by the air forces of other countries to track their engines [9].

The ETS tracks engines/components requiring time change and/or Time Compliance Technical Order (TCTO) action.

Transfer/download of data from the EDU is accomplished using Engine Monitoring Support Equipment (EMSE), which consists of the following:

a) Comprehensive Engine Diagnostic System (CEDS) provides complete capability to interface with the EDU/DEEC and to monitor/record engine operation in a lightweight unit.

b) The downloaded data is used to aid maintenance personnel and is transferred to the engine tracking section

The Comprehensive Engine Diagnostic Unit (CEDS) is a ground-based data collection and diagnostic system (Fig. 9) that supports F100 engines using the Engine Monitoring System (EMS). The CEDS acquires, processes, and displays engine data to maintenance crews and can transfer the data to Air Force tracking systems, such as:

a) Comprehensive Engine Management System Increment IV (CEMS IV)

b) Advanced Compact Engine Tracking System (ACETS).

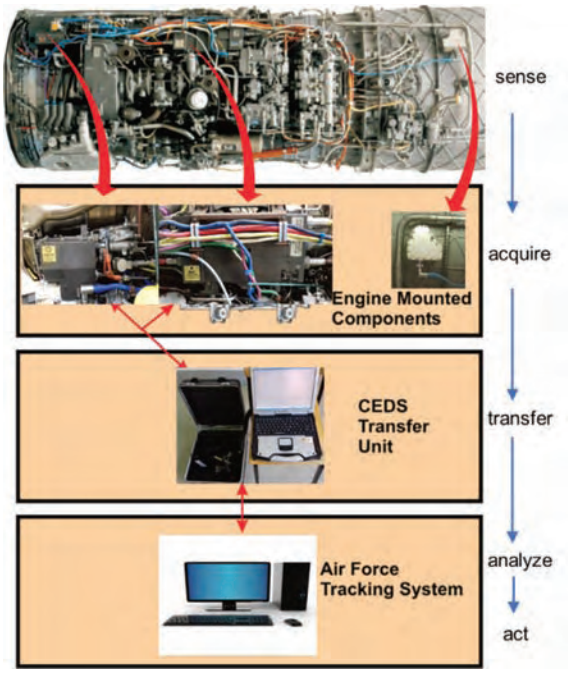

Fig. 9. Typical Engine Monitoring System

The CEDS is used to communicate with the Engine Diagnostic Unit (EDU), Digital Electronic Engine Control (DEEC), and Data Collection Unit (DCU).

Engine Downloading

Downloading is usually performed using a single CEDS transfer unit (Fig. 10) to download all aircraft in a section.

Fig. 10. Comprehensive Engine Diagnostic Set CEDS

This configuration is typically used at the end of the flying day, if the pilot reported an engine anomaly, or in the event of an EMS-reported engine malfunction (aircraft NO-GO flag tripped).

DEEC download capability supports special investigations and is not required during normal maintenance.

Only fault code data will be downloaded (without a time stamp). This data is for read-only purposes and will not be stored in the CEDS.

4. Engine Monitor

CEDS allows the operator to perform real-time monitoring of an aircraft-installed engine (O-Level) [3].

This is typically performed during engine troubleshooting or operational checks, as required by the applicable Technical Order (T.O.).

The Intermediate Maintenance (IM or I-Level) is used at the test cell, after engine maintenance, or when troubleshooting, as required by the applicable T.O. The CEDS transfer unit is permanently mounted in the control room of the Hush House in conjunction with the interconnecting box (Fig. 11).

Fig. 11. Engine Monitoring System at I-Level

The EDU downloads are normally done at the end of the day for flight-line operations, at the end of the acceptance test for test cell operations, or when faults are detected by the EMS.

The EDU download summary report (Fig. 12) provides a brief summary of downloaded data. An option is provided for the operator to examine the download data in detail. When downloading data from the EDU, CEDS will store identical data into two locations. One location is a file to transfer data to Air Force tracking systems. The other location stores the data in the CEDS database (internal memory). Up to 500 complete downloads may be stored in CEDS memory at a time.

Once CEDS memory is full, subsequent downloads are accommodated by deletion of the oldest data in CEDS memory. The transfer file grows continuously until the data is transferred to Air Force tracking systems or CEDS runs out of memory.

If CEDS detects an error during its operations, messages will be displayed to inform the operator of a malfunction.

CEDS (Fig. 10) allows the operator to download/view DEEC fault codes, clear DEEC fault codes, update DEEC logic, perform an LOD test, and view the memory locations within the DEEC that may be required to support special investigations, as requested by P&W.

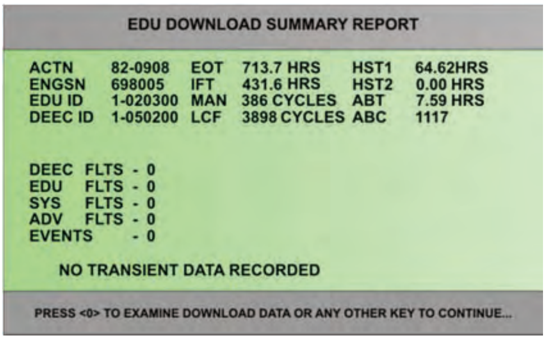

```
EDU DOWNLOAD SUMMARY REPORT

ACTN     82-0908   EOT  713.7 HRS    HST1  64.62HRS
ENGSN    698005    IFT  431.6 HRS    HST2  0.00 HRS
EDU ID   1-020300  MAN  386 CYCLES   ABT   7.59 HRS
DEEC ID  1-050200  LCF  3898 CYCLES  ABC   1117

DEEC  FLTS - 0
EDU   FLTS - 0
SYS   FLTS - 0
ADV   FLTS - 0
EVENTS     - 0

  NO TRANSIENT DATA RECORDED

PRESS <0> TO EXAMINE DOWNLOAD DATA OR ANY OTHER KEY TO CONTINUE...
```

Fig. 12. EDU Download Summary Report

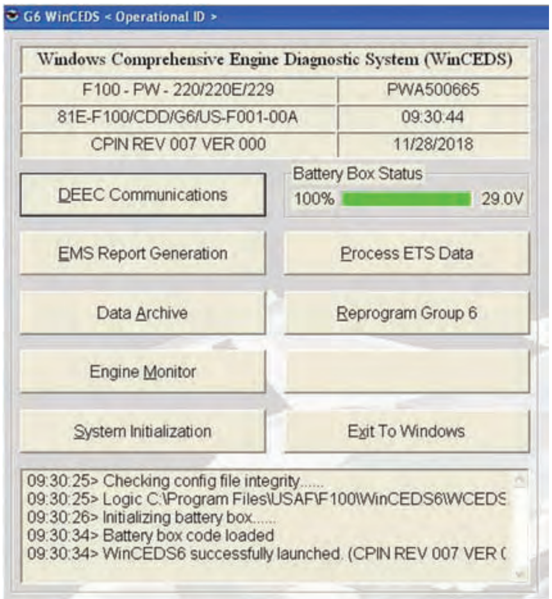

F100 - PW - 220/220E/229 | PWA500665
81E-F100/CDD/G6/US-F001-00A | 09:30:44
CPIN REV 007 VER 000 | 11/28/2018
100% 29.0V

```
09:30:25> Checking config file integrity......
09:30:25> Logic C:\Program Files\USAF\F100\WinCEDS6\WCEDS
09:30:26> Initializing battery box......
09:30:34> Battery box code loaded
09:30:34> WinCEDS6 successfully launched. (CPIN REV 007 VER (
```

Fig. 13. CEDS menu

EMS Report Generator

The EMS Report Generator option (Fig. 13-14) allows the generation and display of EMS data in several different screen formats.

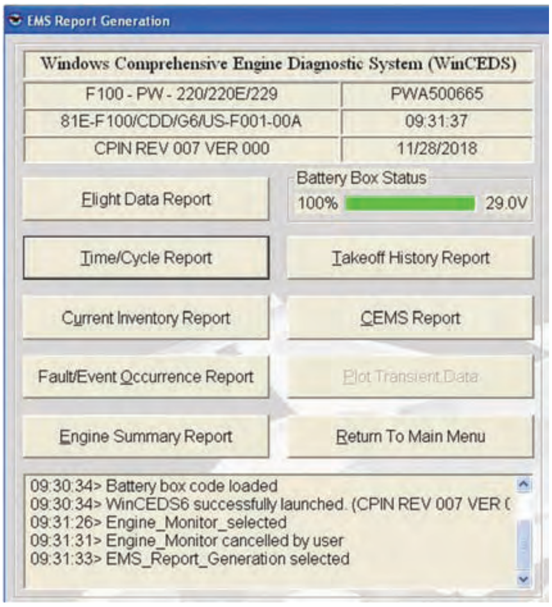

F100 - PW - 220/220E/229 | PWA500665
81E-F100/CDD/G6/US-F001-00A | 09:31:37
CPIN REV 007 VER 000 | 11/28/2018
100% 29.0V

```
09:30:34> Battery box code loaded
09:30:34> WinCEDS6 successfully launched. (CPIN REV 007 VER (
09:31:26> Engine_Monitor_selected
09:31:31> Engine_Monitor cancelled by user
09:31:33> EMS_Report_Generation selected
```

Fig. 14. EMS Report Generator submenu

The secondary menu options are described on the following pages.

1. Flight Data Report – This option allows the operator to view all or selected parts of information recorded from a selected engine for a single download.

The data may be contained on several different screens (Fig. 15-20). It shows all downloads stored in CEDS for the engine selected like:

1. Documentation data and time/cycle data:

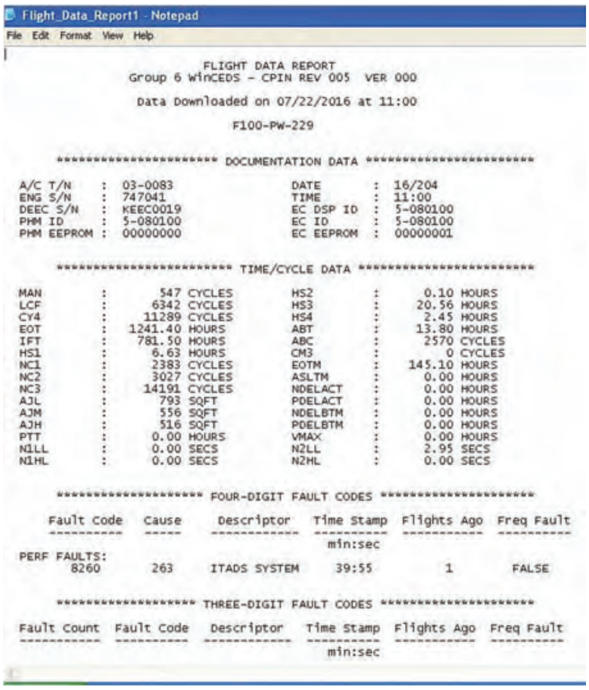

```
                     FLIGHT DATA REPORT
          Group 6 WinCEDS - CPIN REV 005  VER 000

           Data Downloaded on 07/22/2016 at 11:00

                         F100-PW-229

   ********************** DOCUMENTATION DATA **********************

A/C T/N     :  03-0083                  DATE       :  16/204
ENG S/N     :  747041                   TIME       :  11:00
DEEC S/N    :  KEEC0019                 EC DSP ID  :  5-080100
PHM ID      :  5-080100                 EC ID      :  5-080100
PHM EEPROM  :  00000000                 EC EEPROM  :  00000001

   *********************** TIME/CYCLE DATA ***********************

MAN         :      547 CYCLES           HS2        :      0.10 HOURS
LCF         :     6342 CYCLES           HS3        :     20.56 HOURS
CY4         :    11289 CYCLES           HS4        :      2.45 HOURS
EOT         :  1241.40 HOURS            ABT        :     13.80 HOURS
IFT         :   781.50 HOURS            ABC        :      2570 CYCLES
HS1         :     6.63 HOURS            CM3        :         0 CYCLES
NC1         :     2383 CYCLES           EOTM       :    145.10 HOURS
NC2         :     3027 CYCLES           ASLTM      :      0.00 HOURS
NC3         :    14191 CYCLES           NDELACT    :      0.00 HOURS
AJL         :      793 SQFT             PDELACT    :      0.00 HOURS
AJM         :      556 SQFT             NDELBTM    :      0.00 HOURS
AJH         :      516 SQFT             PDELBTM    :      0.00 HOURS
PTT         :     0.00 HOURS            VMAX       :      0.00 HOURS
N1LL        :     0.00 SECS             N2LL       :      2.95 SECS
N1HL        :     0.00 SECS             N2HL       :      0.00 SECS

   ******************* FOUR-DIGIT FAULT CODES *******************

   Fault Code   Cause    Descriptor   Time Stamp  Flights Ago  Freq Fault
   ----------   -----   ------------  ----------  -----------  ----------
                                        min:sec
PERF FAULTS:
     8260        263    ITADS SYSTEM     39:55         1          FALSE

   ****************** THREE-DIGIT FAULT CODES ******************

Fault Count  Fault Code   Descriptor   Time Stamp  Flights Ago  Freq Fault
-----------  ----------  ------------  ----------  -----------  ----------
                                         min:sec
```

Fig. 15. Documentation data and time/cycle data

2. Engine Fault Data:

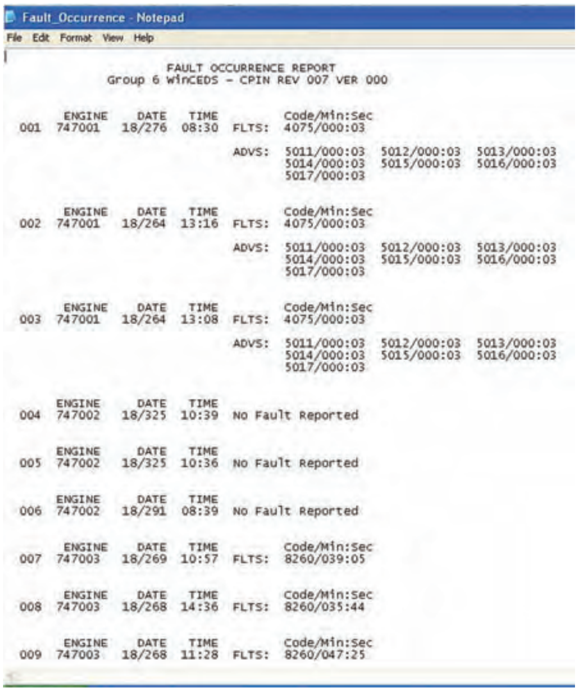

```
                 FAULT OCCURRENCE REPORT
         Group 6 WinCEDS - CPIN REV 007 VER 000

      ENGINE    DATE    TIME          Code/Min:Sec
001  747001    18/276  08:30  FLTS:  4075/000:03

                              ADVS:  5011/000:03  5012/000:03  5013/000:03
                                     5014/000:03  5015/000:03  5016/000:03
                                     5017/000:03

      ENGINE    DATE    TIME          Code/Min:Sec
002  747001    18/264  13:16  FLTS:  4075/000:03

                              ADVS:  5011/000:03  5012/000:03  5013/000:03
                                     5014/000:03  5015/000:03  5016/000:03
                                     5017/000:03

      ENGINE    DATE    TIME          Code/Min:Sec
003  747001    18/264  13:08  FLTS:  4075/000:03

                              ADVS:  5011/000:03  5012/000:03  5013/000:03
                                     5014/000:03  5015/000:03  5016/000:03
                                     5017/000:03

     ENGINE     DATE    TIME
004  747002    18/325  10:39  No Fault Reported

     ENGINE     DATE    TIME
005  747002    18/325  10:36  No Fault Reported

     ENGINE     DATE    TIME
006  747002    18/291  08:39  No Fault Reported

      ENGINE    DATE    TIME          Code/Min:Sec
007  747003    18/269  10:57  FLTS:  8260/039:05

      ENGINE    DATE    TIME          Code/Min:Sec
008  747003    18/268  14:36  FLTS:  8260/035:44

      ENGINE    DATE    TIME          Code/Min:Sec
009  747003    18/268  11:28  FLTS:  8260/047:25
```

Fig. 16. Engine Fault Data

3. Engine Performance data:

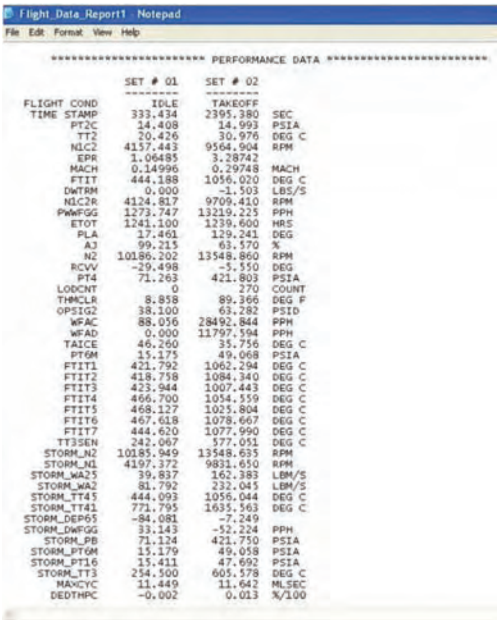

```
Flight_Data_Report1 - Notepad
File  Edit  Format  View  Help

 ************************ PERFORMANCE DATA ************************

                    SET # 01      SET # 02
                    --------      --------
   FLIGHT COND          IDLE       TAKEOFF
    TIME STAMP       333.434      2395.380  SEC
          PT2C        14.408        14.993  PSIA
           TT2        20.426        30.976  DEG C
          N1C2      4157.443      9564.904  RPM
           EPR       1.06485       3.28742
          MACH       0.14996       0.29748  MACH
          FTIT       444.188      1056.020  DEG C
         DWTRM         0.000        -1.503  LBS/S
         N1C2R      4124.817      9709.410  RPM
        PWWFGG      1273.747     13219.225  PPH
          ETOT      1241.100      1239.600  HRS
           PLA        17.461       129.241  DEG
            AJ        99.215        63.570  %
            N2     10186.202     13548.860  RPM
          RCVV       -29.498        -5.550  DEG
           PT4        71.263       421.803  PSIA
        LODCNT             0           270  COUNT
        THMCLR         8.858        89.366  DEG F
        OPSIG2        38.100        63.282  PSID
          WFAC        88.056     28492.844  PPH
          WFAD         0.000     11797.594  PPH
         TAICE        46.260        35.756  DEG C
          PT6M        15.175        49.068  PSIA
         FTIT1       421.792      1062.294  DEG C
         FTIT2       418.758      1084.340  DEG C
         FTIT3       423.944      1007.443  DEG C
         FTIT4       466.700      1054.559  DEG C
         FTIT5       468.127      1025.804  DEG C
         FTIT6       467.618      1078.667  DEG C
         FTIT7       444.620      1077.990  DEG C
        TT3SEN       242.067       577.051  DEG C
      STORM_N2     10185.949     13548.635  RPM
      STORM_N1      4197.372      9831.650  RPM
    STORM_WA25        39.837       162.383  LBM/S
     STORM_WA2        81.792       232.045  LBM/S
    STORM_TT45       444.093      1056.044  DEG C
    STORM_TT41       771.795      1635.563  DEG C
   STORM_DEP65       -84.081        -7.249
   STORM_DWFGG        33.143       -52.224  PPH
      STORM_PB        71.124       421.750  PSIA
    STORM_PT6M        15.179        49.058  PSIA
    STORM_PT16        15.411        47.692  PSIA
     STORM_TT3       254.500       605.578  DEG C
        MAXCYC        11.449        11.642  MLSEC
       DEDTHPC        -0.002         0.013  %/100
```

Fig. 17. Engine Performance Data

4. Event (maintenance) Data;

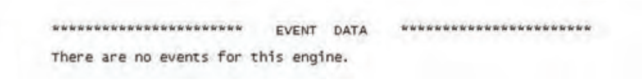

```
************************   EVENT  DATA   ************************
There are no events for this engine.
```

Fig. 18. Event (maintenance) Data

5. Engine Advisory Data:

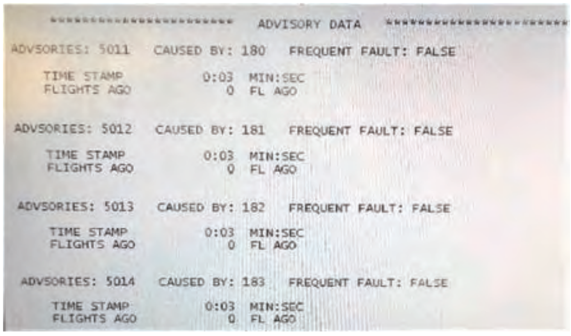

```
************************   ADVISORY DATA   ************************
ADVSORIES: 5011   CAUSED BY: 180   FREQUENT FAULT: FALSE

   TIME STAMP          0:03   MIN:SEC
   FLIGHTS AGO            0   FL AGO

ADVSORIES: 5012   CAUSED BY: 181   FREQUENT FAULT: FALSE

   TIME STAMP          0:03   MIN:SEC
   FLIGHTS AGO            0   FL AGO

ADVSORIES: 5013   CAUSED BY: 182   FREQUENT FAULT: FALSE

   TIME STAMP          0:03   MIN:SEC
   FLIGHTS AGO            0   FL AGO

ADVSORIES: 5014   CAUSED BY: 183   FREQUENT FAULT: FALSE

   TIME STAMP          0:03   MIN:SEC
   FLIGHTS AGO            0   FL AGO
```

Fig. 19. Engine Advisory Data

6. Transient data.

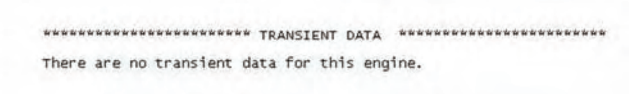

```
************************ TRANSIENT DATA ************************
There are no transient data for this engine.
```

Fig. 20. Engine Transient Data

Engine Monitor

The engine monitor option allows the operator to view/record real-time EDU (Fig. 21) or DEEC (Fig. 22) with the engine running or view DEEC parameters when the engine is static. The operator is presented with a display of selected parameters and may select up to four additional parameters.

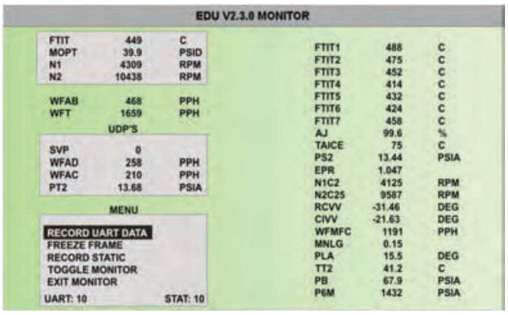

```
                         EDU V2.3.0 MONITOR

FTIT      449     C                  FTIT1     488     C
MOPT      39.9    PSID               FTIT2     475     C
N1        4309    RPM                FTIT3     452     C
N2        10438   RPM                FTIT4     414     C
                                     FTIT5     432     C
WFAB      468     PPH                FTIT6     424     C
WFT       1659    PPH                FTIT7     458     C
       UDP'S                         AJ        99.6    %
                                     TAICE     75      C
SVP       0                          PS2       13.44   PSIA
WFAD      258     PPH                EPR       1.047
WFAC      210     PPH                N1C2      4125    RPM
PT2       13.68   PSIA               N2C25     9587    RPM
                                     RCVV      -31.46  DEG
       MENU                          CIVV      -21.63  DEG
                                     WFMFC     1191    PPH
RECORD UART DATA                     MNLG      0.15
FREEZE FRAME                         PLA       15.5    DEG
RECORD STATIC                        TT2       41.2    C
TOGGLE MONITOR                       PB        67.9    PSIA
EXIT MONITOR                         P6M       1432    PSIA
UART: 10          STAT: 10
```

Fig. 21. EDU Real Time Monitor

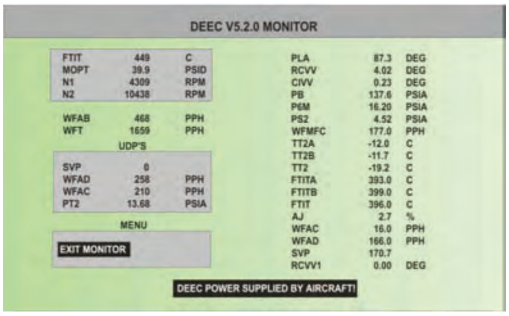

```
                        DEEC V5.2.0 MONITOR

FTIT      449     C                  PLA       87.3    DEG
MOPT      39.9    PSID               RCVV      4.02    DEG
N1        4309    RPM                CIVV      0.23    DEG
N2        10438   RPM                PB        137.6   PSIA
                                     P6M       16.20   PSIA
WFAB      468     PPH                PS2       4.52    PSIA
WFT       1659    PPH                WFMFC     177.0   PPH
       UDP'S                         TT2A      -12.0   C
                                     TT2B      -11.7   C
SVP       0                          TT2       -19.2   C
WFAD      258     PPH                FTITA     393.0   C
WFAC      210     PPH                FTITB     399.0   C
PT2       13.68   PSIA               FTIT      396.0   C
                                     AJ        2.7     %
       MENU                          WFAC      16.0    PPH
                                     WFAD      166.0   PPH
EXIT MONITOR                         SVP       170.7
                                     RCVV1     0.00    DEG

              DEEC POWER SUPPLIED BY AIRCRAFT!
```

Fig. 22. DEEC Real-Time Monitor

Troubleshooting scenario for flightline operations

When the aircraft returns, the ground crew performs the required postflight inspections including a check of aircraft system fault indicators. The ground crew takes the following actions based on the fault indicator flags.

When neither flag (Fig. 4) is tripped (NO-GO or EMS), the aircraft is released. When the NO-GO or EMS BIT flags are tripped, the technician uses Engine Maintenance Support Equipment (EMSE) to download the EDU and extract fault data.

If a fault has been recorded by the EMS, the technician refers to the Technical Order (T.O.) work package, which contains information required to troubleshoot the fault and return the engine to service.

There may be instances when the pilot or engine operator may complain about improper engine operation, but the EMS will not indicate a need for troubleshooting (no fault or event codes).

Aircraft Indications

Troubleshooting usually begins with an engine malfunction reported by the pilot. Most engine anomalies will be reported by the pilot and recorded by the EMS. However, some engine faults will be recorded only by the EMS (without the pilot noticing any fault exists). The pilot may report some engine anomalies only (no EMS data).

Cockpit indicators can be verified to ensure that the fault exists with the engine and not the airframe. It is done by using the Comprehensive Engine Diagnostic System (CEDS) to check the engine EMS faults that are recorded. Indicators in the cockpit may be erroneous due to an airframe malfunction.

The pilot monitors engine parameters through gauges mounted in the cockpit (Fig. 23).

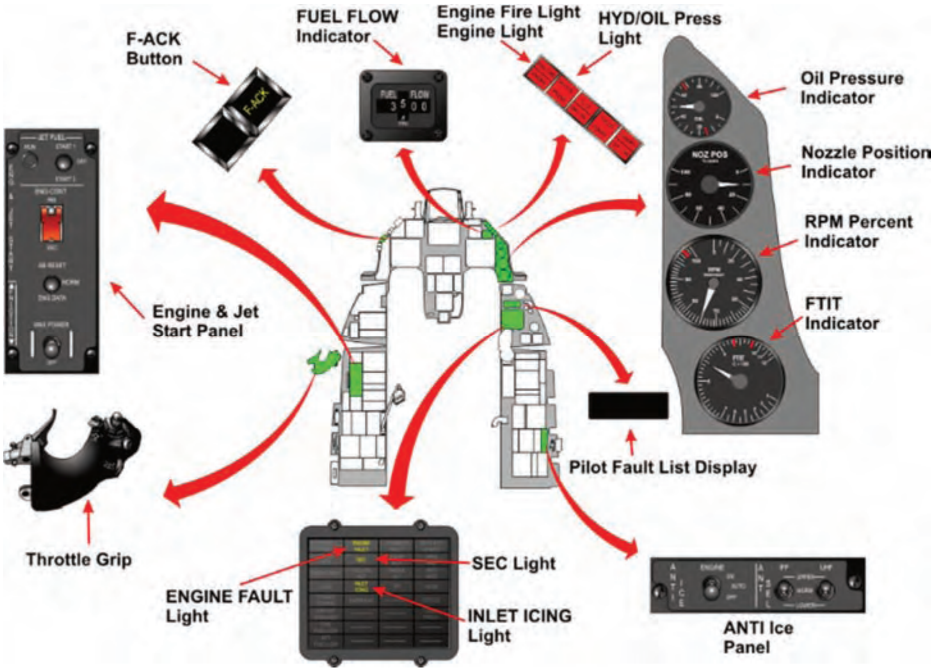

Fig. 23. Engine Controls and Indicators [1]

Table 1. Engine indicators

Indicator	Description
HUD (Head-Up Display)	Warnings, Fuel, Pilot Fault List (PFL)
Master Caution	Illuminated for all warnings displays and PFLs
Engine Fire	Engine Bay Temperature >765°F
HYD/OIL	Engine Oil Pressure < 10 PSI
ENGINE	Engine overtemperature, flameout or stagnation
PFLs (located on the data entry display)	Pilot Fault List
A/B Failure	Augmentor Failure
Mach No. Failure	Loss of the Mach signal to the DEEC
DEEC/EDU Communication Failure	Loss of the multiplex (MUX) communication to the EDU/DEEC
Anti-ice overtemperature	Anti-ice problems
Anti-ice valve Failed Closed	Anti-ice problems
Engine Low Thrust (indicates both FTITA and FTITB signals failed)	Engine Low Thrust
A/C Engine MUX-Bus Failure	Caution Panel, Engine in Secondary Mode (SEC)
Engine Fault	PFL Fault present
Overheat	Engine bay overheat
Inlet Icing	Icing Condition Present
Fuel/Oil Hot	Fuel temperature is hot causing a hot oil condition
UCADC	Upgraded Central Air Data Computer Failure

The engine parameters that are monitored in the cockpit are:

1. Core rotor speed: N2 (% RPM)
2. Fan turbine inlet temperature: FTIT (°C)
3. Fuel flow: (PPH)
4. Exhaust nozzle position: ENP (%)
5. Main oil pressure: MOP (PSI).

Caution lights alert the pilot to warnings or malfunctions and indicate the engine system affected. The pilot takes appropriate action required by the indication.

F-16 engine indicators are shown in Table 1.

5. Engine fault troubleshooting procedure

Engine troubleshooting procedures are the part of Technical Manual Fault Isolation Power Plant MODEL F100-PW-229 [12]. This manual provides fault identification, description and isolation procedures for power plant system.

Fault Identification and Description.

The fault diagnostic logic information appears in the body of the page in block flow form (Fig. 24). This form identifies the fault as well as relevant conditions leading to a specific eight-character numeric-alphanumeric code. It provides the conditions existing at the time the fault occurred and/or, when applicable, a crossreference listing from self-test failed test number to a fault code.

As an example, a complete fault code as would appear on a fault identification page or in a job guide test result (except for location code) is as follows: 70-00-AD-00. The fault code elements are broken down as follows:

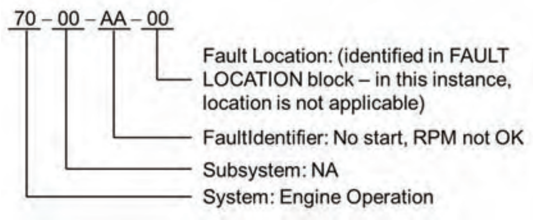

The two-letter fault identifier used to identify faults is assigned so that the first letter identifies the basic fault. The second letter identifies a subfault found within the basic fault.

Fault Isolation Procedures

The user will find the fault isolation procedure for the required fault code on the appropriate fault isolation procedure flow chart. Each fault code is followed by a series of action instructions contained in rectangular blocks with the monitored results of the actions outside the blocks (Fig. 24). These actions terminate with fault correction instructions or reference to a schematic diagram or another system fault isolation manual for further fault analysis. The action blocks also contain any required reference to locator data, schematic or wiring diagrams, or job guide function in parentheses (Fig. 24).

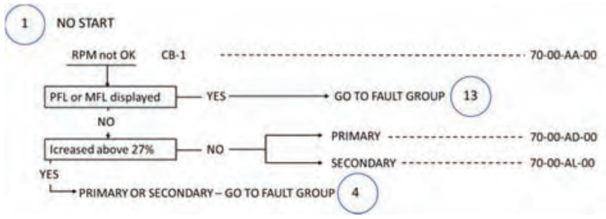

Fig. 24. Fault Isolation Flow Chart [12]

The next step of the fault troubleshooting it to follow the procedures in the LOG BOOK REPORT (70-00-00) section of the aforementioned fault isolation manual (Fig. 25).

Information from the Log Book Reports leads to the fault tree. In this case: 70-00-AA (Fig. 25). Fault tree of our interest is described in the Fault Isolation Information (70-00-00) (Fig. 26).

In our case scenario first step of the fault isolation procedure is to review even/fault data in accordance with the supplemental data described in Tables 9-1 and 9-5 (Fig. 26). Supplemental data from Table 9-1 provides the information about EMS data downloading procedures (Table 2).

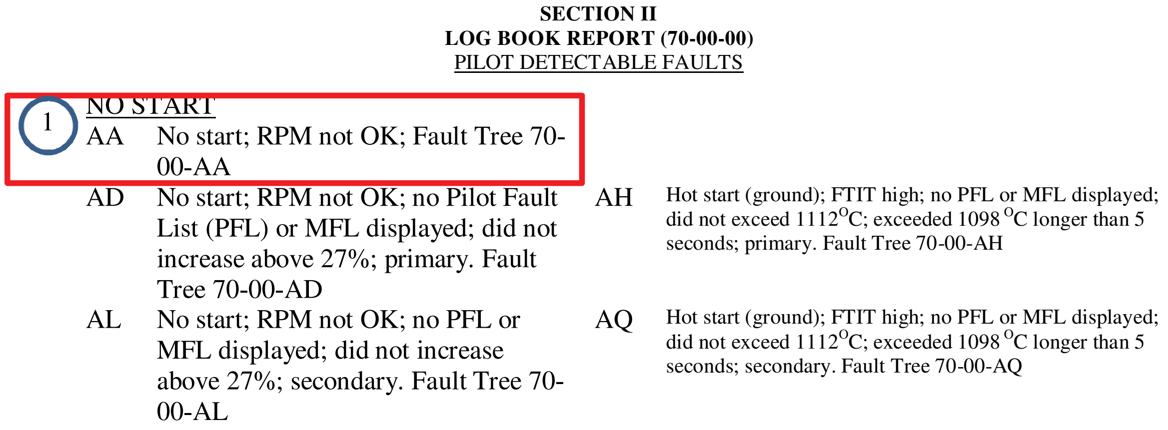

SECTION II
LOG BOOK REPORT (70-00-00)
PILOT DETECTABLE FAULTS

① NO START

AA	No start; RPM not OK; Fault Tree 70-00-AA		
AD	No start; RPM not OK; no Pilot Fault List (PFL) or MFL displayed; did not increase above 27%; primary. Fault Tree 70-00-AD	AH	Hot start (ground); FTIT high; no PFL or MFL displayed; did not exceed 1112^{O}C; exceeded 1098 ^{O}C longer than 5 seconds; primary. Fault Tree 70-00-AH
AL	No start; RPM not OK; no PFL or MFL displayed; did not increase above 27%; secondary. Fault Tree 70-00-AL	AQ	Hot start (ground); FTIT high; no PFL or MFL displayed; did not exceed 1112^{O}C; exceeded 1098 ^{O}C longer than 5 seconds; secondary. Fault Tree 70-00-AQ

Fig. 25. Log book report (Fault code 70-00-AA) [12]

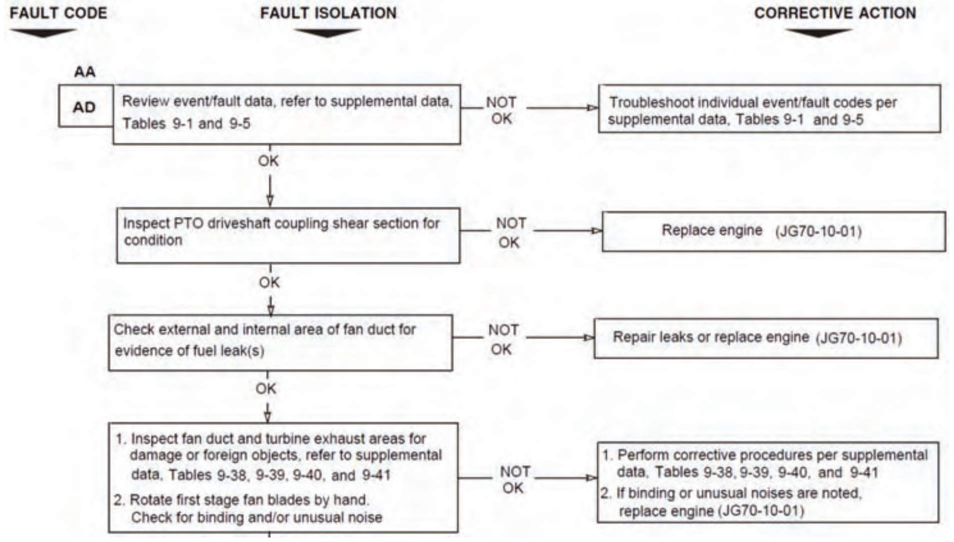

Review event/fault data, refer to supplemental data, Tables 9-1 and 9-5

Troubleshoot individual event/fault codes per supplemental data, Tables 9-1 and 9-5

Inspect PTO driveshaft coupling shear section for condition

Replace engine (JG70-10-01)

Check external and internal area of fan duct for evidence of fuel leak(s)

Repair leaks or replace engine (JG70-10-01)

1. Inspect fan duct and turbine exhaust areas for damage or foreign objects, refer to supplemental data, Tables 9-38, 9-39, 9-40, and 9-41
2. Rotate first stage fan blades by hand. Check for binding and/or unusual noise

1. Perform corrective procedures per supplemental data, Tables 9-38, 9-39, 9-40, and 9-41
2. If binding or unusual noises are noted, replace engine (JG70-10-01)

Fig. 26. Fault tree. Fault isolation information [12]

Table 2. Fault Data Review procedure

PROCEDURE	NORMAL INDICATION	REMEDY FOR ABNORMAL INDICATION
Aircraft safe for maintenance (JG10-30-01) Power source: Battery Support Equipment: Common Engine Transfer Set 1. Open access door 3309 and 3316 2. Connect data download cable to receptacle J1 on CETS unit 3. Connect data download cable to receptacle J146/1 4. Position laptop power switch to ON 5. Select WinCEDS from menu shell program or double click on WinCEDS icon 6. With CET unit on main menu, select EDU COMMUNICATIONS 7. Select EDU DOWNLOAD. Verify cable connection. Select OK	No faults/events displayed	Troubleshoot existing events/faults per supplemental data, Table 9-5. If communication error is displayed, replace CETS and cables. If problem persists go to fault code 77-00-ZF

If there are no engine fault codes downloaded from either EDU or DEEC then one should follow the Fault tree branch downwards from (Fig. 26). In case there are some fault codes downloaded one should follow the supplemental data in Table 9-5 (Table 3 and Table 4).

There are six basic types of events/faults. Each event/fault is identified with a four-digit code. A different series of numbers is used for each fault type; i.e., EDU events are 1000 to 1999, DEEC faults 2000 to 2999, EDU faults 3000 to 3999, system faults 4000 to 4999, and EDU advisory faults 5000 to 5999, and 8000 series ITADS faults.

Intelligent trending and diagnostics system (ITADS) faults are displayed as four digit code numbers (8000 series) on the comprehensive engine trending and diagnostics system (CETADS) only after engine data is downloaded from the EDU and uploaded to the engine management computer running the CETADS software. ITADS only utilized takeoff performance data sets. It does not utilize ground performance data sets or test cell performance data [9].

Let us assume that the fault code downloaded was the 1120 (Table 5).

Corrective action should be followed in accordance with the chart “P” (Table 6). If the engine control mode was the PRIMARY MODE then one should go to fault code 70-00-AD. In case it was SEC MODE – fault code 76-00-BG.

Following the Log Book Report (Fig. 27) one may find the right corrective action searching for the Fault tree 70-00-AD.

Part of the fault isolation procedure of the fault tree 70-00-AD is shown in the Fig. 28.

Table 3. EDU event. EDU fault, DEEC fault, System fault and EDU advisory code reference

MFL / PFL CODES	FAULT CODES	EVENT/FAULT DESCRIPTION	CORRECTIVE ACTION		
			CHART	TABLE	MIDAS FAULT CODE

Table 4. Supplemental data for EDU event, EDU fault, DEEC fault, system fault, cont.

MFL/PFL CODES	FAULT CODES	EVENT/FAULT DESCRIPTION	CORRECTIVE ACTION		
			CHART	TABLE	MIDAS FAULT CODE
023	4054	RCVV Resolver Number 2 Position			76-00-ZY
024	4050	RCVV Resolver			76-00-ZS
025	1000	Stagnation	A		

Table 5. Supplemental data for EDU event, EDU fault, DEEC fault, system fault, cont.

MFL/PFL CODES	FAULT CODES	EVENT/FAULT DESCRIPTION	CORRECTIVE ACTION		
			CHART	TABLE	MIDAS FAULT CODE
036	1090	N2 Overspeed	G		
037	1120	Engine No Start	P		
038	1151	Axial RCVV Flutter	H		

Table 6. CHART P. Engine no start corrective procedures

CHART P. ENGINE NO START	
NOTE • If fault was recorded during wet or dry motoring procedure, or engine depreservation, trouble shooting is not required. • Following data may be obtained during engine data review to determine appropriate troubleshooting procedure: control mode (primary or secondary)	
PRIMARY	SECONDARY
A	B
CORRECTIVE ACTION	
“A” – Go to fault code 70-00-AD	“B” – Go to fault code 76-00-BG

Let us assume one have reached to the point when we should check main fuel gear pump filter assembly IAW supplemental data from Table 9-32 (Table 7).

While inspecting fuel filter one finds it clogged by a foreign material. Then one should install filter IAW Job Guide JG73-00-09 (Table 8).

The next step of the troubleshooting procedure is to perform engine start and leak check IAW (JG70-00-01) as a follow-on maintenance of the MFGP Fuel Filter element, removal and installation procedure IAW T.O PL1F-16CJ-2-73JG-00-21 (Table 9).

This step ends fault isolation procedure. As a result of the case study research we may propose the Engine Discrepancy Removal Schematic Diagram (Fig. 29).

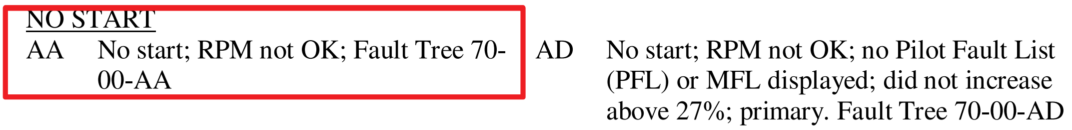

NO START

AA No start; RPM not OK; Fault Tree 70-00-AA

AD No start; RPM not OK; no Pilot Fault List (PFL) or MFL displayed; did not increase above 27%; primary. Fault Tree 70-00-AD

Fig. 27. Log Book Report (Fault code 70-00-AD)

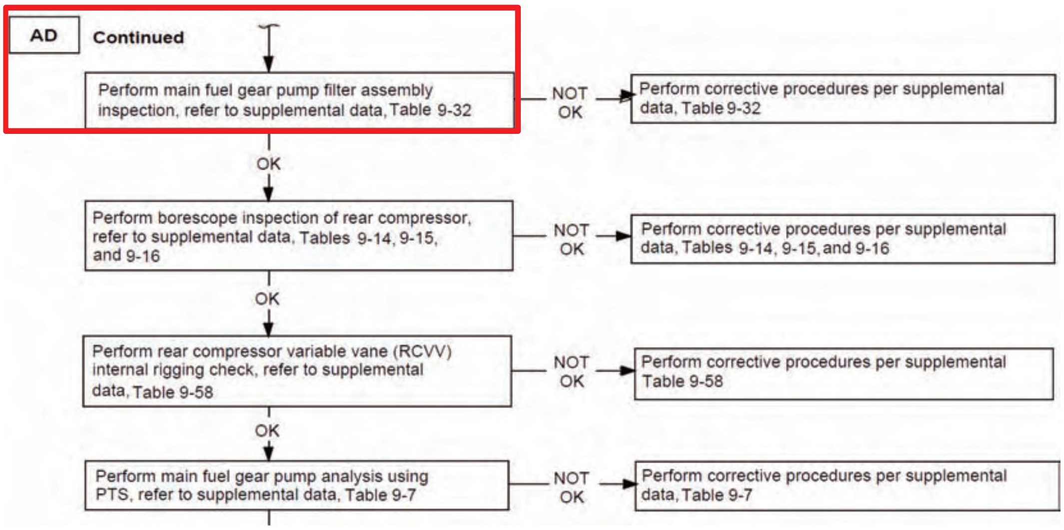

Fig. 28. Part of the Engine Fault Tree (Engine Fault 70-00-AD)

Table 7. Supplemental data. Main fuel gear pump filter assembly inspection procedure (part of Table 9-32)

NOTE Instructions for main fuel gear pump filter assembly inspection are unique to gear / pump bypass valve configuration 1. Remove main fuel gear pump filter (JG73-00-09) 2. Visually inspect filter assembly (Figure 9-48) as follows:			
INSPECTION AREA	CONDITION	MAXIMUM SERVICEABLE LIMITS	CORRECTIVE ACTION
Fuel filter cover	Cracks or distortion	None	Replace cover
	Stripped, crossed or worn threads	None	Replace cover
	Packing groove for wear and foreign material build-up	None	Remove foreign material. If grooves are damaged, replace cover
	Differential pressure indicator housing operation	None	If housing is damaged or operation is not smooth, replace cover. After check, reset differential pressure indicator by inverting fuel filter cover and pressing button. If indicator does not reset, replace differential pressure indicator (JG73-00-25)

Table 8. Troubleshooting procedure for the clogged filter (part of Table 9-32), cont.

PROCEDURE
3. Install main fuel pump filter (JG73-00-09)

Table 9. Part of the MFGP Fuel Filter element, removal and installation procedure

TO PL1F-16CJ-2-73JG-00-21
FOLLOW-ON MAINTENANCE:
• (2) Perform engine start and leak check (JG70-00-01).

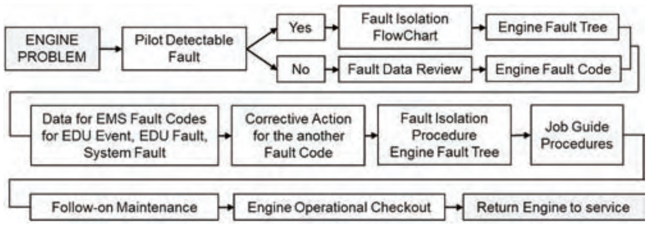

Fig. 29. Engine discrepancy removal schematic diagram. Own elaboration

6. Summary

Engine Monitoring System (EMS) is the key element in the engine prognostic and health monitoring. This is also the integral part of the engine performance trending. It allows to track engine performance parameters and their projections using historical data. In cooperation with Prognostic Health Monitor (PHM) and Engine Management And Tracking System (EMATS) it allows engine maintenance personnel for an easier troubleshooting and improvements implementation (right maintenance in right time), Time Accumulated Cycles TACs counting, engine parameters analysis, life time usage and the possibility of forecasting engine life remaining time. As a result, it is possible to manage engine components replacement, modules, and forecasting spare parts in advance.

As most of the complex systems it requires special preparation and experienced personnel. It supports engine tracking personnel in their work but it will never replace experienced and qualified personnel in engine diagnosis and prognostics.

It is very important to stress that while performing engine discrepancies removal sometimes corrective actions described in the fault isolation manual are just the most probable solution of the encountered problem. It does not guarantee that all engine discrepancies found during flight operations could be removed with the proposed corrective actions. In many cases one goes through the whole engine troubleshooting process, reaches the end of the engine fault tree and does not find the solution for the encountered engine problem.

Nomenclature

AJ	Exhaust nozzle area
AJRATIO	Exhaust nozzle area ratio (Aj CENC feedback / calculated Aj for choked nozzle)
CEDS	Comprehensive Engine Diagnostic Set
CEMS	Comprehensive Engine Management System
CENC	Convergent Exhaust Nozzle Control
CETADS	Comprehensive Engine Trending And Diagnostic System
CETS	Common Engine Transfer System
CIVV	Compressor Inlet Variable Vanes
DEEC	Digital Electronic Engine Control
EDU	Engine Diagnostic Unit
EHM	Engine Health Management
EMB	Engine Management Branch
EMS	Engine Monitoring System
EOT	Engine Operating Time
EPR	Engine Pressure Ratio
FLT	Fault
FTIT	Fan Turbine Inlet Temperature
GSC	Ground Station Computer
ITADS	Intelligent Trending And Diagnostic System
LODCNT	Light Off Detector Count
MFC	Main Fuel Control
MNAC	Aircraft Mach Number
MOP	Main Oil Pressure
N1	Fan speed
N1C2	Corrected fan speed
N2	Core speed
PB	Burner pressure
PLA	Power Lever Angle
PT4	Combustion chamber discharge
TAC	Total Accumulated Cycles
Tt2	Fan Inlet Total Temperature
WFAC	Augmentor fuel flow, core
WFAD	Augmentor fuel flow, duct
WFMFC	Main fuel control fuel flow

Bibliography

[1] Lockheed Martin STM 16-329PL (Poland Block 52) F100-PW-229 Power Plant.
[2] F100 Pratt&Whitney F100 WUC, October 2018.
[3] F100-PW-229 Periodic Engineering Excellence Reviev.
[4] Lockheed Martin Aero Flight Safety, Operations and Maintenance, June 2018.
[5] International Engine Management Program, October 2018.
[6] Technical Manual T.O.00-20-1 Aerospace Equipment Maintenance Inspections, Documentation, Policies and procedures.
[7] F100 Pratt&Whitney F100 WUC, October 2018.
[8] Technical Manual General System Organizational Maintenance Power Plant Model F100-PW-229 Technical Order PL1F-16CJ-2-70GS-00-21.
[9] Engine Management and Tracking System EMATS Maintenix
[10] F100-PW-229 Engine Interactive Electronic Technical Manuals.
[11] Technical Manual Maintenance Instructions Intermediate Level Introduction and General Information Aircraft Engine F100-PW-229 Technical Order 2J-F100-56-1.
[12] Technical Manual Fault Isolation Organizational Maintenance Power Plant Model F100-PW-229 Technical Order PL1F-16CJ-2-70FI-00-21.

Sławomir Szrama, DEng. – Squadron Commander at 31^{st} Air Force Base Poznań-Krzesiny.
e-mail: *s.szrama@ron.mil.pl*

Article citation info:
CUPER-PRZYBYLSKA, D. Pressure measurement in the cylinder of four-stroke marine engine – simulation analysis. *Combustion Engines*. 2019, **177**(2), 36-39. DOI: 10.19206/CE-2019-206

Dominika CUPER-PRZYBYLSKA

CE-2019-206

Pressure measurement in the cylinder of four-stroke marine engine – simulation analysis

The measurement of combustion pressure relies on connecting a pressure sensor to a four-stroke marine engine cylinder by a channel led out from the engine cylinder. The geometry of the channel distorts the results of combustion pressure measurements. The purpose of the work is to create a model of combustion processes in engine cylinders. The model uses a mathematical description of the indicator channel on one of the engine cylinders. The input data to the model and the data necessary for its verification came from the direct measurements on the research facility. The test object was a four-stroke Sulzer 3AL25/30 engine loaded by an electric power generator. During calculations, different diameters and lengths of measurement channel were simulated. The obtained results allowed to formulate the conclusion that the geometry of the measurement channel has a significant impact on the measurement results. The increase of the length of the measuring channel as well as the diameter of the channel causes disturbances in the measurement of the maximum pressure.

Key words: *diesel engine, marine engine, combustion pressure, indicator channel*

1. Introduction

Measurement of combustion pressure is a very important parameter in the diagnosis of marine Diesel engines. The measuring of combustion pressure allows detecting e.g.: a problem with piston rings leakage or a problem with fuel injection. Ship engines operate continuously for hundreds of hours, powering a ship or operating as an auxiliary engine on a ship that generates electrical energy. Therefore, proper diagnostics will enable early detection of a technical problem related to the proper functioning of the engine and avoid the withdrawal of the engine of operation as well as costly repairs.

However, measurement directly in the cylinder of the engine is often impossible due to the engine's construction as well as the high temperatures prevailing in the cylinder during engine operation. Mounting sensors that would be able to record cylinder pressure changes would increase engine costs.

Therefore, for measuring the combustion pressure in medium and low speed marine engines, a drainage channel is used from the piston engine cylinder ended with an indicator cock, later called the indicator channel. The main task of the channel is to remove water and impurities from the engine cylinder during initial engine rotation and blowdown. This way it protects the engines against damage caused by hydro-impact. During the engine operation, this channel is also used to measure the combustion pressure. The sensor is mounted on an indicator cock, i.e. at the end of the indicator channel. Such assembly causes the sensor to be removed from the cylinder. This assembly reduces the cost of combustion pressure measuring. However, the results of the pressure measurement show a discrepancy between the actual cylinder pressure and the pressure on the sensor in the indicator cock.

The shape of the indicator channel can cause discrepancies. Between the cylinder and the sensor on the indicator cock, the diameter of the channel changes as well as bends appear at different angles in the channel. The Kistler company, which produces piezoelectric pressure sensors, already indicates the problem of combustion pressure measurement, caused by the shape of the channel resulting from the natural frequency of the indicator channel. In order to correct the measurement carried out, they indicate that the use of the Bergh and Tijdeman model based on flow equations [1].

Engin Oezatay also mentions this problem of the actual measurement of the combustion pressure, but the reason for the distortion is the phenomenon of Helmholtz resonance occurring in the indicator channel [2].

The article aims to show the influence of the dimensions of the indicator channel to values of measured maximum combustion pressure. Special attention is paid to the maximum pressure in the indicator channel deviates from the value of the combustion pressure in the engine cylinder.

2. Research facility

The implementation of the work objective requires the selection of a research facility. The requirement for the test facility is the possibility of obtaining detailed data related to the geometry of the charge system and the fuel system. The facility consists of 3-cylinder Al25/30 Sulzer engine and electric power generator. The engine is in the marine version. This means, among other things, that the engine cooling system is based on a high and low-temperature water circuit, with the low-temperature circuit being sea water, in this case the external water system, cooled by two cooling towers. The engine is charged by the VTR 160 Brown-Boveri turbocharger and intercooled.

The fuel system consists of Bosch type injection pumps, controlled by the rotational speed governor through fuel racks and multi-hole fuel injectors. Fuel injectors are centrally located in the engine cylinder heads.

The AL25/30 engine is coupled with the GD8-500-50 generator which transmits the generated electrical energy to the water resistor. The engine is installed in the Maritime Laboratory of Gdynia Maritime University and operates at a constant rotational speed of 750 rpm.

The detailed parameters of the test facility are presented in Table 1 and Figure 1 [7].

Table 1. AL25/30 engine parameters [5]

Parameter	**Unit**	**Value**
Rotational speed	rpm	750
Cylinder number	–	3
Cylinder diameter	mm	250
Stroke	mm	300
Compression ratio	–	12.7
Injection timing	° before TDC	18

Fig. 1. Photo of the SULZER 3AL25/30 piston engine facility [7]

During the tests, the engine operated with a 250 kW load determined on the basis of the electrical output power from a generator. The measurement results were recorded in quasi-steady conditions.

During the tests, the combustion pressure was registered in all engine cylinders using Kistler 6613CG1 sensors coupled to a voltage amplifier. Each observation involved 7 revolutions of the crankshaft with a sampling rate of 720 measurements per crankshaft rotation.

3. Assumptions of the model and its validation

3.1. Description of the model

The main purpose of the work need to develop a combustion model of a marine piston engine and its verification based on the actual data of the 3AL25/30 engine.

This goal can be achieved by using a one-dimensional model. This model includes the following partial models: combustion process model, model of heat exchange in the engine cylinder construction elements, model of flows in air and exhaust channels, emission model of exhaust gases, mechanical friction model, model of phenomena occurring in the turbocharger and heat exchange model in the radiator [5].

Functional dependence between individual models is presented in Figure 2.

The C1, C2 and C3 are engine cylinders in which the combustion and heat exchange process was modelled. The model also includes mathematical descriptions of cylinder valve timing, piston movement, and direct fuel injection. The cylinders are connected to the pulse exchangers J1 and J2 via the exhaust ducts The exhaust gases flow through channels 6–8 and 11 to the T turbine and exit outside via channel 9.

The ambient air parameters are entered into the model at the SB1 and SB2 nodes. The air through the channel 1 is supplied to the compressor C, then through the channel 2 to the air cooler CO1. After cooling, the air enters to engine cylinders via channels 3, 4 and 5.

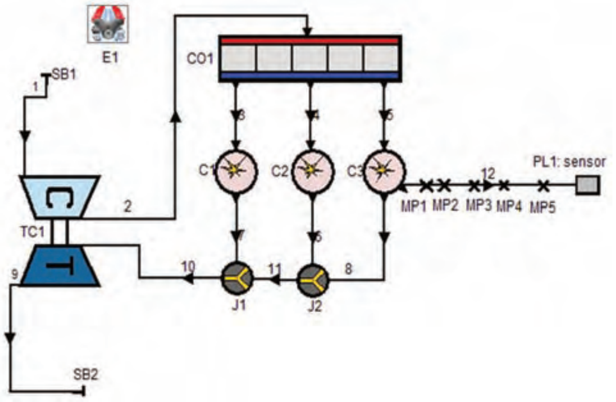

Fig. 2. Model of the research object in the AVL Boost program

The pipe number 12 it's the indicator channel MP symbols are the marked places then find the pressure sensor.

The E1 icon allows the basic engine and model parameters. The most important of them are:

- order of ignitions – in cylinders presented in the values of the rotation angle of the crank shaft, 0°, 480^0 and 240^o respectively,
- oil temperature – SAE10 equal to 67^oC [5]

3.2. Flow model

The flow through all air channels was determined based on the isentropic flow equation, taking into account the mass inertia. In order to determine the mass flow rate, the geometric dimensions of the channels, the value of the isentropic exponent, temperature and pressure as well as the composition of the exhaust gas were needed. The geometrical dimensions were measured on the real object, while the initial values of thermodynamic parameters were adopted. In the case of air ducts as for the measured parameters after the air cooler, and for exhaust gases as for the measured gas parameters. The calculated thermodynamic parameters were determined using the Runge-Kutta iterative method [3].

It should be noted that the geometry of the exhaust gas channels behind the engine cylinders can contribute to the backflow of exhaust gases to adjacent cylinders. For this reason, these channels need to be routed to the collector collecting at an angle. In order to model this state of affairs, the so-called pulse exchangers (J1 and J2 in Fig. 2) are implemented.

Resistance movement in the channels was model using Equation 1:

$$\frac{F}{V} = \varphi \frac{\lambda_f}{2d} \rho u^2 \tag{1}$$

where: F – resistance [N], V – volume [m^3], φ – Fanning coefficient of friction [-], value for the round section is 1, λ_f – coefficient of resistance depending on the type of flow (laminar, mixed, turbulent), d – channel diameter [m], u – flow speed [m/s], ρ – gas density [kg/m^3].

In all gas channels, there is also heat exchange with the environment through convection. The heat transfer coefficient for channels was determined by the Reynolds analogy method [4].

3.3. Model validation

The pressure sensor in the indicator channel on the real object is mounted as shown in Figure 3.

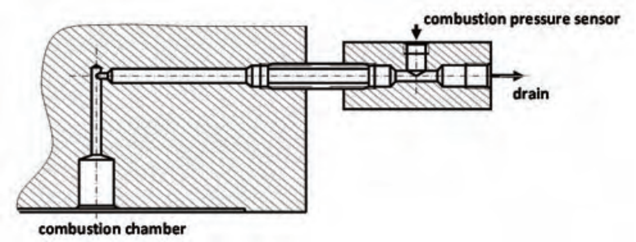

Fig. 3. The mounting position of the pressure sensor in the indicator channel

For the purpose of validation, the actual shape of the indicator channel was designed in the engine model compared to the results on the real object. Validation consisted in a comparison of measured and calculated values. According to the presented data, the majority of parameter values obtained by modeling do not differ from the measured values. The difference between the measured maximum pressure (Pmax) and the calculated by modeling was 0.94% and the position of the Pmax differs by 1 deg of the crankshaft position.

4. Analysis of results

A positively valid model of the research object was used to analyse the phenomena taking place in the indicator channel. Results of the simulation on base on Eq. 1. are presented as follow. Figure 4 shows a model indicator channel in which points 100, 200, 300, 400 and 500 mm were used to calculate pressure changes in points MP1 to MP5. The length of L was 500 mm and 1000 mm. Indicator channel was closed at the end of the indicator cock.

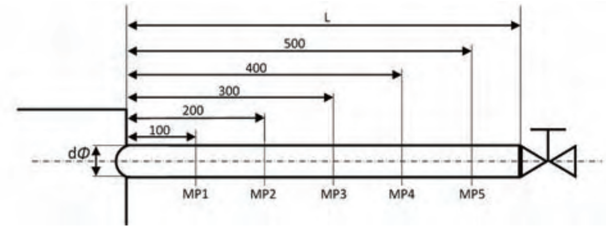

Fig. 4. Simulation indicator channel

Figure 5 shows a graph of pressure changes in the indicator channel in relation to the distance from the combustion chamber at diameters 5, 10, 15, 20, 25 mm. It can be noticed that the calculated pressure increases in relation to the in-cylinder pressure by average 13.7%. For the diameter of 5 mm, the pressure decreases up to 300 mm from the cylinder and for the measuring places 400 mm and 500 mm increases.

It was decided to check whether the diameter of the indicator channel directly affects the combustion process. The upper side of Figure 6 presents graph of combustion pressure in the combustion chamber for various diameters of the indicator channel. The lower side of Figure 6 presents the dependence between differences between the combustion pressure in the cylinder and pressures obtained from measurement points and the diameter of the indicator channel. According to presented results of calculation, the highest combustion pressure occurs at the diameter of the 5 mm indicator channel. The increase of the indicator channel diameter causes observed decrease of the combustion pressure. Probably its effect of increase of the volume of combustion chamber by the volume of the indicator channel. The dependence presented on the lover side of Figure 6 shows that the distance of pressure sensor not more than 100 mm from the cylinder causes only little changes is the pressure measurement.

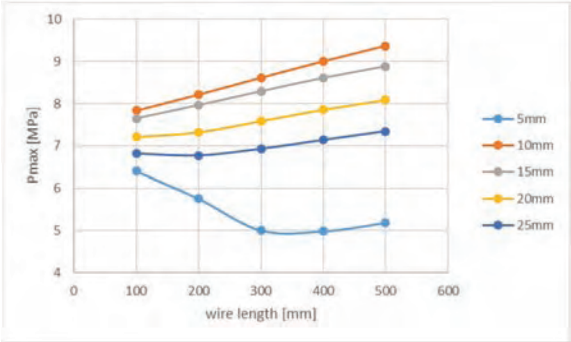

Fig. 5. Changes in the pressure in the indicator channel in relation to the distance from the combustion chamber

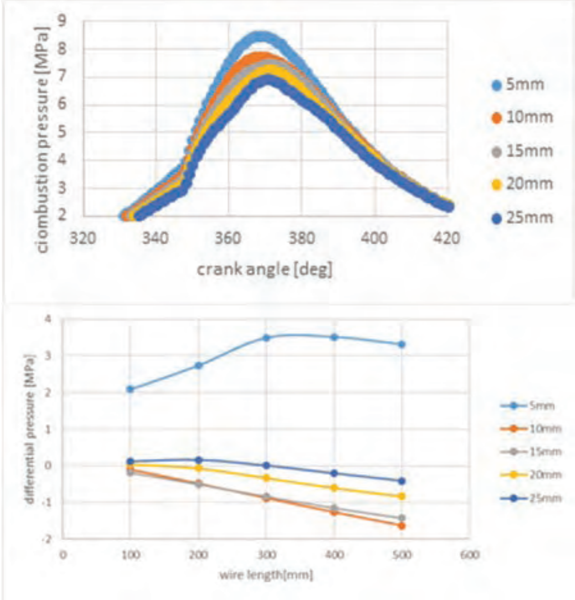

Fig. 6. The graph of combustion pressure in the combustion chamber with different diameters of the indicator channel (up) and a graph of the differences between the pressure in the combustion chamber and the indicator channel (down)

This result is convergent with conclusions presented by Kistler [1]. It should be noted, that the diameter of indication duct equals 5mm causes significant decrease of the measured pressure. Moreover, its important that in the marine engines usually the length of indicator channel is longer than 100mm and according to obtained results the increase of indicator duct length causes significant increase of the measured pressure. It means that long channel causes intensification of the wave phenomena in the channel.

Then, the indicator channel was extended after the last MP5 calculation point by 500 mm, thus the length of the indicator channel extended to 1000 mm. Figure 7 shows a graph of pressure changes in the indicator channel with a diameter of 25 mm in relation to the distance from the combustion chamber.

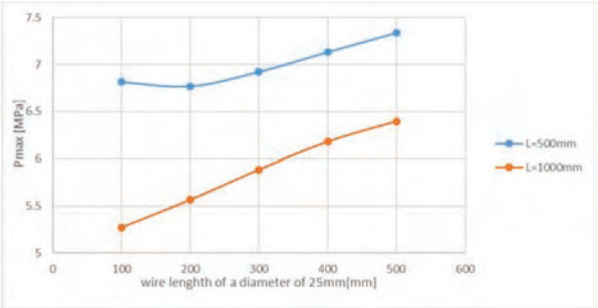

Fig. 7. Pressure changes in the indicator channel with a diameter of 25 mm in relation to the distance from the combustion chamber

It can be noticed that the decrease of the length of the indicator channel causes the decrease of the calculated pressure in the MP5 point. The maximum combustion pressure in a channel with a length of 500 mm increases in relation to the pressure in the cylinder by about 43.1% and at a length of 1000 mm by 24.7%. This result prove the conclusion of possible influence of the wave phenomena on the measurement result.

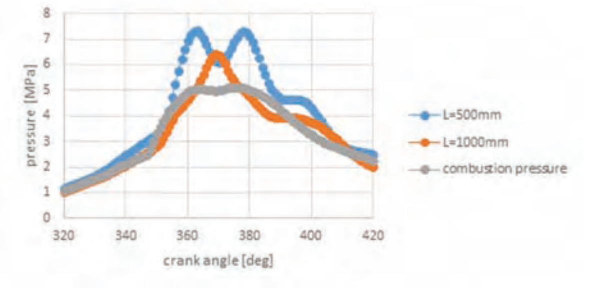

Fig. 8. Pressure at MP5 of the cylinder at different lengths of the indicator channel

Figure 8 shows the pressure diagram measured at 500 mm from the cylinder at different lengths of the indicator channel.

In the graph for a length of 500 mm it can be seen two local maxima of pressure. After extending the indicator channel to 1000 mm the local maximum of the pressure is only one. Both results are for the same combustion pressure in the engine cylinder. Grey graph present the example result of direct measurement of the pressure by the indicator channel with construction presented in Fig. 3.

5. Conclusions

The paper presents the results of calculations of the pressure in the indicator channel in a four-stroke marine engine, using CFD. According to the obtained results, the maximum pressure in the indicator channel deviates in relation to the value of the combustion pressure in the engine cylinder. In most cases, the pressure is even higher. Therefore, there is a possibility that in the indicator channel pressure accumulation occurs, possibly caused by wave phenomena, which are the effect of compressibility of gases. So it is necessary to pay special attention to the shape and dimensions of the indicator channel during the design.

It has been shown that the place where the sensor is installed along with the shape of the indicator channel is important in the diagnosis of the internal combustion engine. Improper installation location of the sensor and the construction of the indicator channel can significantly degrade the diagnostic information for the operator of the marine engine.

According to the results of the calculation of the dependence on the dimensions of the indicator channel, the value of the maximum pressure can range from –21% to + 43% of the maximum combustion pressure. If the indicator channel is incorrectly designed or the sensor is installed in the wrong place, it may not be possible to determine the location of the maximum combustion pressure.

Acknowledgements

The project was supported by AVL Company according to University Partnership Program and license of AVL Boost software.

Bibliography

[1] WALTER, T. Application of an Improved Model for the Determination of Acoustic Resonances in Indicator Passages for Combustion Pressure Measurements in Large Bore Gas Engines. *Kistler Instruments AG,* Winterthur 2007.

[2] OEZATAY, E., ONDER, C. Model based sensor reconstruction of in cylinder pressure trace using indicator cock pressure information. *CIMAC Congress 2010*, **166**, 1-9.

[3] BADER, P., MCLAREN, D., QUISPEL, G.R.W., WEBB, M. Volume preservation by Runge–Kutta methods. *Applied Numerical Mathematic*s. 2016, **109**, 123-137, DOI: 10.17863/CAM.1184.

[4] INCROPERA, F.P., DEWITT, D.P. et al. Fundamentals of heat and mass transfer. *John Wiley & Sons*, 2011.

[5] CUPER-PRZYBYLSKA, D. Model of processes of the AL25/30 marine engine and its verification. *New Trends in Production Engineering*, 2018, **1**(1), 285-29, DOI: 10.2478/ntpe-2018-0035.

[6] CUPER-PRZYBYLSKA, D. Przegląd modeli procesów spalania w cylindrze silnika tłokowego. *Autobusy : technika, eksploatacja, systemy transportowe*. 2018, **19**(4), 48-52, DOI: 10.24136/atest.2018.020.

[7] CUPER-PRZYBYLSKA, D., WYSOCKI, J. Research injection pressure with the Kistler 4067E pressure transmitter on Sulzer engine 3AL25/30. Journal of KONES Powertrain and Transport. 2017, **24**(3), 29-36, DOI: 10.5604/01.3001.0010.3061.

Dominika Cuper-Przybylska, MEng. – Faculty of Electrical Engineering, Gdynia Maritime University.
e-mail: *d.cuperprzybylska@we.umg.edu.pl*

Article citation info:
KOWALSKI, J. The CFD analysis of influence the start of fuel injection (SOI) on combustion parameters and exhaust gas composition of the marine 4-stroke engine. *Combustion Engines*. 2019, **177**(2), 40-45. DOI: 10.19206/CE-2019-207

Jerzy KOWALSKI

CE-2019-207

The CFD analysis of influence the start of fuel injection (SOI) on combustion parameters and exhaust gas composition of the marine 4-stroke engine

The paper presents a theoretical analysis of the impact of injection timing on the parameters of the combustion process and the composition of exhaust gas from a 4-stroke engine designed to shipbuilding. The analysis was carried out based on a three-dimensional multi-zone model of the combustion process. This model has been prepared on the basis of properties of the research facility. The input data to the model were obtained through laboratory tests. Results of calculations showed that the change of the start of injection angle (SOI) from the value of 14 degrees before TDC to 22 degrees before TDC results in changes in the combustion rate and thus an increase in the temperature of the combustion process as well as the increase of nitric oxides fraction in the exhaust gas. Simultaneously the maximum combustion pressure increases also.

Key words: *marine 4-stroke engine, NO_x emission, CFD model, combustion, SOI*

1. Introduction

Diesel engines are still irreplaceable source of mechanical energy in heavy vehicles and ships. For this reason the research work to improve the efficiency of this kind of machines are important and continued. Generally the improve of Diesel engines efficiency may be done by increasing the share of energy taken from the fuel combustion to moving the piston, recovery the energy from the exhaust gas or the decreasing of cooling the engine. All presented ways may be improved by the regulation of the combustion process in the engine cylinder. Mentioned regulation is usually conducted by modification of fuel injection process. Properly prepared combustion mixture in the engine cylinder has crucial role in the combustion process. It should be noted that fuel injected into the cylinder is broken-up, evaporated and mixed with air in quick and turbulent process. The auto ignition is occur in the cylinder area and time in which is proper pressure, temperature and composition of mixture. According to this the start of fuel injection (SOI) beside the fuel spray geometry is significant for improving the engine efficiency and decreasing the emission of toxic combustion products into the atmosphere.

Researches on the influence of SOI value on parameters and the emission from Diesel engines are commonly presented in the literature. Both methods i.e. the decreasing of the engine cooling and SOI changes strategy are presented in [7]. Authors tested the 6 cylinder LHR (Low Heat Rejection) engine. The effect of LHR was prepared by ceramic coating the cylinder. The thermal efficiency was increased from 28–36% to 35–41% but the side effect is the increase of the nitric oxides (NO_x) emission at high speed and load due to the increase of the combustion temperature. The method of the NO_x emission decreasing is the delay of fuel injection. Authors changes the SOI angle from original 20° before top dead center of the piston position (BTDC) to 18° and 16°. The result of this regulation was decreasing of NO_x emission and a little decreasing of brake specific fuel consumption (BSFC) for high load and all considered speeds for 18°BTDC. Further reduction of the SOI angle causes the decrease of NO_x emission but rapid increase of BSFC. In the opposition to this result are observations presented in [11]. Authors of this research present results for the small, single cylinder, diesel engine with common rail system and the range of the SOI from 40 to 0 degrees BTDC. According to presented results the decrease of the SOI causes the decrease of indicated specific fuel consumption. Similar to [7] results are presented in [8]. Some optimal SOI value is observed in another type of the engine (naturally aspirated, single-cylinder, 4-stroke, direct injection). It should be noted that use biodiesel blend of fossil diesel oil and fish oil changes this optimal value of the SOI, but changing of the engine compression ratio not influence on the optimal for BSFC SOI value [12]. The change of optimal value of SOI is observed for ceiba pentandra biodiesel [16]. This optimal value of SOI was not observed for diesel-propane blends on the range of SOI from 19 to 15 degrees BTDC [21], diesel canola oil methyl ester blends (SOI 15, 20, 25) [3] and castor diesel blends (SOI 25, 23, 21) [1]. The possible reason of this fact is too small range of SOI. The largest range of tested SOI is presented in [2] (from 50 to 10 degrees BTDC). Authors of this research present results of model and laboratory tests. According to presented results the maximum NO_x emission was observed for SOI equals 30 degrees BTDC and the increase and the decrease of the SOI causes the decrease of NO_x emission. Higher range of the SOI was presented in [18]. Authors present laboratory test results for small (498 cm^3) single cylinder, diesel engine with common-rail system and the range of the SOI from 200 to 50 degrees BTDC. This dramatically increase of the SOI causes decrease of in-cylinder pressure and heat release rate (HRR). The high reduction of NO_x content in the exhaust gas is observed but the increase of the SOI over the 80 degrees BTDC not changes of this value. Authors stated that minimum content of NO_x is observed for 6.5 ms of ignition delay independently from the engine speed and the value of compression ratio. According to [5] combination of the SOI changing strategy with exhaust gas recirculation EGR causes the decrease of NO_x emission and the increase of BSFC. The decrease of NO_x content in the exhaust gas is observed for multi injection strategies also [10]. The increase of the SOI for first pulse of fuel injection decreases the NO_x content and increases the BSFC for single, duo and triple strategy of injection for diesel blends with coconut oil biodiesel (B20 and B50).

Less attention is paid for modeling aspect of this phenomena. Work [15] present the CFD model of combustion for diesel engine as a segment of cylinder volume, corresponding with one hole of fuel nozzle and results of exhaust gas composition for different SOI. Rakopoulos et al. [17] present simple two-zone model of combustion for the SOI and the EGR investigations. Both research present similar results for NO_x content in exhaust gas.

This short review of literature show that investigations on influence of the SOI are intensive but some shortcomings may be observed. It should be noted that most research are done for small engines on the basis of the laboratory research. There are only a few works about CFD modeling of this aspect. According to this the research target of this work is the CFD analysis of influence the value of the SOI of the large marine engine parameters and exhaust gas composition.

2. Materials and methods

The research object is 3 cylinder, 4 stroke, turbocharged and intercooled Diesel engine to marine applications. The cylinder bore equals 250 mm and 350 mm of the cylinder stroke. During the tests the engine was operated at constant speed equals 750 rpm and constant load equals 250 kW measured as an electric power on the generator. This type of engine is commonly used in the marine applications as a propulsion of electric power generators or main propulsion of relatively small vessels. Parameters of the research object and the measurement equipment as well as the scheme of the laboratory test stand and fuel properties were presented in [13]. The fuel nozzle consists of 9 holes with 0.325 mm of diameter and 158 degrees of holes angle. The data collected during the laboratory test was used to prepare and validate the CFD model of combustion in the engine cylinder. Model is prepared on the base of the moving 3D mesh of the combustion chamber with the inlet and outlet ducts and cylinder valves. Model consists of the fuel injection and brake-up model on the basis of WAVE mechanism [9] with the Wakisaka modification [20], the Dukowicz fuel evaporation model [6]. The 3Z-ECFM [4] model of combustion process was chosen. This model allows to the auto-ignition point calculation also. Model is developed by the heat transfer and turbulent flow models. Closer parameters of the model and its validation was presented in [14]. During laboratory tests the engine was operated with the SOI equals 18 degrees BTDC and delayed SOI to 13.5 degrees BTDC also. The model, presented in [14] was validated for fuel injection delaying also. Prepared model for delayed SOI calculates maximum combustion pressure (pick pressure) with 6.2% error and mean combustion pressure with 2.8% error. The calculation errors for oxygen and NO_x fractions in the exhaust gas equals 3.2% and 9.2% respectively. Mentioned model was used to calculate parameters of the combustion process in the engine cylinder and the composition of the exhaust gas. During the calculation the SOI was changed as follows: 22, 20, 18, 16 and 14 degrees BTDC.

3. Results and discussion

The delaying of the SOI value is commonly used method to reduction NO_x emission from Diesel engines. Left side of Figure 1 presents the mass of fuel evaporated to the engine cylinder. The delay of fuel injection causes evident move the evaporation function to the expansion stroke direction but it should be noted that at the early stage of evaporation the quantity of evaporated mass increases. For example the 0.2g of evaporated fuel mass is reached at 9.2° of crankshaft after SOI 22deg BTDC and only 7.9° of crankshaft for SOI 14deg BTDC.

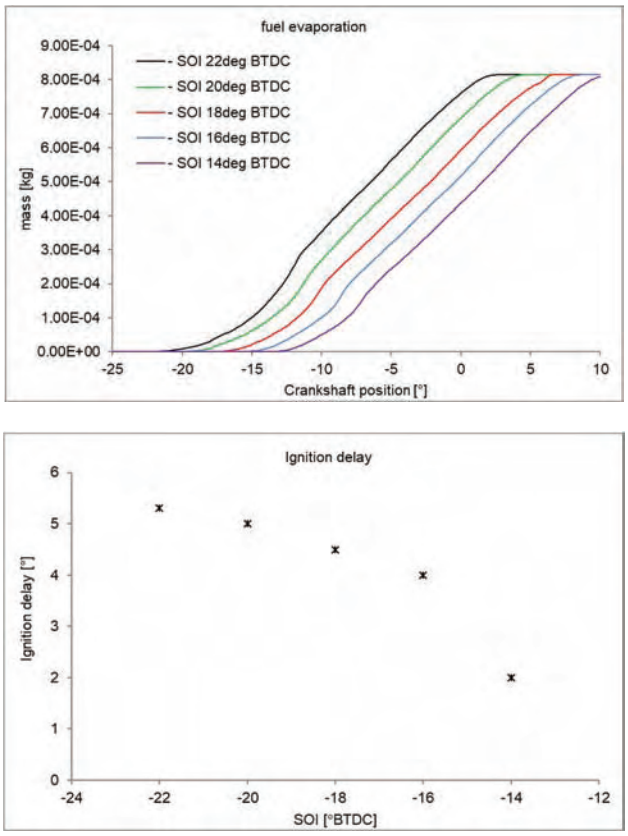

Fig. 1. Fuel mass evaporation and ignition delay

The effect of this is shortening the auto ignition delay from 5.3° for SOI 22 deg BTDC to 2.0° for SOI 14 deg BTDC. The right side of the Figure 1 presents this dependence. It means that the position of auto ignition point depends mainly on the thermodynamic parameters in the combustion chamber than combustion mixture. The delay of the SOI causes decreasing of the intensity of combustion during the early stage (kinetic chemistry controlled combustion). It should be noted that this stage of combustion is responsible for the maximum temperature of combustion. The dependence of the heat release rate (HRR) is presented on the left side of Figure 2. Simultaneously with the decrease of the intensity of the kinetic stage of combustion the diffusion stage of combustion decreases also, but the maximum HRR for diffusion stage of combustion is higher than maximum HRR for kinetic stage. The delaying of SOI causes increasing time of combustion also. The low temperature heat release rate [19] for the beginning of combustion is practically not visible at all considered calculations. Right side of Figure 2 presents the time of combustion of 5, 10, 50 and 90 percent of fuel. The increase of the time of combustion with delaying the SOI is observed for all phases of combustion.

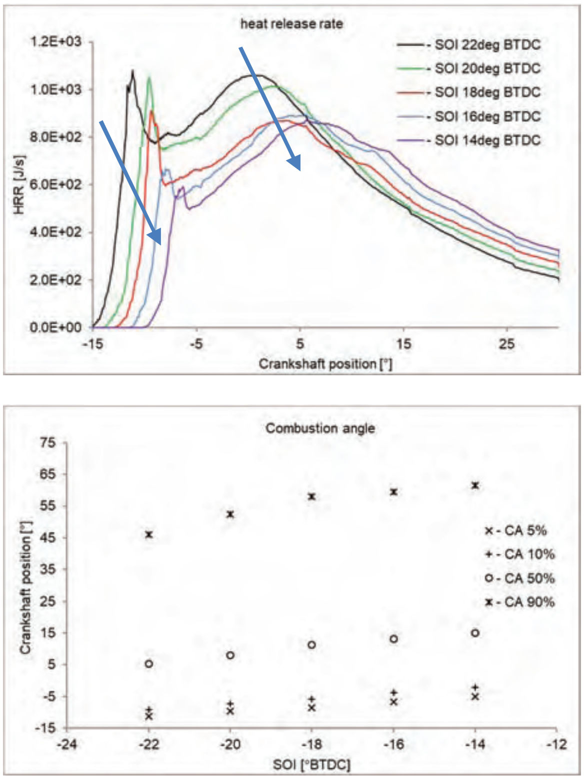

Fig. 2. The heat release rate and the combustion characteristics

Figure 3 and 4 present the HRR (calculated as a mean value for the overall combustion chamber volume) rate in the cross section of the combustion chamber as well as the velocity of the combustion mixture at 12 degrees of the crankshaft position after the SOI. According presented results the increase of the angle of the SOI causes the decrease of intensity of combustion near the fuel nozzle and the increase of the combustion intensity on the front of the fuel spray. This phenomenon is confirmed by results of velocity calculation (Fig. 4). The area with maximum values of the velocity is closer to the fuel nozzle for high values of the SOI.

The intensity of the combustion process may be asses by the observation of fractions of unburned fractions of the combustion mixture. Figure 5 presents fractions of hydrogen (H) and carbon monoxide (CO). According to presented results H fraction rapidly increase in the initial stage of combustion for the early SOI. It should be considered that hydrogen is dominant precursor of combustion process. It means that high rate of the hydrogen content causes intense combustion and increase of the pressure and temperature of combustion due to low activation energy of the chemical reaction of this species. The right side of the Figure 5 present fraction of CO in the combustion chamber. According this point of view the combustion process is slower for the delaying of the SOI, but the CO fraction in the combustion chamber is larger at the end of combustion process.

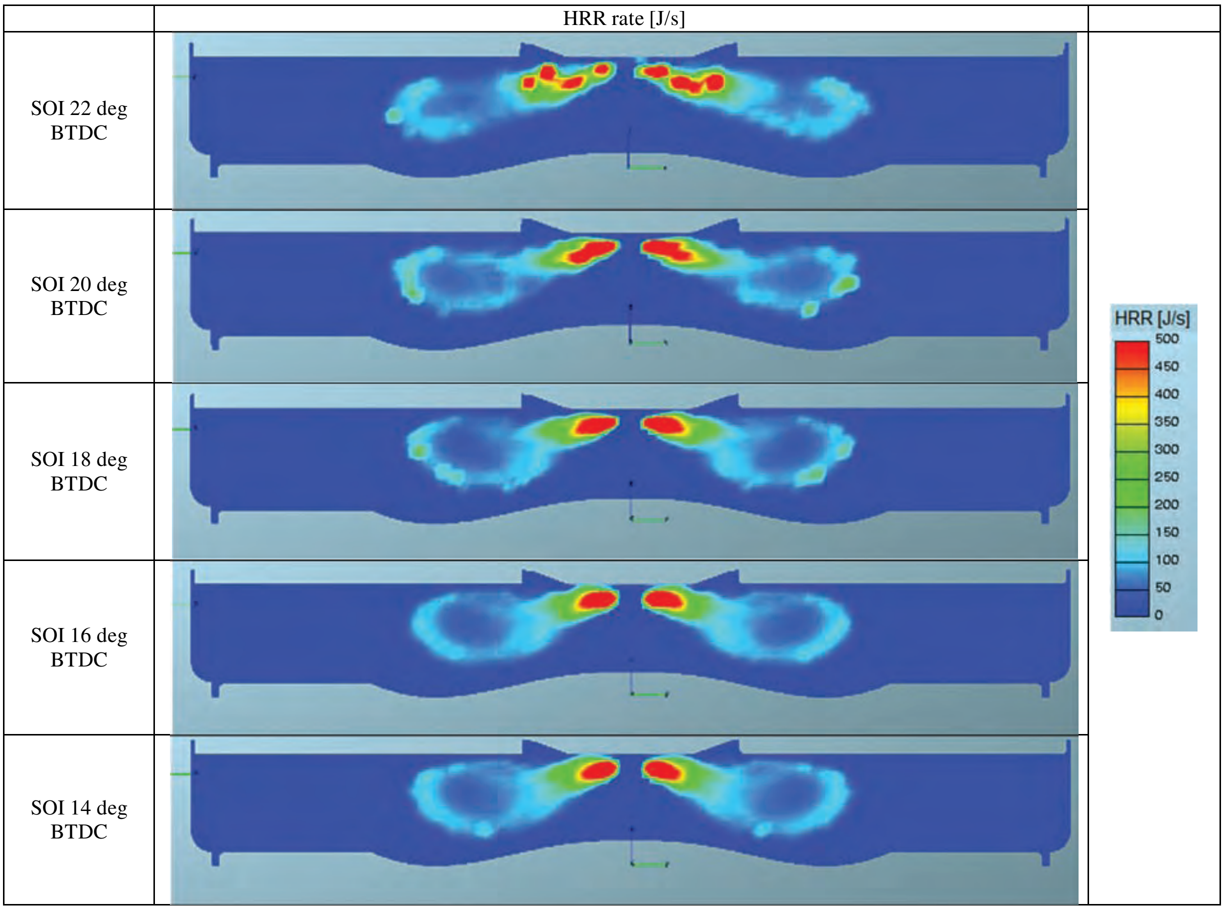

Fig. 3. Heat release rate distribution in the combustion chamber at 12 degrees of the crankshaft position after the SOI

The increase of kinetic stage of combustion causes the increase of the maximum temperature of combustion because the combustion process is rapid. It happens for large values of the SOI. According to results presented in the Figure 6, the delaying of the SOI by 8 degrees causes the decrease of the maximum temperature in the combustion chamber (calculated as a mean temperature of overall cylinder volume) of almost 200 K. Changes in the start of the combustion are clearly visible in the Figure 6 also. It should be noted that the prolongation of the combustion process with the delaying of the SOI do not change the temperature of combustion at the end of the combustion process.

The delaying of the SOI causes the decrease of the maximum combustion pressure (pick pressure). The left side of Figure 7 present dependences of the combustion pressure and values of the SOI. According to presented results considered changes of the SOI causes the change of pick pressure by 2 MPa. A little delaying of the pick pressure position is observed also (less than 2 degrees of the crankshaft position).

The right side of the Figure 7 presents values of pick pressure and the mean indication pressure (MIP) for all considered SOI. According to presented results visible changes of the pick pressure values not influence on the visible change of the MIP value. Considered changes of the SOI cause only 0.25 MPa change of MIP. The explanation of this phenomena is the decrease of the value of the pick pressure and simultaneously increase of the time of combustion. It means that the combustion process is slower and smooth. On the other hand the decrease of MIP and increase of the CO fraction at the end of the combustion process clearly proves the decrease of the combustion efficiency. It is important that presented results come from calculations. It means that the quantity of injected fuel and delivered air are not changed. The deterioration of the combustion process at constant load of the engine cause increase of the fuel dose injected to the cylinder and change the cooperation the engine with turbocharger due to the engine speed governor operation. Result of this is increase of MIP to the value enough to keep constant engine speed at current load.

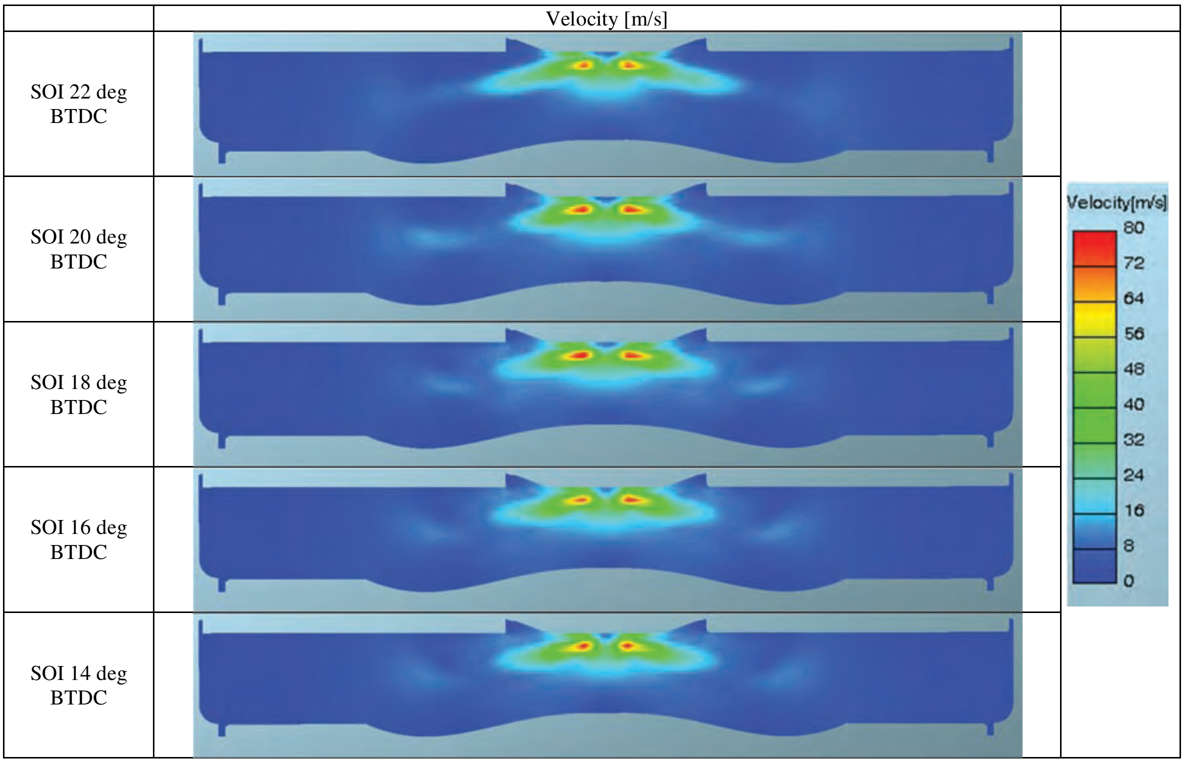

Fig. 4. Velocity distribution of gases in the combustion chamber at 12 degrees of the crankshaft position after the SOI

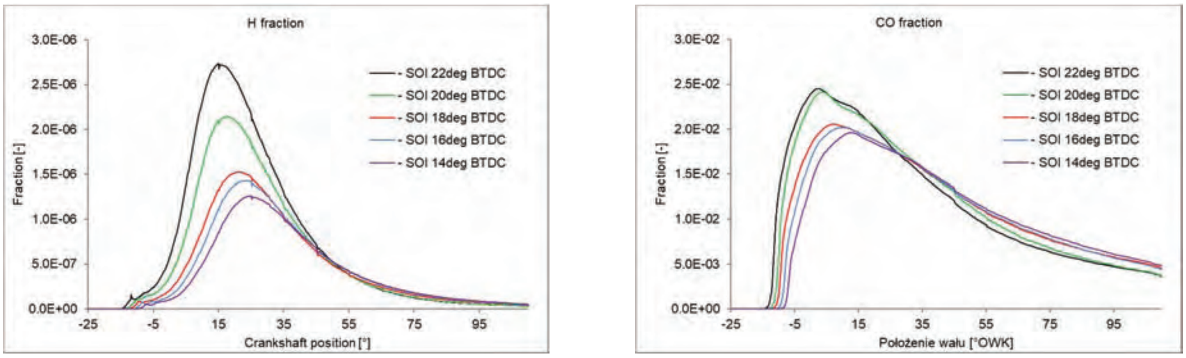

Fig. 5. Hydrogen and carbon monoxide fraction in the combustion chamber

The lower temperature of combustion and the slower combustion process contribute to the decrease of nitric oxides (NO_x) fraction in the combustion chamber and the consequently in the exhaust gas. This phenomenon is presented in the Figure 8. The NO_x fraction is calculated as a sum of the nitric oxide and the nitric dioxide in this model. It should be noted that model of NO_x formation consisted of thermal and prompt mechanisms with NO oxidation [14]. Considered delaying of the SOI causes decrease of the NO_x fraction in the combustion chamber at the end of the combustion process from 1760 ppm to 520 ppm. This trend is expected but the scale of NO_x decreasing is high.

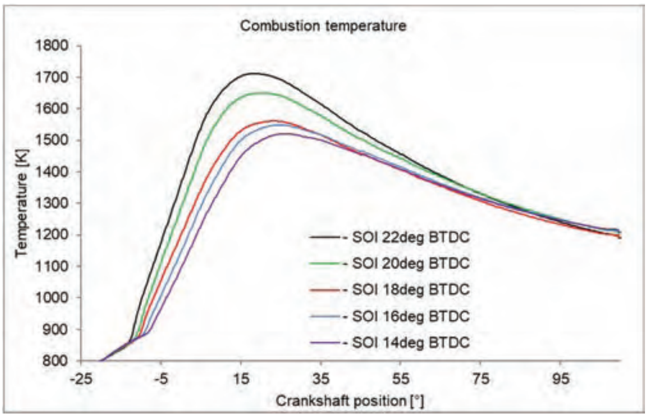

Fig. 6. Temperature of the combustion process

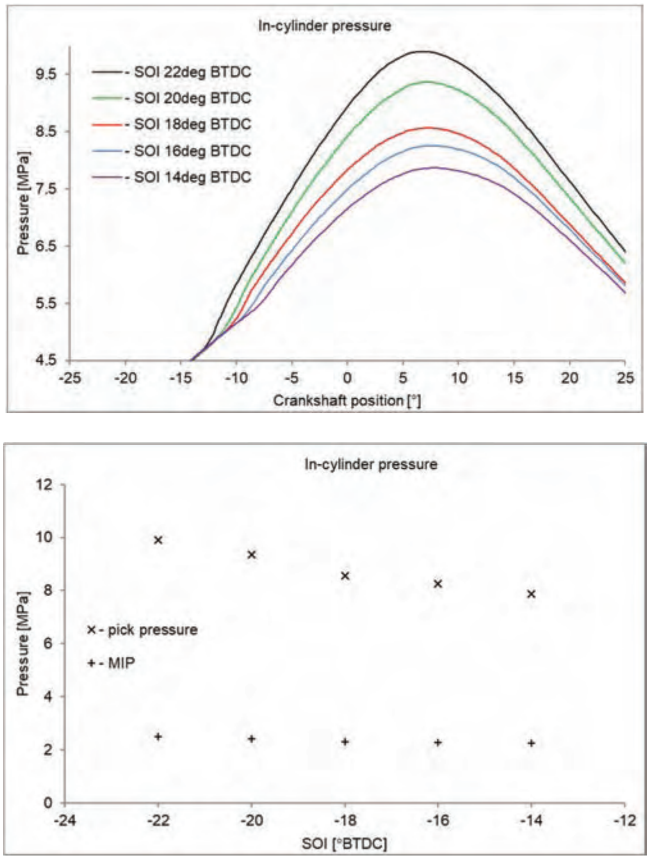

Fig. 7. Pressure of combustion

4. Conclusions

The work presents the influence of the SOI on parameters of the combustion process and the exhaust gas composition in the marine 4-stroke Diesel engine. The analysis is based on the three dimension CFD calculations on the model validated for real laboratory stand. On the basis of presented results following conclusions has been made:

– The delay of fuel injection causes the increase of the evaporated mass of fuel at the early stage of evaporation.

– Thermodynamic parameters in the combustion chamber causes that the shortening of the auto ignition delay is observed also.

– After auto ignition the quantity of evaporated fuel is biggest near the fuel nozzle and the kinetic stage of combustion in less intensive.

– Simultaneously with the decrease of the intensity of the kinetic stage of combustion the diffusion stage of combustion decreases also, but the maximum HRR for diffusion stage of combustion is higher than maximum HRR for kinetic stage.

– The delaying of SOI simultaneously causes increasing time of combustion due to decrease of both stages of combustion.

– The decrease of the SOI angle causes the increase of intensity of combustion near the fuel nozzle and the decrease of the combustion intensity on the front of the fuel spray. This phenomenon is confirmed by results of velocity calculation. The area with maximum values of the velocity is closer to the fuel nozzle for high values of SOI.

– Result of this is the decrease of the maximum combustion pressure as well as the maximum combustion temperature.

– Delaying the SOI causes the decrease of the NO_x fraction and the increase of CO fraction at the end of combustion.

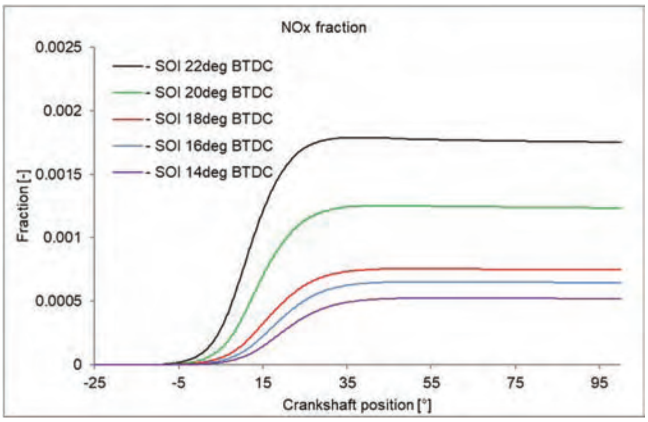

Fig. 8. Nitric oxides fraction in the combustion chamber

Acknowledgements

The project was supported by AVL Company according to University Partnership Program and license of AVL Fire software.

Bibliography

[1] BUYUKKAYA, E., CERIT, M. Experimental study of NO_x emissions and injection timing of a low heat rejection diesel engine. *Int. J. Therm. Sci.* 2008, **47**(8), 1096-1106, DOI: 10.1016/j.ijthermalsci.2007.07.009.

[2] COLIN, O., BENKEIDA, A. The 3-Zones Extended Coherent Flame Model (ECFM3Z) for computing premixed/diffusion combustion. *Oil & Gas Science and Technology*. 2001, **59-60**, 593-609, DOI: 10.2516/ogst.2004043.

[3] DAMODHARAN, D., SATHIYAGNANAM, A., RANA, P., et al. Combined influence of injection timing and EGR on combustion, performance and emissions of DI diesel engine fueled with neat waste plastic oil. Energy Convers. Manag. 2018, **161**, 294-305, DOI: 10.1016/j.enconman.2018.01.045.

[4] DEEP, A., SANDHU, S.S., CHANDER, S. Experimental investigations on the influence of fuel injection timing and pressure on single cylinder C.I. engine fueled with 20% blend of castor biodiesel in diesel. *Fuel*. 2017, **210**, 15-22, DOI: 10.1016/j.fuel.2017.08.023.

[5] DUKOWICZ, J.K. Quasi-steady droplet change in the presence of convection. *Informal Report Los Alamos Scientific Laboratory*. LA7997-MS, 1979.

[6] FUSHUI, L., LEI, Z., BAIGANG, S. et al. Validation and modification of WAVE spray model for diesel combustion simulation. *Fuel*. 2008, **87**(15-16), 3420-3427, DOI: 10.1016/j.fuel.2008.05.001.

[7] HIRKUDE, J., BELOKAR, V., RANDHIR, J. Effect of compression ratio, injection pressure and injection timing on performance and smoke emissions of ci engine fuelled with waste fried oil methyl esters-diesel blend. *Mater. Today Proc.* 2018, **5**(1), 1563-1570, DOI: 10.1016/j.matpr.2017.11.247.

[8] HOW, H.G., MASJUKI, H.H., KALAM, M.A. et al. Influence of injection timing and split injection strategies on performance, emissions, and combustion characteristics of diesel engine fueled with biodiesel blended fuels. *Fuel*. 2018, **213**, 106-114, DOI: 10.1016/j.fuel.2017.10.102.

[9] JIAQIANG, E. Effects of injection timing and injection pressure on performance and exhaust emissions of a common rail diesel engine fueled by various concentrations of fish-oil biodiesel blends. *Energy*. 2018, **149**, 979-989, DOI: 10.1016/j.energy.2018.02.053.

[10] KASHYAP CHOWDARY, P., GANJI, P.R., SENTHIL KUMAR, M. et al. Numerical analysis of C.I engine to control emissions using exhaust gas recirculation and advanced start of injection. *Alexandria Eng. J.* 2016, **55**(2), 1881-1891, DOI: 10.1016/j.aej.2016.03.008.

[11] KIM, H.J., PARK, S.H., LEE, C.S. Impact of fuel spray angles and injection timing on the combustion and emission characteristics of a high-speed diesel engine. *Energy*. 2016, **107**, 572-579, DOI: 10.1016/j.energy.2016.04.035.

[12] KOOK, S., PARK, S., BAE, C. Influence of early fuel injection timings on premixing and combustion in a diesel engine. *Energy and Fuels*. 2008, **22**(1), 331-337, DOI: 10.1021/ef700521b.

[13] KOWALSKI, J. The influence of the fuel spray nozzle geometry on the exhaust gas composition from the marine 4-stroke diesel engine. *Combustion Engines*. 2018, **172**(1), 59-63, DOI: 10.19206/ce-2018-107.

[14] KOWALSKI, J. The model of combustion process in the marine 4-stroke engine for exhaust gas composition assessment. *Combustion Engines*. 2016, **165**(2), 60-69, DOI: 10.19206/CE-2016-208.

[15] MA, Z., HUANG, Z., LI, C. Effects of fuel injection timing on combustion and emission characteristics of a diesel engine fueled with diesel−propane blends. *Energy & Fuels*. 2007, **21**(3), 1504-1510, DOI: 10.1021/ef060574a.

[16] RAKOPOULOS, C.D., RAKOPOULOS, D.C., MAVROPOULOS, G.C. et al. Investigating the EGR rate and temperature impact on diesel engine combustion and emissions under various injection timings and loads by comprehensive two-zone modeling. *Energy*. 2018, **157**, 990-1014, DOI: 10.1016/j.energy.2018.05.178.

[17] SAYIN, C., GUMUS, M., CANAKCI, M. Effect of fuel injection timing on the emissions of a direct-injection (DI) Diesel engine fueled with canola oil methyl ester−diesel fuel blends. *Energy & Fuels*. 2010, **24**(4), 2675-2682, DOI: 10.1021/ef901451n.

[18] SZYMKOWICZ, P., BENAJES, J. Single-cylinder engine evaluation of multi-component diesel surrogate fuel at a part-load operating condition with conventional combustion. *Fuel*. 2018, **226**, 286-297, DOI: 10.1016/j.fuel.2018.03.157.

[19] TAMILSELVAN, R., RAMESHBABU, R., THIRUNAVUKKARASU, R. et al. Effect of fuel injection timing on performance and emission characteristics of ceiba pentandra biodiesel. *Mater. Today Proc.* 2018, **5**(2), 6770-6779,

[20] WAKISAKA, T. Numerical prediction of mixture formation and combustion processes in premixed compression ignition engines. *COMODIA*. 2001, 426.

[21] YOUSEFI, A., BIROUK, M., GUO, H. An experimental and numerical study of the effect of diesel injection timing on natural gas/diesel dual-fuel combustion at low load. *Fuel*. 2017, **203**, 642–657, DOI: 10.1016/j.fuel.2017.05.009.

Jerzy Kowalski, DSc., DEng. – Faculty of Ocean Engineering and Ship Technology, Gdansk University of Technology.

e-mail: *jerzy.kowalski@pg.edu.pl*

Article citation info:
SZRAMOWIAT, M. The concept of a new refrigerant in combustion engines in aspect of the requirements of modern drive systems. *Combustion Engines*. 2019, **177**(2), 46-49. DOI: 10.19206/CE-2019-208

Mateusz SZRAMOWIAT

CE-2019-208

The concept of a new refrigerant in combustion engines in aspect of the requirements of modern drive systems

The article presents currently applied construction solutions for currently used cooling systems for internal combustion engines. There were presented their defects and possible development directions were indicated. On this basis the concept of a cooling system which will enable the improvement of heat exchange in the internal combustion engine has been proposed.

Key words: *combustion engine, engine cooling system, electromagnetic pump*

1. Introduction

The internal combustion engine is a thermal machine in which there is a need to remove heat from elements subject to high temperature. This function is performed by the cooling system, which is also responsible for maintaining the correct operating temperature having a significant effect on thermodynamic efficiency. Therefore, there is a need to ensure a strictly determined temperature value of individual structural elements of the engine, at which the assumed thermodynamic efficiency is achieved, and at the same time the correct cooperation of individual structural elements is guaranteed [1].

Running the process of heat emission in an internal combustion engine on the one hand is limited by the effects of combustion anomalies, which in a short time lead to destruction of the engine, and on the other, the exploitation of the engine at too low temperature results in reduced efficiency, increased emission of incomplete combustion products and accelerated consumption of cooperating construction elements.

Due to the conditions imposed on contemporary sources of vehicle and machine propulsion, aspects related to energy efficiency and impact on the environment are currently the main priorities. For this reason, there is an urgent need for development research, also in the area of cooling systems for thermal machines which results from a significant impact on the listed conditions, including an efficient cooling system for internal combustion engines. This is all the more important as there are still significant development reserves in this area of technology. Therefore, undertaking scientific research on the development of cooling systems for internal combustion engines is justified in all respects, and the results of this type of work are in great demand in the sphere of technical practice.

2. Currently used cooling systems for internal combustion engines

Requirements for cooling systems of thermal machines are very complex. As already mentioned in the introduction, conducting the process of heat production at high temperature is beneficial due to thermodynamic efficiency, but too high thermal load of cooperating structural elements of an internal combustion engine can cause operational problems. This is mainly due to changes in the assembly clearances and lubricating oil operating conditions. The effect is usually accelerated consumption or destruction of cooperating surfaces. Even temporary, local exceeding of the admissible temperature of the elements of the internal combustion engine may cause extreme or dry friction resulting from the lack of adequate lubrication.

As a result, an important task of the cooling system is to discharge the corresponding heat flux from each structural element of the motor which is thermally loaded.

Due to the engine's operational safety, heat dissipation streams from individual structural elements are usually oversized and are not suited to real needs. The modern development of technology, especially in the field of regulation and control, allows the development of a cooling system in which the most appropriate thermal conditions for the work of individual components can be obtained. Therefore, it is advisable to undertake development works in the field of cooling systems, which will have wider application to the implementation of the entire thermal management in a vehicle.

In the current designs of internal combustion engines, both air and liquid cooling systems are used. The air cooling systems are characterized by a simple construction, because the basic heat exchange takes place without an intermediate medium, between the surface of the internal combustion engine and the environment. Due to the construction of such a cooling system it is maintenance-free and does not generate additional operating costs [2].

However, it should be emphasized that the lack of vibration damping by the cooling liquid and the resonant effect of the surface of the ribbed heat exchange surface causes that the motors using the air cooling system generate more noise than the motors with the liquid cooling system. The guarantee of correct heat exchange is also often the need to use ribs of individual cylinders and heads, which results in increased dimensions and weight of the engine.

In air-cooled heat engines, the basic heat transfer takes place only on the external surface, while the internal components are not cooled, which may lead to local temperature rise above the limit values, overheating of these elements and their irreversible damage. In air cooling systems, its efficiency depends on the air flow rate and the heat exchange surface. There is a significantly limited control over the thermal load of individual engine components. Usually in this type of constructions the combustion process is carried out at a higher temperature, which results in the necessity of using fuels with higher anti-knock resistance and oils with greater thermal stabilization. Due to the features mentioned, the air cooling systems have a limited application, mainly in engines with low unit power or stationary motors.

Limits of emissions of toxic exhaust components and the tendency to increase the unit power of internal combustion engines, forces the constructors to reach for new, often more complex solutions of cooling systems. In engines with a liquid cooling system, a number of additional components are required that make for a more complex construction compared to engines equipped with an air-cooling system. These are various types of elements, such as: heat exchanger, mechanically driven coolant pump, expansion tank, heater, thermostat, fan, coolant supply pipes, which significantly complicate the structure, increase weight and dimensions, and increase the production and operation costs of the engine. A better feature of the liquid cooling system is better vibration and noise damping thanks to filling the hull and the cylinder head with cooling liquid [3].

In addition, in this type of cooling system it is possible to cool the internal structural nodes of the engine and to achieve greater thermal stabilization, preventing the local formation of areas with unfavourable thermal features. The design and features of the liquid cooling system also allow maintaining a stable temperature of the internal combustion engine regardless of the operating status and ambient conditions. Usually however, the coolant pump is mechanically coupled to the crankshaft of the internal combustion engine, which prevents independent control of its, flow rate suited to current needs. One of the disadvantageous effects is for example, the prolongation of the heating time of the engine, which affects the durability of components and increased emission of toxic exhaust components.

Nowadays, for marketing reasons, motor vehicles with very high nominal power are used in motor vehicles, whereas under real operating conditions the engine usually operates in low or medium load conditions, not exceeding typically 20–40% of nominal value and the full load is used sporadically. In this case, the role of the constructor is to design such a cooling system for a reciprocating internal combustion engine, which after many hours of operation in urban traffic with a low load guarantees optimum cooling conditions also during operation with maximum load, e.g. during highway traffic.

This is a difficult task, because the thermal inertia of the coolant and the speed of cooling liquid displacement in the system significantly limit the possibility of regulating the heat pickup in the rapidly changing thermal conditions of the engine. The effect of this is increased fuel consumption, increased emission of toxic exhaust components and reduced durability of cooperating construction elements. In the few new designs, the mechanical coolant pump is assisted or replaced by an electric pump. This solution, to a limited extent, creates the possibility of controlling the heat reception, this type of regulation being global, limited to controlling the average temperature of the cooling medium, not always suitable for all local engine components [4].

Since heat exchange between the cooled walls of the motor and the cooling medium is strongly dependent on the flow rate of the refrigerant, cavitation may occur in some of the nodes. This is particularly true for areas with a variable cross-section, in which there is a significant change in the speed of the cooling agent. The appearance of cavitation is related to the disruption of the continuity of the flowing liquid and the formation of embryos in the form of cavitation bubbles.

Cavitation bubbles collapse, and often violently implode, creating a local shockwave. Its speed may be sufficient to create wear of the erosive surface of the engine components. The basic symptom of cavitation on the components of a reciprocating internal combustion engine is the progressive loss of material, which after degradation of the primary structure is dispersed in the liquid in the form of fine grains. Therefore, cavitation is a source of impurities in the cooling liquid, leading to a change in its properties. The complex geometry of the liquid channels of the reciprocating internal combustion engine, as well as other components, make the liquid cooling systems a place of occurrence of the phenomenon of cavitation. Usually elements such as: thermostat, coolant pump rotor, coolant ducts and cylinder liners are subject to erosive damage. Fig. 1 shows a brand new coolant pump at the factory, while Fig. 2 shows a coolant pump destroyed by the erosive effect of cavitation [5].

Fig. 1. Brand new, mechanical coolant pump

Fig. 2. A mechanical coolant pump destroyed by the erosive action of cavitation

Considering the features of modern systems for cooling internal combustion engines with air or liquid, in order to improve their efficiency, various types of support devices are used.

One of such systems, supporting the heat exchange in a piston combustion engine, is the lubricating oil cooling system. The oil circulating in the lubrication system of the internal combustion engine, in addition to the lubrication function of the cooperating surfaces, also acts as a coolant. Therefore, for example in engines with high unit power, as well as in industrial engines, engine oil is used as a cooling medium for pistons, supporting the basic cooling system.

3. A new concept for the cooling system of the internal combustion engine

Considering insufficient possibilities of matching air and liquid cooling systems of piston combustion engines to the requirements of modern internal combustion engines, it is necessary to find new solutions in this area. The cooling system of modern internal combustion engines should provide cooling conditions adequate to the state of the engine operation, with particular emphasis on the efficiency of energy conversion and the emission of toxic exhaust components. This is possible by using a coolant with a greater heat transfer capability and another coolant transport strategy.

The most important feature of the developed concept of a modern cooling system for a reciprocating internal combustion engine is the use of a new type of coolant in the form of a ferromagnetic liquid with good heat transfer properties.

It also results from the possibility of using a new type of pump, responsible for the movement of the coolant in individual cross-sections of the cooling system. This type of pump, using an electromagnetic field for transporting a ferromagnetic liquid, is characterized by a simple construction as well as a wide possibility of regulating the flow of the medium. By using an electronic controller, it is possible to control the flow of refrigerant in the piston cooling system of the internal combustion engine, independent of the engine crankshaft speed.

The proposed cooling system is universal, possible to be used not only in piston combustion engines, but also in other types of thermal machines, where there are specific conditions regarding the thermal state of individual structural elements. This type of cooling system also allows the development of an individual cooling strategy for selected construction nodes by forming independent refrigerant circuits inside the entire cooling system structure of a given machine. This enables individual adaptation of the cooling agent's speed in the given nodes, controlled by additional electromagnetic pumps. The entire system can be centrally controlled based on signals from temperature sensors placed in the cooled machine structure.

The proposed cooling system concept can bring the following effects:

- increase in general efficiency;
- increase in mechanical efficiency;
- improvement of thermal stabilization of the internal combustion engine and shortening the heating time;
- reduction of toxic components emissions;
- better management of heat exchange in the combustion engine and other peripheral devices of the vehicle, such as: interior heating system, vehicle ventilation system, drive transmission system, and in hybrid drive systems: cooling of the inverter, batteries and electrical machines.

This cooling system is a liquid heat exchange system operating in a closed circuit. In the conceptual design, the centrifugal mechanical pump was replaced by an electromagnetic pump for the coolant. This type of pump is made of a solenoid wound on a casing made of a diamagnetic material. In the discussed solution, the coil carcass simultaneously functions as the pump body together with connection stubs. The diagram of the construction of an electromagnetic pump for a coolant composed of one and many solenoids is depicted in Fig. 3 and Fig. 4. The presented concept of the cooling medium pump causes its movement due to the magnetic field created by the electric current flowing through a solenoid or a set of solenoids. The phenomena of magnetism were used to create the motion of the cooling agent. The cooling agent used nanoparticles of ferromagnetics suspended in a liquid, commonly known as "ferrofluid". When the electromagnetic pump is activated, a very large current flows through the solenoid, resulting in a strong magnetic pulse. Ferromagnetic nanoparticles suspended in the liquid at one end of the coil (or even some distance away) are pulled into the pump body, where they begin to accelerate rapidly. The acceleration force stops working around the centre of the coil. The magnetic pump should be designed so that the current in the coil stops flowing from the moment when the stream of nanoparticles of ferromagnetic suspended in the liquid reaches the area around the centre of the coil - otherwise it will be braked on further movement.

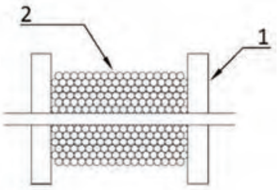

Fig. 3. The design of the electromagnetic pump: 1 – core of the coil, 2 – coil

Fig. 4. Prototype of electromagnetic pump

Figure 5 shows a model test stand, where the prototype pump has been installed. Preliminary tests of the electromagnetic liquid cooling pump were carried out in the presented position. During the tests, it was found that the magnetic field produced by the coil causes the flow of ferrofluid. It has also been shown that by changing the length of the control pulse or changing its frequency, it is possible to change the flow rate of the cooling liquid.

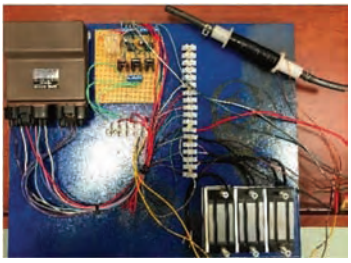

Fig. 5. A model test stand for an electromagnetic pump

In Institute of Vehicles and Internal Combustion Engines at Cracow University of Technology there were developed various concepts of cooling systems using an electromagnetic pump and a cooling agent consisting of ferromagnetic nanoparticles forming a suspension in a liquid. The presented systems differ from each other by the construction of a coolant pump.

Figure 6 shows a cooling system consisting of an electromagnetic one-stage ferromagnetic liquid pump which, if necessary, generates flow in the system from the combustion engine to the heat exchanger. The electronic controller is responsible for the correct operation of the electromagnetic ferromagnetic fluid pump. It simultaneously controls the value of time intervals and the maximum current flowing through the coil, based on electrical signals from such sensors as engine temperature sensor, coolant temperature, oil temperature, crankshaft speed, throttle angle or fuel injection time. After processing in the control unit, they allow precise control of the algorithm and procedures based on the rotational speed of the crankshaft. This method of control also allows complete shutdown of the refrigerant flow, resulting in a shorter heating time for the internal combustion engine. However, due to the rapidly changing processes in the internal combustion engine, the total shutdown of the coolant flow can be risky and lead to engine damage. To implement such a solution, it is necessary to conduct long-term durability tests on many types of engines. The reduction of the heating time of an internal combustion engine can be received by using an additional coolant circuit with low flow rate.

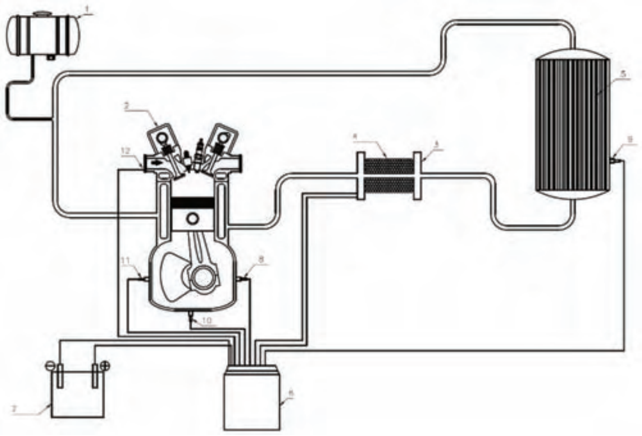

Fig. 6. Diagram of the piston cooling system of an internal combustion engine with an electromagnetic pump: 1 – compensating tank, 2 – combustion engine, 3 – coil core, 4 – coil, 5 – heat exchanger, 6 – electronic controller, 7 – supply source, 8 – temperature sensor, 9 – coolant temperature sensor, 10 – oil temperature sensor, 11 – crankshaft speed sensor, 12 – throttle angle sensor

This solution of the cooling system together with the control system allows obtaining the required cooling liquid flow, regardless of the crankshaft rotational speed. The possibility of such a control of the cooling system significantly improves the heat exchange regulation range. In conventional cooling systems of the internal combustion engine, the lack of control over the cooling agent flow significantly limits the heat exchange control range. When operating an internal combustion engine with maximum load and low speed, the coolant flow must be sufficient to ensure correct heat exchange conditions. This situation adversely affects the overall efficiency of the engine in other work states. In transient states, and when the engine is operated with low load and high speed, unnecessary mechanical losses are generated due to the resistance of the coolant flow. The possibility of controlling the electromagnetic pump can significantly reduce the consumption of energy lost on the drive of the refrigerant pump and eliminates the possibility of cavitation, which can lead to destruction of the pump impeller, and consequent damage to the engine.

4. Summary

The dynamic development of drive systems with thermal engines forces designers to reach for newer technical solutions in the field of cooling and maintaining thermal equilibrium. In the current form, cooling systems for heat engines no longer meet the requirements set by modern vehicle drive systems.

It is necessary to find new, universal solutions that would allow a rational heat exchange economy, not only in the internal combustion engine, but in the whole vehicle drive system.

The use of a cooling system in an internal combustion engine in which an electromagnetic pump was used to create the flow rate and as a cooling agent used ferromagnetic nanoparticles suspended in a liquid can bring benefits related to heat exchange. Depending on the results obtained, it will be possible to assess the applicability of the cooling system in question not only in the internal combustion engine, but also in other elements of the vehicle's drive system that require cooling and other industries.

It is necessary to conduct experimental tests using an internal combustion engine as a test object, which will aim to determine whether it is possible to produce controlled movement of a ferromagnetic fluid by using a pump that uses a magnetic field of sufficient intensity to operate.

Bibliography

[1] WIŚNIEWSKI, S. Obciążenia cieplne silników tłokowych. *Wydawnictwa Komunikacji i Łączności*. Warszawa 1972.

[2] OGRODZKI, A. Chłodzenie trakcyjnych silników spalinowych. *Wydawnictwa Komunikacji i Łączności*. Warszawa 1974.

[3] WAJAND, J.A., WAJAND, J.T. Tłokowe silniki spalinowe średnio- i szybkoobrotowe. *WNT*. Warszawa 2005.

[4] HEYWOOD, J.B. Internal Combustion Engines Fundamentals. *McGraw-Hill* Inc., 1988.

[5] IGNACIUK, P., GIL, L. Uszkodzenia kawitacyjne w silnikach spalinowych. *Autobusy*. 2014, **5**.

Mateusz Szramowiat, MEng. – Institute of Vehicles and Internal Combustion Engines, Cracow University of Technology.

e-mail: *mateusz.szramowiat@pk.edu.pl*

Article citation info:
ANDRYCH-ZALEWSKA, M., CHŁOPEK, Z., MERKISZ, J., PIELECHA, J. Static internal combustion engine operating states in vehicle driving tests. *Combustion Engines*. 2019, **177**(2), 50-54. DOI: 10.19206/CE-2019-209

Monika ANDRYCH-ZALEWSKA
Zdzisław CHŁOPEK
Jerzy MERKISZ
Jacek PIELECHA

CE-2019-209

Static internal combustion engine operating states in vehicle driving tests

The article presents the compression-ignition engine test results of static operating states in driving tests: NEDC (New European Driving Cycle), RDE (Real Driving Emissions) and the Malta custom test cycle, developed at the Poznan University of Technology. The NEDC and Malta tests were carried out as drive cycle simulations on the engine test bench, the RDE test was carried out in the real driving conditions. The engine operating states are described by the physical quantities of speed and torque. For each of the tests, zero-dimensional characteristics of the values describing the engine operation states were determined, including: mean value and average standard deviation and coefficient of variation. Histograms of quantities describing the engine's operating states for considered tests and driving conditions were also determined. A large diversity of zero-dimensional characteristics of the quantities describing the engine's operating states for the considered driving tests and driving conditions was found.

Key words: *combustion engines, drive tests, engine operating conditions*

1. Introduction

The knowledge gap about the usable properties of internal combustion engines in their real operating conditions means that the results of tests that are only compatible with the type approval procedures are no longer sufficient. The functional properties of internal combustion engines, determined in approval procedures, are in fact significant for the tested objects only under the conditions of these procedures [4] – in other conditions these properties can vary considerably [3, 4], and for this reason such a great attention is paid to engine control algorithms [8]. The functional properties of internal combustion engines, which are particularly strongly dependent on the operating conditions of the engines, both static and – most of all – dynamic, are the values characterizing the exhaust emission [3, 4] and, to a lesser degree, fuel consumption. In order to assess the exhaust emission in conditions deviating from the conditions of type approval procedures, and additionally burdened with a certain uncertainty of accidental processes, the tests of car engines in real operating conditions were introduced. The Real Driving Emissions (RDE) [6, 7] procedure allows the study of exhaust emissions from a car engine through the use of Portable Emissions Measurement System (PEMS). The procedure for selecting the speed curve in the RDE test is defined in the regulations in a very precise and restrictive way [1, 6, 7]. Nevertheless, there is a significant margin of indeterminacy in the vehicle speed, which means that this process can be treated as random [3, 4]. The specific realizations of this process, which are the speed curves of the vehicle used in research, may differ significantly from the speed curves in official type approval procedures. Therefore, the task was undertaken to investigate these differences. The tests were performed for the engine's operating states, determined by the vehicle speed. Engine states selected for testing were determined by the NEDC test [9], the Malta test [1], which simulated the NEDC test in road conditions, and states registered in one of the actual RDE tests. The tests were carried out for the same test object. The subject of the research were static states of combustion engine operation, corresponding to dynamic states in real engine operation conditions.

2. Research aim and objects

The aim of the research was to assess the static operating states of a combustion engine vehicle in conditions corresponding to its real operation. To do this, the results of tests in both real conditions as well as on the engine dynamometer were used. Real-world tests were conducted in accordance with the RDE procedure. On the engine test bench, NEDC tests and the Malta test were carried out, developed at the Poznan University of Technology to simulate the NEDC test in road conditions.

The test objects were: an engine and a car equipped with the same engine. The engine tested was a Fiat 1.3 JTD (MultiJet) 4-cylinder compression-ignition engine with a turbocharged displacement of 1.3 dm^3, Euro 4 exhaust emission class. The tested vehicle was a Fiat Idea passenger car with a mileage of 92,000 km.

The Dynoroad 120 kW AVL engine dynamometer station was used to test the engine. Road tests were conducted using the PEMS apparatus. Measurement values in dynamic conditions were recorded at a frequency of 10 Hz.

Research objects and test equipment were described in detail in [1, 2].

3. Empirical test results

Figures 1–3 show the engine speed trends in research tests. Figures 4–6 show the relative torque curves. The relative torque has been defined in relation to the torque at the full engine control setting, i.e. under conditions corresponding to the maximum power characteristics of the engine. The relative torque is:

$$M_{er}(n) = \frac{M_e(n)}{M_{e\,max}(n)} \tag{1}$$

where: $M_e(n)$ – torque at engine speed n, $M_{e\,max}(n)$ – maximum torque at engine speed n, n – engine speed.

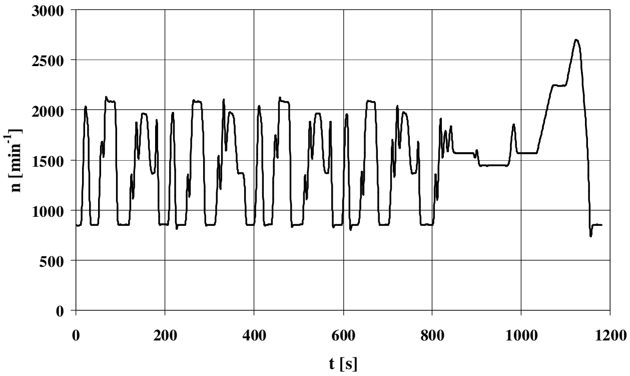

Fig. 1. Engine speed characteristic in the NEDC test

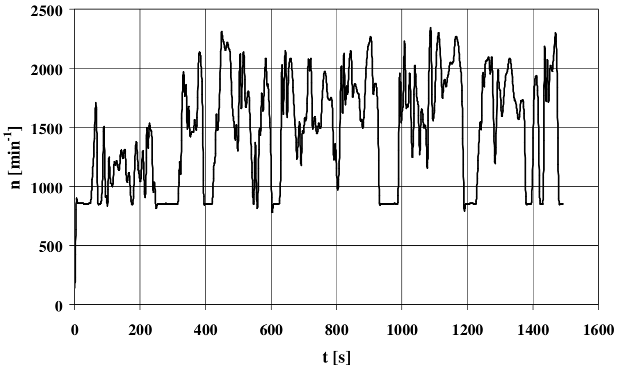

Fig. 2. Engine speed characteristic in the Malta test

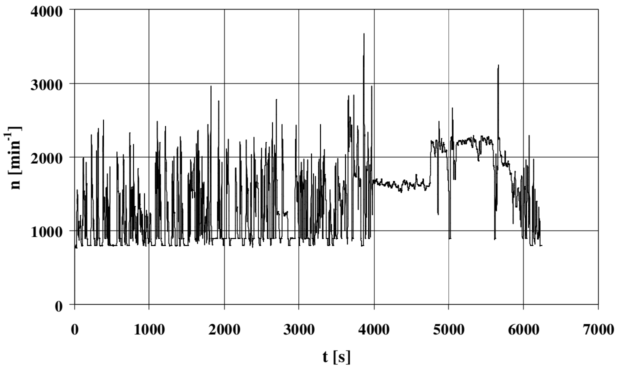

Fig. 3. Engine speed characteristic in the RDE test

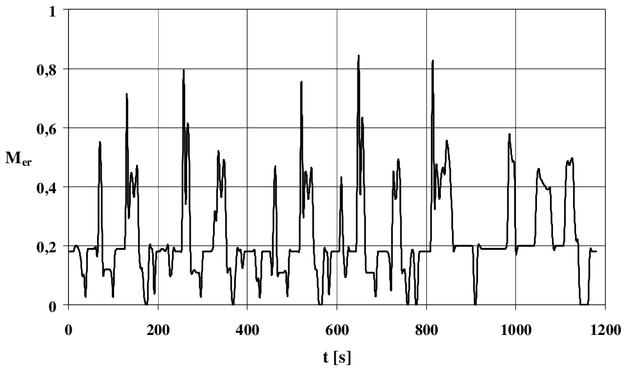

Fig. 4. The relative torque characteristic in the NEDC test

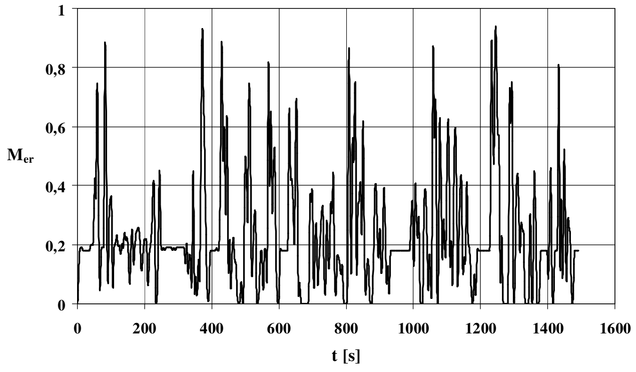

Fig. 5. The relative torque characteristic in the Malta test

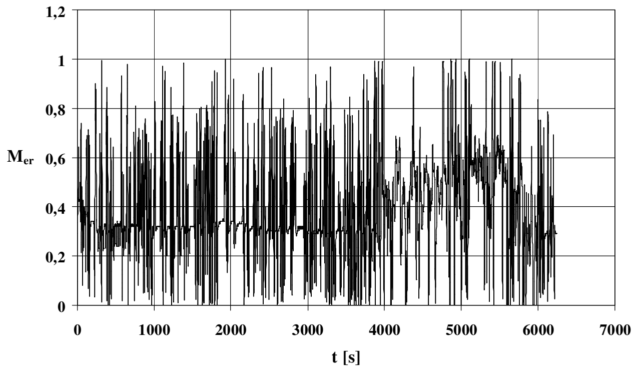

Fig. 6. The relative torque characteristic in the RDE test

The duration of NEDC and Malta tests are similar, while the RDE test lasts 4–5 times longer. The Malta test was developed at the Poznan University of Technology in order to simulate road conditions of the NEDC test, but the fundamental difference in the properties of both tests results from the method of their creation. The NEDC test is created in accordance with the principle of similarity of zero-dimensional characteristics, primarily the vehicle speed, while the Malta test was created based on an accurate simulation of the vehicle speed characteristic in the time domain [5]. This is due to the stronger dynamic properties of the Malta test, but this is not the subject of this work.

4. Analysis of an internal combustion engine operating states

Figures 7–9 present the results of static states corresponding to dynamic states in the empirical research tests. The results are shown in the coordinates of the engine rotational speed – relative torque.

There are significant similarities between the NEDC and Malta tests due to the zero-dimensional characteristics shown in Figures 10–13.

In the case of engine rotational speed, the similarity of characteristics is significant, both the mean value (Fig. 10) and the coefficient of variation (Fig. 11).

In the case of engine load there is a large similarity between the average relative torque value for NEDC and Malta tests, while the average engine load in the RDE test is much larger (Fig. 12).

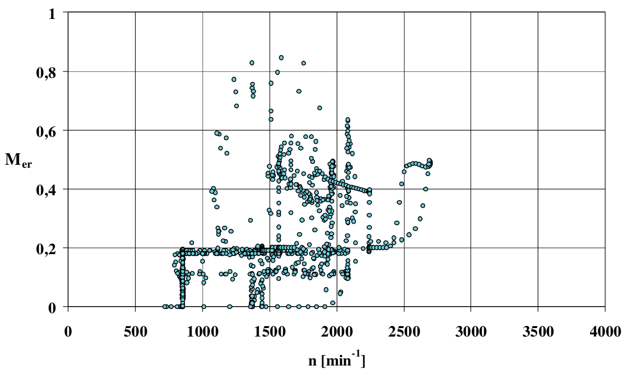

Fig. 7. A set of points in coordinates of engine rotational speed–relative torque in the NEDC test

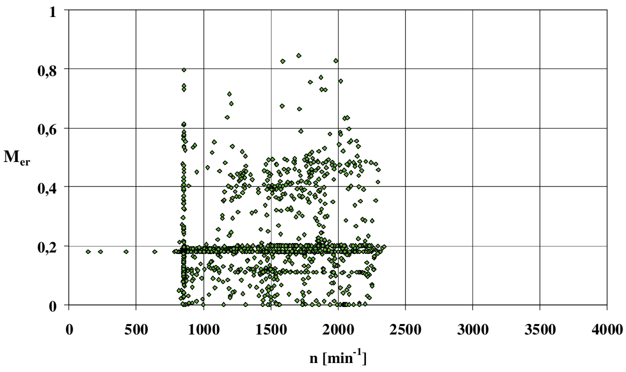

Fig. 8. A set of points in coordinates of engine rotational speed–relative torque in the Malta test

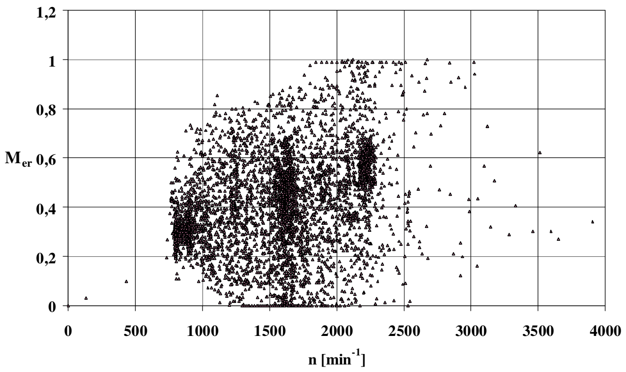

Fig. 9. A set of points in coordinates of engine rotational speed–relative torque in the RDE test

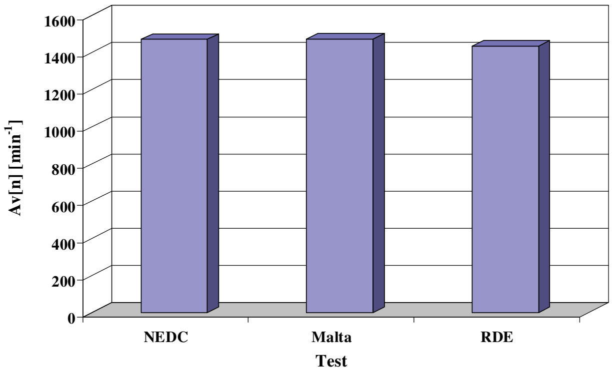

Fig. 10. Average engine speed value in NEDC, Malta and RDE tests

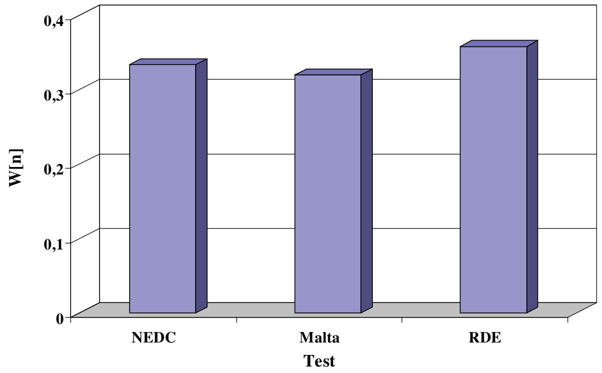

Fig. 11. Coefficient of variation of rotational speed in NEDC, Malta and RDE tests

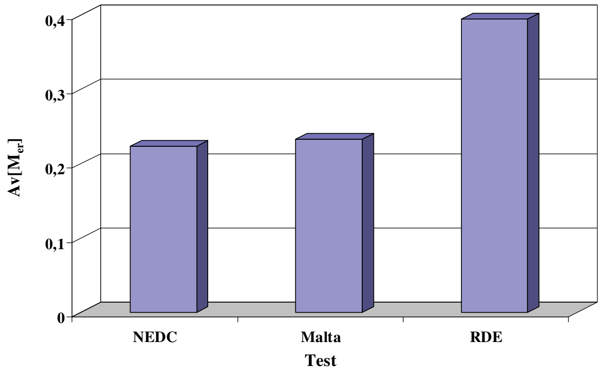

Fig. 12. Mean relative torque value in NEDC, Malta and RDE tests

It is also significant that the coefficient of variation of the relative torque reached the highest values for the Malta test (Fig. 13).

Figures 14 and 15 present the analysis results of the mean value and the coefficient of variation for the relative engine power. Relative engine power is defined as the product of relative torque and relative engine speed compared to the rated speed:

$$N_{er}(n) = M_{er}(n) \cdot \frac{n}{n_N} \tag{2}$$

where: M_{er} – relative torque, n – engine speed, n_N – rated engine speed.

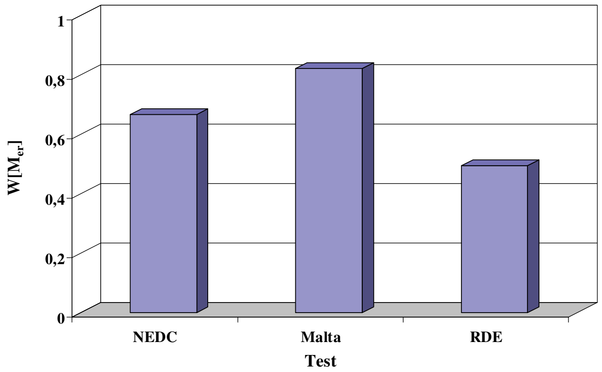

Fig. 13. The relative torque variation coefficient in the NEDC, Malta and RDE tests

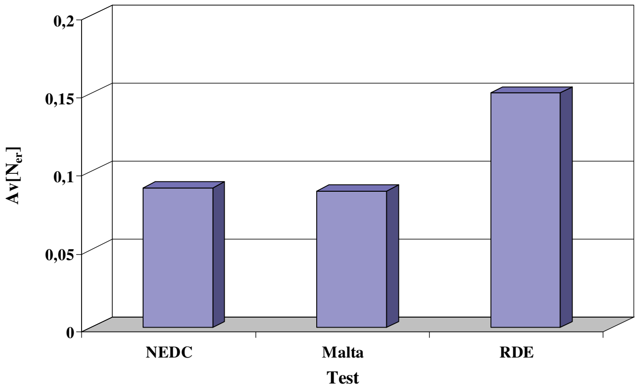

Fig. 14. The average value of the relative engine power in the NEDC, Malta and RDE tests

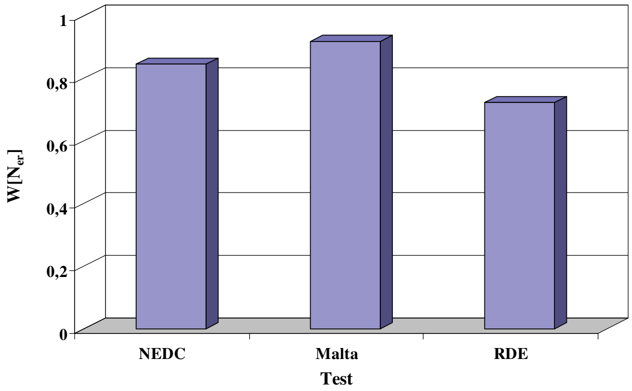

Fig. 15. The relative engine power variation coefficient in the NEDC, Malta and RDE tests

The average value of the relative engine power is almost twice as high for the RDE test compared to the other tests (Fig. 14). At the same time, the RDE test has the smallest coefficient of relative power variation (Fig. 15).

Figure 16 shows the set of average engine speed values and the relative torque in the NEDC, Malta and RDE tests as a function of rotational speed – relative torque, while in Figure 17 – the set of average engine speed values and the average relative engine power values in the coordinates of rotational speed – relative power.

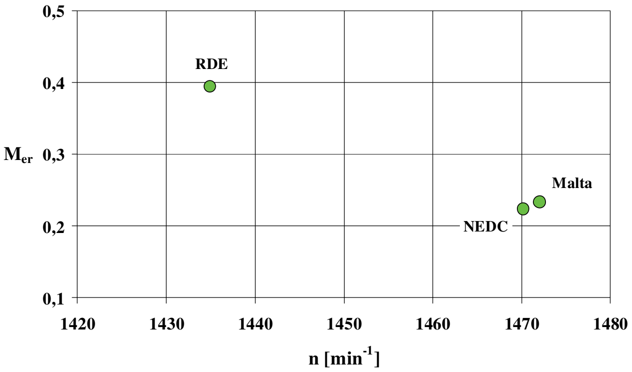

Fig. 16. A set of average engine speed points and an average relative torque value in coordinates: rotational speed–relative torque in NEDC, Malta and RDE tests

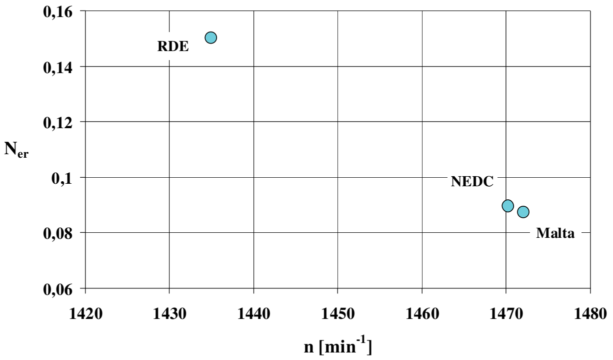

Fig. 17. Collection of points of average engine speed value and average value of relative engine power in coordinates of rotational speed–relative power in NEDC, Malta and RDE tests

It is clearly visible that for the NEDC and Malta tests the average values of the rotational speed, relative torque and – as a consequence of the relative engine power – are close to each other. In the RDE test, the quantities that characterize the engine load are almost twice as large.

Figures 18–20 show the relative number of occurrences of: speed, relative torque and relative power engine states in the analyzed tests.

The relative number of occurrences in the histogram is

$$h = \frac{H}{L} \tag{3}$$

where: H – the number of elements of the set within the counting interval, L – set size (number of elements of the set).

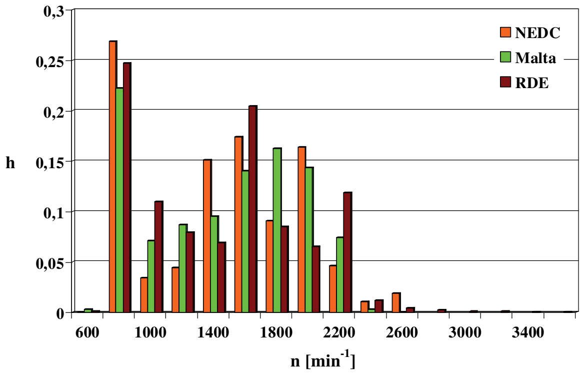

Fig. 18. Engine speed histogram in NEDC, Malta and RDE tests

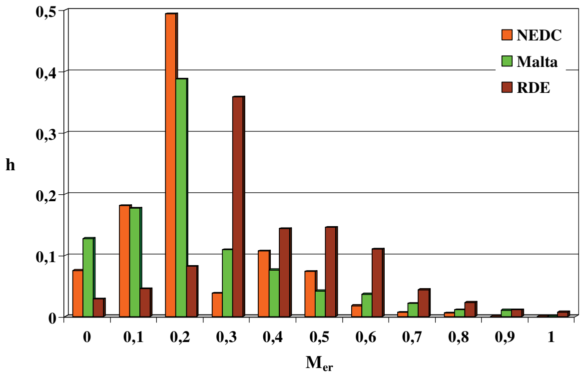

Fig. 19. Histogram of relative torque in NEDC, Malta and RDE tests

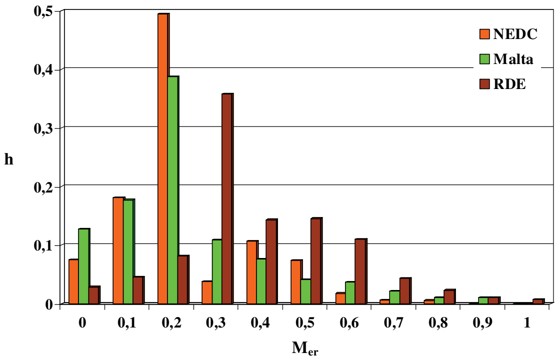

Fig. 20. Histogram of relative engine power in the NEDC, Malta and RDE tests

The process value results also confirmed the conclusions drawn from the assessment of the average value and the coefficient of variation. For rotational speed, the differences in histograms for individual tests are not significant, while for the relative torque and relative engine power much higher relative values were found in the RDE test with the increased occurrence of states with high values compared to the other tests.

Conclusions

The analysis of the internal combustion engine static operating states, corresponding to the operating conditions of the engine under dynamic conditions in drive tests, was carried out for the characteristics of zero-dimensional processes characterizing the engine operation status and in the field of values of these processes. The analyzed processes and values of the engine's operating states were: rotational speed, relative torque and relative engine power. The zero-dimensional characteristics of the processes studied were: mean value and coefficient of variation. In the field of process values, histograms were analyzed.

Based on the static operating states analysis of the internal combustion engine, the following conclusion can be drawn: there is a large similarity between the analyzed characteristics for NEDC and Malta tests, while the RDE test is distinguished by a significantly higher engine load. Therefore, it can be concluded from the analysis of static states of engine operation that conditions in the RDE test favor the increased emission of nitrogen oxides. Of course, the results of the pollutant, which is averaged throughout the road emissions tests, are also influenced by the dynamic conditions of engine operation [1, 3, 4].

Bibliography

[1] ANDRYCH-ZALEWSKA, M., CHŁOPEK, Z., MERKISZ, J., PIELECHA, J. Evaluation of the test drive cycle conditions impact on exhaust emissions from an internal combustion engine. *Combustion Engines*. 2018, **175**(4), 3-9.

[2] ANDRYCH-ZALEWSKA, M. Wpływ katalizatora wewnętrznego na emisję spalin w stanach pracy silnika o zapłonie samoczynnym odpowiadających jego użytkowaniu trakcyjnemu. *Rozprawa doktorska*. Poznań 2018.

[3] CHŁOPEK, Z. Modelowanie procesów emisji spalin w warunkach eksploatacji trakcyjnej silników spalinowych. „Mechanika" z. 173. *Oficyna Wydawnicza Politechniki Warszawskiej*. Warszawa 1999.

[4] CHŁOPEK, Z. Some remarks on engine testing in dynamic states. *Silniki Spalinowe–Combustion Engines*. 2010, **4**(143), 60-72.

[5] CHŁOPEK, Z. Synthesis of driving cycles in accordance with the criterion of similarity of frequency characteristics. *Eksploatacja i Niezawodnosc – Maintenance and Reliability*. 2016, **18**(4), 572-577.

[6] Commission Regulation (EU) 2016/427 of 10 March 2016 amending Regulation (EC) No. 692/2008 as regards emissions from light passenger and commercial vehicles (Euro 6), Verifying Real Driving Emissions, Official J. European Union, L 82, 2016.

[7] Commission Regulation (EU) 2016/646 of 20 April 2016 amending Regulation (EC) No. 692/2008 as regards emissions from light passenger and commercial vehicles (Euro 6), Verifying Real Driving Emissions, Official J. European Union, L 109, 2016.

[8] GUZZELLA, L., ONDER, C.H. Introduction to modeling and control of internal combustion engine systems. *Springer*. 2004.

[9] Worldwide emission standards. Passenger cars and light duty vehicles. Delphi. Innovation for the real world. 2016/2017.

Monika Andrych-Zalewska, DSc. DEng. – Faculty of Mechanical Engineering, Wrocław University of Technology.

e-mail: *monika.andrych@pwr.edu.pl*

Prof. Jerzy Merkisz, DSc., DEng. – Faculty of Transport Engineering, Poznan University of Technology.

e-mail: *jerzy.merkisz@put.poznan.pl*

Prof. Zdzisław Chłopek, DSc. DEng. – Faculty of Automotive and Construction Machinery Engineering, Warsaw University of Technology.

e-mail: *zdzislaw.chlopek@pw.edu.pl*

Prof. Jacek Pielecha, DSc., DEng. – Faculty of Transport Engineering, Poznan University of Technology.

e-mail: *jacek.pielecha@put.poznan.pl*

Article citation info:
NAKASHIMA, K., UCHIYAMA, Y. Experimental development of apparatus to measure piston assembly friction in an eco-mileage vehicle engine. *Combustion Engines*. 2019, **177**(2), 55-59. DOI: 10.19206/CE-2019-210

Kohei NAKASHIMA
Yosuke UCHIYAMA

CE-2019-210

Experimental development of apparatus to measure piston assembly friction in an eco-mileage vehicle engine

Apparatus was developed to measure piston assembly friction with a floating cylinder liner against crank angle, using components of an eco-mileage vehicle engine as much as possible. This apparatus was then used to investigate the effect of different sets of piston rings on piston assembly friction in an eco-mileage vehicle engine. Results indicated that, compared to the piston with all three rings (a top ring, a second ring and an oil ring), the piston with two rings (a top ring and an oil ring) reduced piston assembly friction at all engine temperatures and engine speeds. Another configuration of two rings, with the top ring and the second ring, but without the oil ring, reduced friction at a lower engine temperature and speed, but was almost the same as the three-ring set at a higher engine temperature and speed. Finally, a one-ring set, with only the top ring, further reduced friction, except at a higher temperature and speed, where friction was greater than the two-ring set without the second ring.

Key words: *eco-mileage vehicle engine, floating cylinder liner, piston assembly friction, piston ring, piston skirt*

1. Introduction

Eco-mileage vehicles (Fig. 1) compete by running a fixed number of laps around a track within a given time. Judges calculate fuel efficiency (km/L), and name a winner. Reducing not only vehicle running resistance but also engine friction, are effective means for improving fuel efficiency. The piston assembly friction (the friction between the piston, the piston rings, and the cylinder liner) makes a significant contribution to engine friction [2, 8]. So it is important to reduce the piston assembly friction. Reports have investigated the effects on the piston assembly friction in automobile engines from piston ring tension [3, 4, 9], surface treatment of the ring [13, 16], piston skirt profile [6, 7], and surface treatment of the piston skirt [10, 12]. In practice, in order to reduce piston assembly friction in an eco-mileage vehicle engine, the typical set of three rings (a top ring, a second ring, and an oil ring) is often replaced with a two-ring set, by removing either the second ring or the oil ring from the piston, or even by removing both the second ring and the oil ring, leaving a one-ring set (with just the top ring). However, no reports have investigated how much piston assembly friction is reduced by such removal of rings from the piston. As candidates for the measurements of such piston assembly friction against crank angle during the engine operation, there are the floating cylinder liner method [1, 3, 7, 13, 15, 16], the three-component force sensor method [4–6, 9–11], and the instantaneous indicated mean effective pressure (IMEP) method [14]. Among these measurement methods, the floating liner method is most commonly used. But the floating liner method generally requires significant engine modifications, such as producing a special cylinder liner. This study developed a friction measurement apparatus with a floating cylinder liner, by using components of an eco-mileage vehicle engine as much as possible. Using this measurement apparatus, the effect of each ring on piston assembly friction was examined, while varying the temperature of the engine and the lubricant, as well as the engine speed.

2. Experimental apparatus and method

Figures 2 and 3 show the measurement apparatus of the piston assembly friction with the floating liner. This measurement apparatus used a commercially-available, four-stroke, air-cooled, horizontal, single-cylinder, gasoline engine, displacing 49 mL, with a bore diameter of 39 mm and a stroke of 41.4 mm. The crankcase of this engine was cut, and a cover was attached to the cut of the crankcase. The engine was turned from horizontal to vertical, to match the orientation in an eco-mileage vehicle. For the floating liner, the outer periphery of the air-cooled cylinder (aluminum finned cylinder casting cast-iron liner) was turned, and the grooves for the joint plates were machined on its outer periphery at the thrust and the anti-thrust side, and then the grooves for the clamping bolts were machined at the thrust, the anti-thrust, the front, and the rear sides. As shown in Fig. 3, joint plates were installed in the grooves on the outer periphery of the floating liner, and then the plates, as well as load washers of piezo type, were mounted in the cylinder block, at both the thrust and the anti-thrust sides. Because the cylinder liner is completely supported by the joint plates, any vertical force in the cylinder liner is applied to the joint plates, and thence to the load washers. Thus it is possible to measure the friction in the sliding directions of the piston. In addition, to suppress lateral displacement due to piston thrust force, clamping bolts were mounted to the cylinder block at the thrust, the anti-thrust, the front, and the rear sides.

Heaters were installed in the cylinder block at the thrust, the anti-thrust, and the rear sides, and thermocouples were installed into the clamping bolts at the front and the rear sides so that the bore surface temperature of the liner could be adjusted and measured.

The measurement apparatus was changed from a wet sump in the commercially-available engine to a dry sump. The heater and the thermocouple were inserted into the oil tank outside the engine. The lubricant was Honda genuine Ultra Green with a lower viscosity for low-fuel consumption engines. The lubricant at a fixed temperature was pumped from the oil tank to the pipe in the upside of the crankcase, and then applied from its pipe to the crankshaft at a flow rate of 600 mL/min.

Figure 4 shows the experimental piston, which is standard part of the commercially-available engine. This piston has three grooves in the skirt. As shown in Fig. 5, the roughness of the skirt sliding surface (other than the grooves) was Ra 2.21 μm on the thrust side and Ra 2.51 μm on the anti-thrust side (after the experiment).

Table 1 shows the experimental rings, which are also standard parts of the commercially-available engine. Table 2 shows the tested combinations of ring sets. The effects of the absence of either the second ring or the oil ring (in the two-ring sets), and of the absence of both the second ring and the oil ring (in the one-ring set) on piston assembly friction were examined, in comparison with the three-ring set (comprising the top ring, the second ring and oil ring) in the commercially-available engine.

Fig. 1. Eco-mileage vehicle

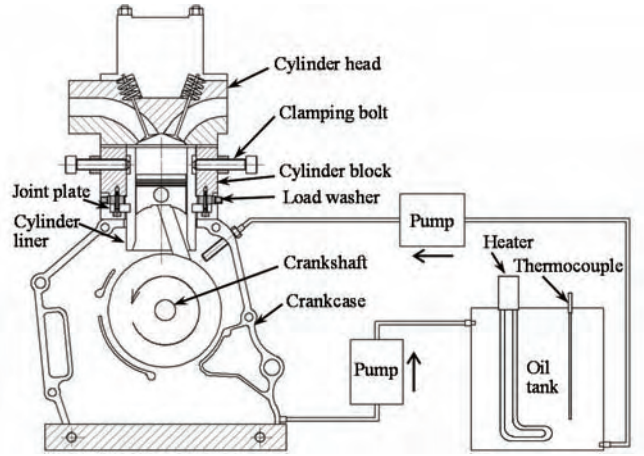

Fig. 2. Measurement apparatus of piston assembly friction

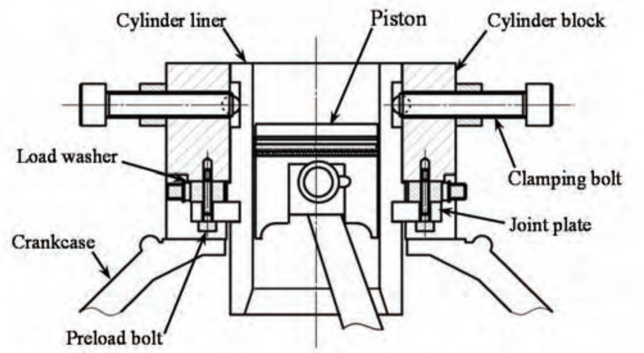

Fig. 3. Measurement unit of piston assembly friction with floating liner

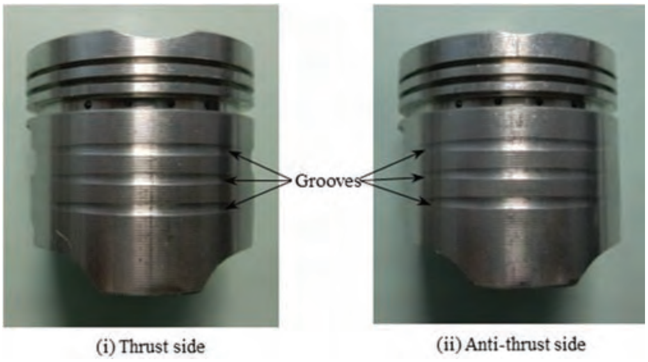

(i) Thrust side (ii) Anti-thrust side

Fig. 4. Experimental piston

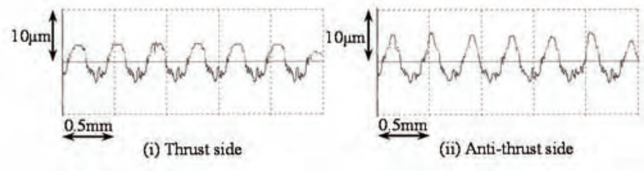

(i) Thrust side (ii) Anti-thrust side

Fig. 5. Roughness of piston skirt sliding surface other than grooves (after experiment)

Table 1. Experimental piston rings

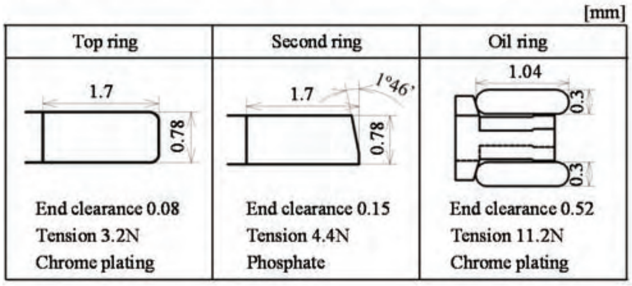

[mm]

Top ring	Second ring	Oil ring
End clearance 0.08 Tension 3.2N Chrome plating	End clearance 0.15 Tension 4.4N Phosphate	End clearance 0.52 Tension 11.2N Chrome plating

Table 2. Combinations of piston ring sets

	Top ring	Second ring	Oil ring
Three-ring set	With	With	With
Two-ring set without second ring	With	Without	With
Two-ring set without oil ring	With	With	Without
One-ring set	With	Without	Without

The roughness of the sliding surface on the liner bore was Rz_{JIS} 1.34 μm (Ra 0.20 μm) on the thrust side and Rz_{JIS} 1.22 μm (Ra 0.22 μm) on the anti-thrust side, after the experiment.

In the experiment, the cylinder head was attached, but the intake and the exhaust valves were not activated, and the piston assembly friction was measured by motoring operation. A preliminary experiment confirmed that the cylinder head (in which the valves were not activated) has a minimum effect on the piston assembly friction, because of the small displacement in this engine. However, in order to make it easy to adjust the temperature on the liner bore, the cylinder head was attached, and an insulation cover was put on the cylinder head and the cylinder block. Before the measurement of the piston assembly fiction, the engine was fully run in. Experiments were performed at temperatures of the liner bore and the lubricant of 40°C to 80°C and at engine speeds of 800 rpm to 1600 rpm.

3. Results and discussion

Figure 6 shows the effect of temperature of the liner bore and the lubricant on piston assembly friction with a three-ring set at an engine speed of 1000 rpm. In Fig. 6, crank angles of 0° and 360° represent engine top dead center (TDC), and 180° bottom dead center (BDC). Since this time the intake and the exhaust valves were not activated, only the two strokes of the piston (downward stroke and upward stroke) were indicated. During the piston downward stroke, a downward force is applied to the liner, and during the piston upward stroke, an upward force is applied to the liner. These forces (frictions) are indicated as negative force and positive force, respectively

As shown in Fig. 6, as the temperature of the liner bore and the lubricant was raised, the friction around TDC and BDC also increased, but the friction in the middle of the stroke decreased. Figure 7 shows the friction mean effective pressure (FMEP) with the three-ring set. Here the FMEP was obtained by integrating the absolute value of friction at crank angles of 0° to 360° and dividing by the stroke volume. In Fig. 7, the FMEP increased with increased engine speed, but the FMEP decreased with increased temperature.

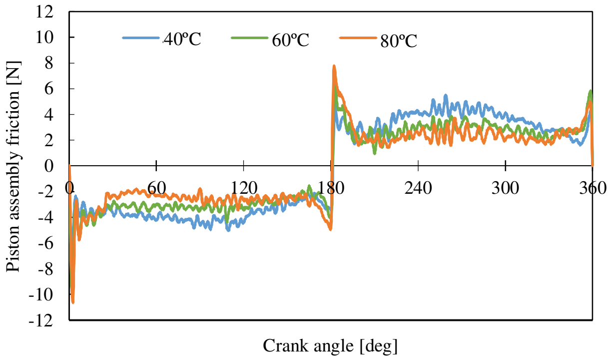

Fig. 6. Effect of temperature on piston assembly friction with three-ring set at 1000 rpm

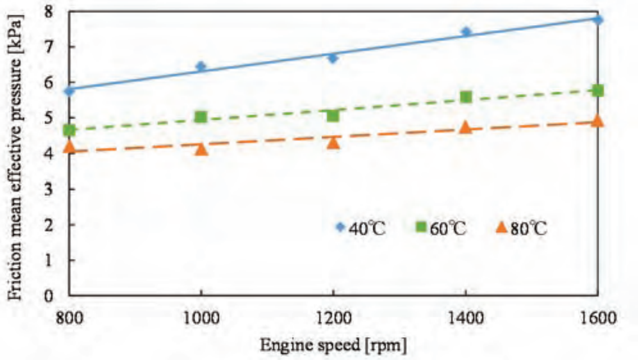

Fig. 7. Friction mean effective pressure (FMEP) with three-ring set

Figure 8 shows the FMEP with a two-ring set without the second ring (with the top and the oil rings). At each temperature and engine speed, the FMEP with this two-ring set without the second ring was lower than that with the three-ring set. As shown in Fig. 9, the friction with the two-ring set was lower around TDC and BDC and in the middle of the stroke, compared with the three-ring set. It appears that friction is decreased when removing the second ring, thus eliminating the contribution of the second ring tension.

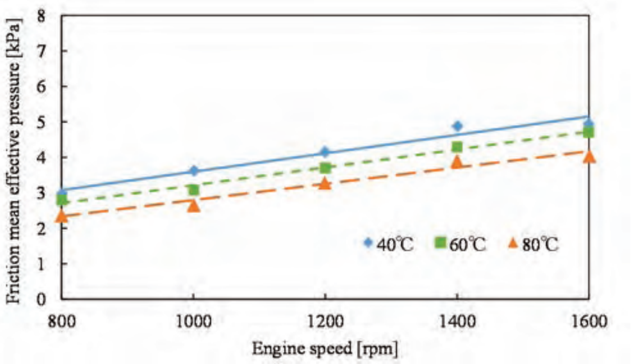

Fig. 8. FMEP with two-ring set without second ring

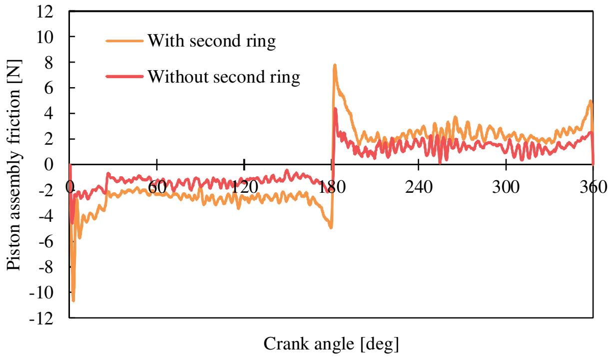

Fig. 9. Effect of absence of second ring on piston assembly friction (80°C, 1000 rpm)

Figure 10 shows the FMEP with a two-ring set without the oil ring (with the top and the second rings). At 40°C, and at 60°C at 800 rpm and 1000 rpm, the FMEP with the two-ring set without the oil ring was lower than that with the three-ring set. However at 60°C at more than 1000 rpm, and at 80°C, the FMEP with the two-ring set without the oil ring was almost the same as that with the three-ring set. At 40°C, and at 60°C at 800 rpm and 1000 rpm, the friction with the two-ring set without the oil ring was lower in the middle of stroke than that with the three-ring set (Fig. 11). At 60°C at more than 1000 rpm, and at 80°C, the friction with the two-ring set without the oil ring was almost the same as that with the three-ring set in the middle of the stroke (Fig. 12). At each temperature and engine speed, the friction with the two-ring set without the oil ring was almost the same as that with the three-ring set around TDC and BDC. It is thought that, by removing the oil ring with the highest tension, a narrow running face of the second ring makes strong contact with the liner around TDC and BDC. Then the reduction of the friction by removing the oil ring is offset by the increase of the friction of the second ring there. At a higher engine speed and a lower load, among the piston assembly friction, the ratio of the piston friction to the ring friction increases [11]. Furthermore, it seems that, by removing the oil ring, the piston skirt makes strong contact with the liner at a higher temperature and a higher engine speed. It is considered that, in the middle of the stroke, the reduction of the friction by removing the oil ring is offset by the increase of the piston friction. So the friction did not decrease at 60°C at more than 1000 rpm, and at 80°C.

Figure 13 shows the FMEP with a one-ring set of only the top ring, without the second and the oil rings. At each temperature and engine speed, the friction with this one-ring set was lower around TDC and BDC and in the middle of the stroke, than that with the three-ring set. So the FMEP with the one-ring set was also lower than that with the three-ring set. However in this one-ring set (with only the top ring), at more than 800 rpm, the FMEP at 80°C was higher than that at 60°C.

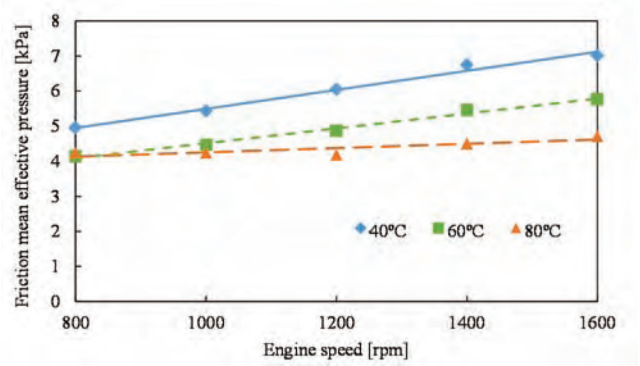

Fig. 10. FMEP with two-ring set without oil ring

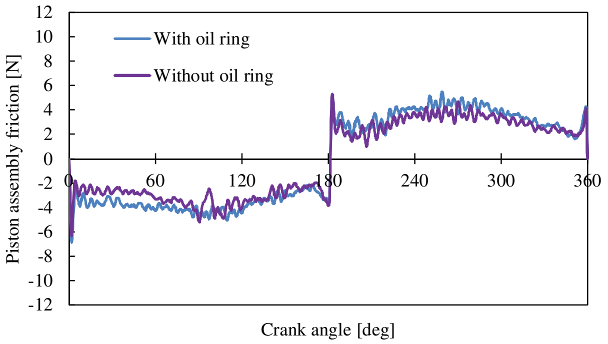

Fig. 11. Effect of absence of oil ring on piston assembly friction at 40°C and 1000 rpm

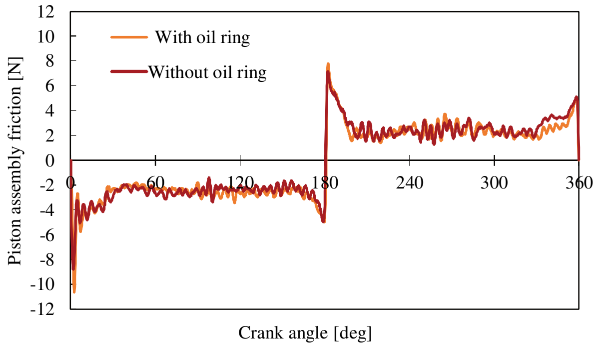

Fig. 12. Effect of absence of oil ring on piston assembly friction at 80°C and 1000 rpm

At more than 800 rpm, the friction with the one-ring set at 80°C increased around TDC and BDC beyond that at 60°C (Fig. 14). At 80°C, the oil viscosity is reduced, so the piston skirt with the one-ring set makes strong contact with the liner around TDC and BDC where the piston speed is lower. It seems that a boundary lubrication condition becomes dominant between the piston skirt and the liner, and then the friction increases there.

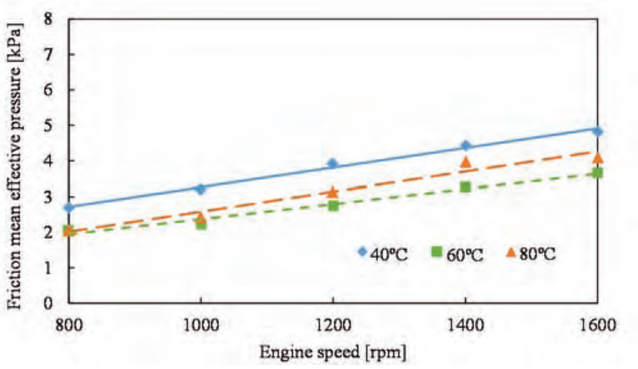

Fig. 13. FMEP with one-ring set without second and oil rings

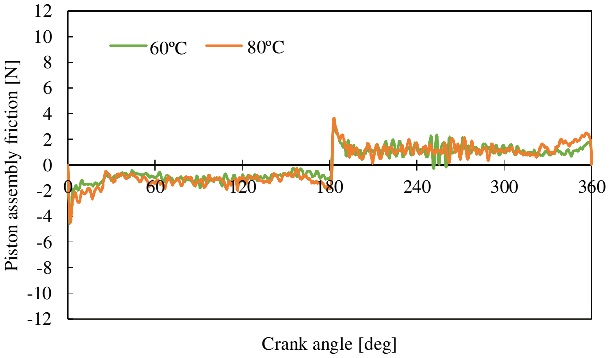

Fig. 14. Effect of temperature on piston assembly friction with one-ring set at 1000 rpm

At 40°C, 60°C, and 80°C at between 800 rpm and 1200 rpm, the one-ring set (of only the top ring) minimized the FMEP. The FMEP was reduced by 27% to 56% for the one-ring set compared to the three-ring set. At 80°C at more than 1200 rpm, the two-ring set (with the top and the oil rings) minimized the FMEP. The FMEP was reduced by 18% for this two-ring set (with the top and the oil rings) compared to the three- ring set.

4. Conclusions

Utilizing a friction measurement apparatus with a floating cylinder liner, the effect of each ring on piston assembly friction was investigated. Results indicate that, at 40°C, 60°C, and 80°C at 1200 rpm or less, the friction is minimized with the one-ring set (of only the top ring), and at 80°C at 1400 rpm or more, the friction is minimized with the two-ring set (with the top and the oil rings).

Future work will investigate the piston assembly friction under firing operation.

Acknowledgements

I would like to thank undergraduate school students Mr. Haruhiko Niwa, Mr. Tomoaki Hayashi, Mr. Kanpei Kobayashi, and Mr. Ryota Ito, of Meijo University, at that time, for fruitful cooperation during this experimental work.

Nomenclature

BDC	bottom dead center	Ra	calculated average roughness
FMEP	friction mean effective pressure	Rz_{JIS}	10-point average roughness
IMEP	indicated mean effective pressure	TDC	top dead center

Bibliography

[1] FURUHAMA, S., TAKIGUCHI, M. Measurement of piston frictional force in actual operating diesel engine. *SAE Technical Paper* 790855. 1979. DOI:10.4271/790855.

[2] HOSHI, M. Introduction to automotive lubrication. *Sankaido Publishing*. 1979, 51-60 (in Japanese).

[3] IIJIMA, N., AOKI, S., IMAMURA, J., TAKIGUCHI, M. An experimental study on effect of lower tension piston rings on piston friction and lubricating oil consumption. *Transactions of the Society of Automotive Engineers of Japan*. 2009, **40**(6), 1477-1482. DOI:10.11351/jsaeronbun.40.1477 (in Japanese).

[4] INOUE, T., MURAKAMI, M., MASUDA, Y., KONOMI, T. A study of friction reduction on piston rings. *Transactions of the Society of Automotive Engineers of Japan*. 1996, **27**(2), 46-50 (in Japanese).

[5] ITOH, Y., KONOMI, T., IWASHITA, Y. Analysis of piston friction on firing conditions by 3-component force sensor method. *Transactions of the Society of Automotive Engineers of Japan*. 1988, **37**, 163-169 (in Japanese).

[6] KONOMI, T., NOHIRA, H., MURAKAMI, M., SANDA, S. Effects of piston skirt profile on friction loss and oil film behaviour. *Proceedings of IMechE* C465/011/93. 1993. 147-154.

[7] MADDEN, D., KIM, K., TAKIGUCHI, M. Part 1: Piston friction and noise study of three different piston architectures for an automotive gasoline engine. *SAE Technical Paper* 2006-01-0427. 2006. DOI:10.4271/2006-01-0427.

[8] MATSUMOTO, K. Friction reduction in an internal combustion engine, *Journal of the Japan Society of Mechanical Engineers*. 1976, **79**(694), 870-876. DOI:10.1299/jsmemag.79.694_870 (in Japanese).

[9] MURAKAMI, M., ITOH, Y., KONOMI, T., NOHIRA, H. Analysis of piston frictional force in engine firing condition -Effects of piston ring specifications on friction-. *Transactions of the Society of Automotive Engineers of Japan*. 1992, **23**(4), 86-91 (in Japanese).

[10] MURAKAMI, M., KONOMI, T., NOHIRA, H. et al. Analysis of piston frictional force under engine firing condition -Effects of surface characteristics of piston skirt on friction-. *Transactions of the Society of Automotive Engineers of Japan*. 1991, **22**(4), 70-73 (in Japanese).

[11] NAKANISHI, K., OKADA, Y., SERA, K. et al. New approach for piston assembly friction analysis based on empirical data, *Transactions of the Society of Automotive Engineers of Japan*. 2010, **41**(2), 301-305. DOI:10.11351/jsaeronbun.41.301 (in Japanese).

[12] OGIHARA, H. Modification of piston sliding surface for internal combustion engine by fine particle peeing of solid lubricant, *Tribologist*. 2002, **47**(12), 895-900 (in Japanese).

[13] OKAMOTO, M., IWASHITA, T. Piston rings for automotive engine. *Engine Technology*. 2002, **4**(3), 98-103 (in Japanese).

[14] URAS, H., PATTERSON, D. Measurement of piston and ring assembly friction instantaneous IMEP method. *SAE Technical Paper* 830416. 1983. DOI:10.4271/830416.

[15] WAKURI, Y., SOEJIMA, M., KITAHARA, T. et al. Characteristics of piston ring friction: Influences of lubricating oil properties. *JSME International Journal Ser. C*. 1995, **38**(3), 593-600. DOI:10.1299/jsmec1993.38.593.

[16] YOSHIDA, H., KUSAMA, K., SAGAWA, J. Effects of surface treatments on piston ring friction force and wear. *SAE Technical Paper* 900589.1990. DOI:10.4271/900589.

Prof. Kohei Nakashima, DEng. – Department of Vehicle and Mechanical Engineering, Meijo University, Japan.
e-mail: *nakasima@meijo-u.ac.jp*

Yosuke Uchiyama, BEng. – Department of Vehicle and Mechanical Engineering, Meijo University Graduate School, Japan.
e-mail: *150446017@ccalumni.meijo-u.ac.jp*

Article citation info:
CZARNIGOWSKI, J., JAKLIŃSKI, P. The influence of the ignition control on the performance of an aircraft radial piston engine. *Combustion Engines*. 2019, **177**(2), 60-65. DOI: 10.19206/CE-2019-211

Jacek, CZARNIGOWSKI
Piotr, JAKLIŃSKI

CE-2019-211

The influence of the ignition control on the performance of an aircraft radial piston engine

Aircraft piston engines are built with compromise on performance and safety. The desire to achieve the highest power-to-weight ratio leads to the search for solutions that optimize the combustion process. On the other hand, the need for maximum reliability leads to the simplification of the design at the costs of performance. An example of such a compromise is the ignition system of the ASz-62IR engine. In this engine there is a double magneto ignition system with a fixed ignition advance angle. As part of the modernisation of this engine, an electronically controlled dual ignition system was developed, which allows for optimum control of the ignition advance angle in terms of power. This article discusses the results of bench tests of the ASZ-62IR-16X engine with fixed ignition timing and variable timing control. Functional parameters and toxicity of exhaust gases were analyzed.

Key words: *aircraft engine, ignition system, power, toxic emission*

1. Introduction

The aviation industry is one of the fastest growing technology sectors [5, 6]. Lightweight and ultralight aircraft propelled by piston engines have an increasing share in this industry [5].

One of the most important requirements for these power units is to obtain as much power from the weight unit [6]. Therefore, design solutions are being developed which allow to increase the power without the necessity to increase the weight of the engine. This is achieved by optimizing the combustion process [9], implementing turbocharging [4] or fuel and ignition advance angle control systems [1, 3]. Another very important factor is the safety and reliability of the design [1]. It is often in contradiction with the limitation of the engine mass: increased safety factors, introduction of redundant systems, etc. The engineers are faced with a dilemma: whether to introduce a new solution that increases engine power but at the same time may reduce the reliability of the structure (in the results of more elements, for example).

Currently, another factor is being introduced: ecology [6–8]. Solutions to reduce carbon dioxide emission [7] and toxic emission [3, 4] are being considered. This is achieved through changes in fuel type [3] and optimization of the combustion process [4]. The introduction of new electronically controlled fuel and ignition control systems also helps in this work [3].

This article presents the results of this type of work: the introduction of electronic ignition timing control system to an aircraft piston engine. The purpose of the analysis is to determine whether the introduction of this system will allow to achieve the objectives of increasing power and reducing engine emissions.

2. Research description

2.1. Research objects

The tests were conducted on the ASz-62IR-16X aviation engine manufactured by the WSK PZL Kalisz S.A. The engine is used in small and medium-sized cargo (Antonov AN-2) and agricultural (M18 Dromader) aircrafts. It is a four-stroke unit of nine cylinders in radial setup, air-cooled with electronic fuel injection control system and magneto ignition. Table 1 lists main parameters of the engine, and Fig. 1 presents the object of research in the test bed.

Table 1. ASz-62IR specification [2]

Parameters	Values
Engine diameter	1380 mm
Length	1130 mm
Dry engine mass	567 kg (±2%)
Cylinder diameter	155.5 mm
Stroke	174.5 mm
Displacement	29.911 dm^3
Compression rate	6.4±0.1
Maximum power at 2200 rpm and PK = 1050 mmHg	1000 KM (735 kW)
Power rating at 2100 rpm and PK = 900 mmHg	820 KM (603 kW)
Power rating at h=1500 m	840 KM (618 kW)
Power (2030 rpm & PK = 830 mmHg)	738 KM (543 kW)
Power (1930 rpm & PK = 745 mmHg)	615 KM (452 kW)
Power (1770 rpm & PK = 665 mmHg)	492 KM (362 kW)
Average fuel consumption	200 dm^3/h
Maximum fuel consumption	330 dm^3/h
Weight to power ratio	0.57 kg/KM (0.42 kg/kW)
Power to displacement ratio	33.43 KM/dm^3 (24.58 kW/dm^3)

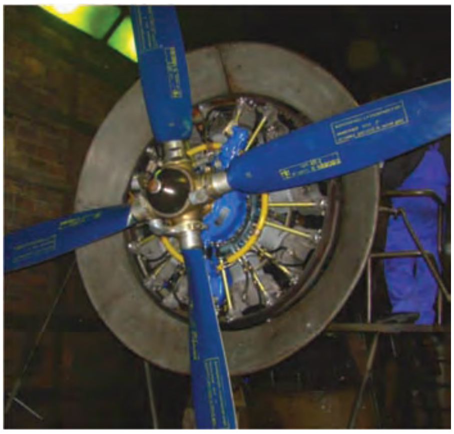

Fig. 1. ASz-62IR-16E engine in test bed

The research was carried out on the ASz-62IR-16E engine equipped with electronic fuel injection system and its modification ASz-62IR-16X equipped additionally with electronically controlled ignition system. This system was designed within the project "Device for power supplying and controlling on-board and ground equipment" INNOLOT/I/1/NCBR/2013 by the team of Lublin University of Technology and WSK "PZL Kalisz" S.A. The diagram of the system is shown in Fig. 2.

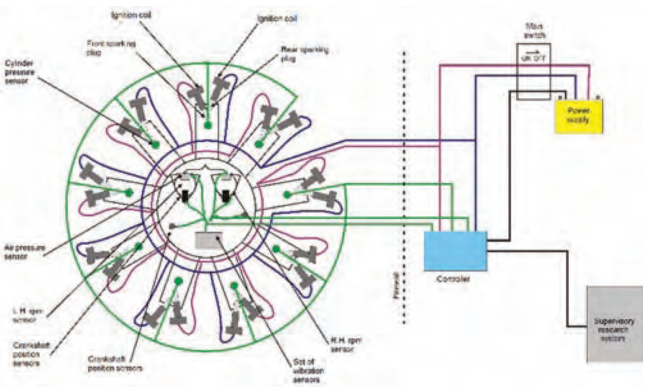

Fig. 2. Ignition system of ASz-62IR-16X engine

2.2. Test stand

The tests were carried out on a test stand located in the WSK „PZL Kalisz" S.A. – research and production stand at the engine manufacturer. The engine was braked by a propeller – Fig. 1. The torque measurement was performed on a reactive basis.

The combustion process was monitored by means of M3.5×0.6 optoelectronic sensors by OPTRAND, placed in the cylinder head. The sensors detected changes of the intensity of light transmitted by two adjacent optic fibers, one connected to a LED, and the other to a photo detector. The change of the intensity of light received by the photodiode was caused by the change of the intensity of light reflected by a steel membrane deformed by the in-cylinder pressure.

The rotational speed and crankshaft position were measured by means of a magnetically induced shaft position sensor. The sensors were located in a purpose-built adapter that enabled determining the TDC position of the first cylinder.

The following signals were measured during the experiment: pressure in 2 cylinders, pressure in inlet manifolds of cylinder 2 (by means of MPX250 sensors) and the position of the crankshaft. The measurement of all the signals were conducted by means of a digital to analogue converter DAQ-Pad 6070E (National Instruments) at the frequency of 30 kS/s per channel. The data were then processed by means of an original program created by the author.

Exhaust gas emissions were measured with the Pierburg Herman HG-400 analyser. Exhaust gas was taken from the exhaust manifold connecting cylinders 2 and 3.

2.3. Scope of research

The aim of the research was to compare the performance of an engine operating with a constant ignition advance angle (ASz-62IR-6E engine) and with an ignition angle dependent on engine operating conditions (according to the calibration of the ASz-62IR-16X engine algorithm). Ignition advance angle for ASz-62IR-16E engine was 15° before GMP for the front spark plug and 20° before GMP for the rear spark plugs. The ignition advance angle for the ASz-62IR-16X engine varied between 10–21° for the front spark plug and 15–26° for the rear spark plug, depending on the rotational speed and intake manifold pressure.

Table 2. Parameters of the exhaust gas analyser HG-400

Component	Measurement range	Measurement resolution	Measurement accuracy
CO	0…10% vol	±0.01% vol.	< 1.2% vol. ±0.06% vol. ≥ 1.2% vol. ±5%
CO_2	0…20% vol.	±0.1% vol.	< 10% vol. ±0.5% vol. ≥ 10% vol. ±5%
HC	0…20000 ppm vol.	±1 ppm vol.	< 220 ppm vol. ±11 ppm vol. ≥ 220 ppm vol. ±5%
O_2	0…22% vol.	±0.01% vol.	< 2% vol. ±0.1% vol. ≥ 2% vol. ±5%
NO_x	0…5000 ppm vol.	±1 ppm vol.	< 500 ppm vol. ±50 ppm vol. ≥ 500 ppm vol. ±10%

The tests were carried out in steady state of engine operation at points corresponding to the acceptance tests of engine production. These points are in line with propeller characteristics and include: take-off power (2200 rpm), nominal power (2100 rpm), 90% of nominal power (2030 rpm), 75% of nominal power (1910 rpm), 60% of nominal power (1770 rpm) and 50% of nominal power (1670 rpm). At each point was measured:

1) The pressure in cylinder 2 in the following 500 cycles;
2) Torque;
3) Engine speed;
4) Exhaust gas composition.

Power was determined on the basis of torque and speed measurements and converted to normal conditions. Cylinder pressure measurements were analyzed and the mean indicated pressure and its standard deviation were determined for 500 consecutive cycles.

3. Results

The following figures show the results of research and analysis of comparison of engine performance with the constant ignition advance angle (ASz-62IR-16E engine) described in the diagrams as Constant and with the variable ignition advance angle (ASz-62IR-16X engine) described in the diagrams as Algorythm.

Figure 3 shows the reduced engine power at the particular measuring points on both ignition systems. It can be seen that the characteristics of the engine practically overlap. In order to show the level of changes, the percentage difference between the power obtained for an engine with a constant and variable ignition advance – Fig. 4. It can be seen that the determined differences do not exceed 2.5% and their average value is 0.7%. Therefore, it can be considered negligible and resulting from the measurement spread.

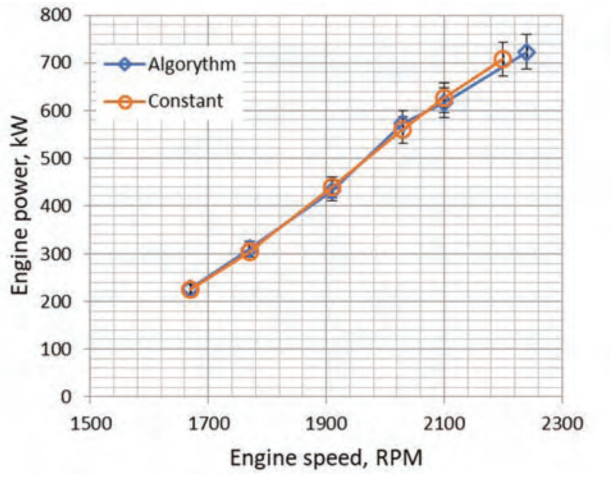

Fig. 3. Relationship between power and rotational speed for constant and variable ignition advance angle

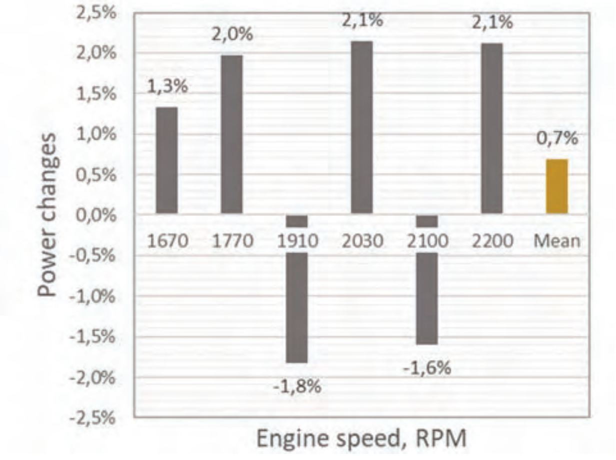

Fig. 4. Differences in reduced engine power between engines with constant and variable ignition advance angle

Figure 5 shows the mean indicated pressure from cylinder no. 2 of the engine at particular measuring points at both ignition systems. Here, too, the characteristics practically overlap. The differences – shown in Fig. 6 – are small and result mainly from the non-repeatability of the measurements.

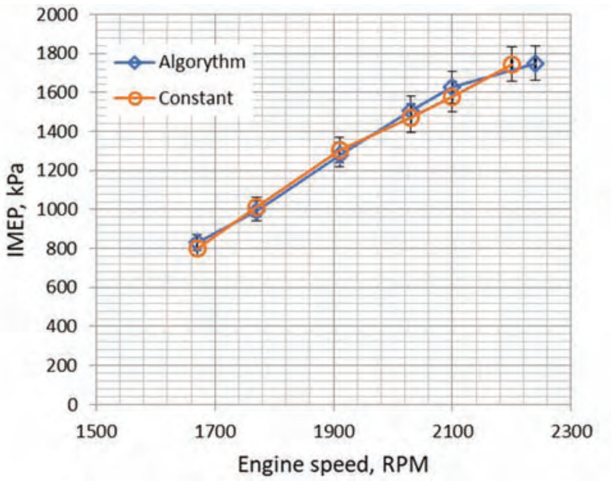

Fig. 5. Relationship between IMEP and rotational speed for constant and variable ignition advance angle

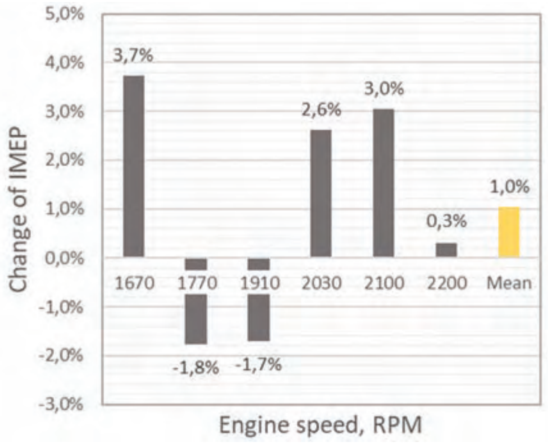

Fig. 6. Differences in IMEP power between engines with constant and variable ignition advance angle

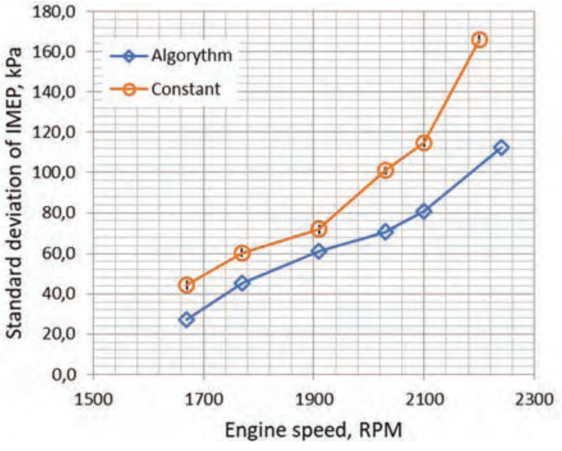

Fig. 7. Relationship between standard deviation of IMEP and rotational speed for constant and variable ignition advance angle

Significant differences were noted in the analysis of the standard deviation of the mean indicated pressure – Figs 7 and 8. The use of electronically controlled ignition system allows to reduce the non-repeatability of the combustion process – lowering the standard deviation of the IMEP. The introduction of a variable ignition advance angle, better adapted to a specific point of work, allows to reduce the non-repeatability by more than 28% on average.

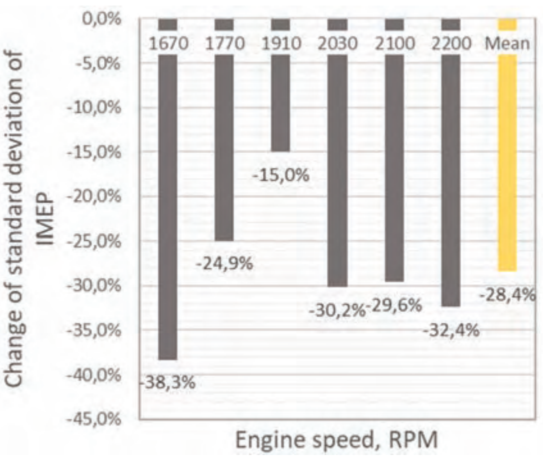

Fig. 8. Differences in standard deviation of IMEP power between engines with constant and variable ignition advance angle

Figures 9 and 10 show carbon monoxide emissions. This engine is characterised by high CO emissions, especially at points of nominal power and take-off power. The emission value reaches 5.8% at nominal power and more than 10% at take-off power respectively. This is due to the regulation of the air-fuel mixture for these points. The mixture is very rich in this case (often exceeds lambda < 0.7) as a result of the use of fuel for engine cooling. This is a characteristic solution for this type of engines. The use of a controlled ignition system results in a slight decrease in emissions at all measuring points. This decrease is on average 3.8% and means that ignition control has improved combustion quality.

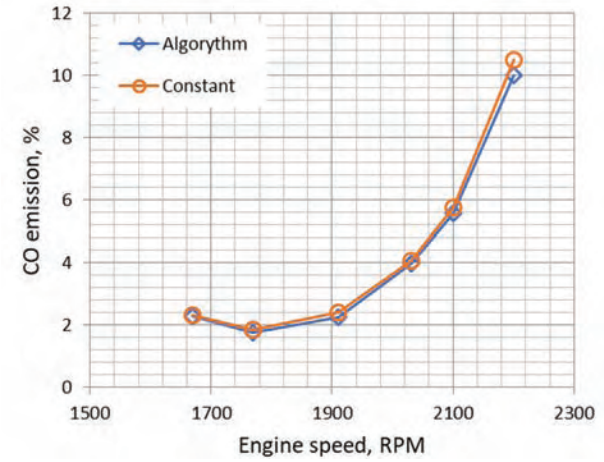

Fig. 9. Relationship between CO emission and rotational speed for constant and variable ignition advance angle

It is also noticeable in the level of emission of non-flammable HC hydrocarbons – Figs 11 and 12. One can also see high emission at points of nominal power and starting power resulting from engine cooling with fuel, reduced by 2.8% on average with improved ignition advance angle.

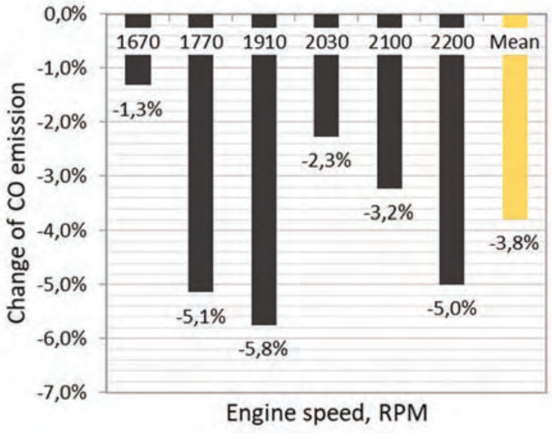

Fig. 10. Differences in CO emission power between engines with constant and variable ignition advance angle

This is also confirmed by the emission of carbon dioxide – Figs 13 and 14. In this case, the improvement of the combustion process results in an increase in CO_2 emissions. This is due to the better oxidation of HC and CO (reduction of their emissions). With the introduction of ignition control, an average increase in emissions of 1.9% was achieved.

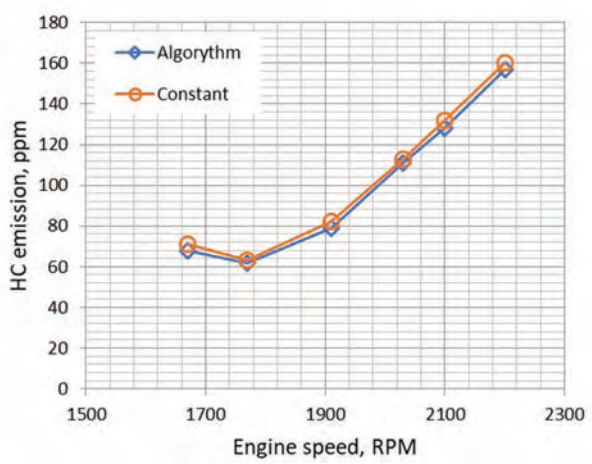

Fig. 11. Relationship between HC emission and rotational speed for constant and variable ignition advance angle

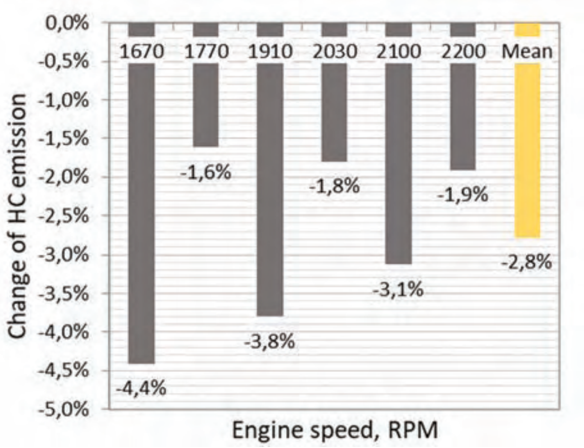

Fig. 12. Differences in HC emission power between engines with constant and variable ignition advance angle

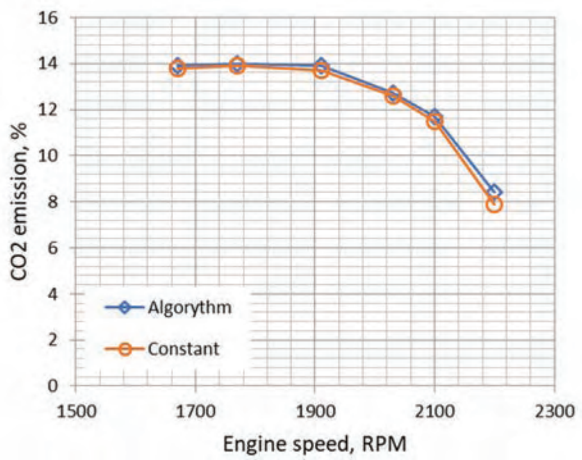

Fig. 13. Relationship between CO_2 emission and rotational speed for constant and variable ignition advance angle

The improvement in combustion can also be seen in NO_x emissions – Figs 15 and 16. At nominal power and 90% of nominal power, NO_x emissions are the highest and exceed 1300 ppm. This is due to the power-optimal setting of both the composition of the mixture and the ignition advance angle. At the take-off power point, this value drops due to the lowering of the combustion temperature through significant enrichment of the mixture (Fig. 17).

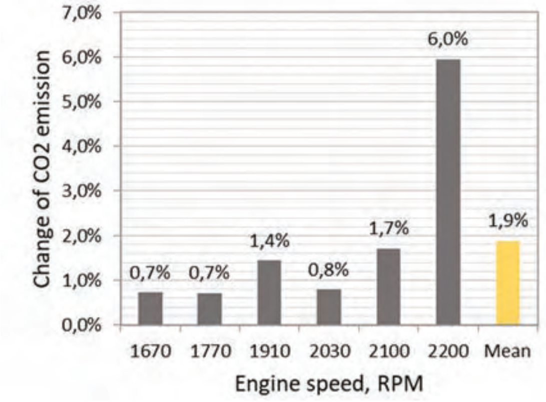

Fig. 14. Differences in CO_2 emission power between engines with constant and variable ignition advance angle

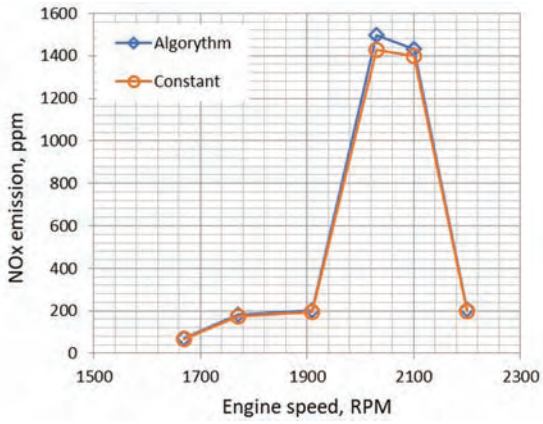

Fig. 15. Relationship between NO_x emission and rotational speed for constant and variable ignition advance angle

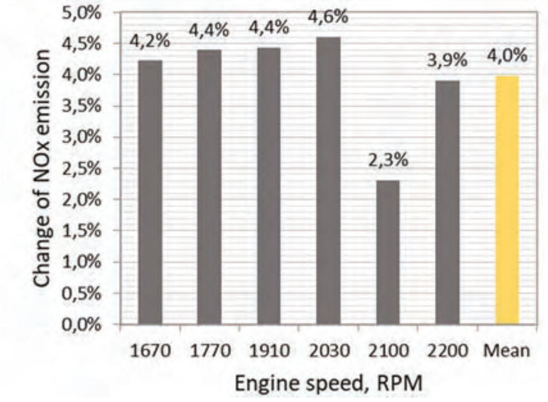

Fig. 16. Differences in NO_x emission power between engines with constant and variable ignition advance angle

The introduction of ignition control improves the combustion process resulting in a reduction in NO_x emissions. In the analyzed case, at each point the emission value was reduced and the average value decreased by 4.0%.

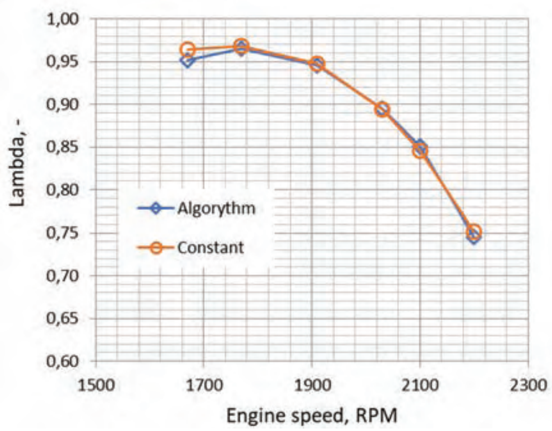

Fig. 17. Relationship between fuel ratio and rotational speed for constant and variable ignition advance angle

4. Conclusions

To summarize, it can be stated that for the tested engine design:

1. The use of ignition advance angle control with respect to engine speed and load has practically no effect on power output. This can be seen both in the obtained mean indicated pressures and reduced power. Therefore, the ignition advance angle in the case of its constant value has been correctly selected.
2. The introduction of ignition timing control has significantly contributed to the reduction of combustion non-repeatability.
3. The introduction of ignition timing control has also improved the fuel oxidation process, which can be seen in the increase in CO_2 in exhaust gases while reducing CO and HC emissions. However, the improvement in combustion resulted in an increase in NO_x emissions.

Therefore, the use of an electronic control system for ignition timing mainly affects the stability of the combustion process, which will result in a reduction in vibrations of the engine. A much more important feature is the ability to easily adapt the ignition control to different types of fuels, which in the case of the previous system required mechanical adjustment.

Acknowledgements

This work was supported by the EU under the project "EPOCA Device for power supplying and controlling on-board and ground equipment" INNOLOT/I/1/NCBR/2013 within the framework the Operational Programme Smart Growth carried out by The National Centre for Research and Development.

Nomenclature

IMEP	indicated mean effective pressure
CO	carbon monoxide emission
HC	non-flammable hydrocarbons emission
NO_x	nitrogen oxides emission
CO_2	carbon dioxide emission

Bibliography

[1] CAO, J., DING, S. Sensitivity analysis for safety design verification of general aviation reciprocating aircraft engine. *Chinese Journal of Aeronautics*. 2012, **25**(5), 675-680. DOI:10.1016/S1000-9361(11)60433-0.

[2] CZARNIGOWSKI, J. Analysis of cycle-to-cycle variation and non-uniformity of energy production: Tests on individual cylinders of a radial piston engine. *Applied Thermal Engineering*. 2011, **31**(10), 1816-1824, DOI:10.1016/j.applthermaleng.2011.02.027.

[3] CZARNIGOWSKI, J., JAKLIŃSKI, P., WENDEKER, M. Fuelling of aircraft radial piston engines by ES95 and 100LL gasoline, *Fuel*. 2010, **89**(11), 3568-3578. DOI:10.1016/j.fuel.2010.06.032.

[4] CZYŻ, Z., GRABOWSKI, Ł., PIETRYKOWSKI, K. et al. Measurement of flight parameters in terms of toxic emissions of the aircraft radial engine ASz62-IR, *Measurement*. 2018, **113**, 46-52. DOI:10.1016/j.measurement.2017.08.035.

[5] DALKILIC, S. Improving aircraft safety and reliability by aircraft maintenance technician training. *Engineering Failure Analysis*. 2017, **82**, 687-694. DOI:10.1016/j.engfailanal.2017.06.008.

[6] DRAY, L. An analysis of the impact of aircraft lifecycles on aviation emissions mitigation policies. *Journal of Air Transport Management*. 2013, **28**, 62-69. DOI:10.1016/j.jairtraman.2012.12.012.

[7] HASSAN, M., PFAENDER, H., MAVRIS, D. Probabilistic assessment of aviation CO_2 emission targets. *Transportation Research Part D: Transport and Environment*. 2018, **63**, 362-376. DOI:10.1016/j.trd.2018.06.006.

[8] KURNIAWAN, J. S., KHARDI, S. Comparison of methodologies estimating emissions of aircraft pollutants, environmental impact assessment around airports. *Environmental Impact Assessment Review*. 2011, **31**(3), 240-252. DOI:10.1016/j.eiar.2010.09.001.

[9] SUJATA, M., MADAN, M., RAGHAVENDRA, K. et al. Unraveling the cause of an aircraft accident. *Engineering Failure Analysis*. 2019, **97**, 740-758. DOI: 10.1016/j.engfailanal.2019.01.065.

Jacek Czarnigowski, DSc., DEng. – Faculty of Mechanical Engineering, Lublin University of Technology.

e-mail: *j.czarnigowski@pollub.pl*

Piotr Jakliński, DSc., DEng. – Faculty of Mechanical Engineering, Lublin University of Technology.

e-mail: *p.jaklinski@pollub.pl*

Article citation info:
DZIUBAK, T. Properties of material with nanofiber layer used for filtering the inlet air of internal combustion engines. *Combustion Engines*. 2019, **177**(2), 66-75. DOI: 10.19206/CE-2019-212

Tadeusz DZIUBAK

CE-2019-212

Properties of material with nanofiber layer used for filtering the inlet air of internal combustion engines

Nanofiber properties, and the possibilities of their application in industry, including the production of car air intake filtration materials for vehicle engines are discussed. The attention is paid to the low efficiency of standard filtration materials based on cellulose in the range of dust grains below 5 μm. The properties of filtration materials with nanofibers addition are described. The conditions, and methodology of material filter paper tests at the station with particle counter were developed. Studies on the filtration characteristics, such as: efficiency, accuracy, as well as pressure drop of filtration materials differing in structure were made: standard paper, cellulose, and these materials with the addition of nanofibers. These are commonly used filter materials for filter inserts production of car air intake systems. Test results show significantly higher values of the efficiency, and filtration accuracy of materials with nanofiber layer addition of dust grains below 5 μm in comparison with standard filter paper. It was found that there are 16 μm dust grains in the air flow behind the insert made out of cellulose,, which may be the reason for the accelerated wear of the engine's "piston-piston ring-cylinder" association. Lower values of dust mass loading coefficient km for filtration materials with the addition of nanofiber layer, in relation to standard filter paper were observed.

Key words: *engine, air filter, filtration materials, nanofiber filter media, filtration efficiency, filtration performance, pressure drop, dust mass loading*

1. Introduction

The dominant filter material of modern inlet air internal combustion engines is filter paper (porous material), characterized by filtration performance $d_z \geq 5$ μm, filtration efficiency at $\varphi_w = 99.9\%$, low thickness $g_m = 0.4–0.8$ mm, and the same small ($k_m = 200–250$ g/m^2) dust absorptivity limited by the permissible pressure drop Δp_{fdop} of the air filter [3, 5, 6–9]. Filter papers stop dust grains on the fibers (which have approx. diameter of 20 μm) of the porous barrier due to the various forces, and filtration mechanisms. Over time, dust grains are deeply embedded in the fibrous structure of the filtration media, preventing the proper air flow. As a result, there is a continuous pressure drop on the filter, until the value of Δp_{fdop} is reached, which is the criterion of air filter usage end, and the exchange of the filter cartridge.

It is believed that all dust grains above $d_z \geq 1$ μm which are of mineral origin cause accelerated components wear of internal combustion engines [2–5, 7, 10]. The air filter responds for supplying air to the engine cylinders of the appropriate quality (purity), to minimize engine components wear.

The development of fiber production technology has caused that more and more often, filter manufacturers, for example: Donaldson, Maan-Hummel, use filtration materials with an additional nanofiber layer. These are the fibers with very small diameters, ranging from 50–1000 nm, which dependins on their production process, and the type of polymer used.

A thin layer of nanofibers applied from the inlet side to a standard filter bed (eg cellulose) retains particles of impurities, before they penetrate into the filter material. The development of fiber production technology has caused that more and more often, filter manufacturers, for example: Donaldson, Maan-Hummel, use filtration materials with an additional nanofiber layer. The dust particles retention on the surface of the layer of nanofibers allows their subsequent removal (filter cleaning) by means of reverse (in the opposite direction to the direction of air flow during operation) of a compressed air pulse under high pressure. If the dust particles are on the filter material surface, they do not damage (break) the structure of the filter cartridge when they are blown out.

In the available literature, the data characterizing the properties of filtration materials with the addition of nanofibers is not very common. Hence, it is advisable to carry out experimental investigations of filtration materials with the addition of nanofibers in terms of efficiency, filtration performance, and pressure drop. Such studies are expensive and labor-intense, however, this is the most reliable research method.

2. Air pollution and their impact on engine components wear

During the operation of combustion engines with air, the significant amounts of contaminants enter into cylinders, but these are mostly dust grains with sizes below 2–5 μm as modern air filters, where filter paper or non-woven fabric is a filter medium, operate with such precision. Larger dust grains enter into the engine cylinders as a result of the failure of the air supply system. The contaminants enter into the engine cylinders also with fuel and oil but their amount is much smaller. The abrasive wear occurs when a hard foreign objects get between two cooperating surfaces, sticking into the different depths, leading to deformation and cutting micro volumes of surface layers of the cooperating components. The literature is dominated by the view that the greatest wear is caused by the dust grains of sizes of d_z equal to the minimum h_{min} thickness of an oil layer needed to create a lubricant film between the cooperating surfaces, that is when there is the following relationship. For any other value of the quotient of h_{min}/d_z, connection wear decreases (Fig. 1) [10].

$$\frac{h_{min}}{d_z} = 1 \tag{1}$$

The minimum thickness of the oil film h_{min} between two abrasively cooperating surfaces is directly proportional to the temperature-dependent oil viscosity η, the C coefficient depending on the bearing dimensions, relative speed of lubricated surfaces υ, and inversely proportional to the P loading force and is expressed with the general dependency:

$$h_{min} = \eta \cdot \frac{C \cdot \upsilon}{P} \qquad (2)$$

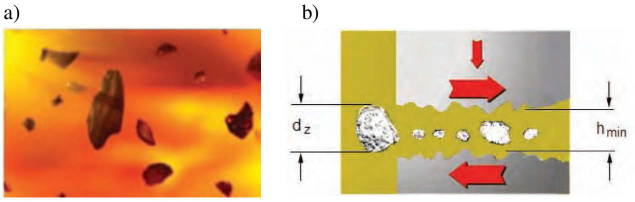

Fig. 1. Effect of solid particulates on a tribological connection: a) contaminations suspended in the oil [1], b) condition of the maximum connection consumption [10]

For the set conditions of the engine operation, the oil film thickness h_{min} changes cyclically in a tribological connections area depending on the connection operating conditions. Between a cylinder liner and a piston rings, the oil film thickness is determined by the piston speed (Fig. 2).

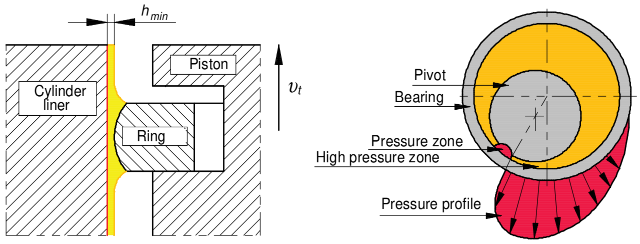

Fig. 2. Formation of an oil film in connections: a) P-R-C, b) pivot – bearing

Between the BDC and UDC dead centres, the piston (piston rings) speed is the largest, thus the thickness of the oil film in this area takes the maximum values. Changing the direction of the piston movement in extreme positions of the cylinder liner makes that its speed in this area is the smallest, and in BDC and UDC is zero, which leads to a reduction of the oil film or its complete disappearance. Therefore, there may be periods of even direct metallic contact between the piston ring and the liner. Under these conditions, in theory, each particle with any small sizes can cause the wear. As a result of the oil film thickness changes, dust grains, which were between the cooperating surfaces, are crushed and grinded and can penetrate between two frictionally cooperating surface, where the oil film thickness takes small values. In typical connections of a combustion engine, the oil film thickness specified in the paper [3] takes different values (Fig. 3).

It is clear that even the smallest dust grains and those below 2–5 µm will result in accelerated wear. It is believed that all the dust grains above 1 µm are the cause of accelerated wear, but the dust's abrasive aggressivity decreases when the dust grains sizes are below 5 µm. However, the dust grains below 1 µm are dangerous because they affect the cylinder sliding surface like polishing paste. Oil particles do not adhere to a polished cylinder bearing surface, which leads to breaking the oil film and accelerated wear. The volume consumption of engine components due to the impact of dust depends on: the parameters of the sucked in dust, clearances between cooperating parts, design and operating engine parameters, material mechanical properties. The dust entering with the air into the engine cylinders affects the first piston ring, the piston, and the top cylinder part the most intensively. Applying by-pass filters in engine lubrication systems resulted exactly from the need to remove contaminants of with the dimension of below 1 µm from the engine oil.

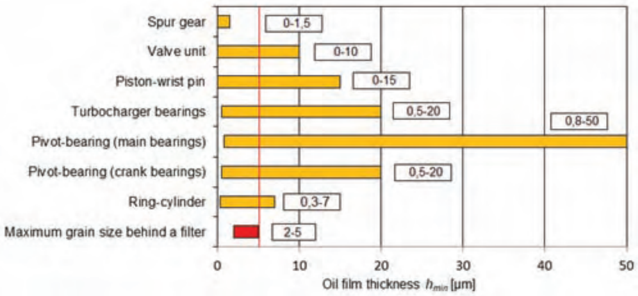

Fig. 3. Oil film thicknesses in typical combustion engine connections [3]

Figure 4 shows the results of the P-R-C connection wear of a 4-cylinder engine with spontaneous ignition (V_{ss} = 1.3 dm^3, N_e = 66 kW at 4,000 rpm, M_o = 200 N·m in the range of 1,750–2,250 rpm), turbocharged, with charge air cooling and exhaust gases recirculation after 1,200 hours of operation according to a specified endurance test [18]. The greatest wear of the cylinder liners was registered in their upper part, in the plane perpendicular to (B-B) the engine axis, which is consistent with other studies results [10]. The cylinder liner and piston rings wear caused by contaminants entering into the cylinder liner with the inlet air and contaminants in the oil causes the decline in the rod side area. As a result, there is a loss of the compressed agent, and thus the pressure drop at the end of a compression stroke, and consequently the tested engine power drop by approximately 2.5% and increase in specific fuel consumption by 3.4% (Fig. 4).

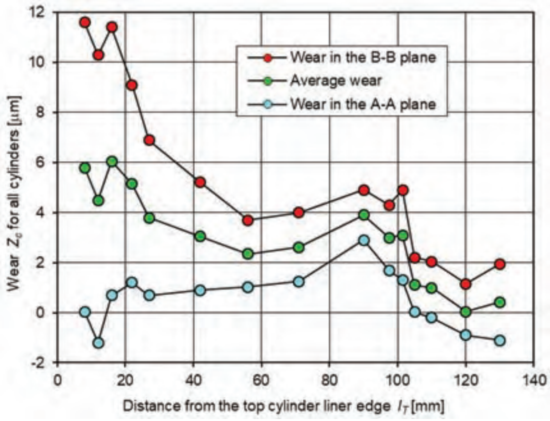

Fig. 4. Cylinder liner wear of a 4-cylinder, turbocharged engine with spontaneous ignition and power N_{emax} = 66 kW in a plane perpendicular (B-B) and parallel (A-A) to the engine axis [18]

The P-R-C connection wear is also the increase in the intensity of exhaust fumes blow-through into a crank case (Fig. 5), which increases the lubricating oil temperature, decreases its lubricating properties and blowing the oil through exhaust gases. The result of this is a loss of "a lubricant film," and as a result of which the system passes from fluid friction conditions to mitigated solid friction.

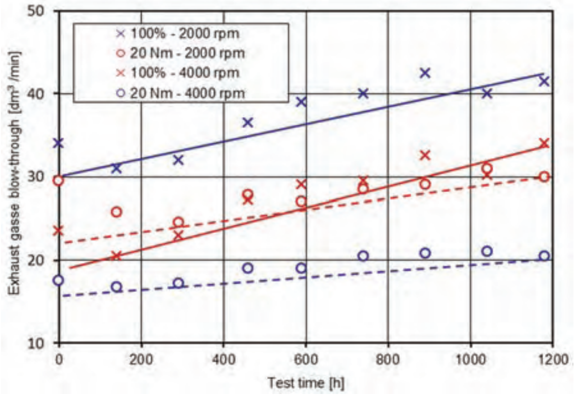

Fig. 5. Effect of the test on: a) the engine exhaust gas blow-through at full and low engine load, b) the engine oil consumption at various engine loads [18]

After 1,200 hours of operation at full load and 4,000 rpm, blow-through intensity increased by 61%. This accelerates considerably the engine oil degradation. The increased looseness in the P-R-C connection intensifies the phenomenon of piston rings operation, thus oil consumption and exhaust fused toxicity increase. At the same time, the engine oil consumption increased by 108%, 96% and 113% respectively at loads of 100%, 33% and 20 N·m (Fig. 6).

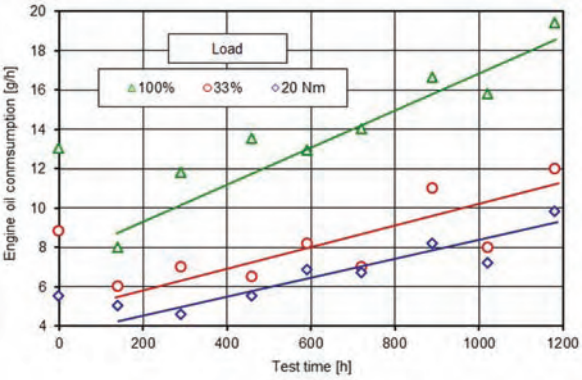

Fig. 6. Effect of the test on: a) the engine exhaust gas blow-through at full and low engine load, b) the engine oil consumption at various engine loads [21]

The accelerated wear of the cylinder liner may be a result of engine operation with an inoperative air filtration system. Figure 7 shows the image of such wear of a truck's cylinder liner.

Abrasive wear of the cylinder bearing surface is visible in the form of parallel, continuous scratches bands along a forming cylinder liner in a cylinder bearing surface top area along approximately 1/5 of the circumference. Scratches were caused by hard and big dust grains. Scratch bands are so intense and deep that traces of final cylinder bearing surface treatment – honing – are invisible (Fig. 7a). Figure 7b shows much less wear of the cylinder bearing surface, seen as single scratches over the traces after surface treatment. Figure 7c shows the view of a truck engine's cylinder bearing surface operated with an operative air filtration system. Honing traces and combustion products deposits on the cylinder liner above upper dead centre of the first piston ring are clearly visible.


a) b) c)

Fig. 7. View of a truck's engine cylinder bearing surface operated with an operative and inoperative air filtration system: a) clear scratches band without honing traces, b) visible single scratches band over surface treatment traces, c) an operative air filtration system [7]

3. Nanofibers filtration materials properties

Proper purity of the air supplied to the internal combustion engine piston cylinders is provided by the air filter together with the intake. In today's passenger cars and vans, there are used single-stage filters, which are equipped with filter inserts made of pleated paper (sometimes made of non-woven fabric) shaped in the form of cuboidal panels. For filtering intake air for vehicle engines used in conditions of high dust concentrations in the air, two-stage or three-stage filters are used. The first stage of filtration is then an inertial filter, and the second is a series of a porous barrier made of filter paper behind it. The development of fiber production technology has caused that more and more often filter manufacturers, for example Donaldson, Mann-Hummel, use filtration materials with an additional nanofibers layer to build filtration inserts.

Nanofibers have completely different properties compared to standard fibers. First of all, in relation to the mass, they have a large surface area, much higher strength, and they are also characterized by higher chemical activity, and higher moisture sorption. They can be used to build filters to separate chemical or biological contaminants from the blood plasma, they can be used as gas filters, and impurities with very small diameters - filters with molecular separation. Due to their structure, nanofibers materials have unique properties, and offer unexpected possibilities of their application in many fields, such as in medicine, energy and air filtration [15].

Nanofibers can be made from different polymers, and thus have different physical properties. Examples of natural polymers include collagen, cellulose, silk fibroin, keratin, gelatine and polysaccharides, such as chitosan and alginate. Nanofibers diameter depend on the type of used polymer, and the method of production [19]. All polymer nanofibers are unique due to their large area, and volume, considerable mechanical strength, and small fiber diameter. Filter media made of nanofibers are characterized by high porosity and small pore sizes [11, 13–15].

In automotive industry, fibers with very small diameter of about 0.05–0.8 μm (50–800 nm) are used. As a comparison [25]:

- cellulose fiber thickness – 10 000–20 000 nm
- human hair thickness –20 000–80 000 nm
- blood red cell diameter – about 7000 nm
- bacteria – 2000 nm.

Figure 8 shows SEM image of nanofibre coated filter medium [23].

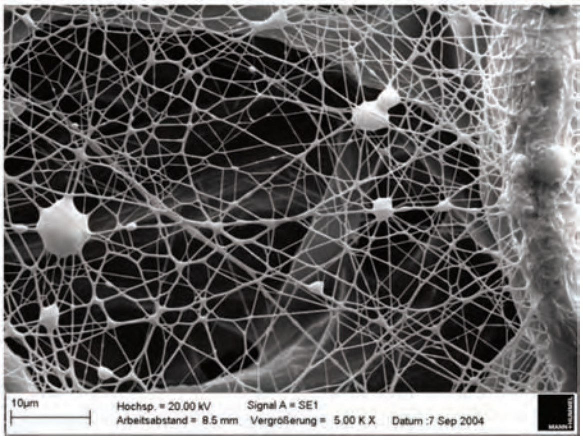

Fig. 8. SEM image of nanofibre coated filter medium [23]

The most widely used method of producing nanofibers is the electrospinning method [19]. It is a process of obtaining fibers from molten polymers or their solutions, using high voltage. This modern technology, using the right polymer, and dissolution system, now allows the production of fibers with diameters ranging from 3 nm to 1000 nm. Virtually any polymer can be obtained in the form of fibers by electrospinning. Nanofibers have many possible technological, and commercial applications in the following areas: tissue engineering, drug delivery (release), diagnosis of carcinogenic changes, lithium-air batteries, optical sensors, and air filtration.

Due to the limited mechanical, and strength properties of the thin layer of nanofibers (1–5 µm), it is applied to the substrate (Fig. 9) from conventional filtration materials that have higher strength. The nanofibers may be laid on one or two sides of the substrate, which may be: cellulose, nylon or polyester. Usage of nanofibers, as an additional layer applied to standard filter materials for air filters used in motor vehicles, significantly increases the efficiency and accuracy of filtration.

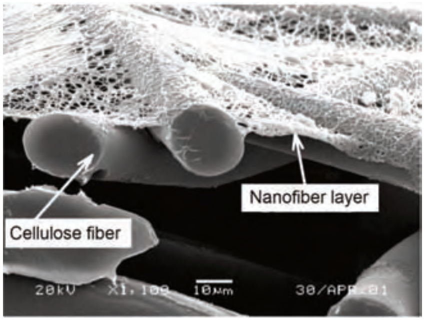

Fig. 9. Nanofibers applied to a cellulose substrate – cross-section view [13]

Figure 10 shows the fractional efficiency of a cellulose-based nanofibre filtration medium, on which a 0.3 mm nanofiber layer, $g_m = 0.1$ g/m^2, and fiber diameter in the range of 40–800 nm was placed [15, 16]. With the increase of the dust grain size, the efficiency of filtration for both filter cartridges gets higher and higher values, but the filtration efficiency of the filter cartridge with the nanofibers layer has higher level. For dust grains with $d_z = 0.25$ µm, filter cartridge filtration efficiency, with the "meltblown" nanofiber layer applied is $\varphi = 80\%$, and for a standard cellulose fiber filter only $\varphi = 20\%$. With the dust grain size, the difference in the filtration efficiency of both cartridges decreases and for $d_z = 4.5$ µm it is 99.8% and 97% respectively. Nanofibers layer usage on a standard filtration substrate also causes an increase in the pressure drop Δp. For the speed $\upsilon_F = 0.3$ m/s, the insert with the addition of nanofibers has a 75% higher flow resistance Δp than the standard [12]. These values are much higher, than those based on cellulose, and commercial materials with the addition of nanofibers (Fig. 3).

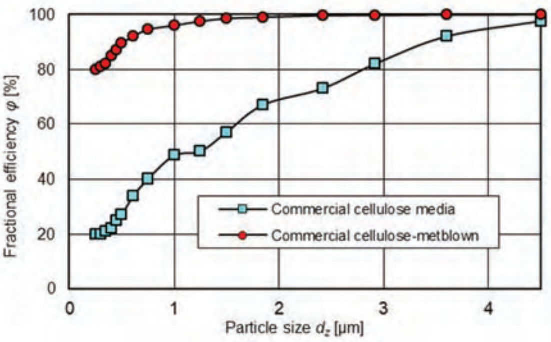

Fig. 10. Pleated filter elements made of cellulose fibers, nanofiber layer and cellulose fibers filtration efficiency [12]

The ratio of the nanofibers to the cellulosic fiber diameter is approximately 1:130. This results in a significant increase in the filtration area for the nanofiber bed. Nanofibers area of 1 g, with a diameter of 200 nm is approximately 20 m^2/g, and only 0.2 m^2/g for cellulose fibers with a diameter of 20 µm. Fiber diameter is the main variable responsible for the filtration efficiency, and flow resistance. The efficiency increases rapidly as the fiber diameter decreases. For example, the use of fibers with a diameter of 1µm instead of 50 µm leads to an increase in the filtration quality factor by 2000 [15, 16].

Filtration efficiency, filtration performance and pressure drop of filtration materials with an additional nanofiber layer depends on the substrate structure (type of material), and the layer of nanofibers thickness. The paper [14] presents the results of filtration effectiveness tests of four samples made of different filtration materials: 1 – nonwoven, 2 – knitted, 3 – woven, 4 – charmeuse (silk nonwoven).

Filtration efficiency, and pressure drop were determined for samples with nanofiber layers with a basis weight of: $g_m = 0.02$ g/m^2, $g_m = 0.1$ g/m^2, $g_m = 0.5$ g/m^2, and without a layer of nanofibers. Photos from the SEM microscope for sample C with a layer of nanofibers with set weights are shown in Fig. 11. The nanofibers had an average diameter of 140 nm with a standard deviation of 30 nm. The average pore size for the nanofiber layer with the basis weight $g_m = 0.02$ g/m^2, $g_m = 0.1$ g/m^2, $g_m = 0.5$ g/m^2 were respectively 1190 nm, 540 nm and 260 nm. The effect of applied nanofiber layer on the filtration efficiency of the filter material (nonwoven fabric 1) is shown in Fig. 12. Material filtration effectiveness without the nanofiber layer is very low, and for particle sizes below 2 µm does not exceed 10%. A small layer of nanofibers with $g_m = 0.02$ g/m^2 increases the filtration efficiency of particles smaller than 2 µm over 60%. Nanofibers layer with $g_m = 0.1$ g/m^2 increased the filtration efficiency of particles with dimensions of 2 µm to the value of about 90%, and for $g_m = 0.5$ g/m^2 – to the value of over 99%.

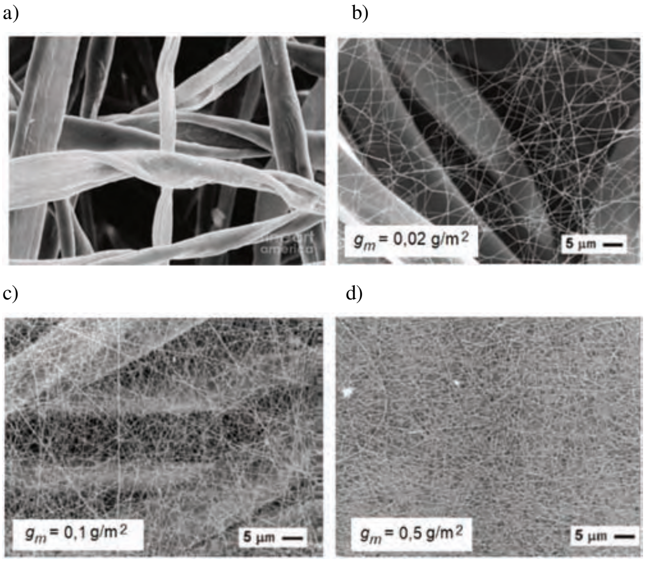
a) b) c) d)

Fig. 11. SEM microscope photographs for sample 3 with nanofiber a basis weight layer: a) without nanofibers, b) $g_m = 0.02$ g/m^2, c) $g_m = 0.1$ g/m^2, d) $g_m = 0.5$ g/m^2 [14]

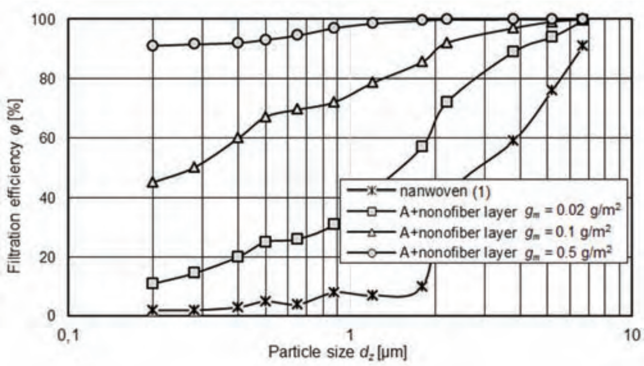

Fig. 12. Material filtration effectiveness (nonwoven fabric sample 1) without a nanofiber layer, and with nanofiber layer with unit weight $g_m = 0.02$ g/m^2, $g_m = 0.1$ g/m^2, $g_m = 0.5$ g/m^2 [14]

There are known constructional solutions for vehicle inlet air filters (Abrams M1 tank), where a filter cartridge with the addition of nanofibers, and a system of automatic impulse purification of the PJCA (Pulse Jet Air Cleaner) filter cartridge is used [12]. It ensures several times longer air filter life, and thus longer vehicle life without the need to operate the filter. The principle of PJAC operation system is that at the time when the pressure drop of the filter inflow does not exceed the permissible value, the air filtration process takes place, as in every vehicle filter. After pressure drop reaches certain value, a pressure modulator is activated for 0.1–0.35 s, producing a pulse in the form of compressed air with a pressure of 0.4–0.6 MPa. Compressed air flowing in the opposite direction, to the air flow direction during the filtration process blows out dust particles from the surface of the filter cartridge, which then fall into the dust collector [20].

Figure 13 shows that the standard filter cartridge, mounted in a tank which moves in the column in desert conditions, reaches the permissible value of pressure drop, $\Delta p_{fdop} = 7.6$ kPa (30 inches of H_2O) after driving about 25 km (16 miles).

When a filter cartridge with a nanofiber layer equipped with an automatic pulse cleaning system reaches maximum pressure drop of approximately 6.3 kPa (25 inches of H_2O), the pulse cleaning system will be activated. After removing the dust from the nanofiber layer, the pressure drop decreases to approximately 5 kPa (20 inches of H_2O), and remains at this level.

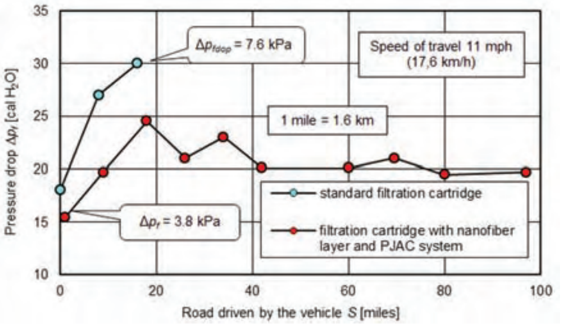

Fig. 13. Air cleaner pressure drop versus miles traveled in 20 mph convoy test in desert conditions and automatic cleaning system [12]

4. Author's own research

4.1. Aim, scope and research subject

The aim of the research was to determine, and compare filtration properties: efficiency and accuracy of filtration, and filter cartridges flow resistance made of various filter materials (cellulose, polyester with the addition of nanofibers) by determining their following characteristics:

- filtration performance $d_{zmax} = f(k_m)$,
- filtration efficiency $\varphi_w = f(k_m)$,
- pressure drop $\Delta p_w = f(k_m)$,

where: k_m – dust mass loading, determining dust mass m_w retained, and evenly distributed over 1 m^2 of filter material active surface, which is expressed by the dependence:

$$k_m = \frac{m_w}{A_w}\,[\mathrm{g/m^2}]. \tag{3}$$

The filtration speed is defined as the quotient of the air stream flowing through the filter cartridge Q_w (equal to the engine air demand), and the area of the active paper filter A_w, and is expressed by the following relationship:

$$v_{Fw} = \frac{Q_w}{A_w \times 3600}\,[\mathrm{m/s}]. \tag{4}$$

The subject of the research were four filter cartridges of the same type, same dimensions, same filtration surface $A_w = 0.153$ m^2, but differing in the filter material (Fig. 14).

On two standard filtration materials, there is a nanofiber layer on the inlet side. In order make test analysis easier, filter materials have been labelled as follows:

- A (cellulose),
- B (polyester),
- C (cellulose + polyester + nanofiber layer),
- D (polyester + nanofiber layer).

Fig. 14. Filter cartridge

Tested filter materials characteristic parameters are summarized in Table 1. Three times higher air permeability, and double the size of the filter material A (cellulose) pores from other materials is noteworthy.

Table 1. Tested filtration materials parameters according to the manufacturer's data

Filter paper identification	Filtration material	Permeability q_p [m^3/m^2/h], 200 [Pa]	Grammage g_m [g/m^2]	Thickness g_z [µm]
A	Cellulose	3017	121	610
B	Polyester	650	180	500
C	Cellulose + polyester + nanofibers	660	120	300
D	Polyester + nanofibers	525	180	500

4.2. Methodology and test conditions

Tests were carried out at the station (Fig. 15), which was equipped with the Pamas-2132 particle counter with the HCB-LD-2A-2000-1 sensor. The meter registers the number and size of dust grains in the air stream Q, behind the tested filter cartridge in the range of 0.7–100 µm in i = 32 measurement intervals, limited by diameters (d_{zimin}–d_{zimax}).

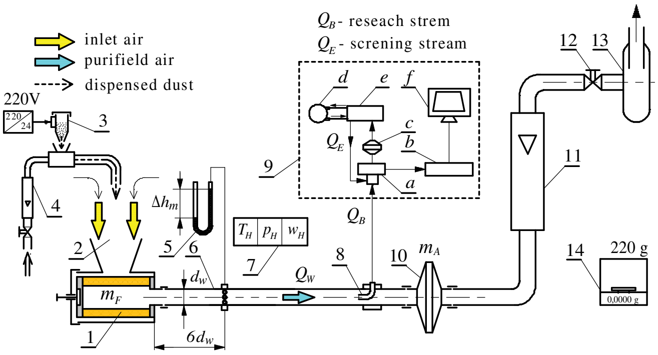

Fig. 15. Filter cartridge test stand functional diagram: 1 – filter cartridge, 2 – dust chamber, 3 – dust dispenser, 4 – rotameter, 5 – U-type manometer tube, 6 – measuring tube, 7 – humidity measurement set , ambient air temperature and pressure, 8 – measuring probe, 9 – particle counter (a – sensor, b - counter microprocessor, c – test stream filter, d – vacuum pump, e – flow control block, f – measuring computer), 10 – absolute filter, 11 – rotameter, 12 – air stream regulation valve, 13 – suction fan, 14 – analytical balance

During the tests, a research cycle was applied, in which five counts of the dust grains in the range 0.7–20 µm were programmed, divided into 20 identical measurement intervals limited with diameters (d_{zimin}–d_{zimax}) with a step of Δd_{zi} = 0.4 µm (0.7–1.1 µm; 1.1–1.5 µm; 1.5–1.9 µm; …; 8.3–8.7 µm) and 11 identical measurement intervals limited with diameters (d_{zimin}–d_{zimax}) with a step of Δd_{zi} = 0.8 µm (8.7–9.5 µm; 9.5–10.3 µm; 10.3–11.1 µm; …; 15.9–16.7 µm). The last measuring compartment had a range of Δd_{zi} = 16.7–20 µm.

At the appropriate distance after tested filter, the tip of the measuring probe is placed centrally in the axis of the cable, which is followed by air suction to the particle counter sensor. The measuring lead ends with a special (absolute) filter, which prevents dust from entering the rotameter, and at the same time it is a measuring filter. The cover in which the cylindrical filter cartridge is located, PTC-D (Fig. 16) test dust is being dispensed as the national replacement for AC fine test dust, whose chemical, and fractional composition is given in [21].

The pressure drop Δp_w in the cartridge was defined as the decrease of the static pressure in the outlet pipe at a distance of $6d_w$ from the edge of the cartridge outlet on the basis of the Δh_{mj} [mm H_2O] indicator on the U-tube liquid manometer, according to the relationship:

$$\Delta p_{wj} = \frac{\Delta h_{mj}}{1000} \cdot (\rho_m - \rho_H) \cdot g \text{ [kPa]}. \qquad (5)$$

where: ρ_m – manometric liquid density [kg/m^{-3}], ρ_H – air density [kg/m^{-3}], g – gravity acceleration [m/s^2].

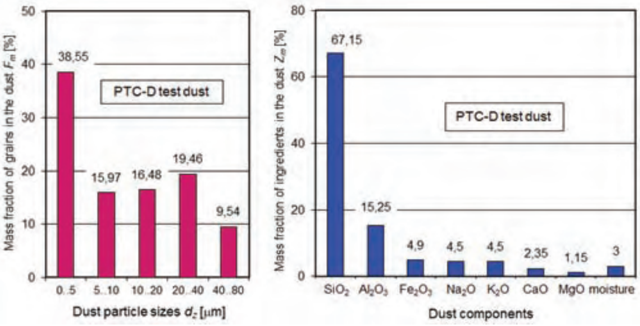

Fig. 16. PTC-D test dust used for testing: a) size distribution, b) chemical composition (PN - ISO 5011)

Cartridges filtration characteristics were determined for the filtration speed υ_{Fw} = 0.1 m/s. For passenger car filters, the maximum speed of paper filtration is in the range of 0.07–0.12 m/s [3, 4, 8, 9, 22]. For the assumed filtration rate (υ_{Fw} = 0,1 m/s), the maximum value of the test stream calculated according to the following relationship has the value Q_{wmax} = 56 m^3/h.

$$Q_{wmax} = A_w \cdot v_{Fw} \cdot 3600 \text{ [m}^3\text{/h]} \qquad (6)$$

where: tested inserts filtration surface A_w = 0.153 m^2.

The RIN 60 rotameter of the measuring range 3–67 m^3/h and the accuracy class 2.5 was assumed for air stream measurement.

Tested filtration materials filtration characteristics were determined by the gravimetric method. Dust mass retained on the tested filter cartridge, and the absolute filter was determined in subsequent measuring cycles with a specified duration. The concentration of dust in the inlet air to the filter cartridge s = 0.5 g/m^3 was used. The tests were carried out in measuring cycles j with duration (time of equal dust dosing) τ_p = 3 min. in the initial period, and τ_p = 9–12 min in the basic period of filter cartridges work. After each measuring cycle j, the parameters necessary to calculate: efficiency, filtration performance, pressure drop and dust mass loading of the filter cartridge were determined. The dust mass was determined by an analytical balance with a measuring range of 220 g and an accuracy of 0.1 mg.

The tests were performed in measurement cycles resulting from time t_p of even dust dispense to the filter. During the measurement cycle at a moment $t_z = \frac{1}{2} t_p$, the procedure of counting of the particle number and measurement of its size was initiated in the counter downstream of the filter.

After each j-th measurement cycle the following were determined:

- The pressure drop Δp_w in the cartridge was defined as the decrease of the static pressure in the outlet pipe at a distance of 6d_w from the edge of the cartridge outlet on the basis of the Δh_{mj} [mm H_2O] indicator on the U-tube liquid manometer, according to the relationship:

$$\Delta p_{wj} = \frac{\Delta h_{mj}}{1000} \cdot (\rho_m - \rho_H) \cdot g \text{ [kPa]}. \qquad (7)$$

where: ρ_m – manometric liquid density [kg/m^3], ρ_H – air density [kg/m^3], g – gravity acceleration [m/s^2].

- The efficiency of filtration, as a quotient of the mass of the dust m_{FFj} trapped by the filter and the mass of the dust m_{Dj} introduced into the filter during the subsequent j-th measurement cycle based on the relation:

$$\varphi_j = \frac{m_{Fj}}{m_{Dj}} = \frac{m_{Fj}}{m_{Fj}+m_{Aj}} 100\%, \qquad (8)$$

- Mass loading of dust k_{mj} of the investigated filtration material:

$$k_{mj} = \frac{\sum_{j=1}^{n} m_{Fj}}{A_w} \text{ [g/ m}^2\text{]}. \qquad (9)$$

- The number N_{zi} of the dust grains in the airflow downstream of the filter (passed through by the filtering material) in the measurement intervals limited with diameters ($d_{zimin} \div d_{zimax}$).
- The accuracy of filtration – as the greatest size of the dust grain $d_{zj} = d_{zmax}$ in the airflow downstream of the filter.
- Percentage share of individual dust grain fractions in the air downstream of the filter for a given test cycle:

$$U_{zi} = \frac{N_{zi}}{N_z} = \frac{N_{zi}}{\sum_{i=1}^{32} N_{zi}} 100\%, \qquad (10)$$

where: $N_z = \sum_{i=1}^{32} N_{zi}$ – total number of dust grains passed through by the filter (from all measurement intervals) in the test cycle.

4.3 Test results analysis

Test results filtration efficiency φ_f, filtration performance d_{zmax}, and pressure drop Δp_f calculations of tested filtration materials are shown in Fig. 17. As the dust mass retained in the filtration layer increases (k_m coefficient increase) the filtration efficiency, filtration performance and pressure drop of filter cartridges assume increasing values. This is the result of the space filling between the fibers (pores), which is consistent with the literature [4, 5, 8, 15, 16].

The work of tested filter cartridges can be divided into two stages. It was assumed that the first (I), the initial stage of filter cartridges operation, lasts until the filtration efficiency stabilizes at the level of φ_w = 99.9%. This stage is characterized by low initial efficiency, filtration performance, and low pressure drop.

For a filter cartridge made of filter material A (cellulose), the initial filtration efficiency is φ_{wA} = 96.5%, and the maximum grain size does not exceed the value of d_{zmaxA} = 16.7 µm. The determined value of filtration efficiency (φ_w = 99.9%) is achieved at the dust mass loading k_{mA} = 91 g/m^2, while the pressure drop increase is insignificant. For the other cartridges made of other filtration materials, the first stage is much shorter.

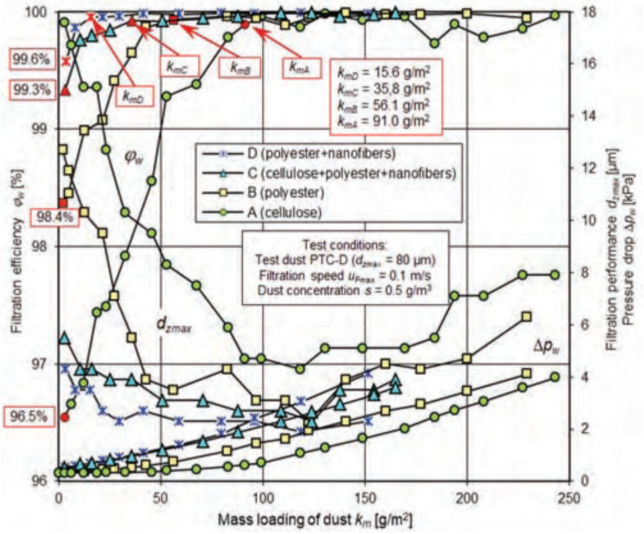

Fig. 17. Filtration efficiency φ_w, filtration performance, d_{zmax}, and pressure drop Δp_w depending on the tested filter cartridges dust mass loading k_m

For the B (polyester) insert, stage (I) ends with the dust mass loading k_{mB} = 56.1 g/m^2, for the cartridge C (cellulose + polyester + nanofibers) k_{mC} = 35.8 g/m^2, and for the contribution D (polyester + nanofibers) coefficient k_{mD} = 15.6 g/m^2. The initial filtration efficiency for the mentioned cartridges is assumed to be higher, respectively: φ_{wB} = 98.4%, φ_{wC} = 99.3%, φ_{wD} = 99.6%. At the end of the first stage filtration, the sizes of the maximum grains for the contributions A, B, C, D are stabilized at the following level: d_{zmaxA} = 4.7 µm, d_{zmaxB} = 3.9 µm, d_{zmaxC} = 3.1 µm, d_{zmaxD} = 3.5 µm.

The initial work stage of the A cartridge made of cellulose is several times longer than the insert D (polyester with a layer of nanofibers) and the contribution of C (cellulose + polyester + nanofibers). At the same time, the required high filtration efficiency of the inserts with nanofiber layer reach much earlier than cartridges made of standard filter material. This confirms the literature information about the positive nanofibers influence on the filtration efficiency, and filtration performance materials used in automotive industry.

In the first filtration stage, the dirt particles deposit on the fibers surface of the porous structure, and on previously deposited particles. In this way, they form slowly growing complicated dendritic structures (agglomerates) that fill free spaces between fibers. They affect the flow field around the fibers. In response to changes in the filter structure, there are changes in the air flow. This has the effect of increasing the flow resistance through the filter bed.

In the second (II) stage of the filtration cartridges, the filtration efficiency remains unchanged, stabilized $\varphi_w = 99.9\%$. In contrast, the pressure drop reaches higher, and higher values, but the intensity of growth is greater for inserts made of materials with nanofibers addition. Filter cartridge D achieves pressure drop $\Delta p_{maxD} = 4.1$ kPa with dust mass loading of $k_{mD} = 151.6$ g/m^2. Filter cartridge A similar pressure drop value ($\Delta p_{maxA} = 3.96$ kPa) achieves at the dust mass loading $k_{mA} = 243$ g/m^2. Inserts with nanofiber layer are characterized by lower dust absorption. This is determined by the surface filtration, as a result of which the dust grains are not allowed into the deposit, but are mostly retained on the nanofiber layer. This is illustrated by the measurement results (Fig. 17) of the maximum dust grains size d_{zmax} in the air after the tested cartridges. In the air after the insert A (cellulose) there are grains with the dimensions of $d_{zmaxA} = 4.3–16.7$ µm, and behind the insert D, where there is nanofiber layer, grains with much smaller dimensions $d_{zmaxD} = 2.3–4.3$ µm.

Filter elements made of cellulose composite and polyester, together with the applied layer of nanofibers, are characterized by higher efficiency, and filtration performance in the whole range of work (smaller dust grain sizes d_{zmax} in the air behind the filter cartridge) than inserts made of filter material without a layer of nanofibers.

With the increase of dust mass retained in the filtration layer (k_m coefficient increase), filter cartridge flow resistance has higher and higher values. The increase in flow resistance is greater for cartridges (C, D) that have an additional nanofiber layer. Therefore, the cartridges will achieve determined permissible resistance value faster during usage of the car $\Delta p_{wdop} = 4$ kPa (Fig. 18).

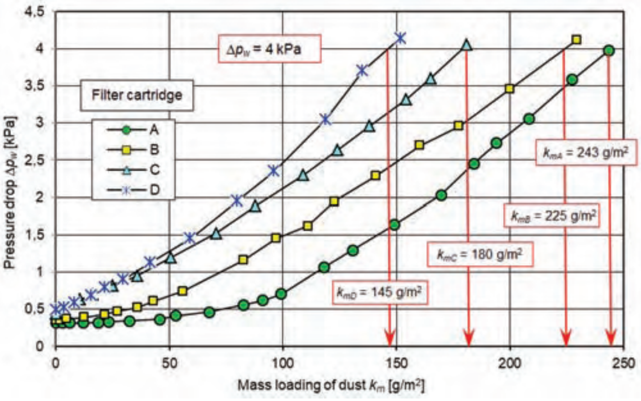

Fig. 18. Filter cartridges pressure drop depending on mass loading coefficient k_m

Filter inserts with a nanofiber layer obtain a maximum mass loading of dust of $k_m = 145–180$ g/m^2 (Fig. 18). For a similar pressure drop value Δp_{wdop} (about 4 kPa) filter cartridges without nanofibers layer obtain dust mass loading in the range of $k_m = 225–243$ g/m^2, which is 50% more value. This is due to the lower pressure drop intensity of the filter cartridges without the nanofibers layer. After the filtration inserts with nanofiber layer have a pressure drop of 4 kPa, the phenomenon of dust agglomeration from the filter bed is observed. This is a proof that in filter beds with nanofiber layer, mainly surface filtration occurs, not deep.

Reaching allowed resistance by the filter (for tested ones $\Delta p_{wdop} = 4$ kPa) forces user to change the filter cartridge. When using filter cartridges with nanofiber layer their exchange intervals will be shorter.

Low efficiency, and filtration performance in the initial period of filter cartridges work without nanofibers layer (this is the case after replacing a contaminated filter cartridge with a new one) causes that dust particles larger than 1 µm in the air entering the engine can have a significant impact on accelerated wear of engine components, mainly cylinder funnel – piston ring-cylinder, association. Such phenomenon is not observed, when using filter cartridges with a layer of nanofibers.

In the final stage of filtration, large dust grains ($d_{zmaxA} = 7.9$ µm) are found in the air behind the filter cartridge A. There is also a noticeable decrease in cartridge filtration (Fig. 17). This indicates that the grains have passed to the outlet side of the filter material. In the final stage, a significant dust mass is accumulated in the form of expanded tree-like dendrites. The dust grains located at the very top of the dendrites are entrained and transferred to the outlet side of the filter material. As a result of this phenomenon, along with the inlet air, dust flows into the engine cylinders. Measurements results of dust grains numbers in the air after the tested filter cartridge (passed through the filter material) are shown in Figs 19 and 21, and after over a dozen measurements in the drawing 20 and 22.

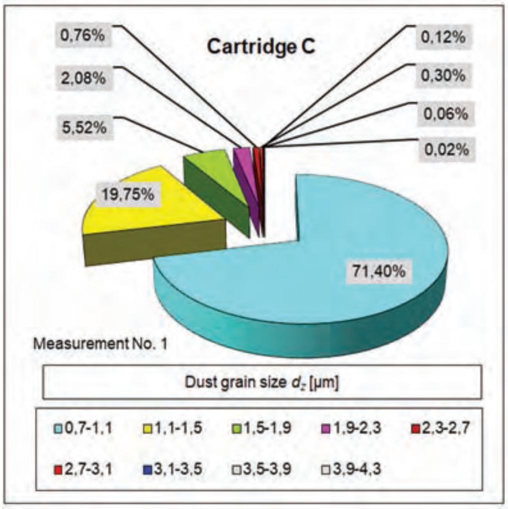

Fig. 19. Granular composition of dust grains assumed by the filter cartridge C (cellulose + polyester + nanofibers) after reaching dust mass loading $k_m = 3$ g/m^2

The largest part in the air are dust grain which have dimensions of 0.7–1.1 µm. For filter cartridge C, this is a constant value, slightly over 70%. For the first measurement, the part of dust grains in the range of 0.7–1.1 µm is

U_{z1} = 71%, for the measurement number 3 – U_{z3} = 73%, and for the measurement number 8 – U_{z8} = 72%. For the remaining measuring compartments, the part of dust grains in the air with each measurement decreases, which indicates the increasing filtration efficiency of the tested material. After the filter achieved the maximum efficiency of $\varphi_{max} =$ 99.99%, there were dust particles smaller than 2.7 µm in purified air.

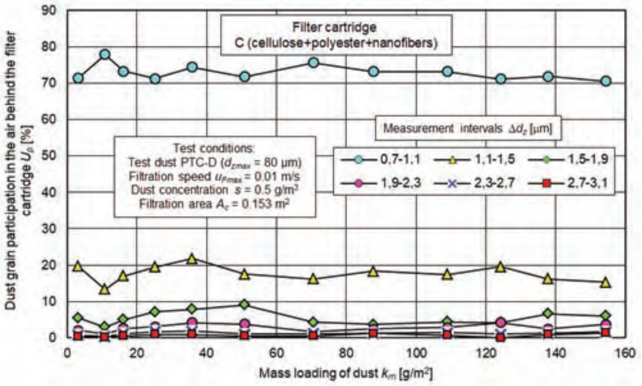

Fig. 20. Dust grains granulometric composition which passed through filter cartridge C (cellulose + polyester + nanofibers)

Part of dust grains of 0.7–1.1 µm for the filter cartridge A (cellulose) is much smaller than the contribution of C (27% at the time of the first measurement) and increases to 85%, and then decreases to about 70% (Fig. 21 and Fig. 22).

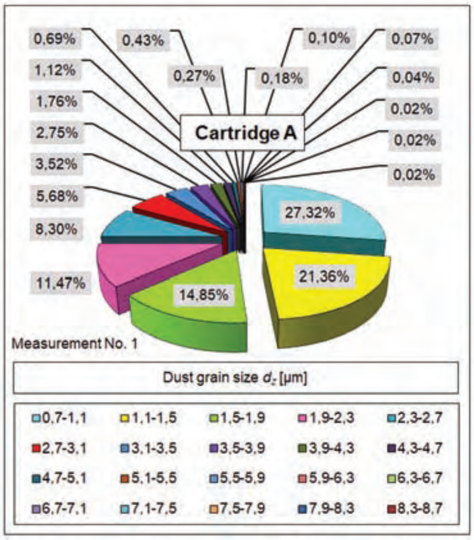

Fig. 21. Granular composition of dust grains assumed by the filter cartridge A (cellulose) after reaching the dust mass loading k_m = 2.8 g/m^2

The share of dust grains of 1.1–1.5 µm size is in the range of 20–27% until reaching the dust mass loading k_m = 67 g/m^2, and then decreases to about 18%, after which it remains at a constant level. For the next measurement intervals, including dust grains above 1.5 µm, the shares of dust grains are getting smaller (Fig. 20), and their changes depending on the k_m coefficient are similar to the shares of dust grains in the 1.1 to 1.5 µm range. In the air behind the filter cartridge A (made of cellulose) after reaching the maximum filtration efficiency φ_{maxA} = 99.96% there were dust grains with dimensions below 4.7 µm.

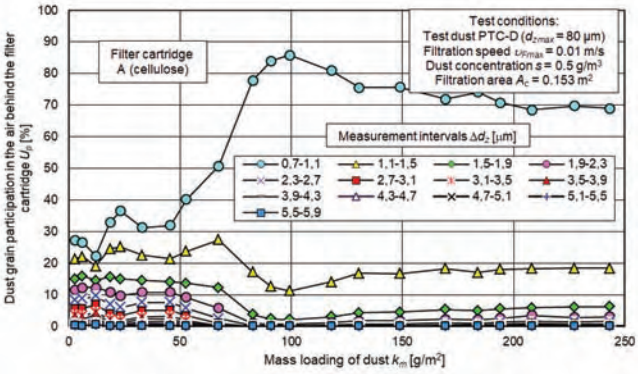

Fig. 22. Dust grains granulometric composition which passed through filter cartridge A (cellulose)

Conclusions

1) Nanofiber layer with a thickness of few micrometers applied on a substrate made of conventional filter materials for car air filters increase the filtration efficiency and filtration performance, especially for dust grains below 5 µm, without a significant pressure drop. As a result, the abrasive wear of engine components, especially those (piston–piston rings–cylinder combination), which decide about the correct combustion process and the power obtained, is reduced.
2) The available literature data has a limited amount of information when it comes to filtration filter inserts properties with nanofiber layer, and all the values of filtration efficiency, and accuracy, hence it is advisable to carry out experimental research.
3) Filtration materials with nanofiber addition create, upon reaching a certain value of the flow resistance, the possibility of impulse cleaning them, with a stream of compressed air, which ensures several times longer usage of the filter cartridge. However, this requires the use of a special air filter design, and additional experimental tests in this area.
4) With the increase of dust mass retained on the filter cartridge (increase in the dust mass loading k_m of the cartridge), the filtering efficiency of the tested cartridges increases dramatically during the initial period, however a more intense increase is observed for the insert with the nanofiber addition. The filter insert with the nanofiber layer achieves the initial filtration efficiency φ_{w0} = 99.34%. Such filtration efficiency value, cellulose cartridge reaches when the dust mass loading k_m = 53 g/m^2. The initial filtration efficiency of this cartridge is φ_{w0} = 96.54%.
5) The filtration cartridge with nanofiber addition in the whole range of work, achieves the filtration performance (maximum size of dust grains d_{zmax}) in the range of d_{z1max} = 2.7–5.5 µm. Filtration performance of the cellulose cartridge in the initial period reaches the value of d_{z1max} = 2.7–5.5 µm, and after obtaining almost 50% of the total working time of the cartridge, the accuracy is at the level of d_{z2max} = 4.7 µm. Such air with mineral dust sucked into car cylinder can accelerate its usage.

6) Flow resistance increase intensity of the inserts with an additional nanofiber layer is significantly higher, therefore the permissible value of $\Delta p_{wdop} = 4$ kPa is reached much faster. This increases filter cartridges exchange frequency, and thus increases operating costs.

Nomenclature

BDC	bottom dead center
UDC	upper dead center
P-R-C	piston–piston rings–cylinder

Bibliography

[1] AVIS, M. Particles: friend or foe? understanding the value of particles in oil analysis. *Machinery Lubrication.* 2012, **6**.

[2] BARRIS, M.A. Total Filtration^{TM}: The influence of filter selection on engine wear emissions, and performance. 1995. SAE Technical Paper 952557.

[3] Diesel engine air filtration, Materiały informacyjne firmy PALL Corporation. 2004, USA.

[4] BUGLI, N. Automotive engine air cleaners – performance trends. SAE Technical Paper 2001-01-1356.

[5] DURST, M., KLEIN, G., MOSER, N. Filtration in Fahrzeugen. Mann+Hummel GMBH, Ludwigsburg, Germany 2005.

[6] DZIUBAK, T. Problems of dust removal from multicyclones of engine air cleaners in cross-country motor vehicles, *The Archives of Automotive Engineering*. 2017, **76**(2), 37-62.

[7] DZIUBAK, T. Operating fluids contaminantions and their effect on the wear of elements of a motor vehicles combustion engine. *The Archives of Automotive Engineering – Archiwum Motoryzacji*. 2016, **72**(2), 93-122.

[8] DZIUBAK, T., SZWEDKOWICZ, S. Operating properties of non-woven fabric panel filters for internal combustion engine inlet air in single and two-stage filtration systems. *Eksploatacja i Niezawodność – Maintenance and Reliability*. 2015, **17**(4), 519-527.

[9] ERDMANNSDÖRFER, H. Lesttingmoglichkeiten von Papierfiltern zur Reinigung der Ansaugluft von Diselmotoren. *MTZ.* 1971, 32, 123-131.

[10] FITCH, J. Clean oil reduces engine fuel consumption. *Practicing Oil Analysis*. 2002, **11**/**12**.

[11] GEORGE, J., FORNA, R., CRAVERO, T. Air filtration with fine polymeric fibers. 16-th Annual Technical Conference and Exposition 2003 Technical Sessions Papers, Reno-Nevada, June 17-20, 2003.

[12] GRAFE, T., GOGINS, M., BARRIS, M. et al. Nanofibers in filtration applications in transportation. Filtration 2001 International Conference and Exposition, Chicago, December 3-5, 2001.

[13] GRAHAM, K., OUYANG M., RAETHER T. et al. Polymeric nanofibers in air filtration applications, 5th Annual Technical Conference & Expo of the American Filtration & Separations Society, Galveston, Texas, April 9-12, 2002.

[14] HEIKKILÄ, P., SIPILÄ, A., PELTOLA, M., HARLIN, A. Electrospun PA-66 Coating on Textile Surfaces, Institute of Fibre Materials Science, Tampere University of Technology, P.O. Box 589, FIN-33101, Tampere, Finland. 2007, 864-870.

[15] JAROSZCZYK, T., PETRIK, S., DONAHUE, K. Recent development in heavy duty engine air filtration and the role of nanofiber filter media. *Journal of KONES Powertrain and Transport*. 2009, **16**(4), 207-216.

[16] JAROSZCZYK, T., FALLON, S. L., SCHWARTZ, S.W. Development of high dust capacity, high efficiency engine air filter with nanofibers. *Journal of KONES Powertrain and Transport*. 2008, **15**(3), 215-224.

[17] KHAJAVI, R., ABBASIPOUR, M., BAHADOR, A. Electrospun biodegradable nanofibers scaffolds for bone tissue engineering. *Journal Applied Polymer Science*. 2016, **133**(3), 42883.

[18] KOSZAŁKA, G., SUCHECKI, A. Changes in performance and wear of small diesel engine during durability test. *Combustion Engines*. 2015, **162**(3), 34-40.

[19] LI, D., XIA, Y. Electrospinning of nanofibers: reinventing the wheel? *Advanced Materials*. 2004, **16**(14), 1151-1170.

[20] LO, L.-M., CHEN, D.-R., PUI, D.Y.H. Experimental study of pleated fabric cartridges in a pulse-jet cleaned dust collector. *Powder Technology*. 2010, **197**, 141-149.

[21] PN-ISO 5011. Filtry powietrza do silników spalinowych i sprężarek. PKNM, 1994.

[22] TAUFKIRCH, G., MAYR, G. Papierluftfilter für Motoren in Nutzfahrzeugen, *MTZ*. 1984, **45**(3), 95-105.

[23] TRAUTMANN, P., PELZ, A., DURST, M., MOSER, N. High performance nanofibre coated filter media for engine intake. Air AFS 2005 Conference and Expo, April 10-13, 2005.

[24] http://www.cottonbangladesh.com/January2009/ElectroSpinning.htm [14.12.2017].

[25] http://www.cottonbangladesh.com/January2009/ElectroSpinning.htm [09.10.2018].

Tadeusz Dziubak, DSc., DEng. – Faculty of Mechanics Military University of Technology, Warsaw, Poland.

e-mail: *tadeusz.dziubak@wat.edu.pl*

Article citation info:
STĘPIEŃ, Z. The influence of particulate contamination in diesel fuel on the damage to fuel injection systems. *Combustion Engines*. 2019, **177**(2), 76-82. DOI: 10.19206/CE-2019-213

Zbigniew STĘPIEŃ

CE-2019-213

The influence of particulate contamination in diesel fuel on the damage to fuel injection systems

The impact of various size particulate contamination on the process of accelerated wear followed by damage to the fuel injection system has been studied in long-term tests on an engine test stand. Also processes of tribological wear of working components of fuel injectors and of high pressure pumps material has been characterised. Measurement results of particulate contamination in diesel fuels available on the Polish market have been presented, referred to requirements of the PN-EN590 standard and of the Worldwide Fuel Charter. In the summary attention has been drawn to the growing problem of particulate contamination in fuels available on the market, and in particular their threat to durability and proper operation of increasingly complex and precisely manufactured HPCR type fuel injection systems.

Key words: *HPCR type fuel injection systems, particulate contamination in diesel oil, tribological wear of HPCR components, tests on engine test stand*

1. Introduction

Operational fluids must fulfil many functions, among which the following are most important:

- supply of energy,
- lubrication of mating surfaces of working components,
- heat removal,
- power transfer in hydraulic systems,
- corrosion protection.

To fulfil their functions such fluids must feature appropriate practical properties and quality parameters specified in appropriate standards, regulations, or ordinances. Durability of automotive vehicle driving units and reliability of their operation depends to a large extent on the quality of operational fluids used in them, including the contained particulate contamination. The existence of particulate contamination in operational fluids causes accelerated wear of mechanically mating components, makes their operation difficult, and finally results in failures, repair shut-downs, and financial losses.

Permanent pursuit of obtaining better and better parameters in the field of unit power and fuel consumption forces significant technical progress in terms of improving the energy performance of engines, at the same time frequently revealing delays in parallel development of manufacturing technology and materials science, and in particular physical metallurgy and accompanying metallographic investigations [1–3]. This leads to reduced durability of crucial components of engine fuel injection systems, resulting both from design and operational reasons. The amount of information proving the occurrence of mechanical failures of actuator components of modern HPCR fuel injection systems, more and more widely used to fuel diesel engines, has been growing for some time. Subassemblies and component of aforementioned systems during the operation are subject to various types of dynamically changing thermal and mechanical cyclical loads, at a complex stress state. This is caused, among other things, by pumping the fuel by the injection pump under a pressure of approx. 250 to 300 MPa, and its quick changes in the high-pressure part of the fuelling system due feeding the fuel via injectors to the engine combustion chambers. The obtaining of so high pressures is inseparably related to the necessity of precise manufacture and matching of the moving, mating parts (frequently with accuracy of approx. 1 μm) [1–5]. Such a high manufacture precisions makes that the aforementioned key actuator components of high-pressure injection systems are very sensitive to any particulate contamination or substances inconsistent with standard PN-EN 590, which can occur in the fuel, causing damage resulting in dysfunction of injection systems and the necessity to carry out usually very costly repairs. The design and way of operation of crucial subassemblies of the fuel injection systems suggest the occurrence of material's tribological wear processes, including attrition, scuffing, fatigue, fretting, diffusive, pitting, and erosive wear, which gives an opinion about the complexity of both damage origination mechanisms, as well as factors that affect them. In practice, in fuel existing in the commercial trade, one can encounter various pollutants, like hard abrasive particulate matter, soft resinous (organic) substances, microbiological structures, water, etc. [4–8].

Hard abrasive particles are the dominating reason for premature damage (wear) to working surfaces of pairs of precise injection pumps (pumping) and injectors (dosing). In this case processes of tribological material wear prevail, including attrition, scuffing, fretting, diffusive, pitting, and erosive wear. As it has been experimentally found, particles 1–5 μm in size are most dangerous, as they can get between moving parts of precise pairs, gradually increasing the existing clearance between them, which has a crucial impact on deterioration of parameters of injection pumps and injectors operation. The erosive wear is caused by hard particles of particulate contamination carried by the fuel hitting with high speed the working surfaces of precise working elements [8–12]. The risk of accelerated wear and damage to components of HPCR type injection systems is affected more by the size distribution of particulate contamination than by its total weight. On average, one litre of diesel fuel contains more than 5×10^4 of hard pollutants bigger than 15 μm (coarse-grained fraction) and more than 5×10^5 hard pollutants bigger than 5 μm (fine-grained fraction) [4].

The main sources of particulate contamination in diesel fuel comprise:

- production – from refinery plants and from ester producing plants
- transport – when pollutants get to diesel fuel
- storage – when pollutants get to diesel fuel
- filling – pollutants get to the fuel from outside
- leaks in the engine fuel system, causing pollutants penetration into diesel oil
- attrition of mating surfaces of working elements
- corrosive destruction of design surfaces of working elements.

Particulate contaminations can substantially differ between each other, and they may be broken down according to the following criteria:

- particle size
- chemical nature (inorganic, organic)
- hardness
- chemical reactivity
- shape
- electrical character.

Standard PN-EN 590 in the requirements for diesel oil defines a permissible amount of pollutants, determined in weight terms (24 mg/kg).

The Worldwide Fuel Charter in the third edition of 2006 [13] for cat. 2, 3, and 4 diesel oil introduced additional requirements related to the particulate matter size distribution in classes: > 4 µm, > 6 µm, and > 14 µm determined pursuant to the ISO 4406 procedure. In the case of category 2, 3, 4, and 5 the Worldwide Fuel Charter (fifth edition) limits the particulate matter content, including:

Mass up to: 10 mg/kg

Distribution of particulate contamination size: 18/16/13 (acc. to ISO code) in accordance with standard ISO 4406.

The particulate contamination content by weight is determined in accordance with the procedure of EN 12662 (mg/kg).

The Worldwide Fuel Charter recommends the standard ISO 4406:2005 as the method to determine the level of pollutants, and to determine the amount of pollutants - the standard ISO 4407 or standards, in which the grain size composition is determined by the method of automatic particle counter, e.g. ISO 11500.

2. Methodology

The HPCR fuel injection system is a separate functional system working directly with a diesel engine. In this system there exist motional matchings, which are tribological systems, where these are systems operating at both sliding and rolling friction.

The HCPR type fuel injection system performs the process and fuel feeding and spraying in diesel engine cylinders and consists of such basic subassemblies as [4]:

- fuel feeding pump
- fuel filters
- high-pressure injection fuel pump
- high-pressure fuel accumulator with high-pressure piping
- fuel injectors
- integrated module controlling the engine operation.

The subassemblies selected for further analysis in the project, such as a high-pressure injection fuel pump and fuel injectors are at the same time subsystems with the following tribological systems:

- high-pressure injection fuel pump: roller–cam, roller–follower, pump piston–follower, eccentric cam–follower, dosing valve
- injector: nozzle needle–guide in the body, nozzle needle –seat, electromagnetic valve plunger–guide.

2.1. Tests on the engine test stand

The engine simulation tests of HPCR system premature wear caused by particulate contamination contained in the Diesel fuel were performed on a multi-purpose test stand equipped with a modern, widely used HSDI (High Speed Direct Injection) FORD 2.0i 16V Duratorq TDCi diesel engine coupled with an Alpha 160 AF eddy current brake from AVL, with a control module allowing the programming of the engine operation parameters (rpm, load, phase time and ramp time between phases). The basic technical parameters of the FORD 2.0i 16V Duratorq TDCi are given in Table 1 [4].

Table 1. Selected technical parameters of the FORD 2.0i 16V Duratorq TDCi engine

Engine type	four-stroke, compression ignition
Fuel injection type	Direct fuel injection, common rail (Delphi) electronically controlled, cooperating with the Levanta engine control system
Cylinders arrangement	In-line, vertical
No. of cylinders	4
Injection sequence	1-3-4-2
Type of timing gear	DOHC/4 VPC
Cylinder diameter	86.0 mm
Piston stroke	86.0 mm
Displacement	1998 cm^3
Maximum power	130 KM (96 kW) at 3800 rpm
Max. torque	330 Nm at 1800 rpm
Max. instantaneous speed	4800 rpm
Idle speed	750±20 rpm
Compression ratio	18.2
Filling	turbocharged with intercooler and “over-boost” function
Valve clearance	Hydraulic adjustment
Capacity of lubrication system with filter	6.0 dm^3
Complies with emission standard	Euro IV

The engine tests were performed in a 4-phase, repeatable cycle which reflected the average engine operating conditions in a low-intensity city traffic. The parameters of the 4-phase cycle are given in Table 2.

Table 2. Parameters of the 4-phase engine cycle

Phase	**Time [s]**	**Engine speed [rpm]**	**Engine load [Nm]**
1	30	800	~0
2	300	1850	100
3	120	3000	70
4	120	1500	50

The test duration time was set as 200 hours. Two engine tests were carried out under the project:. In the first test to fuel the engine a commercial diesel fuel was used, meeting requirements of the standard PN-EN 590 + A1: 2017, containing 4.8 mg/kg of particulate contamination. In the second test a fuel with the maximum permitted amount of particulate contamination, acc. to PN-EN 590 + A1: 2017 equal to 24 mg/kg of fuel, was used to feed the engine, however, it did not meet the limit specified for this parameter acc. to the Worldwide Fuel Charter (max. 10 mg/kg of fuel). An assumption was also made that the size distribution of contaminants contained in the fuel for tests will not be consistent with the recommendations of the Worldwide Fuel Charter in that respect (18/16/13 acc. to ISO 4406). The fuel was prepared based on the same commercial diesel fuel as used in test one. Additional particulate contamination was introduced to this fuel, in the form of Standardized Arizona Test Dust Contaminant ISO 12103-1 Fine Grade (A2) (SAE J726/ISO5011 Fine Grade) at such an amount as to obtain the permitted, described above, amount of contaminants, i.e. 24 mg/kg. In addition, the fuel was prepared so as to guarantee the contaminant size distribution corresponding to code 18/17/15 per ISO 4406. New sets of fuel injectors were used in tests.

Also tests of particulate contamination content in random sampled, on various petrol stations, samples of commercial diesel fuels of various producers were performed.

The particulate contamination content by weight was determined in accordance with the procedure of PN-EN 12662 (mg/kg). Distribution of particulate contamination size: 18/16/13 (acc. to ISO code) was determined in accordance with standard ISO 4406.

3. Results

3.1. Results of HPCR system components evaluation after the test of diesel oil consistent with PN-EN 590 + A1: 2017 with a low particulate contamination content

After the test completion the high-pressure pump and fuel injectors of HPCR system were disassembled to perform visual inspection of working surfaces of element's mating pairs. No damage of working surfaces of the assessed elements was found visible to the naked eye. To continue the evaluation, the components of fuel injectors were cut on a diamond saw to prepare specimens reflecting forms of wear in those parts of the system. Surface examinations on a HITACHI S-2600 N scanning electron microscope were performed to identify the forms of wear existing on selected injector components. No major forms of wear were found inside the nozzle tips (only material oxidation along the line of machining is visible and few shallow attrition places in a direction skew to the machining line) – Fig. 1.

Also needles, apart from small oxidation and clear traces of machining on majority of their length, have not shown traces of major surface wear. Visible small traces of needles attrition (asymmetric in nature) were found only on surfaces of their cylindrical guiding parts - Fig. 2.

No traces of wear (attrition) whatsoever were found on the working elements of the high-pressure pump.

In addition, tests of surface roughness and development were conducted, limited (due to a pretty complicated and costly procedure) to elements of selected nozzle needles. Tests were carried out in 3 random selected micro-areas (of approx. 1 mm^2 area each) of each needle representing a set originating from the performed test, at a distance of 5 to 15 mm from the place, where the needle cone passes into its guiding, working cylindrical part.

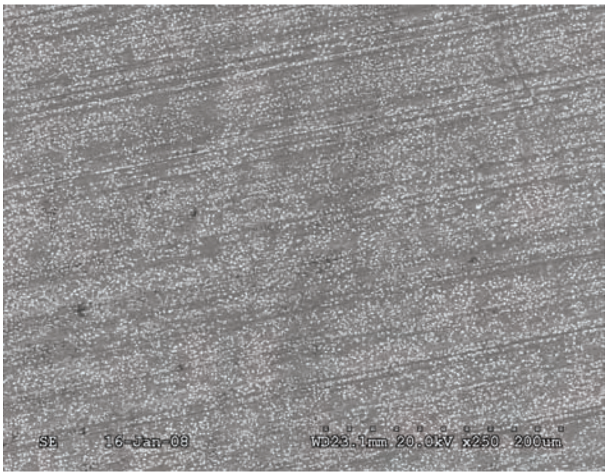

Fig. 1. Image of inside working surface of the nozzle tip body. Visible lines of machining shaping the surface of mating with the nozzle needle. Oxide bands arranged in accordance with the machining lines draw attention

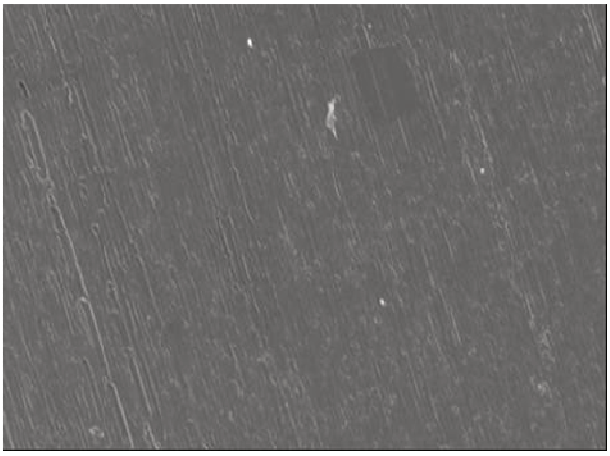

Fig. 2. Image of nozzle needle surface structure in its bottom, cylindrical (guiding) part. Characteristic places of attrition passing perpendicular to the needle axis draw attention in the image. No traces of surface oxidation. The surface of greater smoothness (worn) than in the central part of the element

For each place of test a height map was determined, 3D visualisation showing the surface topography and representative roughness profiles in the direction aligned with the needle axis (red line), and also in the direction perpendicular to the needle axis.

At the same time, for each place of test basic parameters describing the surface roughness were determined, i.e.: Ra – average roughness, Rq – mean square deviation of roughness, and Rt – maximum roughness height and selected parameters describing the profile line. Fig. 3 presents evaluation results of the first from the three tested micro-areas.

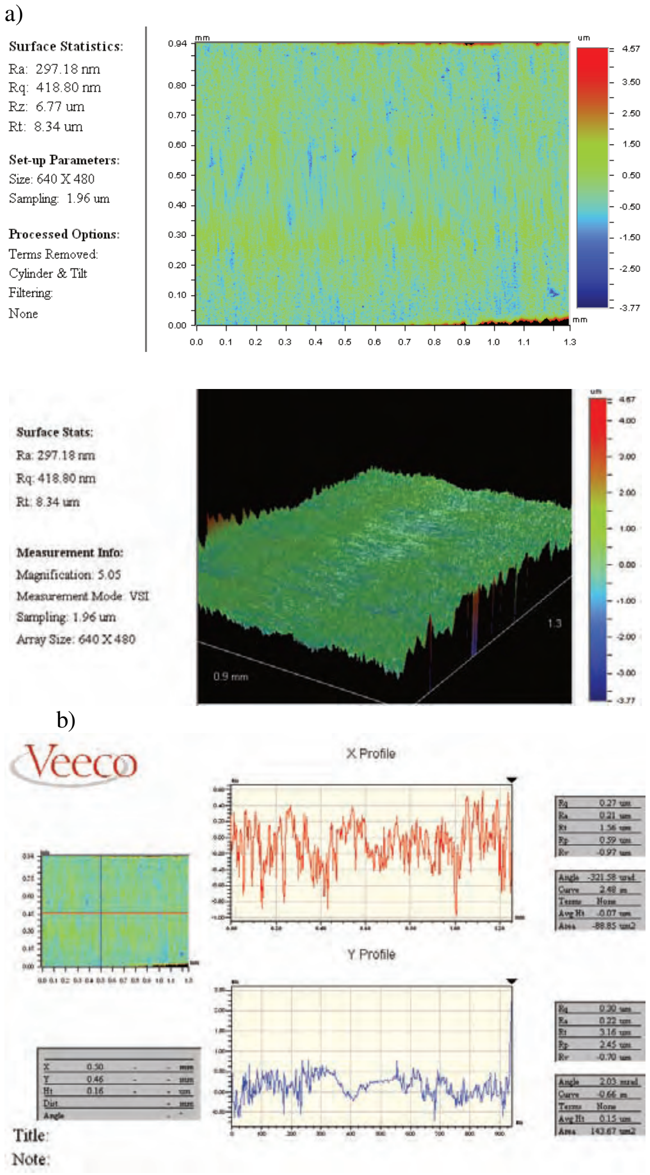

Fig. 3. Graphical results of testing the development (a) and roughness (b) of nozzle needle surface after the first test, for the first evaluated micro-area [4]

3.2. Results of HPCR system components evaluation after the test of diesel oil consistent with PN-EN 590 + A1: 2017 with an increased amount of particulate contamination

After working during 178 hours difficulties occurred related to the maintaining the engine operation parameters in the test and at its starting. After starting, attempts to load it resulted in uneven operation and in effect, the engine stopped. The basic inspection of injectors in terms of flow, hence comparison of fuel dosage evenness via the measurement of overflow from individual injectors gave a clearly negative outcome. Differences in the amount of fuel dosed by individual injectors exceeded 30%.

Like in the case of the first test, after the second test completion the high-pressure pump and fuel injectors of HPCR system were disassembled to perform visual inspection of working surfaces of element’s mating pairs. Visible damage traces (mainly in the form of attritions) were found on working surfaces of needles and plungers of valves controlling the fuel flow – Fig. 4.

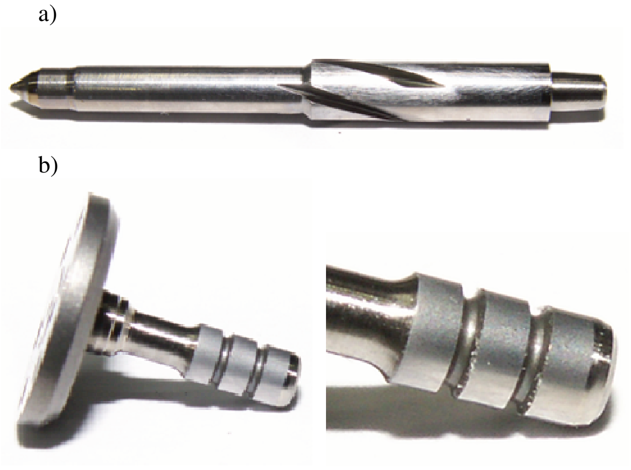

Fig. 4. Traces of mechanical damage originated from the impact of hard particulate contaminations acting on the working parts of a) injector needle, and b) piston of valve controlling the fuel flow

Figure 5 presents selected components of the injection pump subject to macroscopic examination. This examination revealed clear traces of abrasive damage (microcutting, scratching, ploughing, adhesive wear) formed on side guiding walls of follower seats in the body of high-pressure part of the considered pump – Fig. 5a. Also characteristic, of this pump design, wear of the raceway of internal cam ring was found in the form of circumferential abrasive scratches and microgrooves (grooves) and thermal changes of colour – Fig. 5b. On side walls of followers damage of fretting nature was visible – Fig. 5c. Damage of similar type was observed on front surfaces of pistons in the high-pressure part of the pump – Fig. 5d.

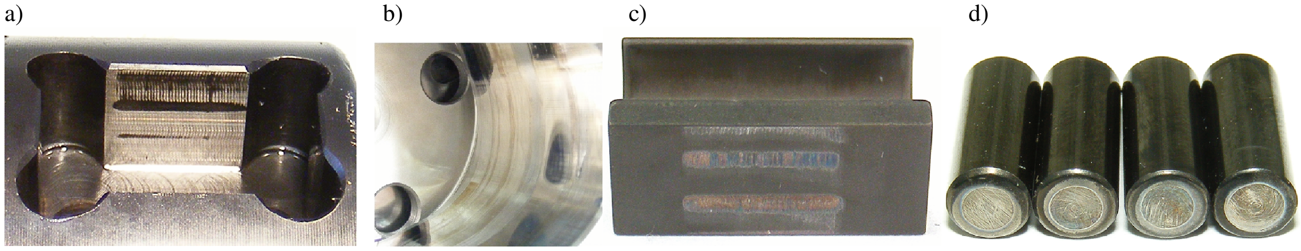

Fig. 5. Traces of abrasive or fretting damage observed on the working surface of high-pressure pump components: a) side guiding walls of follower seats in the pump body, b) raceway of internal cam ring, c) side follower walls, d) front piston surfaces

Before further evaluation, the nozzles of fuel injectors were cut on a diamond saw to prepare specimens reflecting forms of wear in those parts of the system. To identify the wear forms existing in selected injector elements the surface was examined on a HITACHI S-2600 N scanning electron microscope. Traces of damage (mainly in the form of attritions) found in internal working surfaces of nozzle bodies have clearly indicated the existence of an abrasive agent in the area between needles and nozzle bodies mating with them – Fig. 6.

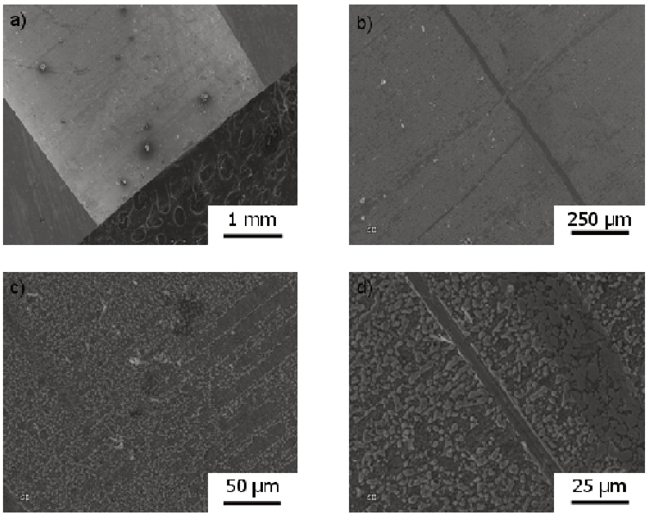

Fig. 6. View of internal working surfaces of injector nozzles, including a) single particulate contaminations of significant size, strongly embedded in the surface, b) an example of material wear, passing parallel to the nozzle axis, c) blooms of oxide nature, which arrange perpendicularly to the nozzle axis, d) local bloom attritions, proven by a line parallel to the nozzle axis not covered by a layer of considered bloom.

Figure 7 presents results of tests of surface roughness and development of selected nozzle needles elements after the second test completion. Test results apply to the first of three studied areas of nozzle needle elements, like in the case of the first test.

Table 3 presents a comparison of selected parameters of surface roughness evaluation results in three studied microareas of needle elements originating from the first and the second test.

Table 3. Comparison of roughness results of evaluated needles surfaces

Roughness Microarea	**Ra [nm]**	**Rq [nm]**	**Rt [µm]**
Nozzle needle after the first engine test			
first	210	281	8.84
second	216	288	8.13
third	229	338	14.46
Nozzle needle after the second engine test			
first	418	536	9.74
second	424	537	10.05
third	431	599	23.98

When comparing roughness results of evaluated nozzle needles after both tests it is possible to state that in the case of nozzle needles originating from the CR system working with diesel fuel containing an increased amount of particulate contamination (second test) – Fig. 7, Table 3, the surface roughness in each of studied areas is much higher as against similar ones, related to needles after the first test – Fig. 3, Table 3.

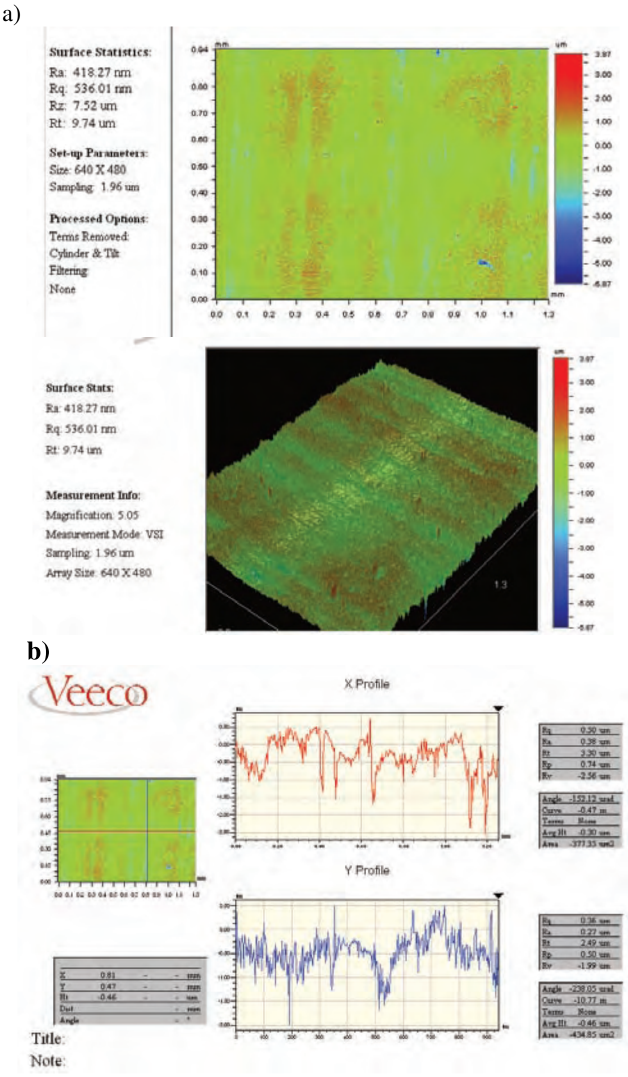

Fig. 7. Graphical results of testing the development (a) and roughness (b) of nozzle needle surface after the second test, for the first evaluated microarea [4]

Moreover, in the case of needles from the second test, apart from a higher surface roughness, grooves passing in the direction aligned with the needle axes are observed and also local extractions of the material and particles of particulate contamination locally embedded in the surface.

The needle surfaces after the first test feature roughness resulting from the applied preliminary mechanical treatment of the surface.

3.3. Results of particulate contamination measurements in commercial diesel fuels

Figures 8, 9, and 10 present results of particulate contamination weight content in random selected, in 2018, samples of commercial diesel fuels. In each of figures the orange line marks the maximum permissible amount of particulate contamination in accordance with requirements of PN-EN 590 + A1. These figures present consecutively the measured number of particles, in diesel fuel samples, broken down into sizes, i.e.: > 4 µm (code ISO 18): 1300–2500 particles – Fig. 8, > 6 µm (code ISO 16): 320–640 particles – Fig. 9, and > 14 µm (code ISO 13): 40–80 particles – Fig. 10. In each of figures the red line marks the maximum permissible amount of particulate contamination in accordance with requirements of the Worldwide Fuel Charter.

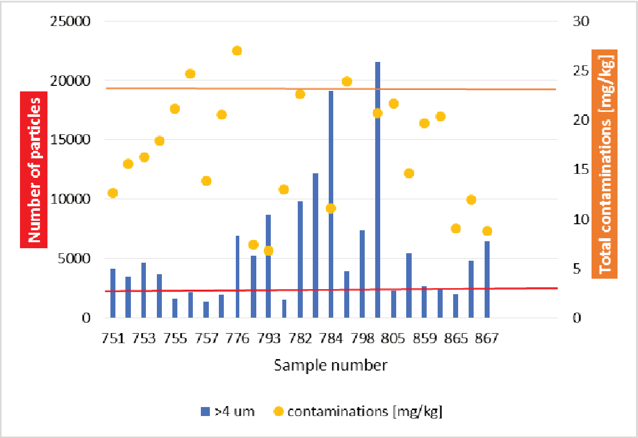

Fig. 8. Weight and quantity content of particulate matter (for particle size > 4 µm) in studied samples of diesel fuels

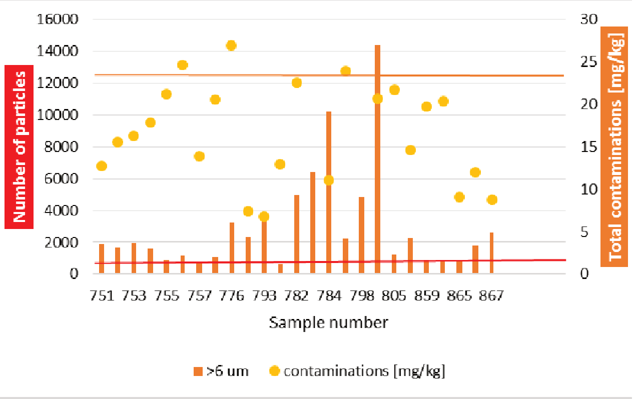

Fig. 9. Weight and quantity content of particulate matter (for particle size > 6 µm) in studied samples of diesel fuels

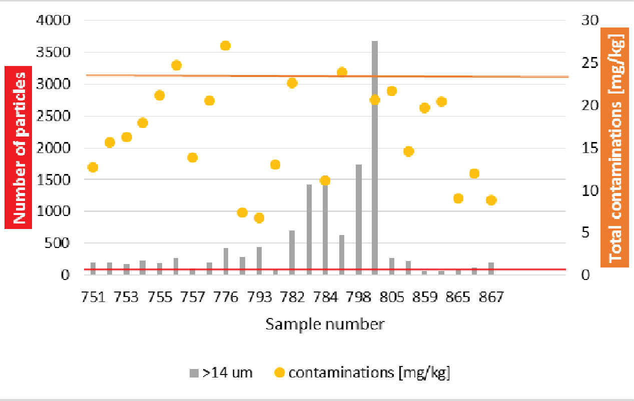

Fig. 10. Weight and quantity content of particulate matter (for particle size > 14 µm) in studied samples of diesel fuels

The obtained results have shown that in the case of weight content measurements for particulate contamination in random taken fuel samples it was found that in approx. 10% of cases the maximum value permitted by the standard PN-EN 590 +A1 was exceeded – Figs. 8, 9, and 10. Much more frequent and higher cases of exceeding were found in the case of particulate matter number measured in the same samples. In the case of particle size > 4 µm (code ISO 18), the cases of exceeding were registered in more than 60% of samples, including cases of exceeding the permissible value twice in approx. 40% of samples – Fig. 8. In the case of particle size > 6 µm (code ISO 16), the cases of exceeding were registered in more than 75% of samples, including more cases of exceeding more than twice in approx. 60% of samples – Fig. 9. While in the case of particle size > 14 µm (code ISO 13), the cases of exceeding were registered in more than 75% of samples, including cases of exceeding the permissible value twice in more than 50% of samples – Fig. 10.

4. Conclusions

The project comprised performance of tests, on an engine test stand, on the impact of particulate contamination quantity and size in diesel fuel on a possibility of accelerated wear and deterioration of operation of modern HPCR fuel injection systems. Also tests of particulate contamination content (total weight content and distribution of contamination size) in random sampled, on various petrol stations, samples of commercial diesel fuels of various producers were performed. The obtained results and observations allowed formulating the following conclusions and hypotheses:

- Particulate contamination in diesel fuel is an increasingly big threat to proper operation and durability of components of modern HPCR type fuel injection system, even if its amount does not exceed the permissible weight determined by the PN-EN 590 standard.
- The rate, size, and form of damage (wear) of working elements of HPCR fuel injection systems is affected not only by the amount (measured by weight) of particulate contamination, but primarily by its size distribution.
- Current studies on fuels available on the market in Poland prove frequent cases of exceeding the amount of particulate contamination in diesel fuel in terms of weight, and in particular in terms of particulate contamination size distribution.
- Further design and technological development of HPCR systems can force introduction of changes in the field of requirements related to particulate contamination of fuels determined by standard PN-EN 590, and even their broadening by parameters so far not subject to limitation (particulate matter size distribution), like it is the case of the Worldwide Fuel Charter.
- Manufacturers of HPCR type fuel injection systems seek lowering the permissible content of particulate matter in fuels, taking into account that further development of those systems will be heading towards obtaining higher and higher pressure of fuel injection, and hence related more and more precise machining and mating of working elements assemblies.

Nomenclature

HSDI	Speed Direct Injection
HPCR	High Pressure Common Rail

Bibliography

[1] DINGLE, P.J.G, LAI M.-C.D. Diesel common rail and advanced fuel injection systems. *SAE International.* 2005.

[2] Zasobnikowe układy wtryskowe Common Rail, *Robert BOSCH GmbH.* 2005.

[3] Diesel Common Rail Technology – Delphi Technische Druckschrift. 2002, **14**.

[4] STĘPIEŃ, Z., URZĘDOWSKA, W., ROŻNIATOWSKI, K. Badanie form zużycia układów wtrysku paliwa w czasie eksploatacji silników z zapłonem samoczynnym. *Raport Nr arch.: DK-4101-1/08, z projektu Nr 0950/T08/2005/28.*

[5] DE MACÊDO NETO, J.C, DE OLIVEIRA, M.A.B., DEL CAMPO, E.R.B. et al. Failure in fuel injector nozzles used in diesel engines. *Journal of Mechanics Engineering and Automation.* 2015, **5**, 237-240.

[6] WIELLIGH, A., BURNER, N., VAAL, P. Diesel injector failures and the consequences – caused by fuel quality. *Conference of the South African Institute of Tribology.* 24 March 2004.

[7] BEJGER, A., GAWDZIŃSKA, K. Fuel system contamination affecting injection equipment of diesel engines. *Applied Mechanics and Materials.* 2016, **817**, 27-33.

[8] IGNACIUK, P., GIL, L. Damages to injectors in diesel engines. *Advances in Science and Technology Research Journal.* 2014, **8**(21), 58-61.

[9] OSMAN, A. Failure of a diesel engine injector nozzle by cavitation damage. *Engineering Failure Analysis.* 2006, **6**, 1126-1133.

[10] BADOCK, C., WIRTH, R., FATH, A., LEIPERTZ, A. Investigation of cavitation in real size diesel injection nozzles. *International Journal of Heat and Fluid Flow.* 1999, **20**(5), 538-544.

[11] QU, J., TRUHAN, J., BLAU, P.J. Investigation of the scuffing characteristics of candidate materials for heavy duty diesel fuel injectors. *Tribology International.* 2005, **38**, 381-390.

[12] STĘPIEŃ, Z., URZĘDOWSKA, W., ROŻNIATOWSKI, K. Influence of fuel quality on advanced diesel injection systems failures. *8th International Congress, Engine Combustion Processes*. Monachium 15-16 marzec 2007.

[13] Worlwide Fuel Charter. Third, Fourth and Fifth Edition.

Zbigniew Stępień, DSc., DEng., Prof. of INIG-PIB, Oil & Gas Institute – National Research Institute in Krakow.

e-mail: *stepien@inig.pl*

Article citation info:
BOGUŚ, P., MERKISZ, J. Analysis of vibration signals using short-time analysis and clustering in parameter space for detection of combustion engine state. *Combustion Engines*. 2019, **177**(2), 83-87. DOI: 10.19206/CE-2019-214

Piotr BOGUŚ
Jerzy MERKISZ

CE-2019-214

Analysis of vibration signals using short-time analysis and clustering in parameter space for detection of combustion engine state

The paper presents a short-time analysis of the vibration signals for the diagnosis of Diesel engine of combustion locomotive by recognition of different engine states using the clustering technique. The main aim of the researches was to distinguish between different engine states represent different wear extends. The proposed method of vibration signal analysis consists on sliding a time window along signal in time and observing the changes of some given statistical parameters. The set of this parameter values creates a multidimensional parameter space where the time evolution can be observed. For recognition and detection of different engine system states some clustering techniques in the parameter space were performed. The results show the possibility of distinguishing different cluster centers within the parameter space which can be assigning to different engine states represented the states before and after a general repair.

Key words: *vibration signals, Diesel engine diagnostic, short-time analysis, clustering*

1. Introduction

Typical combustion engine after a long usage time usually grow old and run down. The engine diagnostic needs new methods for estimation of the engine state in time of it exploitation. The rail vehicle diagnostic has not the same long history as for example car diagnostic. It starts in seventies of XX century when the number of steam locomotives decrease rapidly and they were substituted by Diesel and electric locomotives. From this time the diagnostic methods in the area of diesel locomotive engines started to develop.

The locomotive Diesel engines the same like other combustion engines are nowadays an important source of pollution. To reduce air pollution for passenger cars the OBD norms were introduced. The main function of the OBD system is a continuous monitoring of basic system parameters. The problem of air pollution concerns also the diesel engines and combustion locomotive engines [14]. The rail area is partially regulated with several regulations considering limits on emission of combustion gases (for example, cart UIC 623 1-2-3 in Europe). But all the time there are no obligatory regulations for systems monitoring the emission critical damages that might play a similar role to that of the OBD for cars. But each year the norms and regulations regarding combustion gases emission regarding vehicles with heavy diesel engines like combustion locomotives are develop. This fact gives an impulse to research for new methods for detection of combustion locomotives Diesel engines faults. To achieve this aim the vibration signals were proposed to use.

The vibration signals were taken from an engine and were processed using the short time analysis and clustering method [7, 9, 11, 17]. The measurements were performed on Diesel locomotive 401Da – 427. Unfortunately in this area the classical methods like spectral analysis appear insufficient. In the paper the analyses consider a vibration signal acquired from the combustion locomotive Diesel engine body in two states: before and after a general repairman. The method of vibration signal analysis proposed in the paper consists on sliding a time window along a signal in time. This gives a possibility to calculate the values of some chosen statistical parameters for a signal in short time for each time moment. This gives also a possibility to observe the changes of these parameters in time. As a result a set of observing parameter values creates a multidimensional parameter space where the time evolution can be observed. For recognition and detection of different system states a clustering in the parameter space can be performed. The results show the possibility of distinguishing different cluster centers in the parameter space corresponding to engine states before and after a general repair of an engine.

2. Measurements

The acceleration measurements before repair of a Diesel engine were done by using acceleration sensors EGCS Entran Devices of the range ±5 g. The signal was registered by cart PCL-818HD ADVANTECH with the sampling frequency f_{Hz} =1004 Hz/channel. The measurement after repair were done using the sensors EGCS and some new sensors PCB PIEZOELECTRONICS 393B04 where the signal was amplify by 3-channel signal conditioning amplifier and next registered using analogue to digital cart. The main research object was the 14D40 no 8849 diesel engine of Diesel combustion locomotive ST44.

A Diesel locomotive ST44 have six wheel sets placed on two bogies, each driven by a separate traction electric engine. The electric transmission gear is transferred to a torque of diesel engine (14D40; power output 1470kW = 2000 KM) onto locomotive axles set. The ST44 locomotive was a typical combustion traction vehicle for railway in Poland about twenty and thirty years ago. Nowadays they are gradually withdrawing from current usage [6, 8, 9].

The little different ways of performing the measurement before and after a repair was imposed by specific of measurement sets and circumstances provided in the diagnostic station. The measurements before repair were done under load (on water recoil) for adapted powers in the given measurement point (Fig. 1). The sensors were located on engine body in the places which correspond of engine crankshaft bearing. In each measuring point acceleration was registered in two directions: vertical and horizontal transversal. For each point two measurement series were done. Because of the limited number of sensors the measurement were performed in three points in one time. The measurements were performed for defined settings describing by fixed values of powers and rotational velocities. The periodic inspection repair included service of subassemblies and assemblies, partial disassembling and change of damaged or worn-out elements.

The measurements after repair were done under load (on water recoil) for adapted powers in the given measurement point. This time the measurements were done in six points. Sensors were the same located on engine body in the places which correspond of engine crankshaft bearing. Each measuring point registered acceleration in two directions: vertical (Entran sensors) and horizontal transversal (PCB sensors). For each point two measurement series were done.

Fig. 1. The example vibration sensors mounted on an engine body in a diagnostic station [1]

3. Data analysis

The global characteristics of the signal like Fourier spectrum do not provide any information about local and instantaneous signal alterations. To find some local characteristic some special short-time methods of analysis can be performed. Nowadays the using of wavelets seems most popular in this area. But the main idea of an approach proposed in the paper was taken from the earlier concept of the short-time Fourier spectrum analysis which bases on the short-time Fourier transformation [2, 3, 15]. For discrete case for function u(i) the following definition can be used

$$U(f,n)=\sum_{i=-\infty}^{+\infty} u(i)h(n-i)e^{-j2\pi fTi} \qquad (1)$$

where h(n) is a time function called a window function. The spectrum calculated from (1) is a continuous spectrum and is periodic in frequency f. It depends on the window function form and the moment n [2, 3, 13, 15]. In a special and most simple case the window can be considered as the rectangular function. And the considerations performed in the look for changes in such a short-time window. The approach performed in the paper based on calculating particular parameters in the window sliding in time along the signal. The main advantage of this approach is it simplicity what gives us the direct possibility of diagnostic application. These methods were applied so far rather to singular parameters just to make a simple one-dimensional comparison [8, 9, 11]. In this paper the analysis was performed for more parameters and to consider a problem a multidimensional parameter space was taken into account. The general schema of proposed algorithm is as follows [5, 10, 11]:

1. Choose the width of the time window.
2. Choose the parameters which will be calculated for each window position.
3. In a sliding window for the each given window position calculate the chosen signal parameters.
4. The set of parameter values for the given time moment represents a point in a multidimensional data space.
5. Sliding the window in time along the whole signal gives the set of points in the multidimensional parameter space, which represent the evolution in the parameter space for successive time moments.
6. The points in multidimensional parameter space can create some groups which should represent the state of an engine.
7. The comparison of different signals for different engine state base on analyzing the clusters in multidimensional parameter space.
8. Eventually the diagnosis will consist of distinguishing between different engine states basing on the different clusters created in the parameter space (comparison of the cluster centers) (see Fig. 2).

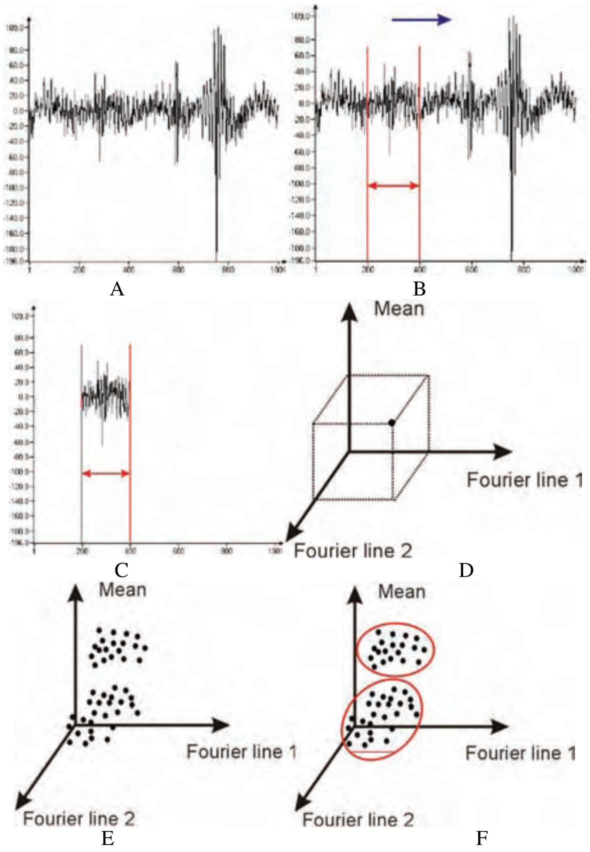

Fig. 2. For the vibration signal (A) the time window is chosen (B) and for the fragment treated as the short-signal (C) the chosen parameters are calculated. The set of parameters values calculated for the given time moment gives the point (vector) in the corresponding parameters space (D). For longer time interval in the parameter space the set of points is observed which represents the time evolution for parameter values (E). Eventually the distribution of points in the parameter space can divide into clusters which can represent different engine states

As a time moment usually a sampled time is taken into account. Many kinds of parameters were taken into consideration: the successive coefficients (lines) of classical Fourier transformation FFT, statistical parameters like median, higher order moments and others. Of course some of they can appear not fully sufficient but from classification point of view the bigger number of parameters gives the higher dimension of the parameter space what make distinguishing between different clusters easier.

Having a point distribution in the parameter space some observation can distinguish between different engine states. To make the observation objective one can perform a clustering in the parameter space. The clustering is one of the most important techniques of pattern recognition. Assume n element data set X. The clustering algorithm finds the number c (lower than the number of elements n) and divide the data set X for c subsets, where elements are most similar to each other [4]. For calculations performed in the paper the classical hard c-means algorithm of clustering was applied. It can be obtained by optimization of the objective function in a form [4, 12]

$$J = \sum_{i=1}^{n} \sum_{j=1}^{c} p_{ij} E_{ij} \qquad (2)$$

where energy E_{ij} is defined as an Euclidean distance $E_{ij} = |x_i - y_j|^2 = d_{ij}$ between the data point x_i and the centroid of cluster y_j and it is assumed that probabilities (membership values) p_{ij} that associates the data point x_i to cluster j are

$$p_{ij} = \begin{cases} 1 & \text{if} \quad x_i \in \text{cluster}_j \\ 0 & \text{if} \quad x_i \notin \text{cluster}_j \end{cases} \qquad (3)$$

4. Results and discussion

The measurements were performed on two ST44 locomotives (number 2045 and 2061). For each signal the set of eleven parameters were calculated for each time moment: 1 FFT line, 2 FFT line, 3 FFT line, 4 FFT line, 5 FFT line, mean, moment 2, moment 3, moment 4, moment 5 and median. This set of eleven parameter values created a point in the corresponding parameter space.

Finally for all time moments one could observe the set of points in the parameter space. The evolution in the parameter space did not create a pattern which could distinguish between signals before after a repair. Rather the irregular balls of puffs were found [7] (see Fig. 3). Therefore the only way to distinguish the signals was to recognize in which part of parameter space the point were placed. And the best parameter here is a center of points calculated using clustering algorithms.

Then for the set of points it center was calculated using the clustering algorithm HCM (classical hard c-means algorithm) [4, 12].

First of all the examinations which were taken into account tried to distinguish the results for signals registered before and after a repair which should represent the states of worn out and right working engine. The comparison was done for some special cases but at the beginning the researches on window size were performed to choose the width of the time window. The introductory researches on influence of window width on parameters values (see Table 1) did not show any interesting dependencies. Generally the values of parameters (especially FFT parameters) grow while the window width rises. Eventually the window width was chosen arbitrary taking into account that the window width should include more than one characteristic periodical signal components. The eventual value of window width taken into calculation was 1000 samples. This time corresponds approximately to the rotation period of crankshaft.

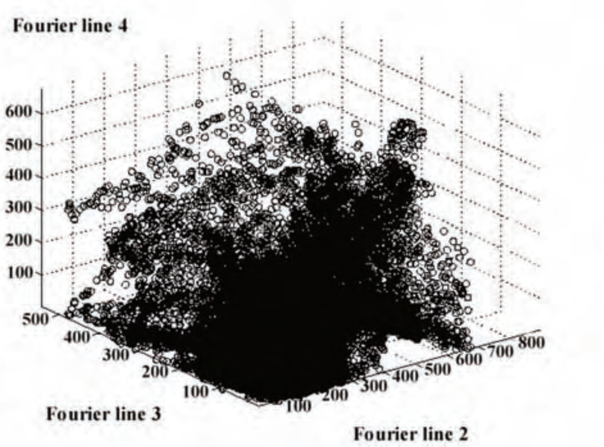

Fig. 3. An example view of a pattern created by points in a parameter space (find out that a dimension parameter space is 9 but at above figure there are only plot of three chosen parameters what can be visualized)

Values of FFT line represent the number of sample in frequency domain which corresponds to the given line. Taking into account that the sample frequency was f = 1004 Hz (approximately 1 kHz) it is easy to calculate the frequencies of coordinates for FFT calculation depending on number of samples. But in the approach presented in the paper the values of successive FFT lines are representing the successive coordinates in parameter space. Therefore the results in Hz are not need and the original data will be using by taking the sample frequency 1 „per unit".

The centers for signals represent wear and good working engines (before and after a repair) were compared in all possible data sets:

- A – all signal,
- A2045 – signals for locomotive 2045,
- A2061 – signals for locomotive 2061,
- V – signals registered in vertical direction,
- V20145 – signals registered in vertical direction for locomotive 2045,
- V20161 – signals registered in vertical direction for locomotive 2061,
- H – signals registered in horizontal transversal direction,
- H2045 – signals registered in horizontal transversal direction for locomotive 2045,
- H2016 – signals registered for horizontal transversal direction for locomotive 2061.

Generally the relative units are used to describe all axis of parameter space. The comparison of the different clusters is performed by calculating the distances between cluster centers corresponding to the given engine states.

Table 1. Dependency of cluster center coordinates obtain using HCM algorithm on number of samples in a window (locomotive ST44-2045 after repair)

Number of samples	FFT 1	FFT 2	FFT 3	FFT 4	FFT 5	Mean	Mom 2	Mom 3	Mom 4	Mom 5	Median
10	7.5	10.4	11.3	15.6	13.9	0.0	20.3	2.9	1769.1	198.7	0.0
20	9.7	13.0	14.9	15.0	15.4	0.0	20.8	6.0	1873.9	1011.9	0.0
50	14.2	16.4	21.3	18.9	27.2	0.0	21.1	6.3	1933.4	916.7	0.0
100	19.4	22.2	23.5	25.6	32.8	0.0	21.2	6.2	1951.2	817.3	0.0
200	27.0	30.4	31.4	30.9	35.3	0.0	21.2	6.2	1959.6	805.9	0.0
500	42.4	48.0	48.5	46.6	48.9	0.0	21.2	6.2	1965.9	798.7	0.0
1000	59.1	66.7	67.1	72.2	68.5	0.0	21.2	6.2	1968.5	802.2	0.0
2000	84.0	92.2	95.8	101.3	92.2	0.0	21.2	6.4	1967.9	848.8	0.0
5000	138.2	134.9	150.8	133.6	153.8	0.0	21.2	6.4	1967.0	841.9	0.0
10000	185.6	216.7	182,5	194.8	233.9	0.0	21.2	6.4	1961.6	726.2	0.0

The Table 2 is showing the distances between the cluster centers corresponding to engine states.

It can be found that the biggest relative distances are for signals registered in horizontal transversal direction. More deep analysis is also showing that the comparison should be performed for signals from the same locomotive.

Table 2. The distances between the data sets for engine working before and after a repair

Signal data set	D
A	817521
A2045	935008
A2061	700295
V	4429
H	1630642
V2045	6402
V2061	2530
H2045	1863622
H2061	1398172

The last step was to perform a trial of a simple classification of an engine state basing on results of clustering in parameter space.

The classification in practice consists of building a classifier which can classify new data and can make a decision about their membership [4, 12, 16]. Taking into account the results from Table 2 only the data of horizontal measurements were taken into account in a classification. In this approach first a training set must be created and allocated. The training set was used just to train a system to distinguish between the engine states before and after a repair. The training set was chosen arbitral taking into consideration a first half of each data set. The applied classification method was classical linear discriminant function approach where a plane in a decision space is found to divide of data space on decision regions, which decide in assigning of an object to the given class. After a training stage, a testing stage was performed. On this stage the second subset of each data set was used to estimate a classification ability of classifier. The results of the testing stage are presented in Table 3. The classification states in Table 3 are described as proper and improper, where proper means the engine working after the repair (right working engine) and improper means the engine working before the repair (worn out engine).

The general conclusion can be formulated as follow: the signals from horizontal measurements can be used to diagnosis of engine state making classification of vibroacoustic signals basing on short tome analysis and clustering in a parameter space.

5. Conclusion

The short-time analysis was performed to distinguish between different engine states which correspond to engine state before and after a repair. Eleven parameters were selected for each time moment what created the evolution in a multidimensional parameter space. In this space the clustering was performed. The obtained results seem quite promising. However, taking into account the great complexity and variety of possible measurement schemes it must be noted that the presented experiments can be treated only as the introductory stage of the research. We have used only signal examples taken from two locomotives. The set of using parameters seems reasonable but of course there is possibility of choosing higher number of them or taking another type of parameters. Calculated in sliding window parameters values give us the points whose coordinates evolve in the parameter space. After calculating of cluster centers the comparison is done by finding distances between the given cluster centers. Observing the parameter space we can find the massive center and some outside traces that can be treated as the improper behavior of an engine. The next and the last was a classification. The results of classification are not perfect but they are showing. The next step of analysis will be performing a classification with using of Support Vector Machine SVM method [1, 16] which seems quite effective in similar problems [10].

Table 5. The result of classification for data sets H – signals registered in horizontal transversal direction, H2045 – signals registered in horizontal transversal direction for locomotive 204 and H2016 – signals registered for horizontal transversal direction for locomotive 2061

	H Percentage of classification as a		H2045 Percentage of classification as a		H2016 Percentage of classification as a	
	Proper	Improper	Proper	Improper	Proper	Improper
Proper (after the repair)	69%	31%	79%	21%	85%	15%
Improper (before the repair)	75%	25%	83%	17%	93%	7%

The future researches need to perform an experiments on bigger set of data what usually increase an expenses of researches.

It seems also that there are the significant differences for the data taken from different locomotives. This shows that to classify and real diagnosis using vibroacoustic signal analysis all measurement must be taken from the same locomotive and for the same installation of injector and accelerometers also.

Nomenclature

A	all signals
A2045	signals for locomotive 2045
A2061	signals for locomotive 2061
FFT	Fast Fourier Transformation
H	signals registered in horizontal transversal direction
H2045	signals registered in horizontal transversal direction for locomotive 2045
H2061	signals registered for horizontal transversal direction for locomotive 2061
OBD	on-board diagnostic system
V	signals registered in vertical direction
V2045	signals registered in vertical direction for locomotive 2045
V2061	signals registered in vertical direction for locomotive 2061

Bibliography

[1] ABE, S. Support vector machines for pattern classification. *Springer-Verlag*. 2005.

[2] ALLEN, J.B., RABINER. A unified approach to short-time Fourier analysis and synthesis. *Proceedings of the IEEE*. 1977, **65**, 1558-1564.

[3] ALLEN, J.B. Short term spectral analysis, synthesis, and modification by Discrete Fourier Transform. *IEEE Transactions on Acoustic, Speech, and Signal Processing ASSP-25*. 1977, 235-238.

[4] BEZDEK, J.C. Pattern recognition with fuzzy objective function algorithms. *Plenum Press*, Second edition, 1987.

[5] BOGUŚ, P., LEWANDOWSKA, K. Short-time signal analysis using pattern recognition methods. *Artificial Intelligence and Soft Computing*. 2004, **3070**, 550-555.

[6] BOGUŚ, P., MERKISZ, J. Short-time analysis of combustion engine vibroacoustic signals through pattern recognition techniques. *SAE Technical Paper*. 2005, 2005-01-2529.

[7] BOGUŚ, P., MERKISZ, J. Misfire detection by short-time analysis with using clustering techniques. *Congress Proceedings, PTNSS KONGRES 2005*, September 25th – 28th, 2005, Bielsko-Biała/Szczyrk.

[8] BOGUŚ, P., SIENICKI, A., WOJCIECHOWSKA, E., MERKISZ, J. The comparison of vibroacoustic signals taken from an engine before and after repair. *Combustion Engines*. 2007-SC3, 300-306.

[9] BOGUŚ, P., SIENICKI, A., WOJCIECHOWSKA, E. Porównanie stanu silnika lokomotywy spalinowej ST44 przed i po remoncie przy użyciu sygnału wibroakustycznego. *Pojazdy Szynowe*. 2007, **2**, 28-36.

[10] BOGUŚ, P., MERKISZ, J., MAZUREK, S. The prospects of artificial intelligence methods in identification and prevention of critical railway accidents. *L. Rutkowski, R. Tadeusiewicz, L. Zadeh, J. Zurada (eds.). Computational Intelligence: Methods and Applications*. EXIT, Warsaw 2008, 445-453.

[11] BOGUŚ, P., GRZESZCZYK, R., WRONA, A. et al. Estimation of fuel spraying from diesel engine injector using multiresolution wavelet analysis of vibroacoustic signals. *Combustion Engines*. 2015, **162**(3), 264-270.

[12] DUDA, R., HART, P. Pattern classification and scene analysis. New York, *Wiley Interscience* 1973.

[13] HARRIS, F.J. On the Use of windows for harmonic analysis with the Discrete Fourier Transform. *Proceedings of the IEEE*. 1978, **66**, 51-83.

[14] MERKISZ, J. Ecological aspects of combustion engines (Part 1 and 2). Poznań: *Wydawnictwo Politechniki Poznańskiej*. 1998 and 1999 (in Polish).

[15] PORTNOFF, M.R. Time-frequency representation of digital signals and systems based on Short-Time Fourier Analysis. *IEEE Transactions on Acoustic, Speech, and Signal Processing*. 1980, **28**, 55-69.

[16] WANG, L. (ed.). Support vector machines: theory and applications. *Springer-Verlag* 2005.

[17] YANG, J., PU, L. et al. Fault detection in a diesel engine by analyzing the instantaneous angular speed. *Mechanical Systems and Signal Processing*. 2001, **15**, 549-564.

Prof. Piotr Boguś, DSc., PhD. – Rail Vehicle Institute TABOR in Poznań, Poland.

e-mail: *piotr.bogus@gumed.edu.pl*

Prof. Jerzy Merkisz, DSc., DEng. – Faculty of Transport Engineering, Poznan University of Technology.

e-mail: *jerzy.merkisz@put.poznan.pl*

Article citation info:
WIŚNIOWSKI, P., GIS, M. Representativeness of toxic substances emissions in bench tests that reflect the traffic conditions of a vehicle. *Combustion Engines*. 2019, **177**(2), 88-90. DOI: 10.19206/CE-2019-215

Piotr WIŚNIOWSKI
Maciej GIS

CE-2019-215

Representativeness of emissions of toxic substances in bench tests reflecting the road traffic conditions of a vehicle

The results of measurements of exhaust emissions in real road traffic differ significantly from the results of stationary homologation tests. One of the solutions, helpful in determining the actual emission, is the creation of stationary exhaust emission tests simulating the use of the vehicle on the road. The article presents the method of reconstructing the synthetic driving test obtained on the basis of road tests and presents the obtained profile of the speed course. The authors discussed the reasonableness of selecting the emission component determining the correctness of the representativity of the stationary test obtained, which determines the amount of work done by the engine.

Key words: driving cycle, road tests, emission of toxic substances, chassis dynamometer, synthesis of road tests

1. Introduction

Research on the ecological properties of automotive combustion engines is carried out at almost every stage of the life cycle of vehicles. The research is carried out in the development phase of the engine concept (basic cognitive research), in the design phase (during prototype tests), in the production phase (during quality control), in the admission stage (approval tests) and in the operation phase (diagnostic tests). The purpose of all these tests is to determine the emission of pollutants in the engine's exhaust gas under given conditions. This goal is carried out in dynamometer tests in which different engine operation conditions are reproduced [3]. Due to the discrepancy of emissions in real traffic conditions with emissions resulting from stationary (eg homologation) tests, it seems reasonable to prepare test conditions imitating the real road conditions in the best way [9, 10].

2. Explanation of the issue

Research to date on the subject of representativeness of bench tests relative to road conditions needs to be clarified and explained. Simulating traffic conditions during stationary tests on a chassis dynamometer is a difficult task due to numerous random factors. Currently used chassis dynamometer tests are perfectly suited for comparative tests aimed at determining the emission values of particular exhaust components during strictly defined engine operating conditions. However, these are not tests that precisely represent real traffic conditions, but rather some kind of patterns for emission tests [6]. It would be necessary to create a bench test, which would be based on the measured operating parameters of the representative group of vehicles in real traffic and additionally introduce a random factor during the test construction. This factor, however, cannot lead to complete randomness of the test [1].

3. Description of the measurements

Taking into account the above assumptions, a series of measurements was carried out on a test vehicle on a designated measurement route. During the registration of vehicle performance parameters, the emission of toxic substances from its exhaust system was also measured using a PEMS mobile analyzer. The results of emission measurements were later used to verify the level of representativeness of the designed test.

3.1. The object of research

The test object was the Ford Focus Flexifuel spark-ignition vehicle shown in Figure 1, produced in 2008. Technical data of the car can be found in Table 1.

Table 1. Technical data of the test car

Name	Data
Make	Ford
Type	Focus
Power	92 kW
Engine stroke volume	1798 cm^3
Location and number of cylinders	In-line, 4
Emission level	Euro 4
Transmission	Manual (five forward gears, one reverse gear)

Fig. 1. Ford Focus car on the test bench

3.2. Measuring equipment

The benchmark emission tests were carried out on a 2-roller chassis dynamometer 2PT220EX type, manufactured by Jaroš with two rollers with a diameter of 372 mm, with electric simulation of motion resistance and mechanical simulation of inertia placed in the low temperature chamber. This dynamometer allows the examination of vehicles (also at ambient temperature up to –14°C) with the following parameters:

- maximum net power on wheels up to 220 kW,
- maximum speed of 130/200 km/h,

- pressure on the drive axle up to 2400 kg,
- drive for one axle or more than one axis with the possibility of disconnecting the drive,
- maximum wheelbase of the drive axle: 2100 mm,
- maximum vehicle height 2900 mm, maximum distance of the rear drive axle from the front of the car 5000 mm.

Emission measurements were made using a set of AMA i60 AVL analyzers. The following pollutants were measured:

- carbon monoxide (low concentrations) (CO_{low}),
- carbon monoxide (high concentrations) (CO_{high}),
- carbon dioxide (CO_2),
- hydrocarbon totals (THC),
- methane (CH_4),
- nitrogen oxides (NO_x), nitric oxide (NO) and nitrogen dioxide (NO_2), nitrous oxide (N_2O).

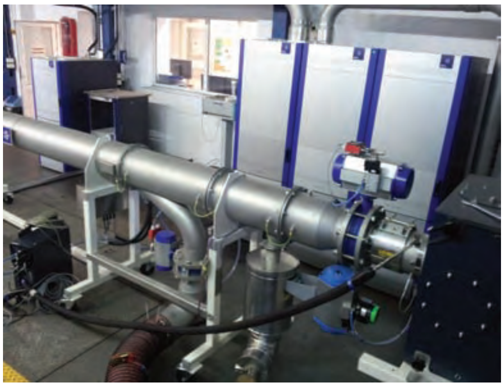

Fig. 2. A set of AMA i60 measuring devices

The Semtech DS analyzer with the GPS module from Sensors Inc. (Fig. 2) was used for measurements and registration of harmful gaseous exhaust gas compounds. It was a PEMS type analyzer that allows measuring the mass flow of exhaust gases and the concentration of harmful compounds such as: carbon dioxide (CO_2), carbon monoxide (CO), hydrocarbons (HC) and nitrogen oxides (NO_x).

Fig. 3. The SEMTECH DS mobile analyzer used in the Ford Focus Flexi-fuel vehicle tests

3.3. Speed registration and mapping

Figure 3 shows an exemplary fragment of the speed course registered in the real road traffic measurements, while Fig. 4 shows a fragment of the speed course of the discussed artificial test, obtained as a result of treating the input data with a specially prepared calculation algorithm [8]. The obtained test is characterized by a representative level of toxic substances emission and fuel consumption as well as the amount of work done by the vehicle's engine during the test.

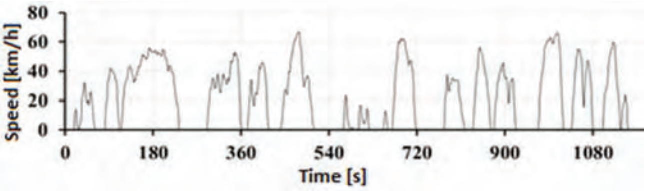

Fig. 4. Selected fragment of the speed course registered in road measurements

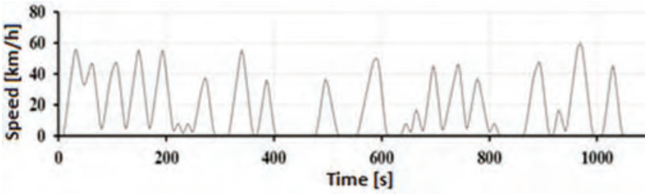

Fig. 5. Selected fragment of the speed course registered in stationary measurements

4. Findings

In order to verify the correctness of the assumptions and the correctness of the construction of the based on road measurements stationary test itself, it was necessary to compare the emission values of individual exhaust components. It turned out that the type of measurement equipment used had a significant influence on the obtained results. In the case of hydrocarbons measurement, in road tests the analyzer operating on the principle of using infrared IR built into the mobile measuring device was used, relatively inaccurate in the case of carbon particle emission measurement, due to the registration of the flow of only part of hydrocarbon compounds. However, in the case of laboratory tests, an FID analyzer was used, which shows high accuracy of measurement, recording real and reliable values of carbon emissions. As a result, the recorded road values of the hydrocarbon emission intensity were proportionally lower than the values recorded in the laboratory tests.

Another difference between road and bench tests was the emission intensity values when the engine was idling. They resulted from the method of flue gases flow meter measurement using a Pitot tube, which explains the phenomenon of oscillating emission intensity (also to zero values), because the emission values are the smallest when the vehicle is stationary, and Pitot tube is characterized by the smallest accuracy at small flows [5, 7].

Finally, it was decided to use the results of measuring the intensity of carbon dioxide emission as a constituent of exhaust, which best describes the level of representativeness of the designed test relative to road tests. The amount of carbon dioxide emitted is proportional to the amount of fuel consumed in the tests and, as a result, proportional to the work done by the engine.

For a more reliable confirmation of the representativeness and repeatability of the results, the Mann-Whitney statistical significance test was carried out. He showed that at the significance level of 0.05 there are no grounds to reject the hypothesis about the lack of significant differences between the results of individual tests [4]. This is the key information that authorizes us to accept the hypothesis about the compatibility and repeatability of the tests performed for the most important exhaust component.

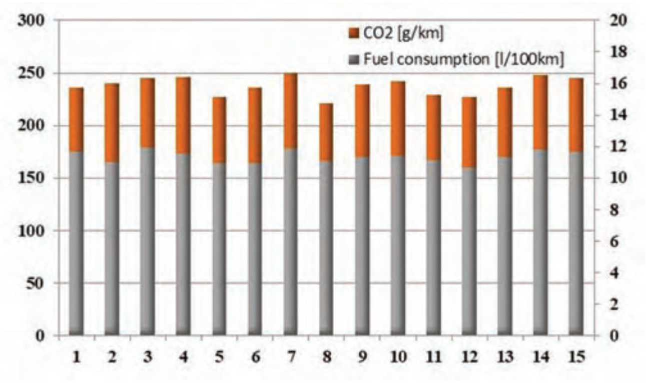

Fig. 6. Fuel consumption and carbon dioxide emissions

In order to more reliably confirm the representativeness of the obtained tests, during the tests mass measurement of fuel consumption was performed during stationary tests both in the designed tests and in the test reproduced directly according to registered vehicle speeds in road ones.

Figure 6 shows the fuel consumption in subsequent tests performed on the chassis dynamometer and the carbon dioxide emission values in these tests. A significant correlation of the obtained results can be observed, which proves the high repeatability of the conducted tests on the chassis dynamometer.

5. Conclusion

Based on the analysis of carbon dioxide emissions, there was significant compatibility between road and stationary tests. The results of synthetic tests differed by no more than 2.5% compared to road tests. They confirm significant correctness of the mapping. Since the discrepancy was much greater for the other components, it can safely be said that of all exhaust components of the exhaust system, carbon dioxide is the best component to determine the comparability of the tests obtained [2].

Nomenclature

CH_4	Methane
CO	Carbon monoxide
CO_2	Carbon dioxide
CO_{high}	Carbon monoxide (high concentration)
CO_{low}	Carbon monoxide (low concentration)
FID	Flame Ionization Detector
IR	Infra Red
N_2O	Nitrogen dioxide
NO	Nitric oxide
NO_2	Nitrogen dioxide
NO_x	Nitrogen oxides
PEMS	Portable Emissions Measurement System
THC	Hydrocarbons

Bibliography

[1] MERKISZ, J., RYMANIAK, Ł. Determining the environmental indicators for vehicles of different categories in relation to CO_2 emission based on road tests. *Combustion Engines*. 2017, **170**(3), 66-72.

[2] WIŚNIOWSKI, P., ŚLĘZAK, M., NIEWCZAS, A., SZCZEPAŃSKI, T. Method for synthesizing the laboratory exhaust emission test from car engines based on road tests. *IOP Conf. Series: Materials Science and Engineering*. 2018, **421**, 042080. DOI:10.1088/1757-899X/421/4/042080.

[3] KUTRZYK, A., FILIPCZYK, J., Określenie poziomu emisji składników spalin dla różnych warunków pracy silnika. *Zeszyty Naukowe Politechniki Śląskiej*. 2008, **64**, 167-174.

[4] HYK, W., STOJEK, Z. *Analiza statystyczna w laboratorium*. 2016, *PWN*, Warszawa.

[5] BIELACZYC, P. O badaniach emisji związków szkodliwych spalin z silników samochodowych w warunkach trakcyjnych metodą RDE (PEMS). *Przegląd Techniczny*. 2016 **24**.

[6] BEBKIEWICZ, K., CHŁOPEK, Z., SZCZEPAŃSKI, K. Estimating pollutant emission from motor vehicles in the years 2000–2015. *Combustion Engines*. 2017, **171**(4), 62-67.

[7] WIŚNIOWSKI, P., ŚLĘZAK, M., NIEWCZAS, A., SZCZEPAŃSKI, T. Dobór metody filtrowania przebiegu prędkości pojazdu. *Autobusy: technika, eksploatacja, systemy transportowe*. 2017, **9**, 24-29.

[8] SZCZEPAŃSKI, T., WIŚNIOWSKI, P. Typowe zadania realizowane przez silnik spalinowy. *Transport Samochodowy*. 2017, **1**, 85-104.

[9] MERKISZ, J., PIELECHA, J., JASIŃSKI, R. Ocena emisji spalin pojazdów kategorii Euro 6 w testach drogowych., *Prace Naukowe Politechniki Warszawskiej*. 2017, **115**, 131-144.

[10] CHŁOPEK, Z. Synteza testów jezdnych zgodnie z kryteriami podobieństwa charakterystyk częstotliwościowych. *Eksploatacja i niezawodność – Maintenance and Reliability*. 2016, **18**(4), 572-577.

Piotr Wiśniowski, DEng. – Environment Protection Center, Motor Transport Institute.
e-mail: *piotr.wisniowski@its.waw.pl*

Maciej Gis, DEng.– Environment Protection Center, Motor Transport Institute.
e-mail: *maciej.gis@its.waw.pl*

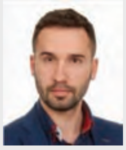

Article citation info:
PROKHORENKO, A., SAMOILENKO, D., ORLINSKI, P. et al. The application of isodromic equation for calculation of PID-controller integrated component. *Combustion Engines*. 2019, **177**(2), 91-94. DOI: 10.19206/CE-2019-216

Andriy PROKHORENKO
Dmytro SAMOILENKO
Piotr ORLINSKI
Dmytro TALANIN
Serhii KRAVCHENKO

CE-2019-216

The application of isodromic equation for calculation of PID-controller integrated component

A functional feature of the application of electronics used for the automatic control of internal combustion engines is necessity in the proportional conversion of ECU electrical signals into the mechanical processes based on corresponding elements motion. For such conversion of information actuating mechanisms are used, referred as actuators. Actuators in the form of electrical machines (stepper or precision electric motors) or electric apparatuses (electromagnets and solenoids) are the mostly widespread in ICE. As a physical object of the research, the unit of Heinzmann, model StG 6-02V that is based on a DC electric drive controlled by a pulse-width modulation signal, was selected in the current work. It has a toothed gearbox and a non-contact reverse positional connection. This actuator provides an output torque of 6 Nm and 36-degree range of output shaft rotational angle. The functional scheme of the electronic system of automatic control of a diesel engine based on mentioned device is developed. The PID regulator with feedback is used to control the actuator. A design formula that can be incorporated in the controller algorithm to calculate the integral component of the PID regulator was also obtained. Values of empirical coefficients were determined in this formula. The results of experimental confirmation of the correctness of the approach taken are presented. Thus, the new formula for determining the integral component of the PID regulator differs positively from the well-known solutions because the new approach is free from storing the whole array of previous data with discrepancy in the controller's RAM, that simplifies the application of the developed algorithm greatly and speeds up the computational capability of the controller.

Key words: *diesel, automatic regulation, electronic system, control algorithm, PID regulator*

1. Introduction

A functional feature of the application of electronics in internal combustion engines for their automatic control is the necessity of the proportional transformation of electrical signals of the electronic control unit into the mechanical processes of moving the corresponding elements. For such information transformation, so-called final controlling drive (FCD) also known as actuators, are used [1].

FCD (actuators) became the most widespread in ICE. These are electric machines (step or precision electric motors) or electric apparatuses (electromagnets and solenoids) of different kinds.

As a physical object, the actuator Heinzmann, model StG 6-02V was used in the current research. This model is based on a DC motor drive controlled by a Pulse-Width Modulation (PWM) signal.

It has a toothed gearbox and a non-contact reverse positional connection. This actuator provides an output torque of 6 Nm and a range for output shaft rotation angle of 36° [2].

The functional scheme of the developed electronic system of the diesel engine automatic control (DEAC) is presented in Fig. 1. The external and internal variables of DEAC are: X – current position of the engine control unit, n – current crankshaft rotation speed, Hp – position of the fuel supply control element (high pressure fuel pump (HPFP) rail position), f – the relative magnitude of the PWM signal. The FCD governor is a part of the ECU engine program. Detailed description of the algorithm of operation of the subsystem developed for the control of the drive positioning is given in the article [3].

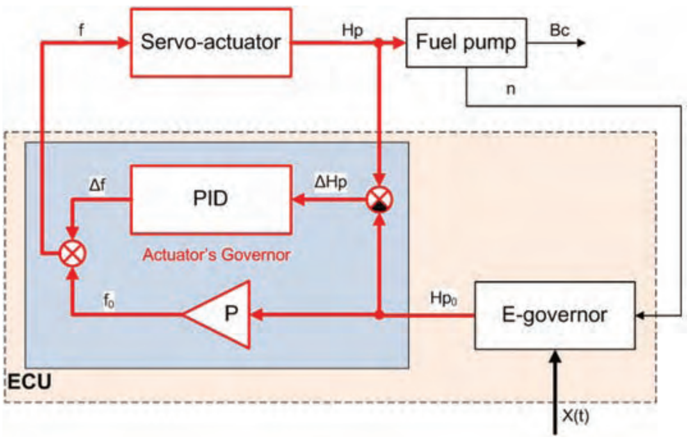

Fig. 1. Functional diagram of the electronic control system of a diesel engine [3]

2. Theoretical study

2.1. A brief description of the algorithm

Taking into account the availability of a reverse positional feedback due to the current HPFP position, the value of "discrepancy" could be calculated:

$$\Delta Hp = Hp - Hp_0 \tag{1}$$

The developed FCD algorithm is based on the parallel work of positional (P) and proportional–integral–derivative (PID) controllers (see Fig. 1).

In this case, the P-controller is a non-inertial amplifier that determines the required level of filling the PWM signal to achieve a given equilibrium position of the rails Hp_0. Its equation has a form:

$$f_0 = K \cdot Hp_0 \tag{2}$$

PID-controller operates in parallel to P-controller and on the basis of the magnitude of the discrepancy, determined by the formula (1), accelerates the achievement of a given position of Hp_0 by means of the program realization of the expression:

$$\Delta f = K_D \cdot \Delta^2 Hp + K_P \cdot \Delta Hp + K_I \cdot S \tag{3}$$

Thus, PWM signal that is sent to the executive mechanism has the following meaning:

$$f = f_0 + \Delta f \tag{4}$$

By analyzing equations (2) and (3), it is not difficult to notice that the first of them provides the static characteristics, and the second determines the dynamic properties of the system.

The differential component in expression (3) is defined as:

$$\Delta^2 Hp = \Delta Hp(t) - \Delta Hp(t - T) \tag{5}$$

where T = 120/n – clock design period, which depends on the current crankshaft speed n and determines the time constant for integration and differentiation.

2.2. An alternative definition of the integral component

The third component in the equation (3) $K_I \cdot S$ defines the integral feedback effect on the PWM control. It is the product of some constant K_I to the finite sum of the discrepancy S.

For the mathematical determination of the current S(t) value, the differential equation of the ideal integral link with the transfer coefficient equal to 1 can be used (or it can be regarded as the coefficient K_I) [4]:

$$\frac{S'(t)}{dt} = \Delta Hp(t)$$

which connects input and output signals: Hp(t) and S'(t) accordingly.

The numerical solution of this differential equation can be represented in the form of a finite sum, provided that the periodicity of the registration of the irregularity and the limitation of the time (number) of the last irregular registrations is constant

$$S'(t) \approx \sum_{i=0}^{N-1} \Delta Hp(t - iT) \tag{6}$$

here N is number of terms in the final sum (the number of recent registrations).

For the simplification of the constant values condition in discrepancy, during all integration time it is accepted $\Delta Hp(t) = \Delta Hp\,(t - iT) = \ldots = \Delta Hp\,(t - NT) = \text{const}$.

Then the limit of this sum will be equal:

$$\lim_{t \to N \cdot T} S'(t) = \lim_{i \to N} \left[\sum_{i=0}^{N-1} \Delta Hp(t - iT) \right] = N \cdot \Delta Hp(t) \tag{7}$$

Equation (6) is an algorithmic-calculated and can be used to determine the third component in equation (3). But its significant disadvantage for practical use in the algorithm is that for calculations it is necessary to have an array of the last N values of the discrepancy, which additionally overloads the controller RAM and reduces processor speed. An alternative approach to defining an integral component in the algorithm of the electronic PID controller is proposed in this study to eliminate this disadvantage.

To determine the same sum for the integral component S(t), the differential equation of the isodromic link is used [4]:

$$\frac{S(t)}{dt} = k \cdot \Delta Hp(t) + k_1 \frac{d\Delta Hp(t)}{dt}.$$

The coefficients k and k_1 in the differential equation have the following physical meaning: k – the transmission factor (amplification), and $k_1/k = T_I$ – time constants of the isodrome [4].

After integrating this differential equation, an expression is obtained (the integral action is replaced by the action of the final summation):

$$S(t) = k \sum_{0}^{t} \Delta Hp(t) + k_1 \Delta Hp(t)$$

Taking into account the recurrence $S'(t) = \sum_0^t \Delta Hp(t) = S'(t - T) + \Delta Hp(t)$ and proceeding from the fact that at each moment of time the following condition must be fulfilled $S(t) = S'(t)$, and after a simple transformation and designation $K_I = k_1 + k$ the expression could be written as:

$$S(t) = k \cdot S(t - T) + K_I \cdot \Delta Hp(t) \tag{8}$$

The resulting equation (8) is a design formula and can be included in the controller algorithm instead of equation (6). Moreover, it devoids the deficiencies of equation (6) because it does not contain the action of the final summation and does not require constant storage of the array of the last discrepancy values. However, equation (8) has uncertain coefficients in the form of coefficients K_I and k.

2.3. Determination of the key coefficients

Determination of the values of constants K_I and k is based on the statement that the boundary of the sum found by equation (6) and equation (8) must coincide. For this condition, the equation (8) must be transformed into the form of an infinite integral sum:

$$S(t) = K_I \sum_{i=0}^{\infty} \left[k^i \cdot \Delta Hp(t - iT) \right] \tag{9}$$

The expression (9) is identical to equation (8), but more complex in practical use. However, the analysis of this equation shows that the coefficient K_I can be attributed to the coefficient K_I. Thus, it was established that $K_I = 1$.

The limit of the sum received by (9) at k < 1:

$$\lim_{t\to\infty} S(t) = \lim_{t\to\infty}\left(K_I \sum_{i=0}^{n}\left[k^i \cdot \Delta Hp(t - iT)\right]\right) =$$

$$= \Delta Hp(t) \cdot \lim_{n\to\infty}\left[\sum_{i=0}^{n} k^i\right] = \Delta Hp(t) \cdot \frac{1}{1-k}$$

Here factors $K_I = 1$ and $\Delta Hp(t - iT) = \Delta Hp(t)$ – are the constants that can be taken as a boundary sign. From the condition of equality of sum of limits $\lim_{t\to N\cdot T} S'(t) = \lim_{t\to\infty} S(t)$, determined by the "integral" (6) and "isodromic" (8) methods, it can be written:

$$N \cdot \Delta Hp(t) = \Delta Hp(t)\frac{1}{1-k}.$$

Hence, the value of the coefficient k in the form of a function from N:

$$k = 1 - \frac{1}{N}.$$

Possible values of the isodromic coefficient k in the restricted interval N = 2 ... 100 are graphically represented in Fig. 2.

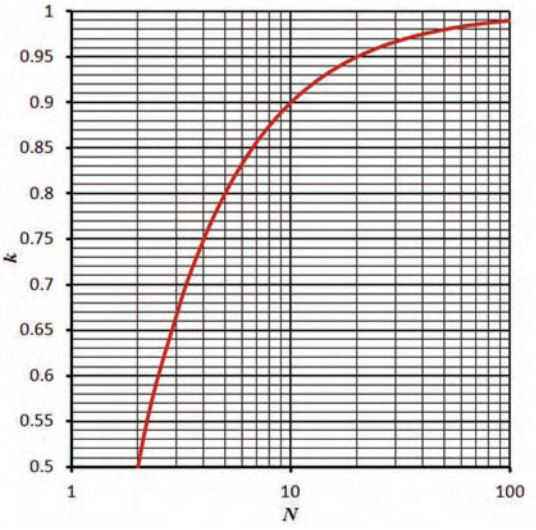

Fig. 2. Possible values of the isodromic coefficient *k*

It should be noted that the nomogram presented in Fig. 2 is used only for the previous choice of the constant coefficients values. The final value, undoubtedly, is determined in the process of PID-controller adjustment and taking into account the physical properties of the control system in general and the executive mechanism characteristics in particular.

3. Experimental validation

The results of experimental confirmation of the theoretical foundations are presented in Fig. 3 and Fig. 4. The experiment was carried out using the experimental setup described in [5]. During the experiment the microcontroller program determined the value of the isodromic coefficient as k = 0.9 (N = 10).

Figure 3 shows the transient process, which is the reaction of the system (Fig. 1) on the external effect in the form of an artificial sharp change in the Hp_0 setting (ΔHp discrepancy) by 50% of the initial value. As it can be seen from Fig. 3, the law of the push F change (torque on the output lever of the actuator) using the proposed "isodromic" method qualitatively differs from the use of the traditional "integral" method - it passes faster at the beginning of the transient process and more smoothly at its end.

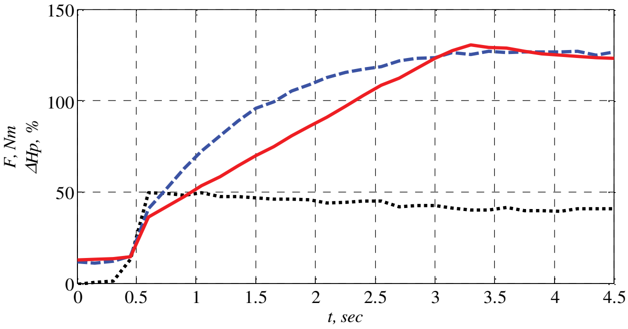

Fig. 3. Discrepancy ΔHp (....) and push F on the output lever: —— "integral" method; - - - "isodromic" method

Additionally it can be illustrated by the rate of change in push during transient process, which in physical sense is the derivative of dF/dt that is shown in Fig. 4. It can be also seen from the chart that in the case of "isodromic" method, the transient process is finished for 1.5 seconds earlier and has no overregulation. It has, undoubtedly, a positive impact on increasing the stability and operation speed of the entire automatic control system.

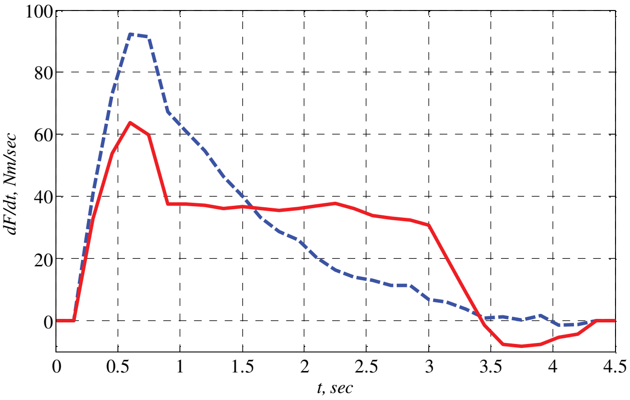

Fig. 4. Rate of the push change at the output lever: —— "integral" method; - - - "isodromic" method

4. Conclusions

Thus, in the current research the new equation was offered for determining the integral component of the PID-controller. It is beneficially different from the traditional algorithm by "integral" method because there is no need to store the array of previous data in the memory of the controller that would significantly simplify the application of algorithm and speeds up the computational capability of the controller.

In addition, such an innovation in the actuator control methods would increase its maximum effort on the input lever by 50% and allow to accelerate the transient process for 1.5 seconds.

Nomenclature

PWM	Pulse-Width Modulation
PID	Proportional-Integral-Derivative
ECU	electronic control unit
P	positional
FCD	final controlling drive
DEAC	diesel engine automatic control
HPFP	high pressure fuel pump

Bibliography

[1] DORF, R.C., BISHOP, R.H. Modern control systems. *11th Edition. — Pearson International Edition.* 2008, 1048.

[2] Heinzmann Actuators – [cited 08.03.2019] – Access: https://www.heinzmann.com/en/engine-and-turbine-management/actuator/electric.

[3] PROKHORENKO, A., SAMOILENKO, D., ORLINSKI, P. et al. Subsystem of positioning the actuator for an electronic diesel control system. *Journal of Machine Construction and Maintenance.* 2018, **1**(108), 103-109.

[4] БЕСЕКЕРСКИЙ, В.А., ПОПОВ, Е.П. Теория систем автоматического регулирования. *М. Наука.* 1975, 768.

[5] ПРОХОРЕНКО, А.О., КРАВЧЕНКО, С.С., САМОЙЛЕНКО Д.Є. и дг. Універсальний електронний регулятор дизеля на основі електричного сервоактуатора. Двигатели внутреннего сгорания. Харьков: *НТУ «ХПИ»*, 2018, **1**, 31-39.

Andriy Prokhorenko, DSc., DEng. – Department of Internal Combustion Engines, National Technical University “Kharkiv Polytechnic Institute”.
e-mail: *prokhorenko@kpi.kharkov.ua*

Dmytro Samoilenko, DEng. – Faculty of Automotive and Construction Machinery Engineering, Warsaw University of Technology.
e-mail: *dmytro.samoilenko@pw.edu.pl*

Serhii Kravchenko, DEng. – Department of Internal Combustion Engines, National Technical University “Kharkiv Polytechnic Institute”.
e-mail: *kravc4enkoserg@gmail.com*

Piotr Orliński, DSc., DEng. – Faculty of Automotive and Construction Machinery Engineering, Warsaw University of Technology.
e-mail: *piotr.orlinski@pw.edu.pl*

Dmytro Talanin – Department of Internal Combustion Engines, National Technical University “Kharkiv Polytechnic Institute”.
e-mail: *dima.kharkiv75@ukr.net*

Article citation info:
SUCHETA, A. Effects of water injection to the fuel and air mixture on equilibrium gas composition in combustion products and selected parameters of the theoretical Otto cycle. *Combustion Engines*. 2019, **177**(2), 95-102. DOI: 10.19206/CE-2019-217

Andrzej SUCHETA

CE-2019-217

Effects of water injection to the fuel and air mixture on equilibrium gas composition in combustion products and selected parameters of the theoretical Otto cycle

Moisturizing the intake air by spraying water in the liquid phase significantly lowers the intake air temperature, mainly due to the high value of latent heat of evaporation. The paper presents a methodology for calculating the parameters of the air-fuel mixture after water injection and during subsequent processes of the Otto cycle: compression, combustion and expansion of exhaust gases. For octane as a fuel, exemplary calculations have been carried out to investigate the effect of water injection on the composition of combustion products and selected parameters of the theoretical Otto cycle (temperature, pressure, output power and thermal efficiency).

Key words: *intake air humidification, water injection, Otto cycle, equilibrium*

1. Introduction

Current and future limits of CO_2 emissions and the need to limit the use of non-renewable fuels are an important impulse for directing research interests towards new solutions. With regard to combustion engines (reciprocating internal combustion engines), the amount of CO_2 emitted by engines depends directly on the fuel consumption. Research in this field is aimed at both reducing passive resistance and at increasing the efficiency of engines operating at stoichiometric composition of the fuel – air mixture in a wide range of parameters (rotational speed and load). Increasing the thermal efficiency of spark-ignition engines operating in accordance with the Otto cycle is associated with an increased the compression ratio. However, increasing the compression ratio increases the combustion temperature, which in turn leads to an increase in NO_x emissions. Combustion techniques are therefore considered at lower temperatures to reduce emissions. Currently, the most commonly used method of reducing the temperature of the mixture is intercooling and so-called cold exhaust gas recirculation (cooled EGR). However, the structure of the so-called cold EGR is complex and must be precisely controlled. The issue is particularly important in the downsizing technique of boosted engines with high thermal loads and an increased tendency to knock.

The technique of water injection into the cylinder makes it possible to significantly reduce the combustion temperature [2]. Injection of water to achieve this goal is not a new concept. It was used for the first time in aviation engines during World War II, primarily to reduce knocking combustion. Unlike EGR, the water injection system can not completely replace the intercooler, but it significantly reduces the temperature of the air-fuel mixture. The effectiveness of cooling the fuel-air mixture by injecting liquid water into it results from two reasons. Liquid water is distinguished by a high value of the latent heat of vaporization, which is 2257 kJ/kg at the evaporation pressure of 1 bar. It is about 7 times higher than the heat of evaporation for octane and about 5.6 times higher than the heat of evaporation for Gasoline RON95 [4]. During the evaporation of drops of water (water mist) the heat, necessary for this process, is collected from the surrounding gases, which reduces their temperature. The vapor formed after evaporation is mixed with the air-fuel mixture, the specific heat of the resulting gas mixture increases and the adiabatic index in the adiabatic compression decreases. The result is that when compressing the air-fuel mixture containing water vapor, lower temperatures will occur.

There are two water injection systems for the engine: injection of water to the inlet channel (Port Water Injection PWI) and injection of water to the cylinder (Direct Water Injection DWI) [4]. Most research works refer to the PWI system because it is cheaper and easier to use. The advantage of water injection to the intake manifold is also the fact that the injected water has a longer time for evaporation, which protects against the inflow of unresolved water to the cylinder which can destroy the oil film of the cylinder liner causing mechanical damage to the engine. The system DWI consists in the injection of water directly into the cylinder in the compression process (compression stroke) to achieve the greatest cooling effect and excluding the formation of water liquid film on combustion chamber walls. The injection of water into the cylinder in this system occurs at a later stage of the compression stroke, when the compressed charge has a correspondingly high temperature. This system is more complex, requires thorough design changes in the engine head and in operation requires the use of higher pressures and precise control.

The subject of the work is a theoretical analysis of the Otto cycle in which air supplied to the cylinder is humidified in the intake manifold by water injection (PWI). The mass of the water injected per cycle is expressed by the parameter s, defined as the ratio between the injected liquid water mass m_w and the stoichiometric fuel mass m_{FUEL} for a given mass of dry air:

$$s = \frac{m_W}{m_{FUEL}} \quad (1)$$

The typical range of parameter s variations in practical applications given in the literature [4] is 20% to 40% which corresponds to a mass fraction of injected water equal approximately to 6% of the total trapped mass per cycle. The maximum value of the parameter s must be selected so precisely that the injected water in the intake manifold can evaporate. Otherwise, getting into the cylinder in excess, in the form of drops, liquid water can damage the oil film on the cylinder liner causing the risk of engine seizure. At the beginning should therefore be determined limit value s_{max}, which will depend on the parameters of the humidified air.

2. Intake air humidification

The air sucked in by the engine can enter the intake manifold directly from the environment or in turbocharged engines is pre-compressed by the compressor and pre-cooled in the intercooler. In the injection system of water to the intake manifold, the spraying of water in the collector is provided by a water injector located at the beginning of the inlet channel [3]. Sprayed into very fine drops, the water evaporates, moisturizes and simultaneously cools the flowing air. It is assumed that in the intake manifold near the intake valve there is a fuel injector that creates a fuel-air mixture supplied to the cylinder. Schematic arrangement of components of the intake system is shown in Fig.1.

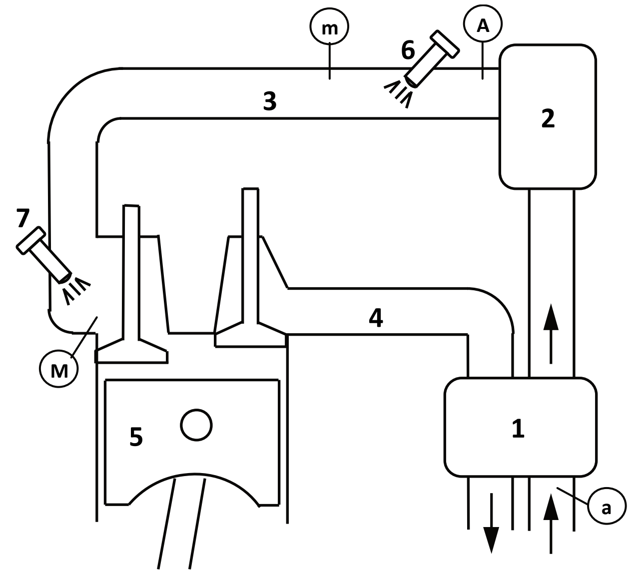

Fig. 1. Engine layout with water injector: 1 – turbocharger, 2 – intercooler, 3 – intake duct, 4 – exhaust duct, 5 – engine bloc, 6 – water injector, 7 – fuel injector; indices for parameters: a – ambient, A – before water injection, m – after water injection, M – after fuel injection

It is assumed that ambient air parameters: temperature ta, pressure p_a and relative humidity φ_a are known.

The amount of water vapour in the combustion air can be specified in various ways. However, the simplest way is to specify the mass of water vapour present in a unit of dry air. This is called specific humidity and is denoted as X and is expressed in kg of water vapour per kg of dry air since

$$X = \frac{m_v}{m_{dry\ air}} = \frac{M_v n_v}{M_{dry\ air}\ n_{dry\ air}} = 0.622\frac{p_v}{p-p_v} \tag{2}$$

where M_v and $M_{dry\ air}$ are the molar masses of water and dry air, respectively whilst n_v and $n_{dry\ air}$ stand for the number of moles of water vapour and dry air, respectively, p_v is partial pressure of water vapour, p is total pressure. In calculations it is more convenient to use a molar specific humidity, denoted as X_Z and is expressed in kmol of water vapour per kmol of dry air since

$$X_Z = \frac{n_v}{n_{dry\ air}} = \frac{p_v}{p_a-p_v} = \frac{\varphi_a p_s(T_a)}{p_a-\varphi_a p_s(T_a)} \tag{3}$$

where $p_s(T)$ is the saturation pressure of water vapour at the given temperature T, n_v is the kmol of water vapour contained in the air, $n_{dry\ air}$ is the kmol of dry air.

The air after passing through the compressor and intercooler has known parameters (temperature T_A, pressure p_A) at the inflow to the inlet channel. The specific humidity of the air after passing through the compressor and cooler does not change $X_a = X_A$, and $X_{Za} = X_{ZA} = X_Z$.

The energy balance sheet diagram for the air humidification process is shown in Fig. 2.

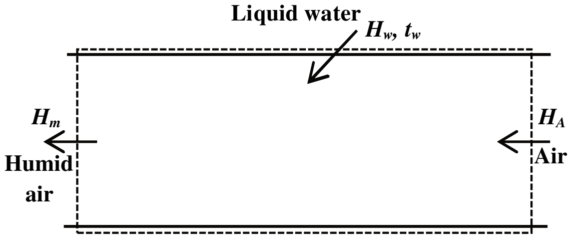

Fig. 2. Illustration of an energy balance for air humidification

The balance is referred to 1 kmole of dry air. It is assumed that the air humidification process in the collector is isobaric and takes place without supplying heat from the outside. After omitting macro kinetic and potential energies of flowing fluids, the energy balance is expressed by the equation:

$$H_A + H_w = H_m \tag{4}$$

where enthalpies

$$H_A = 0.79(Mh)_{N2}(T_A) + 0.21(Mh)_{O2}(T_A) + \\ +X_Z(Mh)_{H2O}(T_A) \tag{5}$$

$$H_w = n_w(Mh)_w(T_w), \ \ (Mh)_w = (Mh)_{H2O} - (Mr)_w \tag{6, 7}$$

$$H_m = 0.79(Mh)_{N2}(T_m) + 0.21(Mh)_{O2}(T_m) + \\ +(n_w + X_Z)(Mh)_{H2O}(T_A) \tag{8}$$

and $(Mh)_{N2}(T)$, $(Mh)_{O2}(T)$, $(Mh)_{H2O}(T)$ means specific enthalpies (mole basis) of nitrogen, oxygen and water vapour respectively at temperature T, $(Mh)_w$ is specific enthalpy (mole basis) of liquid water, $(Mr)_{H2O}$ is the enthalpy of vaporization of water, n_w is the mass (in kmol) of injected liquid water and T_w is the temperature of the injected liquid water. The energy balance equation is valid provided that the injected water evaporates completely, which means that the partial pressure of water vapor p_{H2O} after humidification satisfies the condition:

$$p_{H2O} = \frac{n_w+X_Z}{1+n_w+X_Z}p_A \le p_s(T_m) \tag{9}$$

Water injection reduced the temperature of the resulting mixture so while also lowers the saturation pressure of water vapor which is contained in the mixture. It is therefore possible to determine on the basis of calculations the acceptable amount of injected water so that it can evaporate completely. This value will depend on the air parameters before moisturizing and on the temperature of the water being injected.

For example, for octane (C_8H_{18}) as a fuel, the maximum value of parameter *s* has been determined, at which it is still possible to completely evaporate the injected water. Figure 3 shows the dependence of the maximum value of parameter s_{max} on the temperature T_A of air flowing into the intake manifold and on ambient air parameters: pressure p_a, temperature t_a and relative humidity φ_a.

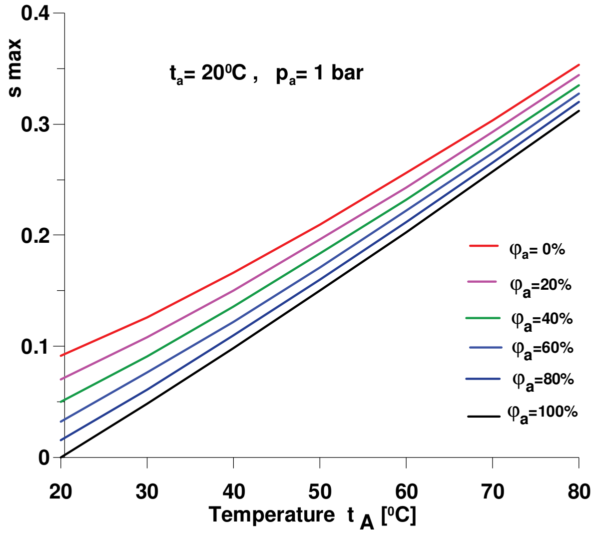

Fig. 3. The dependence of s_{max} on the temperature T_A at the inlet to the collector and the ambient air parameters t_a, p_a, φ_a.

Figure 4 shows the drop in air temperature after water injection in the amount resulting from the value of s_{max} depending on the air temperature at the intake manifold inlet T_A and ambient air parameters.

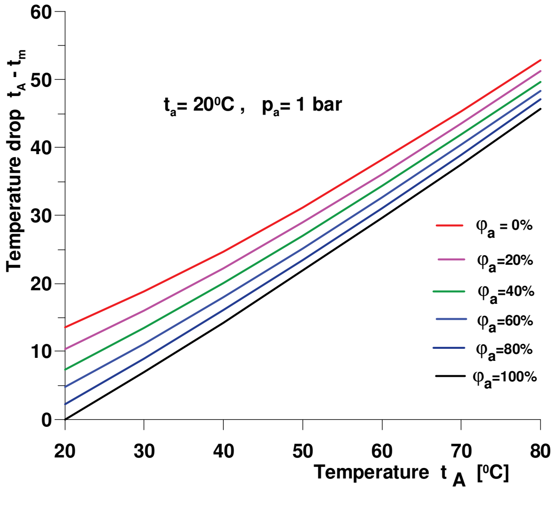

Fig. 4. Decreasing the air temperature in the intake manifold T_A-T_m after the water injection

Figures 3 and 4 show that at a lower air temperature T_A before humidification and at higher relative humidity φ_a in the environment, the amount of water that can be evaporated in the collector is reduced. The drop of the humidified air temperature is also reduced.

3. Calculation of the exhaust composition

It is assumed that the exhaust gases in the engine resulting from the combustion of fuel in the humid air have an equilibrium composition. The methodology for determining the equilibrium composition of exhaust gases was the subject of many works [6, 8].

In [8] the chemical equilibrium of fuel combustion products with the chemical formula $C_\alpha H_\beta O_\gamma N_\delta$ in wet air was analyzed assuming the presence of exhaust gas recirculation. It has been presented in detail the methodology of calculation of the equilibrium composition of the exhaust gases which included ten components: 1 – CO_2, 2 – H_2O, 3 – N_2, 4 – O_2, 5 – CO, 6 – H_2, 7 – H, 8 – O, 9 – OH, 10 – NO, depending on the equivalence ratio Φ (which is the reverse of the excess air ratio λ) and thermal parameters of temperature and pressure.

When combustion takes place in air with a known moisture content and provided denotation of components, the chemical reaction with respect to one kmole of dry air is expressed by the equation:

$$\begin{aligned}&\nu_p\Phi\, C_\alpha H_\beta O_\gamma N_\delta + 0.21\, O_2 + 0.79\, N_2 + n_w + X_Z = \\ &= \nu_1\, CO_2 + \nu_2\, H_2O + \nu_3\, N_2 + \nu_4\, O_2 + \nu_5\, CO + \nu_6\, H_2 + \\ &\quad \nu_7\, H + \nu_8\, O + \nu_9\, OH + \nu_{10}\, NO \end{aligned} \tag{10}$$

In this formula, ν_p is the number of kmol of fuel referenced to one kmol of dry air for stoichiometric combustion; $\nu_p = 0.21/(\alpha + 0{,}25\beta - 0{,}5\gamma)$; Φ is the equivalence ratio; n_w is the mass of injected liquid water (in kmol) referred to 1 kmole of dry air.

In the combustion process, mass balances for individual elements must be met, which leads to the dependencies:

- for the carbon balance: $LC = \nu_p\Phi\alpha = \nu_1 + \nu_5$,
- for the hydrogen balance: $LH = \nu_p\Phi\beta + 2n_w + 2X_Z = 2\nu_2 + 2\nu_6 + \nu_7 + \nu_9$,
- for oxygen balance: $LO = \nu_p\Phi\gamma + 0.42 + n_w + X_Z = 2\nu_1 + \nu_2 + 2\nu_4 + \nu_5 + \nu_8 + \nu_9 + \nu_{10}$,
- for the nitrogen balance: $LN = \nu_p\Phi\delta + 1.58 = 2\nu_3 + \nu_{10}$.

The equilibrium composition of the exhaust gas can be determined additionally using the data of equilibrium constants of formation of six exhaust gas components. A detailed methodology for calculating the exhaust gas composition is presented in [6, 8].

4. Thermochemical data for calculations

Knowledge of the exhaust gas composition is essential for the calculation of thermodynamic functions: internal energy, enthalpy, entropy. The change of thermal parameters of temperature and pressure during expansion stroke also causes a change in the composition of exhaust gases, which should be taken into account when mass and energy balancing of combustion processes are considered.

For computer calculations of thermodynamic functions for exhaust gases (e.g. specific heat at constant pressure Mc_p, specific enthalpy Mh), polynomial approximations of data [1, 6] are used. Thermochemical tables JANAF [5] are considered to be a very reliable source of data. The numerical values of thermodynamic functions given in them enable their polynomial approximations as a function of temperature. In general, to increase the accuracy of calculations, the approximation of the fourth order polynomial for specific heat (Mc_p) and the 5th order polynomial for specific enthalpy (Mh) was applied in two sub-ranges: 300 K–1000 K and 1000 K–5000 K.

Table 1. Coefficients of the approximation functions for specific heat at constant pressure (Mc_p) and standard state enthalpy (Mh) for gas components

Component	Range T	a1	a2	a3	a4	a5	a6
CO_2	1000–5000	4.45362300E+00	3.14016800E–03	–1.27841050E–06	2.39399600E–10	–1.66907766E–14	–4.8964031649E+04
	300–1000	2.27572400E+00	9.92207200E–03	–1.04091130E–05	6.86668600E–09	–2.11727956E–12	–4.8370220993E+04
H_2O	1000–5000	2.67214500E+00	3.05629300E–03	–8.73026000E–07	1.20099640E–10	–6.39112900E–15	–2.9896941613E+04
	300–1000	3.38684200E+00	3.47498200E–03	–6.35469600E–06	6.96858100E–09	–2.50658849E–12	–3.0205840648E+04
N_2	1000–5000	2.92664000E+00	1.48797680E–03	–5.68476000E–07	1.00970380E–10	–6.75406550E–15	–9.2296876792E+02
	300–1000	3.29867700E+00	1.40824040E–03	–3.96322200E–06	5.64151500E–09	–2.44485329E–12	–1.0210718780E+03
O_2	1000–5000	3.69757800E+00	6.13519700E–04	–1.25884200E–07	1.77528100E–11	–1.13730755E–15	–1.2338285229E+03
	300–1000	3.21293600E+00	1.12748640E–03	–5.75615000E–07	1.31387730E–09	–8.76855698E–13	–1.0051470506E+03
CO	1000–5000	3.02507800E+00	1.44268850E–03	–5.63082700E–07	1.01858130E–10	–6.91149050E–15	–1.4266701882E+04
	300–1000	3.26245100E+00	1.51194090E–03	–3.88175500E–06	5.58194400E–09	–2.47495046E–12	–1.4308890656E+04
H_2	1000–5000	2.99142300E+00	7.00064400E–04	–5.63382800E–08	–9.23157801E–12	1.57275135E–15	–8.2613824429E+02
	300–1000	3.29812400E+00	8.24944100E–04	–8.14301500E–07	9.47541505E–11	2.23969543E–13	–1.0131004781E+03
H	1000–5000	2.50000000E+00	0.00000000E+00	0.00000000E+00	0.00000000E+00	0.00000000E+00	2.5474035858E+04
	300–1000	2.50000000E+00	0.00000000E+00	0.00000000E+00	0.00000000E+00	0.00000000E+00	2.5474035858E+04
O	1000–5000	2.54205900E+00	–2.75506100E–05	–3.10280300E–09	4.55106700E–12	–4.36805100E–16	2.9227890256E+04
	300–1000	2.94642800E+00	–1.63816650E-03	2.42103100E–06	–1.60284310E–09	3.89069600E–13	2.9144731860E+04
OH	1000–5000	2.88273000E+00	1.01397430E–03	–2.27687700E–07	2.17468300E–11	–5.12630500E–16	3.8870046299E+03
	300–1000	3.63726600E+00	1.85091000E–04	–1.67616460E–06	2.38720200E–09	–8.43144200E–13	3.6068984347E+03
NO	1000–5000	3.24543500E+00	1.26913830E–03	–5.01589000E–07	9.16928300E–11	–6.27575887E–15	9.8000694105E+03
	300–1000	3.37654100E+00	1.25306340E–03	–3.30275000E–06	5.21781000E–09	–2.44626304E–12	9.8171893575E+03

$$\frac{(Mcp)}{(MR)} = a1 + a2 * T + a3 * T^2 + a4 * T^3 + a5 * T^4 \qquad \frac{(Mh)}{(MR)} = a1 * T + \frac{a2}{2} * T^2 + \frac{a3}{3} * T^3 + \frac{a4}{4} * T^4 + \frac{a5}{5} * T^5 + a6$$

(MR) = 8.3144126 kJ/kmol·K ; T [K] ; (Mc_p) [kJ/kmol·K] ; (Mh) [kJ/kmol]

Based on data [5] the calculated values of polynomial coefficients a1, a2, … , a6 have been included in the Table 1.

The calculated kilomolar enthalpy $(Mh)_i$ is the sum of the enthalpy of formation of component "i" at the reference state T_f = 298.15 K and the excess of the physical enthalpy above the reference state. So there is so-called total enthalpy. When performing energy balance calculations, internal energy is also used. Calculation of the kilomolar internal total energy (including chemical energy) of the gas mixture component $(Mu)_i$ is possible from the Gibbs equation, which can be represented for the ideal gas:

$$(Mu)_i = (Mh)_i - (MR)T \tag{11}$$

Calculations of thermodynamic quantities for a mixture of gaseous components with a known molar composition y_i and known thermal parameters: p, T enable the following relationships:

$$(Mh) = \sum_{i=1}^{N} y_i (Mh)_i \tag{12}$$

$$(Mu) = \sum_{i=1}^{N} y_i (Mu)_i = (Mh) - (MR)T \tag{13}$$

$$(Mc_p) = \sum_{i=1}^{N} y_i (Mc_p)_i \tag{14}$$

$$(Mc_v) = (Mc_p) - (MR) \tag{15}$$

molecular weight for the mixture:

$$M = \sum_{i=1}^{N} y_i M_i \tag{16}$$

gas constant for the mixture:

$$R = (MR)/M \tag{16}$$

equation of state:

$$pV = mRT = n(MR)T \tag{17}$$

5. Otto cycle simulation

In order to analyze the effect of water injection into the intake manifold on the pressure and temperature of the working medium in the SI piston engine, simulation calculations for a single cycle were carried out. The calculation does not take into account exhaust gas recirculation. The injected water will affect the composition of the gas mixture which is subjected to compression and the initial and final temperature of the charge during compression in the engine. In order to investigate the impact of water injection on the parameters of the Otto cycle, a computer program was developed.

The air temperature after humidification was determined from the energy balance for the isobaric and adiabatic mixing with the air the adopted in the calculation amount of water injected (at a given temperature). The amount of water supplied allowed its complete evaporation in the intake manifold, it did not exceed the value of s_{max} (Fig. 3).

The initial temperature of the air-fuel mixture fed to the cylinder was determined also from the energy balance for the isobaric and adiabatic mixing of humidified air with atomised liquid fuel at given temperature. Here, also, the temperature decreases due to evaporation of the fuel.

The following simplifying assumptions were made.

1. The simulation calculations concern the theoretical Otto cycle consisting of the following processes:
   1–2 adiabatic compression of a gaseous fuel-air-water vapour gas mixture of known composition,
   2–3 isochoric temperature increase resulting from fuel combustion,
   3–4 adiabatic exhaust expansion,
   4–1 isochoric exchange of charge in the cylinder, i.e. introduction of a fresh fuel mixture with moist air instead of expanded exhaust gas.
2. It is assumed that the gaseous components are semi-perfect and that the exhaust gases during the expansion are in the chemical equilibrium determined for the conditions (temperature and pressure) that are in a given point of their expansion.
3. The temperature T_1 of the mixture of fuel vapour, air and water vapor at the beginning of compression results from the previous processes of air humidification and fuel atomization. The initial pressure of the mixture is $p_1 = 1$ bar.
4. The proportion of fuel to dry air determines the equivalence ratio Φ. The numerical values of equivalence ratio assumed in the example calculations refer to the stoichiometric mixture (Φ = 1).
5. Combustion of the mixture is isochoric, runs in TDC infinitely fast.
6. Compression (1–2) and expansion (3–4) are adiabatic (the heat exchange between the gas charge and the cylinder walls is omitted).

In formulating mass and energy balances a control volume boundary is assumed, the position of which determines the surfaces of the cylinder wall, the piston crown and the surface of the combustion chamber. For compression 1–2 the mass and composition of the mixture does not change. For two, close each other (a) and (b), thermal states of compressed mixture the equation of energy balance can be written:

$$E_{\text{in a-b}} = U_b - U_a + Q_{a-b} \tag{18}$$

The supplied energy $E_{\text{in a-b}}$ is the elementary work of compression $W_{a\text{-}b}$, whereas the heat of the process $Q_{a\text{-}b} = 0$ which results from the assumption of adiabaticity of the compression. To calculate the elementary work of compression can be used the exact relationship:

$$W_{a-b} = \frac{p_a V_a}{\kappa - 1}\left[1 - \left(\frac{p_b}{p_a}\right)^{\frac{\kappa-1}{\kappa}}\right] \tag{19}$$

or approximate relation, which is correct if the elemental process (a–b) in the p–V diagram approximates a straight line:

$$W_{a-b} = (p_a + p_b)(V_b - V_a)/2 \tag{20}$$

The parameters of compressed mixture for the state "a" are known (at the beginning of compression they are equal to the parameters in point 1, and for subsequent steps of integration are equal to the resultant parameters "b" from the previous calculation step). Unknown final parameters T_b and p_b of each elemental step must satisfy the system of equations:

energy balance

$$U_b(T_b) = U_a(T_a) + W_{a-b} \tag{21}$$

equation of state

$$\frac{p_b V_b}{T_b} = \frac{p_a V_a}{T_a} \tag{22}$$

Assuming the reversibility of adiabatic compression, the final temperature for a single integration step $\Delta V = V_a - V_b$ can also be calculated from the isentropic equation:

$$T_b = T_a \left(\frac{p_b}{p_a}\right)^{\frac{\kappa-1}{\kappa}} \tag{23}$$

in which the adiabatic index κ is temperature dependent and should be calculated for known temperature T_a (variable during isentropic compression).

From the calculations results a high agreement in the pressure and temperature course for both of these methods. The first (balance) method is more general, because it allows for the exchange of heat between the wall of the working space and the charge in the cylinder for polytropic process.

Process 2–3 is an isochoric during which the fuel combustion reaction takes place. The combustion products contain gas components of unknown mole fractions y_{i3} corresponding to chemical equilibrium for thermal parameters: temperature T_3 and pressure p_3. The thermal parameters for state "3" meet the equations of energy and substance balance:

$$U_3(T_3, y_{i3}, p_3) = U_2(T_2) \tag{24}$$

$$m_3 = m_2 \Longrightarrow \frac{p_3}{R_3(T_3, y_{i3}) T_3} = \frac{p_2}{R_2 T_2} \tag{25}$$

Thermal parameters at the point "3" of the cycle (the beginning of the expansion process) were determined by solving the above system of nonlinear equations, where the input data for the calculation is: composition y_{i2}, temperature T_2 and pressure p_2 of the mixture in state "2" and assuming that process 2–3 is adiabatic and isochoric and exhaust gases in the state of "3" (with 10 components) have an equilibrium composition.

In adiabatic process 3–4 is assumed that the composition of the exhaust gases will be equilibrium, depending on equivalence ratio Φ and on the current thermal parameters T and p on the expansion line. This composition will be variable as a result of changes in temperature and pressure during expansion. For sufficiently small change in volume $\Delta V = V_b - V_a$ the energy balance equation for the elementary process a–b applies:

$$0 = U_b - U_a + W_{a-b} \tag{26}$$

where: $U_b(T_b, p_b, y_{ib})$ – is the total internal energy of the exhaust (physical and chemical), whereas

$$W_{a-b} = \frac{p_a V_a}{\kappa - 1}\left[1 - \left(\frac{p_b}{p_a}\right)^{\frac{\kappa-1}{\kappa}}\right] \approx (p_a + p_b)(V_b - V_a)/2 \tag{27}$$

is the elementary work of this process, and the equation expressing together the mass balance and the equation of state:

$$m_b = m_a \Longrightarrow \frac{p_b V_b}{R(T_b, y_{ib}) T_b} = \frac{p_a V_a}{R(T_a, y_{ia}) T_a} \qquad (28)$$

The above set of balance equations is nonlinear, with unknown T_b and p_b. This system for each calculation step corresponding to the volume increase ΔV of the system was solved iteratively.

In case the expansion 3–4 passes with heat exchange to the walls of the engine working space, the heat $Q_{a\text{-}b}$ determined on each elementary calculation step should be involved into the energy balance equation. The elementary work $W_{a\text{-}b}$ can then be calculated based on the simplified relationship. Such an extension of the model will not cause changes in the methodology of further calculations.

The model of the Otto cycle described above was used to perform simulation calculations for the following data.

1. The volume at the node points of the cycle is: $V_1 = V_4 = 445\ cm^3$; $V_2 = V_3 = 45\ cm^3$.
2. The environment air parameters are: temperature $t_a = 20^oC$, pressure $p_a = 1$ bar, relative humidity $\varphi_a = 0$.
3. Value of pressure $p_1 = 1$ bar.
4. Motor fuel is octane C_8H_{18}. Thermodynamic properties of the fuel [1, 6, 7] for referenced temperature $T_f = 298.15$ K are:

- Lower calorific value – LCV = 5073 MJ/kmol,
- Enthalpy of fuel condensation $(Mr)_{FUEL} = 35.34$ MJ/kmol,
- Standard enthalpy of gaseous fuel formation $(Mh)_{FUEL} = -216.27$ MJ/kmol,
- Specific heat at constant pressure for gaseous fuel $c_p = 0.005\ T + 6.75 \cdot 10^{-3}\ T - 3.67 \cdot 10^{-6}\ T^2 + 7.75 \cdot 10^{-10}\ T^3$ kJ/kg K,
- Specific heat at constant pressure for liquid fuel $c_p = 2.23$ kJ/kg K,

5. Combustion of fuel is stoichiometric ($\Phi = 1$),
6. Compression 1–2 and expansion 3–4 are adiabatic,
7. In the expansion stroke 3–4, the composition of the exhaust gases is equilibrium, determined for the current thermal parameters: temperature and pressure.

The calculation results for the above assumptions and the assumed ratio s of the mass of water injected into the intake manifold to the mass of fuel are summarized in Table 2 below. For three variants of calculation differing in the assumed parameter: s = 0 (no water injected); s = 0.1, s = 0.2 the table contains parameters: temperature of air after water injection t_m, temperature fuel-humid air mixture after fuel injection t_1, temperature and pressure in the points of the Otto cycle. The table also includes the results of calculations of compression work W_k, expansion work W_{exp} and the theoretical efficiency of the cycleη_t,

$$\eta_t = \frac{W_{exp} - |W_k|}{n_{FUEL}\ LCV} \qquad (29)$$

where n_{FUEL} is a number of kmol of fuel for one cycle, LCV is lower calorific value of the fuel.

The graphs below present the results obtained from simulation calculations for stoichiometric combustion of octane in dry air and humidified air at parameter s = 0.2.

Table 2. Parameters in the points of Otto cycle and fuel conversion efficiency for different water to fuel ratio s

Parameter	Unit	s = 0	s = 0.1	s = 0.2
Temperature t_m	^oC	70	54.7	39.8
Temperature t_1	^oC	47.8	34.3	21.0
Temperature T_1	K	320.9	307.4	294.2
Pressure p_1	bar	1	1	1
Temperature T_2	K	675.0	650.5	626.2
Pressure p_2	bar	20.8	20.9	21.1
Temperature T_3	K	2899.7	2878.8	2857.4
Pressure p_3	bar	96.2	99.7	103.3
Temperature T_4	K	1837.7	1804.3	1765.8
Pressure p_4	bar	6.06	6.22	6.37
Compression work	J	–153.1	–153.6	–154.1
Expansion work	J	800.4	827.0	853.9
Theoretical efficiency η_t	%	46.31	46.67	46.85

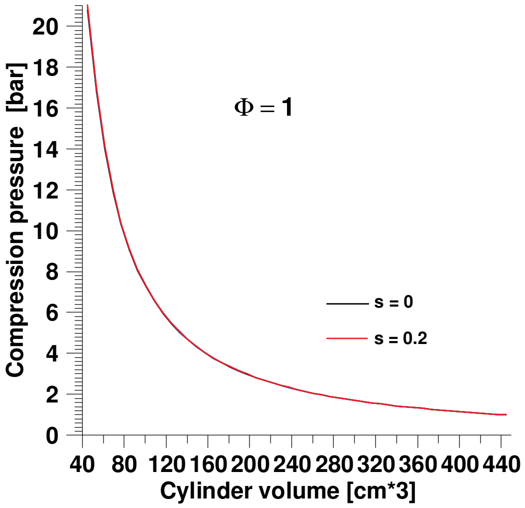

Fig. 5. Pressure-volume diagram for compression for different parameter s

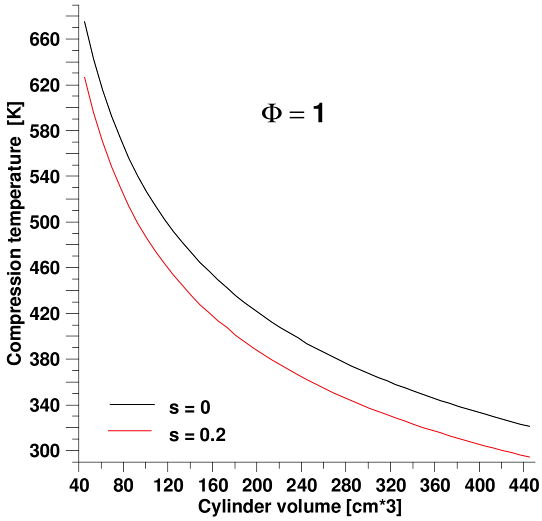

Fig. 6. Temperature-volume diagram for compression for different parameter s

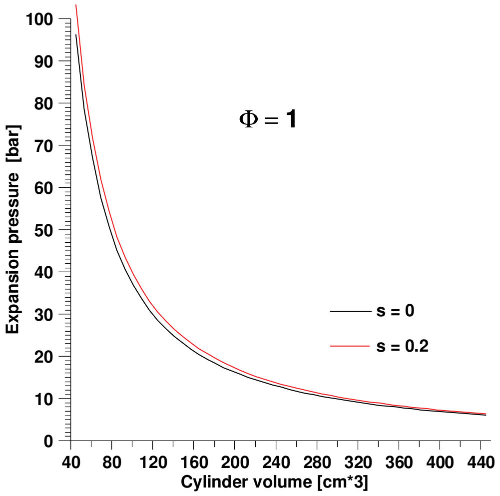

Fig. 7. Pressure-volume diagram for expansion for different parameter s

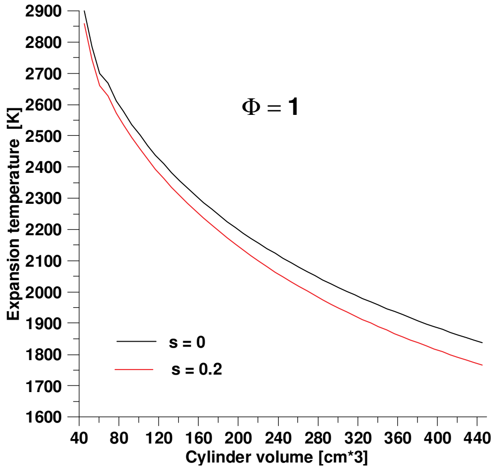

Fig. 8. Temperature-volume diagram for expansion for different parameter s

The next graphs illustrate the variability of the composition of the exhaust gas for the expansion for the cycle without water injection (Fig. 9) and with the water injection at s = 0.2 (Fig. 10). Additionally Fig. 11 illustrates the composition of exhaust gases upon combustion with excess air (Φ = 0.9) and with water injection at s = 0.2.

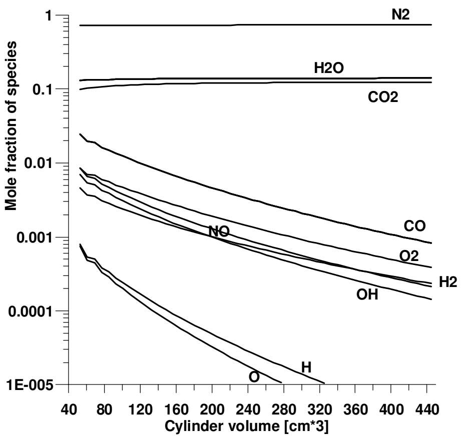

Fig. 9. Equilibrium gas composition for expansion stroke (fuel octane, Φ = 1, no water injection s = 0)

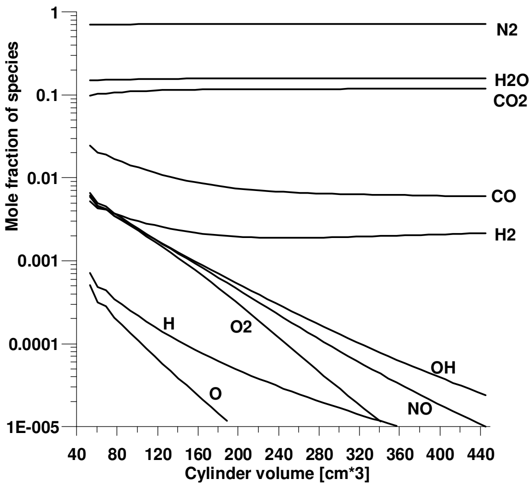

Fig. 10. Equilibrium gas composition for expansion stroke (fuel octane, Φ = 1, with water injection s = 0.2)

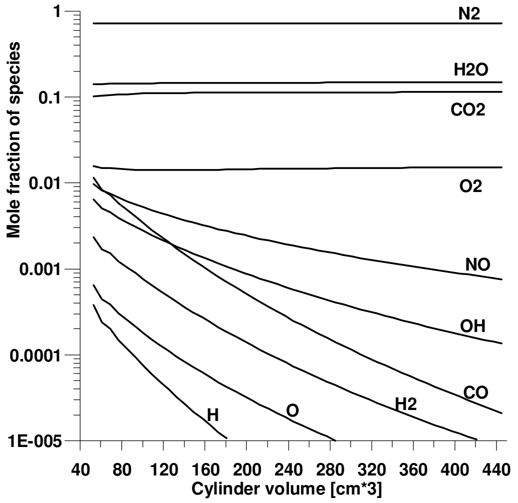

Fig. 11. Equilibrium gas composition for expansion stroke (fuel octane, Φ = 0.9, with water injection s = 0.2)

6. Conclusion

1. Water to fuel ratio s is fundamental parameter of water injection systems. In PWI systems, the amount of water injected must be selected so exactly that it can be evaporated in the intake manifold. Otherwise, drops of liquid water can damage the oil film on the cylinder liner causing the risk of engine seizure.
2. The amount of liquid water which can be actually vaporised is yet limited by the equilibrium state between liquid water and steam. For this reason, the amount of sprayed water in the intake manifold depends on the ambient air parameters and on the air parameters before moisturizing.
3. Evaporation of water in the intake manifold reduces the temperature of the humidified air. When the ambient humidity increases the attainable temperature drop decreases because of the decreasing amount of injected water required.
4. Lowering the temperature of the fuel-wet air mixture obtained by water injection reduces the initial T_1 and the final compression temperature T_2.

5. The load pressure p_2 at the end of compression is slightly dependent on the amount of water injected. The consequence of this fact are the similar numerical values of work calculated for the compression process for the analyzed cases.
6. During fuel combustion (process 2–3) the temperature T_3 decreases with the increase of the amount of water injected. The probability of knock phenomena is thus reduced, higher compression ratios can then be reached.
7. The pressure in the expansion process is higher (Fig. 7) for higher values of the parameter s. Consequently, the mechanical work generated by the expansion stroke as well as the thermal efficiency of the Otto cycle is preferably higher.
8. A comparison of the results shown in Fig. 9 (for s = 0) and in Fig. 10 (for s = 0.2) leads to the conclusion that the water injection significantly reduces the O_2, NO, OH concentrations in the exhaust gas at the end of the expansion, whereas it causes an increase in the concentration of CO and H_2. In the case of combustion with excess air ($\Phi = 0.9$) and s = 0.2 in the final exhaust composition, the H_2 and CO concentrations are greatly reduced while the NO concentration increases. (Fig. 11).

Nomenclature

c_p	specific heat at constant pressure	$kJ\ kg^{-1}\ K^{-1}$
H	enthalpy	kJ
LCV	lower calorific value	$kJ\ kmol^{-1}$
m	mass	kg
M	molal mass	$kg\ kmol^{-1}$
$(Mh)_i$	specific enthalpy of component i	$kJ\ kmol^{-1}$
(Mc_p)	specific heat at constant pressure	$kJ\ kmol^{-1}\ K^{-1}$
(Mr)	specific enthalpy of vaporisation	$kJ\ kmol^{-1}$
(MR)	universal gas constant	$kJ\ kmol^{-1}\ K^{-1}$
n	amount of matter	kmol
p_s	saturation pressure	bar
p	pressure	bar

R	gas constant	$kJ\ kg^{-1}\ K^{-1}$
s	water to fuel ratio	$kg\ kg^{-1}$
t	temperature	^{o}C
T	temperature	K
U	internal energy	kJ
W	work	kJ
φ	relative humidity of air	
Φ	equivalence ratio	
κ	adiabatic index	
η	thermal efficiency	
ν	stoichiometric coefficient	

Bibliography

[1] ANNAMALAI, K., PURI, I. Advanced thermodynamics engineering. *CRC Press*. 2002.

[2] BORETTI, A. Water injection in directly injected turbocharged spark ignition engines. *Applied Thermal Engineering*. 2013, **52**, 62-68. DOI: 10.1016/j.applthermaleng.2012.11.016.

[3] CHEN, B., ZHANG, L., CHEN, X., ZHANG, Q. Thermodynamics and numerical analysis of intake air humidification of a turbocharged GDI engine. *Sadhana-Academy Proceedings in Engineering Science*. 2018, **43**(5), art. no. 79. DOI:10.1007/s12046-018-0871-5.

[4] FALFARI, S., BIANCHI, G., CAZZOLI, G. et al. Basic on water injection process for gasoline engines. *73rd Conference of Italian Thermal Machines Engineering Association. ATI2018. Energy Procedia.* 2018, **148**, 50-57. DOI:10.1016/j.egypro.2018.08.018.

[5] JANAF Thermochemical Tables, NSRDS_NB, US Bureau of Standards, IV ed. 1998.

[6] RYCHTER, T., TEODORCZYK, A. Teoria silników tłokowych. *WKŁ*. Warszawa 2006 (in polish).

[7] SONNTAG, R., BORGNAKKE, C., VAN WYLEN, G. Fundamentals of thermodynamics. *John Wiley&Sons*. 2003.

[8] SUCHETA, A. Obliczanie składu równowagowego spalin, *Silniki Spalinowe*. PTNSS, 2007-SC2 (in polish).

Sucheta Andrzej DSc., DEng.– Faculty of Mechanical Engineering and Computer Science, University of Bielsko-Biala.

e-mail: *asucheta@ath.bielsko.pl*

Article citation info:
SLAVINSKAS, S., LABECKAS, G., MICKEVIČIUS, T. Effect of biodiesel on the development of split injection characteristics.
Combustion Engines. 2019, **177**(2), 103-107. DOI: 10.19206/CE-2019-218

Stasys SLAVINSKAS
Gvidonas LABECKAS
Tomas MICKEVIČIUS

CE-2019-218

Effect of biodiesel on the development of split injection characteristics

The paper presents the experimental test results of a common rail injection system operating with biodiesel and the diesel fuel. The three fuel split injection strategies were implemented to investigate the effects made by biodiesel and a fossil diesel fuel on the history of injector inlet pressure and the injection rate. In addition, the three intervals between split injections and the different injection pressures were used to obtain more information about the studied subjects. The obtained results showed that the peak mass injection rates of the main injection phase were slightly higher when using biodiesel than the respective values measured with the normal diesel fuel. Because the first injection phase activated the fuel pressure fluctuations along the high-pressure line and in front of the injector, the time-span between injections has an impact on the injector inlet pressure and thus the fuel injection rate during the second injection phase. Since the nozzle closes little later for biodiesel, the injector inlet pressure also occurred latter in the cycle.

Key words: *split injection, injection rate, common rail injection system, diesel fuel, biodiesel fuel*

1. Introduction

Fuel split injection characteristics play a significant role in the fuel spray development [1, 2], the fuel-air mixture stratification [3], as well as the ignition delay and the subsequent combustion process [4, 5] characteristics of the diesel engine.

Han et al. [6] experimentally investigated the split injection process of fatty acid esters on a common rail injection system. The test results show that the fuel properties caused modest changes in the pressure fluctuation after the end of injection as well in the injection mass. The injection dwell time was also found to influence the injector inlet pressure characteristics at the start of the main injection event and thus the amount of fuel injected during main injection was slightly changed.

Han et al [7] also carried out numerical study on fuel physical properties made effects on the split injection processes of a common rail injection system. In that study a one-dimensional model based on AVL HYDSIM was established to identify the effect of fuel density, viscosity and bulk modulus of compressibility on split injection characteristics. Researchers found that fuel physical properties effects were modest at the pilot injection stage, but more noticeable at the main injection stage.

Park et al. [8] experimentally and theoretically investigated the spray and atomization characteristics of biodiesel fuel. It was found that the peak injection rate increased and advanced, when the injection pressure increased due to initial injection momentum. The injection rate of the soybean oil methyl ester, which has a higher density than diesel fuel, is higher than that of diesel fuel despite its low injection velocity.

Boudy and Seers [9] investigated the impact of physical properties of biodiesel on the injection process in a common rail direct injection system using a single and triple injection strategies. The results showed that fuel density is the main property that affects the injection process, such as total mass injected and pressure wave in the common rail system. While the fuel's viscosity and bulk modulus influenced the injection parameters to a lesser degree of extension.

Wang et al. [10] conducted fuel injection and combustion study by the combination of mass flow rate and heat release rate with single and multiple injection strategies. The test results showed that the fuel injection duration is obviously longer than the injection energizing duration. Split injection strategy revealed complicated interaction among splits with the first injection duration and dwell interval dominating the interaction degree. It was also noted that the interaction also considerably depends on the number of splits.

Despite of considerable number of experimental and numerical studies on the subject, in the technical literature still is a lack of knowledge related with the effects of the intervals between the splits and this is especially important in case of using biodiesel. The purpose of the research was to obtain a deeper knowledge about the impact of the widely differing properties of biodiesel on the main injection parameters such as the fuel injection rate and the injector inlet pressure for the three split injection strategies under various biodiesel and the diesel fuel injection pressures.

2. Materials and method

The fuel injection rates were measured and analysed using an injection rate measuring system based on Bosch method [11].

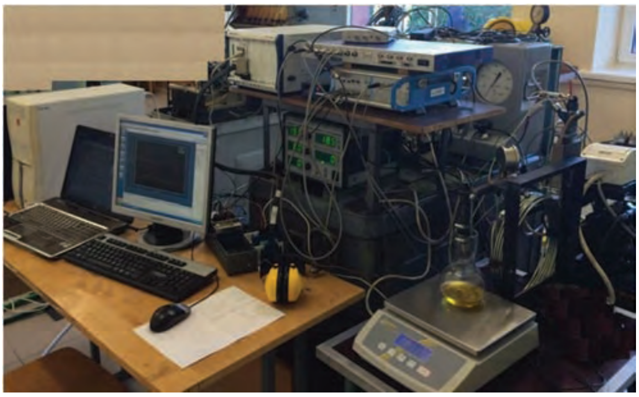

Fig. 1. Test stand used in the experiments

The experimental setup consists of two parts: the fuel injection system and injection rate measuring system (Fig. 1). The fuel injection system includes an electrically driven high-pressure pump, a rail and an injector. The injector nozzle has 6 holes and the diameter of each hole is 0.24 mm. The NI PXIe 1062Q system with DI Driven D000020 module was used to control the injection process.

The injection rate measuring system consists of the injector mount on which the injector and the pressure sensor are mounted, the measuring and following tube, the orifice plate separating them and the check valve. The injection rate measuring method is based on measuring a dynamic increase in pressure produced by the fuel injection into measuring tube filled with fuel. The shape of the fuel pressure increase correspondents to the injection rate.

The pressure variation in the tube was measured with a piezoelectric pressure sensor type 6052C (Kistler) coupled to the Kistler charge amplifier-module 5064 with an accuracy of ±0.5% in the pressure range of 0–25.0 MPa. The fuel pressure at the injector inlet was measured with a piezoresistive high-pressure Kistler Inc. sensor 4067A2000 and amplified by an amplifier-module 4665. Both amplifier-modules were mounted on the signals conditioning platform-compact 2854A. The injector energizing pulses, fuel injection rate, fuel pressure and back pressure signals were continuously recorded by using an AVL IndiModul 622 data acquisition system.

Table 1. Properties of the tested fuels

Fuel	Density at 30°C [kg/m^3]	Kinematic viscosity at 40°C [mm^2/s]
Diesel fuel	832.7	2.13
RME	883.6	4.44

The fuel studied was rapeseed methyl ester, the split injection characteristics of which were compared with the respective values of a fossil diesel fuel (DF). The main physical properties of the tested fuels are listed in Table 1. Four injection pressures (rail pressures) of 45, 85, 110 and 135 MPa were used for the experimental tests. The back pressure in the tube was adjusted to 4.0 MPa.

The fuel pressure traces over the 100 consecutive injection cycles were recorded and averaged for the analysis. The quantity of the fuel injected (by mass) was determined as a mean value of the 1000 consecutive injection cycles, measured by a precision scale.

Table 2. Test matrix for split injection

Injection duration [ms]	0.15–1.0	0.5–0.5	1.0–0.15
Injection interval [ms]	0.8; 1.0; 1.2	0.8; 1.0; 1.2	2.0; 2.15; 2.3

The three groups of the experimental tests with the different injection durations and injection intervals were carried out to reveal the interaction between the splits. The test matrix is shown in Table 2.

3. Results and discussion

Modern diesel engines are equipped with a common rail fuel injection system that can be adapted to implement split injection strategy. In this case, the pressure oscillations in the high-pressure line caused by the first injection affected the subsequent injection process.

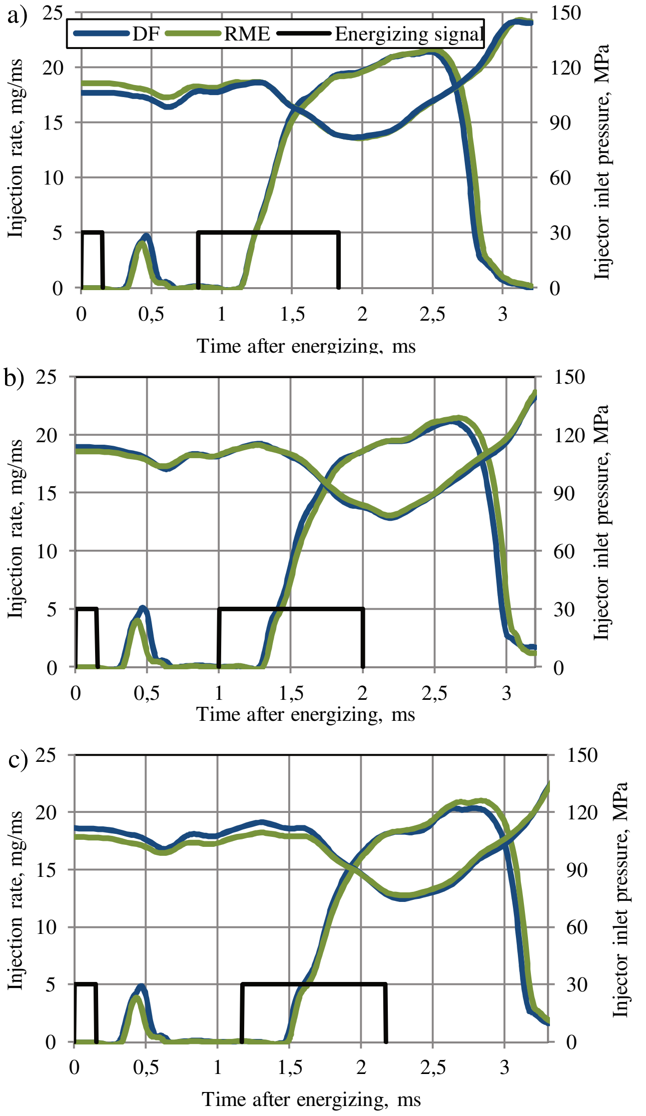

Fig. 2. Effects of pilot injection energizing pulse and split injection interval on the injector inlet pressure fluctuation and the injection rate of the fuels at the injection intervals: a – 0.8 ms, b – 1.0 ms, c – 1.2 ms

Figure 2 shows variations in the fuel mass injection rate and the injector inlet pressure in a time scale during the split injection process, with the duration of 0.15 ms and 1.0 ms and a variable interval between injections.

As can be seen in Fig. 2, the short pilot injection pulse causes low-magnitude inlet pressure fluctuation that quickly damps without causing observable influences on the main injection. Higher density of biodiesel fuel causes the reduction of the peak mass injection rate in the pilot stage. While, on the contrary, the peak mass injection rates of the main injection stage were slightly higher when using RME than the respective values measured with the diesel fuel. As can be seen at the end of the main injection, the end of injection takes place slightly earlier in the cycle with diesel fuel. This occurs mainly due to lower viscosity of the diesel fuel. Since the viscosity of biodiesel is higher more time is needed to close the injector due to the viscous forces slowing down the needle movement. While changes in the injection intervals did not have a noticeable effect on the injection characteristics.

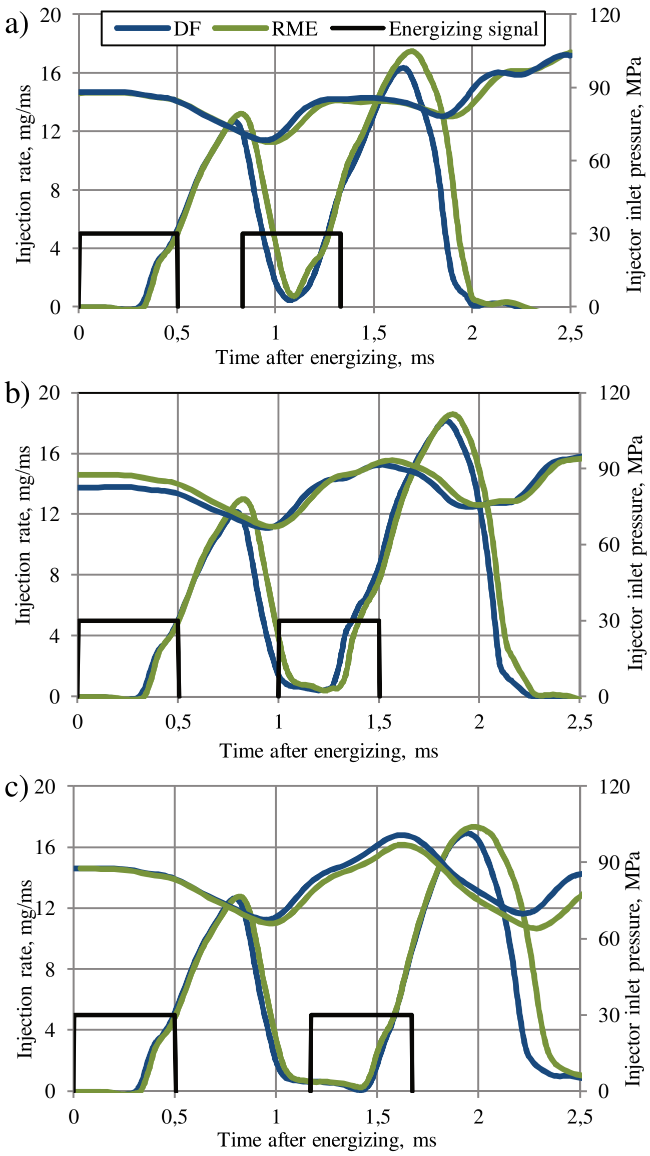

Fig. 3. Effects of fuel types on injector inlet pressure and the injection rate under split injection at the intervals: a – 0.8 ms, b – 1.0 ms, c – 1.2 ms

Figure 3 presents variations in the fuel mass injection rate and the injector inlet pressure during the two-stage injection process for biodiesel and a fossil diesel fuel. The injector energizing duration was equal to 0.5 ms for each injection event, while the injection intervals were changed for 0.6 (a), 1.0 (b) and 1.2 ms (c) as can be seen in figure.

As the injection process starts, significant oscillations are observed in the inlet pressure. The first injection causes temporary pressure drops and then subsequently pressure rise caused by the water-hammer effect when the needle moves back into closed position. With an increase in the interval between injections, the fluctuations amplitude of the injector inlet pressure increased correspondingly. At the tested injection intervals of 0.8, 1.0 and 1.2 ms the respective injector inlet pressure fluctuations amplitudes were equal to 16, 26 and 31 MPa. Since after the first injection, the nozzle closes little later for RME than for diesel fuel, the pressure increase is also delayed.

As can be seen in Figure 3, the pressure fluctuations affect the injection rate of the second injection. Due to fuel pressure fluctuations in the high-pressure line evoked by the first injection, the second injection proceeds under the increasing inlet pressure at the injector. For this reason, the fuel injection rate during the second stage of the process was higher than that measured in the first stage of injection. Maximum injection rate is affected by the duration of injection interval between the pulses. Therefore, the maximum injection rate was approximately 32.8% higher during the second injection than that determined in the first injection stage for both types of the fuels tested with the injection interval of 0.8 ms between splits.

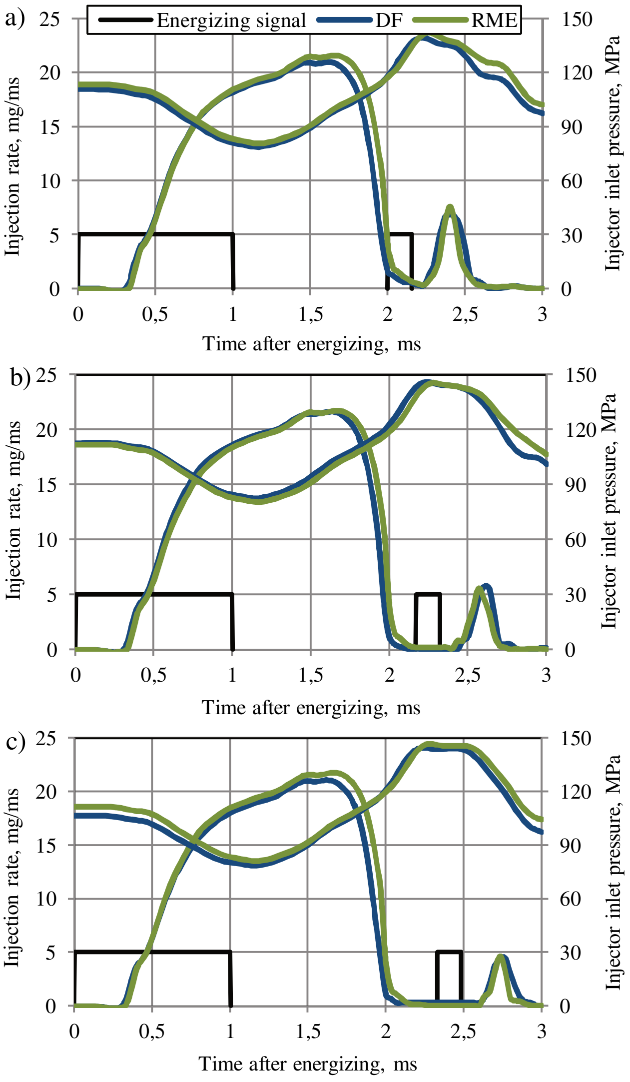

Fig. 4. Effects of fuel types on injector inlet pressure and the injection rate under split injection at the intervals: a – 2.0 ms, b – 2.15 ms, c – 2.3 ms

After the injection interval was increased from 0.8 to 1.0 ms (Fig. 3b), maximum fuel injection rate during the second injection increased by 43.3% for biodiesel and 49.9% for the normal diesel fuel. While further increase of the injection interval between splits to value of 1.2 ms (Fig. 3c), maximum injection rate over the second stage increased with a lower intensity – by 36.3% and 33.6% for biodiesel and the mineral diesel fuel, respectively. This occurrence can be associated with the fact that the biggest part of the second injection coincided with the reduction phase of fuel pressure caused by fluctuation of fuel pressure waves in the high-pressure line activated by the first fuel injection phase.

After the injection interval was increased from 0.8 to 1.0 ms (Fig. 3b), maximum fuel injection rate during the second injection increased by 43.3% for biodiesel and 49.9% for the normal diesel fuel. While further increase of the injection interval between splits to value of 1.2 ms (Fig. 3c), maximum injection rate over the second stage increased with a lower intensity – by 36.3% and 33.6% for biodiesel and the mineral diesel fuel, respectively. This occurrence can be associated with the fact that the biggest part of the second injection coincided with the reduction phase of fuel pressure caused by fluctuation of fuel pressure waves in the high-pressure line activated by the first fuel injection phase.

Figure 4 presents the history of fuel mass injection rate and the injector inlet pressure during the main injection and post injection events for biodiesel and a fossil diesel fuel for the various injection intervals of 2.0, 2.15 and 2.3 ms. As can be seen in figure, the fuel pressure fluctuations in the high-pressure line have noticeable influence on the shape of a very small time-span characteristic following after the main injection process. The post-injection started just after the fuel pressure at the injector reached the maximum value of about 140 MPa, therefore the fuel-mass injection rate was of the biggest values for both injections of biodiesel and the mineral diesel fuel at the injection interval between pulses of 2.0 ms (Fig. 4a).

As the interval between the injections increased, the maximum injection rate of the second injection gradually decreased because during this phase of process the fuel pressure in the high-pressure line progressively decreased with regard to its maximum value. For this reason, during the second injection the maximum value of injection rate decreased by 26.7% for biodiesel and 18.8% for the diesel fuel at the 2.15 ms interval between injections (Fig. 4b). The interval between injections increased to 2.3 ms, the maximum injection rate additionally reduced by 19% for both fuel types. Hence, the maximum injection rate developed during the second injection phase depends on the injector inlet pressure fluctuation phase at that instance when the process occurs, i.e. whether the fuel line-pressure increases or decreases at the considered moment.

Figure 5 presents the dependencies of fuel mass injected during two-stage injection process for the three fuel injection intervals between splits and the three initial injection pressures. As expected, for both biodiesel and mineral diesel fuels the cycle injection quantities increased with increasing injection pressure. In case with a small pilot injection (Fig. 5a), cycle injection quantity was not noticeably affected by the time interval between pilot and main injection events because the fuel fluctuations after the first injection were negligible.

In case of the fuel split-injection with the two 0.5 ms injector energizing pulses, the effect of the injection interval on the mass cycle injection quantity was significand as can be seen in Fig. 5b. As show Fig. 3 and Fig. 5, the cycle injected fuel quantity correlate well with the pressure fluctuations at the injector inlet. At an initial injection pressure of 85 MPa, the increase in the injection interval from 0.8 to 1 ms resulted in the amplitude of pressure fluctuations 17.7% higher. While, at the same time, the cycle injection mass of mineral diesel and biodiesel increased by 19% and 8.5% respectively. As the injection interval increased up to 1.2 ms, the amount of fuel-mass injected decreased as did the pressure fluctuations amplitude.

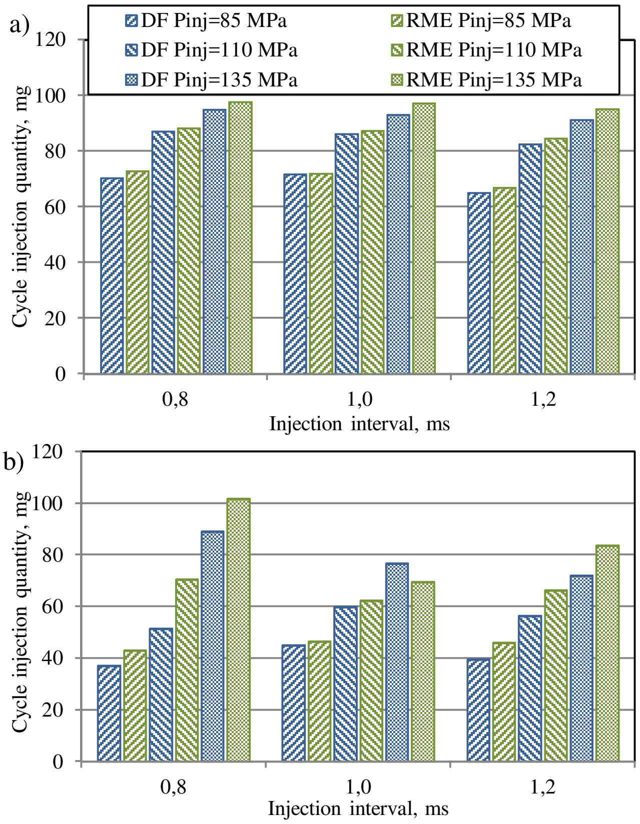

Fig. 5. The effect of injection interval on cycle injection quantity for various injection pressures: a – injector energizing pulses of 0.15–1.0 ms; b – injector energizing pulses 0.5–0.5 ms

4. Conclusions

The three fuel split injection strategies were implemented to investigate the effects made by biodiesel and a fossil diesel fuel on the history of injector inlet pressure and the injection rate. At the same time, the intervals between split injections and the injection pressures were changes to obtain more information about the studied subjects.

The short pilot injection pulse caused low-magnitude inlet pressure fluctuations those quickly have been damped without causing any observable effect on the main injection process. The peak mass injection rates of the main injection phase were slightly higher when using biodiesel than the respective values measured with the normal diesel fuel

Because the first injection phase activated the fuel pressure fluctuations along the high-pressure line and in front of the injector, the time-span between injections has an impact on the injector inlet pressure and thus the fuel injection rate during the second injection phase. Since the nozzle closes little later for biodiesel, the injector inlet pressure also occurred latter in the cycle.

Acknowledgements

The authors are Thankful to the Company AVL-AST, Graz, Austria, which according the University's Partnership Program, has granted to Power and Transport Machinery Engineering Institute of Vytautas Magnus University the AVL-BOOST program that enhanced the reliability and accuracy of the data obtained.

Nomenclature

RME	rapeseed methyl ester
DF	diesel fuel

Bibliography

[1] LEE, C.S., LEE, K.H., REITZ, R.D., PARK, S.W. Effect of split injection on the macroscopic development and atomization characteristics of a diesel spray injected through a common-rail system. *Atomization Spray*. 2006, **16**(5), 543-562.

[2] WANG, Z.M., XU, H.M., JIANG, C.Z., WYSZYNSKI, M.L. Experimental study on microscopic and macroscopic characteristics of diesel spray with split injection. *Fuel*. 2016, **174**, 140-152.

[3] MA, S.Y., ZHENG, Z.Q., LIU, H.F. et al. Experimental investigation of the effects of diesel injection strategy on gasoline/diesel dual-fuel combustion. *Applied Energy*. 2013, **109**, 202-212.

[4] LIM, J., LEE, S., MIN, K. Combustion modeling of split injection in HSDI diesel engines. *Combustion Science and Technology*. 2011, **183**(2), 180-201.

[5] SARANGI, A.K., GARNER, C.P., MCTAGGART-COWAN, G.P. et al. The effects of split injections on high exhaust gas recirculation low temperature diesel engine combustion. *International Journal of Engine Research*. 2013, **14**(1), 68-79.

[6] HAN, D., DUAN, Y.Z., WANG, C.H. et al. Experimental study of the two-stage injection process of fatty acid esters on a common rail injection system. *Fuel*. 2016, **163**, 214-222.

[7] HAN, D., LI, K., DUAN, Y. et al. Numerical study on fuel physical effects on the split injection processes on a common rail injection system. *Energy Conversion and Management*. 2017, **134**, 47-58.

[8] PARK, S.H., KIM, H.J., SUH, H.K., LEE, CH.S. A study on the fuel injection and atomization characteristics of soybean oil methyl ester (SME). *International Journal of Heat and Fluid Flow*. 2009, **30**(1), 108-116.

[9] BOUDY, F., SEERS, P. Impact of physical properties of biodiesel on the injection process in a common-rail direct injection system. *Energy Conversion and Management*. 2009, **50**, 2905-2912.

[10] WANG, Z., WYSZYNSKI, M.L., XU, H. et al. Fuel injection and combustion study by the combination of mass flow rate and heat release rate with single and multiple injection strategies. *Fuel Processing Technology*. 2015, **132**, 118-132.

[11] BOSCH, W. The fuel rate indicator: a new instrument for display of the characteristic of individual injection. *SAE Technical Paper* 660749, 1966.

Prof. Stasys Slavinskas, DSc. – Institute of Power and Transport Machinery Engineering, Faculty of Agricultural Engineering, Vytautas Magnus University.
e-mail: *stasys.slavinskas@vdu.lt*

Prof. Gvidonas Labeckas, DSc. – Institute of Power and Transport Machinery Engineering, Faculty of Agricultural Engineering, Vytautas Magnus University.
e-mail: *gvidonas.labeckas@vdu.lt*

Tomas Mickevičius, DSc. – Institute of Power and Transport Machinery Engineering, Faculty of Agricultural Engineering, Vytautas Magnus Univer-sity.
e-mail: *tomas.mickevicius@vdu.lt*

Article citation info:
PUZDROWSKA, P. Identification of damages in the inlet air duct of a diesel engine based on exhaust gas temperature measurements. *Combustion Engines*. 2019, **177**(2), 108-114. DOI: 10.19206/CE-2019-219

Patrycja PUZDROWSKA

CE-2019-219

Identification of damages in the inlet air duct of a diesel engine based on exhaust gas temperature measurements

The temperature of the exhaust gas of a diesel piston engine, measured in the characteristic control sections of its thermo-flow system, can be a valuable source of diagnostic information about the technical condition of the elements limiting the working spaces thus separated, including the turbocharging system, but also its fuel supply system and replacement of the medium. In standard marine engine measurement systems equipped with an impulse turbocharging system, the exhaust gas temperature is measured at the outlet of individual cylinders and before and after the turbocharger turbine, using traditional thermocouples with high measurement inertia (time constant of tenths of a second and more). This means that for further diagnostic analyses, the average value of the periodically changing temperature of the exhaust stream leaving individual engine cylinders, the exhaust stream in the collective duct feeding the turbine and the exhaust stream in the exhaust duct of the turbine is used.

This article proposes a new approach to the issue of diagnostic informationiveness of the exhaust gas temperature of a diesel engine, extending its observations with the dynamics of changes in the duration of one working cycle. The aim of the tests carried out on the laboratory stand of Farymann Diesel engine type D10 was to determine the diagnostic relations between the loss of permeability of the inlet air channel filter baffle and selected standards of the quick-changing signal of the exhaust gas temperature. On the basis of the calculations carried out, the following dynamic features of the recorded signal were determined: maximum amplitude of instantaneous exhaust gas temperature values (peak-to-peak value), its rate of increase and decrease, and the specific enthalpy of exhaust gases within one engine work cycle.

Comparative analysis of numerical data characterizing the recorded quick-changing exhaust gas temperature courses clearly indicates obvious thermodynamic and energy consequences of partial loss of flow capacity of the air channel supplying the combustion chamber of the test engine.

A further development of the experimental test programme is foreseen in order to determine a diagnostic matrix to support the diagnostic inference about the technical condition of the diesel engine on the basis of measurements and analysis of the quick-changing exhaust gas temperature.

Key words: *diesel engine, intake air channel, diagnostics tests*

1. Introduction

Quick-changeable engine exhaust gas temperature allows the users to obtain diagnostic information on the technical condition of structural elements limiting the cylinder's working spaces, as well as inlet air and exhaust gas ducts [1, 2, 12]. In order to develop a diagnosis method based on this parameter, it is necessary to reconcile such requirements as: high accuracy of measurements, their cost-effectiveness and technological efficiency. It is also important to minimize the influence of external factors on the accuracy of measurements. Therefore, it seems appropriate to use the method of measuring quick changeable temperatures with water-cooled thermocouple [5, 6, 19][1].

2. Conditions for laboratory testing

Empirical tests were carried out on the laboratory test bed of a single-cylinder four-stroke diesel engine Farymann Diesel type D10 (Fig. 2). The research was aimed at recording in the selected control sections of the exhaust gas duct[2] the temperatures of quick-changing exhaust gases. Then, on their basis, diagnostic parameters were determined for two states: the reference one and the simulated loss of permeability of the inlet air channel filter baffle.

During the tests, the following control parameters and indicators of engine operation were recorded (described in Table 1):

- temperature of exhaust gases, by means of thermocouple type K cooled additionally with water jacket,
- exhaust gas pressure in the outlet duct,
- exhaust gas pressure in the combustion chamber,
- a signal of the upper dead position of the piston,
- load current of the generator (armature),
- voltage at the terminals of the generator armature,
- exhaust outlet valve opening signal.

A multifunctional measurement and recording module type DT-9805 from Data Translation was used to record quick-changing exhaust gas temperatures and pressures as well as the piston dead position signal,

Fig. 1. A view of the inlet air duct supplying the engine: 1 – supply air control valve (degree of shutdown of the valve as during the laboratory

---

[1] If the thermocouple is not cooled, the recorded signal is disturbed, which results from the heating of the thermocouple from the surrounding gas, which is discussed in the publication [15].

[2] Variable: the temperature and pressure of the exhaust gas was recorded in the straight exhaust gas duct, at the same distance from the cylinder outlet valve, so that the signals were comparable and to prevent interference and reflection of pressure waves in the duct due to changes in the pipeline shape.

while Matlab and Microsoft Excel software was used to record and mathematically process the recorded values of quick-changing exhaust gas temperatures. During the test, a constant crankshaft speed of the 1445 min^{-1} engine and a constant engine load were maintained. The sampling frequency was 7000 Hz.

The test was carried out for two different technical states of the intake air channel: defined as state 1 (reference) and state 2, which caused changes in the active cross-sectional area of the air flow through the valve mounted between the cylinder valve and the filter – Fig. 1. In this way, a reduction in the permeability of the filter baffle as a result of its contamination was simulated, which is quite often the state of inoperability of every internal combustion engine [3, 13].

The presented test results are the average of 90 consecutive measurements recorded under the same engine operating conditions, determined by the engine load, crankshaft rotational speed and environmental parameters. During the tests, distillation fuel ORLEN ECODIESEL was burnt in the engine.

In order to undergo mathematical treatment and statistical analysis of the obtained results of diagnostic tests of the engine, it is necessary to decide to compare the same data groups. The most reliable and comparable "portion" of data obtained during the recording of the observed quick-variable quantities was considered to be the results within one engine work cycle (from 0 to 720°CSR). In order to allow for such an approach, it shall be assumed that the signal of the exhaust gas temperature variation is a periodic

Table 1. The parameters of the Farymann D10 single cylinder diesel engine recorded on the laboratory test stand

Item	Parameter	Measuring device	unit	Measurement range
1.	Exhaust gas temperature – T_{sp1}	Exposed junction type K thermocouple (junction diameter 0.2 mm, ceramic sheath)	°C	0–1000
2.	Exhaust gas temperature – T_{sp2}	Grounded type K thermocouple with the junction of external diameter of 0.5 mm, made from inconell	°C	0–1000
3.	Exhaust gas pressure in the exhaust channel – p_{sp}	Optical pressure sensor – Optrand C12296	V	0–689475.73 Pa (0–100 psi), sensitivity $6.01 \cdot 10^{-8}$ V/Pa (41.43 mV/psi)
4.	Engine speed (angular position °CA) – n Top dead center – TDC	Induction engine speed sensor and TDC sensor	min^{-1}	0–3000
5.	Load Current of the generator (armature) – I_{tw}	Electric current meter	A	0–15
6.	Voltage at the armature terminals– U_{tw}	Voltmeter	V	0–250
7.	Exhaust valve opening signal	Gap type opto-isolator with a comparator LM393	V mm	0–5 10 (gap)

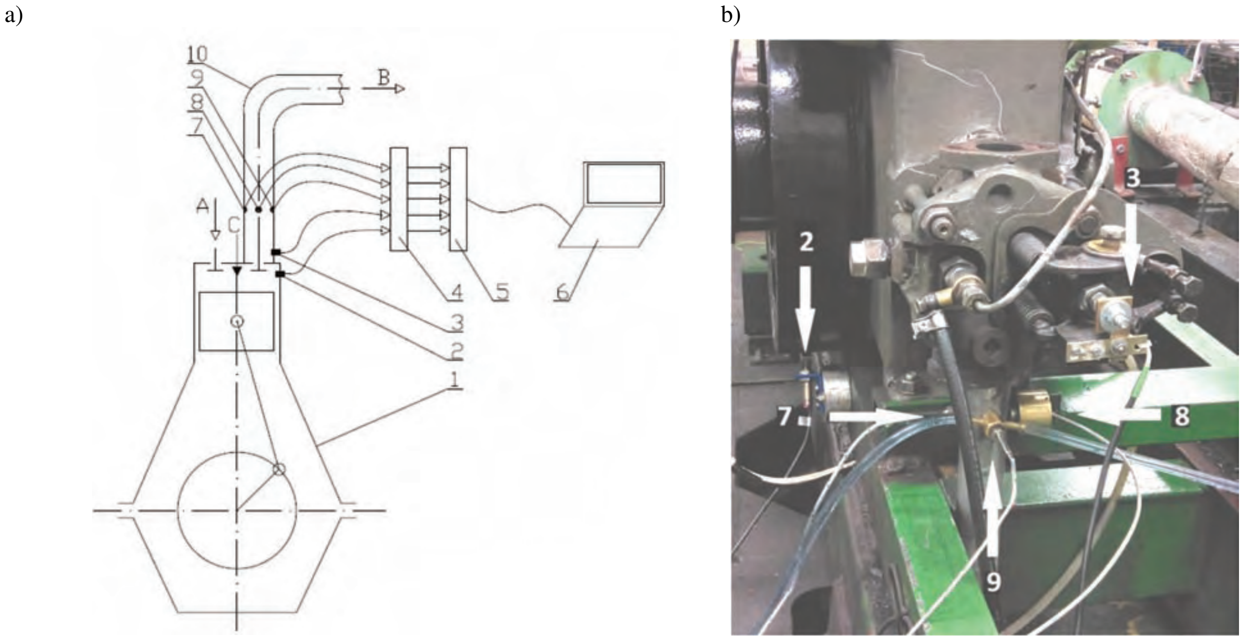

Fig. 2. a) Diagram of the laboratory test stand with the fitting spots of the sensors marked: 1 – Farymann D10 engine, 2 – engine speed and TDC sensor, 3 – exhaust valve opening sensor, 4 – A/C converter, 5 – recorder, 6 – analysis software, 7 – thermocouple in a ceramic sheath, 8 – pressure sensor, 9 – water cooled thermocouple, 10 – exhaust gas channel, A – intake air, B – exhaust gas, C – fuel line; b) a view of the laboratory test stand with the fitting spots of the sensors of the recorded parameters marked: 2 – engine speed and TDC sensor, 7 – thermocouple in a ceramic sheath, 9 – water cooled thermocouple, 3 – exhaust valve opening sensor, 8 – pressure sensor

signal. The time intervals analyzed in this study meet the conditions for their recognition as quasi-periodic, which is also acceptable [7, 8, 10, 11]. The recorded signal of the engine exhaust gas temperature is periodically time-dependent. Its values are repeated in constant intervals, lasting for a time called a period, that is:

$$x(\tau + T) = x(\tau) \tag{1}$$

The necessary condition is that the period (T) is any non-zero measurable number. This condition has been met in the case of analyzed signals of fast changing exhaust gas temperature [15, 17, 18].

3. Diagnostic parameters

The results of the laboratory tests presented in this chapter refer to the temperature variation rates for a single diesel engine cycle. Four different measurement signal standards were analyzed, allowing to assess the technical condition of structural elements limiting the working spaces of the cylinder, as well as the air intake channel only on the basis of measurements and analysis of the quasi-periodic signal, which is the quasi-periodic temperature of the exhaust gas in the outlet duct [9, 14, 16].

Dynamic exhaust gas temperature measurements in the selected control sections of the engine exhaust outlet channel make it possible to determine:

- the average peak to peak variable exhaust gas temperature (difference between maximum and minimum for the signal, within one engine cycle);
- specific enthalpy of subsequent temperature pulses of the exhaust gas leaving the cylinder;
- the rate (intensity) of increase and decrease in the value of the quick-changeable exhaust gas temperature for the single engine cycle.

On the basis of the course of quick-changeable temperature of the exhaust gases, the above mentioned standards of measurement signal values were determined, which may constitute adequate diagnostic parameters for the tested states of unfitness of the intake air channel. The results of their analysis are presented in the next chapters.

3.1. An average peak-to-peak value of the quick-changeable temperature

The average peak-to-peak value of the quick-changeable exhaust gas temperature is determined as the difference between the maximum and minimum temperatures for each engine cycle (Fig. 3). The value of this diagnostic value was determined according to the relation:

$$\Delta T_{śr} = t_{max} - t_{min}\ [K] \tag{2}$$

where: $\Delta T_{śr}$ – average peak-to-peak value [K], t_{max} – maximum temperature of the exhaust gas within one engine cycle [^{o}C], t_{min} – minimum temperature of the exhaust gas within one engine cycle [^{o}C].

3.2. A specific enthalpy of the exhaust gas

The study of the temperature and pressure variability of exhaust gases leaving the cylinder of a diesel engine in the range of one work cycle gives the possibility of direct qualitative and quantitative assessment of the specific enthalpy of exhaust gases. The value of this parameter was determined by integrating the course of the quick-changeable temperature of exhaust gases within the limits specified by the values of the crankshaft rotation angle for one cycle, as well as by the known value of the specific heat of exhaust gases, depending on their average temperature:

$$h = \int_0^{720} c_{p(t_{sp})} \cdot t_{sp} d\alpha_{OWK} \left[\frac{J}{kg}\right] \tag{3}$$

where: h –specific enthalpy of the exhaust gas [J/kg], $c_{p(tsp)}$ – average specific heat of the exhaust gas [kJ/kg·deg], t_{sp} – the temperature of the exhaust gas recorded within one engine cycle [^{o}C], α_{OWK} – the angle of the engine crankshaft revolution [^{o}CSR].

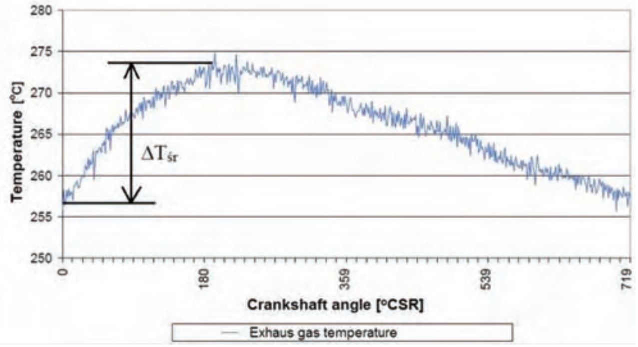

Fig. 3. The course of fluctuation of the quick-changing exhaust gas temperature for one engine cycle and the graphical interpretation of the peak-to-peak temperature value

The average specific heat of stoichiometric exhaust gases was determined on the basis of the chemical composition of exhaust gases recorded for each state of work of a diesel engine.

3.3. A rate of the exhaust gas temperature's alterations

Knowledge of the rate of increase and decrease in temperature of exhaust gases allows to determine the dynamics of this flow process. Figure 4 shows the graphical interpretation of the method of determining this diagnostic parameter for one engine cycle, based on a signal of a quick-changing exhaust gas temperature.

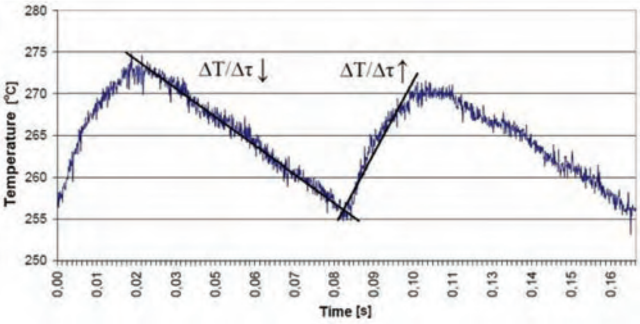

Fig. 4. The course of fluctuation of the quick-changing exhaust gas temperature for one engine cycle and the graphical interpretation of determining the rate of temperature increase and decrease

The rate of increase (decrease) of temperature of exhaust gases was determined according to the relation:

$$\frac{\Delta T}{\Delta \tau} = \frac{t_{max} - t_{min}}{\tau(t_{max}) - \tau(t_{min})} \tag{4}$$

where: $\Delta T/\Delta\tau$ – rate of increase (decrease) of temperature of exhaust gas [K/s], t_{max} – the maximum exhaust gas temperature within one engine cycle [^oC], t_{min} – the minimum exhaust gas temperature within one engine cycle [^oC], $\tau(t_{max})$ – the time during which the temperature of the exhaust gases within one engine cycle reaches its maximum value [s], $\tau(t_{min})$ – the time during which the temperature of the exhaust gases within one engine cycle reaches its minimum value [s].

4. The results of measurements and calculations

Diagnostic measures (parameters) described above have been determined for 2 experimental tests simulating various operating states of a diesel engine. Figures 5 and 6 show the time courses of quick-changeable exhaust gas temperature obtained from ten consecutive engine operation cycles for the two considered technical states of the intake air channel. The presented signals of quick changing temperature were subjected to mathematical treatment in order to remove interference from the measuring network. The measured exhaust gas temperature values achieved during the laboratory engine test were filtered using the method of least squares in the Microsoft Excel software environment.

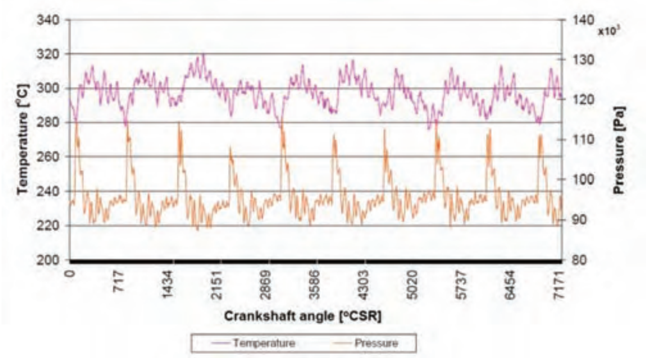

Fig. 5. Time courses of the quick changeable temperature and exhaust gas pressure obtained from ten consecutive engine cycles for state 1 – with the valve regulating the air supply to the engine cylinder fully open

Table 2 presents a summary of the diagnostic parameters determined during the testing of the Farymann engine type D10 in the two considered technical conditions of the intake air channel. The data presented in the table are average values, given for a group of 90 engine operating cycles recorded during the measurements. They refer to a single engine cycle for comparative analysis of defined measurement standards of recorded signals. Figures 7 and 8 show the achieved values of diagnostic parameters in a graphical form for a more readable interpretation of numerical data.

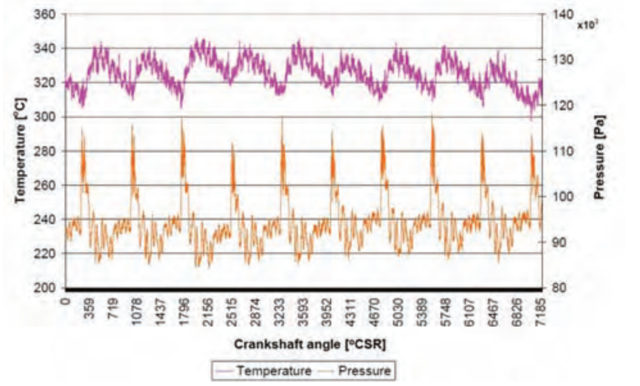

Fig. 6. Time courses of the quick-changeable temperature and exhaust gas pressure obtained from ten consecutive engine cycles for state 2 with the partially closed valve regulating the air supply to the engine cylinder (as in Figure 1)

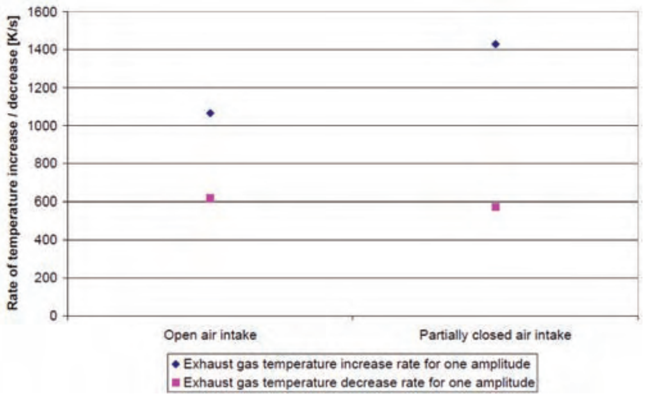

Fig. 7. Values of diagnostic parameters, such as the average rate of increase and decrease of exhaust gas temperature within one engine operating cycle, depending on the technical condition of the intake air channel

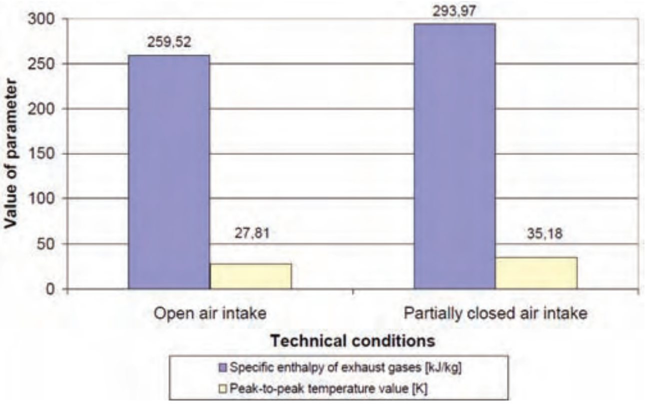

Fig. 8. Values of diagnostic parameters such as specific enthalpy and peak-to-peak exhaust gas temperature within one engine cycle, depending on the technical condition of the intake air channel

Table 2. Summary of determined values of diagnostic parameters with their standard deviations

Diagnostic parameter		$\Delta T_{\acute{s}r}$ [K]	h [kJ/kg]	$\Delta T/\Delta\tau \uparrow$ [K/s]	$\Delta T/\Delta\tau \downarrow$ [K/s]
Technical condition	Operating condition	Peak-to-peak temperature value [K]	Specific enthalpy of exhaust gas [kJ/kg]	Exhaust gas temperature increase rate for one amplitude [K/s]	Exhaust gas temperature decrease rate for one amplitude [K/s]
1	Average value	27.81	259.52	1064.71	615.80
	Standard deviation	2.20	5.33	226.91	110.08
2	Average value	35.18	293.97	1428.78	573.72
	Standard deviation	2.73	4.03	272.17	74.33

5. Comparison of the calculation results

The peak-to-peak value of the exhaust gas temperature was significantly higher for a partially closed air intake duct than in the reference state (differences exceeding the standard deviation). The diagnostic parameter that is averaged over one engine work cycle of the exhaust gases specific enthalpy showed a much higher value (apart from the standard deviation) for a test with a partially closed air intake relative to the reference state. For the diagnostic parameter, i.e. the exhaust gas temperature increase rate within one engine cycle, large standard deviations of this parameter are visible (even 20% of the average value). There is also a significant discrepancy in the results obtained for each technical condition. Significantly higher value compared to the reference state was observed for a state with a partially closed air intake. The exhaust gas temperature increase rate also informs about the dynamic properties of the thermocouple used during laboratory tests [15]. The rate of exhaust gas temperature's decrease is also characterized by significant standard deviations (up to 17% of the average value), as is the case with the rate of exhaust gas temperature increase. However, there is less discrepancy between the achieved average values of this diagnostic parameter. A value significantly lower than the reference state was observed for a study with a partially closed air intake. It is also visible that the rate of decrease of quick changing exhaust gas temperature is about 2 times lower than the rate of increase of this parameter. This is due to the slower cooling of the thermocouple than heating.

Diagnostic parameters determined on the basis of measurements of quick-changeable exhaust gas temperature, such as specific enthalpy, peak-to-peak value and temperature increase rate, react similarly to changes in the structure of the engine intake air channel during the laboratory engine tests.

In the next step of the laboratory tests it is planned to determine Sankey's stream charts. They will be used as an energy background for studies of the influence of selected diesel engine defects on the quick-changing signal of exhaust gas temperature [4, 20].

Bibliography

[1] BROWN, C., KEE, R.J., IRWIN, G.W. et al. Identification applied to dual sensor transient temperature measurement. UKACC *Int. Control Conference*. Manchester 2008.

[2] JAREMKIEWICZ, M. Odwrotne zagadnienia wymiany ciepła, występujące w pomiarach nieustalonej temperatury płynów. Rozprawa doktorska. *Wydawnictwo Politechniki Krakowskiej*. Kraków 2011.

[3] JAREMKIEWICZ, M., TALER, J. Inverse determination of transient fluid temperature in pipelines. *Journal of Power Technologies*. 2016, **96**(6), 385-389.

[4] KORCZEWSKI, Z. Badania efektywności energetycznej nowo produkowanych paliw żeglugowych z zastosowaniem silnika diesla. *Journal of Polish CIMEEAC*. **13**, 1(5), 53-64.

[5] KORCZEWSKI, Z. Exhaust gas temperature measurements in diagnostics of turbocharged marine internal combustion engines. Part I. Standard Measurements. *Polish Maritime Research*. 2015, **22/1**(85), 47-54.

[6] KORCZEWSKI, Z. Exhaust gas temperature measurements in diagnostics of turbocharged marine internal combustion engines. Part II. Dynamic Measurements. *Polish Maritime Research*. **23/1**(89), 68-76.

[7] KORCZEWSKI, Z. Diagnostyka eksploatacyjna okrętowych silników spalinowych – tłokowych i turbinowych. Wybrane zagadnienia. *Wyd. Politechniki Gdańskiej*. Gdańsk 2017.

[8] KORCZEWSKI, Z. The method of energy-efficiency investigations of the newly produced marine fuels through the application of a diesel engine. Materiały Konferencji MAPE, *Explo-Ship 2018*. Zawiercie.

[9] KORCZEWSKI, Z., PUZDROWSKA, P. Analytical method of determining dynamic properties of thermocouples used in measurements of quick – changing temperatures of exhaust gases in marine diesel engines. *Combustion Engines*. 2015, **162**(3), 300-306.

[10] KORCZEWSKI, Z., ZACHAREWICZ, M. Alternative diagnostic method applied on marine diesel engines having limited monitoring susceptibility. *Transactions of the Institute of Measurement and Control*. 2012, **34**(8), 937-946.

[11] KORCZEWSKI, Z., ZACHAREWICZ, M. Diagnostyka symulacyjna układu turbodoładowania okrętowego tłokowego silnika spalinowego. *Zeszyty Naukowe Akademii Marynarki Wojennej*. 2007, **2**(169).

[12] KOWALSKI, J., Laboratory study on influence of air duct throttling on exhaust gas composition in marine four-stroke diesel engine, *Journal of KONES*. 2015, **19**(1), 191-198.

[13] KOWALSKI, J. The emission and combustion characteristics of marine diesel engine with extreme throttled of air or exhaust ducts. *New Trends in Production Engineering*. 2018, **1**(1), 427-433.

[14] MARSZAŁKOWSKI, K., PUZDROWSKA, P. A laboratory stand for the analysis of dynamic properties of thermocouples. *Journal of Polish CIMEEAC*. 2015, **10**(1), 111-120.

[15] OLCZYK, A. Koncepcja pomiaru szybkozmiennej temperatury gazu z uwzględnieniem dynamicznej składowej temperatury. *Pomiary Automatyka Kontrola*. 2007, **53**/9, 576-579.

[16] PUZDROWSKA, P. Determining the time constant using two methods and defining the thermocouple response to sine excitation of gas temperature. *Journal of Polish CIMEEAC*. 2016, **11**(1), 157-167.

[17] PUZDROWSKA, P. Metoda wyznaczania stałej czasowej termopary na podstawie pomiaru szybkozmiennej temperatury spalin wylotowych silnika o ZS. *Zeszyty Naukowe Akademii Morskiej w Gdyni*. 2018, **108**, 115-133.

[18] PUZDROWSKA, P. Signal filtering method of the quick-varying diesel exhaust gas temperature. *Combustion Engines*. 2018, **175**(4), 48-52.

[19] RUDNICKI, J., PUZDROWSKA, P., MARSZAŁKOWSKI, K. Osłona termopary chłodzona wodą jako narzędzie zapobiegające zakłóceniom zewnętrznym podczas pomiarów temperatur szybkozmiennych spalin w kanale wylotowym silnika okrętowego. *Journal of Polish CIMAC*. 2017, **12**(1), 97-104.

[20] ZACHAREWICZ, M. Metoda diagnozowania przestrzeni roboczych silnika okrętowego na podstawie parametrów procesów gazodynamicznych w kanale zasilającym turbosprężarkę. *Rozprawa doktorska*. AMW, Gdynia 2009.

Patrycja Puzdrowska, MEng. – Faculty of Ocean Engineering & Ship Technology, Gdansk University of Technology.
e-mail: patpuzdr@pg.edu.pl

Article citation info:
NOGA, M., GORCZYCA, P. Development of the range extender for a 48 V electric vehicle. *Combustion Engines*. 2019, **177**(2), 113-121. DOI: 10.19206/CE-2019-220

Marcin NOGA
Paweł GORCZYCA

CE-2019-220

Development of the range extender for a 48 V electric vehicle

The article deals with the concept, development and results of preliminary tests of a range extender for an electric light commercial vehicle Melex with a 48 V electrical system. The purpose of the project is to build a prototype of the range extender powered by an internal combustion engine that will increase the range of the vehicle with electric drive, and at the same time will be characterized by a high efficiency and low exhaust emissions. The developed range extender is a combination of a 163cc single-cylinder combustion engine with a generator joined through a ribbed belt transmission. The 3-phase generator from a heavy-duty vehicle was used. In order to match the output voltage of the generator to the system voltage of the electric vehicle, an external adjustable regulator and a rectifier bridge with an increased operating voltage were used. The range extender was attached to a body of the electric vehicle by means of a welded frame made of thin-walled steel profiles. Initial tests of the developed range extender showed its proper interaction with both the lead-acid battery of the vehicle as well as with the nickel-metal hydride battery (NiMH) adapted to 48 V voltage from a hybrid electric vehicle. A maximum output power exceeding 2 kW was obtained. Maximum value of the overall efficiency of the range extender reaches up to 18.8%, which is a high value considering the small size of the used engine and the type of generator. The directions for further development of the range extender were also revealed in this paper.

Key words: *electric vehicle, range extender, spark ignition engine, overall efficiency, three-way catalyst*

1. Introduction

Nowadays, the emphasis is on the ecology of transport, with a special place for reducing carbon dioxide emissions. It is one of the ways to fight the greenhouse effect as well as environmental pollution. For this reason, hybrid- or all-electric vehicles are becoming more and more popular. In hybrid vehicles, part of the electrical energy needed to drive a vehicle is obtained from an electric machine that recovers energy while braking the vehicle [11]. It allows for a significant reduction of fuel consumption by a combustion engine [17]. In pure electric vehicles, all the energy needed to drive the vehicle is drawn from the batteries in the vehicle. In highly developed countries, where renewable sources or nuclear energy are used to produce electricity, it allows significant reducing greenhouse gas emissions. In Poland, electricity which is used to charge electric vehicle batteries, is mostly obtained at power plants or combined heat and power plants fired with coal or lignite. In countries producing electric energy in similar way, the use of electric vehicles as a way of fighting against carbon dioxide emissions is not very well justified until now. It is true that an electric vehicle does not emit pollutants and this is itself very beneficial, but its use does not eliminate emissions in a wider context. Emissions are moved from the place where the vehicle is used to a place where the power plant is. For example, in Poland, CO_2 emissions for each kWh of energy drawn from the electric grid currently amount to over 800 g [16], which is one of the highest values in Europe. With the energy demand of about 0.15–0.20 kWh per 1 km driving for an average passenger car [21], this gives CO_2 emissions related to the use of an electric vehicle equal to about 120–160 g for each kilometer driven. Additionally, the above estimation does not take into account battery and charger efficiencies, which are significantly lower than 1 [15]. Modern vehicles with hybrid drive achieve in road tests a fuel consumptions, which give results of CO_2 emissions of around 100 g/km [20].

One of the most serious disadvantages in the fast extending the use of electric vehicles, even in highly developed countries, is the limited range of these vehicles [8]. This limitation results from the relatively low energy density for currently available batteries [5]. In order to mitigate this inconvenience for end-users, some manufacturers of electric vehicles provide, as additional equipment, a so-called range extender [10, 14]. The device is essentially an auxiliary power unit that usually consists of an electric generator powered by an internal combustion engine with a power up to about 30 kilowatts. Such device is automatically activated when the battery state of charge drops below the limit [19]. It is possible to continue driving, usually at a limited speed. The most famous electric car with a range extender optionally available is BMW i3.

Based on the facts provided above in an outline, in the Students Club of Combustion Engines operating in the Institute of Automobiles and Internal Combustion Engines of the Cracow University of Technology, an idea appeared to create the range extender for an electric vehicle with a 48 V electric system. The concept of the range extender was adopted, consisting of a single-cylinder spark-ignition internal combustion engine driving a three-phase alternating current generator. The main objective of the project is to obtain the highest possible efficiency and the lowest possible CO_2 emission of the auxiliary power unit by selecting the optimal operating conditions, modifications of the engine and its additional systems, and then through the use of alternative fuels. In addition, the development of the range extender allows Students to use knowledge achieved in the course of their studies in many fields: design and operation of machines, combustion engines, electrical engineering, electronics, control engineering, programming, etc.

In the first phase of development, the use of a gasoline-powered engine has been proposed, but in the future the possibility of using more environmentally friendly fuels, such as bioethanol, natural gas or even hydrogen, is foreseen. Compared to conventional fuels the use of bioethanol or natural gas would significantly reduce CO_2 emissions in a process of electricity production for the vehicle [22]. The use of hydrogen would practically eliminate the carbon compounds from the exhaust gases emitted by the engine [2, 6].

2. Range extender for an electric light commercial vehicle

2.1. Vehicle

The prototype range extender described in the next section has been designed for the light commercial vehicle Melex 945DS. A general view of the vehicle that is in the equipment of the Laboratory of Mechatronics of the Cracow University of Technology is presented in Fig. 1.

Fig. 1. Electric light commercial vehicle Melex 945DS

Vehicles of this type in many varieties has widespread use for transporting goods inside industrial plants, warehouses, or as golf carts. They can be also found at airports and in many Polish city-centers as a transport mean for tourists. The model used for research purposes is a two-person vehicle (driver + passenger). The vehicle can also carry loads up to 150 kg in a cargo space located over a rear axle. The nominal voltage of the electric system is 48 V. The energy storage system consists of eight 6V-lead-acid batteries in series with a capacity of 221 Ah (10 h). The batteries are located under the driver's and passenger's seat. The propulsion source is an electronically controlled separately-excited DC motor with a rated power of 3.9 kW at 4300 rpm. The power is transmitted from the motor to the rear wheels through a two-stage gear reducer. The vehicle in this configuration achieves a top speed of around 30 km/h. The nominal amount of energy stored in the batteries equal to approx. 10.6 kWh, what allows to drive the distance of 60 km. The described vehicle has a curb weight of 620 kg (with batteries). The vehicle is equipped with a lighting system necessary to use in public roads [15].

2.2. Adopted concept of the range extender

The concept of the student project of range extender foresaw the use of generally available, inexpensive and easy to control devices. A three-phase alternating current generator with electromagnetic excitation was used. Alternator propulsion using a single-cylinder spark-ignition combustion engine through a ribbed-belt transmission was used, and rectification of the electric current generated in the alternator was carried out using a 6-diode rectifier bridge. A diagram of the concept of the range extender is shown in a Fig. 2.

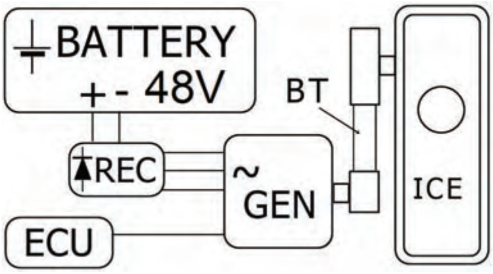

Fig. 2. Adopted concept of the range extender; ICE – Internal Combustion Engine, BT – Belt Transmission, GEN – Generator, REC – Rectifier Bridge, ECU – Electronic Control Unit

The estimated nominal output power of the power unit is about 2 kW. According to this value and the nominal voltage of the vehicle electrical system, individual components have been selected, which will be described in detail below.

2.3. Engine of the range extender

After estimating the power required to drive the generator, it was determined that it would be most reasonable to use a low power industrial four-stroke engine. A single-cylinder, forced air-cooled WEIMA 168FA engine with a displacement of 163 cm^3 and a maximum power of 3.8 kW obtained at 3600 rpm was chosen. This is the license version of the Honda GX 160 engine, which is popular all over the world.

The basic engine specifications are summarized in Table 1.

Table 1. Technical specifications of the engine used in the project

Parameter	Value
Engine type	four-stroke, SI, single-cylinder, OHV, forced air cooling
Displacement	163 cm^3
Bore x Stroke	68 × 45 mm
Compression ratio	8.5
Maximum power	3.8 kW at 3600 rpm
Maximum torque	10 Nm at 2500 rpm
Length x Width x Height	304 × 362 × 335 mm
Fuel system	float carburetor
Ignition system	transistorized magneto
Lubrication system	splash-type
Shaft rotation	counterclockwise
Net weight	15.0 kg

The engine is equipped with a centrifugal speed governor, which is very convenient for a propulsion of a generator. In order to be able to automatically start the engine of the range extender, apart from a recoil starter, an electric starter was also used. The float-type, horizontal carburetor of the engine is equipped with a manually controlled choke valve. Because of the use of a splash lubrication, the engine crankshaft is supported in ball bearings. The engine has a forced air-cooling system. The fan made of plastic is mounted on the flywheel. As an ignition system a transistorized magneto was used. The ignition timing is fixed at 25°CA BTDC.

Currently, in industrial engines with an output power of about 3.5 kW, a side-valve arrangement is still relatively often used, which gives a simple cylinder head design and low price of the engine, but does not allow to achieve high performance, thermal efficiency and low exhaust emissions [4]. The chosen engine is an OHV-type. Two valves are driven by rocker arms and pushrods from the camshaft located in a cylinder block. A location of the valves in the cylinder head allowed a favorable shape of the combustion chamber, hence the minimum brake specific fuel consumption of the engine at the factory carburetor settings is around 330 g/kWh. For an engine of this size this can be considered a beneficial result. The mentioned BSFC results were obtained by the authors of the work as part of research conducted in another project.

2.4. Generator and other electrical components

In the project the three-phase AC generator from a heavy-duty vehicle was used. The used alternator with the symbol A004TA0592 was produced by Mitsubishi. The general view of the used generator is shown in Fig. 3.

Fig. 3. General view of a generator used the project [24]

The generator's rated voltage is 28 V, while the nominal charging current is equal to 90 A and can be obtained starting from a rotational speed of 6000 rpm. The generator is excited electromagnetically by a rotor with 6 pole pairs. Stator windings are connected in a star. The weight of the alternator is equal to 7 kg. In the factory version, the alternator was equipped with an integrated rectifier bridge and an electronic voltage regulator.

In order to match the generator's output voltage to the battery of the electric vehicle, both the rectifier bridge and the voltage regulator were removed. Due to a need to obtain a significantly increased output voltage of the generator, the connection of the stator's windings in the star was retained. The original rectifier bridge was made of Zener diodes with a breakdown voltage of approx. 50 V. This value was too low due to the voltage needed to fully charge the Melex vehicle batteries, which exceeds 60 V. The range extender design uses an external six-diode bridge with a maximum reverse voltage of 1200 V and a continuous output current of 60 A. After attaching the aluminium heat sink to the rectifier, it was placed on the support frame bracket in such a way that it was cooled by air outflowing from the alternator ventilation gaps. The generator's excitation circuit uses an adjusted electronic current stabilizer. The regulator allows to maintain the set value of the battery charging current under given operating conditions. In a final form of the range extender, it will be replaced by an automatic regulator of the generator's output parameters that implements a predetermined battery charging strategy.

2.5. Power transmission

As mentioned earlier, the range extender concept adopted simple solutions, hence transmission with a ribbed belt was used to transmit the drive from the engine to the generator. A belt of 6PK-type for automotive applications was used. Transmissions with a ribbed belt are characterized by simple construction, low price, they are quiet and do not require lubrication. The efficiency of such a transmission reaches up to 97% at rated load, with a load equal to half the rated load, the efficiency is slightly lower and amounts to approximately 95% [23]. These can be considered a high values, especially taking into account average values of efficiency obtained by internal combustion engines.

The maximum regulated engine speed is 3600 rpm. At 28 V, the generator requires a speed of at least 6000 rpm to obtain a nominal output current. The characteristics of the used generator at the output voltage increased to above 50 V were not known. However, from the fundamentals of electric machines, it is known that at the same load and the same excitation magnetic field, obtaining an increased output voltage requires approximately proportional increase of the generator's rotational speed [1]. For this reason, it was decided to use a multiplier transmission with a gear ratio of approximately 0.5. Finally, the original 69 mm diameter pulley was left in the generator, while a 126 mm diameter wheel was used on the motor shaft, which gives a gear ratio of about 0.55. The generator pulley width has been reduced to the width of the 6PK belt by turning method.

The internal combustion engine of range extender has a counterclockwise rotation direction, while the generator rotates in a clockwise direction in a powertrain which it originates. It is true that due to the generation of alternating current, the direction of rotation of the generator is irrelevant, however, both the fan and the excitation circuit brushes are adapted (optimized) to work in only one direction. As a result, the internal combustion engine and generator had to be placed on opposite sides of the belt transmission. On the one hand, this increases the transverse dimension of the engine-transmission-generator assembly, but on the other hand it allows the use of a small-length belt, which does not require additional tensioning pulleys. In addition, the longitudinal dimension of the engine-transmission-generator assembly is clearly smaller in this case.

2.6. Support frame

As part of the project, it was planned to mount the prototype range extender in a rear part of the electric vehicle in a place intended for the cargo space.

In order to be able to mount the system on the vehicle, it was necessary to design and make a special support frame. The developed 3D model of the designed item is shown in Fig. 4.

The support frame is made of thin-walled steel square pipes. The object has dimensions of 850 mm × 500 mm. The frame is attached to the vehicle body through rubber-metal elements in four points. The purpose of the dampers is to diminish vibrations caused by the single-cylinder engine of range extender. Unfortunately, the engine has no balancing shaft, so the role of rubber-metal elements is the more important. The dampers are attached to the vehicle via special brackets. Direct mounting of the damping elements to the vehicle was not possible due to a fact that the body of the vehicle is made of a plastic of a relatively low mechanical strength.

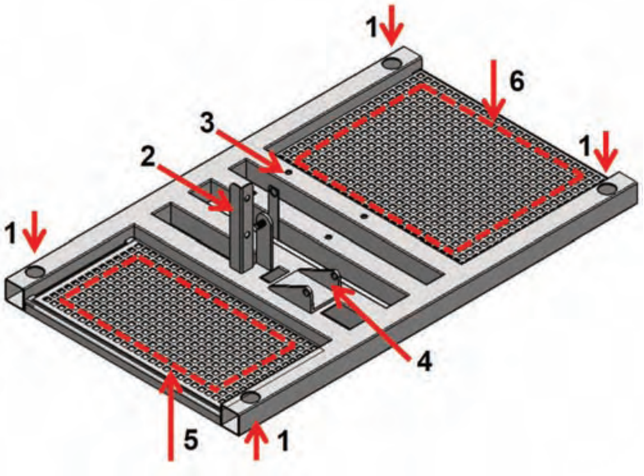

Fig. 4. Support frame of the range extender: 1 – hole for mounting of damping elements, 2 – bracket of a rectifier bridge, 3 – hole for mounting an engine, 4 – bracket of a generator, 5 – area for mounting control devices, 6 – area for mounting an engine management system (in future)

The support frame has a bracket that holds the generator and a bracket that allows to adjust the belt tension of the transmission by turning the alternator. The frame is also equipped with mounting brackets for the rectifier bridge with heatsink and engine speed sensor. Two shelves were made in the free spaces of the frame, thanks to which it was possible to mount the range extender control systems. Perforated steel sheets were used to make shelves. Frame elements were joined together by MAG-method welding. After finishing the construction works, the frame was cleaned and covered with two layers of anticorrosive coating.

2.7. Developed prototype of the range extender

After making the support frame, the range extender components were mounted on it. Then the ready auxiliary power unit was mounted on the Melex electric vehicle. The view of the developed range extender mounted on the electric vehicle at the place for the cargo space of is shown in Fig. 5.

The electrical leads of the rectifier bridge have been connected to the poles of the vehicle battery. Connections were made using cables with a 6 mm^2 cross-section. For safety reasons, double-insulated wires and over-current protection in the form of fuses were used.

The generator control system has been equipped with devices for measurements the battery voltage, charging current and rotational speed of the internal combustion engine. The generator excitation circuit switch, engine off switch and starter button are located both on the control panel of the generator control unit and on the dashboard of the vehicle so that the range extender can be started and stopped while the vehicle is being driven. A potentiometer for adjusting the charging current was placed on the generator control panel.

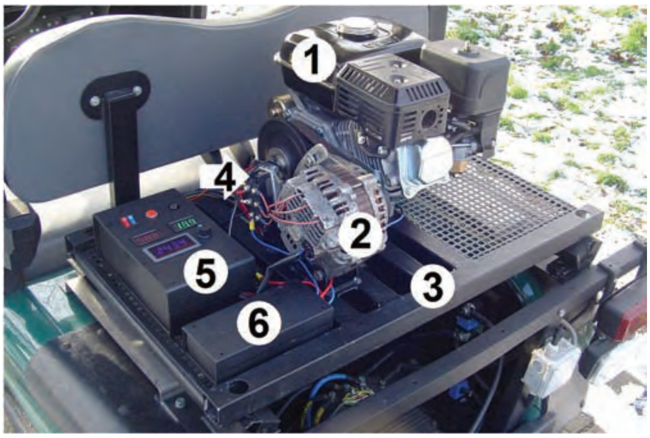

Fig. 5. View of the developed 48 V range extender: 1 – engine, 2 – generator, 3 – support frame, 4 – rectifier bridge, 5 – generator control unit, 6 – relays and voltage converter for a starter motor

The used engine electric starter is intended for operation at 12 V. To avoid the need to use an additional battery with this voltage, the starter is supplied from 48 V vehicle batteries via a DC-DC voltage converter.

3. Stationary research of the range extender

3.1. Preliminary tests of an efficiency of the range extender

Preliminary tests of the developed range extender were carried out when the engine with the generator was mounted on the test frame, and the electric vehicle was equipped with a nickel-metal hydride (NiMH) battery instead of a lead-acid battery. These batteries were adapted to an electric vehicle from a hybrid car. The main issue of the adaptation was the proper connection of the modules so that the output voltage of the pack match the system voltage of the Melex vehicle. Finally, a package with a nominal voltage of 50.8 V and a capacity of 32.5 Ah was obtained. The aim of the work was to develop a lightweight battery pack allowing for increasing the payload of an electric vehicle. More information for readers interested in this topic can be found in [16].

The carried out preliminary research was aimed at verifying the feasibility of the range extender project built according to the adopted concept and using the chosen components.

Already the first tests have confirmed that the adapted generator powered by the chosen combustion engine enables effective charging of the battery of the electric vehicle. A NiMH battery pack charging current exceeding 35 A was obtained.

A quantitative assessment of the range extender's operation consisted in examining the overall efficiency of the power unit at selected operating points (engine rotational speed–battery charging current). The overall efficiency means that this is considered as an energy delivered to the battery pack referred to an amount of used fuel. In particular, the overall efficiency of the range extender was calculated using formula (1):

$$\eta_{RE} = 100 \cdot \frac{E_{RE}}{m_f \cdot LHV} \tag{1}$$

where: η_{RE} – overall efficiency of the range extender, %, E_{RE} – energy delivered by the range extender, kJ, m_f – mass of a gasoline consumed in the test, kg, LHV – lower heating value of the gasoline, kJ/kg.

A denominator of the formula (1) represents the amount of chemical energy of fuel consumed by the engine during each test. The petrol LHV value of 43,000 kJ/kg was used for calculations [13].

The energy delivered to the battery by the range extender E_{RE} was calculated using the following general formula:

$$E_{RE} = \int_{t_0}^{t_1} V_{bat} \cdot I_{RE} \, dt \tag{2}$$

where: V_{bat} – battery voltage, V, I_{RE} – current delivered by the range extender, A, t – time, s, 0/1 – start/end of the measurement.

The registration of measurement results was carried out using a digital data acquisition card, thus finally the formula for calculating the energy delivered to the battery has the form:

$$E_{RE} = \sum_{t=t_0}^{t_1} V_{bat} \cdot I_{RE} \cdot \Delta t \tag{3}$$

The measurement frequency was 10 Hz, so the time step Δt was 0.1s in the formula. The measurement of fuel consumption was carried out using a laboratory digital scale. Due to the measuring range of the data acquisition card for measuring the battery voltage, a resistive divider with 1: 6 attenuation was used. The charging current was measured with a contactless transducer using the Hall effect. The measuring range of the transducer was 70 A, while its sensitivity was 33 mV/A.

The efficiency measurements were carried out at three operating points. In each of the tests, the consumption time of 100 g of fuel was measured. As the system was assembled in the test version, it was decided to perform measurements at a charging current not exceeding the safe value of 20 A. The first test was carried out at a speed of 2,900 rpm and an adopted load of 20 A. The second measurement was made for the same lever position of the engine speed governor, but with a reduced load value – 9 A. Due to the reduced engine load, the rotational speed in this test was slightly higher – around 3000 rpm. The last, third experiment was made at a set speed reduced to 2550 rpm. In the third test, the load was adopted to be the same as in the first measurement, i.e. 20 A.

Figure 6 shows exemplary graphs of the range extender operating parameters at 20 A load and an engine speed set to 2550 rpm (Test No. 3).

The value of the excitation current allowing to obtain the desired value of the charging current was set at the beginning of the test, and then it was not corrected anymore. Because of this, the current delivered by the range extender decreased slightly during the test. This was the result of a gradual increase in the battery voltage. During the test no. 3 the range extender delivered about 585 kJ of electric energy to the battery.

Results of the overall efficiency tests of the range extender for the three measurement points are summarized in Table 2.

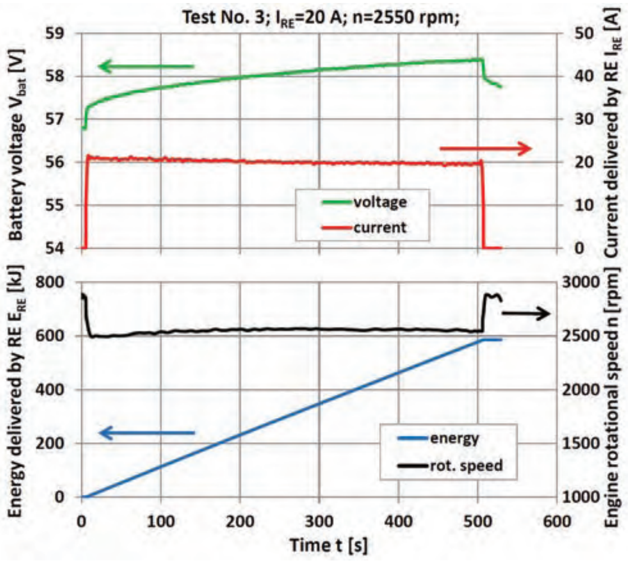

Fig. 6. Range extender operating parameters in the function of a charging time at 2550 rpm and $I_{RE} \approx 20$ A

Table 2. Summary of the results of measurements of an overall efficiency of the range extender

Parameter		Test No.		
		1	2	3
Current delivered by RE, I_{RE} [A]	setpoint	20	9	20
	average in the test	18.9	8.6	20.1
Engine rotational speed, n [rpm]		2900	3000	2550
Charging time, t [s]		505	688.2	501.6
Fuel consumption, m_F [kg]		0.1	0.1	0.1001
Energy delivered by RE, E_{RE} [kJ]		523.31	335.83	584.95
Overall efficiency of RE, η_{RE}		**12.2**	**7.8**	**13.6**

Due to slight variability of the range extender output current during the test, the table lists both current setpoints as well as averaged values from the actual measurement. Figure 7 presents a comparison the overall efficiency of the range extender.

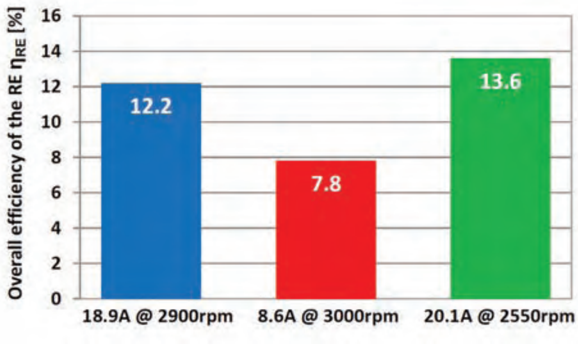

Fig. 7. Comparison of the overall efficiency of the range extender in different operating points

The maximum efficiency of the range extender in the preliminary experiments was 13.6% and was obtained at the load 20 A and at the engine rotational speed 2550 rpm.

This can be explained by the fact that under the given conditions the engine load was the highest. Similarly, due to the properties of the used generator, it is advantageous that the desired current value is obtained at the lowest possible rotor speed, i.e. at the lowest frequency of the generated alternating current [1]. The result obtained in the second test confirms that the operation of the power unit at the low load is inefficient. For this reason, the operation of the range extender in the low load region should be avoided.

3.2. Overall efficiency and exhaust gas toxicity of the range extender with air-fuel ratio correction

After installation the range extender assembly on the electric vehicle, further research and development work was carried out. One of the directions of further development of the design was the adaptation of a motorcycle exhaust system with an integrated three-way catalytic converter. These actions were taken to reduce the noise emitted by the power unit [7], but also to reduce concentrations of toxic exhaust compounds in the future. The used silencer comes from a Yamaha Majesty S XC125R motorcycle with a 125 cm^3 displacement engine and a maximum power of 8.8 kW at 7500 rpm. A view of the range extender with the adapted motorcycle exhaust system is presented in Fig. 8.

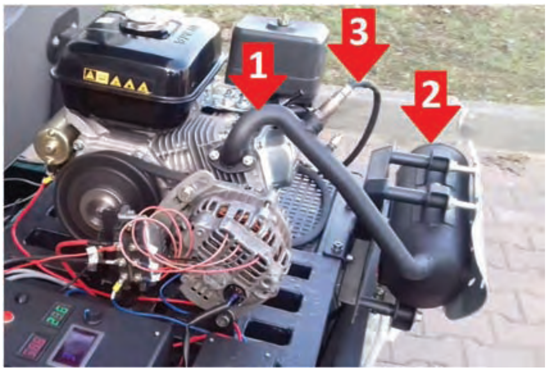

Fig. 8. An adapted exhaust system mounted to the range extender: 1 – exhaust pipe, 2 – muffler with TWC, 3 – wideband oxygen sensor

Adaptation of the exhaust system for mounting to the range extender required the use of a new pipe connecting the cylinder head exhaust port to the muffler. An oxygen sensor was installed in the new exhaust pipe to allow a regulation of the air-fuel ratio in a closed loop. In the next stage of development of the range-extender, a system for maintaining the stoichiometric air-fuel ratio of the mixture will be prepared so that the catalytic converter integrated in the exhaust system can operate effectively [12]. The research of the range extender equipped with a new exhaust system was aimed at verifying the considered method of the maintaining stoichiometric AFR, as well as an evaluation of the operation of the catalytic converter under these conditions. As the result of previous activities, it was revealed that with the carburetor factory settings, the engine is fed with a rich mixture. The value of relative AFR (λ) is variable between 0.8 and 0.9, depending on the engine load and rotational speed. This makes, that it is possible to supply additional air downstream from the carburetor in order to dilute the mixture so as to obtain a stoichiometric air-fuel ratio.

In addition, as part of the carried out work, the overall efficiencies of the range extender fed with the mixture without modifying its air-fuel ratio, and after obtaining the stoichiometric AFR were compared.

In order to supply an air stream after the carburetor, a stub pipe was added to the intake port of the cylinder head, which was connected to an additional throttle valve via a rubber hose. The purpose of the valve was to regulate the air flow that dilutes the air-fuel mixture formed in the carburetor. The concept of modification of the intake system is shown in Fig. 9.

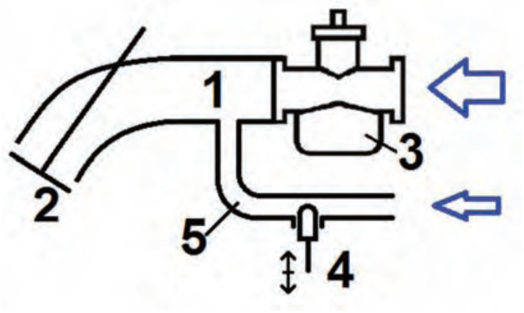

Fig. 9. Scheme of a modification of the air intake system: 1– intake port, 2 – intake valve, 3 – carburetor, 4 – additional-air valve, 5 – additional-air port

Comparative tests using the mixture composition regulation were carried out at a rotational speed of approximately 3400 rpm and a load of about 42 A. With a battery voltage of 52–53V, this gives the output power of the range extender within 2.2 kW, which is significantly higher than that obtained in the previous tests. This was possible because the range extender was already mounted in the vehicle on the support frame made in a target form. The methodology of the conducted research was analogous to that described in subsection 3.1. The only difference was that the range extender was mounted in the space previously occupied by the NiMH battery, hence the load for the range extender was this time lead-acid batteries. However, this fact did not affect the results. As before, the period of registration of the operating parameters of the range extender was determined until the engine consumed 100 g of fuel. Arcon Oliver K-4500 gas analyzer was used to determine the exhaust composition and conversion efficiency of the catalyst. The analyzer allows the measurement of CO, CO_2, HC, NO_x and O_2 concentrations in dry exhaust gas. The relative air-fuel ratio is calculated by the analyzer based on the exhaust gas composition. In order to measure the composition of the exhaust gas, two exhaust gas intake points were made, one in the pipe in upstream from the catalyst, and the other in the muffler downstream from the reactor support.

During the first measurement the engine operated with a closed additional-air valve. As the second, a test was carried out in which the mixture formed by the carburetor was diluted by additional air supplied downstream from the throttle. The opening degree of the additional air valve was adjusted so as to obtain a stoichiometric AFR.

Figure 10 presents graphs of energies delivered to the battery and overall efficiencies of the range extender obtained in the both measurements.

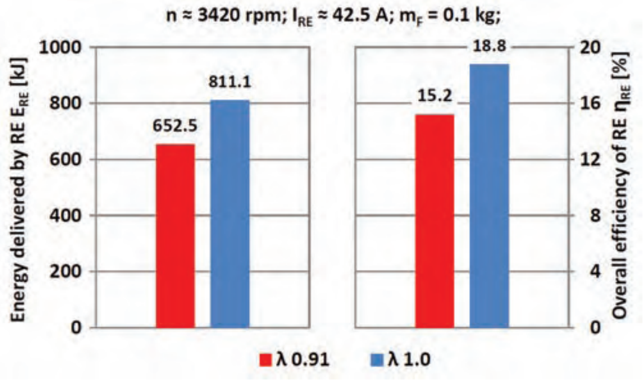

Fig. 10. Comparison of energies delivered to battery and efficiencies of the range extender working with factory settings (λ 0.91) and with a modified relative AFR (λ 1.0) by the supplying of additional air

When the engine was running without additional air, the mixture composition oscillated around the value of relative air-fuel ratio of 0.91. When using the dilution of the mixture with additional air, the fuel consumption of the engine decreased, hence the time of consumption of 100 g of fuel increased. For this reason, in the second test, the generator delivered a significantly larger amount of electricity to the battery, and this gave a significant increase in the overall efficiency of the range-extender when fed with a mixture of stoichiometric air-fuel ratio.

Figure 11 shows the results of the exhaust composition measurement in the both experiments. In the first measurement, with the unmodified air-fuel ratio of the mixture, the composition of the exhaust gases upstream from the catalytic converter (λ 0.91) was recorded. During the second measurement, the compositions of exhaust gas both upstream from (λ 1.0 upstr. TWC) and downstream from the catalytic reactor (λ 1.0 dwnstr. TWC) were recorded. This made it possible to evaluate the conversion efficiency of the reactor being part of the new exhaust system.

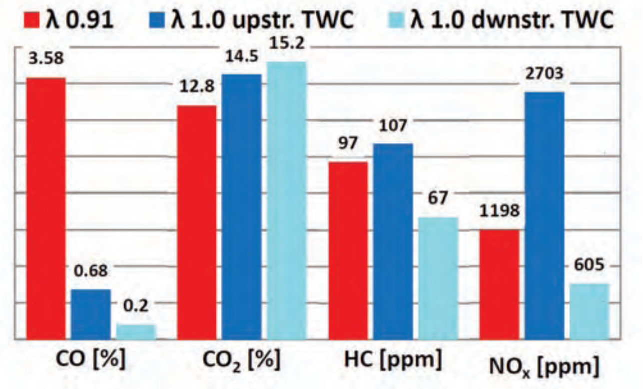

Fig. 11. Comparison of CO, CO_2, HC and NO_x concentrations in exhaust of the RE engine working with factory settings (λ 0.91), as well as with AFR modification (λ 1.0)

During operation without adding air downstream from the carburetor, the engine was fed with a rich mixture, hence a high CO concentration and a relatively low NO_x concentration in the exhaust. The correction to the stoichiometric AFR resulted in a significant decrease in the concentration of carbon monoxide, but also in an increase in the concentration of NO_x upstream from the catalytic converter. This was expected when shifting from a rich to stoichiometric mixture. It was also observed, that the concentration of hydrocarbons upstream from the catalytic converter was higher by 10 ppm in relation to the result for the composition of the mixture $\lambda = 0.91$. This may be due to the deterioration of the fuel atomization conditions associated with the reduction of the air flow rate through the carburetor when additional air is supplied. However, this was not a particularly large increase. It should also be noted that particularly for a low-power engine fed by a carburetor, a very favorable proportions of CO to CO_2 upstream from the catalytic converter was observed when the engine was fed with a stoichiometric mixture. This indicates that the mixture was correctly prepared, as well as combustion process occurred properly.

Figure 12 shows the results of conversion efficiency when engine was fed with a stoichiometric mixture. Efficiencies were calculated from exhaust gas compositions upstream from and downstream from the catalytic converter that were presented above.

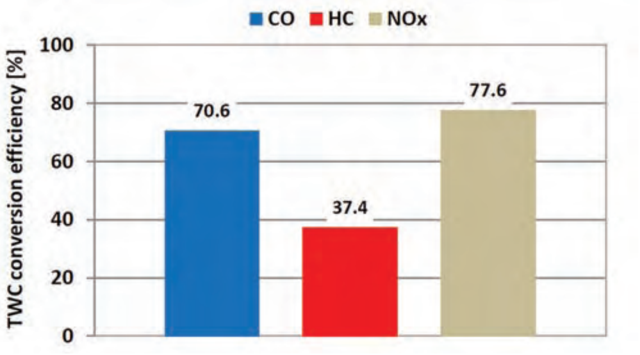

Fig. 12. Conversion efficiency of TWC during operation of the engine with stoichiometric air-fuel ratio

The use of modification of the air-fuel ratio by dilution with additional air caused that the catalytic reactor integrated in the new exhaust system started to work. The conversion efficiency for CO and NO_x obtained relatively high values. In the case of hydrocarbons, a lower efficiency was obtained. This is usually observed for reactors, that were aged in a some extent, like the one used. In any case, the concentrations of toxic compounds downstream from the catalytic converter, when the engine is running with the stoichiometric mixture are clearly lower than those recorded when working with the unmodified AFR ($\lambda = 0.91$). This confirms the correctness of the adopted concept of the air-fuel ratio adjustment in order to enable decreasing of toxic components emissions of the developed range extender.

4. Road tests of the vehicle equipped with RE

In order to determine the impact of the range extender implementation on the traction parameters of the electric vehicle, road tests were carried out. During the tests the vehicle behavior was compared at an acceleration from $v = 0$ to $v = v_{max}$ with RE off, and then with RE turned on. In tests, the vehicle load was the driver and passenger, which together with a weight of the range extender gives the total vehicle weight of 820 kg. The engine rotational speed was set at 3450 rpm, while the current delivered to the battery was approximately 40A. During the tests, the vehicle batteries remained charged at around 70%. With a higher state of charge, turning on the range extender could adversely affect the life of the batteries.

Figure 13 presents a comparison of waveforms of the battery voltage, the battery current and the vehicle speed in acceleration tests with the range extender switched off and then running.

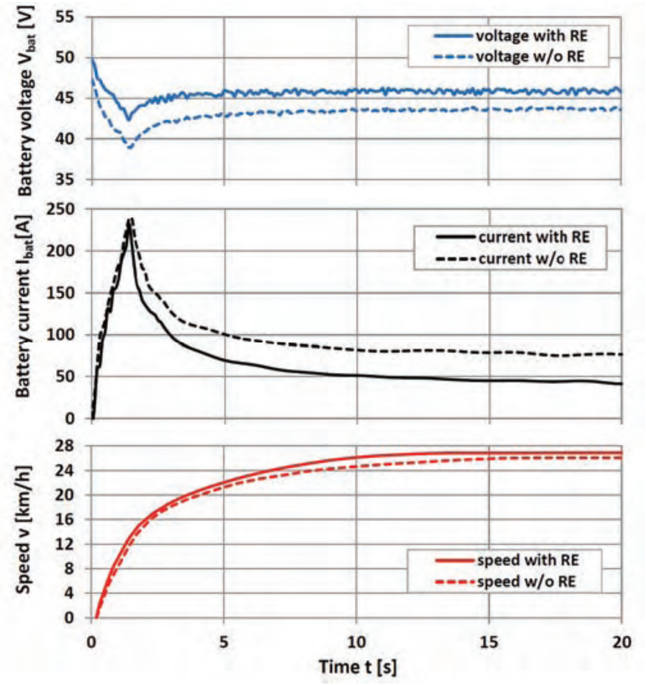

Fig. 13. Comparisons of battery parameters and vehicle speed during acceleration with the range extender off (dashed) and running (solid)

The use of the range extender causes a significant decrease in the current drawn from the batteries while driving at a speed close to maximum. The decrease of the current drawn from the battery causes that proportionally smaller decrease in battery voltage under load are observed. The increase in the voltage of the battery operating under load by about 2 V, caused by the decrease of the voltage drop on the internal resistance of the batteries [9], resulted that the maximum speed of the vehicle with the range extender running increased by approx. 1 km/h. The use of the auxiliary power unit also had an impact on reducing the acceleration time of the vehicle from 0 to 24 km/h. With the range extender off, it was 8.4 s, and when driving with the RE turned on, this time has been shortened to 6.8 s.

5. Conclusions and further development

The first stage of the project development was completed. The developed range extender works correctly both in stationary conditions and when driving a vehicle. At several selected measurement points, the overall efficiency tests were carried out, during which promising results were obtained. In the further part of the work, the engine exhaust system was modified by using a muffler with a three-way catalytic converter. The use of a simple method of regulating the air-fuel ratio of the mixture allowed to verify the efficiency of the engine's cooperation with the exhaust gas aftertreatment system. The use of a three-way catalytic reactor, when the engine is running a stoichiometric mixture, significantly reduces the emission of toxic exhaust components. In addition, the leaning the mixture formed by the carburetor up to stoichiometric ratio in the last of the analyzed measurement points resulted in obtaining the most favorable, so far, result of the overall efficiency of the developed RE amounting to 18.8%. Taking into account the low output power of the auxiliary power unit, the efficiency can be considered very beneficial. A positive result of the verification of the method of regulation the stoichiometric mixture, confirms the desirability of developing the AFR automatic correction system.

The results of the carried out work allowed also to determine the area and extent of further work on the developed range extender. In the next step, these activities will be focused on the development of an automatic control system of the range extender. The next research of the efficiency of the power unit at various points of its operation map will allow to determine the effective algorithm for controlling the engine speed depending on the demand for electrical power. As mentioned in the introduction, it is also planned to introduce modifications to the engine and fuel system oriented at increasing the overall efficiency and the use of alternative fuels, what will allow for a significant reduction of CO_2 emissions. To accomplish these goals it will be necessary to equip the engine with an integrated injection-ignition system [3]. Among engine modifications, an application of a strategy of the late intake valve closing allowing the implementation of a work cycle with increased expansion (Miller–Atkinson) is considered [18].

Acknowledgements

This research was conducted in the framework of task No. M-04/406/2018/DS, which was a subsidy for research granted by the Ministry of Science and Higher Education of the Republic of Poland.

Nomenclature

η_{RE}	overall efficiency of the range extender, %
λ	relative air-fuel ratio
AFR	air-fuel ratio
APU	auxiliary power unit
BSFC	brake specific fuel consumption, g/kWh
BT	belt transmission
BTDC	before top dead center
CA	crank angle, degrees
dwnstr.	downstream from
ECU	electronic control unit
E_{RE}	energy delivered by the range extender, kJ
GEN	generator
I_{bat}	battery current, A
I_{RE}	current delivered by the range extender, A

ICE	internal combustion engine
LHV	lower heating value, kJ/kg
m_f	mass of a gasoline consumed in the test, kg
MAG	metal active gas
n	engine rotational speed, rpm
OHV	overhead valve
RE	range extender
REC	rectifier bridge
SI	spark ignition
t	time, s
TWC	three-way catalyst
upstr.	upstream from
v	vehicle speed, km/h
V_{bat}	battery voltage, V
w/o	without

Bibliography

[1] ADAMIEC, M., DZIUBIŃSKI, M., SIEMIONEK, E. Research of the alternator on the stand – efficiency aspect. *IOP Conference Series: Materials Science and Engineering*. 2018, **421**, 022001. DOI:10.1088/1757-899x/421/2/022001.

[2] BRZEŻAŃSKI, M., MARECZEK, M., MAREK, W. et al. The realized concept of variable chemical composition fuel gas supply systems, for internal combustion engines. *Combustion Engines*. **170**(3), 2017, 108-114. DOI:10.19206/CE-2017-318.

[3] DZIUBIŃSKI, M. Ecological aspect of electronic ignition and electronic injection system. *Environmental Engineering V*. 2016. DOI:10.1201/9781315281971-42.

[4] EICHLSEDER, H., KLÜTI□G, M., PIOCK, W.F. Grundlagen und Technologien des Ottomotors: Der Fahrzeugantrieb, *Springer*. Vienna 2008.

[5] GIS, W., MENES, M. The development of the world electric vehicles fleet in years 2010-2017. *IOP Conference Series: Materials Science and Engineering*. 2018, **421**, 022008. DOI:10.1088/1757-899x/421/2/022008.

[6] GIS, W., PIELECHA, J., WAŚKIEWICZ, J. et al. Use of certain alternative fuels in road transport in Poland. *IOP Conference Series: Materials Science and Engineering*. 2016, **148**, 012040. DOI:10.1088/1757-899x/148/1/012040.

[7] HEBDA, R. Adaptation of the exhaust system with a catalytic converter for a low power industrial engine. *Cracow University of Technology*. Master Thesis, Cracow 2019.

[8] HUSAIN, I. Electric and hybrid vehicles: design fundamentals. *CRC Press, Taylor&Francis Group*. Boca Raton 2010.

[9] JUDA, Z., NOGA, M. The influence of battery degradation level on the selected traction parameters of a light-duty electric vehicle. *IOP Conference Series: Materials Science and Engineering*. 2016, **148**, 012042. DOI:10.1088/1757-899x/148/1/012042.

[10] KARPUKHIN, K., TERENCHENKO, A. The creation of energy efficient hybrid vehicles in the Russian Federation. *Combustion Engines*. 2017, **168**(1), 145-148. DOI:10.19206/CE-2017-123.

[11] KHAJEPOUR, A., FALLAH, S., GOODARZI, A. Electric and hybrid vehicles: technologies, modeling and control – a mechatronic approach. *John Wiley&Sons*. Chichester 2014.

[12] KOZIOŁ-JAROSZ, M., BRZEŻAŃSKI, M. The role and tasks of the support mats in the construction of catalytic converters. *Combustion Engines*. 2017, **170**(3), 96-99. DOI:10.19206/CE-2017-315.

[13] MICHAELIDES, E.E. Energy, the environment, and sustainability. *CRC Press, Taylor&Francis Group*. Boca Raton 2018.

[14] NOGA, M. Application of the internal combustion engine as a range extender for electric vehicles. *Combustion Engines*. 2013, **154**(3), 781-786.

[15] NOGA, M., JUDA, Z. Energy efficiency and equivalent CO$_2$ emissions of a light-duty electric vehicle depending on driving distance. *IOP Conference Series: Materials Science and Engineering*. 2018, **421**, 022023. DOI:10.1088/1757-899x/421/2/022023.

[16] NOGA, M., JUDA, Z. The application of NiMH batteries in a light-duty electric vehicle. *Czasopismo Techniczne*. 2019, **1**, 197-222. DOI:10.4467/2353737xct.19.014.10054.

[17] PIELECHA, I., CIEŚLIK, W., BOROWSKI, P., CZAJKA, J., The development of combustion engines for hybrid drive systems. *Combustion Engines*. 2014, **158**(3), 2014, 23-35.

[18] PIELECHA, I., CZAJKA, J., BOROWSKI, P., WISŁOCKI, K. Thermodynamic indexes of Atkinson cycle combustion engine operation under transient conditions. *Combustion Engines*. 2013, **154**(3), 517-524.

[19] RIBAU, J., SILVA, C., BRITO, F.P. et al. Analysis of four-stroke, Wankel, and microturbine based range extenders for electric vehicles. *Energy Conversion and Management*. 2012, **58**, 120-133. DOI:10.1016/j.enconman.2012.01.011.

[20] RODAK, Ł., SZRAMOWIAT, M. Comparison of fuel consumption between a vehicle with standard and hybrid drive system. *IOP Conference Series: Materials Science and Engineering*. 2018, **421**, 042068. DOI:10.1088/1757-899x/421/4/042068.

[21] SLASKI, G., OHDE, B. A statistical analysis of energy and power demand for the tractive purposes of an electric vehicle in urban traffic – an analysis of a short and long observation period. *IOP Conference Series: Materials Science and Engineering*. 2016, **148**, 012027. DOI:10.1088/1757-899x/148/1/012027.

[22] STELMASIAK, Z., PIETRAS, D. Utilization of waste glycerin to fuelling of spark ignition engines. *IOP Conference Series: Materials Science and Engineering*. 2016, **148**, 012087. DOI:10.1088/1757-899x/148/1/012087.

[23] STOCKMAN, K., DEREYNE, S., DEFREYNE, P. et al. An efficiency measurement campaign on belt drives. *Proceedings of Energy Efficiency in Motor Driven Systems (EEMODS 2015)*. Helsinki 2015, 366-377.

[24] https://www.motorcityreman.com/20366n.html – accessed on 2019-03-25.

Marcin Noga, DEng. – Faculty of Mechanical Engineering, Cracow University of Technology.
e-mail: *noga@pk.edu.pl*

Paweł Gorczyca, Eng. – Faculty of Mechanical Engineering, Cracow University of Technology.
e-mail: *gorczycap7@gmail.com*

Article citation info:
KRAKOWSKI, R. Assessment of the technical condition of a marine diesel engine based on the analysis of the exhaust gases chemical composition. *Combustion Engines*. 2019, **177**(2), 122-126. DOI: 10.19206/CE-2019-221

Rafał KRAKOWSKI

CE-2019-221

Assessment of the technical condition of a marine diesel engine based on the analysis of the exhaust gases chemical composition

In the article, the concept of technical diagnostics in relation to marine engines was characterized. The compression ignition piston engine was presented as a diagnostic object. The next part of the article discusses the composition of exhaust gases with particular emphasis on compounds harmful to the environment. The available test methods for exhaust composition are also briefly described by means indication of the engine and exhaust gas analyzer. The reduction of emission of harmful compounds in the exhaust gases is also described in the article. The main part of the article presents the research object, i.e. the marine diesel engine piston and the exhaust gases analyzer, as well as tests carried out. The tests were performed for the engine in working order and inefficient condition in order to compare them with the simulated damages of injection pump and turbocharger. The article was completed conclusions.

Key words: *technical diagnostics, exhaust composition, engine indication, exhaust gas analysis, marine diesel engine*

1. Introduction

As a result of the marine engine operation, its elements wear. Therefore, it is very important to constantly diagnose it in order to keep the engine in the best possible technical condition. The construction of the engine and the physicochemical processes occurring during the engine operation process are used during the diagnosis. The most useful parameters of work processes include, among others, combustion, fuel supply, and air supply. In addition to the parameters of the work processes, physicochemical parameters such as pressure, temperature, vibrations and exhaust composition are also important [1].

Examination of the technical condition of the engine belong to the group of control tests, which include research and measurements that enable the assessment of the engine's operation and determination of the wear of its components. Therefore, there are many ways to assess the technical condition of a marine piston engine. One of them is the analysis of the chemical composition of exhaust gases presented in this article.

2. Marine diesel engine as a diagnostic object

The marine engine is characterized by a complicated construction, which consists of many functional systems [5, 10].

The quantity and complex structure of these systems makes the ship engine a special object of technical diagnostics. Each of them has a very large impact on the reliability of the engine and the safety of people and the ship.

3. Exhaust gas composition in marine diesel engines

Exhaust gases are created as a result of a complex combustion process with intense heat discharge. In addition, there is also the emission of harmful compounds along with other combustion products. Nitrogen oxides (NO_x), sulfur oxides (SO_x), hydrocarbons (C_nH_m), particulates (PM), carbon dioxide (CO_2), carbon monoxide (CO), aldehydes (RCHO) are considered to be the basic components of the exhaust [2].

These compounds can take the gaseous, liquid or solid form. The composition of the exhaust depends on the technical condition of the engine, fuel quality and air parameters [6, 7, 9].

4. Diagnosing the technical condition of the marine diesel engine

4.1. Exhaust gas analyzers

Flue gas analyzers allow for accurate evaluation and analysis of exhaust fumes. These analyzers must be properly selected and used in accordance with the control tests. The exhaust gas analyzers can be distinguished [4, 8]:

- non-dispersive analyzers – mainly used to determine the content of carbon oxides and carbon dioxide in engines,
- flame-ionization – are used to analyze the concentration of hydrocarbons,
- chemiluminescence – allows the examination of the exhaust gas composition in terms of content NO_x.
- magnetic – in this case, the oxygen content tests in the exhaust gas are carried out.

5. Exhaust gas analysis

5.1. Methodology for determining the amount of air supplied to the fuel

The amount of air supplied to burn fuel is one of the most important factors affecting the actual course of the combustion process. The appropriate air content causes the fuel combustion process is complete. There are no harmful compounds in the exhaust.

In order to achieve complete and total combustion of fuel, the air supplied to the cylinder should be in excess. The theoretical amount of air is not enough due to the limited time of air flow through the combustion space and improper fuel grinding.

Excess air is determined by the excess air factor λ, which can be defined as the ratio of the amount of air supplied to the amount theoretically needed to completely burn fuel [11] and is determined by the equation:

$$\lambda = \frac{L}{L_t} \qquad (1)$$

where: L – the actual mass of dry air in which the fuel is burned, L_t – theoretical demand for dry air.

The excess air factor λ depends on the quality of the fuel and its fragmentation, the structure of the combustion space and the method of feeding fuel and air to the combustion space. It is closely related to total and incomplete combustion. As a result of the low coefficient λ, incomplete combustion of fuel occurs, which causes thermal losses. On the other hand, too high value of the excess air coefficient causes incomplete combustion resulting in an increase in the amount of heat. To determine the air excess coefficient λ, the formula (1) is used, which takes the form for incomplete combustion:

$$\lambda = \frac{21\%\ O_2}{21\%\ O_2 - U_{O2}} \quad (2)$$

where: U_{O2} – the amount of unburned air (oxygen), (21% O_2 – U_{O2}) – amount of air (oxygen) consumed during combustion.

The excess air ratio λ is calculated assuming that the amount of excess air is proportional to the measured proportion of oxygen in the exhaust gas. Under normal conditions, the molar ratio of oxygen in the air is 21%.

In order to analyze the composition of exhaust gases, it is necessary to use graphs showing the relationships between components of exhaust gases and illustrating the excess air ratio, among others Ostwald's chart. If the percentage chemical composition of the fuel is known (c% carbon, h% hydrogen, o% oxygen, s% sulfur in% nitrogen) and volume proportions of individual exhaust gas compounds (b% carbon dioxide, t% carbon monoxide, ns% nitrogen and os% oxygen), an equation for the balance of oxygen contained in the exhaust components and the air supplied for combustion may be used:

$$(1 + b)\cdot b + (0.605 + a)\cdot t + o_s = 21\% \quad (3)$$

where the fuel differentiator is defined by the formula:

$$a = 2.37\frac{h - 0.125(o - s)}{c} \quad (4)$$

The equation of the simplified percentage balance of exhaust gases is expressed by the formula:

$$b + t + 0_s + n_s = 100\% \quad (5)$$

The maximum percentage of carbon monoxide is calculated from the formula:

$$t_{max} = \frac{21}{0.605 + a} \quad (6)$$

6. Reduction of emission of harmful compounds in the exhaust gases

6.1. The primary method

The main feature of the primary method of reducing the emission of harmful compounds is to prevent the formation already during combustion in the combustion chamber [3].

This method intervenes in the fuel combustion process and requires engine design changes.

6.2. The secondary method

This method is based on purification of exhaust gases after the fuel combustion process. The advantage of these methods is better efficiency in the reduction of nitrogen oxides as opposed to primary methods.

One of the best and most effective methods is the method of selective catalytic reduction (SCR) [3].

7. Research on the laboratory test stand

The engine test stand is located in the laboratory engine room of the Maritime University of Gdynia. It is a diesel-electric unit consisting of an internal combustion engine cooperating with an electric generator. On the test stand it is possible to make a thermal balance of the engine and load characteristics. The stand has the UNITEST 201 diagnostic system, which enables electronic motor indication. It is also possible to analyze combustion and injection processes with simulated engine damage. Basic technical data are presented in Table 1.

Table 1. Characteristics of the SULZER 3AL25/30 engine

Engine manufacture	Metal Industry Works H. Cegielski
Type	3AL25/20
Current type	Variable
Electric voltage	400 V
Current frequency	50 Hz
Rotation speed	750 rev/min
Cylinder diameter	250 mm
Piston stroke	300 mm
Engine power	396 kW

The SULZER 3AL25/20 engine shown in Figure 1 is a four-stroke self-ignition diesel engine, charged with a VTR 160 Brown-Boveri turbocharger. The air supercharging and the lubricating oil are cooled by means of a water system. The pistons are cooled with lubricating oil.

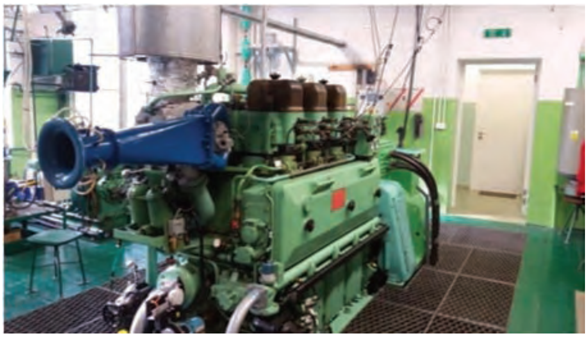

Fig. 1. SULZER 3AL25/30 engine

The UNITEST 201 diagnostic system is a computer engine monitoring system that is designed for continuous monitoring of motor and installation parameters.

The measurements were made for the following technical conditions of the engine:

- engine without damage at loads 50 kW, 120 kW, 200 kW,
- damaged injection pump no. 2 (reduced fuel dose) at loads 50 kW, 120 kW, 200 kW,
- damaged turbocharger – leakage in the intake system at loads 50 kW, 120 kW, 200 kW.

During the tests EURODIESEL fuel was used for diesel engines in accordance with the European PN-EN 590 standard. Fuel properties are shown in Table 2.

Indicator diagrams were made with each engine load and technical condition (they were not included in this article), as well as the exhaust gas composition test with the MRU 95/3CD exhaust gas analyzer was carried out.

Table 2. EURODIESEL fuel properties

No.	Parameters	Value	Unit
1.	Density in temp. 15°C	0.8287	g/cm^3
2.	Kinematic viscosity in temp. 40°C	2.789	mm^2/s
3.	Cetane number	51.0	–
4.	Solid impurities content	6	mg/kg
5.	Polycyclic aromatic hydrocarbons	0.5	%(m/m)
6.	Content of fatty acid esters	7.0	%(V/V)
7.	Calorific value of fuel	42657	kJ/kg
8.	Density of fuel	828.7	kg/m^3

8. Exhaust gases analyzer type MRU 95/3CD

The MRU 95/3CD type exhaust gas analyzer, shown in Fig. 2, is an electrochemical analyzer. It is mainly used in power plants, brickyards, laboratories, heating plants and in environments with high dustiness. The analyzer has such functions as:

- measurement of exhaust gas temperature up to 650°C,
- ambient temperature up to 100°C,
- content: O_2 in the range of 0–21%, CO in the range of 0–10000 ppm, NO_x in the range of 0–4000 ppm and SO_2 in the range of 0–2000 ppm.

Fig. 2. Exhaust gases analyzer type MRU 95/3CD

9. Principle of operation and description of the procedure for starting the exhaust gas analyzer

The MRU 92/3CD analyzer was used for testing emissions of toxic compounds in exhaust gases. The principle of operation of the flue gas analyzer consists in generating electricity as a result of chemical reactions of the gas with the electrolyte. The gas is introduced into the electrolyte through a diffusion membrane. After completing the gas reaction with the electrolyte, the generated current is transferred to two separate electrodes included in two electrochemical sensors. The material type of electrodes, electrolyte and membranes depends on the type of gas detected by the sensor. Measurement results can be sent to a computer or printed in a built-in printer.

The analyzer used during measurements consists of two suitcases (gas preparation system and analyzer), enabling its transport and probes together with gas sampling lines. Before starting the tests, the calibration of the measuring device should be performed, consisting in examining the air composition in the laboratory.

10. Test results

10.1. Oxygen content in the exhaust gases

The oxygen content in the exhaust depends on the engine load (Table 3). The higher load causes the amount of oxygen in the exhaust gas decreases for operational state and simulated damage, where for a good condition falls from 15% to 12.5%.

Table 3. The oxygen content in the exhaust gases

Oxygen (O_2)			
Engine load	50 kW	120 kW	200 kW
Engine without damage	15%	13.7%	12.5%
Damaged injection pump No 2	15.4%	13.9%	12.3%
Air outlet in the turbocharger	15.3%	13.3%	11.5%

For the damaged injection pump and turbocharger the amount of oxygen in the exhaust gas is higher compared to the normal state, but then also decreases respectively from 15.4% to 12.3% and from 15.3% to 11.5%.

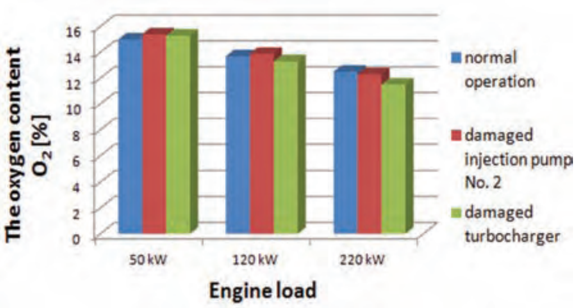

Fig. 3. The influence of the engine load on the oxygen O_2 [%] content indicated by the analyzer for various engine states

Figure 3 shows that the highest oxygen consumption occurs in the simulation of a damaged injection pump. The decreasing amount of oxygen is related to fuel consumption, which is lower for simulated malfunctions, for 50 kW and 120 kW, while for the largest load, i.e. 220 kW, the fuel consumption is at a similar level (Fig. 4).

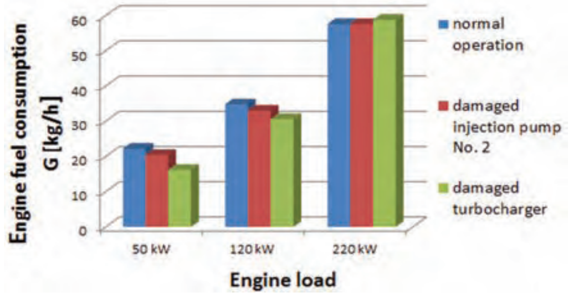

Fig. 4. Fuel consumption by a marine engine for three loads in different engine states

In addition, the composition of the fuel and air mixture affects the combustion process and the products of the combustion process. Depending on the conditions in which combustion takes place, complete and total combustion, incomplete and non-total combustion occur. Typically, due to imperfect combustion conditions, which will also occur in the event of engine damage, the products contain flammable substances, i.e. flammable gases in the case of incomplete combustion and solid combustible components in the case of non-total combustion [2, 3]. The essential toxic components of exhaust gases include: carbon monoxide (CO), unburnt hydrocarbons (HC) and nitrogen oxides (NO_x). In addition, PM particulate matter are also formed, mainly in self-ignition engines [4].

10.2. The carbon monoxide content in the exhaust gases

The content of carbon monoxide (CO) in the exhaust gas tends to increase with increasing load and for the normal state increases from 651 ppm to 1471 ppm (Table 4).

Table 4. The carbon monoxide content in the exhaust gases

Carbon monoxide (CO)			
Engine load	50 kW	120 kW	200 kW
Engine without damage	651 ppm	967 ppm	1471 ppm
Damaged injection pump No 2	773 ppm	1038 ppm	1653 ppm
Air outlet in the turbocharger	753 ppm	1137 ppm	2108 ppm

According to what was written above, the state of disability is conducive to the formation of incomplete combustion components, which include carbon monoxide. For example, for a damaged injection pump, the amount of carbon monoxide was more than 200 ppm higher than for a normal state at the same load.

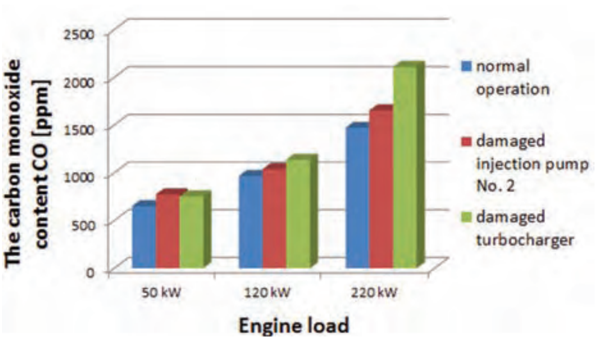

Fig. 5. The influence of engine load on the carbon monoxide CO [ppm] content indicated by the analyzer for various engine states

However, for the damaged turbocharger the increase in carbon monoxides was almost threefold (Fig. 5). Such results clearly indicate the occurrence of damage to engine components.

10.3. The nitrogen oxides content in the exhaust gases

As in previous cases, the increase of nitrogen oxides (NO_x) in the exhaust gases is caused by the increase in engine load (Table 5) and additionally by the higher and higher exhaust gases temperature.

Table 5. The nitrogen oxides content in the exhaust gases

Nitrogen oxides (NO_x)			
Engine load	50 kW	120 kW	200 kW
Engine without damage	700 ppm	1130 ppm	1201 ppm
Damaged injection pump No 2	820 ppm	1179 ppm	1271 ppm
Air outlet in the turbocharger	842 ppm	1289 ppm	1362 ppm

The increase in temperature is influenced by both the increasing load and the states of engine failure. In addition, it can be seen (Fig. 6) that damage to the turbocharger has a greater influence on the increase of this temperature than the faulty injection pump.

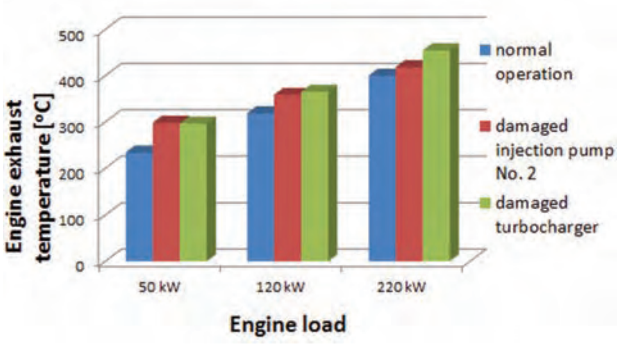

Fig. 6. Engine exhaust temperature 3AL25/30

The graph presented in Figure 7 shows that a larger impact on the growth of nitrogen oxides has a damaged turbocharger than an injection pump, i.e. similar to an increase in the exhaust gas temperature.

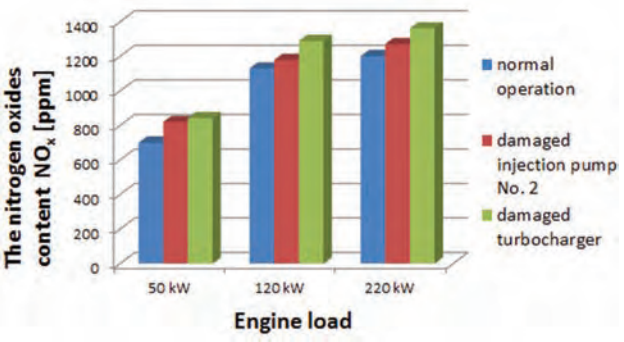

Fig. 7. The influence of engine load on the content of nitrogen oxides NO_x [ppm] indicated by the analyzer for various engine states

Engine failure conditions also affect the increase of nitrogen oxides and for example at 200 kW, the content of this compound increased from 1201 ppm to 1271 ppm for a damaged pump and up to 1362 ppm for turbocharger malfunctions.

10.4. The carbon dioxide content in the exhaust gases

As for the content of carbon dioxide in the exhaust, it also increases depending on the load increase, but compared to other states, there are no such differences (Table 6).

Table 6. The carbon dioxide content in the exhaust gases

Carbon dioxide (CO_2)			
Engine load	50 kW	120 kW	200 kW
Engine without damage	4.3%	5.3%	6.2%
Damaged injection pump No 2	4%	5.1%	6.3%
Air outlet in the turbocharger	4.4%	5.6%	6.9%

These similar values may be due to the fact that there is a greater increase in carbon monoxide as a result of incomplete combustion. On the other hand, imperfect combustion conditions affect the level of carbon dioxide, which has not been created as much as in the case of complete combustion (Fig. 8).

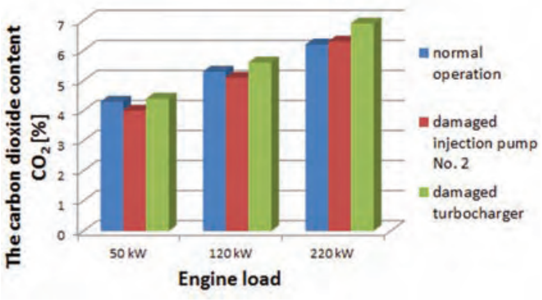

Fig. 8. The influence of engine load on the content of carbon dioxide CO_2 [%] indicated by the analyzer for various engine states

11. Conlusions

The aim of the research was to assess the technical condition of the 3AL25/30 marine engine based on the analysis of the exhaust gases chemical composition. After analyzing the obtained results, it can be concluded that after using simulated malfunctions of the 3AL 25/30 engine, we get different results, which indicate the inefficiency of the combustion engine operation. It follows that the analysis of the exhaust gas composition can be used to assess the technical condition of the engine. The content of each of the compounds contained in the exhaust gases clearly differed in the states of disability in comparison to the normal state, i.e. there was a noticeable increase in the proportion of particles in the exhaust gases depending on the engine failure and load. The composition of the exhaust gases is affected by the pressure and temperature in the combustion chamber, and thus the engine load.

The flue gas analyzer also has the option of measuring the sulfur dioxide content. However, due to the fact that the marine engine was powered by marine diesel oil (MDO), which does not contain sulfur in the chemical composition, no readings of this compound were made.

The obtained results allow to evaluate this state, nevertheless marine engine diagnostics based on analysis of the composition of the exhaust gases during operation of the vessel is rarely used. In order to have a full spectrum of the technical condition of the engine, it is necessary to compare these results with fuel consumption, exhaust gas temperature, as well as with engine indicator diagrams made simultaneously with the exhaust composition measurements. Such graphs were made during the research, but they were not included in the article.

Nomenclature

C_nH_m	hydrocarbons	O_2	oxygen
CO	carbon monoxide	PM	particulate matter
CO_2,	carbon dioxide	RCHO	aldehydes
DO	diesel oil	SCR	selective catalytic reduction
NO_x	nitrogen oxides	SO_x	sulphur oxides

Bibliography

[1] BOCHEŃSKI, C., JANISZEWSKI, T. Diagnostyka silników wysokoprężnych. *Wydawnictwa Komunikacji i Łączności*. Warszawa 1996.

[2] BORKOWSKI, T. Emisja spalin przez silniki okrętowe. *Fundacja Rozwoju Wyższej Szkoły Morskiej w Szczecinie*. Szczecin 1999.

[3] GIERNALCZYK, M. Metody redukcji emisji do atmosfery związków toksycznych oraz CO_2 przez statki. *Logistyka*. 2014, **6**, 655-665.

[4] GOLA, M., JANUŁA, J., LITWIN, J. Laboratorium Silników Spalinowych: Red. A. Kowalewicz. *Wydawnictwo Politechniki Radomskiej*. Radom 1996.

[5] KLUJ, S. Diagnostyka urządzeń okrętowych. *Studium Doskonalenia Kadr S.C. Wyższej Szkoły Morskiej*. Gdynia 1995.

[6] KOŁWZAN, K., ADAMKIEWICZ, A. Zapobieganie zanieczyszczeniu powietrza przez statki w świetle najnowszych wymagań Załącznika VI do Konwencji MARPOL. *Zeszyty Naukowe Akademii Morskiej w Szczecinie*. 2009, **18**(90), 66-70.

[7] KOWALSKI, J. Ocena stężenia tlenków azotu w gazach wylotowych silnika okrętowego za pomocą sztucznej sieci neuronowej. *Zeszyty Naukowe Akademii Morskiej w Gdyni*. 2009, **60**, 73-83.

[8] MERKISZ, J. Ekologiczne problemy silników spalinowych. Tom I. *Wydawnictwo Politechniki Poznańskiej*. Poznań 1998.

[9] USTRZYCKI, A. Laboratorium silników spalinowych. Ocena procesu spalania na podstawie wykresu indykatorowego. *Wydawnictwo Politechniki Rzeszowskiej*. Rzeszów 2011.

[10] WITKOWSKI, K. Stan diagnostyki technicznej okrętowych silników tłokowych. *Diagnostyka*. 2005, **34**, 85-92.

[11] PIOTROWSKI, I., Witkowski K., Okrętowe silniki spalinowe. *Trademar*. Gdynia 2003.

Rafał Krakowski, DEng. – Faculty of Marine Engineering, Gdynia Maritime University.
e-mail: *r.krakowski@wm.umg.edu.pl*

Article citation info:
LESIAK, K., BRZEZANSKI, M., PROSTANSKI, D. Concept of using the heat pipes in the heat exchanger of diesel engine exhaust system intended for use in potentially explosive atmospheres. *Combustion Engines*. 2019, **177**(2), 127-131. DOI: 10.19206/CE-2019-222

Krzysztof LESIAK
Marek BRZEZANSKI
Dariusz PROSTANSKI

CE-2019-222

Concept of using the heat pipes in the heat exchanger of diesel engine exhaust system intended for use in potentially explosive atmospheres

Limiting the temperature of exhaust gases to below 150°C is one of the necessary conditions for diesel engine to be used in a potentially explosive atmosphere. For this purpose heat exchangers are necessary to be used. This article presents the concept of exchanger in which heat pipes are used to transport thermal energy from the exhaust gases to the cooling medium.

Key words: *exhaust system, heat exchanger, heat pipes, temperature of exhaust gases, hard coal mining*

1. Introduction

Operation of diesel engines in the areas threatened by methane and/or coal dust explosion hazard is possible only after meeting the required technical conditions [1, 3, 4, 13]. Limitation of surface temperature as well as temperature of exhaust gases below 150°C are among these conditions. Diesel engines used in the areas threatened by explosion hazard most frequently have the useful power within the range from 80 to 160 kW [5]. As the heat transported with exhaust gases is similar to the heat transformed into useful work [8], it is necessary to collect big amount of energy from exhaust gases and then to dispersed it or to recuperate it [7].

Different types of the heat exchangers e.g. those described in [3, 6] are used to reduce exhaust gases temperature.

Air quality i.e. emission of pollutants by diesel drives is the other especially important aspect. In 2016 the Regulation of the European Parliament and of the Council [12] on the accepted level of harmful substances emission by mobile machines operating in a potentially explosive atmospheres was issued. The requirements can be compared with the requirements of stage IIIA of the diesel engine directive repealed by this regulation [11]. For the reasons described in [1, 3], diesel engines used so far by the Polish manufacturers meet the requirements of the repealed directive [11]. in the scope of the stage II and in some cases the stage IIIA.

To improve the quality of exhaust gases emitted to a potentially explosive atmosphere, the concept of outlet system, described in [3] was suggested. This article is focused on the concept of heat exchanger based on heat pipes and/or thermosiphon pipes.

2. Heat pipes and thermosiphon pipes

Heat pipe is a passive device of a very long lifetime [14]. Generally the heat pipe is a vacuum, tightly closed thin-wall pipe filled with capillary structures, so called wick, and partially with the working fluid. Heat pipes have a very high heat transfer coefficient from 10 000 to 100 000 W/mK comparing to 400 W/mK for copper [21]. They use two-stage, close evaporation circuit and then condensation of the working fluid. The following three zones can be distinguished in a heat pipe:

- evaporation zone – heat is delivered to this zone and evaporation of working fluid takes place,
- adiabatic zone – where there is a heat transportation between evaporation zone and condensation zone without heat exchange to atmosphere,
- condensation zone – where heat from vapour is transferred to pipe outer space, so the vapour is condensed. The condensed fluid returns to the evaporator through the wick structure by capillary action.

The phase change processes and two-phase flow circulation continue as long as the temperature gradient between the evaporator and condenser is maintained.

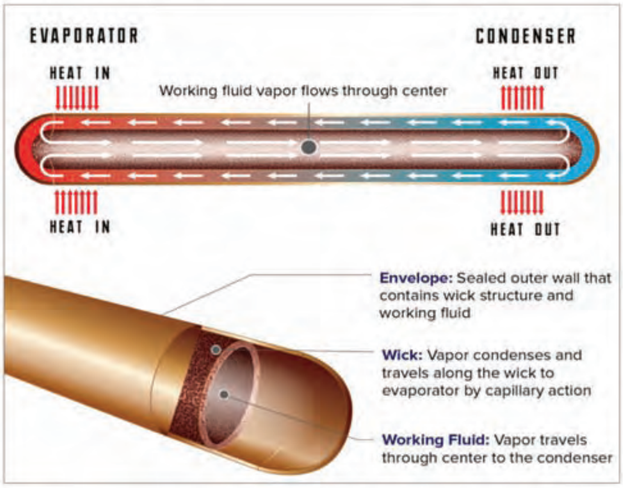

Fig. 1. Illustration of heat pipe operation [21]

Temperature range in which the heat pipes operate properly as well as their lifetime depend on a type of working fluid used and the envelope. In Table 1 sample fluids and the respective operational temperature ranges are given.

Use of heat pipes in place of homogeneous heat conductors (rods), allows to limit the dimensions and mass of heat exchangers. For instance, a heat pipe of a diameter 6 mm, length 30 cm, at temperature difference of 3°C can transfer 180 W of heat. To achieve the same effects using a homogeneous copper pipe of the same length, its diameter would have to be 24.4 cm and the weight would be around 125 kg [10].

Table 1. Working fluid with practical temperature limits [19]

Operating min temp., °C	Operating max temp., °C	Working fluid
–271	–269	Helium
–170	0	Ethane
–150	40	Propylene
–60	~ 25 to 100	Methanol
–50	~ 100	Acetone
20	280, short term to 300	Water
100	350	Naphthalene
200	300	Dowtherm A/Therminol VP
200	400	AlBr3
400	600	Cesium
500	700	Potassium
600	1100	Sodium
1100	1825	Lithium

Thermosyphons are one of different types of heat pipes [23]. Unlike the heat pipes, which, due to the capillary structure (wick), can work at any orientation [24], thermosiphons use gravity at the return of the condensed liquid in the condenser zone. For this reason, the evaporator zone must be located below the condenser zone.

The above feature of thermosiphons may be treated as their disadvantage, however, it should also be borne in mind that by changing the orientation of a heat pipe with a wick, its possibilities in terms of the amount of transported heat change as well. The highest efficiency of the heat pipe is achieved in vertical operation when the evaporation zone is below the condenser zone. Then the return of condensed working medium from the condenser zone to the evaporator zone, in addition to the capillary forces, is supported by the force of gravity.

The superiority of thermosiphons over heat pipes should primarily include the fact that they are able to transfer higher thermal power while maintaining the same diameter, and that their length can be almost unlimited – a typical heat pipe length is < 25 cm, while for geothermal applications thermosyphons with a length of more than 50 m are manufactured [24].

3. Concept of an exhaust system and a heat exchanger for the mining diesel drive

It is suggested to use diesel oxidation catalyst (DOC) and a diesel particulate filter (DPF) to improve quality of exhaust gases. Thanks to the use of the DOC reactor, a significant reduction of CO and HC concentrations in exhaust gases is expected (> 90%) [2].

In order to meet the safety requirements related to meeting the surface temperature limit of 150° C, it is necessary to equip the reactor with a water jacket. On the other hand, cooling the reactor surface can reduce the efficiency of the DOC reactor. For this reason, it is suggested to apply additional air insulation between the surface of the reactor and the water jacket (Fig. 2).

The heat exchanger concept using heat pipes (Fig. 3) provides using two separate sections: the exhaust section and the cooling water section. Heat transfer between the sections will be mainly through heat pipes / thermosiphons. Due to the fact that heat pipes obtain the highest efficiency at operation, where the evaporator part is located below the condenser part, the exhaust section is provided below the cooling water section. To increase the area of heat transfer from exhaust gases, lamellas (radiators) will be placed on the pipes. In order to achieve greater efficiency in heat transfer from exhaust gases, the stream of exhaust gas and cooling water will be directed countercurrently.

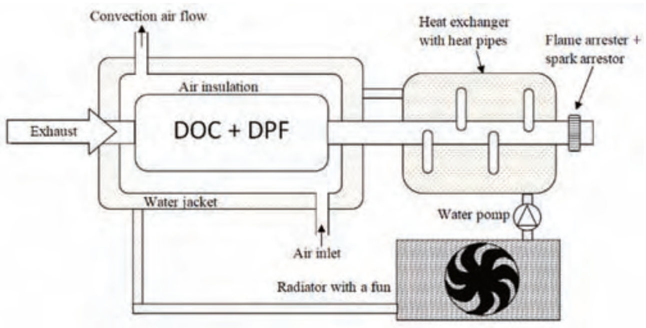

Fig. 2. Exhaust system concept with an aftertreatment system, adapted to operate in potentially explosive atmospheres

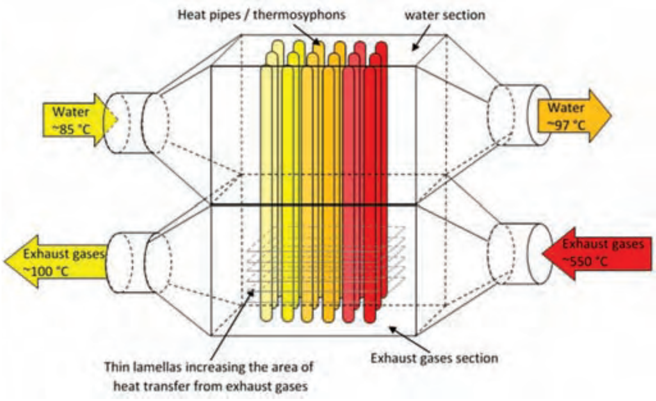

Fig. 3. Heat exchanger concept using heat pipes/thermosyphons

Number of heat pipes required for construction of the heat exchanger cooperating with an engine of maximum power 80 kW was assessed within the project. It was assumed the for maintaining the safety coefficient, exhaust gases should be cooled down to temperature 100°C (instead of limit value equal to 150°C). Heat conveyed with exhaust gases can be calculated according to the following formula:

$$Q_W = (G_F + G_A)\, c_p\, (T_H - T_L) \tag{1}$$

where GF – fuel consumption per hour, GA – air consumption per hour, c_p – specific heat of exhaust gases, T_H – temperature of hot gases, T_L – ambient temperature

Basing on [5], for determination of heat conveyed with the exhaust gases, it was assumed that $Q_e \approx Q_W$ (Q_e – heat converted to the useful work). Temperature increase is an expected result of using the catalytic reactor in the discussed concept of exhaust system. It was assumed that temperature increase would be not greater than 80°C [9]. Impact of temperature increase on amount of heat conveyed with exhaust gases will be compensated by an assumption that the gases will be cooled down to 100°C and not to ambient temperature – constant temperatures T_H and T_L does not affect Q_W in formula (1).

Finally it was assumed that $Q_e \approx Q_W$ and for the discussed engine of maximum useful power ~ 80 kW, it was assumed that power which should be taken from exhaust gases to reduce gases temperature to 100°C is Q_{Wmax} = 80 kW.

Expected maximum temperature of exhaust gases is 550°C. Taking into account the fact that heat pipes operate in limited temperature range (Table 1), to cover the required temperature range from 100°C to 550°C, different types of heat pipes should be used. For the discussed case, the heat pipes filled with the following liquids: Water, Naphthalene, $AlBr_3$ (Aluminium bromide) and Caesium were selected. Most often, heat pipes manufacturers inform about the maximum conveyed power only for one engine operating point. Additionally, the available data relate only to the heat pipes filled with water or methanol. For the above reasons, the characteristics that can be obtained using the calculator for heat pipes filled with water of one of the manufacturers [22] was used for further analyses. Characteristics of heat pipe of length 400 mm, diameter ½", length of evaporator and condenser equal to150 mm, operating in a vertical position, where the evaporator zone is below the condenser zone, is presented in Fig. 4.

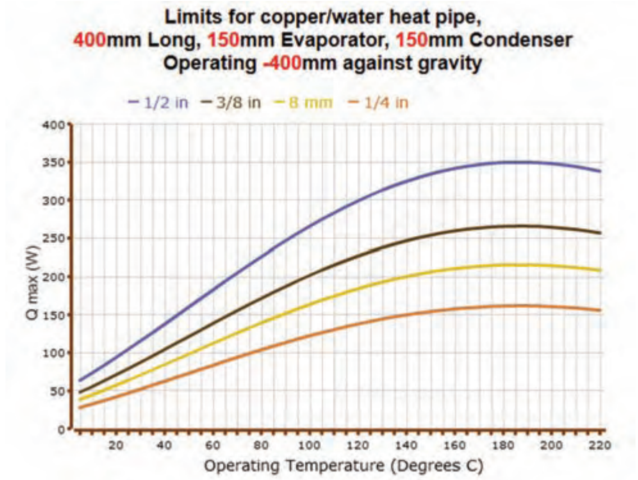

Fig. 4. Curve Q_{max} = f(operating temperature) for a water heat pipe [22]

The above characteristics are not available for the heat pipes other than water filled ones. But, for Intermediate Temperature heat pipes the characteristic given in Fig. 5 is available.

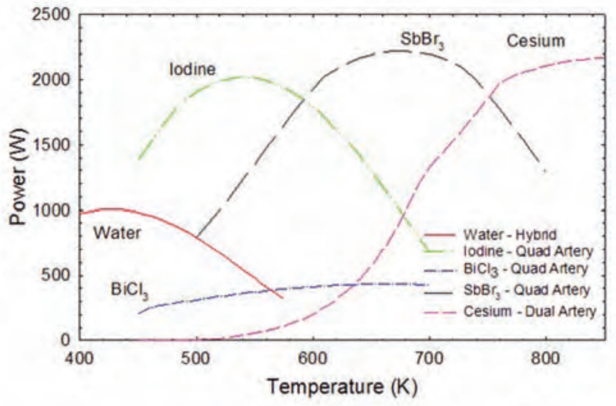

Fig. 5. Theoretical heat pipe power for different fluids [20]

Considering the fact that in the case of intermediate temperature heat pipes, the transferred power is greater than for a heat pipe filled with water, for the discussed range of operating temperatures and each of the selected heat pipes has a similar range of operation, it was assumed that for the same geometric dimensions (diameter, total length as well as size of each heat pipe zone) having an impact on transferred power, ability in heat transfer will be similar.

By transposition of the characteristics from Fig. 4 (for the pipe ½") to the pipes filled with naphthalene, $AlBr_3$ and Caesium within the operating temperatures as in Table 1, we obtain a family of characteristics presented in Fig. 5. Part of the characteristics delivered by the manufacturer [22] is drawn by a solid line. As the characteristics delivered by the manufacturer was limited to 220°C and the manufacturer in his information material accepts possibility of using this pipe to temperature 280°C (Table 1), further part of this characteristics was extrapolated using the polynomial degree 2. Extrapolated part of the characteristics for a water pipe is presented as dashed line. The relationships for other pipes were also determined by extrapolation and they were also presented as dashed lines.

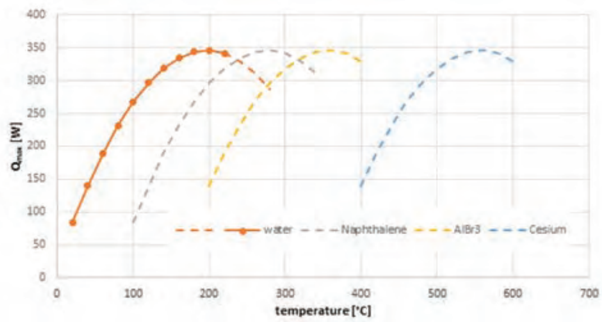

Fig. 6. Curves Q_{max} = f(operating temperature) for analysing the type of working fluid

Basing of the above figure, transferred heat power was assumed depending on temperature range given in Table 2 – for the safety reason heat power values lower than those resulting from the characteristics were accepted.

Table 2. Transferred heat power depending of the working fluid and operating temperature range accepted for the analysis

T_1 [°C]	T_2 [°C]	Working Fluid	Q [W]
100	150	Water	250
150	220	Water	300
220	300	Naphthalene	300
300	400	AlBr3	300
400	480	Caesium	150
480	550*	Caesium	300

* – maximum temperature of exhaust gases

Due to the fact that information on fuel burning process and air demand for the discussed engine, the product $(G_F + G_A) * c_p$ was determined from the following relationship:

$$\left.\begin{array}{l} Q_w = (G_F + G_A) \cdot c_p \cdot (T_H - T_L) \\ Q_w = 80\ \text{kW} \\ T_H = 550°\text{C} \\ T_L = 100°\text{C} \end{array}\right\}$$

$$(G_F + G_A) \cdot c_p = 178\ \mathrm{W/°C} \qquad (2)$$

To estimate the power which should be taken from exhaust gases in each temperature range given in Table 2, the following formula was used:

$$Q_{wi} = 178\,(T_2 - T_1) \qquad (3)$$

where T_2 and T_1 – higher and lower temperature for the i^{th} temperature range from Table 2.

From the product of heat (Q_{wi}), which should be transferred in the given temperature range as well as from heat which can be transferred by a single pipe (Q_{hp1}), minimum number of required pipes was calculated. Calculation results are given in Table 3.

Table 3. Calculation results

Working Fluid	T_2 [°C]	T_1 [°C]	Q_{Wi} [W]	Q_{hp1} [W]	Q_{Wi} / Q_{hp1} [pcs.]
Caesium	550	480	12444	300	42
Caesium	480	400	14222	150	95
AlBr3	400	300	17778	300	60
Naphthalene	300	220	14222	300	48
Water	220	150	12444	300	42
Water	150	100	8889	250	36
Total			80000		323

Q_{hp1} – assume power of a single heat pipe in the given temperature range [W]

Q_{Wi} / Q_{hp1} – number of pipes of the given type [pcs]

4. Safety

Safety is the most important aspect, especially in the underground coal mining industry. In connection with the above, the safety solutions should be taken into account. Heat pipes do not pose any danger if proper operate. However, in the risk analysis, also emergency states should be considered. This is particularly important for the pipes where substances such as water are used as a working fluid. Unsealing of the tube, e.g. as in a result of vibrations during operation is the main risk that can happen. As a result of leakage of the tube, the working fluid may escape to the atmosphere if the leakage is in the exhaust section, and / or to the cooling medium, if the leakage is in the water section. Hazard statements being a part of Globally Harmonized System of Classification and Labelling of Chemicals (GHS) [16] are used for assessment of hazards resulting from chemical substances or their mixtures. In Table 4, the hazards posed by each working fluid used in the discussed heat pipes, are listed.

Table 4. Type of hazards for each working fluid

Working Fluid	Hazards
Caesium [15]	H260 – During a contact with water self-ignited flammable gases are released. H314 – Causes a serious skin burns and injuries to eyes.
AlBr3 [18]	H314 – Causes a serious skin burns and injuries to eyes. EUH014 – Reacts violently with water. In the result of hydrolysis, HBr is released.
Naphthalene [17]	H228 – flammable in the solid state H410 – Is very toxic to water organisms, causing long-lasting effects.

5. Conclusions

The article presents the concept of exhaust gases outlet system. The expected benefits of the presented concept are as follows:

- significant reduction of CO, HC emission with exhaust gases (> 90%),
- smaller dimensions of the heat exchanger used for cooling the exhaust gases,
- lower weight of the entire exhaust system.

Heat pipes have much greater heat transfer power comparing to solid conductors of the same dimensions. This is why their use is a very attractive option in relation to the current solutions.

For the safety reason, use of the pipes filled with other fluid than water, exclude them from using in underground mine workings.

In further research work the analysis of using the water-filled heat pipes to increase the efficiency of the currently used heat exchangers, e.g. for dissipation of the coolant heat, is considered.

The use of thermosiphons instead of the analysed heat pies enables a reduction in the number of the required pipes.

Due to the lack of characteristics of power transferred in heat pipes and thermosiphons in a function of temperature, further tests are planned to determine them.

Bibliography

[1] DOBRZENIECKI, P. Dostosowanie silnika spalinowego z układem wtryskowym common rail górniczej maszyny roboczej do obowiązujących wymagań i przepisów. *Maszyny Górnicze*. 2016, **3**, 45-53.

[2] KRUCZYŃSKI, S., DANILCZYK, W. Ograniczanie szkodliwości gazów wylotowych silników spalinowych poprzez zastosowanie reaktorów katalitycznych. *MOTROL*, 2007, **9**, 93-102.

[3] LESIAK, K., BRZEZANSKI, M. Concept of the exhaust system of combustion engines used in underground mining. *Combustian Engines*. 2017, **169**(2), 97-100. DOI: 10.19206/CE-2017-217

[4] PIECZORA, E., DOBRZANIECKI P. About requirements for diesel drives used in hard coal mine underground workings. *Minig – Informatics, Automation And Electrical Engineering*. 2018, **2**, 31-48.

[5] PIECZORA, E., DOBRZANIECKI, P., KACZMARCZYK, K., SUFFNER, H. Rozwój dołowych maszyn transportowych z napędem spalinowym. *Maszyny Górnicze*. 2016, **2**, 20-33.

[6] SUFNER, H. Chłodzenie spalin w górniczych napędach spalinowych dla kopalń węgla kamiennego. *Maszyny Górnicze*. 2018, **3**, 67-80.

[7] ŚWIDER, J., WOSZCZYŃSKI, M., STANKIEWICZ, K. Integracja i zarządzanie działaniem źródeł i odbiorników prądu w pojazdach z układami rekuperacji energii cieplnej. *Maszyny Górnicze,* 2013, **4**, 10-19.

[8] WALENTYNOWICZ, J. Wyznaczanie bilansu cieplnego silnika spalinowego o zapłonie samoczynnym. *Biuletyn WAT VOL. LV.* 2006, **2**, 265-277.
[9] LEPREUX, O. Model-based temperature control of a diesel oxidation catalyst. *Mathematics. Ecole Nationale Sup´erieure des Mines de Paris*. 2009.
[10] YUNUS CENGEL, A. Heat transfer – a practical approach, *Mcgraw-Hill*, 2nd edition, 2002.
[11] Commission Directive 2012/46/EU of 6 December 2012 amending Directive 97/68/EC of the European Parliament and of the Council on the approximation of the laws of the Member States relating to measures against the emission of gaseous and particulate pollutants from internal combustion engines to be installed in non-road mobile machinery.
[12] Regulation (EU) 2016/1628 of the European Parliament and of the Council of 14 September 2016 on requirements relating to gaseous and particulate pollutant emission limits and type-approval for internal combustion engines for non-road mobile machinery, amending Regulations (EU) No 1024/2012 and (EU) No 167/2013.
[13] EN 1679-1:1998+A1:2011 Reciprocating internal combustion engines. Safety. Compression ignition engines.
[14] https://www.1-act.com/innovations/heat-pipe-materials-working-fluids-and-compatibility/?hilite=%27luiqid%27%2C%27material%27
[15] https://en.wikipedia.org/wiki/Caesium
[16] https://en.wikipedia.org/wiki/GHS_hazard_statements
[17] https://en.wikipedia.org/wiki/Naphthalene
[18] https://pl.wikipedia.org/wiki/Bromek_glinu
[19] https://www.1-act.com/compatible-fluids-and-materials/
[20] https://www.1-act.com/innovations/heat-pipe-materials-working-fluids-and-compatibility/intermediate-temp-heat-pipes/
[21] https://www.1-act.com/innovations/heat-pipes/
[22] https://www.1-act.com/resources/heat-pipe-calculator/
[23] https://www.1-act.com/resources/heat-pipe-fundamentals/different-types-of-heat-pipes/
[24] https://www.1-act.com/resources/heat-pipe-fundamentals/different-types-of-heat-pipes/thermosyphons/

Krzysztof Lesiak, MEng. – KOMAG Institute of Mining Technology.
e-mail: *klesiak@komag.eu*

Prof. Dariusz Prostański, DSc., DEng. –KOMAG Institute of Mining Technology.
e-mail: *dprostanski@komag.eu*

Prof. Marek Brzeżański, DSc., DEng. – Faculty of Mechanical Engineering, Cracow University of Technology.
e-mail: *mbrzez@pk.edu.pl*

Article citation info:
LABECKAS, G., SLAVINSKAS, S., MICKEVICIUS, T., KREIVAITIS, R. Tribological study of high pressure fuel pump operating ethanol-diesel fuel blends. *Combustion Engines*. 2019, **177**(2), 132-135. DOI: 10.19206/CE-2019-223

Gvidonas LABECKAS
Stasys SLAVINSKAS
Tomas MICKEVIČIUS
Raimondas KREIVAITIS

CE-2019-223

Tribological study of high-pressure fuel pump operating with ethanol-diesel fuel blends

This paper presents comparative experimental study's results of ethanol-diesel fuel blends made effects on operational properties of a high-pressure fuel pump of a common rail injection system. The two identical fuel injection systems mounted on a test bed of the fuel injection pumps were prepared for the experimental durability tests. The lubricity properties of ethanol-diesel fuel blends E10 and E20 blends were studied using a four-ball tribometer. The test results showed that long-term (about 100 hours) using of ethanol-diesel blends produced a negative effect on the durability of the high-pressure fuel pump. Due to the wear of plunger-barrel units the decrease in the fuel delivery rate occurred of about 39% after the 100 h of continuous operation with ethanol-diesel fuel blends. The average friction coefficients of ethanol-diesel fuel blend E10 was lower than that of the normal diesel fuel. After the 100 hours of operation with ethanol-diesel fuel blend E10, the measured wear scar diameter was 10% higher than that of a fossil diesel fuel.

Key words: *diesel fuel, ethanol-diesel fuel blends, lubricity, four ball test rig, plunger-barrel units, wear scar diameter*

1. Introduction

In the recent decades, the scientists continue to work on the rational global energy using as well as urgent ecological and environmental problems. The requirements stated by the EU parliamentarians to intensify the development of renewable energy sources, strict environmental requests associated with the reduction of greenhouse gas emissions and wastes in the municipal economy, agricultural and forestry sectors encourage the researchers to investigate alternative and renewable energy strategies including a wider use of biofuels. Up to now, the researchers have not offered new technological solutions that would completely replace internal combustion engines by other mechanical energy sources. For this reason, oil and the natural gas reserves rapidly decrease over the recent decades. Moreover, smoke and exhaust emissions produced by internal combustion engines cause serious damage to the ecological system.

Agriculture and transport sectors are among the largest fossil fuel consumers and therefore can be regarded as the biggest contributors to the environmental pollution. The mineral diesel fuel traditionally remains the most popular among the others motor fuels. Consumption of the diesel fuel has been growing steadily over the last two decades.

The physical properties of the fuel such as density, viscosity and bulk modulus of compressibility affect the delivery rate and the injection characteristics and thus the quality of the air and the fuel mixture, which in turn affects the combustion process, brake thermal efficiency and the ecological parameters of the diesel engine. Specific properties of alternative and renewable biofuels such as density, viscosity, calorific value, cetane number, freezing point, etc. differ from those of the normal diesel fuel. Mixing diesel fuel with ethanol or other alcohols reduces viscosity of the blend [1]. In case the viscosity of biofuels (ethanol) is too low, this can result in more intensive wear of plunger-barrel and the needle-valve-nozzle units. The fuel injection systems for Euro 6 and beyond will have to generate extremely high fuel injection pressures and controlled injection events to meet the strictest legislations associated with engine out emissions [2]. A higher boiling point and aromatic, nitrogen, and sulphur contents appear to improve lubricity of the diesel fuel [3].

The three main methods can be using to measure the lubrication properties of the fuel: the High Frequency Reciprocating Rig (HFRR), Scuffing Load Ball On Cylinder Lubricity Evaluator (SLBOCLE) and the four-ball test machine method [4].

The scientists conducted the lubricity studies of ethanol and the diesel fuel by using HFRR method. They found that ethanol addition of up to 14% (v/v) to diesel fuel meets the EN 590 standard requirements and thus has minor effect on the values of the average Wear Scar Diameter (WSD) [5]. The limits of diesel lubricity standards of the wear scar are established as 460 and 520 µm. The others authors showed that the wear scar diameter for diesel fuel is lower, while for the blend with ethanol is higher [6]. In contrast to other studies the authors reported that the addition of ethanol assisted to improve lubricity of the diesel fuel [8]. The results of these studies show that there is no consensus on the effect of ethanol on the fuel lubricity and reliability of fuel injection systems.

When the amount of ethanol in the diesel fuel is increased, the cetane number (CN) is decreased proportionally. However, the auto-ignition delay period for diesel fuel, especially synthetic biofuel, does not always directly depend on the cetane number value [7–9]. The auto-ignition delay depends on chemical composition and physical properties of the fuel as well as on gas maximum pressure and the temperature inside the combustion chamber. Significant influence on the ignition delay also provide such factors as the shape of combustion chamber, compression ratio, chemical structure of the fuel and the fuel injection characteristics that affects the quality of combustible mixture and the temperature variations prior to TDC during the compression stroke.

The calorific value of ethanol is lower than that of the diesel fuel. When alcohols are added to diesel fuel, net heating value of the blend decreases and the brake specific fuel consumption increases [1, 7–9]. Actually, application oxygenated additives in the diesel fuel results in relatively higher brake specific fuel consumption, slightly higher brake thermal efficiency of an engine operating in the most common load and speed conditions. The increased brake thermal efficiency of an engine can be attributed to the fact that the fuel-bound oxygen provides an essential help in burning the fuel completely during the diffusive combustion phase. Ethanol added to diesel fuel considerably reduces flash point of the blend and increases the possibility to catch a fire. Ethanol solubility in the diesel fuel depends on the hydrocarbon composition of the fuel, temperature, content of water and wax in the blend and ambient humidity [8].

Authors of the studies [7–9] noted that using of ethanol and other oxygenated additives reduces the amount of nitrogen oxides in the exhaust gases due to lower combustion temperature of biofuel blends and higher overall relative air/fuel ratio. The amount of total unburned hydrocarbons in exhaust gases depends on engine load and has tendency to increase with increasing ethanol content of the fuel. Ethanol added to diesel fuel has the potential to reduce the production of carbon monoxide, but higher than the 4–5 wt% ethanol-oxygen content may result in higher CO emissions when running a fully loaded engine at the high speed of 2200 rpm [7].

However, the long-term impact of ethanol-diesel fuel blends with relatively lower density, viscosity and lubricity properties on the reliability of a Common Rail Direct Injection (CRDI) system remains unexplored to a greater degree of extension and thus requires specific experimental tests. The aim of the research is to investigate the effect of bioethanol on the durability of the main components of a high-pressure common rail fuel pump.

2. Materials and methods

The experimental investigation was carried out in the fuel systems testing laboratory at Power and Transport Machinery Engineering Institute, Faculty of Agricultural Engineering of Vytautas Magnus University – Agricultural Academy.

The common rail injection system has been used for the experimental tests. The principal arrangement of the test stand, equipment and apparatus are shown in Fig. 1.

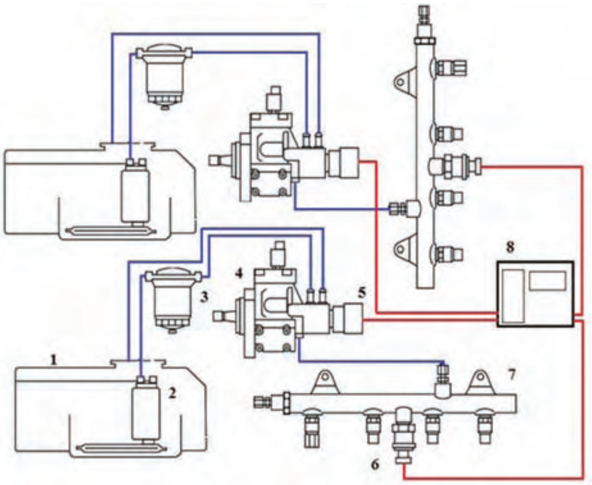

Fig. 1. Scheme of the testing stand: 1 – fuel tank; 2 – fuel supply pump; 3 – fuel filter; 4 – high-pressure pump; 5 – pressure control valve; 6 – rail-pressure sensor; 7 – fuel rail; 8 – fuel pressure control

The two Bosch-type high-pressure fuel pumps were connected by the same belt driven in the same mode at speed of 1000 rpm. The electric delivery pump (2) mounted in the fuel tank (1) supplied the fuel through the fine-porous fuel filter (3) to the high-pressure fuel pump (4). Moreover, both fuel pumps maintained the changeable pre-set pressure values depending on the on-going time of every 30 minutes. Powered by an electrical motor, the high-pressure fuel pumps operated continuously to build up the needed injection pressure, which was retained in the volume of the fuel accumulator (7). The pressure was adjusted via a pressure regulator (5) connected to the control unit (8). The sensor installed in the pressure accumulator transferred the resulting signals to the control unit to evaluate the present fuel pressure.

The fuel-flow was cooled in order to assure that the temperature does not exceed the 35°C during the reliability tests of the fuel pumps.

The changes in the fuel delivery rates determined for the various pressure values built up by both fuel pumps at the very beginning (0 hours) of the experiments are illustrated by the columns in Fig. 2.

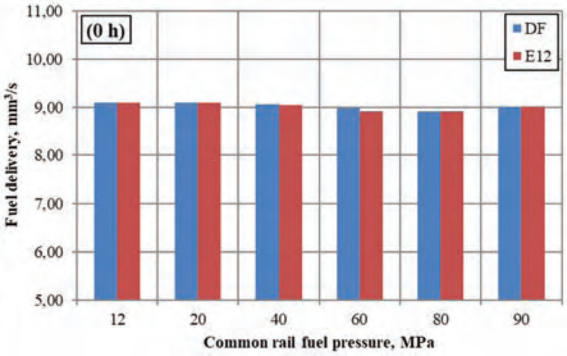

Fig. 2. Changes in a high-pressure pump's fuel delivery rate as a function of fuel pressure built up by a common rail injection system for the beginning of experiments (at zero hours of operation)

Diesel fuel (DF) and the three ethanol-diesel fuel blends E10, E12 and E20 have been used for the experimental tests. The main properties of the tested fuels are listed in Table 1.

Lubricating properties of the fuels were determined by using the four-ball test machine shown in Fig. 3 [4, 5].

Table 1. Properties of the tested fuels

Parameter	Diesel	E12	Ethanol
Density at 40°C (kg/m^3)	812.6	804.9	788
Kinematic viscosity at 40 °C, mm²/s	2.06	1.8	1.2
Lower heating value (MJ/kg)	42.88	40.56	26.95
Cetane number	51.5	44.4	8.0
Flash point, °C	55	13	13
Carbon (% w/w)	87	81.8	52.2
Hydrogen (% w/w)	12.6	12.7	13.0
Oxygen (% w/w)	0.4	5.6	34.8
Sulphur (ppm w/w)	4.1	3.6	–
Molecular weight (g/mol)	200	179.91	46

The load of 150 N was used during the experiments. The tests continued over 1 hour. Before each experimental test, the all appropriate parts of the machine, i.e. bottom and upper ball holders, fuel vessel and test balls were cleaned up in an ultrasonic bath, and then all parts were dried completely.

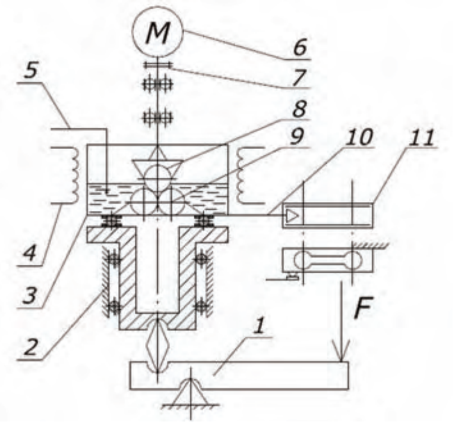

Fig. 3. The scheme of the four-ball tribotester: 1 – load transfer lever; 2 – vertical centre bearing; 3 – oil sample compartment; 4 – oil heater; 5 – thermocouple; 6 – electrical motor; 7 – clutch; 8 – upper rotary ball; 9 – lower stationary balls; 10 – torque transfer lever; 11 – force transducer

The temperature of the fuel was maintained to be of a constant value of about 30° C during the lubricity tests.

The intensity of the balls' surface wear images was evaluated by using Nikon Elipse MA100 optical microscope.

3. Analysis if the results and discussions

The primary purpose of the fuel-injection system is to supply the fuel to the cylinder of a diesel engine. The fuel-injection pump builds up the fuel pressure needed for injection and then at the required rate delivers the fuel to the engine's cylinders [11].

The columns in Fig. 4 illustrate the changing trends in fuel delivery rate determined for various pressure values built up by the both fuel pumps at the end (after 100 h) of the experimental tests.

Analysis of the obtained results shows that the resulting decrease in the fuel delivery rate was about 16% higher with ethanol-diesel fuel blend E12 at the injection pressure of 60 MPa, while the relative decrease was equal to 39% at a higher pressure of 90 MPa. From the observation of the test results, it can be assumed that the wear intensity of the plunger-barrel units was significantly greater when using ethanol-diesel fuel E12 blend that is especially a case at the injection pressure of 90 MPa. Most likely, that the delivery rate of ethanol-diesel fuel E12 blend was reasonably lower due the resulting wear and thus the leakage of the fuel. The revealed decrease in fuel delivery rate shows that the pump has lost the ability to operate with fuel blend E12, so further experimentations were suspended. The obtained test results actually differ from those effects noted by Armas et al. (2012) illustrating that using of fuel blend with a lower ethanol content (7.7% vol.) does not significantly affect the durability of the common rail fuel pump [12].

The plunger-barrel unit is one of the most overloaded components of the fuel system [11]. It can be assumed that this element is one of the most friction-sensitive units operating in the heaviest friction conditions in the diesel engine and therefore it can be chosen to evaluate the effects done by the relatively worse lubricating properties of ethanol-diesel fuel blends. Columns in Fig. 5 show how the average wear scar of the test ball changed when using the normal diesel fuel and ethanol-diesel fuel blends E10 and E20.

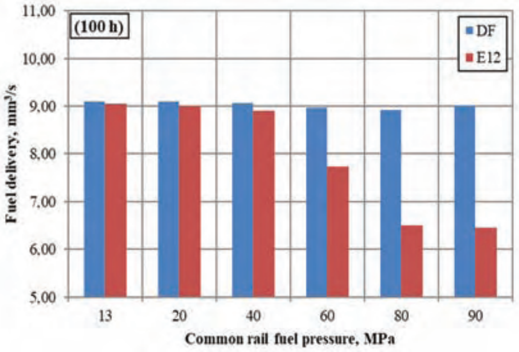

Fig. 4. Changes in a high-pressure pump's fuel delivery rate as a function of fuel pressure built up by a common rail injection system for the end of experiments (after 100 hours of operation)

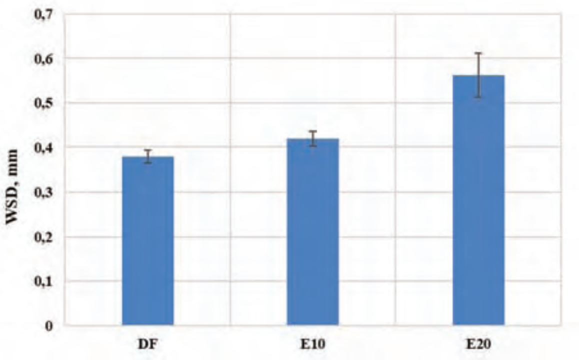

Fig. 5. The dependency of the average wear scar caused by the diesel fuel and ethanol-diesel fuel E10 and E20 blends

The test results demonstrate that the average wear scar with maximum decrease in the diameter of 0.56 mm was obtained when using diesel-ethanol fuel E20 blend. While the minimum wear scar with the diameter of 0.38 mm was recorded with the normal diesel fuel. At the same time, the wear scar diameter was equal to 0.42 mm when running with ethanol-diesel fuel blend E10.

The changing trends in variation of the friction coefficients are illustrated by the diagrams presented in Fig. 6. As can be seen in the diagrams, the friction coefficient was relatively lower and its variation was more stable when using the lowest ethanol-diesel fuel blend E10.

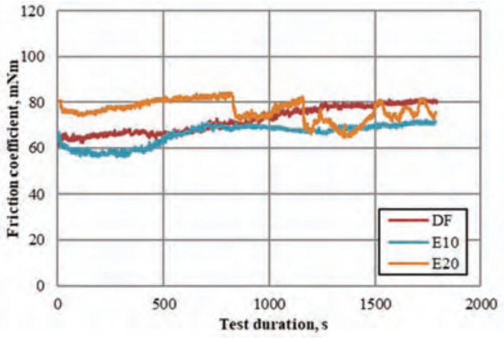

Fig. 6. Variations of friction coefficient for diesel fuel and ethanol-diesel fuel blends E10 and E20 as a function of time

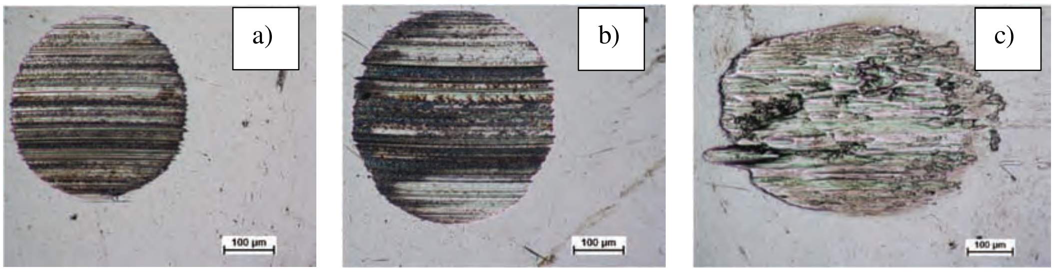

Fig. 7. Images of the worn surfaces areas obtained when lubricating with: a) DF; b) E10; c) E20

Figure 7 shows the images of the worn steel ball surface. The obvious difference in the worn surface area can be seen by comparing the friction pairs lubricated with the different fuels. The images show that using of the diesel fuel resulted in a relatively lower the worn surface area if compared to that caused by ethanol-diesel fuel blends.

Conclusions

1. The capacity (fuel delivery rate) of a high-pressure fuel injection pump decreased by 39% after the 100 hours' of operation with ethanol-diesel fuel blend E12 under close to real operating conditions.
2. Maximum mean diameter of the wear scar was equal to 0.56 mm when using ethanol-diesel fuel blend E20 and the minimum value of the wear scar was measured when running with the normal diesel fuel.
3. Maximum averaged frictional coefficient was measured when using ethanol-diesel fuel blend E20.
4. Analysis of the experimental data shows that the resulting area of a ball surface wear scar was relatively lower when using diesel fuel due to its better lubricating properties.

Nomenclature

E	ethanol
E10	10 vol% ethanol/90 vol% diesel fuel
E12	12 vol% ethanol/88 vol% diesel fuel
E20	20 vol% ethanol/80 vol% diesel fuel
WSD	wear scar diameter

Bibliography

[1] TORRES-JIMENEZ, E., JERMAN, M.S., GREGORC, A. et al. Physical and chemical properties of ethanol–diesel fuel blends. *Fuel*. 2011, **90**(2), 795-802.

[2] MATZKE, M., LITZOW, U., JESS, A. et al. Diesel lubricity requirements of future fuel injection equipment. SAE International *Journal of Fuels and Lubricants*. 2009, **2**(1), 273-286.

[3] LAPUERTA, M., GARCÍA-CONTRERAS, R., AGUDELO, J.R. Lubricity of ethanol-biodiesel-diesel fuel blends. *Energy & Fuels*. 2009, **24**(2), 1374-1379.

[4] HU, E., HU, X., WANG, X. et al. On the fundamental lubricity of 2, 5-dimethylfuran as a synthetic engine fuel. *Tribology International*. 2012, **55**, 119-125.

[5] KUSZEWSKI, H., JAWORSKI, A., USTRZYCKI. A. Lubricity of ethanol–diesel blends – study with the HFRR method. *Rzeszow University of Technology*. 2017, 491-498.

[6] ODZIEMKOWSKA, M., MATUSZEWSKA, A., CZARNOCKA, J. Diesel oil with bioethanol as a fuel for compression-ignition engines. *Applied Energy*. 2016, **184**, 1264-1272.

[7] LABECKAS, G., SLAVINSKAS, S., MAŽEIKA, M. The effect of ethanol–diesel–biodiesel blends on combustion, performance and emissions of a direct injection diesel engine. *Energy Conversion and Management*. 2014, **79**, 698-720.

[8] HANSEN, A.C., ZHANG, Q., LYNE, P.W. Ethanol–diesel fuel blends – a review. *Bioresource Technology*. 2005, **96**(3), 277-285.

[9] ERKAL, G. Comparıson of engıne performance and emıssıons for conventıonal petroleum dıesel fuel and dıesel-ethanol blends. *Master of Science in Mechanical Engineering Department Middle East Technical University*. 2010.

[10] XU, B.Y., QI, Y.L., ZHANG, W.B., CAI, S.L. Fuel properties and emissions characteristics of ethanol-diesel blend on small diesel engine. *International Journal of Automotive Technology*. 2007, **8**(1), 9-18.

[11] HEYWOOD, J.B. Internal combustion engine fundamentals. 1988.

[12] ARMAS, O., MATA, C., MARTÍNEZ-MARTÍNEZ, S. Effect of an ethanol–diesel blend on a common-rail injection system. *International Journal of Engine Research*. 2012, **13**(5), 417-428.

Prof. Stasys Slavinskas, DEng. – Faculty of Agricultural Engineering at Vytautas Magnus University.
e-mail: *stasys.slavinskas@vdu.lt*

Prof. Gvidonas Labeckas, DEng. – Faculty of Agricultural Engineering at Vytautas Magnus University.
e-mail: *gvidonas.labeckas@vdu.lt*

Tomas Mickevicius, DEng. – Faculty of Agricultural Engineering at Vytautas Magnus University.
e-mail: *tomas.mickevicius1@vdu.lt*

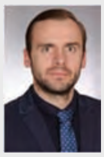

Raimondas Kreivaitis, DSc., DEng. – Faculty of Agricultural Engineering at Vytautas Magnus University.
e-mail: *raimondas.kreivaitis@vdu.lt*

Article citation info:
WRÓBEL, R., ŁOZA, Ł., HALLER, P., WŁOSTOWSKI, R. The effect of fuel mixture on engine vibrations. *Combustion Engines*. 2019, **177**(2), 136-138. DOI: 10.19206/CE-2019-224

Radosław WRÓBEL
Łukasz ŁOZA
Piotr HALLER
Radosław WŁOSTOWSKI

CE-2019-224

The effect of fuel mixture on engine vibrations

In the article, the authors analyze the effect of a fuel mixture (iso-octane, butanol and ethanol) on the generation of engine vibrations. The paper presents the results in the form of frequency response (using the Fast Fourier Transform – FFT) for three mixtures of different proportions. The measurements were made with the use of accelerometers and data acquisition cards, conditioning the received signal. The vibration component, in the form of acceleration, will be subjected to a FFT and presented in graphical form (periodogram). The authors put a special emphasis on a comparative analysis, indicating changes in harmonics, which may be a potential cause of engine degradation.

Key words: *engine's vibrations, fuel mixture, FFT, frequency response*

1. Introduction: fuel mixture

From the beginning of the introduction of the combustion engine, as the most popular method of supply engines, engineers sought optimal fuels. The direction of the search was multivariable (the extent of the influence of variables was mainly dependent on "political factors"). Initially, when the fuels were underdeveloped, they tried to obtain the most energy-efficient fuel, without taking into account the effects of such an operation. Today, research is conducted to maintain power while reducing toxicity of exhaust gases (unfortunately this is usually done by reducing one toxic factor, at the expense of increasing another). In addition to the energy and environmental aspects, one can notice and other problems resulting from the use of experimental fuel mixtures, such as changing the vibroacoustic deviation map of the engine. The article presents the results of tests of vibration changes in relation to the content of individual components of the fuel mixture.

Due to the fact that fuels available on the market contain an admixture of biofuels (alcohol) in research, it was decided to use iso-octane as a reference fuel to determine the octane number, RON (Research Octane Number) octane number equal to 100.

Ethyl alcohol is one of the most available alternative fuels obtained in the treatment of biological waste. It is characterized by a higher octane number relative to commercial gasolines equal to 130 (RON), for gasoline 91–99, and a lower calorific value equal to 26.8 MJ/kg (calorific value of gasoline 42.6 MJ/kg) Due to the high heat of evaporation (0.92 MJ/kg, gasoline 0.36 MJ/kg) the addition of ethyl alcohol causes the cooling of the fuel and air mixture, increasing the density, thus increasing the fill factor. Butanol is one of the fuels that can be an alternative to fossil fuels. It is obtained in the biomass fermentation process. Physicochemical properties are similar to gasoline (calorific value 36 MJ/kg, evaporation heat 0.43 MJ/kg, RON 96). Butanol can be used as a replacement for gasoline without modifying engine components [1–3].

The mixtures were composed based on the experimental design for ternary mixtures. Due to the lower calorific value of alcohols relative to the reference fuel, fuel consumption with the use of mixtures is higher, while the improvement of the engine's ecological parameters can be expected due to lower temperatures achieved in the combustion process (reduction of NO_x [3]).

2. Research object

The object of the research was the Fiat 1,2 spark-ignited engine (capacity 1242 cm^3, power 44 kW (60 horses), max torque 102 Nm, four-stroke engine, 8-valve, spark-ignition, powered by multipoint injection) [6]. The engine was located on the test bench of the electro-dynamic test bench, allowing it to control its parameters. The following figure shows the unit under test.

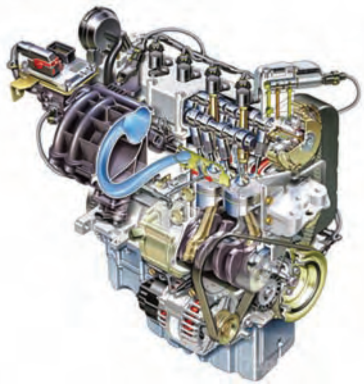

Fig. 1. Research object: Fiat 1.2 spark-ignition engine [3]

Fiat created a unit of 1.2 Fire in 1993. Over more than two decades, the motor has gained, among others, 16-valve head and was produced in four power versions. Drivers were dealing with a 60, 75, 80 or 86-horsepower spark ignition versions. The engine usually suffers from minor failures, well tolerates gas supply, and 8-valve models have collision-free timing. 1.2 Fire was mounted under the hood of two generations of Punto, Grande Punto, Bravo and Bravo, Palio, two generations of Panda, Stilo, Idea, Pentecost and Lancia Ypsilon and Y. This is a real sales hit that is really common in the aftermarket [4].

The facility was located on a measuring stand, equipped with an electrowired brake. The full schematic diagram of the position is shown in Fig. 2.

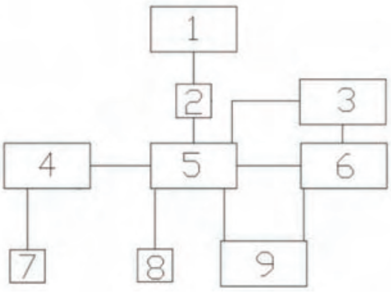

Fig. 2. Schematic diagram of the research place: 1 – fuel tank, 2 – fuel gauge, 3 – cooling system, 4 – exhaust system, 5 – engine, 6 – brake, 7 – PEMS, 8 – accelerometer, 9 – driver

The measurements were based on proprietary diagnostic system based on single axis axial accelerometer PCB353A (sensitivity 10.19 mV ±5%, measuring range ±491 m/s^2/peak, frequency range1 to 4000 Hz ±5%, frequency range 0.7 to 6500 Hz ±10%, resolution (1 to 10 Hz) 0.0005 g RMS for 1 to 10 Hz [5]). Accelerometer was connected to National Instruments type 9215 data acquisition card with USB connector (measuring range ±10 V, 4 multiplexed channels, max. sampling rate 100 kS/s/channel, 16 bit resolution [6]). The accelerometer was mounted along the vertical axis (perpendicular to the ground) on the head housing (8192 samples, 0.5 sec).

3. Results

Obtained signal (Fig. 3) is transformed to the frequency domain, using the fast Fourier transform with a base of 2. The way in which the FFT algorithm is introduced has been known since 1965 and it is widely described in the literature [7–9]. The fast Fourier transform used for discrete signals is expressed as follows:

$$X(k) = \sum_{j=1}^{N} x(j)\omega_N^{(j-1)(k-1)} \qquad (1)$$

The time domain response is showed below is related to two extreme measured values. Below (Fig. 4) is shown the frequency response of extreme values.

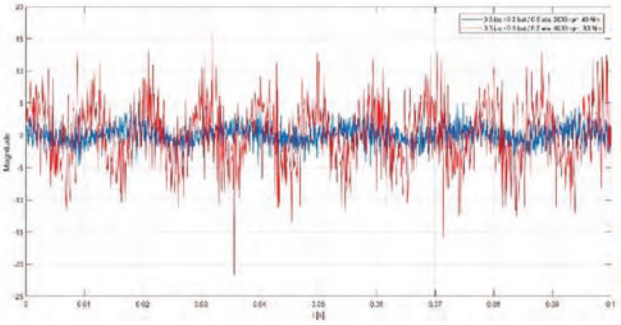

Fig. 3. Time response signal for extreme research values (blue – mixture of 0.3 izo/0.2 but./0.5 eta, red – 0.3 izo/0.5 but/0.2 eta, 2000 rpm, 40 Nm)

The table shown below shows the normalized values of magnitude as a function of frequency. The engine corresponds to 4 has basic harmonics. The first one is a direct derivative of the motor engine load (it is 51, 78, 105 Hz for the next 3 engine load states). Subsequent values of harmonic dominant frequencies (which are further derivatives of the motor load) are: 1200, 3750 and 7000 Hz.

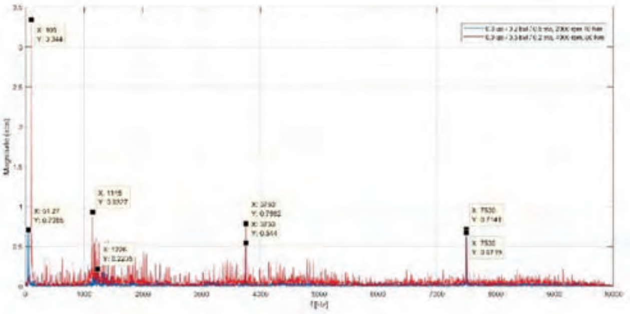

Fig. 4. Frequency response signal (periodogram) for extreme research values (blue – mixture of 0.3 izo/0.2 but/0.5 eta, red – 0.3 izo/0.5 but/0.2 eta, 2000 rpm, 40 Nm)

Table 1. Amplitude values of 4 dominant harmonics (only in the first case there are frequency fluctuations depending on the load). The values are presented for mixtures of fuel: 0.3 isooctane/0.2 butanol/0.5 ethanol (red); 0.3/0.35/0.35 (green) and 0.3/0.5/0.2 (blue)

	Dominant harmonic no.				
	1		2	3	4
Engine's load	f [Hz]	Mag (abs)	Mag (abs) f = 1200 Hz	Mag (abs) f = 3750 Hz	Mag (abs) f = 7500 Hz
2000 rpm/ 40 Nm	51	0.71	0.22	0.54	0.67
3000 rpm/ 60 Nm	78	1.83	0.61	0.59	0.72
4000 rpm/ 80 Nm	105	3.40	1.95	0.72	0.84
2000 rpm/ 40 Nm	51	0.74	0.19	0.52	0.66
3000 rpm/ 60 Nm	78	1.85	0.70	0.61	0.68
4000 rpm/ 80 Nm	105	2.94	1.19	0.68	0.74
2000 rpm/ 40 Nm	51	0.77	0.33	0.59	0.74
3000 rpm/ 60 Nm	78	1.81	0.52	0.59	0.70
4000 rpm/ 80 Nm	105	3.30	0.93	0.79	0.71

The following figure shows changes in the absolute value of dominant harmonics depending on the fuel mixture (mix 1: 0.3 isooctane/0.2 butanol/0.5 ethanol, mix 2: 0.3/0.35/0.35, mix 3: 0.3/0.5/0.2). The graph applies to all applications used (Fig. 5: 2000 rpm/40 Nm, Fig. 6: 3000 rpm/60 Nm, Fig. 7: 4000 rpm/80 Nm).

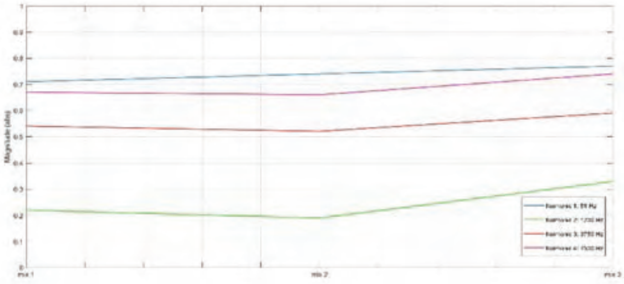

Fig. 5. Absolute values of dominant harmonics for 3 researches mixtures of fuel, 1st load (2000 rpm/40 Nm), blue: harmonic 1 (51 Hz), green: harmonic 2 (1200 Hz), red: harmonic 3 (3750 Hz), purple: harmonic 4 (7500 Hz)

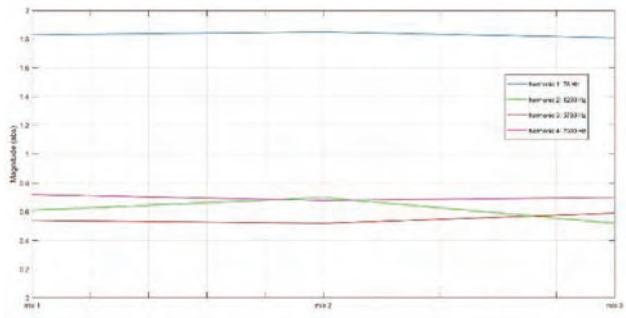

Fig. 6. Absolute values of dominant harmonics for 3 researches mixtures of fuel, 2nd load (3000 rpm/50 Nm), blue: harmonic 1 (51 Hz), green: harmonic 2 (1200 Hz), red: harmonic 3 (3750 Hz), purple: harmonic 4 (7500 Hz)

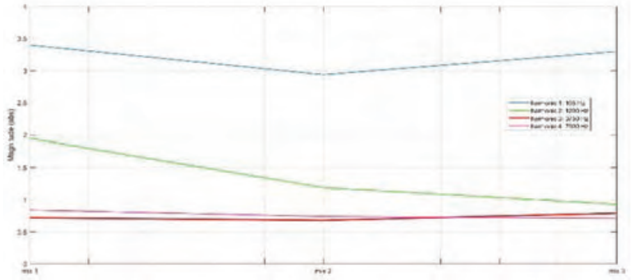

Fig. 7. Absolute values of dominant harmonics for 3 researches mixtures of fuel, 3rd load (4000 rpm/60 Nm), blue: harmonic 1 (105 Hz), green: harmonic 2 (1200 Hz), red: harmonic 3 (3750 Hz), purple: harmonic 4 (7500 Hz)

3. Conclusions

The first dominant harmonic, which is a direct derivative of the engine load, takes on the largest size, regardless of the type of mixture used. The frequency value of this harmonic is variable and depends on the load, however, regardless of the type of mixture.

The last dominant harmonic (represented in Figures 5–7 in violet solid line), whose value is constant, regardless of the composition of the mixture (7500 Hz) generates high vibrations, but only for smaller load values.

The type of fuel mixture affects the fluctuations in the magnitude of the dominant harmonics, especially for small and large loads.

The biggest magnitude of vibration (the first dominant harmonic) generates a blend with the highest ethanol content. This conclusion applies to all loads tested (Table 1).

The mixture consisting of 0.3 isooctane/0.35 butanol/ 0.35 ethanol generates the highest vibration fluctuations. This can be a potential cause of engine degradation.

Acknowledgements

Research financed from Wroclaw University of Science and Technology statutory funds no. 0401/003/18.

Nomenclature

FFT	Fast Fourier Transform
RON	Research Octane Number

Bibliography

[1] CHMIELEWSKI, A., BOGDZIŃSKI, K., GUMIŃSKI, R. et al. The test stand research on Honda NHX 110 powered with alternative fuels: a case study. *Advances in Intelligent Systems and Computing*. 2019.

[2] FARIAS, M.S., SCHLOSSER, J.F., RUSSINI, A. et al. Performance of an agricultural engine using mineral diesel and ethanol fuels. *Ciencia Rural*. **47**(3), e20151387, 2017.

[3] HUSSEIN, A.A. The effect of the heavy alcohol additive to base fuel of spark ignition engine. *Raporty Wydziału Mechanicznego Politechniki Wrocławskiej*. Ser. PRE, **3**. 140, 2017.

[4] An article about FIAT engines. *fiatklubpolska.pl.*

[5] PCB Homepage, Accelerometers. *www.pcb.com/TestMeasurement/Accelerometers.*

[6] NI9215 datasheet.www.ni.com/pdf/manuals/373779g.pdf.

[7] STRANNEBY, D. Cyfrowe przetwarzanie sygnałów. Metody, algorytmy, zastosowanie. *Wydawnictwo BTC*, Warszawa 2004.

[8] ZIELIŃSKI, T.P. *Cyfrowe przetwarzanie sygnałów,* Wydawnictwo WKŁ, Warszawa 2005.

[9] LYONS, R.G. Understanding digital signal processing. *Wydawnictwo Prentice Hall,* 2018.

Radosław Wróbel, DSc., DEng. – Faculty of Mechanical Engineering, Wroclaw University of Science Technology.
e-mail: *radoslaw.wrobel@pwr.edu.pl*

Piotr Haller, MEng. – Faculty of Mechanical Engineering, Wroclaw University of Science Technology.
e-mail: *piotr.haller@pwr.edu.pl*

Łukasz Łoza, MEng. – Faculty of Mechanical Engineering, Wroclaw University of Science Technology.
e-mail: *lukasz.loza@pwr.edu.pl*

Radosław Włostowski, MEng. – Faculty of Mechanical Engineering, Wroclaw University of Science Technology.
e-mail: *radoslaw.wlostowski@pwr.edu.pl*

Article citation info:
KNIAZIEWICZ, T., ZACHAREWICZ, M. Method for assessing the technical condition of marine diesel engine driving the synchronous generator. *Combustion Engines*. 2019, **177**(2), 139-144. DOI: 10.19206/CE-2019-225

Tomasz KNIAZIEWICZ
Marcin ZACHAREWICZ

CE-2019-225

Method for assessing the technical condition of marine diesel engine driving the synchronous generator

The paper presents an innovative method for assessing technical condition of a marine diesel engine that drives synchronous generator. It is based on the measurement and analysis of generator's phase-to-phase voltage. Additionally, it requires the measurement of a pseudoperiodic signal [3] with a period equal to duration of engine's working cycle. The basis for developing method was the assumption that rotational speed fluctuations of an engine's crankshaft (and also the generator) depend on a course of a working process carried out in it. The generator's phase-to-phase voltage is directly dependent on a rotational speed fluctuation of its rotor. It must therefore be possible to assess a course of a working process of an engine based on a voltage waveform of a synchronous generator that cooperates together.

Key words: *diagnosis, diesel-electric unit, model research, empirical studies*

1. Introduction

An important group of engines used in shipbuilding (it is estimated that about 50% [10]) diesel engines propelling ship's generators. According to the SOLAS Convention, each ship must have at least two independent power supply units [1]. In most cases, there are more (usually three or four). These are usually diesel engines not equipped with indicator valves [10]. This makes it difficult to apply operation strategies according to technical condition to them. They are operated according to so-called hourly recharge (time resource for correct work). Such a strategy imposes an exchange of their elements of a construction structure every specific number of working hours (regardless of their actual technical condition, often fit) [9].

Therefore, works were carried out to develop parametric, non-invasive methods for assessing their technical condition. One of them is method presented in the article based on the measurements of an phase-to-phase voltages of an synchronous generator constituting with a diesel engine (DG). The basis for the development of the method was the observation that both a load of the engine with torque and its technical condition affect on phase-to-phase voltages of a synchronous generator cooperating with it [5, 8] (which in theory should have a sinusoidal shape [2, 10]). An example of a phase-to-phase voltage of a generator as a function of time recorded during empirical studies is shown in Figure 1. In addition, the figure shows the reference waveform of the phase-to-phase voltage (theoretical).

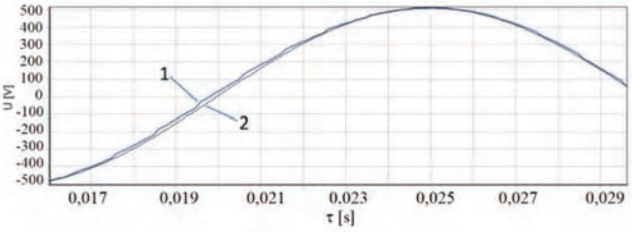

Fig. 1. The chart of line voltage synchronous generator as a function of time: 1 – waveform measurements obtained from 2 – course model

On the basis of analysis of a phenomena occurring in the DG, it was considered that a reason for a observed deformations of the interfacial tension waveform is fluctuations of the angular velocity of a generator rotor (Fig. 2).

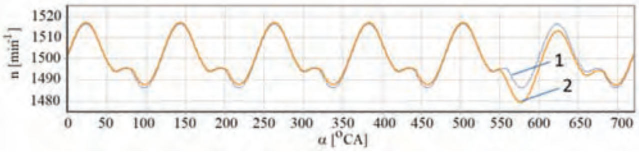

Fig. 2. The rotational speed of the generator rotor as a function of an angle of rotation of an engines crankshaft for: 1 – for an operational engine, 2 – for a damaged engine (reducing the dose of fuel supplied to the No. 1 cylinder by 50%)

The direct cause of rotation speed fluctuation of a generator rotor are the rotational speed fluctuations of an engine crankshaft. They result from the variable torque of a crankshaft and depend on the value of indicated pressure in the engine cylinders [7]. Figure 3 shows the torque curve obtained in the result of modelling for the six-cylinder engine 1 – operational, 2 – damaged.

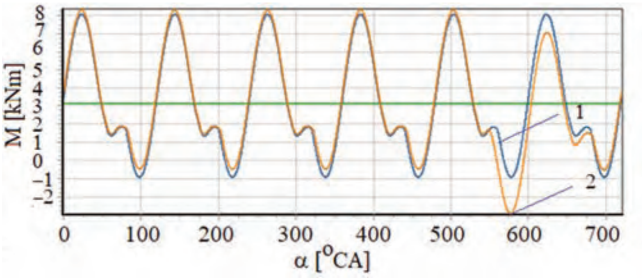

Fig. 3. The chart of engine torque as a function of an angle of crankshaft rotation for: 1 – operational engine, 2 – damaged engine (reducing the dose of fuel supplied to cylinder No. 1 by 50%)

The analysis of the waveforms presented in Fig. 1 and 2 clearly indicates that a working process occurring in cylinders (indicated pressure) affects the torque values. However, the torque directly affects course of a rotational speed of an engine crankshaft (generator rotor).

2. Model of diesel-electric unit

Development of presented method for assessing technical condition of a marine diesel engine required conducting a thorough analysis of selected phenomena occurring in engine and generator. For this purpose, a mathematical model of a diesel-electric unit was developed. The mathematical model includes a possibility of simulating known and recognizable engine damage such as: change of fuel dose, change of valves cross-section area, change of the injection opening angle, leakage in a piston-rings-cylinder system. Development of the DG mathematical model has been divided into two stages (Fig. 4).

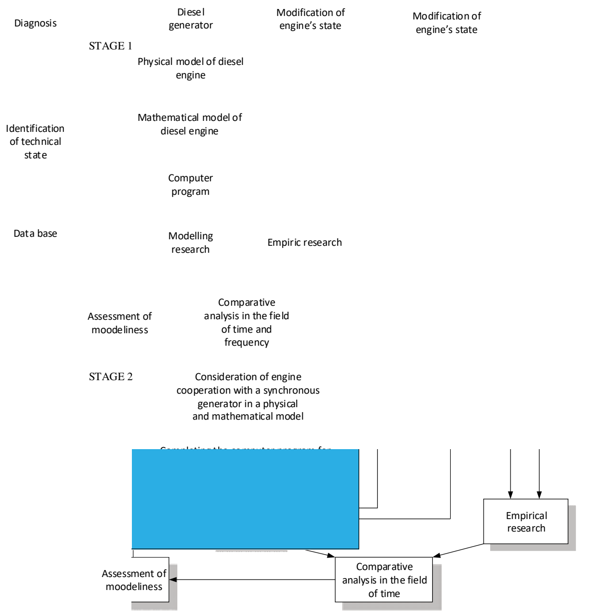

Fig. 4. Research program

The first stage involved development of a mathematical model of a diesel engine. The adequacy of this model has been verified on a basis of a comparative analysis of a results of model and empirical studies. Empirical studies were carried out on a laboratory engine with high diagnostic susceptibility. Obtaining a positive result of an adequacy assessment (quantitative and qualitative) of the mathematical model of the engine allowed for a transition to the second stage – the development of the DG mathematical. This approach to modelling issue was dictated by the fact that in the case of engines driving marine generators, model verification would be extremely difficult. In most cases, these engines are not equipped with indicator valves.

The stage of developing the mathematical model of the engine was preceded by the development of a physical model of the processes taking place in the DG. The basis for the development of the physical model was identification of phenomena occurring in team and a mutual relations between a functional components of a subprograms. The identification was based on the built models: functional and topological.

The developed mathematical model of the unit was the basis for writing a computer program (often called a numerical model) that allows solving the equations included in the model.

The result of the solution of the equations of the mathematical model of the DG were a phase-to-phase voltages of a L_{1-2}, L_{2-3}, L_{3-1} generator, waveforms of a crankshaft of an engine (generator rotor) as a function of time or angle of rotation of a crankshaft. Course of factor parameters in engine cylinders such as: temperature, pressure, mass, individual gas constant, etc. as functions of an angle of a crankshaft rotation.

3. Model and empirical research

3.1. Research plan

Recognition of the DG model as adequate enabled development of a determined, selective research plan [6, 10]. It was assumed that according to the same program model and empirical studies will be carried out. Empirical research was carried out on three DG powered by 6SW 400 type engines cooperating with GCPf – 94c/1 type generators. Research objects are installed at the stand in the Laboratory for the Operation of Electric Ship Equipment (Fig. 5).

Fig. 5. Research object in the Laboratory for the Operation of Electric Ship Equipment

The test program is shown in Tables 1 and 2. Table 1 shows the test program for the engine in full technical condition. However, Table 2 presents the test program for the damaged engine. The tests were carried out for the engine damaged for a following partial technical condition. First, cylinder No. 1 was turned off. Then cylinder No. 6 was turned off. The last stage of the research consisted in excluding cylinders no. 1 and 6 from operation.

Table 1. Study plan for DG in full technical condition

Load with electrical loads	Measurement number
2 kW	1
10 kW	2
20 kW	3

Table 2. Study plan for DG in full technical condition

Load with electrical loads	Measurement number
Cylinder No. 1 excluded from work	
2 kW	1
10 kW	2
20 kW	3
Cylinder No. 6 excluded from work	
2 kW	1
10 kW	2
20 kW	3
Cylinders No. 1 and 6 excluded from work	
2 kW	1
10 kW	2
20 kW	3

3.2. Measuring apparatus

The implementation of the research required the development of proprietary measuring apparatus [4]. It was assumed that the apparatus must allow for implementation of measurements of a synchronous generator voltage (three channels) while maintaining the galvanic isolation of high voltages at the terminals (user's computer). An additional role of the developed measuring instrument was to adjust a levels of measurement signals to the range accepted by the Advantech USB-4711A measuring card used. In addition, it was necessary to measure a parameter enabling a synchronization of recorded phase-to-phase voltages with an engine working cycle. The acceleration measured at the engine head in the injector needle's operating axis was considered to be an optimal parameter. It was assumed that measurements must be carried out with a sampling frequency of not less than 10 kHz (for each measurement channel). This frequency provides about 400 signal samples per revolution of an engine crankshaft at a typical (for DG) rotational speed of 1500 min^{-1}. The Advantech USB-4711A card with a resolution of 12 bit was used for the measurements. It allows measuring the voltage signal in the following ranges:

- ±10 V measurement accuracy is 0.00244 V,
- ±5 V measurement accuracy is 0.00122 V,
- ±2, measurement accuracy is 0.00061 V,
- ±1.25 measurement accuracy is 0.000305 V,
- ±0.625 V measurement accuracy is 0.000153 V.

The computer cooperating with the measuring card was used to acquire values of measured parameters.

3.3. The research data analysis

Regardless of the source (model or empirical study), the data was saved in a same format. This allowed to use a proprietary computer program for their processing. In addition, it ensured that an analysis of a research results will be carried out (regardless of whether the results will come from empirical or model studies) in the same way.

The first stage in the analysis of measurement data consists in use of so-called averaging synchronic [9]. The acceleration of an injector (Fig. 6) is registered with the reference signal in the averaging process.

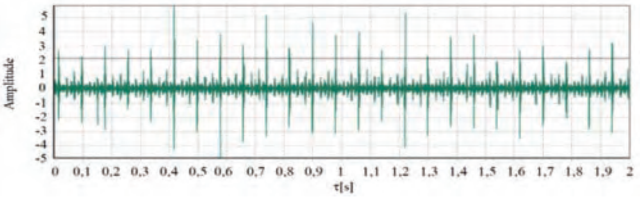

Fig. 6. The chart of accelerations measured in the axis of the injector needle

As a result of synchronous averaging of recorded phase-to-phase voltage waveforms, the waveforms corresponding to the engine cycle shown as a function of time were obtained (Fig. 7).

The next stage in the analysis of a measurement data was to obtain the plot considered to be a reference (corresponding to the work of the generator rotor with constant rotational speed). The course found to be a reference one was obtained by using a Fourier transform relative to the registered phase-to-phase voltage waveform. Subsequently, the output course was reconstructed on the basis of the inverse Fourier transform for a first harmonic. This is illustrated by dependence:

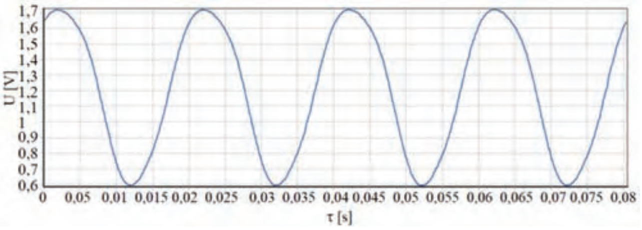

Fig. 7. Synchronous average of the generator phase-to-phase voltage as a function of time for one engine working cycle

$$a_1 = \frac{2}{T} \cdot \int_{-\frac{T}{2}}^{\frac{T}{2}} f(\tau) \cdot \cos\left(\frac{2 \cdot \pi}{T}\right) d\tau \tag{1}$$

$$b_1 = \frac{2}{T} \cdot \int_{-\frac{T}{2}}^{\frac{T}{2}} f(\tau) \cdot \sin\left(\frac{2 \cdot \pi}{T}\right) d\tau \tag{2}$$

$$U_{wz} = \frac{a_0}{2} + a_1 \cdot \cos\left(\frac{2 \cdot \pi}{T} \cdot \tau\right) + b_1 \cdot \sin\left(\frac{2 \cdot \pi}{T} \cdot \tau\right) \tag{3}$$

The course of interfacial tension $L_{1\text{-}2}$ and the reference waveform as a function of time are shown in Fig. 8.

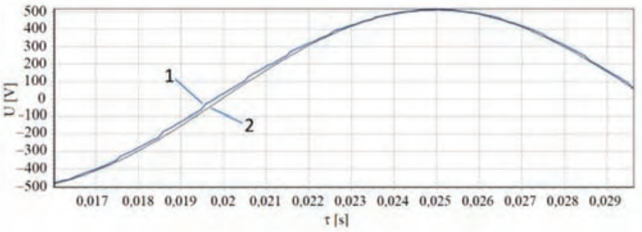

Fig. 8. A fragment of the registered phase-to-phase voltage waveform as a function of time: 1 – waveform obtained from measurements, 2 – reference waveform

The next stage of the analysis of the courses obtained as a result of empirical and model research was development of measures proportional to the value of an engine crankshaft angular velocity fluctuation. The decision was made that the most promising method would be to conduct time-domain analysis. It is based on a calculation (for each value of the ordinate of an average wave) of the difference between the time values for the runs of the synchronously averaged and the reference $\Delta\tau_i = \tau_{ave\,i} - \tau_{ref\,i}$. The time difference can take both: positive and negative values. The value $\Delta\tau_i$ greater than zero means that for a given moment of time an angular velocity of a crankshaft is greater than an average for a working circuit. The negative difference indicates a lower value of an angular velocity of a crankshaft from an average for a working circuit. The applied method of data analysis is shown in Fig. 9.

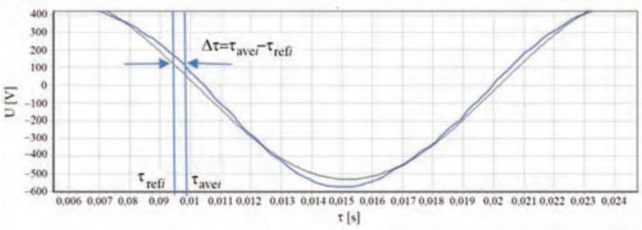

Fig. 9. A fragment of generator's phase-to-phase voltage with the method of calculating the time increment value

Analysing the voltage waveforms shown in Fig. 9, it can be seen that in a range of a largest amplitude values of a generator phase-to-phase voltage there may be areas for which it is not possible to meet the condition $U_{refi} \approx U_{avei}$. In this case, it was decided to take the value of the time difference $\Delta\tau_i$ as equal to „100" – a difference of this value does not occur during the research, so it could act as a marker.

By analysing the phase-to-phase voltage waveform as a function of time shown in Fig. 9, it can be observed that the time difference values are not linear with respect to the phase-to-phase voltage value and depend on a generator's phase-to-phase voltage. The largest values of time differences occur for a voltage value of 0 V. However, closer to the maximum and minimum voltage amplitude, these values decrease. To minimize an effect of nonlinearity, it was decided to use a proportionality factor described by the dependence:

$$\mathrm{wsp}_\tau = \frac{a_0}{2} + a_1 \cdot \cos^2\left(\frac{2\cdot\pi}{T}\tau\right) + b_1 \cdot \sin^2\left(\frac{2\cdot\pi}{T}\tau\right) \qquad (4)$$

where: a_1 – factor calculated from the equation 1, b_1 – factor calculated from the equation 2.

The calculated time differences $\Delta\tau_i$ have been multiplied by the proportionality coefficient wsp_τ (described by the dependence (4)). According to a described method, the time difference values for all three generator's phase-to-phase voltages were calculated. Then, for each moment of time, the arithmetic mean of the time difference values was determined (for all analyzed phase-to-phase voltage waveforms). In the case when the value of time difference for any of runs was indeterminate (the $\Delta\tau_i$ tag equals 100), the mean value from a smaller number of passes was determined for a given abscissa (time) value (the uncertainty values were omitted). An exemplary course of time differences as a function of time is shown in Fig. 10.

In addition, in Fig. 10, an areas corresponding to individual engine cylinders were determined, an influence of which was the highest on the engine speed fluctuation (from a cylinder opening of a given cylinder until a cylinder cylinder's next cylinder opening). Next, an area under a obtained time differences was calculated as a function of time within integration limits corresponding to an opening times injector of a given cylinder injector until the next cylinder injection opening (according to the order of cylinders).

$$Z = \int_{\tau_{owtr\,i}}^{\tau_{owtr\,i+1}} \Delta\tau(\tau)d\tau \qquad (5)$$

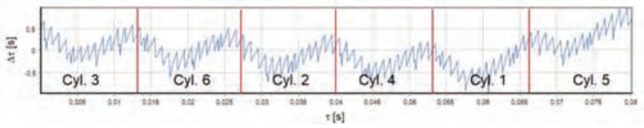

Fig. 10. The chart of time differences as a function of time for the engine with a damaged cylinder no. 1 (measurement of acceleration of the injector carried out on cylinder No. 3)

The values of a surface area under a plot of time differences as a function of time for individual damaged engine cylinders (Z measure values) are shown in Fig. 11.

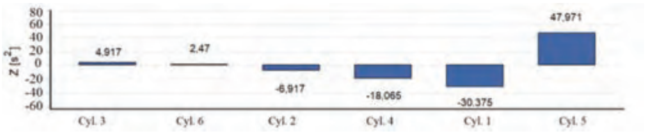

Fig. 11. Z measure as a function of time for individual engine cylinders for a damaged engine (disabling fuel supplying cylinder No. 1)

The proposed measure Z allowed to analyse a results of model and empirical research. The tests were carried out on a basis of the test plan proposed in section 3.1.

3.4. Research results

Conducted research [10] allowed to conclude that the developed mathematical model of a diesel-electric unit is not adequate in quantitative relation to the examined real objects. Whereas values of the Z measure calculated for the efficient and damaged cylinders in a case of model and empirical tests are convergent, which allows the model to be considered qualitatively adequate. Noteworthy is the fact that results of empirical research (Z measure) differ in a fundamental way. However, in a case of damaged engines, some regularities can be observed, which allowed to draw the following conclusions:

- For all simulated partial technical airworthiness states, in each case a value of the Z parameter calculated for a damaged engine cylinder is clearly smaller (this is evidenced by on a decrease of angular velocity of a crankshaft) from the other cylinders.
- All empirical research results are subject to significant errors resulting from the limitations of the measuring instrument used (optoisolation and low signal sampling frequency of 10 kHz).
- The significance of errors decreases with the increase of the engine load with the moment of resistance (increase of the generator load).
- Failure of any of a cylinder sections results in a significant change in a value of the Z measure both in an area of a damaged cylinder and other cylinders. Values of the damaged cylinders are always negative, while as a result of a work of an engine speed controller values of the other cylinders usually have values greater than those of an efficient engine.

When developing a method of assessing a technical condition of an engine, one had to find an unambiguous measure informing about the damage and identifying the damaged cylinder section. The process of technical condition evaluation was divided into two main stages:

- the first stage consisted in determining whether there is damage in the case of the tested DG,
- the second stage consisted in locating the damage occurring on an indication of a particular cylinder section.

In the first stage, it was decided to use a standard deviation value – σ calculated for the Z measures for each of engine's cylinders.

This step is based on observation made regarding a value of the standard deviation of the Z measure for the engine in various technical states. It was observed that in the case of a defective engine, standard deviation takes on a value higher than in the case of engine that is efficient for same loads. This is due to larger fluctuations in an angular velocity of a crankshaft of a damaged engine, which results in a greater spread of the Z value. The standard deviation values for engine cylinders in various technical conditions are shown in Table 3.

Table 3. List of values of standard deviations for various technical states of the engine

Technical state and load	Empirical research for DG no. 1			Model research
	1	2	3	[σ]
	[σ]	[σ]	[σ]	
Efficient – 2 kW	5.98	5.47	6.21	2.51
Off cyl. 1 – 2 kW	10.66	8.92	8.35	5.40
Off cyl. 6 – 2 kW	7.29	7.78	6.44	5.90
Off cyl. 1 and 6 – 2 kW	6.79	4.93	5.31	5.65
Efficient - 10 kW	8.90	8.74	7.23	0.72
Off cyl. 1 – 10 kW	15.05	11.59	15.26	11.46
Off cyl. 6 – 10 kW	13.68	16.14	11.77	11.90
Off cyl. 1 and 6 – 10 kW	11.03	10.38	10.54	10.72
Efficient – 20 kW	8.60	7.55	5.98	1.82
Off cyl. 1 – 20 kW	22.67	17.81	19.14	21.52
Off cyl. 6 – 20 kW	18.09	23.02	18.82	22.21
Off cyl. 1 and 6 – 20 kW	16.40	18.18	19.66	19.63

Based on value of standard deviation of the Z measure, it was possible to assess whether an engine was functional or damaged. At the same time, it can be observed that discrepancies in standard deviation values for a damaged engine increased as load of generator increased. It was considered that in a case of a generator loaded with 10 kW and 20 kW load power, standard deviation value of less than 10 means a motor for which no damage was introduced, while a deviation value greater than 10 indicates engine damage.

The second stage is based on observation that in a case of a damaged engine value of the Z measure for damaged cylinders is significantly greater than value of standard deviation. The value of standard deviation beyond range of standard deviation also exceeds a value of Z for undamaged cylinders, but absolute value of Z is less for them than those of damaged cylinders. The value of Z measure in the case of cylinders with a given damage (for one cylinder turned off) exceeds a value of product 1.5 σ in each case. However, in case of undamaged cylinders, in none of cases examined, value of adopted measure exceeded value of 1.5·σ. It was considered that measure allowing identification of a damaged single cylinder is whether any of the measures Z exceeds 1.5·σ. Exceeding it clearly shows that cylinder is turned off. Failure to meet this condition may indicate that there is no damage or damaged cylinders.

With information from first stage of the analysis (whether there is damage) and knowing if the measure Z exceeds value of one-and-a-half times standard deviation, it is possible to distinguish between engine that is efficient and a damaged cylinder with more than one cylinder. In a case of damage to a larger number of engine cylinders, unambiguous statement of which cylinder was damaged is possible. When conducting analysis, the standard deviation σ should be used to identify damaged cylinders, instead of product 1.5·σ. The proposed method of analysing technical condition of an engine is shown schematically in Fig. 12.

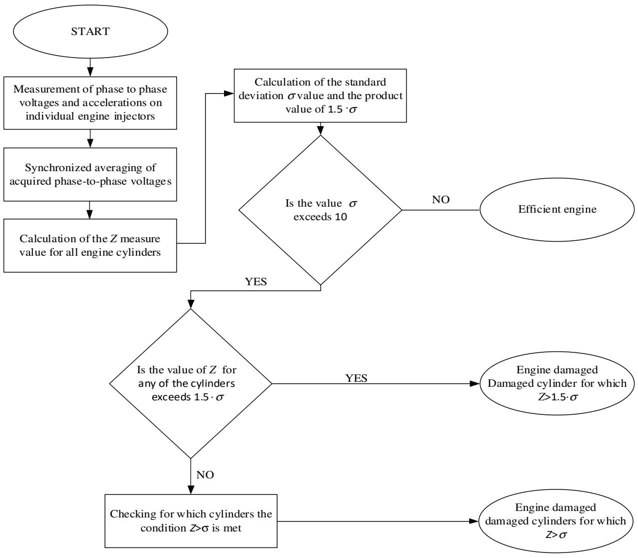

Fig. 12. An algorithm for assessment of technical condition of engine driving synchronous generator based on the phase-to-phase voltages

In addition to presented model and empirical tests, it was decided to carry out additional model tests for partial technical condition, impossible to implement on a real object. Limitations of empirical research resulted from necessity to interfere in the engine, which could potentially lead to its damage.

It was decided to carry out tests for various technical properties and for two loads of loads with a capacity of 10 kW and 20 kW respectively. The tests carried out for a full and partial technical condition were:

- reducing a dose of fuel supplied to cylinders by 10%, 20%, 30%, 40% and 50% in relation to nominal dose,
- reducing an injection advance angle by 5^{o}CA,
- increase of an injection advance angle by 5^{o}CA,
- introduction of a leak in the piston–cylinder–cylinder system of 5% of maximum cross-sectional area of a outlet valves,
- reducing a cross-sectional area of an injector holes by 10% and 20%,
- increase in cross-sectional area of an injector holes by 10% and 20%.

Based on the analysis of the data [10], the following conclusions can be made:

- Simulated partial technical health conditions consisting in reducing a fuel dose delivered to a damaged cylinder and a simulated leak in the TPC system can be detected and located using the developed method.

- Failure conditions consisting in changing an active cross-section of an injector holes and changing an injection advance angle for a damaged cylinder cause some deviations of the Z-measure value in relation to efficient engine. However, the values Z of these deviations are minimal, therefore these damages probably cannot be detected using proposed method.
- The inability to identify part of a damage may be caused by a need to adapt format of data recording from the computer program to a measuring instrument used. (The computer program simulates the measuring frequency of measuring instrument of 10 kHz for each channel, which gives about 800 samples per working cycle of the engine).

4. Summary

Despite the inclusion of a series of partial engine technical states in a diesel-electric unit model, in the case of empirical studies, it was decided to ask only one failure in the individual engine cylinders. It resulted from the inability to introduce modifications to test object due to risk of its damage. However, the study was conducted model for other states of partial technical suitability arguing that it should be possible to detect and identify damage involving:

- reducing a dose of fuel supplied to a cylinder by more than 20% of a nominal dose,
- change of injection timing,
- leaks in the piston-rings-cylinder system,
- changing an active cross-section of an injector holes.

The study proves that selected states of partial technical suitability of a diesel-electric unit's engines cause a deformation of voltage line of the generator's. As a result of conducted tests, control parameters were identified that allow for unambiguous identification of engine damage. The results of model and empirical studies carried out in the work showed that their continuation is justified. Further research should be mainly focused on:

- increasing the accuracy of generator phase voltage measurements, which can be achieved by:
  - increasing a sampling rate,
  - reducing a device's non-linearity,
  - increasing a resolution of a measuring instrument from 12 bits to at least 16 bits;
- conducting tests for other typical engine damages of a diesel-electric unit.

Nomenclature

a_0, a_1, b_1	Fourier ratio
i	iteration
$L_{1-2}, L_{2-3}, L_{3-1}$	applies to phase-to-phase voltages
owtr	applies to opening of the injector
T	period
U	electric voltage
Uśr	applies to synchronized average values
wsp	proportionality factor
wz	applies to the reference course
Z	measure describing the technical condition of the engine
σ	standard deviation
τ	time

Bibliography

[1] International Convention for the Safety of life at Sea, *1979 SOLAS, Tekst ujednolicony.* Polish Register of Ships, Gdańsk 2002.

[2] BIAŁEK, R. Electrical engineering and ship electronics. *Maritime University of Gdynia*. Gdynia 2002.

[3] CHŁOPEK, Z., PIASECZNY, L. Research of fast-changing processes in the combustion engine. *AMW, Scientific Papers*. 2004, **2**(157).

[4] CWALINA, A., ZACHAREWICZ, M. Conception and practical application of a measuring device for energetic parameters measurement of a mechatronic object. *Solid State Phenomena*. 2012, **180**, 185-193.

[5] CWALINA, A., ZACHAREWICZ, M. The conception of diagnosing the technical condition of marine diesel engine driving a synchronous generator. *Combustion Engines*. 2011, **4**, 1-5.

[6] POLAŃSKI, Z. Planning experiments in technology. *PWN*, Warszawa 1984.

[7] WAJAND, J.A., WAJAND, J.T. Mid-speed and high-speed diesel engines. *WNT*. Warszawa 2005.

[8] ZACHAREWICZ, M. Internal test of the technical condition of an uncharged marine diesel engine based on measured of gasodynamic parameters in the exhaust channel. *AMW Scientific Papers*. 2011, **4**(187), 125-132.

[9] ZACHAREWICZ, M. The method of diagnosing engine working spaces based on gasodynamic parameters in the turbocharger inlet channel. *Polish Naval Academy*. Dissertation. Gdynia 2009.

[10] ZACHAREWICZ, M. Possibilities of parametric evaluation of the technical condition of a marine diesel engine with low diagnostic susceptibility. *Polish Naval Academy*. Gdynia 2019.

Tomasz Kniaziewicz, DSc., DEng. – Faculty of Mechanical and Electrical Engineering, Polish Naval Academy.

e-mail: *t.kniaziewicz@amw.gdynia.pl*

Marcin Zacharewicz, DEng. – Faculty of Mechanical and Electrical Engineering, Polish Naval Academy.

e-mail: *m.zacharewicz@amw.gdynia.pl*

Article citation info:
LASOCKI, J., GIS, M. The influence of driving pattern on pollutant emission and fuel consumption of hybrid electric vehicle. *Combustion Engines*. 2019, **177**(2), 145-150. DOI: 10.19206/CE-2019-226

Jakub LASOCKI
Maciej GIS

CE-2019-226

The influence of driving pattern on pollutant emission and fuel consumption of hybrid electric vehicle

Hybrid electric vehicles (HEVs) have an increasing presence in passenger transport segment. They have been designed to minimize energy consumption and pollutant emission. However, the actual performance of HEVs depends on the dynamic conditions in which they are used, and vehicle speed is one of the key factors. A lot of excess emission and fuel consumption can be attributed to rapid changes of vehicle speed, i.e. accelerations and decelerations. On the other hand, dynamic driving favours energy recovery during braking. This study examines the relationship between HEVs speed, pollutant emission and fuel consumption. The considerations were based on the results of testing vehicles in WLTC and NEDC driving cycles, performed on a chassis dynamometer. The test objects were two light-duty passenger vehicles, one with series-parallel, gasoline-electric hybrid system and the other, used as a reference, with conventional spark-ignition engine. Both vehicles had similar technical parameters and combustion engines supplied with gasoline. The driving cycles were divided into several parts according to the speed range. For each part, pollutant emission and fuel consumption were determined and appropriate values of selected parameters of driving pattern were calculated. Combining the results of empirical research and calculated parameters allowed to obtain characteristics. Their analysis provided valuable insight into the impact of driving pattern on actual emission and fuel consumption of HEV.

Key words: *hybrid electric vehicle, HEV, pollutant emission, fuel consumption, driving pattern*

1. Introduction

With the rapid development of world transportation, environment pollution and the depletion of non-renewable energy resources have become two serious problems. The need to address these concerns led many academic institutions and automobile manufacturers to adopt research and development programs that included not only more efficient and cleaner ways to use fossil fuel in internal combustion engine vehicles (ICEVs), but also the development of alternative propulsion systems and energy carriers. In recent years, battery electric vehicles (BEVs) have received increased attention worldwide and their production numbers for large markets has increased. However, despite remarkable achievements in the development of BEVs in the last years [5], there are still two serious problems to be solved: low operational range of BEVs due to relatively limited capacity of batteries and considerably high vehicle and battery costs, which reduces the number of potential buyers.

BEVs and ICEVs features are combined in hybrid electric vehicles (HEVs), with the variety of subtypes available, including plug-in hybrid electric vehicles (PHEVs). HEVs usually consist of two different power sources – an internal combustion engine and an electric motor. Some powertrain configurations of HEVs enable them to switch between two power sources, which allows for the use of pure electric mode under certain driving conditions or in low-emission zones of city centers. HEVs certainly do not have the operational range restriction of BEVs and they are beneficial in terms of environmental impact due to reduction in tailpipe emissions and fossil fuel consumption [8–10]. In the case of PHEVs there is also potential to diversify transportation energy sources and stimulate real opportunities on the integrating renewable energy into the power system. On the other hand, two separate power sources increase vehicle mass, which in turn lead to a higher consumption of both electricity and fuel.

The actual performance of HEVs depends on the dynamic conditions in which they are used [8–10], and vehicle speed is one of the key factors. A lot of excess emission and fuel consumption can be attributed to rapid changes of vehicle speed, i.e. accelerations and decelerations. On the other hand, dynamic driving favors energy recovery during braking.

The present study aims at investigating the impact of driving pattern on pollutant emission and fuel consumption of HEVs. It involves empirical testing of two light-duty vehicles – HEV with series-parallel hybrid system and ICEV with conventional spark-ignition combustion engine – on a chassis dynamometer in the WLTC and NEDC driving cycles.

2. Parameters of driving pattern

Vehicle driving pattern is usually defined by the variation of vehicle speed with time [5]. Some researchers extend this definition to other factors like gear changing, driving distance etc. [6, 12]. It is possible to quantify driving patterns using certain parameters, also known as zero-dimensional or point characteristics [2–6]. A large number of such parameters has been proposed [6], Among them, those related to speed and acceleration are most often considered for investigating the influence of driving pattern on vehicle pollutant emission and fuel consumption [3, 4].

The examples of driving pattern parameters used in previous research works [1, 6, 7, 11] can be divided into five categories:

1. Average value, in relation to: speed, driving speed (excluding stops), acceleration, deceleration, driving time within one driving period (from start to stop), number of acceleration-deceleration changes (and vice versa) within one driving period, etc.
2. Time share, in relation to: stop ($v = 0$), acceleration, deceleration, driving at constant speed, etc.

3. Standard deviation, in relation to: speed, acceleration, deceleration, etc.
4. Relative and joint distribution, in relation to: speed, acceleration, deceleration, etc.
5. Complex parameters: relative positive acceleration, positive kinetic energy, product of the speed and acceleration, product of the squared speed and acceleration, average absolute value of product of speed and acceleration, number of stops per distance, etc.

One of the classic examples of employing driving pattern parameters to examine their influence on pollutant emission and fuel consumption is the research of Ericsson [6]. She collected driving data from a vehicle driven in urban conditions and used the results to determine the values of 62 independent parameters, including commonly used variables based on speed and acceleration as well as newly proposed variables related to engine rotational speed and gear changing. After statistical analysis of the results obtained, 9 parameters were found to have significant environmental effects [6].

3. Materials and methods

The general concept of this study was to obtain data on pollutant emission and fuel consumption of vehicles tested in driving cycles that simulate dynamic driving conditions on the chassis dynamometer. Next, values of the selected driving pattern parameters for the speed profiles of these driving cycles were determined. Combining the results of empirical research and calculated parameters allowed to obtain dependencies for pollutant emission and fuel consumption on driving pattern parameters.

Empirical part of the research concerned two vehicles:

- HEV, with a series-parallel drive system, consisting of spark-ignition combustion engine, electric motor and continuously variable transmission e-CVT,
- ICEV, with spark-ignition combustion engine and continuously variable transmission CVT.

HEV was treated as the main object of research, while ICEV served as a reference, to compare test results. Both vehicles had similar technical parameters and combustion engines supplied with gasoline (Table 1).

Table 1. Specifications of the vehicles tested

Parameter	HEV	ICEV
Combustion engine displacement	1798 cm^3	1798 cm^3
Maximum power	90 kW at 5200 rpm	108 kW at 6400 rpm
Maximum torque	142 N·m at 3600 rpm	180 N·m at 4000 rpm
Combustion engine compression ratio	13	11
Fuel type used	Gasoline	Gasoline
Fuel injection type	Multi-point (MPI)	Multi-point (MPI)
Gearbox type	e-CVT	CVT

Vehicles were tested in two type-approval driving cycles: the Worldwide Harmonized Light Vehicles Test Cycle class 3.2 (WLTC) and the New European Driving Cycle (NEDC). The driving cycles were divided into parts according to the vehicle speed range – WLTC into four parts: low speed, medium speed, high speed and extra high speed, while NEDC into two parts: Urban Driving Cycle (UDC) and Extra Urban Driving Cycle (EUDC).

Driving cycles were performed in laboratory conditions on the chassis dynamometer at Motor Transport Institute in Warsaw. The tests were repeated several times for each vehicle, with the combustion engine warmed up. The influence of the cold engine start was outside the scope of the current study. For a detailed description of test conditions, refer to previous publications [8–10].

The results obtained included averaged values of:

- fuel consumption (Q), expressed in $dm^3/100$ km,
- road emission of: carbon dioxide (CO_2), total hydrocarbons (THC), nitrogen oxides (NO_x) and carbon monoxide (CO), expressed in g/km.

In the second part of the study, the parameters of driving pattern were determined for each part of the driving cycle. The analysis involved:

- average speed – v_{AV} [km/h],
- average acceleration – a^{+}_{AV} [m/s^2],
- average deceleration – a^{-}_{AV} [m/s^2],
- relative positive acceleration – RPA [m/s^2],
- average absolute value of the product of speed and acceleration – $|v \cdot a|_{AV}$ [m^2/s^3],
- time share of vehicle stop (v = 0) – u_{stop} [%].

The parameters listed above are regarded as relevant for experimental investigation and modelling of pollutant emission and fuel consumption of light-duty vehicles [6]. Vehicle's average speed is the basic parameter used to determine the characteristics of internal combustion engines under dynamic conditions, e.g. for the inventory of pollutant emissions and fuel consumption [2]. Average acceleration determines the demand for maximum engine torque, while average deceleration indicates the intensity of braking [5]. Besides, both average acceleration and average deceleration can be considered as criteria for an aggressive driving style. Relative positive acceleration is calculated as the integral of speed multiplied with positive acceleration and the time interval when the acceleration is positive, divided by the total distance of the drive [6]. Relative positive acceleration value is large for driving pattern that includes a lot of high power-demand accelerations and is found to increase fuel consumption [5]. The average value of absolute value of product of speed and acceleration can be interpreted as a measure of engine power output per unit mass of the vehicle [5].

In order to determine the characteristics of pollutant emissions and fuel consumption, their values were normalized to the highest value obtained for one of the vehicles in a given category (fuel consumption or road emission of each exhaust component). In this way, differences in values are clearly visible and at the same time it is possible to compare the characteristics for both vehicles in one graph, without losing information relevant for the qualitative assessment of the course of the given dependence.

4. Results and discussion

The dependence of normalized fuel consumption on individual parameters of driving pattern is shown in Fig. 1. The sets of points were approximated by second degree polynomial functions.

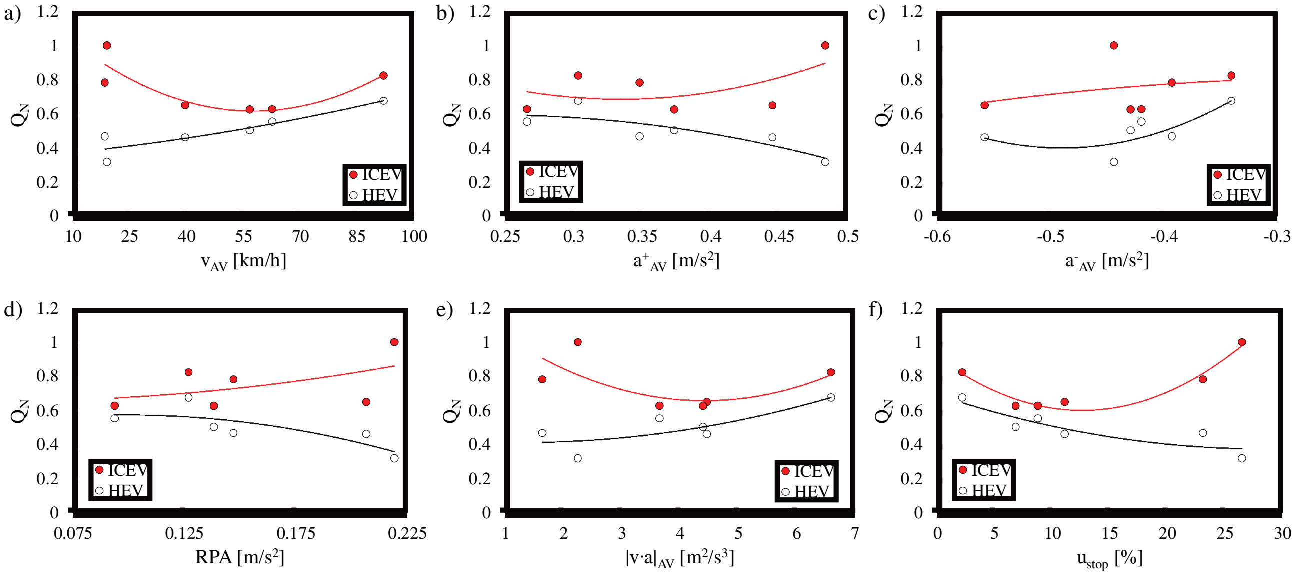

Fig. 1. The dependence of normalized fuel consumption on driving pattern parameters: average speed (a), average acceleration (b), average deceleration (c), relative positive acceleration (d), average absolute value of the product of speed and acceleration (e), time share of vehicle stop (f)

The dependencies of fuel consumption on the driving pattern parameters show considerable regularity along curves of approximation. By far the most effective parameters in this case are the average speed and time share of vehicle stop, followed by the product of speed and acceleration. On the other hand, average deceleration can be considered the worst parameter among those analyzed. Interestingly, smaller spread of points along the curves of approximation can be observed for HEV, which may result from more stable operating conditions of the internal combustion engine in the hybrid system and lower sensitivity to dynamic states of operation than in the case of ICEV.

The characteristics determined for ICEV are consistent with those known from the literature [4–5] and databases implemented in specialized software such as INFRAS or COPERT. In principle, fuel consumption of ICEVs is high in heavy traffic conditions, characterized by low average vehicle speed, high time share of vehicle stop with engine working at idle speed and high dynamics of driving, as reflected in the frequent acceleration and deceleration. For HEV it is just the opposite, because at a low speed a significant part of the power used to drive the vehicle's wheels comes from the electric motor, hence the fuel consumption is low. In addition, in the dynamic driving conditions, the share of energy recovered by recuperative braking increases. Perhaps because of this the impact of the deceleration on fuel consumption is more pronounced for HEV than ICEV.

There is also a significant increase in fuel consumption of HEV and ICEV at high average speed, which corresponds to high engine load. This time, however, both the power generated by the electric motor and the intensity of recuperative braking are relatively low and do not allow a significant reduction in fuel consumption. Last but not least, high average speed implies low time share of vehicle stop, hence high fuel consumption observed.

For obvious reasons, the dependencies of normalized road emission of carbon dioxide are almost identical to those of normalized fuel consumption. Factors determining their courses are largely the same as those affecting fuel consumption. Hence, they were not presented here and included in the discussion.

The dependence of normalized road emission of total hydrocarbons on individual parameters of driving pattern is shown in Fig. 2. The sets of points were mostly approximated by second degree polynomial functions. A power function was proposed only for average speed, average acceleration (HEV) and average absolute value of the product of speed and acceleration.

Comparing the dependences obtained for the emission of total hydrocarbons to those regarding fuel consumption, it can be concluded that they are much less regular (which is understood as a large spread of points on the graphs). Average speed, average absolute value of the product of speed and acceleration and time share of vehicle stop can be assessed as moderately effective in the description of the total hydrocarbons emission. On the contrary, average acceleration, deceleration and relative positive acceleration are not useful in this application. These conclusions are valid for both HEV and ICEV.

Difficulties in outlining the trend regarding the dependence of hydrocarbons emission on driving pattern parameters indicates a high sensitivity of hydrocarbons emission to the operating states of the internal combustion engine. Nevertheless, these results confirm observations from other research works, e.g. [3], according to which road emission of hydrocarbons is the highest for low average speed (and therefore large time share of vehicle stop) and very low for high average speed (and low time share of vehicle stop) corresponding to high engine load.

The dependence of normalized road emission of nitrogen oxides on individual parameters of driving pattern is shown in Figure 3. The sets of points were mostly approximated by second degree polynomial functions. The exemptions were: average speed and average absolute value of the product of speed and acceleration, for which a power function was proposed, and time share of vehicle stop, for which an exponential function was used.

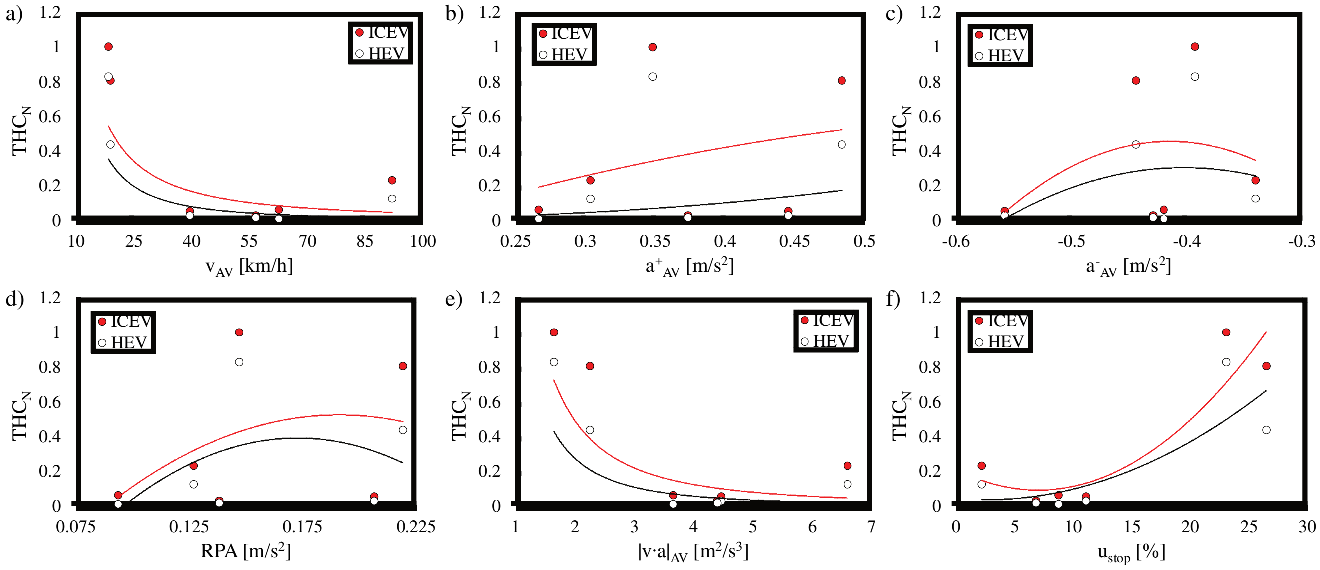

Fig. 2. The dependence of normalized road emission of hydrocarbons on driving pattern parameters: average speed (a), average acceleration (b), average deceleration (c), relative positive acceleration (d), average absolute value of the product of speed and acceleration (e), time share of vehicle stop (f)

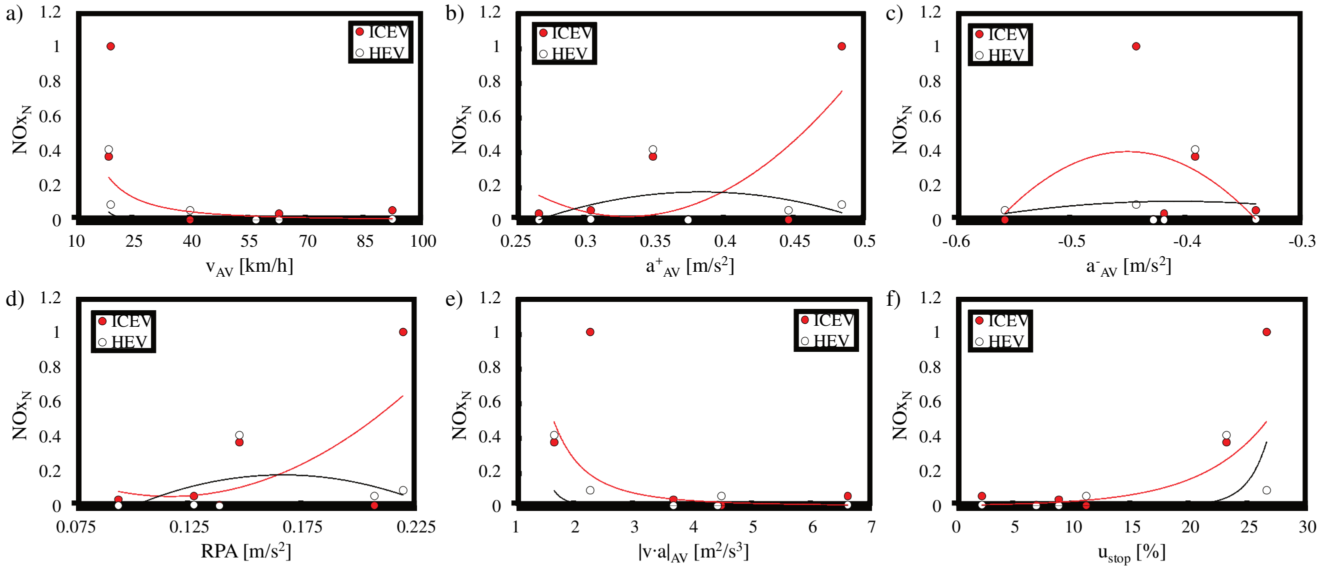

Fig. 3. The dependence of normalized road emission of nitrogen oxides on driving pattern parameters: average speed (a), average acceleration (b), average deceleration (c), relative positive acceleration (d), average absolute value of the product of speed and acceleration (e), time share of vehicle stop (f)

The relation of road emission of nitrogen oxides with driving pattern parameters should be assessed as relatively weak. For most of the parameters, the proposed approximation curve is for illustration only and does not allow to conclude on the relationship of parameters with the emission of nitrogen oxides. Only in the case of average speed, average absolute value of the product of speed and acceleration and time share of vehicle stop it is possible to determine the nature of dependence, at least to some extent. This is similar to the trends that have been discussed with reference to hydrocarbons emission.

It is worth noting that among all the pollutants that were included in this study, it is the emissions of nitrogen oxides that reached nearly the same values for both vehicles. The differences in values are very small, the only large discrepancy occurred for the 'low speed' part of the WLTC.

The dependence of normalized road emission of carbon monoxide on individual parameters of driving pattern is shown in Figure 4. The sets of points were approximated by second degree polynomial functions. The only exemption was the time share of vehicle stop, for which an exponential function was used.

When analyzing the shapes of dependencies plotted for carbon monoxide emission, differences may be noticed between results obtained for individual vehicles. The dependencies for HEV are regular and reveal some trends, whereas for ICEV there is a large spread of points, hence it is more difficult to draw the right conclusions.

Generally, the emission of carbon monoxide from HEV is much lower than from ICEV and is influenced by driving pattern. If the dependencies in Figure 5 did not apply to normalized values, this effect would be more clearly visi-

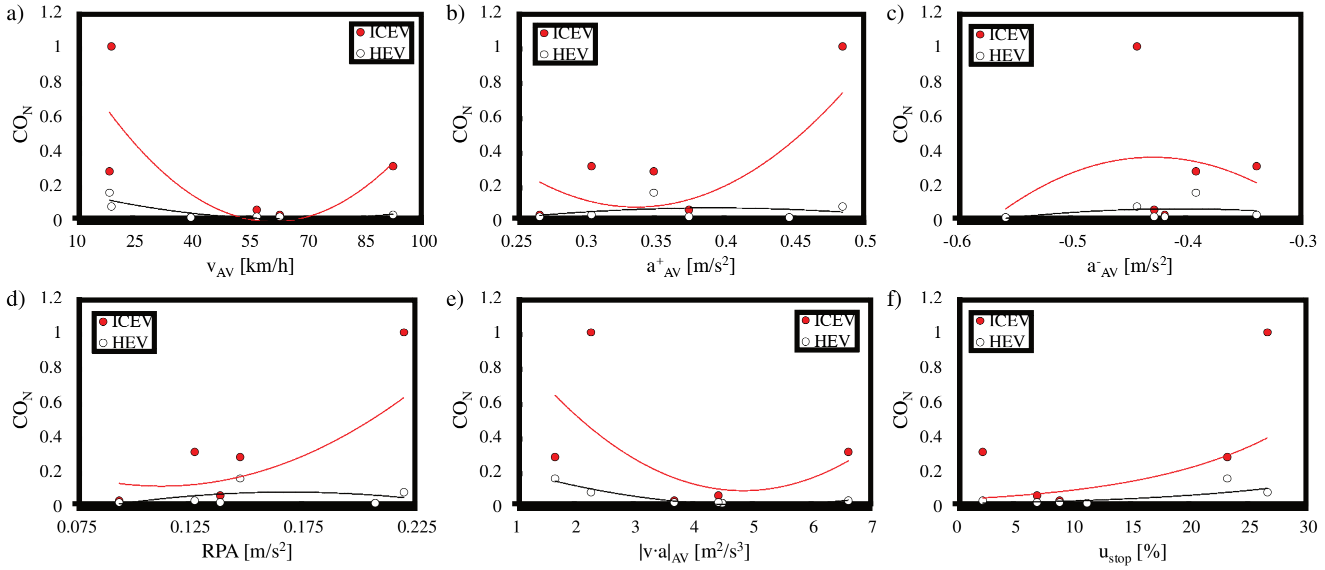

Fig. 4. The dependence of normalized road emission of carbon monoxide on driving pattern parameters: average speed (a), average acceleration (b), average deceleration (c), relative positive acceleration (d), average absolute value of the product of speed and acceleration (e), time share of vehicle stop (f)

ble. Starting from the average speed, i.e. the basic driving pattern parameter, the maxima of carbon monoxide emission for low and high speed values can be noticed. The largest emission is for low speed, which is confirmed in the literature [3, 4]. The same applies to average absolute value of the product of speed and acceleration. This is reflected in the dependence determined for the time share of vehicle stop, which is high for low average speed (typical in urban traffic) and implies high carbon monoxide emission. For parameters related to acceleration and deceleration, a maximum carbon monoxide emission may be indicated for moderate values of these parameters.

In the case of ICEV, there are similar, but less accurate, trends observed in the relationships between carbon monoxide emission and average speed, average absolute value of the product of speed and acceleration, and time share of vehicle stop. However, dependences based on average acceleration, average deceleration and relative positive acceleration are rather difficult to interpret.

5. Conclusions

The impact of vehicle driving pattern on combustion engine's fuel consumption and pollutant emission is clearly visible and unquestionable. It is then possible to quantify this impact using statistical parameters of driving pattern, determined for a given course of vehicle speed over time. Such parameters are the most useful and effective to analyze trends in fuel consumption, but relatively less in the case of pollutant emissions.

The influence of driving pattern on fuel consumption and pollutant emission of HEV depends strongly on the structure of vehicle drive system and its control strategy. The decisive factor is the algorithm, according to which the electric motor assists the combustion engine, thus reducing pollutant emission and fuel consumption under certain driving conditions. Energy recuperation during braking, with intensity depending on the driving pattern, also has a significant impact. This makes HEVs different from ICEVs in terms of the influence of driving pattern on pollutant emission and fuel consumption, which has been confirmed by the results of this study.

Nomenclature

a^+_{AV}	average acceleration
a^-_{AV}	average deceleration
BEV	battery electric vehicle
CO	carbon monoxide
CO_N	normalized road emission of carbon monoxide
CO_2	carbon dioxide
CO_{2N}	normalized road emission of carbon dioxide
CVT	continuously variable transmission
EUDC	Extra Urban Driving Cycle
HEV	hybrid electric vehicle
ICEV	internal combustion engine vehicle
MPI	multi-point injection
NEDC	New European Driving Cycle
NO_x	nitrogen oxides
NO_{xN}	normalized road emission of nitrogen oxides
PHEV	plug-in hybrid electric vehicle
Q	fuel consumption
Q_N	normalized fuel consumption
RPA	relative positive acceleration
THC	total hydrocarbons
THC_N	normalized road emission of total hydrocarbons
UDC	Urban Driving Cycle
u_{stop}	time share of vehicle stop
$\|v\cdot a\|_{AV}$	average absolute value of the product of speed and acceleration
v_{AV}	average speed
WLTC	Worldwide Harmonized Light Vehicles Test Cycle

Bibliography

[1] ANDRÉ, M. Driving cycles development: characterisation of the methods. *SAE Technical Paper 961112*. 1996.

[2] CHŁOPEK, Z. Propozycja charakterystyk emisji zanieczyszczeń z silników spalinowych pracujących w warunkach dynamicznych. *Archiwum Motoryzacji*. 2009, **2**, 111-134.

[3] CHŁOPEK, Z., BIEDRZYCKI, J., LASOCKI, J., WÓJCIK, P. Comparative examination of pollutant emission from an automotive internal combustion engine with the use of vehicle driving tests. *Combustion Engines*. 2016, **164**(1), 56-64.

[4] CHŁOPEK, Z., BIEDRZYCKI, J., LASOCKI, J., WÓJCIK, P. Investigation of pollutant emissions from a motor vehicle engine in tests simulating real vehicle use in road traffic conditions. *Combustion Engines*. 2013, **154**(3), 202-207.

[5] CHŁOPEK, Z., LASOCKI, J., WÓJCIK, P., BADYDA, A.J. Experimental investigation and comparison of energy consumption of electric and conventional vehicles due to the driving pattern. *International Journal of Green Energy*. 2018, **15**(13), 773-779, DOI:10.1080/15435075.2018.1529571.

[6] ERICSSON, E. Independent driving pattern factors and their influence on fuel-use exhaust emission factors. *Transportation Research Part D: Transport and Environment*. 2001, **6**(5), 325-345.

[7] FOMUNUNG, I., WASHINGTON, S., GUENSLER, R. A statistical model for estimating oxides of nitrogen emissions from light duty motor vehicles. *Transportation Research Part D: Transport and Environment*. 1999, **4**(5) 333-352. DOI:10.1016/S1361-9209(99)00013-9.

[8] GIS, M., BEDNARSKI, M. Comparative studies of harmful exhaust emission from a hybrid vehicle and a vehicle powered by spark ignition engine. *IOP Conference Series: Materials Science and Engineering*. 2018, **421** 042022. DOI:10.1088/1757-899X/421/4/042022.

[9] GIS, M., BEDNARSKI, M., WIŚNIOWSKI, P. Comparative analysis of NEDC and WLTC homologation tests for vehicle tests on a chassis dynamometer. *Journal of KONES Powertrain and Transport*. 2018, **25**(3), 189-196.

[10] GIS, M., LASOCKI, J. Advantages of using hybrid vehicles based on empirical studies on the chassis dynamometer in the WLTC test. *Journal of KONES Powertrain and Transport*. 2018, **25**(4), 103-109.

[11] KUHLER, M. KARSTENS, D. Improved driving cycle for testing automotive exhaust emissions. *SAE Technical Paper 780650*. 1978.

[12] NEUBAUER, J.S., BROOKER, A., WOOD, E. Sensitivity of battery electric vehicle economics to drive patterns, vehicle range, and charge strategies. *Journal of Power Sources*. 2012, **209**, 269-277.

Jakub Lasocki, DEng. – Faculty of Automotive and Construction Machinery Engineering, Warsaw University of Technology.

e-mail: *jakub.lasocki@pw.edu.pl*

Maciej Gis, DEng. – Environment Protection Centre in Motor Transport Institute.

e-mail: *maciej.gis@its.waw.pl*

Article citation info:
SIADKOWSKA, K., WENDEKER, M., GRABOWSKI, Ł. An investigation of the fuel injector dedicated to the aircraft opposed-piston two-stroke diesel engine. *Combustion Engines*. 2019, **177**(2), 151-155. DOI: 10.19206/CE-2019-227

Ksenia SIADKOWSKA
Mirosław WENDEKER
Łukasz GRABOWSKI

CE-2019-227

An investigation of the fuel injector dedicated to the aircraft opposed-piston two-stroke diesel engine

The paper presents the research results of the injector construction with the modified injection nozzle. The injector is designed for a prototype opposed-piston aircraft diesel engine. The measurements were based on the Mie scattering technique. The conditions of the experiment corresponded to maximum loads similar to those occurring at the start. The measuring point was selected in line with the analysis of engine operating conditions: combustion chamber pressure at the moment of fuel delivery (6 MPa) and fuel pressure in the injection rail (140 MPa). The analysis focused on the average spray range and distribution, taking into account the differences between holes in the nozzle. As a result of the conducted research, the fuel spray range was defined with the determined parameters of injection. The fuel spray ranges inside the constant volume chamber at specific injection pressures and in the chamber were examined, and the obtained results were used to verify and optimize the combustion process in the designed opposed-piston two-stroke engine.

Key words: *diesel engine, injector, opposed-piston engine, spray range*

1. Introduction

The correct process of fuel spraying in the combustion chamber is extremely important because the engine achieves optimal operating parameters and minimizes the emission of toxic substances. Injection equipment has a significant role in the formation of an air-fuel mixture and influences the fuel flow rate from nozzles, the range of the fuel flow front and the way of distribution of fuel droplets in the combustion chamber [1]. Registration of images inside the combustion engine cylinder meets with a number of difficulties, mainly related to high temperature and pressure, limited access to the cylinder and very high dynamics of recorded phenomena [7]. However, optical techniques are becoming more and more popular, as evidenced by studies using fixed volume chambers in universities and R&D centres in China [5], Spain [5, 9] or simulation studies conducted in centres in Korea and the USA [6] or in Germany and Slovenia [10].

The research engine was a newly designed internal Diesel engine. The unit is characterized by three cylinders with three pairs of opposed-pistons. The engine will generate a power output equal to 100 kW at a crankshaft rotation speed of 3800-4000 rpm, with a capacity of about 1.6 l, with a Diesel cycle. The engine will be equipped with a direct Diesel injection system [3]. It was assumed initially that the chamber to test fuel spray in the engine injection analysis should maintain nitrogen or air pressure at the level of P_{pow} = 5–8 MPa. Due to the examination of the spraying process only, without combustion, high temperatures will not be reached. The diameter of these chambers is in the range of 70–220 mm, their height is 33–120 mm, and optical access is from 2–6 sides of the chamber. The studies carried out at the Poznań University of Technology [7, 13, 14] used windows made of 30 mm thick quartz glass instead, which enabled the researchers to set the compression pressure at the level of 10 MPa and to record the penetration of the spray with a camera.

In the test engine injection chamber, there is no need to install a piston inside the chamber, but it is necessary to install an injector, pressure and temperature sensors and a gas supply valve in order to maintain a given pressure during the tests. Three windows will provide optical access for sufficient observation of the spray distribution. Due to the diameter of the test engine cylinder of 65–70 mm, the chamber parameters of Φ = 100 and H = 120 can ensure convenient testing capabilities to obtain a volume of nearly 1 dm^3. Figures 1–4 below present a graphical documentation of constant volume chambers used in selected studies.

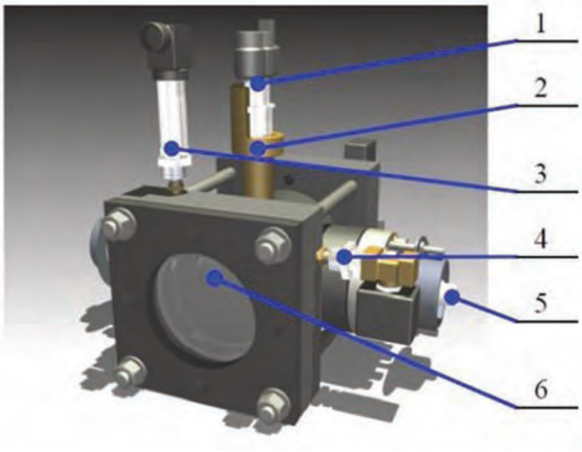

Fig. 1. View of the constant volume chamber – Poznań University of Technology: 1 – injector, 2 – injector housing, 3 – air pressure sensor, 4 – electromagnetic air valve outflow, 5 – lighting, 6 – quartz glass [13]

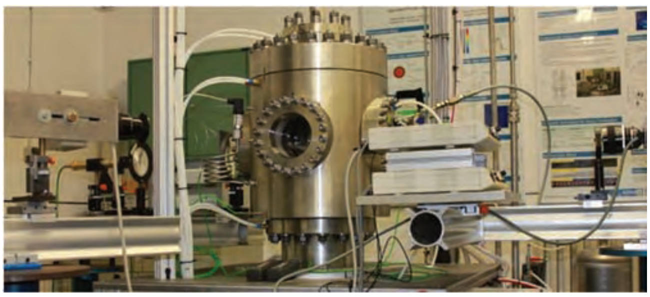

Fig. 2. Constant volume chamber at RWTH Aachen, Germany [8]

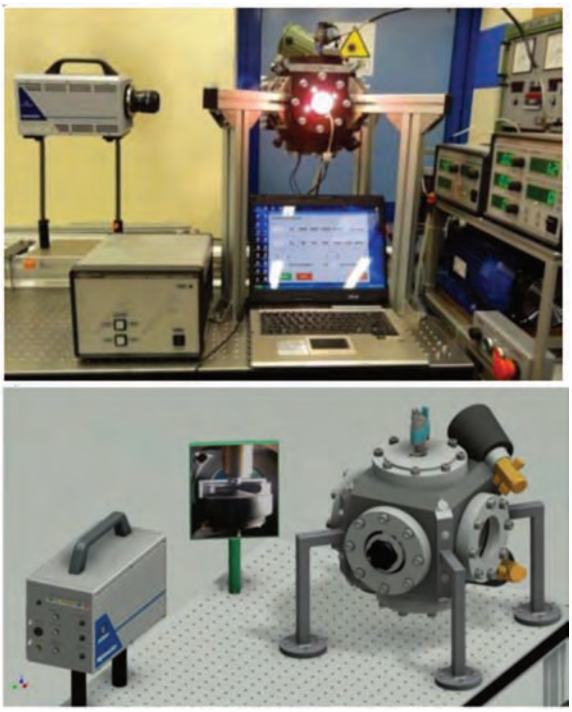

Fig. 3. A research stand for the optical tests of fuel injection and spraying process – Poznań University of Technology [13]

Fig. 4. Constant volume test chamber – Technical University of Valencia [11]

2. Research scope

In order to do the analysis of optical tests of the fuel injection process, a series of measurements of the spray range in a constant volume chamber at the injection pressure of 140 MPa and in the chamber (counter pressure) of 6 MPa was carried out. The aim of the research was to determine the range of the fuel spray at specific parameters of its injection. The studies were to enable the evaluation of the range of fuel spray inside the constant volume chamber at a specific injection pressure and in the chamber. The conditions of the experiment corresponded to the maximum loads similar to those occurring at the start. The measuring point was selected on the basis of the analysis of engine operating conditions: combustion chamber pressure (6 MPa) at the moment of fuel delivery and fuel pressure in the injection rail (140 MPa).

The investigations of fuel jet penetration were carried out in a constant volume chamber with the following parameters: maximum working pressure of 15 MPa, optical access in the shape of a circle with a diameter of 160 mm, volume of about 5.5 dm^3. A piezoelectric Kistler sensor (0–25 MPa) measured the pressure in the chamber, while a piezoresistive Kistler sensor (0–200 MPa) measured the fuel pressure. To generate fuel pressure, a Common Rail system with a pressure control of 0-200 MPa was used. The chamber was equipped with two M12×1.5 or M14×1.5 connections sealed on a 60 deg cone. In order to carry out the tests, a dedicated injector mounting was made to the chamber.

The Photron FAST-CAM SA1.1 UltraHigh-Speed Video System used in this research is applied in ballistics, material research, the defence and aerospace industries, fluid dynamics and PIV. It uses a modern CMOS sensor to achieve sensitivity and speeds that were previously unavailable. Its maximum speed exceeds 600,000 fps, its global shutter operates regardless of the selected refresh rate, and its dead time between successive stages is less than a microsecond. Figure 5 shows the camera. The tests were performed at 5400 fps and 1024 × 1024 resolution, which ensured optimal results.

Fig. 5. Photron FASTCAM SA1.1 – a camera view [12]

The evolution of the range of the fuel spray in the high-pressure chamber was measured. The research included the measurements with a high speed camera based on the Mie scattering technique with global lighting (7 repetitions for a specific measurement point).

The preparation of the test stand and measurements for a single measurement point included:

a) designing and making assembly elements of the researched injector.

b) measuring (7 repetitions) the injection at a frequency of min. 10 000 Hz for a given injection pressure (fuel pressure) and counter pressure (chamber pressure).

c) graphic processing the collected images - determination of the relationship between the spray range and time.

The Bosch Injector No. 0 445 110 135 was used for the optical testing of the fuel injection process. This injector is shorter than typical electromagnetic injectors. The holes in the nozzles were electro-drilled, and their edges were rounded. There are two holes with a diameter of $\Phi = 0.14$ mm, placed on the circumference every 180° (Fig. 6).

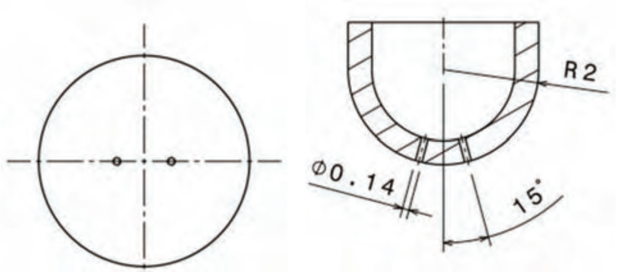

Fig. 6. Location of the spray holes

In order to determine the precise geometry of the inside of the nozzle and verify the correctness of hole welding, a tip scanning was carried out with the SkyScan 1173 device. It is a high-energy (130 kV) micro-scanner dedicated to large objects and capable of spiral scanning allowing for a 2D/3D image analysis and a realistic visualization of the internal structure with a spatial accuracy of at least 7 μm [2].

Figure 7 shows the scanner capabilities on the example of the injector. Figure 8 shows the scanned tips of the nozzle used in the engine, while Figure 9 shows the scanning effects.

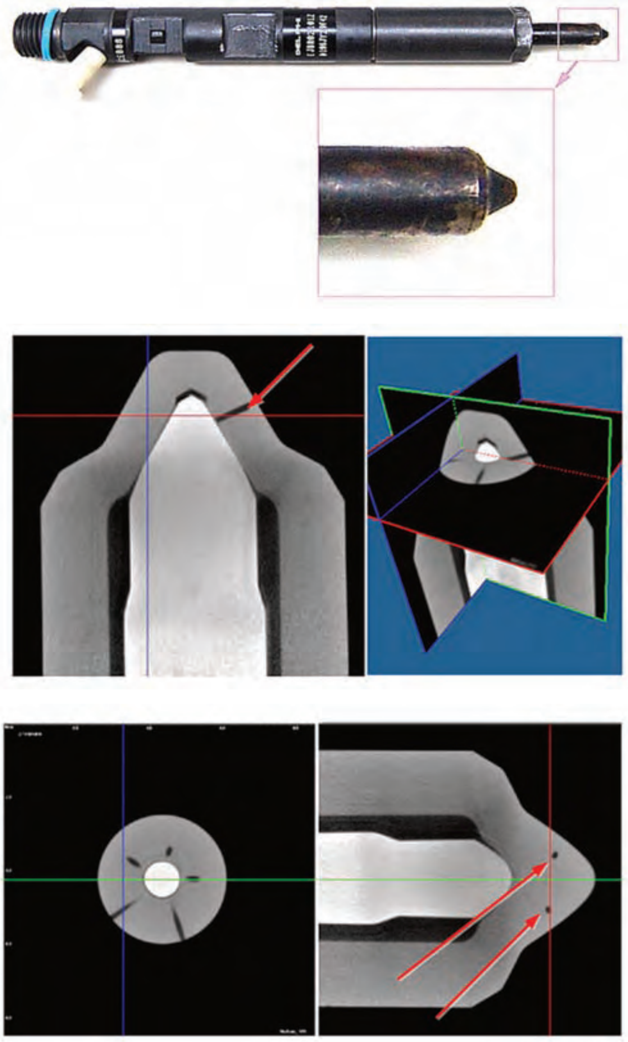

Fig. 7. Sample scanning [2]

Fig. 8. Scanning of the spray tip

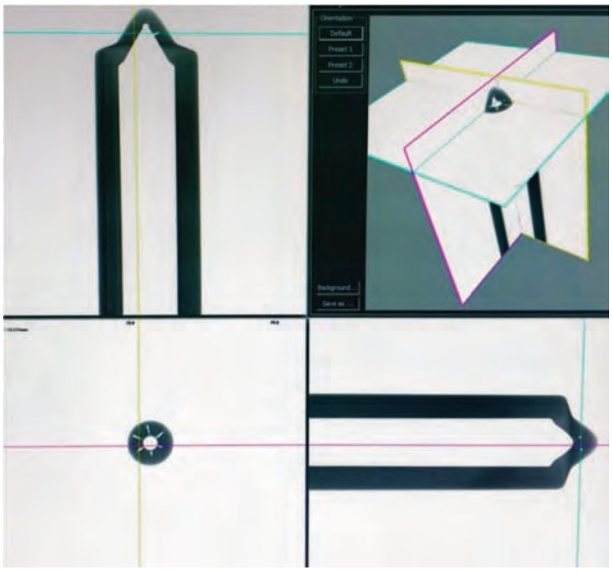

Fig. 9. Results of the scanning of the spray tip with its welded holes – scanning accuracy 10 μm

3. Test results and analysis

Figures 10 and 11 show the measurement results for seven repetitions, separately for the left and right nozzle holes. The total registration time was 10 ms, but the most important is the period from 0 to 2 ms, because such injection time will occur in the designed engine, for which the injector is dedicated. The diameter of the combustion chamber is 65–70 mm. The injector is placed perpendicularly to the cylinder axis, so that the range of the spray does not exceed the dimensions of the cylinder. Obtained after

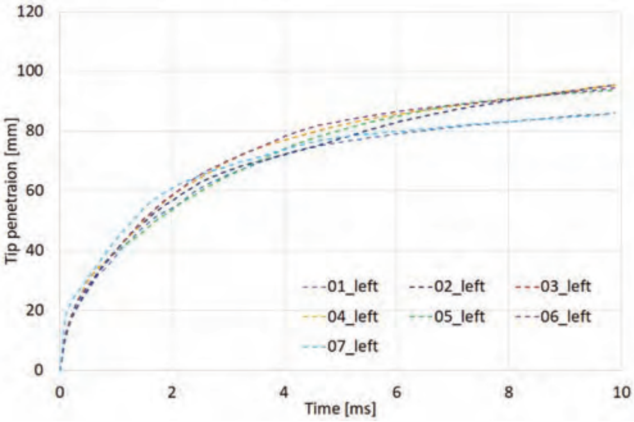

Fig. 10. Fuel spray ranges at the measurement point: injection pressure 140 MPa, in the chamber 6 MPa, left hole

2 ms range of 60 mm is correct, because during this time the spray does not reach the wall of the opposed-piston engine. The achieved spray ranges within 2 ms are repeatable, and overlapping. Initially, the shape of the curve is similar to a parabola, then, after 4 ms, it is flattened almost to a straight line. This is due to the fact that as the distance from the atomizer increases, the kinetic energy of the stream decreases. The effect of counter pressure is also visible. Figure 12 shows the average range of the spray at the measuring point for both nozzle holes. The mean ranges from left and right holes do not differ significantly from each other. The combustion chamber is symmetrical, so the same propagation of the spray was expected.

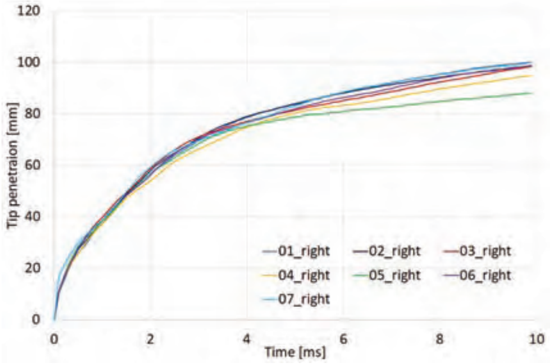

Fig. 11. Fuel spray ranges at the measurement point: injection pressure 140 MPa, in the chamber 6 MPa, right hole

Table 2 shows the images recorded at the selected period of time, showing the average range of individual sprays at the indicated measuring points. The research was carried out at a single measurement point for which 7 repetitions were made. The ranges from the left and right spray tip hole were analysed separately. The sizes of the ranges for the left and right sprays tips are significantly similar. A further development of the spray pattern results in a different size of the spray ranges because of partial evaporation of individual sprays and a change in fuel concentration at the liquid-air border [13].

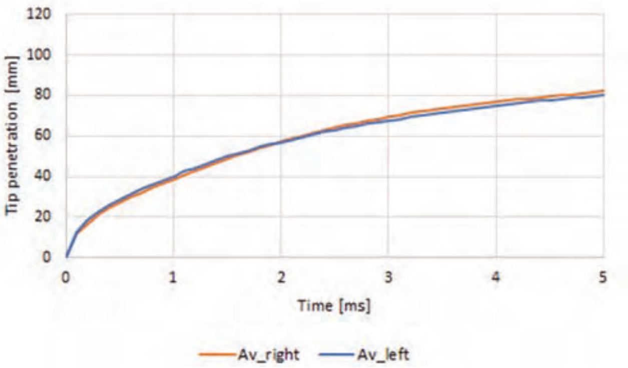

Fig. 12. Average fuel spray ranges at the measurement point: injection pressure 140 MPa, in the chamber 6 MPa

Table 2. Range of the spray at the measuring point

Measuring point (140/6 MPa)			Length [mm]	Number of droplets
0,5 ms	1,0 ms	2,0 ms		
	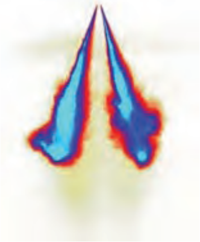	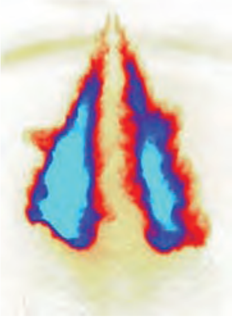	0 10 20 30 40 50 60	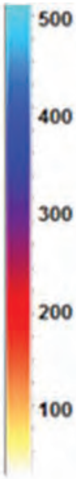 500 400 300 200 100
3,0 ms	4,0 ms	5,0 ms		
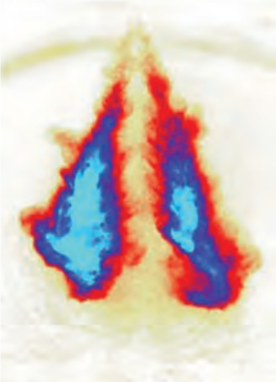	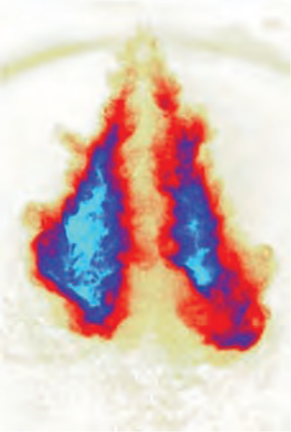	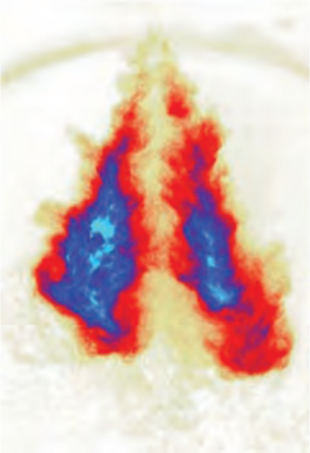	0 10 20 30 40 50 60 70 80 90	

Conclusions

The research was dedicated to the spray range in the constant volume chamber with a high speed camera. The analysis of the injection process enabled us to determine the nature of fuel spraying as well as the length and speed of the spray.

As a result of the study, the range of fuel spray was determined at constant injection parameters. The fuel spray penetration ranges inside the constant volume chamber at specific injection pressures and in the chamber were examined. The obtained results will be used to verify and optimize the combustion process in the research engine.

Acknowledgements

This work has been realized in the cooperation with The Construction Office of WSK "PZL-KALISZ" S.A." and is part of Grant Agreement No. POIR.01.02.00-00-0002/15 financed by the Polish National Centre for Research and Development.

Bibliography

[1] ANDREASSI, L., UBERTINI, S., ALLOCCA, L. Experimental and numerical analysis of high pressure diesel spray-wall interaction. *International Journal of Multiphase Flow*. 2017, **33**, 742-765, DOI:10.1016/j.ijmultiphaseflow.2007.01.003.

[2] Bruker microCT. Description SkyScan1173. 2018, http://bruker-microct.com/products/1173.htm.

[3] CZYŻ, Z., SIADKOWSKA, K., SOCHACZEWSKI, R. CFD analysis of charge exchange in an aircraft opposed-piston diesel engine. *MATEC Web of Conferences*, 2019, ***252***, 4002, DOI:10.1051/matecconf/201925204002.

[4] DESANTES, J.M., GARCÍA-OLIVER, J.M., XUAN, T. et al. A study on tip penetration velocity and radial expansion of reacting diesel sprays with different fuels. *Fuel*. 2017, **207**, 323-335, DOI:10.1016/j.fuel.2017.06.108.

[5] DESANTES, J.M., PASTOR, J.V., GARCÍA-OLIVER, J.M. et al. An experimental analysis on the evolution of the transient tip penetration in reacting diesel sprays. *Combustion and Flame*. 2014, **161**, 2137-2150, DOI:10.1016/j.combustflame.2014.01.022.

[6] HOON, C., REITZ, R.D. CFD simulations of diesel spray tip penetration with multiple injections and with engine compression ratios up to 100:1. *Fuel*. 2013, **111**, 289-297, DOI:10.1016/j.fuel.2013.04.058.

[7] IDZIOR, M., STOBNICKI, P., PIELECHA, I. et al. Research and analysis of the influence of the injection pressure on spraying fuel in the chamber about the fixed volume. *Combustion Engines*. 2013, **154**(3), 811-819.

[8] ITV RWTH Aachen. Spraykammer. 2018, https://www.itv.rwth-aachen.de/index.php?id=41.

[9] LI, F. et al. Experimental study on spray characteristics of long-chain alcohol-diesel fuels in a constant volume chamber. *Journal of the Energy Institute*. 2017, C, 1-14, DOI:10.1016/j.joei.2017.11.002.

[10] MARCIC, S., MARCIC, M., WENSING, M. et al. A simplified model for a diesel spray. *Fuel*. 2018, ***222***, 485-495, DOI:10.1016/j.fuel.2018.02.152.

[11] PAYRI, R., GARCÍA-OLIVER, J.M., BARDI, M. et al. Fuel temperature influence on diesel sprays in inert and reacting conditions. *Applied Thermal Engineering*. 2012, **35**(1), 185-195, DOI:10.1016/j.applthermaleng.2011.10.027.

[12] Photron. Specyfikacja FASTCAM SA1.1. 2018, www.photron.com.

[13] PIELECHA, I. et al. Problems of determining of fuel spray geometric parameters when based on optical investigations. *Combustion Engines*. 2015, **162**(3), 307-315.

[14] STOBNICKI, P. Badawcza analiza wtrysku paliwa w aspekcie właściwości ekologicznych silnika o zapłonie samoczynnym. 2013.

Ksenia Siadkowska, MEng. – Faculty of Mechanical Engineering, Lublin University of Technology.
e-mail: *k.siadkowska@pollub.pl*

Łukasz Grabowski, DEng. – Faculty of Mechanical Engineering, Lublin University of Technology.
e-mail: *l.grabowski@pollub.pl*

Prof. Mirosław Wendeker, DSc., DEng. – Faculty of Mechanical Engineering, Lublin University of Technology.
e-mail: *m.wendeker@pollub.pl*

Article citation info:
KURCZYŃSKI, D., WARIANEK, M., ŁAGOWSKI, P. Analysis of the uniqueness of the combustion process of the Perkins 1104D-E44TA engine in dual-fuel operation powered by natural gas and diesel fuel. *Combustion Engines*. 2019, **177**(2), 156-164. DOI: 10.19206/CE-2019-209

Dariusz KURCZYŃSKI
Michał WARIANEK
Piotr ŁAGOWSKI

CE-2019-228

Analysis of the uniqueness of the combustion process of the Perkins 1104D-E44TA engine in dual-fuel operation powered by natural gas and diesel fuel

The paper presents the results of the research on the uniqueness of the combustion process in the Perkins 1104D-E44TA engine already equipped with a Common Rail injection system, and then adapted on an engine test stand to dual-fuel operation. The result of the combustion process is an indicator diagram. The combustion process in the cylinder of the tested engine was evaluated by determining the uniqueness indicators of subsequent operating cycles, such as: the uniqueness indicator for the maximum pressure of the operating cycle, the uniqueness indicator for the mean indicated pressure, the uniqueness indicator for the indicated diagram and the uniqueness indicator for the partial indicator diagram. The conducted tests and the analysis of the results showed the impact of dual-fuel power supply of the tested engine on the combustion process, as compared to supplying the engine only with diesel fuel, for which it has been optimized.

Key words: *dual-fuel, natural gas, combustion process, indicator diagram, uniqueness of combustion process*

1. Introduction

Fuels for compression-ignition combustion reciprocating engines must have high atomization, evaporation and air mixing capability, so as to ensure easy engine start-up as well as long service life and reliability. The conventional fuels used to power these engines are diesel fuels obtained from crude oil in the process of its distillation and in the process of secondary processing of heavy distillation residues. Diesel fuels are a mixture of many different hydrocarbons with different properties and structure of molecules, containing from 14 to 20 carbon atoms in a molecule, boiling at a temperature from 150°C to 380°C [1]. Its density at a temperature of 15°C is approximately 817-856 kg/m^3. Diesel fuels include the following hydrocarbons: linear paraffinic, branched isoparaffinic as well as naphthenic and aromatic with a ring structure. The number of individual hydrocarbon groups in diesel fuel determines its physicochemical properties affecting the efficiency of engine operation and the toxicity of exhaust fumes. In the elemental composition, diesel fuels contain about 86% of carbon and 14% of hydrogen [23, 24]. The properties of modern diesel fuels used to power compression-ignition engines are well known, defined in detail and adapted to engine requirements. They are mainly characterized by good compression-ignition properties. They have a high calorific value per unit of mass as well as per unit of volume. Diesel fuels are relatively easy to store, transport and use as a fuel for combustion engines. The properties of diesel fuels change as needed, by modifying their hydrocarbon composition and introducing various additives.

Natural gas is an interesting alternative to power reciprocating combustion engines. It presents smaller risk to the environment compared to crude oil or coal. It is a fuel which occurs in large quantities and is characterized by favorable properties in terms of possibilities to power combustion engines [3, 21, 28]. First and foremost, by a simple chemical structure, which determines fast and complete combustion, low content of toxic compounds and solids, as well as a smaller quantity of carbon dioxide in exhaust fumes. It consists mainly of one, the simplest carbon-hydrogen compound, methane. Its content in natural gas may be 85–99% [5]. Natural gas also includes other hydrocarbons such as ethane, propane, butane, isobutane, hexane, heptane, octane, pentane, isopentane. It may also contain impurities such as carbon dioxide, nitrogen, hydrogen sulphide, helium and small amounts of water vapor [2]. Natural gas is lighter than air. In the case of tank leaks, it quickly rises up to higher atmospheric layers. It forms explosive mixtures with air. The autoignition temperature of compressed natural gas can range from 480°C to approximately 630°C [11]. Under normal conditions, the density of natural gas vapor is 0.72–0.76 kg/m^3 [8]. The properties of natural gas are largely determined by the properties of methane, which is its main component. The boiling point of methane is –161.0°C and the melting point is –182.0°C [9]. Its autoignition temperature is 595°C [10]. It has a high octane number of about 130, which means that it is resistant to detonation.

The properties of diesel fuel and natural gas presented above are significantly different. They make natural gas easier to use for powering spark-ignition engines. According to [26, 27], the autoignition temperature of natural gas can be 650°C and for diesel fuel 250°C. Diesel fuels have the ability of autoignition at the level of the cetane number of 45–55, whereas natural gas is resistant to detonation described by the octane number at the level of 120–130 [12]. This makes it more difficult to use natural gas in compression-ignition engines. The natural gas/air mixture compressed in the cylinder will not self-ignite. An ignition source is required to initiate the combustion of a natural gas/air mixture. In addition, natural gas burns slower than liquid petroleum fuels for supplying high-speed combustion engines.

The calorific value per unit of mass for natural gas is greater than the calorific value of diesel fuel [4, 28, 29]. However, the density of natural gas at ambient conditions is, of course, much lower than that of diesel fuel. Thus, the calorific value of the gaseous fuel per volume unit at ambient conditions is smaller than of diesel fuel. In order to increase the energy density of natural gas, it is necessary to compress it to high pressures (about 20 MPa) or to condense it at a temperature of about –162°C and ambient pressure. Compression or condensation of natural gas is technologically and technically possible, but also causes additional problems in terms of transport, storage and use for powering the engines.

There are two options of the use of natural gas for powering compression-ignition engines. The first is the introduction of significant changes in the engine structure, i.e. a reduction in the compression ratio and the introduction of the ignition system. In fact, a compression-ignition engine becomes a spark-ignition engine and can no longer be powered by diesel fuel. The second option is the use of dual-fuel supply [13, 14, 22, 25]. This means that two fuels can be burned simultaneously in a cylinder of a dual-fuel engine: natural gas and diesel fuel. Diesel fuel, injected at the end of the compression process, is the source of ignition of the natural gas. This approach allows the engine to be powered by two fuels simultaneously or by diesel fuel only. The technology of dual-fuel powering of compression-ignition engines by natural gas and diesel fuel is still being developed. The conducted research concerns, among others, the processes of fuel-air mixture formation and combustion while simultaneously powering the engine with natural gas and diesel fuel.

2. Object of the study

The object of the study was a four-cylinder compression-ignition engine Perkins 1104D-E44TA equipped with a Common Rail injection system with direct fuel injection and electromagnetically controlled injectors. It meets the Tier 3 emission standard for engines with non-road applications [19]. It is equipped with a forced induction with a turbocharger controlled by a blow off valve connected to the solenoid valve controlled by an electronic unit controlling the engine operation. On the basis of information provided by the sensors determining the engine operating conditions, this unit calculates the injected fuel dose, controlling the value of pressure in the fuel tank and the time of injection as well as charging pressure. The basic technical data of the tested engine are presented in Table 1.

Table 1. Basic technical data of the Perkins 1104D-E44TA diesel engine

Parameter	Unit	Value
Cylinder arrangement	–	straight
No of cylinders	–	4
Injection type	–	direct
Type of fuel system	–	Common Rail
Max. engine power	kW	96,5
Engine speed at maximum power	rpm	2200
Max. torque	Nm	516,0
Engine speed at max. torque	rpm	1400
Engine cubic capacity	m^3	$4.4\cdot10^{-3}$
Cylinder diameter	mm	105
Piston stroke	mm	127
Compression ratio	–	16.2
Air supply system	–	turbocharger, intercooler

Perkins 1104D-E44TA engine, located at the engine test stand in the Heat Engines Laboratory at the Kielce University of Technology, has been adapted to dual-fuel operation using the compressed natural gas CNG and diesel fuel ON. This engine is equipped with a CNG powering system with an electronic control unit of the OSCAR-N DIESEL system [7]. The flow chart of the Perkins 1104D-E44TA engine powering system by CNG of the OSCAR-N DIESEL system is shown in Figure 1. Gaseous fuel is delivered to the intake system between the turbocharger and the intercooler. Natural gas is fed by means of four injectors mounted on a common rail. Injectors supply gas fuel through flexible hoses to the hose, where the air from the turbocharger flows to the cooler. The mixture of gaseous fuel and air after passing through the cooler is fed to the engine cylinders. It is compressed in the engine cylinders. At the end of the compression process, a reduced amount of diesel fuel is injected into the cylinder, which then ignites itself and starts the process of combustion of the gas fuel accumulated in the cylinder. The amount of gaseous fuel supplied to the engine intake system shall be determined by the controller of the system for powering the engine with this fuel. This depends on the operating conditions of the engine. The amount of natural gas supplied to the cylinder must not exceed the amount causing detonation and exceeding the permissible temperatures. This means that at higher loads, the dose of natural gas is reduced and the dose of diesel fuel is increased. In the absence of gaseous fuel, the engine is conventionally powered by diesel fuel.

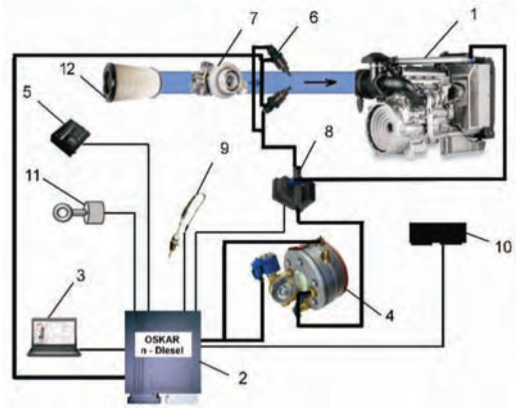

Fig. 1. The flow chart of the natural gas fuelling system OSCAR-N DIESEL: 1 – Perkins 1104D-E44TA engine, 2 – controller of the engine gas fuelling system, 3 – computer, 4 – reducer, 5 – gas system switch, 6 – gas injectors, 7 – turbocharger, 8 – gas pressure regulator, 9 – temperature sensor, 10 – emulator, 11 – ignition switch, 12 – air filter

3. Engine test stand

The tests were carried out on an engine test stand located in the Heat Engines Laboratory at the Kielce University of Technology. Perkins 1104D-E44TA engine being tested at this stand is connected with an eddy current brake, which enables the engine to operate under various load and crankshaft speed conditions. The change of the engine test stand's operational parameters is carried out by means of a control module located in the control room of the test stand. The measurement of the mass consumption of diesel fuel in the tested engine is carried out using the fuel gauge manufactured by Automex. Mass consumption of natural gas is measured at the test stand using the Coriolis flow meter by Emerson. An accurate measurement of the mass of air supplied to the cylinders is carried out using an ABB flow meter. The diagram of the engine test stand on which the tests were performed is shown in Fig. 2.

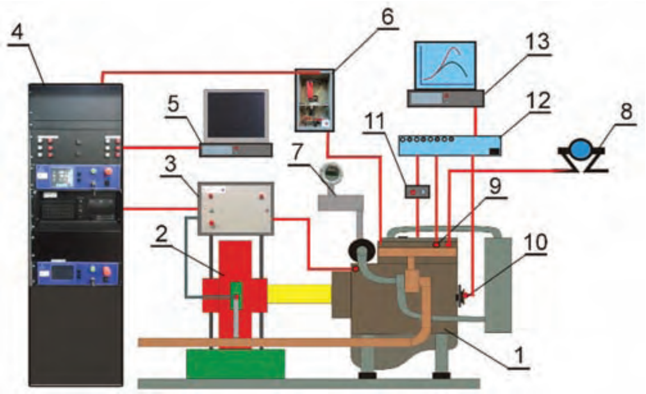

Fig. 2. Test stand elements: 1– Perkins 1104D - E44TA engine, 2 – Automex AMX 200/6000 brake, 3 – measurement module, 4 – measurement cabinet with stand control system, 5 – computer to control station parameters and archive test results, 6 – Automex ATMX2040 mass fuel dosimeter, 7 – ABB mass air flow meter, 8 – Coriolis flow meter for measurement of CNG consumption, 9 – sensor of the pressure in the engine cylinder, 10 – engine crank angle encoder AVL 365C, 11 – converter for measuring the current controlling the operation of the injector LA25NP, 12 – AVL IndiSmart 612 system for indicating fast-changing quantities, 13 – computer for archiving fast-changing quantities

The tests of the working medium pressure in the Perkins 1104D - E44TA engine cylinder were carried out using the AVL IndySmart 612 measuring system. It consisted of the following elements:

- AVL IndiSmart 612 data acquisition system,
- piezoelectric pressure sensor in the AVL GH13P/AG04 engine cylinder,
- optical encoder of an engine crank angle AVL 365C.

The piezoelectric sensor enables the continuous measurement of the pressure in the engine cylinder. The analogue signal from the sensor is sampled at high frequency. The AVL 365C photoelectric encoder used in the system generates 720 electrical impulses per revolution. This allows the pressure to be measured in increments of 0.5°of the crank angle. The measurement system enables the multiplication of this signal, which allows to increase the resolution of the measurement to 0.1° of the crank angle. AVL Indicom Mobile 2012 is used to operate the engine cylinder pressure measuring system. It allows, among other things, to record pressure for subsequent operation cycles and to draw up mean indicator diagrams. It also enables the analysis of the combustion process based on the heat released during this process. The system for measuring the fast-changing quantities of the tested engine has been additionally equipped with a system for measuring the current controlling the operation of the injector. This system was connected in series to the line controlling the operation of the injector of this cylinder, in which the pressure was recorded. It made it possible to record the profile of the current controlling the operation of the injector as a function of the crank angle. The flow chart of the fast-changing quantity measurement system used during the tests is shown in Fig. 3.

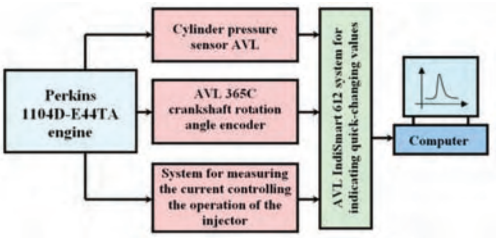

Fig. 3. The flow chart of the measurement system of fast-changing quantities of Perkins 1104D-E44TA engine used for testing

4. Indicator diagrams for Perkins 1104D-E44TA engine in dual-fuel operation

Tests of Perkins 1104D-E44TA engine running on compressed natural gas and diesel CNG + Diesel in dual-fuel operation and, for comparison, when powered by diesel fuel only, were conducted when it was operating according to the external speed characteristics and the load characteristics for crankshaft speed n = 1800 rpm. Using the AVL IndiSmart 612 system for measuring fast-changing quantities, the pressure waveform in the cylinder of the engine under test were recorded for subsequent fifty operating cycles under steady state conditions. The measurements of the pressure in the cylinder were carried out with a resolution of 0.1° of the crank angle. Diagrams constituting Figure 4 show example results of pressure measurements in the engine cylinder as a function of the crank angle for subsequent fifty operating cycles of the Perkins 1104D-E44TA engine in dual-fuel operation and powered by diesel fuel only. The diagrams show that in the case of an engine powered by CNG and diesel fuel, the spread of the maximum combustion pressures is significantly greater than the spread of these values obtained in an engine powered by diesel fuel only. It should be noted that the diagrams presented were developed at low engine load, where the share of natural gas in total fuel consumption is high. The sets of indicator diagrams determined under the steady state operating conditions, while powering the tested engine with a specific fuel, were used to calculate the uniqueness of the combustion process. Figure 5 shows a comparison of the pressure waveforms during the combustion process in the Perkins 1104D-E44TA engine cylinder operating according to external speed characteristics for selected crankshaft speeds n = 1400, 1800 and 2200 rpm, in dual-fuel operation CNG + Diesel and powered by diesel fuel only. For the two different powering methods tested, slight differences in the pressure waveforms were obtained. Figure 6 shows a comparison of the pressure waveforms during the combustion process in the Perkins 1104D-E44TA engine cylinder operating according to the load characteristics for crankshaft speed n = 1800 rpm, with selected loads of the engine T = = 20, 200 and 450 Nm, in dual-fuel CNG + Diesel operation and powered by diesel fuel only. In this case, greater differences in pressure waveforms during the combustion process at lower loads can be noted. These differences become smaller as the load increases. This is due to the fact that as the load increases, the energy share of natural gas in the total amount of energy supplied to the engine cylinders significantly decreases. The energy share of natural gas in the total energy supplied to the engine cylinders for the tests performed is shown in Fig. 7.

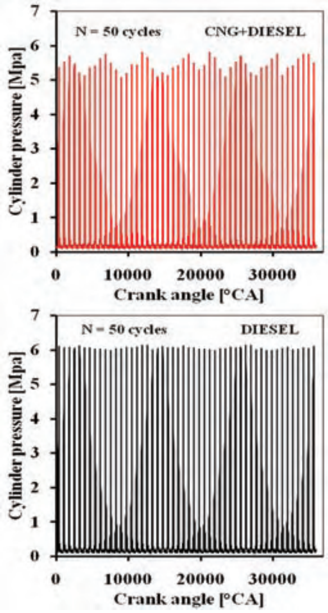

Fig. 4. Example sets of indicator diagrams determined under steady state conditions for subsequent operating cycles of Perkins 1104D-E44TA engine in dual-fuel CNG + Diesel operation and powered by diesel fuel only, operating according to the load characteristics for crankshaft speed n = 1800 rpm and load T = 20 Nm

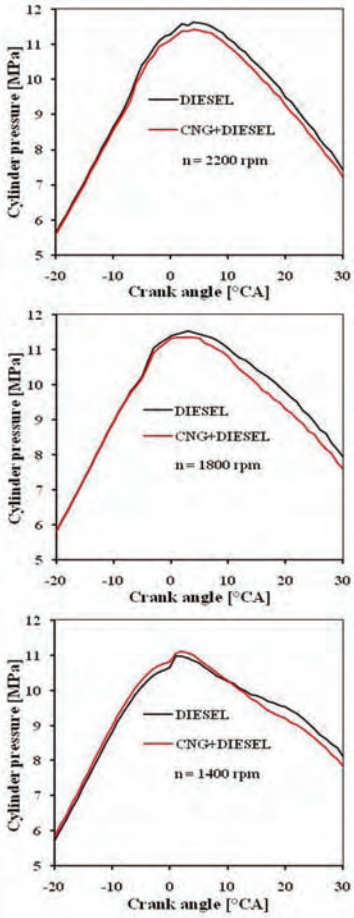

Fig. 5. Comparison of the pressure waveforms during the combustion process in the Perkins 1104D-E44TA engine cylinder operating according to external speed characteristics for selected crankshaft speeds n = 1400, 1800 and 2200 rpm, in dual-fuel CNG + Diesel operation and powered by diesel fuel only

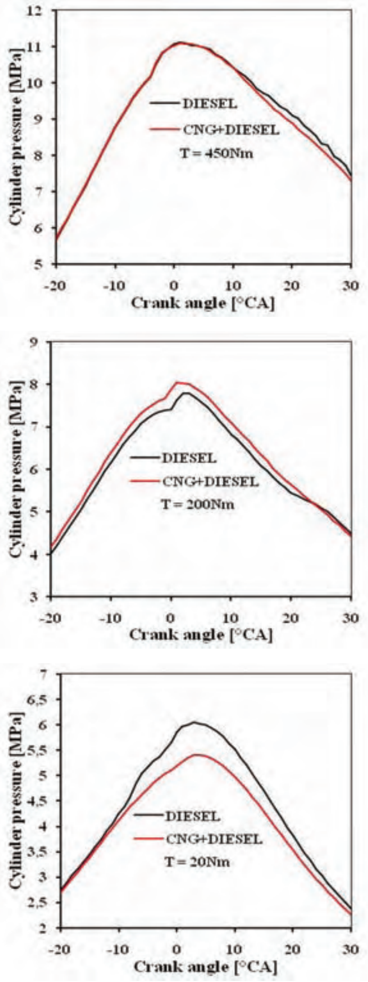

Fig. 6. Comparison of the pressure waveforms during the combustion process in the Perkins 1104D-E44TA engine cylinder running according to the load characteristics for crankshaft speed n = 1800 rpm, with selected loads of the engine T = 20, 200 and 450 Nm, in dual-fuel CNG + Diesel operation and powered by diesel fuel only

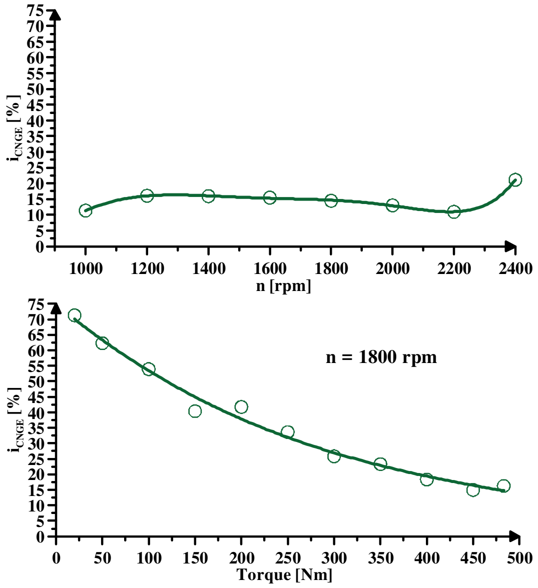

Fig. 7. The energy share of natural gas in the total energy input to the cylinders of the Perkins 1104D-E44TA engine running in dual-fuel CNG + Diesel operation and according to external speed characteristics and load characteristics for crankshaft speed n = 1800 rpm

5. Combustion process uniqueness indicators

The result of the processes taking place in a reciprocating combustion engine is an indicator diagram. It makes it possible to determine the basic indicators of engine operation and combustion process parameters. With subsequent indicator diagrams of the operating engine, it is possible to assess the correctness of the combustion process. The aim is to ensure that the indicator diagrams of the engine running under steady operating conditions are the same. In fact, these diagrams vary. Each subsequent pressure waveform in the cylinder is different from the previous one. This is the result of the variability of the processes occurring in the engine: air supply process, fuel injection process, fuel-air mixing process, ignition initiation or autoignition process, environmental condition variability. An important factor affecting the course of subsequent operating cycles in the engine cylinder during its tests on the test stand is the ability to ensure stable engine operation parameters [20]: crankshaft speed, torque curve, constant temperatures and pressures of: collector air, engine lubricating oil and cooling liquid. The lack of repeatability of these processes occurring in the engine and the variability of the engine operating conditions causes that the subsequent cycles of its operation differ. This may affect the values of the engine's performance indicators, including engine noise and exhaust fumes composition. In addition, the problem of the uniqueness of subsequent indicator diagrams should be taken into account when analyzing them. A single recorded pressure waveform may not be representative of the engine and the indicators determined on its basis. Therefore, usually for the analysis of the indicator diagram, a mean diagram of several dozen operating cycles measured under steady conditions of the engine operation is prepared. It may then be assumed that such an indicator diagram is representative of an engine operating under the specified conditions.

Uniqueness is a statistical parameter used to characterize the variability of the data set obtained from measurements. The uniqueness of the combustion process can be assessed by determining the uniqueness of the parameters characterizing this process [15–18, 20]. Classical indicators of the uniqueness of the combustion and fuel injection process have been discussed, among others, by Heywood [6]. The combustion process is analyzed on the basis of indicator diagrams and parameters determined on its basis. The uniqueness or, in other words, variability of these parameters shall be determined by dividing the standard deviation of a given parameter by its mean value in the set of results:

$$X_Y = \frac{\sigma_Y}{\overline{Y}} \tag{1}$$

where: σ_Y – standard deviation of parameter Y, $\overline{Y}$ – average value of the parameter under consideration.

The paper includes the analysis of the uniqueness for the combustion process of Perkins 1104D-E44TA engine running on compressed natural gas and diesel fuel in dual-fuel operation and on diesel fuel only. The values of four uniqueness indicators for subsequent engine operating cycles were determined: the uniqueness indicator for the maximum combustion pressure of the operating cycle, the uniqueness indicator for the mean indicated pressure, the uniqueness indicator for the indicator diagram and the uniqueness indicator for the partial indicator diagram.

The values of the uniqueness indicator for the maximum combustion pressure of the operating cycle were calculated with the equation:

$$X_{p_{max}} = \frac{\sigma_{p_{max}}}{\overline{p}_{max}} = \frac{\sqrt{\frac{1}{N}\sum_{i=1}^{N}\left(p_{max,i} - \overline{p}_{max}\right)^2}}{\overline{p}_{max}} \tag{2}$$

where: $p_{max,i}$ – maximum combustion pressure of the i-th operating cycle of the engine, $\sigma_{p_{max}}$ – standard deviation of the maximum combustion pressure, $\overline{p}_{max}$ – average maximum combustion process pressure calculated from N engine's subsequent operating cycles, N – number of subsequent engine operating cycles recorded.

The indicator of the uniqueness of the mean indicated pressure has been calculated using the equation:

$$X_{p_i} = \frac{\sigma_{p_i}}{\overline{p}_i} = \frac{\sqrt{\frac{1}{N}\sum_{i=1}^{N}\left(p_{i,i} - \overline{p}_i\right)^2}}{\overline{p}_i} \tag{3}$$

where: σ_{p_i} – standard deviation of the mean indicated pressure value, $\overline{p}_i$ – average value of the mean indicated pressure from the subsequent N operating cycles of the engine, $p_{i,i}$ – average indicated pressure of the i-th cycle.

The uniqueness indicator for the indicator diagram was determined from the following formula:

$$X_S = \frac{\sigma_S}{\overline{S}} = \frac{\sqrt{\frac{1}{N}\sum_{i=1}^{N}\left(S_i - \overline{S}\right)^2}}{\overline{S}} \tag{4}$$

where: σ_S – standard deviation of the area under the opened indicator diagram, $\overline{S}$ – mean value of the area under the opened indicator diagram calculated for subsequent N operating cycles of the engine, S_i – area under the i-th opened indicator diagram.

The area under the opened indicator diagram was calculated from the formula:

$$S = \int_{\alpha_p}^{\alpha_k} p\,d\alpha \tag{5}$$

where: α_p, α_k – values of the crank angle corresponding to the first and last point on the analyzed indicator diagram.

The uniqueness indicator for the partial indicator diagram has been calculated using the equation:

$$X_{S_C} = \frac{\sigma_{S_C}}{\overline{S}_C} = \frac{\sqrt{\frac{1}{N}\sum_{i=1}^{N}\left(S_{C,i} - \overline{S}_C\right)^2}}{\overline{S}_C} \tag{6}$$

where: σ_{S_C} – standard deviation of the area under the curve of the opened indicator diagram from the closing of inlet valves to the opening of outlet valves, $\overline{S}_C$ – mean value of the area for the following N diagrams calculated under the opened indicator curve from the closing of inlet valves to the opening of outlet valves, $S_{C,i}$ – value of the area under the curve of the i-th opened indicator diagram from the closing of inlet valves to the opening of outlet valves.

The surface area under the curve of the partial indicator diagram limited by the crank angle at which the inlet valves close and the crank angle at which the outlet valves begin to open is calculated from the formula:

$$S_C = \int_{\alpha_{zd}}^{\alpha_{ow}} p d\alpha \qquad (7)$$

α_{zd}, α_{ow} – values of the crank angle corresponding respectively to the closing of inlet valves and opening of outlet valves.

6. Analysis of the uniqueness indicators for the combustion process of the Perkins 1104D-E44TA engine in dual-fuel operation running on natural gas and diesel fuel

The diagrams below present the comparison of the uniqueness indicators of the combustion process of Perkins 1104D-E44TA engine running on compressed natural gas and diesel fuel CNG + Diesel in dual-fuel operation and, for comparison, on diesel fuel only. The results of the calculation of the uniqueness indicator for the maximum combustion pressure of the operating cycle of the tested engine operating according to the external speed characteristics are shown in Figure 8. They obtain similar values for engines in dual-fuel operation powered by CNG + Diesel fuel and by diesel fuel only. The obtained values of this indicator do not show an unambiguous correlation for the two methods of powering. It should be noted, however, that the energy share of natural gas in the total amount of energy supplied to the engine during its operation according to its external speed characteristics is practically below 20%. As a result, there are no significant differences in the combustion process on the indicator diagram. The values of the uniqueness indicator for the maximum combustion pressure of the operating cycle of the Perkins 1104D-E44TA engine running according to the load characteristics are shown in Figure 9. For loads of 20, 50 and 100 Nm, higher values of this ratio were obtained in the case of dual-fuel supply. However, they decrease significantly as the load increases. For loads above 100Nm, similar values of the uniqueness indicator for the maximum combustion pressure of the cycle of the tested engine in dual-fuel operation and running on diesel fuel were obtained. As the load increases, the energy share of natural gas in the total amount of fuel supplied to the cylinders decreases.

Figures 10 and 11 present the values of uniqueness indicators of the mean indicated pressure of the Perkins 1104D-E44TA engine, operating according to external speed characteristics and load characteristics for crankshaft speed n = 1800 rpm, in dual-fuel operation powered by CNG + Diesel and by diesel fuel only. In the case of dual-fuel operation of the engine, greater values of the uniqueness indicator of the mean indicated pressure as compared to the engine running on diesel fuel were obtained. Definitely greater values of this indicator were obtained for the smallest loads (20 Nm and 50 Nm) at engine operation according to the load characteristics. Under these engine operating conditions, the energy share of natural gas in dual-fuel operation was 71% and 62%, respectively. With an increase in engine load and a decreasing share of natural gas from about 54% to about 16%, the differences in the analyzed indicator for the two methods of powering are not so significant.

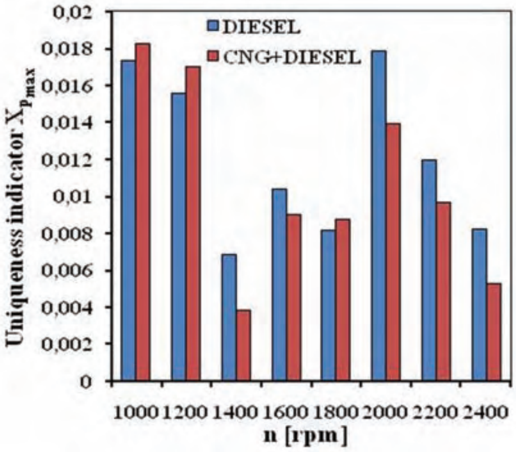

Fig. 8. Comparison of the value of the uniqueness indicator for the maximum pressure of the combustion process of the operating cycle of the Perkins 1104D-E44TA engine operating according to external speed characteristics, in dual-fuel operation, powered by CNG + Diesel and by diesel fuel only

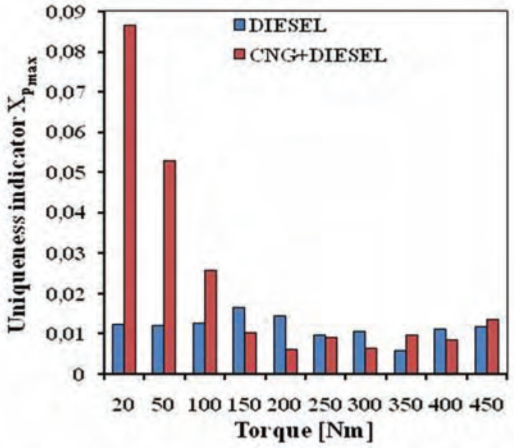

Fig. 9. Comparison of the value of the uniqueness indicator for the maximum pressure of the combustion process of the operation cycle in the Perkins 1104D-E44TA engine cylinder, running according to load characteristics for crankshaft speed n = 1800 rpm, in dual-fuel operation powered by CNG + Diesel and by diesel fuel only

The values of the uniqueness indicator for the indicator diagram and the uniqueness indicator for the partial indicator diagram of the Perkins 1104D-E44TA engine in dual-fuel operation powered by CNG + Diesel and diesel fuel only are shown in Figures 12 to 15. For a dual-fuel engine, both during operation according to external speed characteristics and load characteristics, higher values of the above-mentioned indicators were obtained. The greatest differences in the values of uniqueness indicators of the indicator diagram and partial indicator diagram for two methods of powering the tested engine were obtained at low engine loads.

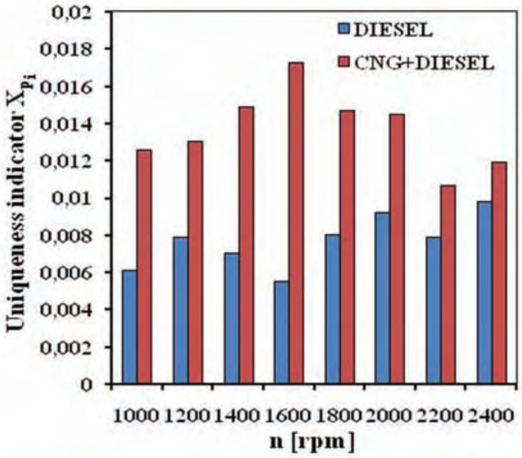

Fig. 10. Comparison of the value of the uniqueness indicator for the mean indicated pressure of the Perkins 1104D-E44TA engine operating according to external speed characteristics, in dual-fuel operation powered by CNG + Diesel and by diesel fuel only

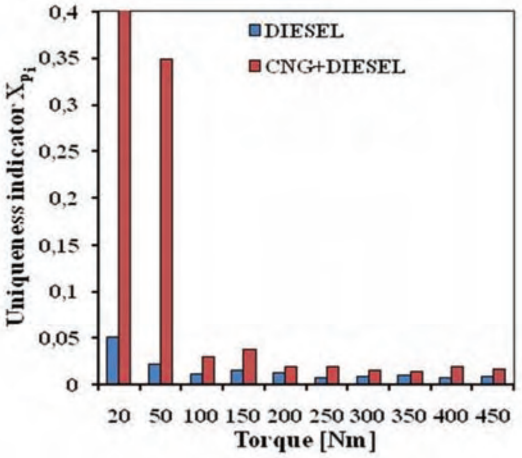

Fig. 11. Comparison of the value of the uniqueness indicator for the mean indicated pressure of the Perkins 1104D-E44TA engine, running according to load characteristics for crankshaft speed n = 1800 rpm, in dual-fuel operation powered by CNG + Diesel and by diesel fuel only

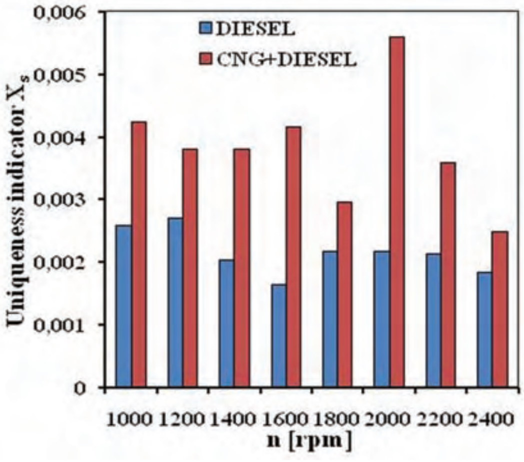

Fig. 12. Comparison of the value of the uniqueness indicator for the indicator diagram of the Perkins 1104D-E44TA engine operating according to external speed characteristics, in dual-fuel operation powered by CNG + Diesel and by diesel fuel only

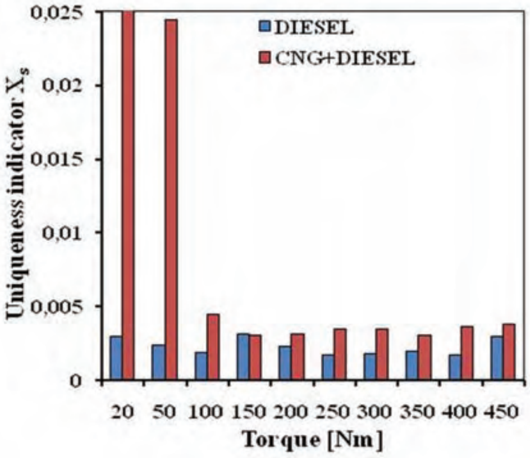

Fig. 13. Comparison of the value of the uniqueness indicator for the indicator diagram for the Perkins 1104D-E44TA engine, operating according to load characteristics for crankshaft speed n = 1800 rpm, in dual-fuel operation powered by CNG + Diesel and by diesel fuel only

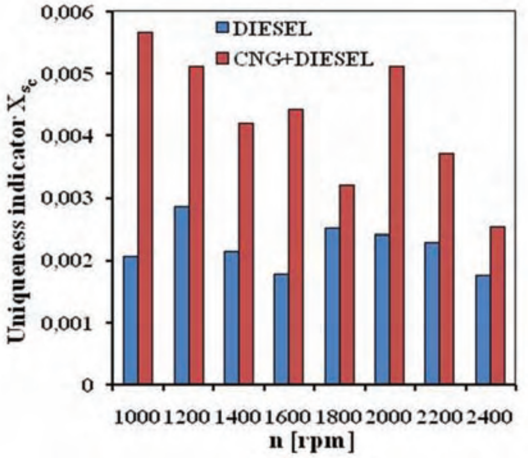

Fig. 14. Comparison of the value of the uniqueness indicator for the partial indicator diagram of the Perkins 1104D-E44TA engine operating according to external speed characteristics, in dual-fuel operation powered by CNG + Diesel and by diesel fuel only

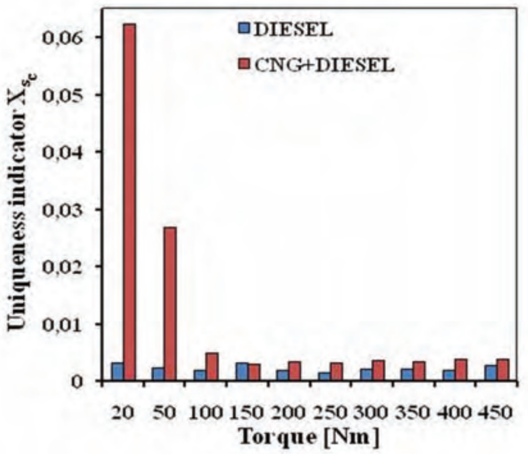

Fig. 15. Comparison of the value of the uniqueness indicator for the partial indicator diagram for the Perkins 1104D-E44TA engine, operating according to load characteristics for crankshaft speed n = 1800 rpm, in dual-fuel operation powered by CNG + Diesel and by diesel fuel only

5. Conclusion

The research showed that when powering the Perkins 1104D-E44TA engine by both natural gas and diesel fuel, the values of uniqueness indicators: mean indicator pressure, indicator diagram and partial indicator diagram are greater than when powering the engine by diesel fuel. Significantly greater values of the above-mentioned indicators were obtained at the lowest loads of the engine operating according to the load characteristics. The obtained values of the uniqueness indicator for the maximum combustion pressure of the operating cycle of Perkins 1104D-E44TA engine for the smallest loads of the engine operating according to the load characteristics are also significantly greater when powering the engine by natural gas and diesel fuel. For the remaining measuring points, the values of this indicator do not differ significantly and are not clearly smaller or greater for one of the two methods of powering the tested engine. The results obtained are certainly influenced by significantly different physical and chemical properties of natural gas and diesel fuel, as well as different shares of natural gas in the total amount of fuel supplied to the engine cylinders. The share of natural gas in the total amount of fuel supplied to the engine cylinders could not be the same, due to the possibility of detonation under greater engine loads. With low engine loads and a high share of natural gas in a dual-fuel supply, this type of supply has a significant impact on the processes occurring in the engine cylinder. The uniqueness of the combustion process is clearly increasing. When the engine is running according to external speed characteristics and at high loads, the uniqueness for most of the indicators determined is greater in the case of dual-fuel supply. However, these differences between dual-fuel operation and powering by conventional fuels are not significant. According to the authors, further research should be carried out on the uniqueness of the combustion process in dual-fuel operation of the engine, with constant load and different shares of natural gas in the total amount of fuel supplied to the engine cylinders.

Bibliography

[1] BOCHEŃSKI, C.I. Biodiesel paliwa rolnicze. *Wydawnictwo SGGW.* Warszawa 2003.

[2] CHEN, H., HE, J., ZHONG, X. Engine combustion and emission fuelled with natural gas: A review. *Journal of the Energy Institute.* 2018, 1-14.

[3] CHO, H.M., HE, B.Q. Combustion and emission characteristics of a lean burn natural gas engine. *International Journal of Automotive Technology.* 2008, **9**(4), 415-422, DOI: 10.1007/s12239-008-0050-5.

[4] GHAREHGHANI, A., HOSSEINI R., MIRSALIM, M. et al. An experimental study on reactivity controlled compression ignition engine fueled with biodiesel/natural gas. *Energy.* 2015, **89**, 558-567, DOI: 10.1016/j.energy.2015.06.014.

[5] GRUDEN, D. Umweltschutz in der Automobilindustrie. Vieweg + Teubner-GWV Fachverlage GmbH, Wiesbaden 2008.

[6] HEYWOOD, J.B. Internal combustion engines fundamentals. *Mc Graw Hill Co.* N.Y. 1988.

[7] Instrukcja montażu i programowania systemu OSCAR-N DIESEL.

[8] Karta charakterystyki. Gaz ziemny (p < 200 kPa). Polskie Górnictwo Naftowe i Gazownictwo PGNiG.

[9] Karta charakterystyki. Metan. Messer 2016.

[10] Karta charakterystyki. Metan sprężony. Linde 2017.

[11] Karta charakterystyki substancji niebezpiecznej. Gaz ziemny w sieciach przesyłowych i dystrybucyjnych. Polskie Górnictwo Naftowe i Gazownictwo PGNiG. Warszawa 30.10. 2010.

[12] KHAN, M.I., YASMIN, T., SHAKOOR, A. Technical overview of compressed natural gas (CNG) as a transportation fuel. *Renewable and Sustainable Energy Reviews.* 2015, **51**, 785-797. DOI:10.1016/j.rser.2015.06.053.

[13] KURCZYŃSKI, D., ŁAGOWSKI, P., TOMYUK, V. Selected aspects of dual-fuelling of the Perkins 1104D-E44TA engine with natural gas and diesel fuel. *Technical Transactions.* 2018, **12**, 173-178. DOI: 10.4467/2353737XCT.18.190.9678.

[14] KURCZYŃSKI, D., ŁAGOWSKI, P., WARIANEK, M. The impact of natural gas on the ecological safety of using Diesel engine. Published in: 2018 XI International Science-Technical Conference Automotive Safety**.** Conference Location: Casta. 18-20 April 2018**.** IEEE Xplore: 17823659. DOI:10.1109/AUTOSAFE. 2018.8373341.

[15] LEJDA, K., KURCZYŃSKI, D., ŁAGOWSKI, P. et al. The evaluation of the Fiat 0.9 Twin air engine powered by petrol and LPG gas work cycles uniqueness. *Journal of KONES Powertrain and Transport.* 2018, **25**(3), 323-330.

[16] LONGWIC, R. Charakterystyka działania silnika o zapłonie samoczynnym w warunkach swobodnego rozpędzania. *Wydawca Politechnika Lubelska.* Lublin 2011.

[17] LOTKO, W. Niepowtarzalność opóźnienia samozapłonu paliwa w silniku o zapłonie samoczynnym. *Archiwum Motoryzacji.* 2008, **3-4**, 195-209.

[18] LOTKO, W., GÓRSKI, K., TRELA, Z. et al. Wpływ parametrów paliwa na niepowtarzalność procesu spalania w silniku o zapłonie samoczynnym. *Autobusy-Technika, Eksploatacja. Systemy Transportowe.* 2018, **12**, 508–513. DOI: 10.24136/atst.2018.442.

[19] Perkins, operation and maintenance manual, Perkins Engines Company Limited, 2012.

[20] PRZYBYŁA, G., POSTRZEDNIK, S. Niepowtarzalność cykli pracy silnika spalinowego przy jego wysokiej prędkości obrotowej oraz różnym obciążeniu. *Czasopismo Techniczne M.* 2008, **7-M**, 151-159.

[21] REIF, K., DIETSCHE, K-H. Kraftfahrtechnisches Taschenbusch. *Vieweg+Teubner Verlag*. Wiesbaden 2011.

[22] SAHOO, B.B., SAHOO, N., SAHA, U.K. Effect of engine parameters and type of gaseous fuel on the performance of dual-fuel gas diesel engines – a critical review. *Renewable and Sustainable Energy Reviews.* 2009, **13**, 1151-1184. DOI:10.1016/j.rser.2008.08.003.

[23] SZLACHTA, Z. Zasilanie silników wysokoprężnych paliwami rzepakowymi. *Wydawnictwo Komunikacji i Łączności.* Warszawa 2002.

[24] TARABET, L., LOUBAR, K., LOUNICI, M.S. et al. Experimental investigation of DI diesel engine operating with eucalyptus biodiesel/natural gas under dual fuel mode. *Fuel.* 2014, **133**, 129-138. DOI: 10.1016/j.fuel.2014.05.008.

[25] THIRUVENGADAM, A., BESCH, M., PADMANABAN, V. et al. Natural gas vehicles in heavy-duty transportation –

a review. *Energy Policy*. 2018, **122**, 253-259. DOI:10.1016/j.enpol.2018.07.052.

[26] WANG, Z., DU, G., WANG, D. et al. Combustion process decoupling of a diesel/natural gas dual-fuel engine at low loads. *Fuel*. 2018, **232**, 550-561. DOI: 10.1016/j.fuel.2018.05.152.

[27] WANG, Z., ZHAO, Z., WANG, D. et al. Impact of pilot diesel ignition mode on combustion and emissions characteristics of a diesel/natural gas dual fuel heavy-duty engine. *Fuel*. 2016, **167**, 248-256. DOI:10.1016/j.fuel.2015.11.077.

[28] WEI, L., GENG, P. A review on natural gas/diesel dual fuel combustion, emissions and performance. *Fuel Processing Technology*. 2016, **142**, 264-278. DOI:10.1016/j.fuproc.2015.09.018.

[29] YANG, B., ZENG, K. Effects of natural gas injection timing and split pilot fuel injection strategy on the combustion performance and emissions in a dual-fuel engine fueled with diesel and natural gas. *Energy Conversion and Management*. 2018, **168**, 162-169. DOI: 10.1016/j.enconman.2018.04.091.

Dariusz Kurczyński, DEng. – Faculty of Mechatronics and Machine Building, Kielce University of Technology.

e-mail: *kdarek@tu.kielce.pl*

Michał Warianek, MEng. – Faculty of Mechatronics and Machine Building, Kielce University of Technology.

e-mail: *mwarianek@tu.kielce.pl*

Piotr Łagowski, DEng. – Faculty of Mechatronics and Machine Building, Kielce University of Technology.

e-mail: *p.lagowski@tu.kielce.pl*

Article citation info:
BEBKIEWICZ, K., CHŁOPEK, Z., LASOCKI, J. et al. Characteristics of pollutant emission from motor vehicles for the purposes of the Central Emission Base in Poland. *Combustion Engines*. 2019, **177**(2), 165-171. DOI: 10.19206/CE-2019-229

Katarzyna BEBKIEWICZ
Zdzisław CHŁOPEK
Jakub LASOCKI
Krystian SZCZEPAŃSKI
Magdalena ZIMAKOWSKA-LASKOWSKA

CE-2019-229

Characteristics of pollutant emission from motor vehicles for the purposes of the Central Emission Database in Poland

Within the Institute of Environmental Protection – National Research Institute the Central Emission Database is being established. The Database will cover the most important emission sectors from anthropogenic activities, including usage of motor vehicles. The intensity of emissions of individual pollutants is the input data to air pollution dispersion models. Based on calculations performed by the air pollution dispersion models concentration of pollutants dispersed in atmospheric air (pollution immission) is provided. The annual average immision for a selected place in Poland is a measure of the threat to environment. In order to determine the intensity of pollutant emissions from motor vehicles it is necessary to recognize the intensity of vehicle motion and the volume of emission of pollutants depending on the type of vehicle motion. The task presented in this article is to determine the characteristics of pollutant emissions from motor vehicles depending on the type of their motion. The mean value of vehicle speeds was used to characterize the type of vehicle motion. The emission of pollutants from vehicles is therefore characterized by the dependence of road emissions of pollutants on the average speed of vehicles. The characteristics were determined for cumulated categories of motor vehicles: passenger cars, light commercial vehicles as well as heavy duty trucks and buses. The results of the inventory of pollutant emissions from motor vehicles in Poland in 2016 were used to determine the characteristics of pollutant emissions.

Key words: *pollutant emission characteristics, motor vehicles, central emission base*

1. Introduction

The Institute of Environmental Protection – National Research Institute has undertaken a global-scale unique enterprise to estimate emission in spatial scale from both natural and anthropogenic sources, as well as modelling of the dispersion of pollutants. As a result of this project, it will be possible to determine the spatial distribution of immission of pollution (concentrations of pollutants dispersed in the air) in Poland, averaged over the year for which immission was determined. Information on pollutant emissions is provided as a part of the Central Emission Database program. Estimated substances are listed below:

- carbon monoxide – CO,
- non-methane volatile organic compounds – NMVOC,
- nitrogen oxides reduced to nitrogen dioxide – NO_x,
- total suspended particles – TSP,
- particulate matter PM10 – PM10,
- particulate matter PM2.5 – PM2.5,
- carbon dioxide – CO_2,
- sulphur oxides reduced to sulphur dioxide – SO_2,
- ammonia – NH_3,
- nickel – Ni,
- cadmium – Cd,
- lead – Pb,
- benzo(a)pyrene – B(a)P,
- mercury – Hg,
- arsenic – As.

In order to model the emission of pollutants it is necessary to provide data of an extensive and intensive nature, on the functioning of the sources of pollutant emissions and data on emission characteristics. This article presents the results of elaboration of emission characteristics from road transport vehicles.

2. Methodology for determining the characteristics of pollutant emissions from motor vehicles

Emission of pollutants from the set of motor vehicles is a superposition of pollutant emissions. This is in line with the assumption that the emissions inventory includes substances in the state emitted from emission sources [2, 5] Emission of pollutants from motor vehicles is modelled as the sum of [2, 4, 5, 10, 11]:

- emission from engine heated to a stable temperature,
- emission during the heating of the engine,
- emission from fuel evaporation from the fuel system of the vehicle,
- particular matter emission related to tribological processes.

The annual emission of pollutants (pollutant emission averaged over 1 year) – E_a from the set of motor vehicles is equal:

$$E_a = \sum_{i=1}^{N} p_i \cdot b_i \qquad (1)$$

where: p – annual mileage of the vehicle, b – emission of pollutant, N – number of vehicles in the set.

According to the Central Emission Database establishing assumptions establishing, there are analyses conducted for the following cumulative categories of motor vehicles:

- passenger cars,
- light commercial vehicles (light duty vehicles),
- heavy duty trucks,
- buses,
- motorcycles and mopeds.

To estimate the emission of pollutants from cumulated categories of motor vehicles, the results of the inventory of pollutants from motor vehicles in Poland in 2017 calculated by COPERT 5 software were used [9].

Input data to COPERT model are [1–3, 9, 10]:

- number of vehicles,
- distance travelled (annual mileage),
- mileage share in the urban areas, rural areas and highways,
- travelling velocity for urban areas, rural areas and highways,
- monthly temperature (min and max),
- the sulphur content in fuels,
- the lead content in fuels,
- fuel compounds,
- heavy metals content in fuels,
- vapour pressure of fuels,
- average trip length.

The methodology of the selection of the COPERT input data has been described in publications [1–3].

With the reference to equation (1), the emission of pollutants from road transport is assumed as the value characterizing the pollutant emission from motor vehicles. The emission of pollutants depends in an operational calculus on the vehicle speed, determining the engine operating states: rotational speed and torque – engine load measures [5]. In pollutants emission modelling, the most frequently used zero-dimensional characteristic is the average vehicle`s speed – v_{AV}. In this article, dependence of emission of pollutants on the average speed of the vehicle is assumed as a characteristic of the emission of pollutants.

The average value of the road emission of the pollutant "j" for the set of vehicles is equal:

$$b_j = \frac{\sum_{i=1}^{N} p_i \cdot b_{ij}}{\sum_{i=1}^{N} p_i} \tag{2}$$

In fact, it is not possible to average the results for individual vehicles, therefore, the results for the elementary categories of motor vehicles in the cumulative categories are averaged:

$$b_j = \frac{\sum_{k=1}^{K} N_k \cdot p_k \cdot b_{kj}}{\sum_{k=1}^{K} p_k \cdot b_{kj}} \tag{3}$$

where: K – number of elementary categories in the cumulative category, N_k – number of vehicles in the category „k".

This paper presents the emission characteristics of motor vehicles for the following pollutants, particularly harmful to the health of living organisms due to the properties of the substances and volume of the emission road: carbon monoxide, non-methane volatile organic compounds, oxides of nitrogen and particulate matter divided into dimensional fractions: total suspended particles, PM10 and PM2.5 particulate matter.

3. Emission characteristics of selected pollutants from motor vehicles in Poland for 2017

According to the equation (3) the average emission of each pollutant was determined (on the basis of the calculated values of the national annual emission for the assumed values of average vehicle speeds for cumulated categories of motor vehicles). The sets of average emissions of pollutants for cumulated vehicle categories in the domain of average vehicle speed have been approximated by a polynomial function from the 3^{rd} to the 6_{th} degree. By that means, the analytical form of the characteristics of road emissions of pollutants was determined for individual categories of motor vehicles. Figures 1–30 present the emission characteristics of selected pollutants from motor vehicles in Poland for 2017. Figures 1–6 present the pollutants emission characteristics from passenger cars.

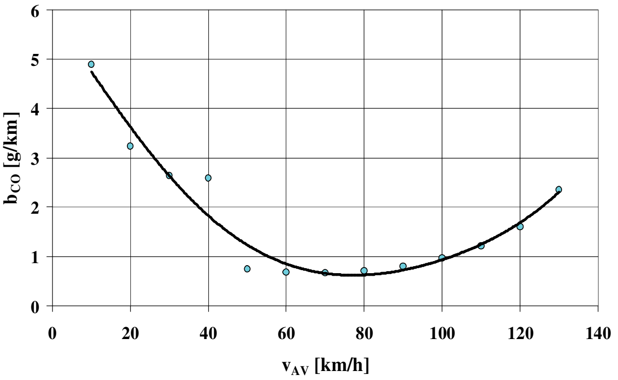

Fig. 1. The characteristic of the specific distance emission of carbon oxide – b_{CO} from passenger cars

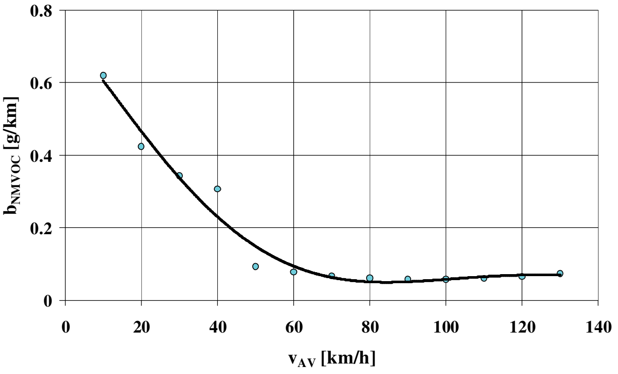

Fig. 2. The characteristic of the specific distance emission of non-methane volatile organic compounds – b_{NMVOC} from passenger cars

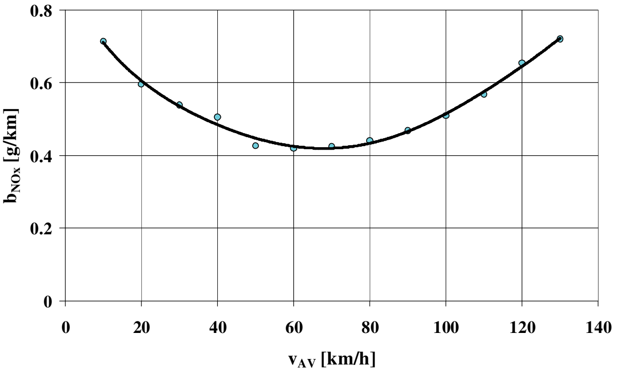

Fig. 3. The characteristic of the specific distance emission of nitrogen oxides – b_{NOx} from passenger cars

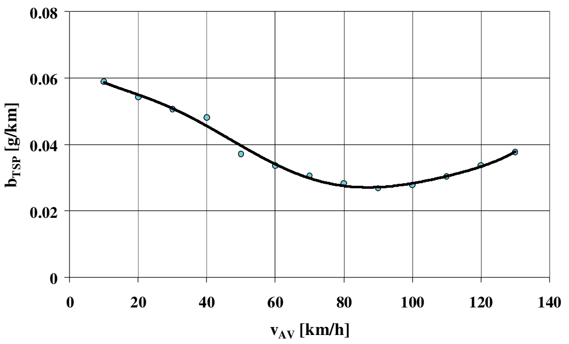

Fig. 4. The characteristic of the specific distance emission of total particulate matter – b_{TPM} from passenger cars

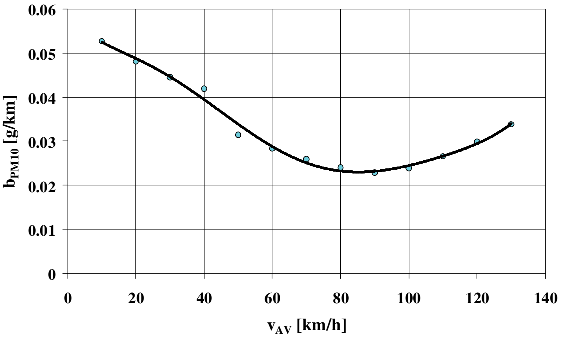

Fig. 5. The characteristic of the specific distance emission of particulate matter PM10 – b_{PM10} from passenger cars

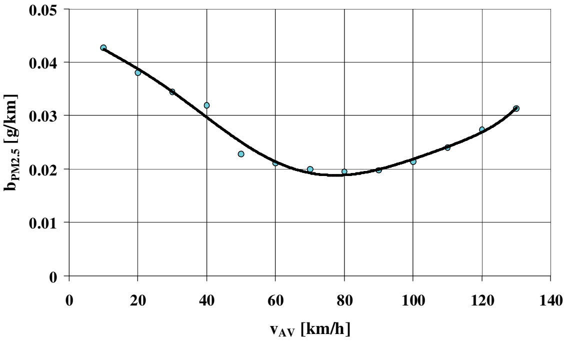

Fig. 6. The characteristic of the specific distance emission of particulate matter PM10 – $b_{PM2.5}$ from passenger cars

For passenger cars, there is a significant sensitivity of emission of pollutants to travel velocity. For low average speed – in conditions of strong dynamic properties of the speed process – in most cases, road emissions are significantly higher than for moderate average speed. The sensitivity of pollutant emissions to the dynamic work states is particularly high for spark-ignition engines [4–6, 11] and the share of these engines in the cumulative category of passenger cars is high [1–3]. There is also a tendency of increasing the emission of road pollutants for a very high average speed, which results in a high engine load. For particulate emissions from sources other than the exhaust system, emission increasing is mainly due to the frictional power at the contact of the wheels with the road surface.

Figures 7–12 present the pollutants emission characteristics from light commercial vehicles.

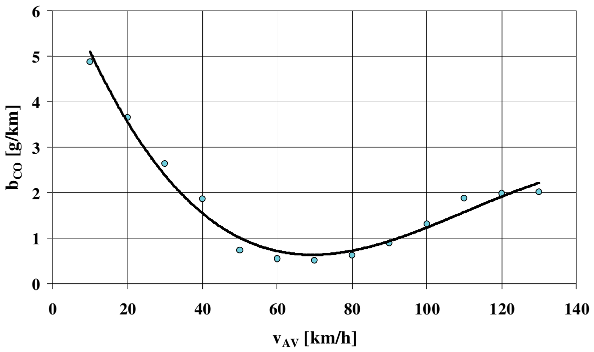

Fig. 7. The characteristic of the specific distance emission of carbon oxide – b_{CO} from light commercial vehicles

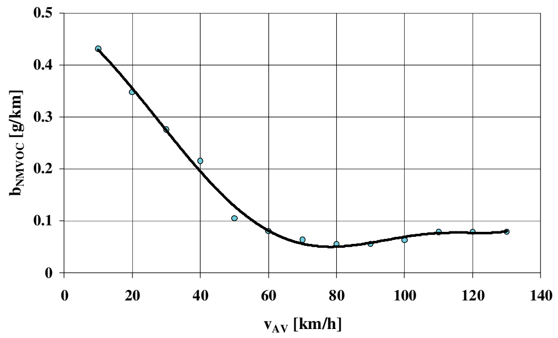

Fig. 8. The characteristic of the specific distance emission of non-methane volatile organic compounds – b_{NMVOC} from light commercial vehicles

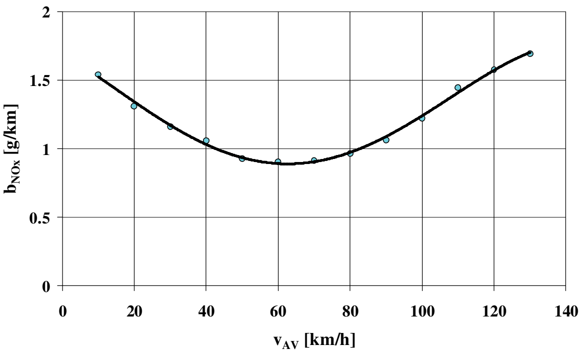

Fig. 9. The characteristic of the specific distance emission of nitrogen oxides – b_{NOx} from light commercial vehicles

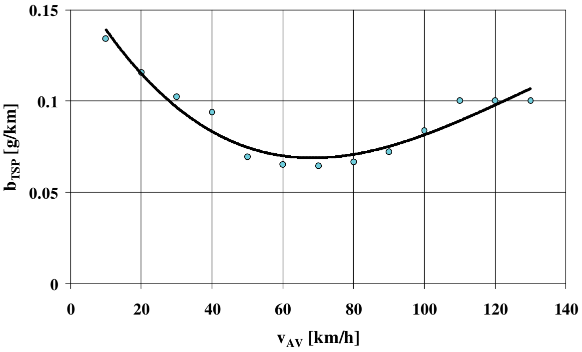

Fig. 10. The characteristic of the specific distance emission of total particulate matter – b_{TPM} from light commercial vehicles

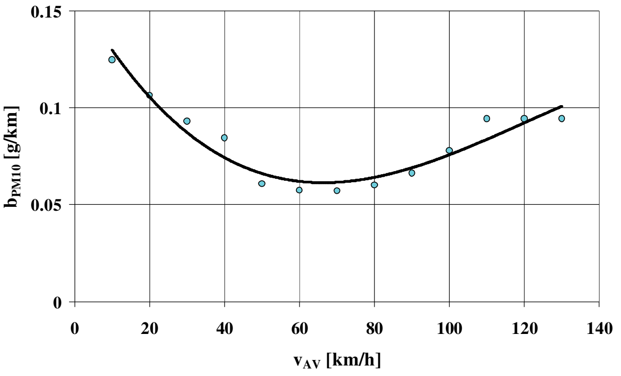

Fig. 11. The characteristic of the specific distance emission of particulate matter PM10 – b_{PM10} from light commercial vehicles

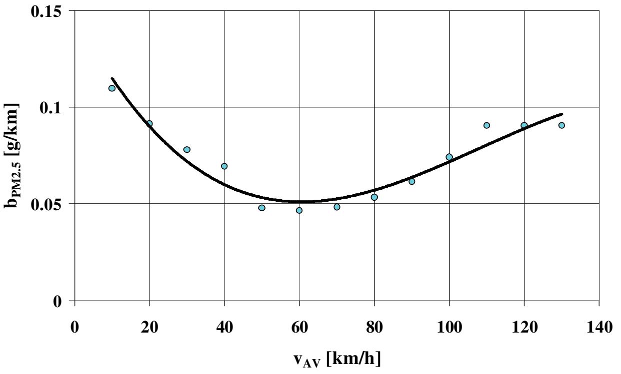

Fig. 12. The characteristic of the specific distance emission of particulate matter PM2.5 – $b_{PM2.5}$ from light commercial vehicles

The pollutant emission characteristics of light commercial vehicles indicate a significant similarity to the characteristics of passenger cars. In the case of substances emission of which strongly depends on the engine and the vehicle load (primarily nitrogen oxides and particulate matter), road emission from light commercial vehicles is higher than for passenger cars.

Figures 13–18 present the pollutants emission characteristics from heavy duty trucks.

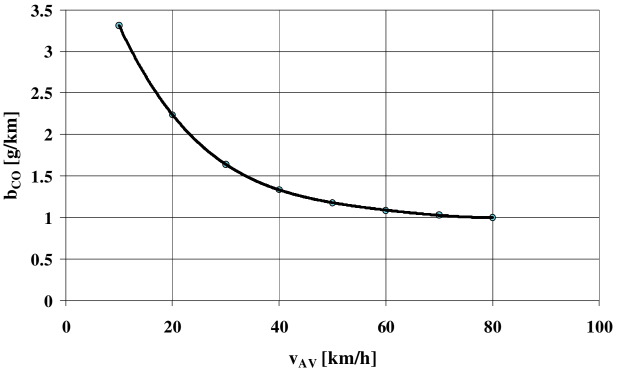

Fig. 13. The characteristic of the specific distance emission of carbon oxide – b_{CO} from heavy duty trucks

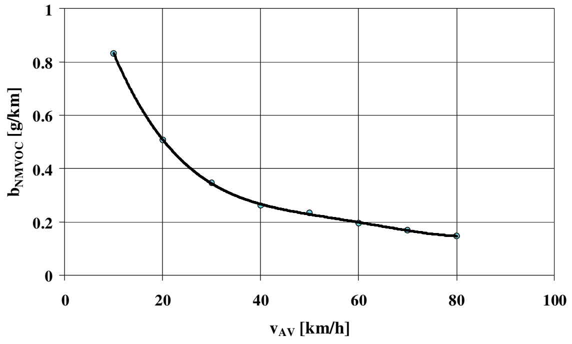

Fig. 14. The characteristic of the specific distance emission of non-methane volatile organic compounds – b_{NMVOC} from heavy duty trucks

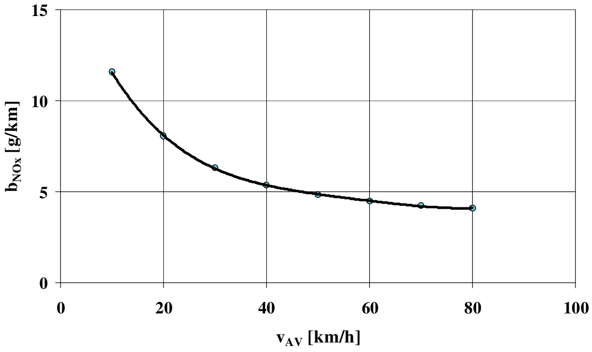

Fig. 15. The characteristic of the specific distance emission of nitrogen oxides – b_{NOx} from heavy duty trucks

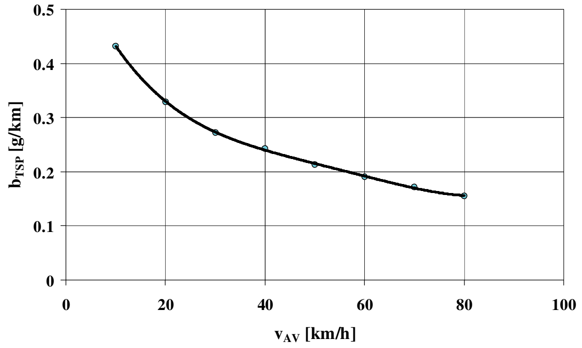

Fig. 16. The characteristic of the specific distance emission of total particulate matter – b_{TPM} from heavy duty trucks

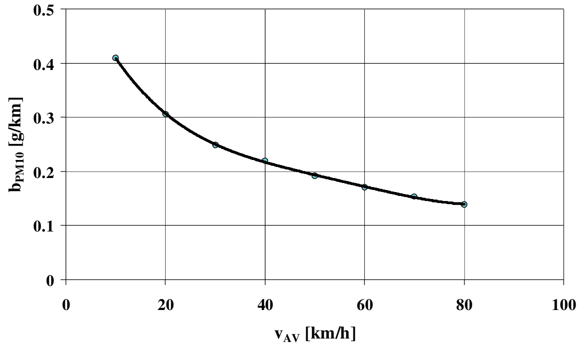

Fig. 17. The characteristic of the specific distance emission of particulate matter PM10 – b_{PM10} from heavy duty trucks

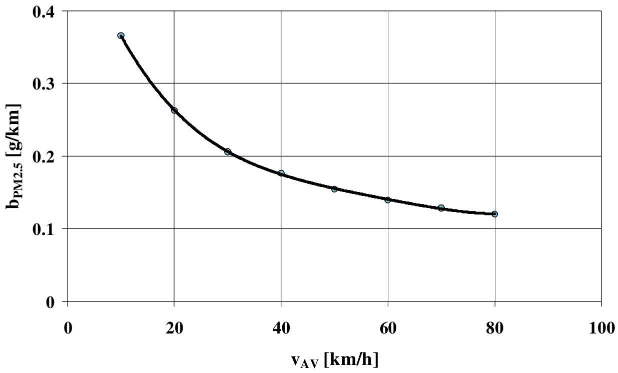

Fig. 18. The characteristic of the specific distance emission of particulate matter PM2.5 – $b_{PM2.5}$ from heavy duty trucks

The dependence of road pollutants emissions on the average speed of vehicles for heavy duty trucks is different than for passenger cars and light commercial vehicles. A tendency of emission decreasing is observed for increasing vehicle speed. This is mainly due to the fact that there are no vehicles with spark ignition engines in the cumulated category of heavy duty trucks. Obviously, road emissions from heavy duty trucks are higher than emissions from light vehicles.

Figures 19–24 present the pollutants emission characterristics from buses.

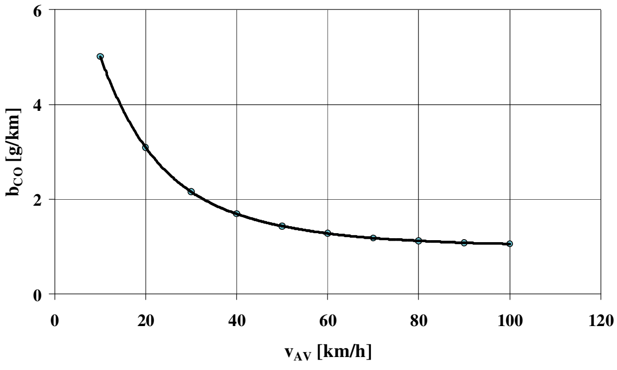

Fig. 19. The characteristic of the specific distance emission of carbon oxide – b_{CO} from buses

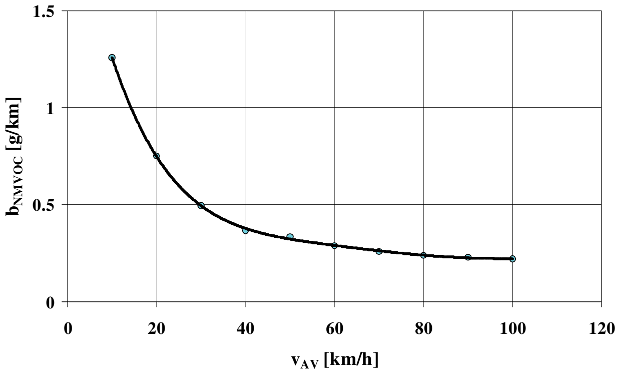

Fig. 20. The characteristic of the specific distance emission of non-methane volatile organic compounds – b_{NMVOC} from buses

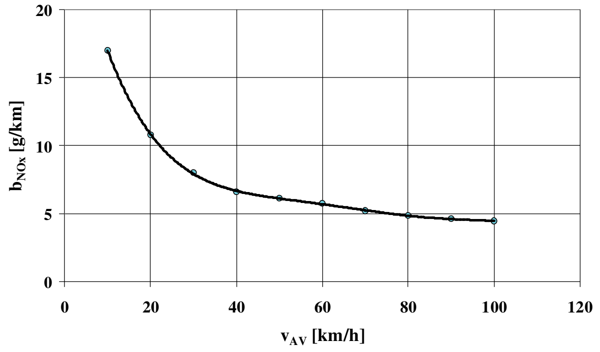

Fig. 21. The characteristic of the specific distance emission of nitrogen oxides – b_{NOx} from buses

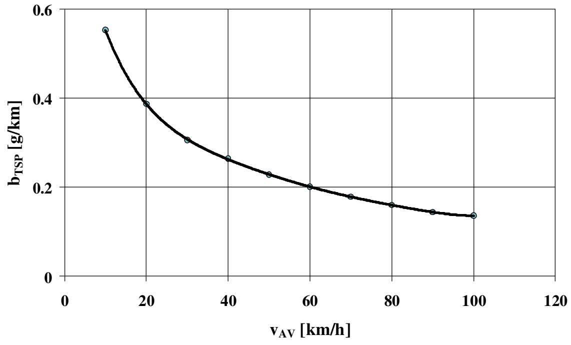

Fig. 22. The characteristic of the specific distance emission of total particulate matter – b_{TPM} from buses

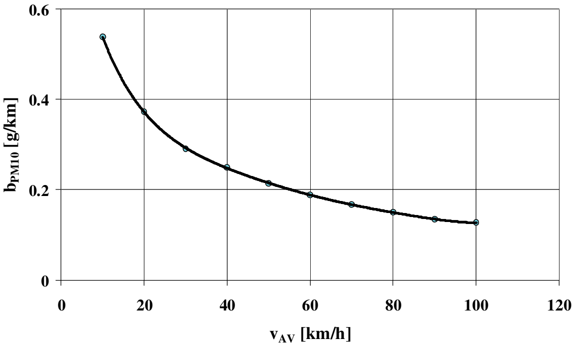

Fig. 23. The characteristic of the specific distance emission of particulate matter PM10 – b_{PM10} from buses

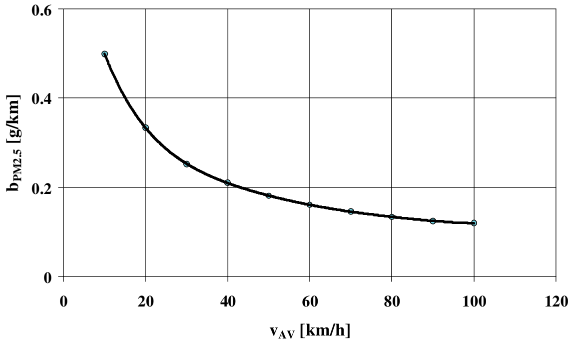

Fig. 24. The characteristic of the specific distance emission of particulate matter PM2.5– b_{PM10} from buses

The emission characteristics for buses are similar to those for heavy duty trucks. Therefore, the cumulative categories of heavy duty trucks and buses are often combined in the modeling of pollutant emissions from motor vehicles.

Figures 25–30 present the pollutants emission characteristics from motorcycles and mopeds.

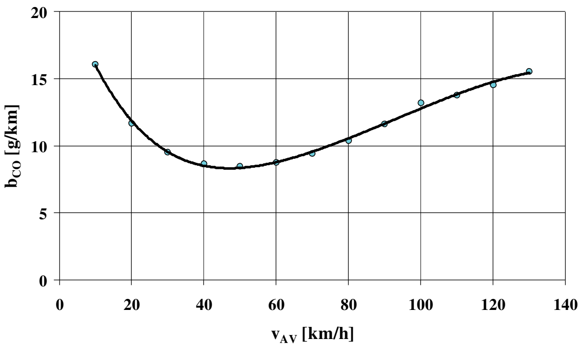

Fig. 25. The characteristic of the specific distance emission of carbon oxide – b_{CO} from motorcycles and mopeds

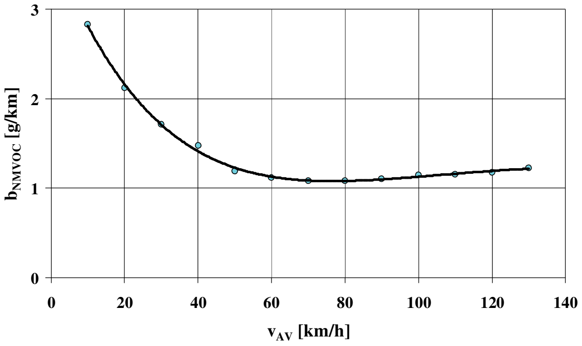

Fig. 26. The characteristic of the specific distance emission of carbon non-methane volatile organic compounds – b_{NMVOC} from motorcycles and mopeds

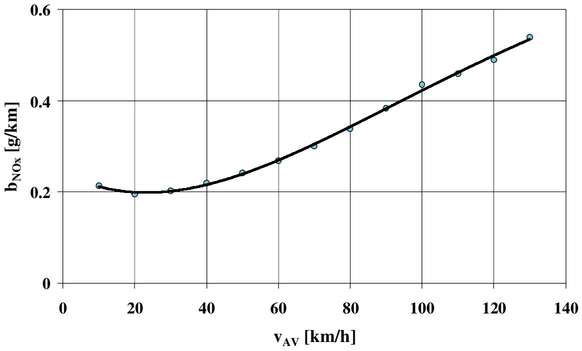

Fig. 27. The characteristic of the specific distance emission of nitrogen oxides – b_{NOx} from motorcycles and mopeds

The pollutant emission characteristics of motorcycles and mopeds significantly differ from emission characteristics of other cumulated vehicle categories. These are primarily vehicles equipped with spark ignition engines, sometimes two-stroke engines. For these engines, there is a significant impact of the engine load on road emissions of carbon monoxide and, in particular, nitrogen oxides.

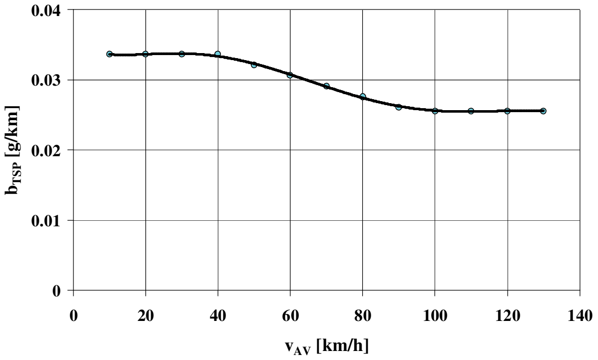

Fig. 28. The characteristic of the specific distance emission of total particulate matter – b_{TPM} from motorcycles and mopeds

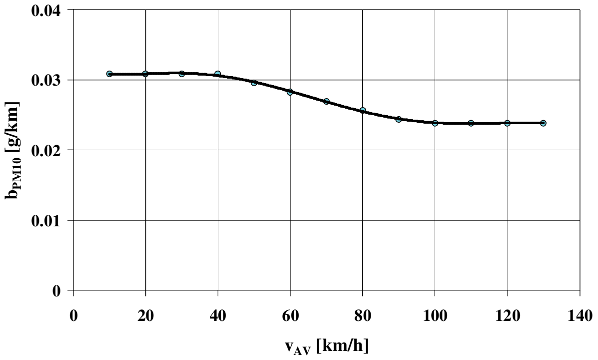

Fig. 29. The characteristic of the specific distance emission of particulate matter PM10 – b_{PM10} from motorcycles and mopeds

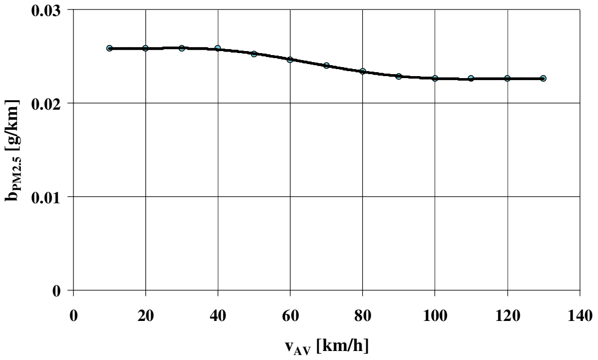

Fig. 30. The characteristic of the specific distance emission of particulate matter PM2.5 – $b_{PM2.5}$ from motorcycles and mopeds

4. Recapitulation

Modeling of pollutants immission is of great practical significance. Measurements of pollution immissions are possible only in selected places, while knowledge about threats in other areas is insufficient. Extensive modeling of emissions and immission of pollution throughout Poland, undertaken by the Institute for Environmental Protection – National Research Institute, is a global-scale unique project.

In order to assess the emission of pollutants from motor vehicles, the knowledge of vehicle motion intensity and character, described by the value of vehicle speed, and emission characteristics are of key importance.

This article presents pollutant emission characteristics determined for cumulated categories of motor vehicles for the first time in Poland based on an inventory of pollutant emissions from road transport [12].

The determined characteristics represent the correlation consistent with the current state of the knowledge, including characteristics presented in the literature [4], determined based on the INFRAS AG software [11] and numerous results of empirical research [6–8]. The results of the current studies on the system developed under the Central Emission Base allow for an optimistic assessment of determined emission characteristics of motor vehicles.

Nomenclature

As	arsenic
b	specific distance emission
Cd	cadmium
CO	carbon monoxide
CO_2	carbon dioxide
E_a	annual emission
Hg	mercury
K	number of elementary categories in the cumulative category
N	number of vehicles
NH_3	ammonia

Ni	nickel
N_k	number of vehicles in the category „k"
NMVOC	non-methane volatile organic compounds
NO_x	nitrogen oxides
Pb	lead
PM10	particular matter PM10
PM2.5	particular matter PM2.5
SO_2	sulphur oxides
TPM	total particular matter
v_{AV}	average velocity

Bibliography

[1] BEBKIEWICZ, K., CHŁOPEK, Z., SZCZEPAŃSKI, K., ZIMAKOWSKA-LASKOWSKA, M. Assessment of results of pollutant emission inventory of the road transport sector in Poland in 2000–2015. *The Archives of Automotive Engineering – Archiwum Motoryzacji*. 2017, **78**(4), 5-25.

[2] BEBKIEWICZ, K, CHŁOPEK, Z., SZCZEPAŃSKI, K., ZIMAKOWSKA-LASKOWSKA, M. Issues of modeling the total pollutant emission from vehicles. *Proceedings of the Institute of Vehicles*. 2017, **1**(110), 103-118.

[3] BEBKIEWICZ, K., CHŁOPEK, Z., SZCZEPAŃSKI, K., ZIMAKOWSKA-LASKOWSKA, M. Results of air emission inventory from road transport in Poland in 2014. *Proceedings of the Institute of Vehicles*. 2017, **1**(110), 77-88.

[4] BUWAL (Bundesamt für Umwelt, Wald und Landschaft), INFRAS AG (Infrastruktur-, Umwelt- und Wirtschaftsberatung). Luftschadstoffemissionen des Strassenverkehrs 1950–2010, BUWAL-Bericht 1995, 255.

[5] CHŁOPEK, Z. The modeling basis of the pollutant emission and the fuel and energy consumption for internal combustion engines of motor vehicles. *Combustion Engines*. 2015, **162**(3), 177-185.

[6] CHŁOPEK, Z., BIEDRZYCKI, J., LASOCKI, J., WÓJCIK. P. Examination of pollutant emissions and fuel consumption at tests simulating the real conditions of operation of a passenger car. *The Archives of Automotive Engineering. Archiwum Motoryzacji*. 2014, **65**(3), 3-18, 81-96.

[7] CHŁOPEK, Z., DĘBSKI, B., SZCZEPAŃSKI, K. Theory and practice of inventory pollutant emission from civilization related sources: share of the emission harmful to health from road transport. *The Archives of Automotive Engineering – Archiwum Motoryzacji*. 2018, **79**(1), 5-22.

[8] CHŁOPEK, Z., LASKOWSKI, P. Pollutant emission characteristics determined using the Monte Carlo Method. *Eksploatacja i Niezawodność – Maintenance and Reliability*. 2009, **2**(42), 42-51.

[9] COPERT Training 5. COPERT 5 vs COPERT 4. European Environment Agency. 2016. http://emisia.com/sites/default/files/COPERT_5_features.pdf. (2019.02.06).

[10] EMEP/EEA air pollutant emission inventory guidebook – 2016. European Environment Agency.

[11] INFRAS AG: Handbuch für Emissionsfaktoren des Strassenverkehrs; Version 3.1; Bern 2010.

[12] Poland's Informative Inventory Report 2018. Submission under the UN ECE Convention on Long-range Transboundary Air Pollution and the Directive (EU) 2016/2284 Warszawa. National Centre for Emission Management (KOBiZE) at the Institute of Environmental Protection – National Research Institute. February 2018.

Katarzyna Bebkiewicz, MEng. – Institute of Environmental Protection – National Research Institute in Warsaw.
e-mail: *katarzyna.bebkiewicz@kobize.pl*

Prof. Zdzisław Chłopek, DSc., DEng. – Professor in the Institute of Environmental Protection – National Research Institute in Warsaw.
e-mail: *zdzislaw.chlopek@kobize.pl*

Krystian Szczepański, DSc., DEng. – Director of the Institute of Environmental Protection – National Research Institute in Warsaw.
e-mail: *krystian.szczepanski@ios.edu.pl*

Magdalena Zimakowska-Laskowska, DSc., DEng. – Institute of Environmental Protection – National Research Institute in Warsaw.
e-mail: *magdalena zimakowska-laskowska @kobize.pl*

Jakub Lasocki, DEng. – Faculty of Automotive and Construction Machinery Engineering, Warsaw University of Technology.
e-mail: *jakub.lasocki@pw.edu.pl*

Article citation info:
STEPANENKO, D., KNEBA, Z. DME as alternative fuel for compression ignition engines – a review. *Combustion Engines*. 2019, **177**(2), 172-179. DOI: 10.19206/CE-2019-230

Denys STEPANENKO
Zbigniew KNEBA

CE-2019-230

DME as alternative fuel for compression ignition engines – a review

The ecological issues and the depletion of crude oil, has led the researchers to seeking for non-petroleum based alternative fuels, along with more advanced combustion technologies, and after-treatment systems. The use of clean alternative fuels is the one of the most perspective method that aiming at resolving of the said issues. One of the promising alternative fuels that can be used as a clean high-efficiency compression ignition fuel with reduced of toxic emissions is dimethyl ether (DME). Moreover, it can be produced from various feedstocks such as natural gas, coal, biomass and others. This article describes the properties and the potential of DME application on the combustion and emission reduction characteristics of the compression ignition engines.

Key words: *alternative fuels, dimethyl ether, DME, internal combustion engine, emission reduction*

1. Introduction

Environmental pollution is the one of the most serious problems that the world is facing today, which is causing by the exhaust gases due to the burning of the fuels. This issue, leads to increasing the stringent regulations that are aimed to lowering the toxic emissions [6–8].

Internal combustion engines (ICE) have been widely used in the different sectors (i.e., transport, industry, agriculture etc.) due to their improved durability and efficiency. Unfortunately, the main energy source for piston engines nowadays is a crude oil, which stocks are significant, but not limitless. Continuously growing of the energy demand (Fig. 1, Fig. 2, Fig. 3) and number of cars (Fig. 4), leads to energy and political crisis related to the rapid depletion of crude oil. Studies indicate that the known reservoirs of the primary energy sources will sufficiently meet the worldwide demand for another 39 years for oil, 61 years for natural gas and 216 years for coal [10, 16].

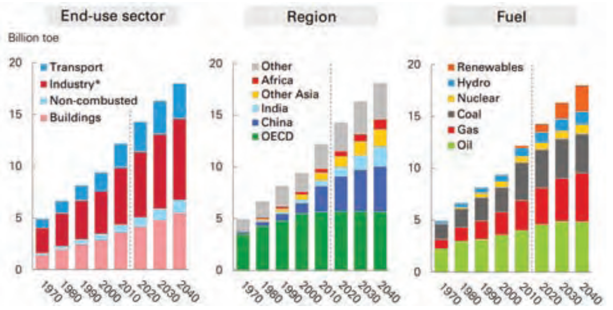

Fig. 1. Primary energy demand [3]

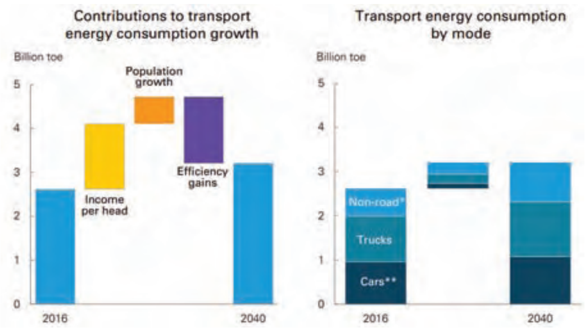

Fig. 2. Growth of fuels used in transport sector [3]: * – Aviation, Marine and Rail, ** – Includes 2- and 3-wheelers

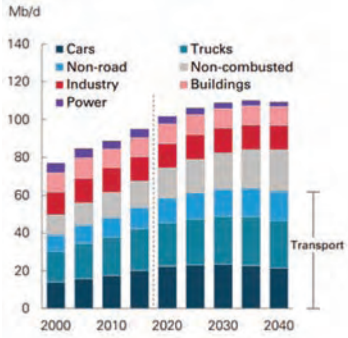

Fig. 3. Liquid fuels demand [3]. Cars include 2- and 3-wheelers, trucks include most SUVs in North America, non-road includes aviation, marine and rail

As presented on the Figure 3 the transport sector continues to dominate global oil demand.

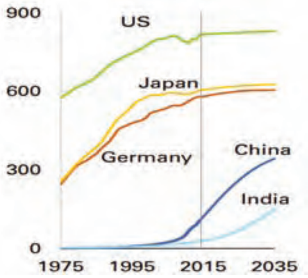

Fig. 4. The number of vehicles per 1000 inhabitants in individual regions in the world [14]

Transportation sector (i.e., cars, trucks, trains, ships, planes and other vehicles) is one of the main air pollution sources. According to different sources, road transport accounts from 23.5% [4] to 28% [9, 26] of all toxic emissions in the world. Air pollution carries significant risks for human health and the environment. The most harmful substances are nitrogen oxides (NO_x), sulfur oxides (SO_x), carbon dioxide (CO_2), hydrocarbons (HC) and particulate matter (PM).

Stringent toxic emission regulations that are concerning on the reduction of the harmful compounds in exhaust gases, greenhouse gases as well as the reduction of fuel consumption are currently one of the most important factors affecting on the development directions of the:

1. Internal combustion engines.
2. Exhaust after-treatment systems.

One of the most perspective methods that allows to solving the environmental pollution issues and the depletion of crude oil reserves, is the use of clean alternative fuels. Whatever fuel is to replace petroleum, it must address the following criteria:

1. There must be enough feedstock materials for the production on a large industrial scale.
2. Relatively low production and transportation costs.
3. Ensure high energy efficiency for the internal combustion engine.
4. Minimal or no negative impact of combustion products and pure fuel on the environment and human health.
5. If possible, use the already existing infrastructure without major changes of the:

- ICE fuel system,
- distribution and transportation of fuels to refill stations.

There are many alternative fuels that can potentially replace conventional petroleum oils including diesel and gasoline, such as biodiesel, light alcohol fuels, biomethane, natural gas, gas-to-liquid (GTL), coal-to-liquid (CTL), biomass-to-liquid (BTL), dimethyl ether (typically abbreviated as DME). Among these fuels the most promising alternative fuel for diesel engines that is suitable for all requirements is DME. The high cetane number over 55 (for diesel usually does not exceed 55), low boiling temperature, relatively low self-ignition temperature and good ecological properties turns out dimethyl ether to be a promising clean alternative fuel that can potentially replace diesel fuel.

The main objective of this paper is to discuss the combustion and emissions characteristics, and environmental effects of DME-fueled vehicles in order to highlight the potential of DME as a fuel in the compression ignition diesel engines and to share this useful information with researchers, engineers and anyone who interested in alternative fuels for diesel engines.

2. Dimethyl ether

DME (dimethyl ether) – it is the simplest ether compound with a formula of $CH_3–O–CH_3$, with some important properties such, as high cetane number, high oxygen content (about 35% of mass), no direct C–C bonds in the molecular structure (which produces considerably less pollutants like smoke and particulate matter (PM) than conventional fuels), low boiling point, low carbon to hydrogen ratio (C/H), has good solubility with diesel, environmentally benign and causes no negative health effects. To detect a leakage, DME does not require an odorant because it has a sweet ether-like odor. Under standard atmospheric conditions DME is a colorless gas, but it can easily condense to the liquid phase under the pressure at 0.5 MPa at 25°C. Liquefied DME has similar properties to those of liquefied petroleum gases (LPG). DME burns with a visible blue flame. The explosion characteristics presented in Table 1.

A tropospheric lifetime of dimethyl ether is 5.1 days [23, 25] therefore, DME does not affect on ozone depletion. The DME global warming potentials is 1.2 (20-year), 0.3 (100-year), and 0.1 (500-year). Based on the analysis and comparison presented in Table 2, it could be concluded that dimethyl ether is environmentally benign.

Thanks to its properties (Table 3) and large variety of raw materials (presented below), DME considered as a promising renewable energy source which can potentially replace conventional diesel fuel. These advantages led the researchers [1, 5, 13, 23–25, 27, 28] and many others, to provide investigations on the analysis of the conventional diesel engines fueled with pure DME or blended with diesel fuel.

Table 1. Explosion and hazard characteristics [23]

Parameters	DME	Diesel	Propane	Butane
Self-ignition temperature [K]	508	523	743	638
Lower explosion limit [vol.%]	3.0–3.4	0.6	2.1	1.9
The upper limit of the explosion [vol.%]	17–18.6	6.5–7.5	9.4	8.4
Minimal ignition energy [mJ]	0.29	–	0.26	0.305

Table 2. Global warming potentials [23, 25]

Chemical compounds	Time horizon (years)		
	20	100	500
DME (CH_3OCH_3)	1.2	0.3	0.1
Carbon dioxide (CO_2)	1	1	1
Methane (CH_4)	56	21	6.5
Nitrous oxide (N_2O)	280	310	170

2.1. DME production

Traditionally, DME is produced as a result of the conversion of various raw materials, such as natural gas, coal, biomass, plastics waste, municipal waste in two distinct ways (Fig. 5) [1, 2, 18, 21, 22]:

1. Indirect route by the dehydrogenation reaction of methanol (Fig. 6).
2. Direct route, in which DME is produced in a single stage by using a bi-functional catalyst directly from synthesis gas (Fig. 7).

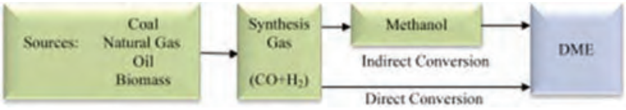

Fig. 5. DME production diagram [2]

2.1.1. Indirect synthesis

In this method DME is produced from syngas in a two-step process (Fig. 6):

- methanol produced from syngas,
- purification and dehydration of methanol.

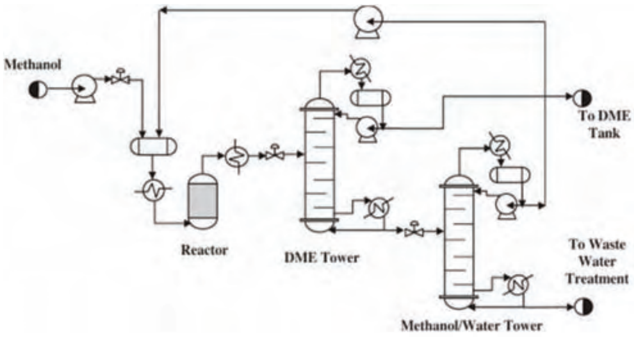

Fig. 6. A scheme of indirect synthesis process [2]

2.1.2. Direct synthesis

Also, known as a single stage method, in which DME is produced directly from syngas (mixture of hydrogen and carbon monoxide ($CO + H_2$)) in a single reactor. The schematic of this process is shown in Fig. 7.

Single stage process is highly exothermic and, therefore, the temperature of the process should be controlled properly in order to avoid run-away [2].

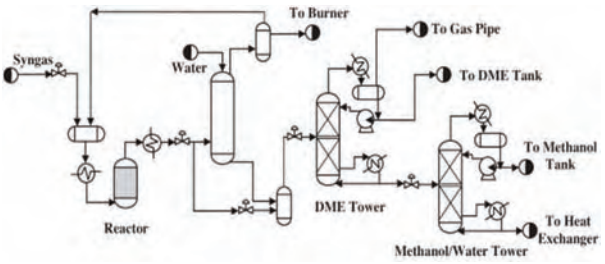

Fig. 7. A scheme of direct synthesis process [2]

2.2. DME infrastructure

The analysis and comparison of the vapor pressure diagram (Fig. 8), shows that the vapor pressure curve for DME falls between butane and propane curves. This means that, the storage, fuel handling, and transportation requirements are similar to those used for LPG and can be used for DME.

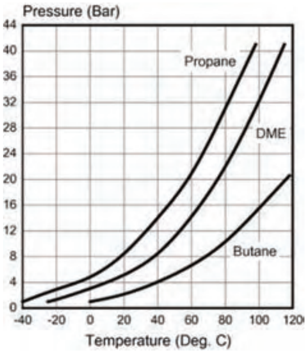

Fig. 8. The vapor pressure characteristics of different fuels [14, 23]

Since there are numerous LPG refilling stations, transitioning to dimethyl ether could be less costly than building a completely new infrastructure, of course the additional refueling stations would be built as the demand for dimethyl ether increases. Dimethyl ether can be offloaded and stored at the refilling station using the same methods and equipment as those used for LPG (Fig. 9). However, due to the different DME properties, LGP infrastructure must be redesigned (discussed in the following chapters).

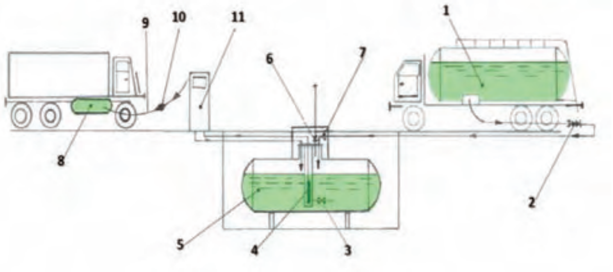

Fig. 9. DME distribution system to the refilling stations [12]

2.3. Advantages and disadvantages

The reasonableness of the DME use in the compression ignition engines can be determined by the detailed examining its advantages and disadvantages.

Advantages:

1. Due to a high cetane number DME has excellent ignition ability and short ignition delay.
2. Low boiling point leads to almost instantaneous evaporation of liquid DME after injection into the engine cylinder.
3. DME can be blended with various fuels such as, diesel, biodiesel, LPG and other.
4. Low carbon to hydrogen ratio than diesel fuel (C/H) results in a lesser amount of CO_2 and greater amount of H_2O generated following full combustion, which is the effect of the combustion of hydrogen [14].
5. High oxygen content together with the absence of any direct carbon-to-carbon (C–C) bonds leads to almost smoke-free combustion, and producing considerably less particulate matter (PM) than conventional diesel fuel.
6. Combustion noise from compression ignition engines is significantly lower when DME is used instead of diesel fuel, due to a slower pressure rise during the premixed burning stage.
7. DME can be applied to the compression ignition engine with minor modifications in the fuel supply system (discussed in the below sections of this paper).
8. Major benefit from this fuel is the big reduction of nitrogen oxides (NO_x), carbon monoxide (CO), hydrocarbon (HC) and particulate matter (PM) emissions, subject to the properly designed injection and combustion strategies [12, 13, 23].

According to the authors [1, 5, 13, 23–25, 27] and others, the most challenging aspects of the DME use in the diesel engines are related to its physical properties and not to its combustion characteristics.

Disadvantages:

1. Because of the low boiling point DME is a gas in the standard atmospheric conditions, therefore it must be pressurized in a fuel system, stored in a pressurized tank, and handled in a liquid form under appropriate pressure.
2. Lower heating value requires a larger injected volume, longer injection period and advanced injection timing in order to deliver the same amount of energy to that provided by diesel fuel. To solve this problem, can be used injectors with a larger nozzle diameter. Moreover, to balance the energy content, the DME fuel tank must be correspondingly larger, which increase vehicle total weight.
3. Low viscosity causes leakage problems within the fuel supply system. To prevent this, issue it is necessary to appropriate sealing the elements in the fuel-injection systems.
4. Low lubricity leads to the surface wear problems of moving parts within the fuel-injection system. According to the authors [12, 23, 24] the lubricity can be enhanced by addition of 500–2000 ppm of a lubricity additive such as, Lubrizol (1000 ppm), Hitec 560 (100

ppm) and Infineum R655 (500 ppm). From the other hand, this issue can be solved by the adaptation of the materials of the bearing surfaces and plunger/barrel interfaces to the low lubricity of DME, however, this solution technically is very complex and expensive.

5. Dimethyl ether non-corrosive, but is an excellent solvent which can dissolve a number of elastomers most commonly used in the diesel engines and other plastic components [1]. To prevent seals quality deterioration after prolonged exposure of DME, it is necessary to carefully select appropriate sealing materials (such as polytetrafluoroethylene (PTFE)).
6. The high vapor pressure of DME means that cavitation can take place, which in turn impedes stable fuel-injection operation. To avoid cavitation the fuel supply pressure (the feed pressure from the storage tank to the fuel pump) must be between 1.2–3 MPa [1, 12].

Table 3. Properties of alternative fuels compared to diesel fuel [10, 11, 13, 20, 23–25]

Parametr	Diesel Fuel	DME	Butane	Propane	Methanol	Ethanol	Biomethane	Biodiesel FAME	GTL
Chemical formula	C_nH_{2n} or C_nH_{2n+2} (n=13~17)	CH_3OCH_3	C_4H_{10}	C_3H_8	CH_3OH	C_2H_5OH	CH_4	–	–
Molecular weight [g/mol]	170	46.07	58.13	44.11	32.042	46.07	16.04	296	259.6
Liquid density at 20°C [kg/m^3]	800–840	668	610	501	791.3	789.4	0.72	919.3	784.6
Liquid viscosity at 25°C [cSt]	2–4	0.12–0.15	0.2	0.2	0.543	1.1	1.12	38	3.497
Vapor pressure at 25°C [bar]	–	5.1	8.4	2.1	–	–	200–250	–	–
Boiling temperature [°C]	125–400	−24.9	−0.5	−42.1	65	79	−162	280–350	72
Self-ignition temperature [°C]	254	235	365	470	385	363	470	261	254
Cetane number	40–55	55–60	10	5	2	11	0	54-56	79
Lower heating value [MJ/kg]	36	28.43	45.74	46.36	20.08	26.83	44.4	34	43.65
Stoichiometric A/F [kg/kg]	14.6	9.0	14.8	15.7	6.47	9.0	10.42	12.5	14.97
Latent heat of evaporation [kJ/kg]	250	410	390	426	1162.64	918.42	511	254	–
Content of carbon, oxygen and hydrogen [% by mass]	86/0/14	52.2/34.8/13	82.8/0/17.2	75/0/25	37.5/50/12.5	52.2/34.73/13.07	74/0/26	77/10.32/12.18	85/0/15
Sulfur content [ppm]	~250	0	0,01	0,01	0	0	0	0.01 max	< 0.05

2.4. Application of dimethyl ether in diesel engine

There are three main application modes of DME fuel in compression ignition engines:

1. Dual fuel combustion mode (fuel mixture ignited by the pilot diesel):

- DME injected into the inlet manifold. In this operation mode DME in gaseous form inducted into the intake air of the inlet manifold to form homogeneous mixtures and then ignited by the direct injected diesel in the cylinder. This mode is inexpensive and requires only minor modifications by adding a separate fuel tank, fuel lines and fuel injector. This method is roughly the same as LPG, demands the same kind of handling and storage considerations as for LPG. The schematic diagram of this mode is shown in Fig. 10.
- DME injected inside the cylinder in a liquid form. In this mode each fuel required a separate fuel supply system as presented in Fig. 11 or they can be injected via one injector.

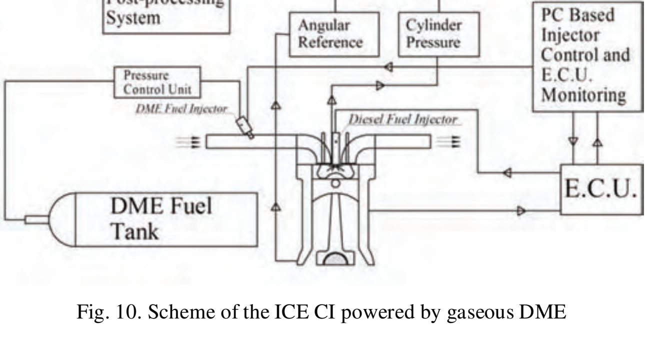

Fig. 10. Scheme of the ICE CI powered by gaseous DME

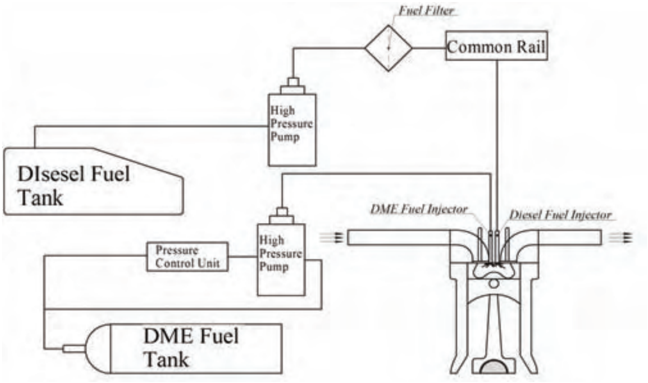

Fig. 11. Fuel system with two injectors

In dual fuel mode when alternative fuel runs out, then electronic control unit automatically switch engine to a reserve tank of diesel fuel.

2. Blended mode:

- One of the major benefits of DME is solubility with various fuels. In this point of view, according to the authors [10, 23] for example the blending of DME with propane improves the lower heating value of DME, the use of DME/biodiesel blend as engine fuel does not require any lubrication additive due to the high lubricity and viscosity of biodiesel. Fuel blended mode is a good inexpensive solution which does not require any modifications in the fuel supply system. Moreover, compared to the conventional diesel fuel, it is found that the blended fuel reduces toxic emissions in the exhaust gases [5, 10, 23].

3. Single fuel mode:

- Due to, the high cetane number and great self-ignition abilities. DME can completely replace diesel fuel. Technically this solution is very complex and expensive, and requires major modifications in the fuel supply system.

2.5. Combustion and emissions characteristics

The evaluation on the combustion and emissions characteristics, include the calculated heat release rate and the cylinder pressure.

The authors [27] studied the operating parameters and emissions characteristics of diesel engine fueled with DME/Diesel blends (DM10 – 10% DME and 90% diesel, DM15 – 15% DME, DM20 – 20% DME). Fuel properties and the constitutions of three oxygenated blends are given in Table 4. According to authors [27] they used a commercial four-cylinder, water-cooled, naturally aspirated diesel engine 4113, made by Wu Xi diesel factory. No more modifications are made on the engine except the fuel pipe and fuel tank. The fuel pipe is changed into the copper one due to the causticity of DME to original rubber pipe. The diesel fuel tank is changed to LPG vessel to prevent DME from evaporating [27].

Table 4. Physical and chemical property of DME, diesel and DME/diesel blend [27]

Properties	DME	Diesel	DM10	DM15	DM20
Liquid density, [g/cm^3]	0.668	0.84	0.823	0.814	0.803
Low calorific value, [MJ/kg]	28.43	42.5	41.1	40.4	39.7
Cetane number	55–60	40–55	> 40	cetane number	< 60
Stoichiometric A/F, [kg/kg]	9.0	14.6	14.04	13.76	13.48
Latent heat of evaporation, [kJ/kg]	410	250	–	–	–
wt.% of carbon	52.2	86	82.2	80.93	79.24
wt.% of oxygen	34.8	0	3.48	5.22	6.96
wt.% of hydrogen	13	14	13.9	13.85	13.8

Figure 12 gives the comparison information of the power output of the engine fueled with four kinds of fuels at speed characteristics with a full load. It can be seen that the more DME percentage in blend is, the lower the power output is. The reasons are [27]:

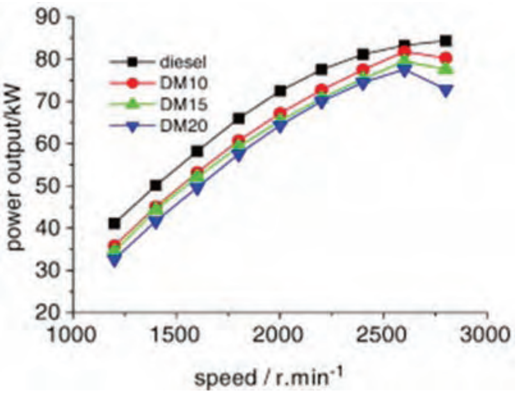

Fig. 12. The comparison of power outputs among various fuels [27]

1. The lower calorific value of blends compared to conventional diesel.
2. The smaller amount of fuel delivery resulted from lower density for blend fuels.

Increasing the amount of fuel delivered per cycle, can improved a power output parameters.

The heat release rate of various fuels is demonstrated in Fig. 13. It can be seen that the amount of heat release of diesel/DME blend fuels during the premixed combustion stage is smaller than that of diesel fuel. The smaller amount of heat release during the premixed combustion stage reduces the combustion pressure and temperature and leads to low NO_x emission [27].

Figure 14 and Figure 15 show comparative values of various toxic compounds in the exhaust gasses. It can be seen that the use of DME/diesel blend as engine fuel can reduce smoke emissions significantly, especially at higher loads, in the same way NO_x emissions are reduced somewhat in comparison with conventional diesel. The emissions of HC and CO are higher than those in diesel fuel.

Authors [27] pointed to a need of the injection strategy optimization to reduce HC and CO emissions. Similar to authors [27], numerous studies [5, 10, 13, 23, 24] shows that NO_x, PM and smoke emissions are slightly lower than those of the diesel fuel operation, however, HC and CO emissions rise. According to the author's [10, 23], the HC and CO emissions could be reduced with an earlier injection period, which would promote the oxidation reaction of the HC and CO emissions. According the authors [13, 23, 24] NO_x emissions reduces due to the larger temperature drop of the mixture due to heat absorption during DME vaporization causes by higher latent heat value of DME.

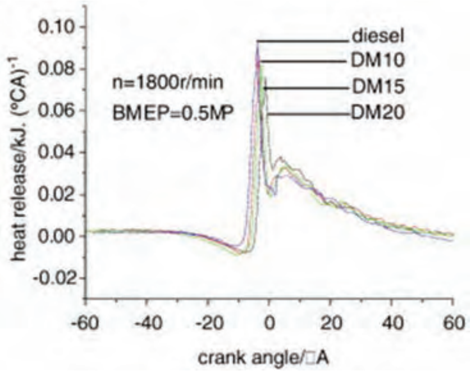

Fig. 13. The comparison of the heat release among various fuels [27]

On the other hand, numerous studies [15, 17, 28], reported that NO_x emissions are higher from DME combustion than diesel combustion, due to rapid ignition and a high combustion temperature.

However, high NO_x emission from DME combustion can be easily reduced to a similar or lower level than that produced by diesel combustion by using a various methods such as exhaust gas recirculation (EGR) and optimization of the injection strategy, what is confirmed by many authors [10, 13, 23, 24].

Different results in the studies shows that, the emission characteristics of DME-fueled engines depends significantly on the engine specifications, fuel supply system, engine operating conditions including injection strategy (single or multiple injections, low or high injection pressure etc.).

Proper adaptation and optimization of the engine operating conditions including the injection strategy and operation algorithms of the diesel engine electronic control unit can helps to reach a state of clean emissions with current combustion technology (Fig. 16 and Fig. 17).

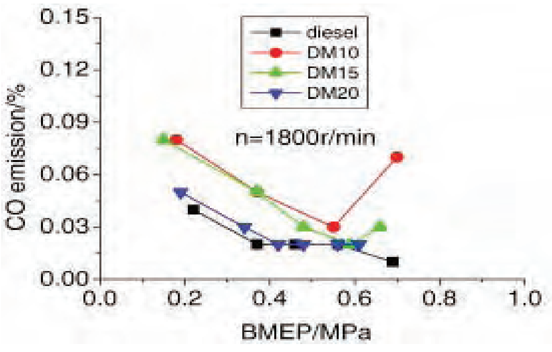

Fig. 14. The comparison of CO emissions [27]

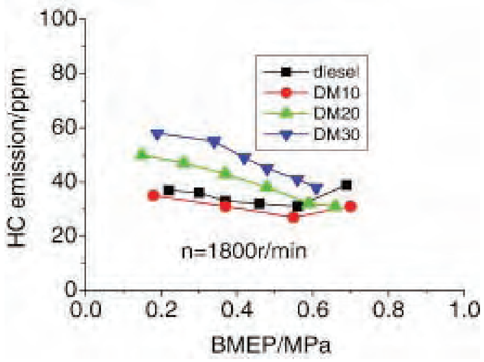

a) The comparison of HC emissions

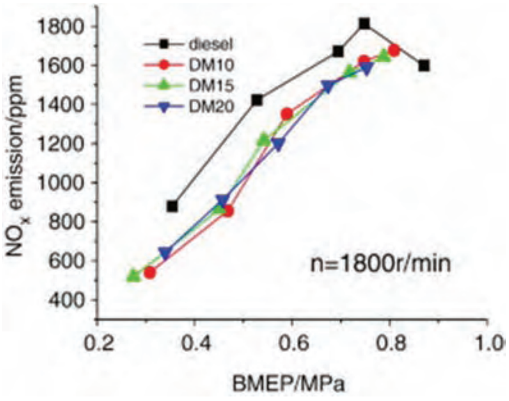

b) The comparison of NO_x emissions

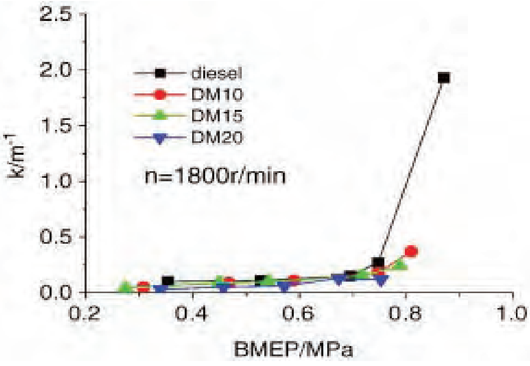

c) The comparison of smoke emission

Fig. 15. The comparison of harmful emissions among various fuels [27]

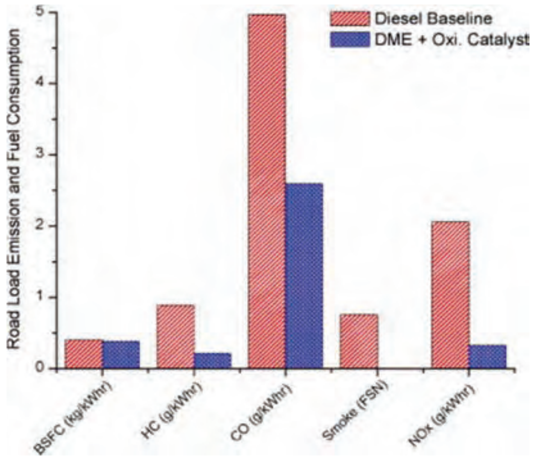

Fig. 16. The comparison of harmful emissions using diesel and neat DME [25]

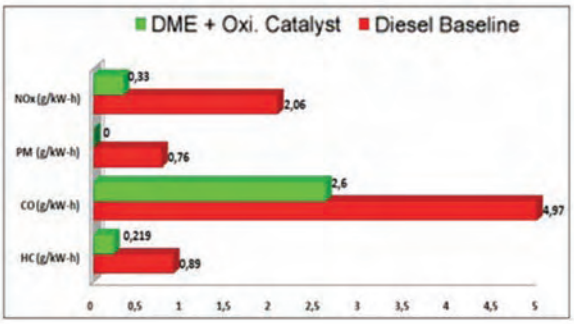

Fig. 17. The comparison of harmful emissions among the DME and diesel fuel [12]

3. Cost of different fuel types

One of the key features that determining the alternative fuels perspectives is price competition with conventional petroleum-based fuels. Simple and easily comparable information on the prices of different fuels could play an important role (Table 5) in enabling vehicle users to better evaluate the relative cost of different fuels available on the market [19], and as result in the consideration of alternative fuel as a substitute for petroleum fuels.

Table 5. Comparison of fuel prices [19]

Type of fuel	Energy content		Fuel price	Fuel price per 10 [kWh]
	[MJ/l]	[kWh/l]		
Petrol	32	8.88	1.536 (€/l)	1.730
Diesel	36	10	1.398 (€/l)	1.398
Natural gas	44.4	12.3	1.103 (€/kg)	0.897
Biomethane	44.4	12.3	1.103 (€/kg)	0.897
LPG	24	6.6	0.693 (€/l)	1.050
DME	28.43	7.9	0.624 (€/l)	0.786
Biodiesel/B7	33	9.16	1.398 (€/l)	1.526

Each fuel has different calorific value so it is important to compare fuels with their energy content as kilowatt hour (kWh) [19]. In this way, the differences between fuels in terms of energy content would be directly visible without the “detour” of a reference fuel [19]. A scaling in 10 kWh would be more familiar to the consumer as 10 kWh is equivalent to the energy content of a liter of diesel [19].

Currently it is quite difficult to determine the consumer cost of DME, and it is mainly depending on the raw material cost and production method. According to International DME Association, the DME consumer cost estimated at 75%–90% of LPG price.

4. Conclusions

Numerous investigations of DME-fueled engines have indicated that the DME offers excellent promise as an alternative fuel for compression ignition diesel engines that can address the pragmatic realization on depleting petroleum reserves and growing concerns on environmental pollution.

The prominent advantages of dimethyl ether as a fuel and energy carrier are high cetane number, superior atomization performance, high oxygen content, no direct C–C bonds, low boiling point, low carbon to hydrogen ratio (C/H) and etc. Moreover, from the environmental benefits point of view, DME is better than diesel fuel, which has been also confirmed by numerous investigations. From technical point of view the DME fuel handling and storage system could be very similar to LPG systems very well-known from automotive industry. In additional, DME may be produced from the renewable materials such as biomass or waste.

Overall, DME has been found to be a very promising alternative fuel for compression ignition engines that can potentially replace diesel fuel.

The further research by the authors of this paper, are the investigations of the DME fuel combustion in the Volkswagen AJM 1.9 TDI engine in dual fuel mode.

Acknowledgements

The authors wish to express their deep thanks to the Nouryon Company (Christian Neefestraat 2, 1077 WW Amsterdam) for the DME fuel and thanks to Elpigaz Company (ul. Perseusza 9, 80-299 Gdańsk) for the DME fuel supply system.

Bibliography

[1] ARCOUMANIS, C., BAE, C., CROOKES, R., KINOSHITA, E. The potential of di-methyl ether (DME) as an alternative fuel for compression-ignition engines: A review. *Fuel*. 2008, **87**(7), 1014-1030.

[2] AZIZI, Z., REZAEIMANESH, M., TOHIDIAN, T., RAHIMPOUR, M.R. Dimethyl ether: a review of technologies and production challenges. *Chem. Eng. Process. Process Intensif.* 2014, **82**, 150-172.

[3] BP Energy Economics. 2018 BP Energy Outlook 2018 BP Energy Outlook. *2018 BP Energy Outlook*. 2018, 125.

[4] CHEN, X., WANG, Z., PAN. S., PAN, H. Improvement of engine performance and emissions by biomass oil filter in diesel engine. *Fuel*. 2019, **235**, 603-609.

[5] CHEN, Y., SU, X. Emissions of automobiles fueled with alternative fuels based on engine technology: a review. *J. Traffic Transp. Eng.* 2018, **5**(4), 318-334.

[6] CRIPPA, M., GRANIER, C. Forty years of improvements in European air quality: regional policy-industry interactions with global impacts. *Atmos. Chem. Phys*. 2016, 16(6), 3825-3841.

[7] EC. Commission Regulation (EU) 2017/1151 of 1 June 2017 supplementing Regulation (EC) No 715/2007 of the European Parliament and of the Council on type-approval of motor vehicles with respect to emissions from light passenger and commercial vehicles Euro 5 a. 2017, **692**, 1-643.

[8] BIELACZYC, P., WOODBURN, J. Current directions in LD powertrain technology in response to stringent exhaust emissions and fuel efficiency requirements. *Combustion Engines*. 2016, **166**(3), 62-75. DOI:10.19206/CE-2016-341.

[9] EPA. Facts. Fast FastFacts acts U.S. Transportation Sect. Greenh. Gas Emiss. July 2018.

[10] GENG, P., CAO, E., TAN, Q., WEI, L. Effects of alternative fuels on the combustion characteristics and emission products from diesel engines: a review. *Renew. Sustain. Energy Rev*. 2017, **71**, 523-534.

[11] GILL, S.S., TSOLAKIS, A., DEARN, K.D., RODRÍGUEZ-FERNÁNDEZ, J. Combustion characteristics and emissions of Fischer–Tropsch diesel fuels in IC engines. *Prog. Energy*

Combust. Sci. 2011, **37**(4), 503-523.
[12] GÓRSKI, W., JABŁOŃSKA, M.M. Eter dimetylowy – uniwersalne, ekologiczne paliwo XXI wieku. *Inst. Naft. i Gazu.* 2012, 631-641.
[13] HOU, J., WEN, Z., JIANG, Z., QIAO, X. Study on combustion and emissions of a turbocharged compression ignition engine fueled with dimethyl ether and biodiesel blends. *J. Energy Inst.* 2014, **87**(2), 102-113.
[14] IDZIOR, M., KARPIUK, W. Assessment of the potential of dimethyl ether as an alternative fuel for compression ignition engines. *Combustion Engines*. 2017, **169**(2), 181-186.
[15] KAJITANI, S., CHEN, Z.L., KONNO, M., RHEE, K.T. Engine performance and exhaust characteristics of direct-injection diesel engine operated with DME. *SAE International*, 1997.
[16] KESSEL, D.G. Global warming — facts, assessment, countermeasures. *J. Pet. Sci. Eng.* 2000, **26**(1), 157-168.
[17] KIM, M.Y., YOON, S.H., RYU, B.W., LEE, C.S. Combustion and emission characteristics of DME as an alternative fuel for compression ignition engines with a high pressure injection system. *Fuel*. 2008, **87**(12), 2779-2786.
[18] KISS, A.A., SUSZWALAK, D.J.-P.C. Innovative dimethyl ether synthesis in a reactive dividing-wall column. *Comput. Chem. Eng.* 2012, **38**, 74-81.
[19] KOLB, O., SIEGEMUND, S. Study on the Implementation of Article 7(3) of the "Directive on the Deployment of Alternative Fuels Infrastructure" – Fuel Price Comparison Study on the Implementation of Article 7(3). Directive on the Deployment of Alternative Fuels Infrastr. 2017, **7**(3).
[20] LAPUERTA, M., ARMAS, O., HERNÁNDEZ, J.J., TSOLAKIS, A. Potential for reducing emissions in a diesel engine by fuelling with conventional biodiesel and Fischer–Tropsch diesel. *Fuel*. 2010, **89**(10), 3106-3113.
[21] LEONZIO, G. State of art and perspectives about the production of methanol, dimethyl ether and syngas by carbon dioxide hydrogenation. *J. CO2 Util.* 2018, 27, 326-354.
[22] LUU, M.T., MILANI, D., WAKE, M., ABBAS, A. Analysis of di-methyl ether production routes: process performance evaluations at various syngas compositions. *Chem. Eng. Sci.* 2016, **149**, 143-155.
[23] PARK, S.H., LEE, C.S. Applicability of dimethyl ether (DME) in a compression ignition engine as an alternative fuel. *Energy Convers. Manag.* 2014, **86**, 848-863.
[24] PARK, S.H., LEE, C.S. Combustion performance and emission reduction characteristics of automotive DME engine system. *Prog. Energy Combust. Sci.* 2013, **39**(1), 147-168.
[25] SEMELSBERGER, T.A., BORUP, R.L., GREENE, H.L. Dimethyl ether (DME) as an alternative fuel. *J. Power Sources*. 2006, **156**(2), 497-511.
[26] U.S. EPA. Inventory of U.S. Greenhouse Gas Emissions and Sinks (1990-2016). *United Stats Environ. Prot. Agency*, 2018.
[27] YING, W., GENBAO, L., WEI, Z., LONGBAO, Z. Study on the application of DME/diesel blends in a diesel engine. *Fuel Process. Technol*. 2008, 89(12), 1272-1280.
[28] YOUN, I.M., PARK, S.H., ROH, H.G., LEE, C.S. Investigation on the fuel spray and emission reduction characteristics for dimethyl ether (DME) fueled multi-cylinder diesel engine with common-rail injection system. *Fuel Process. Technol.* 2011, 92(7), 1280-1287.

Denys Stepanenko, MEng. – Faculty of Mechanical Engineering, Gdansk University of Technology.
e-mail: *denstepa@student.pg.edu.pl*

Zbigniew Kneba, DSc., DEng. – Faculty of Mechanical Engineering, Gdansk University of Technology.
e-mail: *zkneba@pg.edu.pl*

Article citation info:
LUFT, S., SKRZEK, T. Research on the effect of diesel fuel injection parameters on the exhaust emissions in the turbocharged CI engine operating on propane. *Combustion Engines*. 2019, **177**(2), 180-186. DOI: 10.19206/CE-2019-231

Sławomir LUFT
Tomasz SKRZEK

CE-2019-231

Research on the effect of diesel fuel injection parameters on the exhaust emissions in the turbocharged CI engine operating on propane

The article presents results of the studies on the charged, dual-fuel CI compression ignition engine fuelled with propane. The main goal of the studies was to fuel the engine so that the amount of energy provided with propane is possibly highest at the high efficiency, low emission of harmful exhaust constituents and proper combustion. As the studies conducted so far have shown, with the increase of energy from propane we observe crucial changes in the combustion process. As these changes may be a barrier in the further increase of energy, we decided to change the injection parameters of the diesel fuel. The changes introduced allowed for the 70% energetic contribution of gas fuel at the subsequent elimination of unfavourable phenomena. The fuel injection was realized divided into two doses. Both proportions and angle at the beginning of the injection for both doses were variable. The angle at the beginning of injection for the first dose was changed in a wide range and depended on the value of charging pressure. The angle at the beginning of injection for the second dose was changed in a much narrower range, mainly due to very clear changes in the nature of combustion process. The studies have been conducted for three values of charging pressure, namely 200; 400 and 600 [mbar], and also for the naturally aspirated version. Study results have been presented in a form of regulation characteristics for the angle of the beginning of injection of the pilot dose for the chosen charging variants, as well as volume and angle of the beginning of injection for the main dose. The obtained results show that the content of exhaust constituents for the dual-fuel CI engine depends highly on assumed regulations of injection parameters of the fuel dose initiating the ignition, as well as engine charging pressure.

Key words: *combustion engines, dual fuel, propane, alternative fuels, air pollution*

1. Introduction

As numerous publications both domestic and foreign show, the idea of dual-fuel CI engine fuelling is attractive and keeps being developed [3]. This type of fuelling is considered to improve emitted exhaust constituents and to limit exploitation costs of engines fuelled in this way. This is the main concern of this article. What makes this fuelling type so attractive is the possibility of using cheaper fuels, available in the market. These may be both renewable fuels and those coming from crude oil refining, for instance mixture of propane and butane (LPG).

This fuel is in the field of interest of the companies adapting the CI engine due to their lower price as well as the problem of its distribution, which has already been solved [1, 2]. Undoubtedly, the desirable feature of dual-fuel supply is replacing a standard fuel oil with its cheaper substitute to the possibly highest extent and, what is more, using possibly easiest and cheapest methods of providing additional fuel without interference with the engine construction. Though, meeting the condition of maximising the contribution of additional fuel is not easy as there are limitations resulting mainly from the significant changes in the course of combustion process. These changes are the effect of supplying additional fuel along with the air in the cylinder filling cycle. Compressed gas is the mixture of fuel and air. The basic parameters of combustion process, and the same, exhaust constituents of the engine fuelled in this way highly depend on the content of this mixture. Fuel supply is most often realized with the use of mixer or injector, as it is the case in the installations supplying spark-ignition engines used already for years. It is though worth to mention that since these methods work for naturally aspirated spark-ignition engines, they do not work so for charged diesel engines with valve coverage, as they considerably contribute to the escape of a part of the load what causes higher emission of hydrocarbons and hinders the efficiency of engine fuelled in this way. As the previous studies have shown [6] it is possible to supply additional fuel in such a way that we possibly limit the phenomenon of escaping of a part of the load. This method has also been applied during the studies, the results of which have been presented in this article. For the purpose of the study we used propane mainly due to the fact that we wanted to avoid mistakes stemming from the lack of knowledge in the content of LPG fuel version.

The main goal of the studies was to obtain comparable parameters characterizing work of a dual-fuel engine with the corresponding parameters of a standard engine with possibly high contribution of propane so that the biggest proportion of energy is supplied along with this fuel. Taking into account the fact that as a result of introducing of dual-fuel supply the course of combustion changes considerably we needed to shape this process so that the main goal is achieved. In order to achieve this goal we used the possibilities of modern supply system of common rail type. As these and further studies have shown, the way of releasing energy from propane greatly depends on the strategy of parameters selection for diesel fuel injection. It is crucial if an ignition-initiating dose is injected once or it is divided into pilot and main dose. The volume of the dose or doses initiating the ignition, as well as the angle of the beginning of injection are also significant. While introducing some changes in the abovementioned parameters of diesel fuel injection it is possible to flexibly shape the combustion process what allows for obtaining similar parameters of combustion process to those which characterize the work of engine fuelled in a standard way.

Being aware of the fact that a variable regulation of diesel fuel dose injection parameters corresponds to the change in exhaust constituents, the basic emitted constituents have been registered during the study. The registration of exhaust composition and pressure inside the cylinder allowed for the analysis of the influence of diesel fuel injection parameters on the combustion process in the engine fuelled in this way.

2. Research object and measuring equipment used

The studies have been conducted on the test bed of the company AVL, equipped with one-cylinder CI engine AVL 5402 adapted to dual-fuel supply. Propane in the gaseous phase has been supplied with the use of injector mounted in the intake manifold of the engine. Both injector mounting place and gas injection parameters have been selected so to limit the possibility of load escape in the moment of valve coverage. These parameters have been approved and determined on the basis of previously conducted studies [6].

General layout of the engine with dual-fuel supply has been presented in Fig. 1.

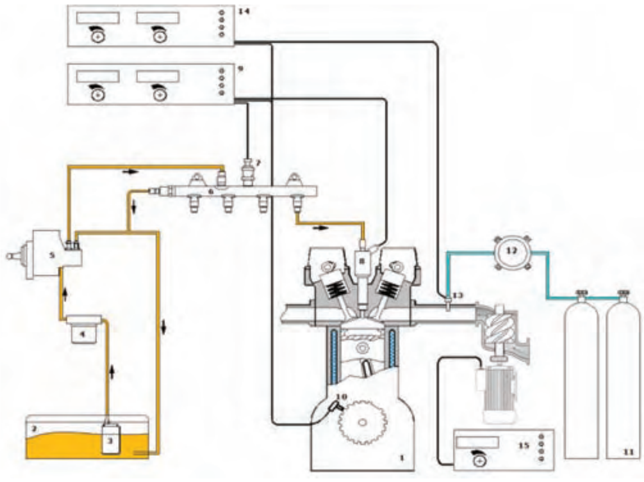

Fig. 1. General layout of dual-fuel system of CI engine supply: 1) dual-fuel engine, 2) diesel fuel tank, 3) electric fuel pump, 4) fuel filter, 5) high-pressure fuel pump, 6) hopper, 7) fuel pressure sensor, 8) diesel fuel injector, 9) controller of common rail supply system, 10) crank shaft location and speed sensor, 11) gas container, 12) pressure regulator, 13) gas injector, 14) controller of gas supply system; 15) engine charging control system

Moreover, the test bed was equipped with the following measurement systems:

- eddy current brake AVL,
- indicating software (IndiCom),
- charging system (AVL boost – electrically powered compressor),
- exhaust analysis system (SESAM I 60),
- system of mass measurement of particle concentration (Micro Soot Sensor),
- system of mass measurement of flow rate of diesel oil used by the engine with temperature conditioning,
- system of mass measurement of flow rate of propane used by the engine (mini CORI-FLOW).

Fuel samples used for the studies came from one batch what aimed to avoid possible discrepancies concerning physical and chemical properties affecting the results of the studies.

An overall scheme of the test bed is presented in Fig. 2.

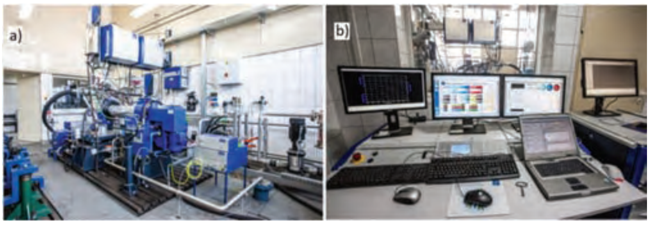

Fig. 2. AVL test bed: (a) general view of the test bed, (b) view of the control room

3. Research programme – assumptions and scope

It was decided to carry out the investigation in the following conditions:

- engine speed n = 2400 rpm,
- three values of diesel fuel pilot dose have been selected: QI (2; 2.25; 2.5 mg),
- a wide range of variability in the injection advance of the diesel fuel pilot dose αI has been chosen (14^o–30^o C.A. before TDC),
- three different values of the angle of the beginning of injection for diesel fuel main dose α II have been chosen (5^o, 6^o, 7^oC.A. before TDC),
- three values of charging pressure p have been adopted (600; 400 and 200 mbar) and uncharged version has been studied, (maximum adopted value of the charging pressure resulted from acceptable maximum combustion pressure, other values have been arbitrarily chosen),
- constant power contribution of propane at the level of 70% of energy supplied to the engine has been adopted,
- constant value of energy dose for diesel fuel at the level of 30% of energy supplied to the engine has been adopted (which means that the change of pilot dose does not affect the energy supplied with the diesel fuel),
- constant value of air-fuel ratio for all measuring points $\lambda = 1.3$ has been adopted.

During realization of each measuring point the concentration of the basic exhaust constituents have been registered: nitrogen oxides NO_x, non-methane hydrocarbons NMHC, propane C_3H_8, and mass concentration of particulate matter PM.

4. Study results

4.1. Variability characteristics of nitrogen oxides' content for different injection parameters of diesel fuel dose initiating ignition

Limiting the emission of this exhaust constituent is still a challenge for diesel engine constructors. Due to its toxic properties it is necessary to look for solutions limiting its concentration. Research results presented below clearly indicate that there is a relation between the concentration of this constituent in the exhaust and adjustment of injection parameters of diesel fuel in the dual-fuel engine.

The results presented above allow to formulate the following conclusions:

- a growth of diesel fuel pilot dose QI is accompanied by the increase in NO_x concentration,
- adjustment of injection advance of QI dose contributes to maximum dozen or so changes in NO_x concentration for a charged engine and over thirty percent changes for an uncharged engine, delaying of injection advance of QII,

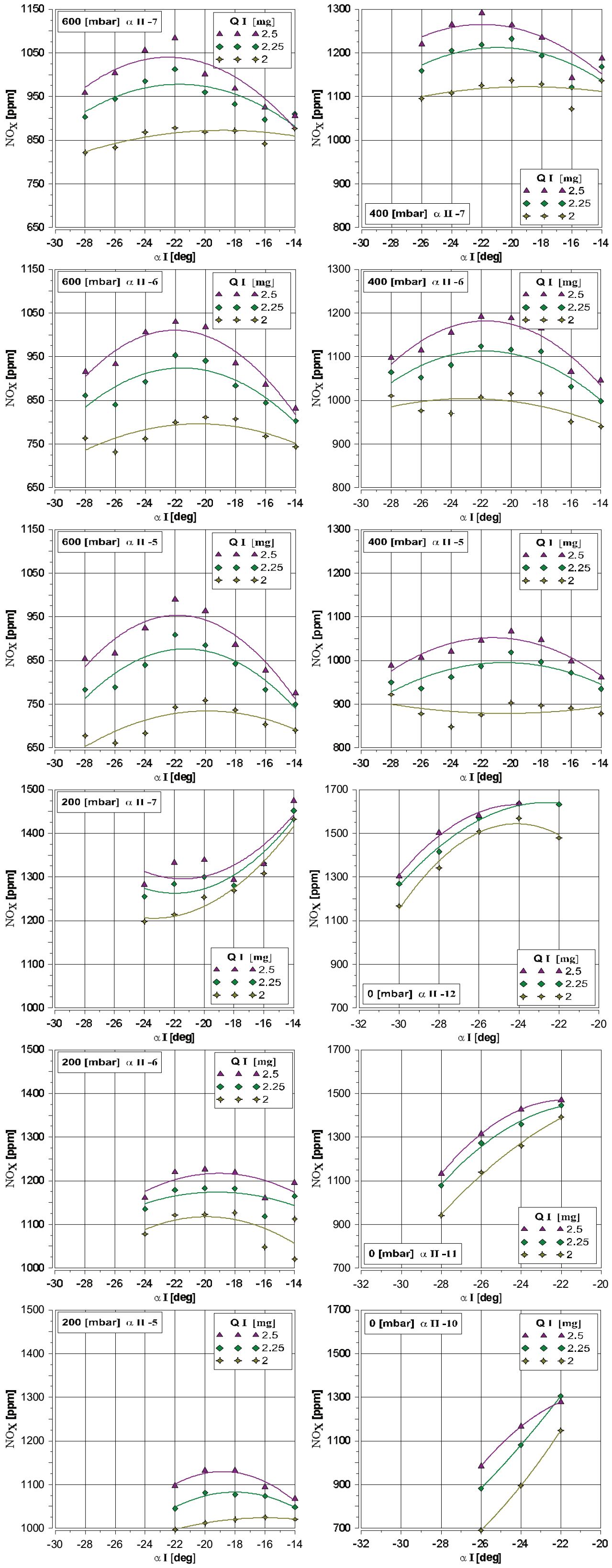

Fig. 3. Characteristics of variability of nitrogen oxides' (NO_x) content in exhaust for different injection parameters of diesel fuel dose initiating ignition

- dose contributes to NO_x reduction for both versions of the engine. In order to justify the first formulated conclusion, one should refer to pressure registered in the cylinder during the time of the study. There is a close relationship between the combustion pressure and the NO_x content inthe exhaust [5, 7, 8]. The highest dose of QI results in the highest combustion pressure and thus the highest temperature in the cylinder. A very small difference in the amount of fuel delivered in the QI dose of only 0.5 mg causes a clear difference in NO_x concentration of about 200 ppm. The dual-fuel supply causes that this effect is more pronounced than in case of standard supply. It is connected with the course of energy release of both fuels. This means that the energy released by the dose Q1 is the sum of the diesel energy of this dose and the energy of the part of propane covered by its range. Thus, a slight increase in the pilot dose rate will translate into the release of more heat before the TDC, and this in turn into the previous combustion of the rest of the charge, the energy of which will be released by the QII dose.

The change in the NO_x concentration due to the change in the injection advance angle of the QI dose also depends on the energy release type of both fuels and more precisely on the location of this process. In almost all considered cases, there is such a position of the angle of the beginning of injection of the QI dose at which the maximum concentration of this component is visible and falls on 20°, 22° C.A. before TDC. Changing this value both towards the previous and later values results in a decrease in the concentration of this component. Earlier advance injection angle for QI makes the dose go to the element of lower concentration and temperature. This leads to extend the delay of self-ignition and consequently to limit the intensity of heat generation. Further increasing the angle of the beginning of injection for QI dose will contribute to the situation at which the dose will not initiate the combustion process. So the combustion process will start after the main dose injection what will cause a considerable delay in the whole process, and the peak value of pressure and temperature will appear much later than in case when pilot dose initiates the combustion process. Such a phenomenon will contribute to lowering the concentration of NO_x, yet one needs to remember that such a change will entail the decrease of thermal efficiency of the engine. On the other hand, delaying the angle of the beginning of injection for QI dose up to some time also results in decreasing the concentration of NO_x. This mechanism is slightly different than the one described earlier. Although, injection of QI dose is realised closer to TDC and the dose takes up the combustion process, the time between the injection of pilot dose and the main dose becomes shorter.

If the time difference between the ignition initiated by the QI dose and the injection of QII dose is shortened (as a result of delaying the injection of QI dose),what effects in decreasing of maximum pressure in the combustion process, then the mechanism of this phenomenon is much dependent on the influence of the former. At the longer time difference which resulted in obtaining maximum combustion pressure when the pilot dose was injected about 20°, 22° before TDC, the time for expansion of heat generated by QI dose is longer and the same the area influenced by this dose will be bigger. So the injection of QII dose realized to the bigger area of higher temperature due to QI dose combustion will cause the intensity increase of evaporation of the fuel supplied in QII dose, shortening of self-ignition time, and consequently earlier and more intense heat generation. Moreover, at a longer time difference it is possible to mix the products of QI dose combustion with the mixture of propane and the air what may also have a positive impact on fuel oxidation supplied in QII dose. So shortening the time difference between the ignition caused by QI dose and QII dose injection one may conclude that the described mechanism is not so effective. The observed phenomenon created the basis for determining the best value of the angle of the beginning of injection of the pilot dose both considering NO_x emission, thermal and general efficiency of the studied engine.

The third formulated conclusion (does not require a thorough analysis) is a result of a simple relation between maximum combustion pressure and the angle of the beginning of injection of the main dose. The change in the angle of the beginning of injection for QII dose causes clear changes in the combustion course which are reflected in form of composition changes of NO_x. It is worthwhile that the combustion pressure depends on the charging pressure so the highest composition of NO_x should be observed for the engine charged with the highest pressure. However, this relation is different. There are few factors that may be responsible for such a relation. One of them is blowing out the cylinder. At the moment of valve overlap the cylinder is blown out with air from the intake system. The intensity of this phenomenon at the constant rotational speed and engine load, as well as constant value of angle of valve overlap depends on the value of charging pressure. It means that the higher charging pressure increases the intensity of blowing out the cylinder what translates into decreasing the temperature of combustion chamber thus improving the filling of the cylinder. As a result, the lower load temperature (substrates) may effect in the lower concentration of NO_x in the exhaust.

Another factor responsible for the lower concentration of NO_x for the charged engine may be slight differences in the air-fuel ratio for the different versions of charging. Both calculated and measured value of this ratio may slightly differ from the reality. The measured mass of air supplied to the engine is not the mass which takes part in the combustion process. The air supplied to the engine includes a part of the air closed in the cylinder and a part goes to the outlet system during valve coverage. Applying this proposal one can assume that with the increase of charging pressure the real air-fuel ratio will decrease. On the basis of these assumptions we need to add that the higher the intensity of blowing out the cylinder, the higher the degree of exhaust dilution with the air taking part in the blowing out process. As a consequence, registered volume concentration of the particular exhaust constituents will be lower.

4.2. Variability characteristics of particulate matter content for different injection parameters of the diesel fuel dose initiating the ignition

Dual-fuel engine supply may considerably influence limiting the emission of particulate matter (PM) in comparison to the emission obtained for the engine supplied in a standard way what is an unquestionable advantage of the engine supplied like this [1, 8]. The concentration of this constituent depends above all on the type of additional fuel, as well as the contribution of this fuel in the combustion process.

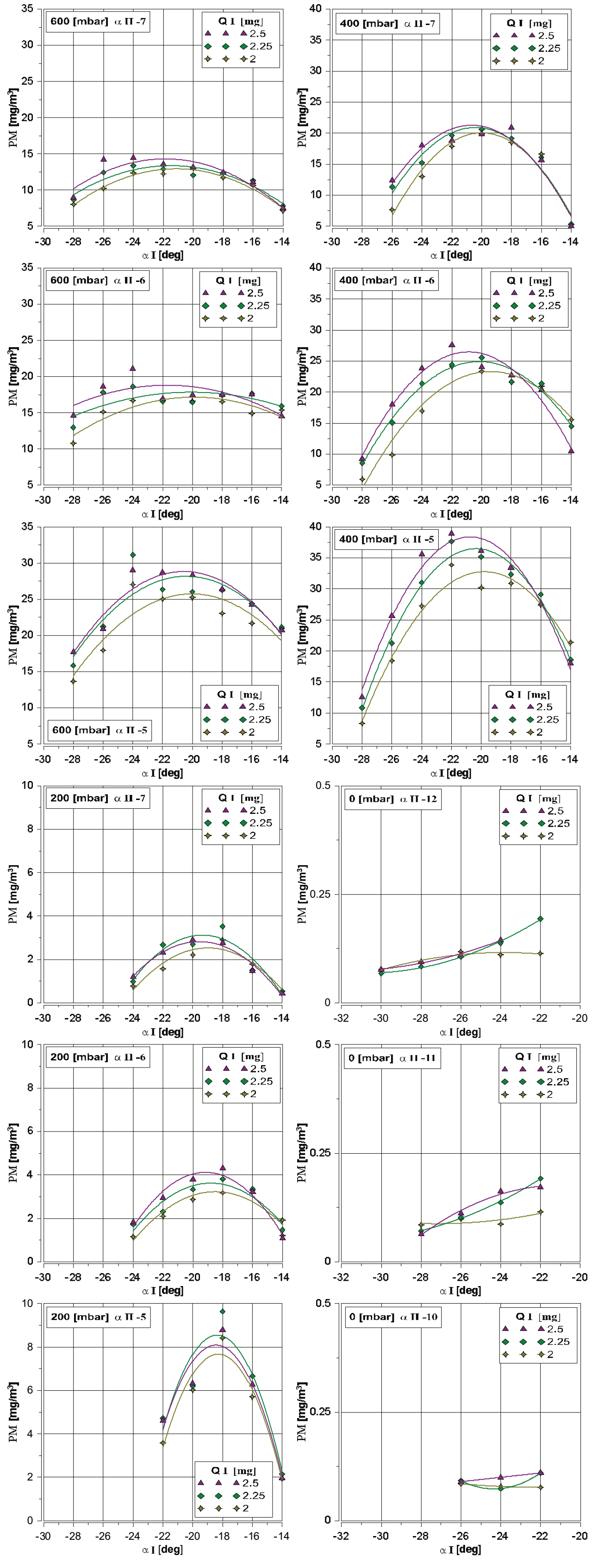

Fig. 4. Characteristics of variability of particulate matter (PM) content in exhaust for different injection parameters of diesel fuel dose initiating ignition

The best results are obtained by supplying the engine with gaseous fuels with a small number of carbon atoms (methane, propane, butane), with the lowest possible contribution of the ignition initiating diesel fuel dose. This means that the main fuel responsible for the emission of particulate matter is standard fuel, the full elimination of which is not possible.

The results presented above allow to formulate the following conclusions:

a) with the increase of QI diesel fuel pilot dose value the concentration of PM also increases,
b) with the increase of charging pressure the concentration of PM also increases (it reaches the smallest value in case of uncharged engine),
c) adjustment of injection advance angle of the QI dose causes the changes in PM concentration; the more delayed the injection angle of the QII, the greater the changes of PM concentration,
d) for the charged engine the delay of angle of the beginning of injection for QII dose is accompanied by the increase in PM concentration.

The nature of particulate matter emission for particular values of the angle of the beginning of injection for the QI dose is similar to the one discussed above regarding NO_x emission. The maximum concentration of particulate matter corresponds to the angle of the beginning of injection for the QI dose in the range 18°–22°C.A. before TDC, it is also the highest for the biggest dose of QI. The most favourable mechanism for the formation of NO_x and PM runs under the same conditions. Due to the 70% contribution of energy supplied with propane, one would expect a considerable reduction in the level of this constituent in relation to the level recorded for the diesel fuel itself. Though, for the cases with the highest charging pressure and the late angle of the beginning of injection for QII dose, i.e. 5°, 6° before TDC, the PM emission level is higher than during the standard supply. This is a consequence of the injection of the main dose into the area devoted to QI dose. This area is characterized by a higher temperature and significant depletion of oxygen. Thus, the main portion of diesel fuel given in the QII dose, reaching such an environment partially underlies the phenomenon of pyrolysis thus creating solid particles. This means that in the dual-fuel engine the in feed of pilot dose may bring about more negative consequences than during standard supply. Unlike in case of NO_x emission, due to the delay of the angle of the beginning of injection for QII dose, the concentration of PM increases. This phenomenon is caused probably by the temperature drop being the result of injection delay of the main dose. Both higher pressure and temperature which accompany the earlier beginning of the injection of the QII dose aids PM reduction.

4.3. Characteristics of variability of non-methane hydrocarbons (NMHC) and propane (C_3H_8) for different injection parameters of diesel fuel dose initiating ignition

Crucial, from the perspective of parameters analysis, the influence of diesel fuel injection parameters on exhaust emission was the need for registration of the concentration of two following exhaust constituents, i.e. non-methane hydrocarbons coming mainly from the diesel fuel combustion, and propane, which is the main energy source for the studied engine. Figure below presents the characteristics of content of non-methane hydrocarbons.

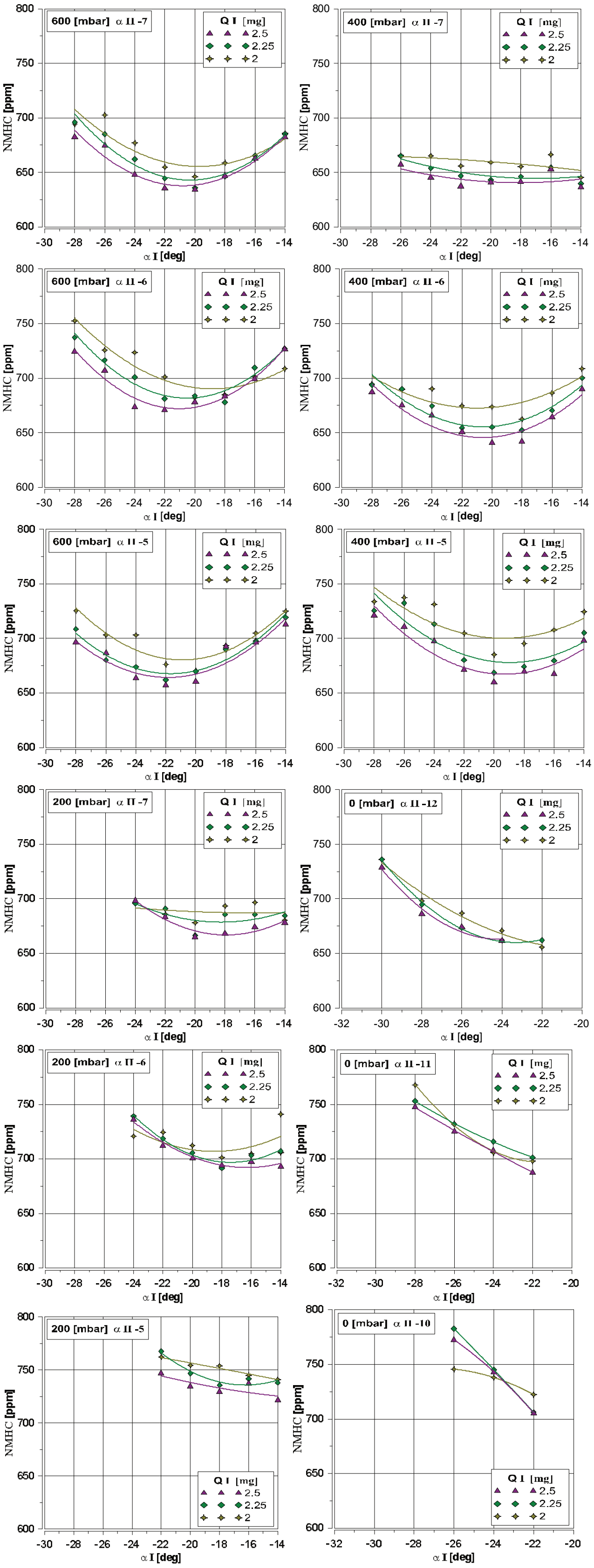

Fig. 5. Characteristics of variability of non-methane hydrocarbons (NMHC) content in the exhaust for different injection parameters of diesel fuel dose initiating ignition

The analysis of the characteristics presented in Fig. 5 leads to formulation of the following conclusions:

a) increase in the diesel fuel pilot dose value QI is accompanied by the decrease of NMHC concentration,
b) adjustment of injection advance angle of the QI dose causes slight, about 10% changes in concentration (NMHC), and the lowest concentrations occur for the adjustment at which maximum value of combustion pressure is reached,
c) delay of injection advance angle for QII dose causes slight increase of the concentration (NMHC).

The abovementioned observations allow to conclude that the content of non-methane hydrocarbons decreases with increasing pressure and, therefore, temperatures in the combustion process. This is the effect of improving the quality of diesel fuel dose combustion.

The injected dose of QI has better conditions for the formation of a combustible mixture compared to the dose of QII. This is mainly due to the easier access to oxygen. Injection of dose QII is carried out to an area in which the oxygen content is lower due to the fact that the QI dose has been burned out.

It should be pointed out that along with the increase in the dose of QI, the dose of QII is proportionally reduced, which has been a condition for maintaining a constant amount of energy supplied with diesel fuel. This means that from the point of view of NMHC hydrocarbons emission, it is beneficial to increase the pilot dose at the expense of the main dose. This is confirmed by previous studies [4, 5, 9]. Unfortunately, the increase in the pilot dose or the elimination of the division of the diesel dose causes a clear increase in the maximum rate of pressure build-up, especially with a significant proportion of propane, which makes the work of such a powered engine impossible. Referring to the main concept of a dual-fuelled engine that concerns the largest possible contribution of additional fuel, it is essential that the energy of this fuel is used as best as possible. One of the ways to determine the quality of this energy use will be to measure the propane concentration in the exhaust. The aim of the studies was to shape the combustion process so that the concentration of propane (the main fuel) in the exhaust gas was as small as possible what has been mentioned in the introduction. The test results presented below indicate that the propane content in the engine exhaust gas is shaped differently to the NMHC component discussed above, while it resembles the NO_x nitrogen oxide emission.

Since the dependence of propane emission on the diesel fuel injection parameters is the same as in the case of nitrogen oxides, the formulated conclusions are similar:

a) the increase of the pilot dose value of diesel fuel for QI is accompanied by the increase in C_3H_8 concentration,
b) adjustment of injection advance angle of the QI dose causes almost 20% changes in concentration of C_3H_8 for the charged engine and slightly bigger changes for the uncharged engine,
c) delay of injection advance angle for QII dose causes C_3H_8 reduction for both versions of the engine.

Analysing the above conclusions, and confronting them with the results characteristic to the combustion process, one can notice a clear correlation between the maximum combustion pressure and the maximum propane concentration. Under the same engine operating conditions (same diesel inject-

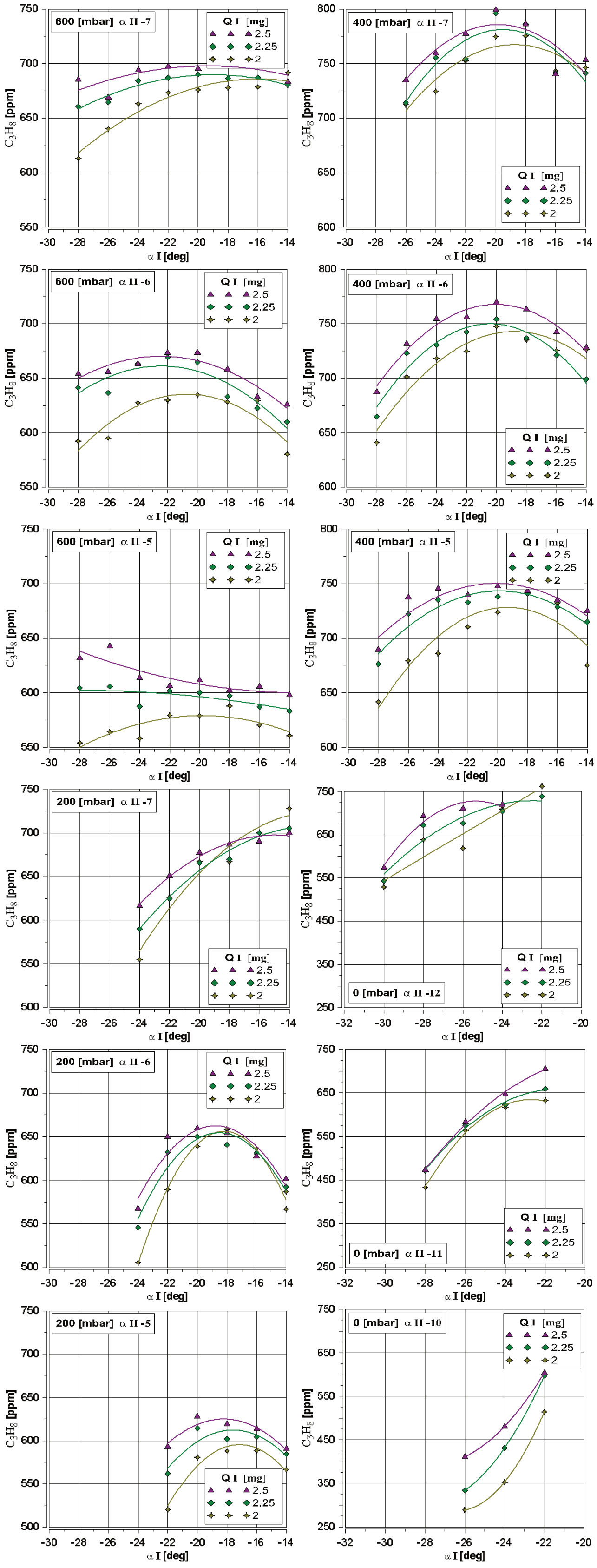

Fig. 6. Characteristics of variability of propane (C_3H_8) content in the exhaust for different injection parameters of diesel fuel dose initiating ignition

tion parameters, and charging pressure) the maximum propane concentration and the maximum combustion pressure are registered, while the decrease in the combustion pressure is accompanied by a drop in propane concentration.

Since the increase in propane emission depends on the increase in the QI dose volume which clearly initiates the combustion process and determines the maximum combustion pressure, it means that the QII injection is realized to the agent with a higher pressure and temperature, which may be the reason for reducing the range of the diesel fuel stream. Thus, the mixture of propane and air away from the central part of the combustion chamber in which the diesel dose is injected is not ignited, which is the main reason for the increase in propane concentration in the exhaust. It should be emphasized that the dose of QII and its range decrease with the increase of QI dose which additionally intensifies this phenomenon. However, increasing concentration of propane in the exhaust does not translate into a decrease in thermal or general efficiency of the engine. This means that the efficiency of the studied engine depends more on the combustion process being shaped by the diesel fuel injection parameters than the propane combustion efficiency measured by the emission of this component. It should also be emphasized that in part the emissions of this component are caused by the escape effect of the load during the valve overlap [6]. Despite the synchronization of the propane injector opening time with the time the cylinder is filled with air, it is very difficult to completely avoid the escape of the load. As shown in the previous studies, at the end of filling the cylinder it is possible that the load regresses to the intake manifold, which in turn takes part in blowing out the cylinder.

5. Conclusions

The possibilities of shaping the combustion process provided by the modern charging system of common rail type contribute to elimination of many limitations resulting from introducing CI charging, especially with the significant contribution of the additional fuel. It is crucial that the choice of diesel fuel injection parameters, namely division of the dose, volume of both pilot and main dose as well as the angle of the beginning of injection depended both on the share of the main fuel, its properties and parameters of engine work, namely: charging pressure, load and rotational speed. It is connected to the need of performing number of regulation characteristics of the engine fuelled this way which would take the aforementioned parameters into account. It is necessary though to determine the criterion for which the adjustment of diesel fuel injection parameters will be realized. As the results of the studies presented in this article have shown, we will need a compromise, since the benefits resulting from improving emission of exhaust composition thanks to the adjustment of diesel oil injection parameters do not equal efficiency improvement of the studied engine. In spite of number of difficulties that introducing a dual-fuel CI engine entails, there are objective benefits in favour of continuation of the studies whose consequence will be more efficient, cheaper in exploitation and environment-friendly engine.

Nomenclature

CI	compression ignition
LPG	liquified petrolum gas
DF	diesel fuel
TDC	top dead center
QI	diesel oil pilot dose
QII	diesel oil main dose

Bibliography

[1] DEO RAJ, T., GOPAL P. SINHA. Performance and emission study of LPG diesel dual fuel engine. *Int. J. Eng. Adv. Technol. (IJEAT)*. 2014, **3**(3).

[2] GARBALA, K., PIEKARSKI, W., ANDRZEJEWSKA, S., WITASZEK, K. Analysis of operating parameters and indicators of a compression ignition engine fuelled with LPG. *Scientific Journal of Silesian University of Technology. Series Transport*. 2016, **93**, 13-22.

[3] PAWLAK, G. The concept of a dual fuel highly efficient internal combustion engine. *SAE Technical Paper*. 2010. DOI:10.4271/2010-01-1480.

[4] POLK, A.C., GIBSON, C.M., SHOEMAKER, N.T. et al. Analysis of ignition behavior in a turbocharged direct injection dual fuel engine using propane and methane as primary fuels. *American Society of Mechanical Engineers*. DOI:10.1115/ICEF2011-60080.

[5] SUNDAR, R.K., KALYAN, K.S., MOSTAFA, S.R. The effect of injection parameters and boost pressure on diesel-propane dual fuel low temperature combustion in a single-cylinder research engine. *Fuel*. DOI:10.1016/j.fuel.2016.07.042.

[6] SKRZEK, T. Assessment of the effect of gaseous fuel delivery mode on thermal efficiency and fuel losses during the valve overlap period in a dual-fuel compression ignition engine. *IOP Conf. Series: Materials Science and Engineering*. 148 012086 DOI:10.1088/1757-899X/148/1/012086, 2016.

[7] SKRZEK, T. Effect of the diesel fuel dose division and the injection angle on operating parameters of a dual-fuel compression ignition engine. *Combustion Engines*. 2015, **3**(162). DOI:10.19206/CE-2017-319.

[8] STELMASIAK, Z., MATYJASIK, M. Exhaust emissions of dual fuel self-ignition engine with divided initial dose. *Combustion Engines*. 2013, **154**(3).

[9] YOUSEFI, A., BIROUK, M. An investigation of multi-injection strategies for a dual-fuel pilot diesel ignition engine at low load. *Journal of Energy Resources Technology*. 2016, **139**(1). DOI: 10.1115/1.4033707.

Prof. Sławomir Luft, DSc., DEng. – Mechanical Engineering Faculty, Radom University of Technology and Humanities.

e-mail: *s.luft@uthrad.pl*

Tomasz Skrzek, DEng. – Mechanical Engineering Faculty, Radom University of Technology and Humanities.

e-mail: *t.skrzek@uthrad.pl*

Article citation info:
FABER, J., JURASZ, Z., BRODZIK, K. Effect of aging and interaction of cooling fluid with heat exchangers material in long-lasting durability test. *Combustion Engines*. 2019, **177**(2), 187-192. DOI: 10.19206/CE-2019-232

Joanna FABER
Zbigniew JURASZ
Krzysztof BRODZIK

CE-2019-232

Effect of aging and interaction of cooling fluid with heat exchangers material in long-lasting durability test

Efforts to improve engine cooling efficiency by usage of heat exchanger as well as research on cooling fluids composition and properties are well described. Studies on heat exchangers are focused mainly on their durability properties, while cooling fluids' development is lately concentrating on nanofluids. In this paper physicochemical properties changes of diluted glycol-based cooling fluid in a long-term durability test of vehicle heat exchanger, were investigated. Following parameters were measured: density of coolant, pH value, elements content in coolant, and reserve alkalinity. Above mentioned analyses were performed on samples collected both in the beginning and periodically after every 500 hours of durability test which lasted for 3000 hours in total. The performed study leads to conclusion that interaction of cooling fluid with material of heat exchanger and changes in glycol composition during long-lasting durability test allows to determine aging effect of applied glycol solution on heat exchanger wear.

Key words: *glycol chemical-physical properties, cooling fluid, heat exchanger, corrosion resistance*

1. Introduction

Heat transfer and efficient cooling of vehicle engine is one of the key processes in proper engine work. Heat produced during engine work and fuel combustion needs to be dissipated, and for that reason a heat exchanger is placed in each vehicle.

The role of heat exchanger, which in automotive the most often is a radiator, is to exchange efficiently heat between two or more fluids. This process leads to heat dissipation, and then to engine cooling [1–3]. Typically radiators are forced air-cooled with crossflow [4], with large enough area for heat transfer.

Vehicle radiators, due to their exposure to high temperatures and temperature changes, have to meet a number of requirements, among them i.e. tightness, thermal efficiency, mechanical durability, corrosion resistance etc. In fact, resistance to thermal shocks is the basic durability parameter of radiators [5, 6]. On the other hand, temperature changes and temperature gradient are the main factors influencing radiator corrosion resistance [3]. For that reason designing of efficient and durable radiator is a complicated matter [1]. The materials used for radiators are typically aluminum alloys, most often aluminum-manganese alloys (Al-Mn) due to their high tensile strength and good corrosion resistance, especially intergranular corrosion resistance [7].

Nowadays, a lot of effort is put into thermal efficiency improvement and fastening of the heat transfer [8–10]. From one point of view this can be achieved by maximizing heat transfer area as heat transfer efficiency is a function of heat exchange relative surface area and fluid temperature [1, 2]. This can be done by using fins or microchannels [9], where the coolant flow is divided into a number of separated tube flows [4]. On the other hand, maximizing heat transfer area by i.e. increasing fins quantity, leads to undesirable increase of vehicle weight influencing fuel combustion efficiency [2]. This fact is in the opposite to another trend in automotive industry: downsizing.

In fact, heat transfer improvement by radiator's construction changes is now limited because of the physical limitations. For that reason the researches are focused now on cooling fluids development. Coolants used in vehicle should have high efficiency of heat dissipation and high thermal conductivity coefficient [2, 10–12], as their role is to act as a heat-exchange medium [8, 13].

Nowadays, the most widely used cooling fluids are water or ethylene glycol-based fluids [12], although their efficiency is relatively low. For this reason the possibility of employing nano-fluids, containing nanoparticles, is now under investigation. The main feature of nano-fluids is their high capacity of thermal properties enhancement [8]. It was observed, that application of nano-fluids can improve heat transfer by 25% [9] to even 50% [8]. Nano-fluids are fluids enriched by nanoparticles, which may be for example ZnO, CuO, Al_2O_3, SiO_2 [2], Cu or TiO_2 [2, 9]. Despite properties of nano-fluids, their usage is limited and OEMs still recommend glycol-based coolants for their automobiles [14].

Many tests for new models of radiators are usually required before their implementation, and are routinely performed, i.e. durability by thermal shocks, vacuum/helium tightness or external corrosion resistance for aggressive salt spray. The results of degradation study of radiator material, durability tests or radiators operational parameters are described in literature. However, data regarding radiator's internal material performance or cooling fluid long-term performance is not easily available

The aim of present work was to monitor changes in chemical and physical properties of selected cooling fluid during long term durability test of three radiators. The radiators were exposed to high temperature of cooling fluid for more than 3000 h, and samples of coolant were collected every 500 h.

This paper discusses elements concentration changes in Glysantin G48, glycol based fluid, which are a reflection of radiator's material wear and cooling fluid condition. Moreover, some physical parameters were also observed: changes in reserve alkalinity, pH value and density, which may also reflect the aging effect of cooling fluid and material.

2. Experimental

2.1. Testing stand

Durability test of three selected heat exchangers (Tested parts #1…#3) were performed in BOSMAL Automotive Research and Development Institute Ltd. The scheme of testing stand is presented in Fig. 1.

The test was performed in three steps and lasted 3003 hours in total. The temperature during the 3000 hours of the test was constant (120°C), and it was increased to 137°C during the last three hours of the test. Cooling fluid was heated with the use of pipe exchanger before introduction to radiators in order to simulate engine work.

The pressure of the fluid was measured in front of the radiators, and was in the range of $(1.5\ldots2.3) \times 10^5$ Pa. The summary of test parameters is presented in Table 1.

Table 1. Durability test parameters

Test step	Time	Temperature	Pressure
–	[h]	[°C]	[$\times10^5$ Pa]
1	2500	120 ±0.5	1.5 ±0.05
2	500	120 ±0.5	2.1 ±0.05
3	3	137 ±2.0	2.3 ±0.05

The flowrate of cooling fluid in each heat exchanger was also monitored and recorded, and was 4200 L h^{-1}. At the start of the test and every 500 hours of test duration a 50 mL sample of cooling fluid was collected, and physical-chemical analysis were performed.

2.2. Cooling fluid

Cooling fluid which was used in durability test was Glysantin G48®. The basis of Glysantin G48 is ethylene glycol, and according to Data Sheet [15] Glysantin G48 contains a corrosion inhibitor package based on organic acids salts and silicates. The main objective of Glysantin G48 is to protect engines against corrosion, overheating and frost damage. Moreover, Glysantin G48 does not contains nitrites, amines and phosphates.

Before use, concentrated Glysantin G48 was diluted with distilled water to concentration recommended by producer [15].

2.3. Physical-chemical analysis

Some physical properties of Glysantin G48 are mentioned in Data Sheet, i.e. density, viscosity, boiling point, flash point, pH value, reserve alkalinity or ash content. Typical values for concentrated Glysantin G48, given by producer, are presented in Table 2 [15]. Besides physical data, no chemical properties or elements content are mentioned in Data Sheet. The only limitations in elements content refer to the water used to dilution of concentrated Glysantin.

Table 2. Physical properties of Glysantin G48 [15]

Parameter	Unit	Value
Density at 20°C	g cm^{-3}	1.121…1.123
Viscosity at 20°C	mm^2 s	24…28
Refractive index at 20°C	-	1.432…1.434
Boiling point	°C	> 165
Flash point	°C	> 120
pH value	–	7.1…7.3
Reserve alkalinity	mL	13…15
Ash content	%	< 1.5
Water content	%	< 3.5

Only few of listed in Table 2 parameters may change during coolant usage as a result of cooling fluid wear, while remaining are typical parameters independent of the wear.

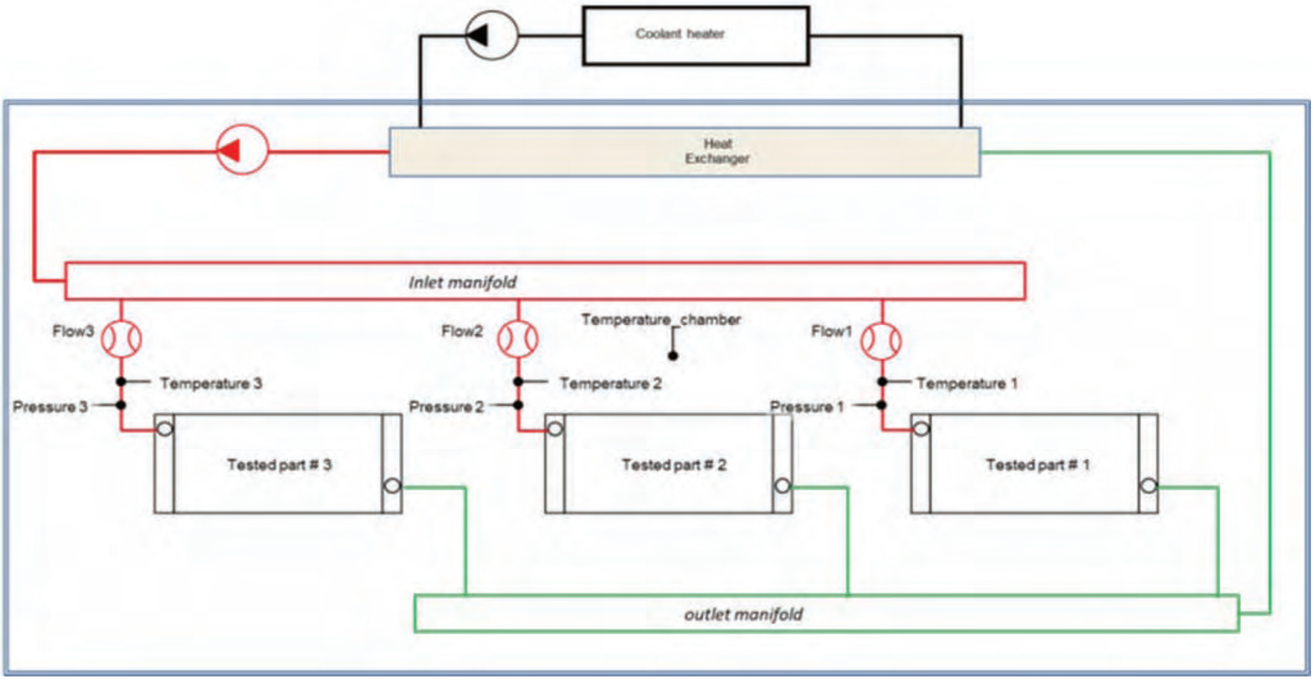

Fig. 1. The scheme of testing stand

Following physical parameters were selected for monitoring the condition of tested fluid during durability test: density at 20°C, pH value and reserve alkalinity, as this parameters may be the indicators of cooling fluid wear.

Polish Standards were applied for above mentioned analysis:
– reserve alkalinity (R.A.) by titration method was measured according to PN-C-40008-05:1993 [16],
– pH value by potentiometric was measured according to PN-C-40008-04:1992 [17],
– density was measured at 20°C by oscillometric method according to PN-EN ISO 12185:2002 [18].

Additionally, twenty different elements (including metals and non-metals) were also measured in each collected coolant sample. Elements concentration was measured by inductively coupled plasma optical emission spectrometer (ICP-OES) Perkin Elmer Optima 8300, with horizontal plasma and binary, radial and axial, observation system. Fluid samples collected every 500 hours and so called ‘zero sample’ (before the introduction to stand and start of the test) were diluted ten times with deionized water before analysis and then measured directly by means of ICP-OES method.

The elements measured were as follows: Al, B, Ba, Ca, Cr, Cu, Fe, K, Mg, Mn, Mo, Na, Ni, P, Pb, Si, Sn, Ti, and Zn. Some of mentioned elements are typically present in Glysantin G48, as a result of organic acids salts package, and the remaining are indicators of heat exchangers’ material wear. The changes in elements concentrations during durability test were monitored.

3. Results and discussion

During the durability test, at the start of the test and every 500h of test, cooling fluid samples were collected. Some changes in physical properties of coolants were observed during the test in comparison to ‘zero sample’.

As presented in Table 3 and in Fig. 2 slightly, but steady decrease in reserve alkalinity and pH value was observed along with test duration. No significant changes in density were observed, which may suggests that no significant changes in chemical composition (i.e. dissolved wear elements increase) occurred.

The changes in R.A. values may be a proof that the capacity of coolant to neutralize acidic glycol oxidation products is decreased, and therefore the protection ability of cooling fluid is decreased. This may effect in radiator’s material corrosion, however the lowest value of reserve alkalinity during the test was still within recommended range (10…14). On the other hand, observed pH value decreased below 7.0 during the test, which value is out of range of safe coolant performance and will result in lower corrosion protection ability of the coolant. It can be stated, that safe working time of diluted Glysantin G48 in presented test conditions, is 1000 hours in maximum, which is not a long time, but it should be still keep in mind that cooling fluid worked simultaneously with 3 radiators, not with one as it usually takes place.

Along with physical properties, concentrations of wide range of elements were also measured. The results obtained can be divided into three groups (Tables 4–6). First group (Table 4) includes elements that are neither from additives package nor wear elements, and their concentration is below method detection limit (MDL). Among this elements are barium (Ba), chromium (Cr), iron (Fe), lead (Pb), tin (Sn), and titanium (Ti). This elements are wear elements (i.e. Fe may derive from cylinder block, Pb may derive from heater core [20]). Because the present test was a stand test of radiators durability with simulation of high temperature from engine work, and not with a real engine, above mentioned elements were not detected in collected cooling fluid samples.

Table 3. Physical properties changes

Coolant sample	R.A. [mL]	pH value	Density at 20°C $[\text{g cm}^{-3}]$
‘zero sample’	13.4	7.5	1.083
after 500 h	13.1	7.4	1.082
after 1000 h	12.9	7.1	1.092
after 1500 h	12.6	6.5	1.095
after 2000 h	11.8	6.4	1.087
after 2500 h	11.4	6.2	1.092
after 3000 h	10.4	6.0	1.089

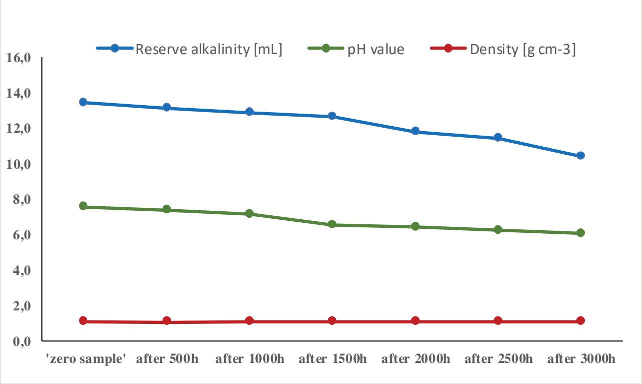

Fig. 2. Physical properties changes

Table 4. Elements not detected in coolant samples [mg/L]

Coolant sample	Ba	Cr	Fe	Pb	Sn	Ti
‘zero sample’	< 0.1	< 0.3	< 0.1	< 0.1	< 0.5	< 0.1
after 500 h	< 0.1	< 0.3	< 0.1	< 0.1	< 0.5	< 0.1
after 1000 h	< 0.1	< 0.3	< 0.1	< 0.1	< 0.5	< 0.1
after 1500 h	< 0.1	< 0.3	< 0.1	< 0.1	< 0.5	< 0.1
after 2000 h	< 0.1	< 0.3	< 0.1	< 0.1	< 0.5	< 0.1
after 2500 h	< 0.1	< 0.3	< 0.1	< 0.1	< 0.5	< 0.1
after 3000 h	< 0.1	< 0.3	< 0.1	< 0.1	< 0.5	< 0.1

The second group of elements includes elements coming from additives package. Among this elements sodium (Na), boron (B), potassium (K), phosphorus (P), molybdenum (Mo), and silicon (Si) have to be mentioned. Boron is usually added to cooling fluid in form of borates, especially sodium borate, and silicon in form of silicates. Potassium may be in form of salt, but the addition of K in tested coolant is not very high. Similarly, addition of Mo and P is not very high in cooling fluid under study. The role of all these additives is to inhibit material corrosion by buffering properties and to act as anti-foam agents [19, 20].

The concentrations levels of elements from additive package during the durability test are presented in Table 5. The changes in concentrations levels of Na and B during the test are graphically presented in Fig. 3, of Si and P in Fig. 4, while concentration changes of Mo and K are presented in Fig. 5. The elements were grouped on the basis of the trends in concentration changes.

Table 5. Changes in additive elements concentrations [mg/L]

Coolant sample	B	Na	K	Si	P	Mo
'zero sample'	988	4407	19.4	116	9.4	1.4
after 500 h	950	4267	27.2	89.4	21.0	1.3
after 1000 h	1078	4692	61.5	86.1	28.1	2.5
after 1500 h	1200	5638	78.0	92.4	22.5	2.8
after 2000 h	1218	5596	79.0	86.5	16.5	2.8
after 2500 h	1236	5560	95.7	87.3	18.0	5.0
after 3000 h	1190	5066	123	76.4	14.5	5.4

It can be seen in Fig. 3 that changes in concentration values are very similar for boron and sodium. After initial slightly decrease in B and Na concentration, increase and then again decrease was observed. Although observed concentration changes of these elements occurred it cannot be stated that they are significant.

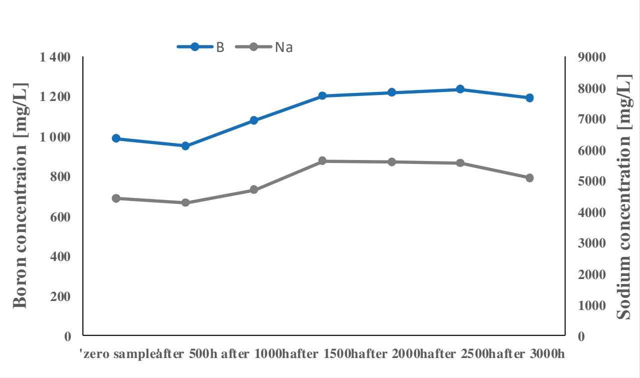

Fig. 3. Changes in B and Na concentration

No significant changes in concentration were observed for phosphorus and silicon, and the changes were very similar (Fig. 4). However, concentration of P and Si slightly decreased during the test, this decrease may testify Si or P additive wear and worsening of cooling fluid properties.

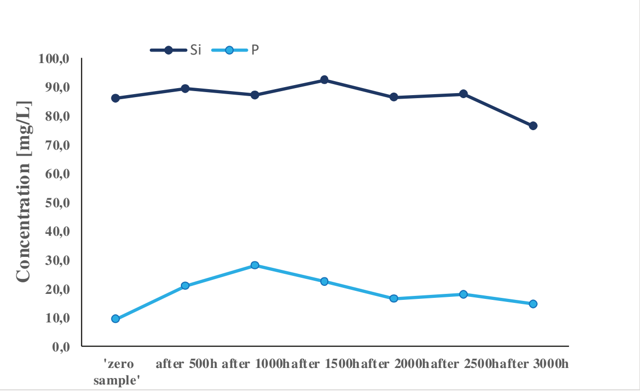

Fig. 4. Changes in P and Si concentration

Significant increase of concentration was observed for potassium and molybdenum (Fig. 5). It is difficult to conclude why concentration of this elements increased. One of the possible reasons is that compounds containing Mo and K have a tendency to precipitate from the solution. Another reason may be slightly decrease of water content in cooling fluid (slightly density increase – Table 3). For that reason concentration level of K and Mo increased from sample to sample.

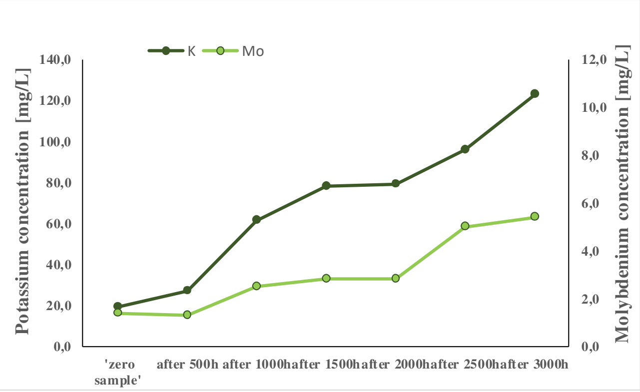

Fig. 5. Changes in K and Mo concentration

Wear metals present in collected fluid samples constitute third group of elements which should be discussed. Concentration changes of following elements were monitored: aluminum (Al), iron (Fe), copper (Cu), zinc (Zn), magnesium (Mg), manganese (Mn), and nickel (Ni). The concentration levels of these elements in collected coolant sample are presented in Tables 6 and 7 and in Fig. 6 and 7.

Table 6. Changes in wear elements concentrations [mg/L]

Coolant sample	Mg	Mn	Ni
'zero sample'	0.47	0.22	0.77
after 500 h	0.18	0.13	0.82
after 1000 h	0.30	0.57	0.66
after 1500 h	0.56	0.49	0.54
after 2000 h	0.22	0.15	0.13
after 2500 h	0.41	0.20	0.32
after 3000 h	0.51	0.19	0.10

As presented in fig. 6 quite big dispersion of results can be observed, but is should be mentioned that observed concentrations levels are below 1 mg/L, which is a very low value. Some concentration changes can take place due to sample collection repeatability, and some other due to measurement reproducibility, and for that reason no significant conclusions can be drawn for these elements.

Another group of wear element is group including Cu, Al, Ca and Zn. Concentrations of these elements were significantly higher than 1 mg/L and some trends in concentration levels changes can be observed (Fig. 7, Table 7). The highest concentration level during the whole test was observed for zinc (Zn), and after initial increase in concentration of Zn, some decrease was observed. Similar situation was observed for calcium (Ca), which is an external contamination, but probably from connections in test stand. The concentration of copper (Cu) was on similar level during the test, so it can be stated that no wear of components including Cu occurred.

The most important observation is that no significant increase of aluminum concentration was observed that clearly prove that no radiator wear took place.

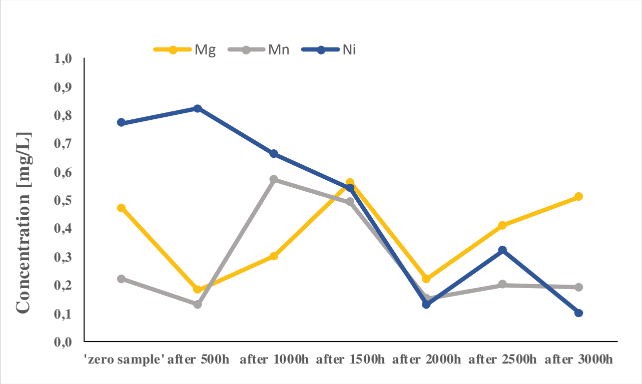

Fig. 6. Changes in Mg, Mn and Ni concentration

Table 7. Changes in wear elements concentrations [mg/L]

Coolant sample	Al	Ca	Cu	Zn
‘zero sample’	7.4	2.1	4.7	12.7
after 500 h	5.8	2.1	2.6	16.2
after 1000 h	4.4	3.6	5.1	19.5
after 1500 h	12.5	6.1	3.8	19.5
after 2000 h	6.8	2.2	3.5	22.0
after 2500 h	12.1	7.3	1.1	19.1
after 3000 h	9.0	5.2	1.6	16.6

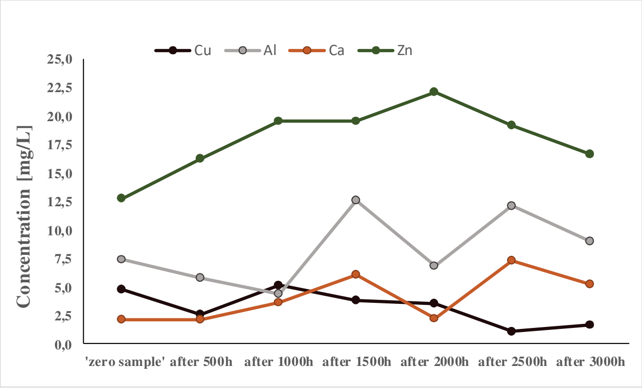

Fig. 7. Changes in Cu, Al, Ca and Zn concentration

4. Conclusions

During the 3003 h durability test of three radiators physical properties changes of cooling fluid were monitored: reserve alkalinity and pH value. It can be stated that coolant wear took place. Further performance of cooling fluid under study in prolonged durability test could be worsen due to further R.A. and pH value decrease. On the other hand no significant increase of wear elements concentrations were noticed, that can prove that no radiator wear occurred.

Periodical chemical analysis along with physical properties changes observations is a simple, but very helpful tool for radiator’s material and cooling fluid wear monitoring.

Acknowledgements

The authors would like to acknowledge Maciej Szczugieł for the help in stand test performance.

Nomenclature

MSDS	Material Safety Data Sheet
ICP-OES	inductively coupled plasma optical emission spectrommetry
R.A.	Reserve Alkalinity
MDL	Method Detection Limit

Bibliography

[1] ZOHURI, B. Heat exchanger types and classifications. *Compact Heat Exchangers: Selection, Application, Design and Evaluation.* Springer 2017. DOI: 10.1007/978-3-319-29835-1.

[2] LALPURWALA, G.J., JANI, D.B. A critical review on heat transfer enhancement in a car radiator by use of nano fluid. *IJRME – International Journal of Research in Mechanical Engineering*. 2017, **04**(04), 25-27. http://researchscript.com/ijrme/ijrmevol4issue4/ijrme040406

[3] ADDEPALLI, S., EIROSA, D., LIEOTRAKOOL, S. et al. Degradation study of heat exchangers. *Procedia. CIRP* 2015, **38**, 137-142. DOI:10.1016/j.procir.2015.07.057.

[4] LIN, CH., SAUNDERS, J., WATKINS, S. The effect of changes in ambient and coolant radiator inlet temperatures and coolant flowrate on specific dissipation. *SAE Technical Paper*. 2000-01-0579. DOI:10.4271/2000-01-0579.

[5] PETA, K., GROCHALSKI, K. The measurements of temperature and deformations of car radiators. *E3S Web of Conferences*. 2017, **19**, 1-4. DOI:10.1051/e3sconf/20171903033

[6] PETA, K., GROCHALSKI, K., PIASECKI, A., ŻUREK, J. The influence of sodium chlorides fog on corrosion resistance of heat exchangers used in automotive. *Archives of Mechanical Technology and Materials*. 2017, **37**, 45-49. DOI:10.1515/amtm-2017-0007.

[7] OYA, Y., KOJIMA, Y., HARA, N. Influence of silicon on intergranular corrosion for aluminium alloys. *Materials Transactions*. 2013, **54**(7), 1200-1208. DOI: 10.2320/matertrans.M2013048

[8] AHMED, A.S., OZKAYMAK, M., SÖZEN, A. et al. Improving car radiator performance by using TiO_2-water nanofluid. *Engineering Science and Technology, an International Journal* 2018, **21**, 996-1005. DOI: 10.1016/j.jestch.2018.07.008.

[9] HARSH, R., SRIVASTAV, H., BALAKRISHMAN, P. et al. Study of heat transfer characteristics of nanofluids in an automotive radiator. *IOPConference Series: Materials Science and Engineering*. 2018, **310**, 1-7. DOI; 10.1088/1757-899X/310/1/012117.

[10] VOON, F.C. Design and development of nanofluid car radiator test rig. *Technical Report.* 2015.

[11] SHEIKHZADEH, G., HAJILOU, M., JAFARIAN, H. Analysis of thermal performance of a car radiator employing

nanofluid. *International Journal of Mechanical Engineering and Applications*. 2014, **2**(4), 47-51. DOI: 10.11648/j.ijmea.20140204.11.

[12] MUTUKU, W.N. Ethylene glycol (EG)-based nanofluids as a coolant for automotive radiator. *Asia Pacific Journal on Computational Engineering*. 2016, **3**(1), 1-15. DOI: 10.1186/s40540-016-0017-3

[13] SAXENA, G., SONI, P. Nano coolants for automotive applications: a review. *Nano Trends: A Journal od Nanotechnology and Its Applications*. 2018, **20**(1), 9-22. techjournals.stmjournals.in/index.php/NTs/article/view/78.

[14] TL 774:2010, Ethylene Glycol-Based Coolant Additive, VW Standard 2010.

[15] BASF: G48® Data Sheet 2013.

[16] PN-C-40008-05:1993, Antifreeze fluids for heat exchangers for combustion engines. Determination of alkalinity reserve.

[17] PN-C-40008-04:1992, Antifreeze fluids for heat exchangers for combustion engines. Determination of pH value.

[18] PN-EN ISO 12185:2002, Crude petroleum and petroleum products. Determination of density. Oscillating U-tube method.

[19] www.borax.com/applications/industrial-fluids-lubricants.

[20] ANDERSON, D.P., MALTE, L., LYNCH, B.K. Diesel engine coolant analysis, new application for established instrumentation. *Spectro Incorporated.* 1998. https://archive.org/details/DTIC_ADA347981.

Joanna Faber, DEng. – Chemical Laboratory Manager, BOSMAL Automotive Research and Development Institute Ltd.

e-mail: *joanna.faber@bosmal.com.pl*

Krzysztof Brodzik, DEng. – Head of Materials Testing Department, BOSMAL Automotive Research and Development Institute Ltd.

e-mail: *krzysztof.brodzik@bosmal.com.pl*

Zbigniew Jurasz, DEng. – Research and Technical Specialist in BOSMAL Automotive Research and Development Institute Ltd.

e-mail: *zbigniew.jurasz@bosmal.com.pl*

INSTYTUT TECHNICZNY WOJSK LOTNICZYCH
ul. Księcia Bolesława 6, 01-494 Warszawa, skr. poczt. 96
tel.: 261 851 300; tel./faks: 261 851 313
www.itwl.pl e-mail: poczta@itwl.pl

Tomograf komputerowy (CT) – badanie nieniszczące NDT

Instytut Techniczny Wojsk Lotniczych oferuje usługi z zakresu badań tomografem komputerowym. Badania prowadzone są na tomografie typu v/tome/x m 300 firmy GE o max. mocy lampy 300kV/500W. Urządzenie posiada również lampę do nanotomografii o mocy 80kV/15W.

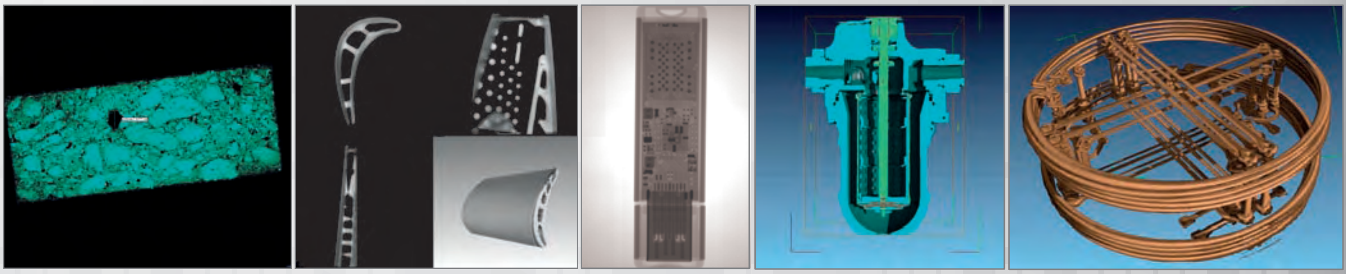

Prowadzimy prace badawcze obejmujące swym zakresem materiały takie jak:

- stopy tytanu
- stale
- materiały kompozytowe
- beton
- guma

Urządzenie umożliwia prowadzenie badań z zakresu:

- wykrywania defektów o rozmiarach powyżej 0,5 μm z wykorzystaniem lampy 180 kV
- materiałów o bardzo dużej gęstości (np. łopatki turbin silników lotniczych) z wykorzystaniem lampy o mocy 300 kV
- układy elektroniczne (scalone)
- materiały pirotechniczne
- złożone agregaty lotnicze

Masa badanych elementów do 50 kg.
Wymiary orientacyjne 50×50×60 cm.

Posiadamy wysoko wykwalifikowany, certyfikowany personel.

Kontakt bezpośredni:
Zakład Silników Lotniczych
tel.: +48 261 851 334; fax: +48 261 851 338
e-mail: jaroslaw.spychala@itwl.pl

Zapraszamy do współpracy!

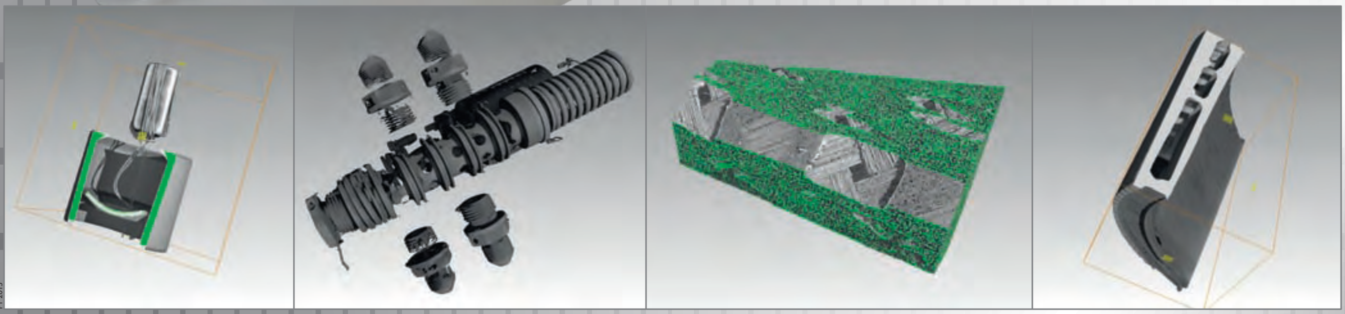

PT 2013

Publisher:

Polish Scientific Society of Combustion Engines

9 772300 989002

ISSN: 2300-9896

Combustion Engines
Polskie Towarzystwo Naukowe Silników Spalinowych

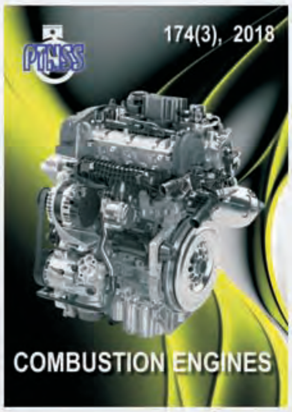

www.combustion-engines.eu

INSTYTUT TECHNICZNY WOJSK LOTNICZYCH

ul. Księcia Bolesława 6, 01-494 Warszawa, skr. poczt. 96
tel.: 261 851 300; tel./faks: 261 851 313
www.itwl.pl e-mail: poczta@itwl.pl

Tomograf komputerowy (CT) – badanie nieniszczące NDT

Instytut Techniczny Wojsk Lotniczych oferuje usługi z zakresu badań tomografem komputerowym. Badania prowadzone są na tomografie typu v/tome/x m 300 firmy GE o max. mocy lampy 300kV/500W. Urządzenie posiada również lampę do nanotomografii o mocy 80kV/15W.

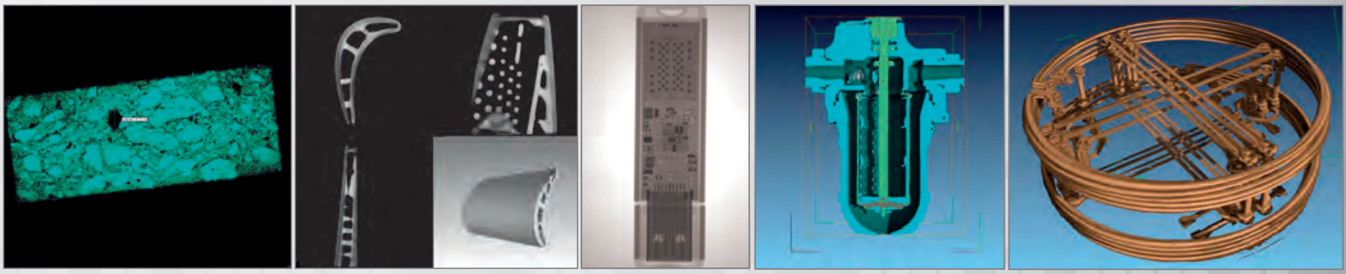

Prowadzimy prace badawcze obejmujące swym zakresem materiały takie jak:

- stopy tytanu
- stale
- materiały kompozytowe
- beton
- guma

Urządzenie umożliwia prowadzenie badań z zakresu:

- wykrywania defektów o rozmiarach powyżej 0,5 μm z wykorzystaniem lampy 180 kV
- materiałów o bardzo dużej gęstości (np. łopatki turbin silników lotniczych) z wykorzystaniem lampy o mocy 300 kV
- układy elektroniczne (scalone)
- materiały pirotechniczne
- złożone agregaty lotnicze

Masa badanych elementów do 50 kg.
Wymiary orientacyjne 50×50×60 cm.

Posiadamy wysoko wykwalifikowany, certyfikowany personel.

Kontakt bezpośredni:
Zakład Silników Lotniczych
tel.: +48 261 851 334; fax: +48 261 851 338
e-mail: jaroslaw.spychala@itwl.pl

Zapraszamy do współpracy!

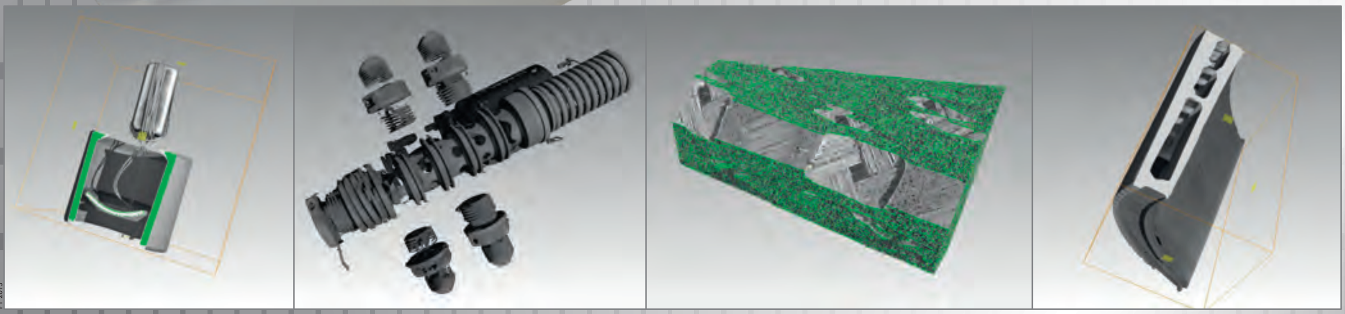

PT 2013

Publisher:

Polish Scientific Society of Combustion Engines

Combustion Engines

Polskie Towarzystwo Naukowe Silników Spalinowych

ISSN: 2300-9896

www.combustion-engines.eu